Synthesis of Terminal Transition Metal Pnictide Complexes by Activation of Small Molecules

Dissertation

Zur Erlangung des mathematisch-naturwissenschaftlichen Doktorgrades

Doctor Rerum Naturalium

Im Promotionsprogramm der Georg-August-University School of Science (GAUSS)

vorgelegt von

M. Sc. Josh Abbenseth

aus Bremervörde

Betreuungsausschuss

Prof. Dr. Sven Schneider

Institut für Anorganische Chemie, Georg-August-Universität Göttingen

Prof. Dr. Franc Meyer

Institut für Anorganische Chemie, Georg-August-Universität Göttingen

Mitglieder der Prüfungskommission

Referent: Prof. Dr. Sven Schneider

Institut für Anorganische Chemie, Georg-August-Universität Göttingen

Co-Referent: Prof. Dr. Franc Meyer

Institut für Anorganische Chemie, Georg-August-Universität Göttingen

Weitere Mitglieder der Prüfungskommision

Prof. Dr. Manuel Alcarazo

Institut für Organische und Biomolekulare Chemie, Georg-August-Universität Göttingen

Prof. Dr. Jörg Behler

Institut für Physikalische Chemie, Georg-August-Universität Göttingen

Jun.-Prof. Dr. Nathalie Kunkel

Institut für Anorganische Chemie, Georg-August-Universität Göttingen

Dr. Christian Sindlinger

Institut für Anorganische Chemie, Georg-August-Universität Göttingen

Tag der mündlichen Prüfung: 08.07.19

This thesis originated in the time between January 2016 and June 2019 at the Institute for Inorganic Chemistry of the Georg-August-University Göttingen.

I am deeply grateful to my supervisor
Prof. Dr. Sven Schneider

Thank you Sven for the trust you put in me and my skills, the constant support, the opportunity to present my work on several conferences and the freedom to pursue my own scientific ideas.
Our inspiring and sometimes heated discussions taught me how to properly address scientific problems.

I also want to express my gratitude to
Prof. Dr. Franc Meyer
for being my second supervisor and the fruitful discussions.

Contents

Introduction

1 Introduction

1.1 Physical and Chemical Characteristics of Pnictogens

The elements belonging to group 15 of the periodic table (nitrogen, phosphorus, arsenic, antimony, bismuth and moscovium) are knows as the pnictogens. The name is derived from the Greek word πνιγ- (to strangle, to choke) and was first proposed by the Dutch chemist Anton Eduard van Arkel.[1]

Nitrogen is an essential element to all biological life.[2] Biological and industrial utilization of nitrogen is achieved upon nitrogen fixation towards ammonia. The Haber-Bosch process facilitates the conversion of N_2 and H_2 towards NH_3 at elevated temperatures using metal catalysts. Due to the high demand of ammonia in the fertilizer and chemical industry this highly optimized industrial process operates on a scale of hundreds of megatons per year.[3],[4] The generally accepted mechanism consists of initial splitting of the dinitrogen molecule on the catalyst surface to form metal nitrides which are further converted by chemisorbed dihydrogen to afford ammonia (Scheme 1.1, left). The harsh reaction conditions (400 bar, 480°C) and the required production of highly pure dihydrogen leads to an overall energy demand of over 1% of the global energy production.[5],[6]

In nature, nitrogen fixation is mediated at ambient conditions by enzymes called nitrogenases.[7] The most active representative of this class is the Fe-Mo nitrogenase which was structurally characterized (Scheme 1.1, right).[8]–[10]
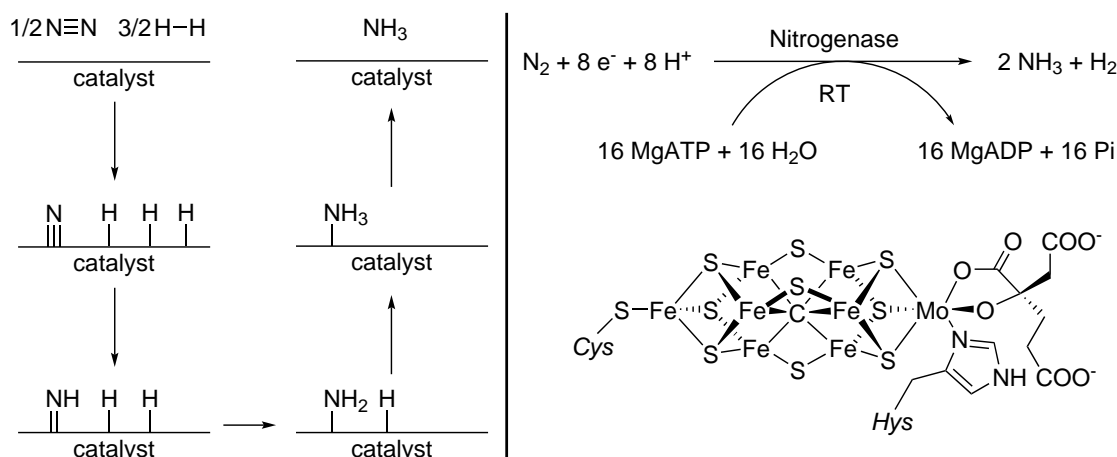
Scheme 1.1: Left: Mechanism of ammonia production by the Haber-Bosch process; Right: Nitrogen fixation by the Fe-Mo nitrogenase.[5]–[7]

While the exact mechanism of nitrogen fixation by Fe-Mo-Nitrogenase is not fully understood yet, the overall stoichiometry requires 16 equivalents of adenosine triphosphate (ATP), rendering this process highly energy demanding.[2],[11] This phosphorus containing molecule is commonly called the energy currency of biological life.[12] Besides

this, phosphorus also plays an important role as phosphate in the construction of bones, phospholipids, DNA and RNA.[12] Therefore, phosphates are important components of fertilizers. White phosphorus (P_4), mainly produced by electrothermal conversion of $Ca_3(PO_4)_2 \cdot CaF_2$, is an essential building block for the production of phosphorus containing chemicals.[13] The heavier elements of the pnictogens do not exhibit comparable relevance due to their higher toxicity and/or lower abundancy.[14] Typical uses are fabrication of alloys (As, Sb, Bi), insecticides (As), flame retardants (Sb), pharmaceuticals and cosmetics (Bi).[12]

At ambient conditions nitrogen is encountered as gaseous dinitrogen. In this molecule the nitrogen atoms are bound *via* a short N≡N triple bond (1.0977 Å) consisting of one σ- and two π-bonds (Scheme 1.2). The large HOMO-LUMO gap of 10.82 eV, the missing dipole moment and the resulting large bond dissociation energy of $225.0 \, \text{kcal} \cdot \text{mol}^{-1}$ render N_2 kinetically and thermodynamically highly stable. Thus, the Haber-Bosch process requires the rather drastic conditions described above.[13] The high stability of the triple bond can be attributed to the almost identical radii of the 2s and 2p orbitals allowing for efficient overlap and hybridization (Scheme 1.2, Figure 1.1). This is attributed to the high degree of penetration of the 2p orbitals into the core.
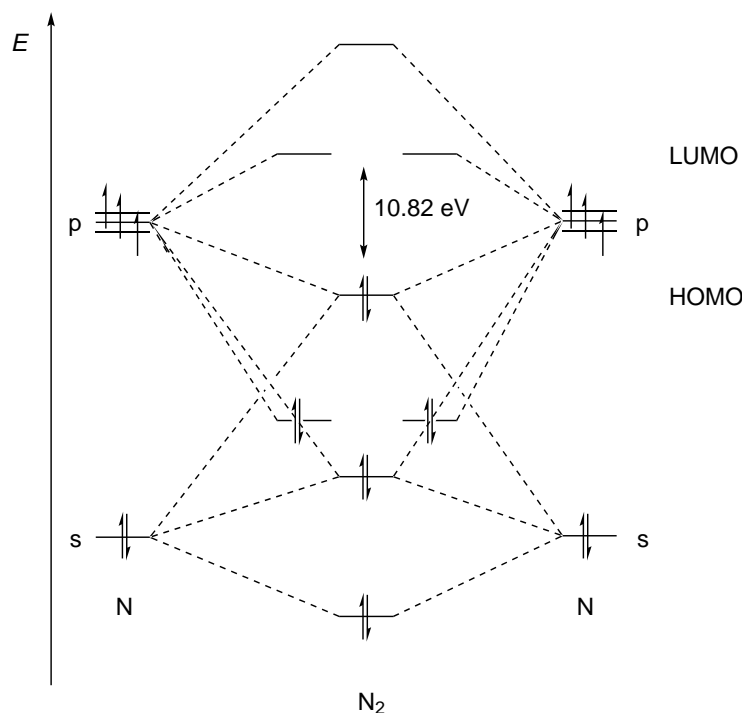
Scheme 1.2: Qualitative MO scheme of the dinitrogen molecule.[13]
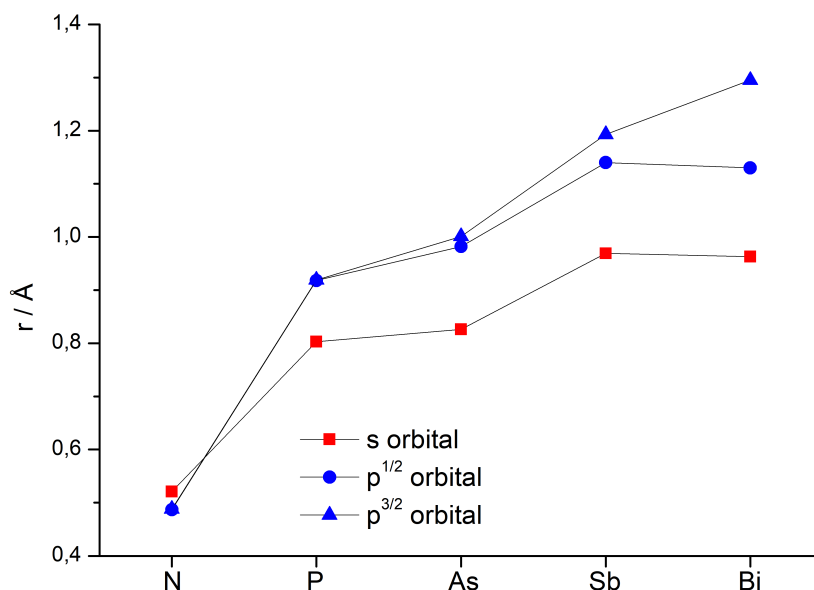
Figure 1.1: Radii of the pnictogens and p orbitals.[15]

This changes drastically when moving to the heavier elements that favor formation of tetrahedral Pn_4. Diphosphorus and its heavier analogues can only be generated at temperatures above $1000\,K$ in the gas phase due to the high reactivity and low bond dissociation energy (Table 1.1).[13],[16] Furthermore, the Pn≡Pn bond distance elongates by ca. $0.8\,Å$ when moving from nitrogen to phosphorus.[16] While for 2nd row elements the s and p orbitals exhibit almost identical radii, the np orbitals with $n \geq 3$ encounter Pauli repulsion with other p core orbitals resulting in a significant increase of the radii compared to the corresponding ns orbitals (Figure 1.1).[15],[17]

Table 1.1: Physical properties of Pn_2, Pn = N, P, As, Sb, Bi.[16]

Compound	Bond distance / $Å$	D_e / $kcal \cdot mol^{-1}$
N_2	1.0977	225.0
P_2	1.8934	116.1
As_2	2.1026	91.3
Sb_2	2.3415	71.3
Bi_2	2.6596	46

Older textbooks rationalize the lower stability of P_2 and its heavier homologues by arguing that π-bonding in heavier elements is considerably weaker due to poorer p(π) orbital overlap when compared to 2nd row elements. However, these statements are not in agreement with quantum chemical calculations that predict the more diffuse p(π) orbitals to allow for similar overlap as the lighter elements.[18] Energy decomposition analysis (EDA)[19] further elucidates this bonding situation. The attractive interaction
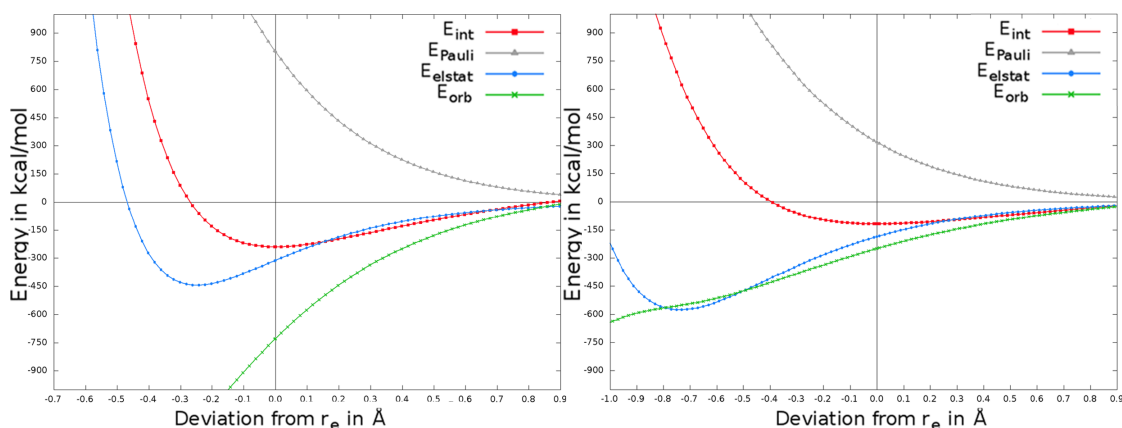
Figure 1.2: Calculated energy terms of the EDA at different bond length of N_2 (left) and P_2 (right), Copyright © 2014, Springer-Verlag Berlin Heidelberg.[18]

between the nitrogen atoms in the dinitrogen molecule mainly arises from covalent orbital interactions ΔE_{orb} (70%) with smaller contribution from the electrostatic coulombic attraction $\Delta E_{\mathrm{elstat}}$ (30%, Figure 1.2).

These contributions are more alike in P_2 ($\Delta E_{\mathrm{orb}}/\Delta E_{\mathrm{elstat}}$: 57%/43%). If the orbital interactions are further separated into σ- and π-bonding contributions it becomes evident that the stabilization by π-bonding in diphosphorus is even greater than in N_2, disproving the general assumption that weak π-interactions are the reason for the tendency of heavier elements to form single bonds with other elements. Further quantum chemical investigation shows that the equilibrium bond distance of the diatomic pnictogens is rather dictated by the Pauli repulsion $\Delta E_{\mathrm{Pauli}}$ since the attractive terms ΔE_{orb} and $\Delta E_{\mathrm{elstat}}$ become larger when the Pn≡Pn bond gets shortened with respect to the equilibrium distance r_e (Figure 1.2). The higher stability of P_4 over P_2 can therefore be linked to the different radii ratios of the s and p orbitals for second row elements and their heavier analogues. Due to Pauli repulsion, N_2 is favored over N_4 whereas P_4 is more stable than P_2. This statement also holds true for heavier elements of group 15 of the periodic table.
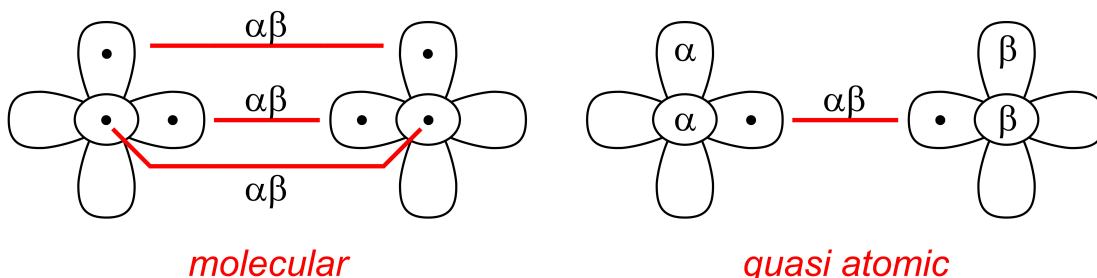
Figure 1.3: Schematic representation of important spin couplings in Pn_2.[20]

Dinitrogen is commonly described as the prototype of an unpolar, covalent triple bond as a product of three singlet spin functions that show almost perfect paring (molecular coupling). Generalized valence bond (GVB)[21] theory suggests that the heavier analogues differ from this description and that the formulation of quasi-atomic coupling become increasingly important in describing the bond.[20] In this formulation two electrons are coupled to a singlet in a σ-bond. The remaining electrons resulting in the two π-bonds adopt triplet states which are antiferromagnetically coupled (Figure 1.3). In As_2, both couplings exhibit the same weight in describing the bonding. The latter one is therefore expected to become dominant in heavier analogues.

1.2 Terminal Transition Metal Pnictide Complexes

Parts of this chapter were adapted from: **J. Abbenseth**, S. C. Bete, M. Finger, C. Volkmann, C. Würtele, S. Schneider, *Organometallics* **2018**, *37*, 802-811. Copyright 2018 American Chemical Society.

1.2.1 Heavy Analogues of Nitride Complexes - First Indications

While terminal transition metal nitride complexes are a well-studied class of compounds, isolation of the heavier analogues was only achieved in 1995.[22],[23] Prior to this finding the possible formation of triply bonded heavy transition metal pnictide species was a subject of much speculation.[24] Becker and co-workers first suggested the formation of a terminal tungsten phosphide species in 1985 upon studying the reaction of $[W_2(O^tBu)_6]$ (**I**, Scheme 1.3) and $^tBuC{\equiv}P$.[25],[26] A four-membered WC_2P heterocycle was identified as one of the reaction product as well as an unstable WCP_2 ring compound which was characterized by ^{31}P NMR spectroscopy. The proposed mechanism involves a breaking of the $W{\equiv}W$ triple bond to form transient alkylidyne and phosphide species (**II**, Scheme 1.3) which form four-membered rings upon addition of another equivalent of $^tBuC{\equiv}P$. A 1,3-O^tBu migration step yields the final products **III** and **IV**.

This mechanistic proposal is supported by the formation of alkylidynes and nitrides when alkynes or nitriles are used instead of the phosphaalkyne $^tBuC{\equiv}P$. Scheer and co-workers further confirmed this mechanistic proposal upon performing the reaction in the presence of Lewis-acidic transition metal carbonyl compounds which allowed for the isolation of $[(^tBuO)_3W{\equiv}P-[M]]$.[27] Later, several additional reports also proposed the possible formation of terminal transition metal phosphides.[24] The first terminal
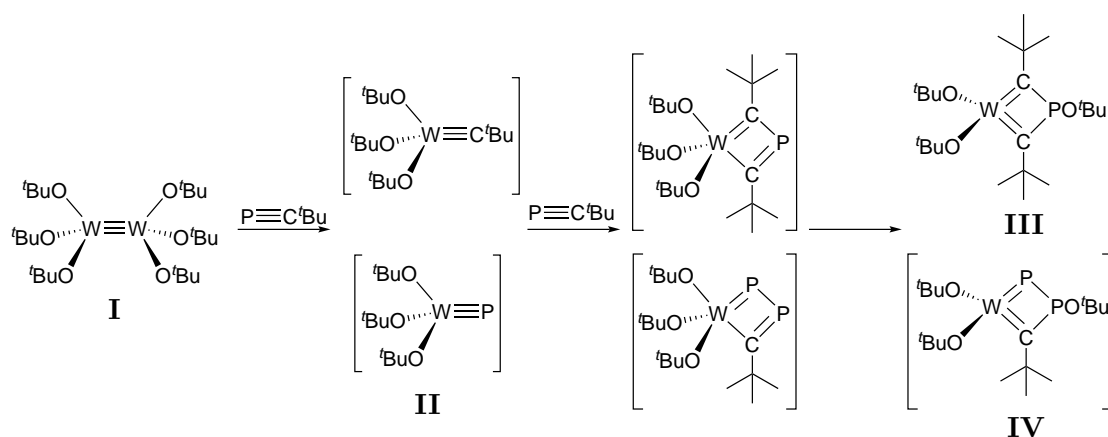
Scheme 1.3: Proposed reactivity of **I** to give the transient terminal tungsten phosphide **II**.[25],[26]

arsenide complex was postulated by Ziegler and co-workers in 1989 based on the results obtained for the thermolysis and co-photolysis of arsenide capped tris-Mo complex $[\{MoCp(CO)_2\}_3(\mu^3\text{-}As)]$. The reaction yields a triply bonded Mo≡Mo complex which suggests formation of the arsenide **V**. This was further substantiated by the addition of $[CoCp(CO)_2]$ which yielded complexes containing a single arsenic atom (Scheme 1.4).[28],[29]
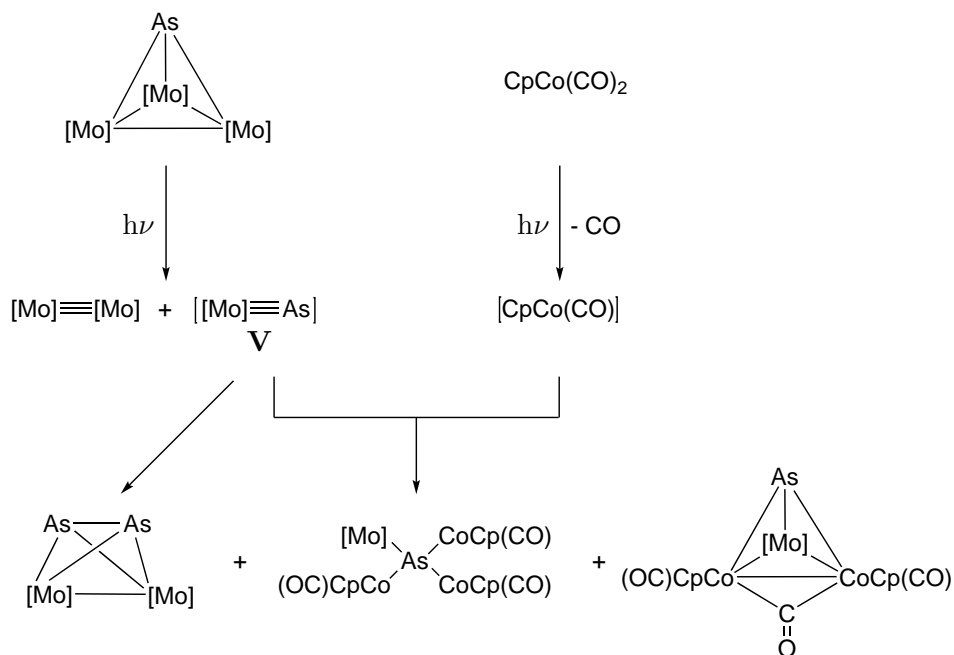
Scheme 1.4: Proposed mechanism of the photolysis of $[\{MoCp(CO)_2\}_3(\mu^3\text{-}As)]$ and $[CoCp(CO)_2]$ to form the postulated arsenide complex **V** and subsequent reactivity with $[CoCp(CO)]$, $[Mo] = [MoCp(CO)_2]$.[28]

Spectroscopic evidence for the formation of terminal stibide complexes was provided by Rheingold and co-workers. The gas-phase reaction of transition metal carbonyl complexes with Sb_2^- allowed for the observation of $[MSb(CO)_n]^-$ (M = Fe, n = 3; M = Cr, Mo, W; n = 4) by Fourier-transform ion cyclotron resonance mass spectrometry (FT-ICR).[30]

1.2.2 Synthesis of Terminal Pnictide Complexes from the Elements

The functionalization of dinitrogen still represents a major challenge in synthetic chemistry. As described in the previous chapter, dinitrogen is a kinetically and thermodynamically highly stabilized molecules which necessitates rather forcing conditions to facilitate full bond cleavage. Today, several systems are available that facilitate the splitting of N_2 into terminal nitrides (dominated by Mo complexes) and even the catalytic conversion of dinitrogen to ammonia and trimethylsilyl amine has been accomplished, while more functionalized nitrogen containing molecules can be generated stoichiometrically.[31]–[39] In this context, photochemical and electrocatalytic approaches have also been investigated, however a complete survey of this field is beyond the scope of this thesis.[31],[35],[40]–[45] Understanding the molecular interactions of transition metal complexes and the dinitrogen molecule in dimeric complexes is crucial for further developments towards more efficient platforms capable of splitting and functionalization of dinitrogen and will be the focus of this chapter.

Complete N≡N bond scission was first reported for the molybdenum trisanilide complex [Mo(NRAr)$_3$] (**VI**, R = C(CD$_3$)$_2$Me, Ar = 3,5-Me$_2$C$_6$H$_3$, Scheme 1.5) in 1995. Storing a solution of **VI** at $-35°$C under a dinitrogen atmosphere yields the N_2-bridged complex [{Mo(NRAr)$_3$}$_2$($\mu-N_2$)] (**VII**) which splits the dinitrogen bond homolytically upon warming to room temperature. The resulting nitrido complex [MoN(NRAr)$_3$] (**VIII**) is formed *via* a zig-zag transition state.[46]–[48] Consideration of the MO scheme of the {MoNNMo} core, constructed by the Mo d and nitrogen p orbitals, gives valuable insights into the required electronic structure to facilitate splitting of dinitrogen (Scheme 1.5). The S_6-symmetric dimer **VII** features 10 π-electrons (formally: $2 \cdot$ Mo(III) = 6; $N_2 = 4$) giving rise to an overall triplet configuration. The zig-zag transition state lifts the degeneracy of the 2e$_u$ π-MOs and allows for mixing with the antibonding σ^*-orbital which is forbidden in the case of **VII**. This interaction, besides the overall π-electron count, seems to be crucial for scission of the N_2 bond since it allows for the population of the σ-bonding orbital set 1b$_u$ in the reaction products.[31] This is showcased by the triamidoamine complex [Mo(R'NCH$_2$CH$_2$)$_3$($\mu-N_2$)] (**IX**, R' = ^{t}BuMe$_2$Si) which would feature an identical π-electron count within the {MoNNMo} core and high similarities in bond distances and angles. However, the ligand in *trans*-position to the dinitrogen bridge destabilizes the σ^*-MO leading to unfavorable kinetic and thermodynamic parameters for splitting into terminal nitrides.[49] Furthermore, the rigidity of the chelate ligand prevents rotation of the amide donors which is proposed to lead to increased charge transfer in the transition state favoring the splitting of N_2.[50],[51]
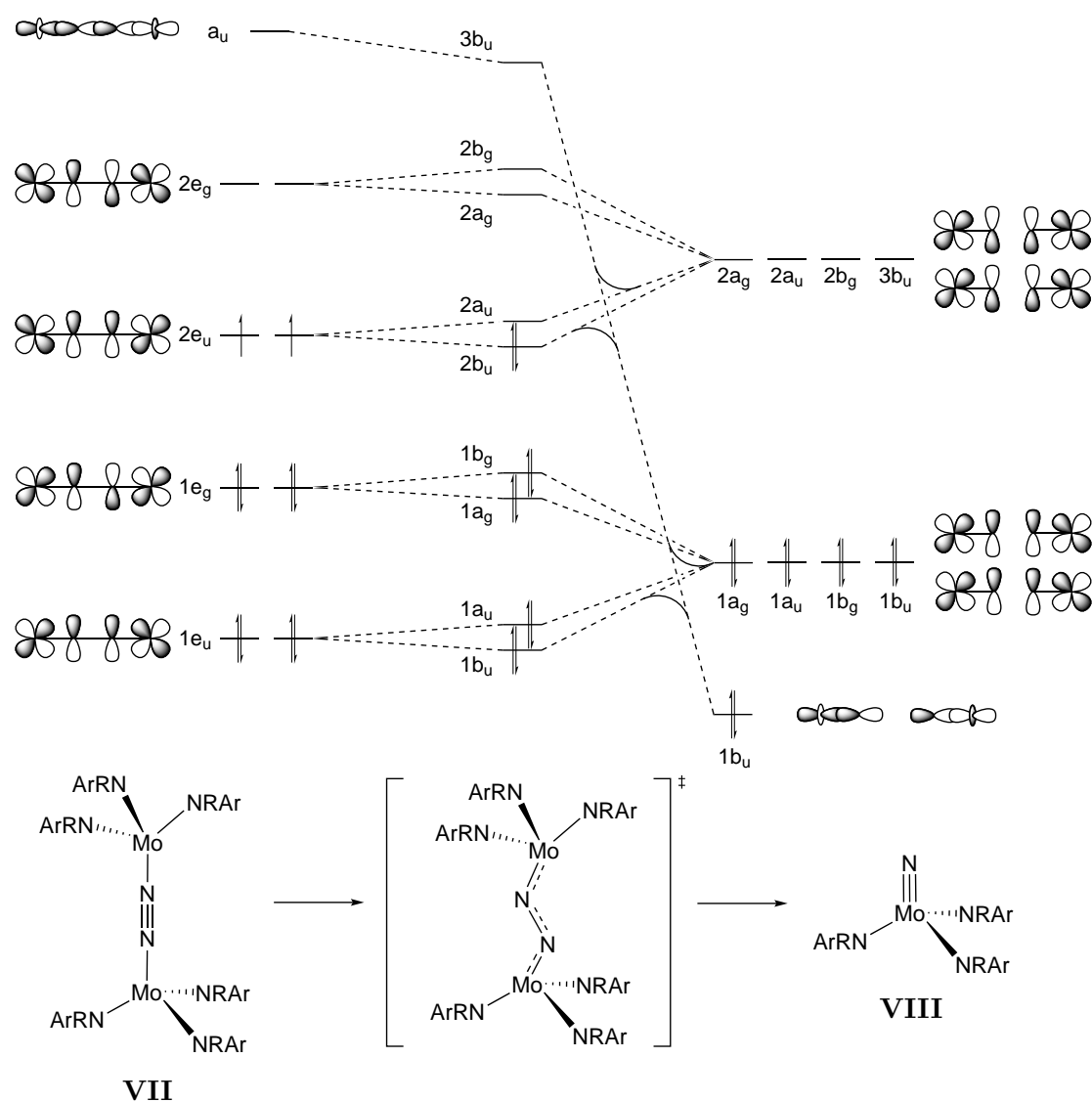
Scheme 1.5: MO scheme for N_2-cleavage by **VII** towards **VIII**.[31]

This MO consideration also explains why strong N_2 activation does not necessarily lead to bond scission. **VII** can be oxidized to cationic **X** and dicationic **XI** which feature a doublet and a singlet state, respectively. Increased N_2 bond activation is observed by Raman spectroscopy ($\tilde{\nu}_{NN}$: $1630\,\mathrm{cm}^{-1}$ (**VII**), $1503\,\mathrm{cm}^{-1}$ (**X**), $1349\,\mathrm{cm}^{-1}$ (**XI**)) due to depopulation of the N-N bonding orbitals sets $2e_u$ upon oxidation. Consequently, no dinitrogen splitting is observed since the decreased amount of π-electrons prevents the formation of stable nitride complexes.[47]
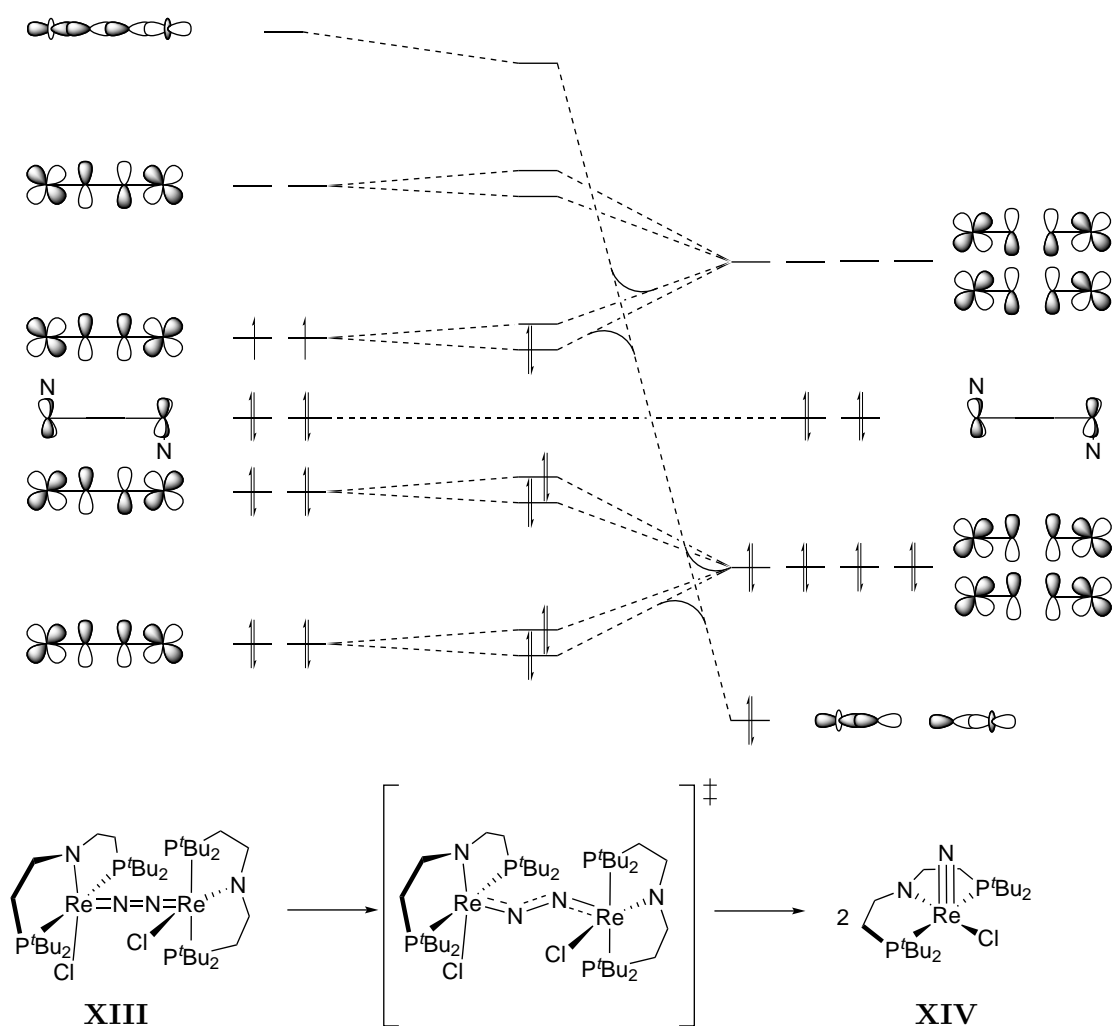
Scheme 1.6: MO scheme for N$_2$-cleavage by **XIII** towards **XIV**.[52]

Schneider and co-workers reported the first example of dinitrogen splitting to a terminal nitride by a well-defined transition metal complex containing a central atom beyond group 6. Upon one-electron reduction of the Re^{III} dichloride complex [ReCl$_2$(L^1)] (**XII**, Scheme 1.6, L^1 = N(CH$_2$CH$_2$P^{t}Bu$_2$)$_2$), dinitrogen is bound within the dimer [{ReCl(L^1)}$_2$(μ−N$_2$)] (**XIII**) which could be characterized crystallographically.[40] Splitting towards the Re^V nitride [ReNCl(L^1)] (**XIV**) is observed in high yield upon warming to room temperature.[53] The obtained nitride could be further functionalized to allow for the synthesis of nitrogen containing organic molecules.[33],[53] Due to the change of the overall geometry of the obtained dinitrogen dimer from S_6 towards C_2, non-bonding, δ-symmetric orbitals have to be considered. The overall increased electron count within the {ReNNRe} core when compared to Cummins' system results in a $\pi^{10}(\delta^4)$-configuration (Scheme 1.6). This result shows that dinitrogen splitting might also be accomplished

n	S	$\tilde{\nu}_{NN}$ / cm^{-1}
0	0	n.a.
1	$\frac{1}{2}$	1530
2	0	1563
3	$\frac{1}{2}$	1482
4	1	1477
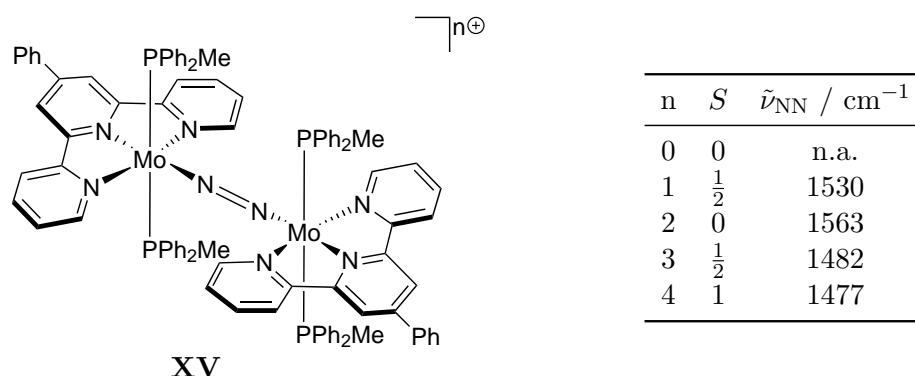
Figure 1.4: Redox series of **XV^{n+}**.[55]

with late transition elements if a suitable coordination geometry and electronic configuration is provided. The formed nitrides should be more reactive due to successive weakening of the M≡N bond along the periodic table.[54]

The participation of ligand centered orbitals can alter the overall picture of bond activation drastically as shown for the redox series $[\{Mo(^{Ph}Tpy)(PPh_2Me)_2\}_2(\mu-N_2)]^{n+}$ (**XV^{n+}**, n = 0 - 4, ^{Ph}Tpy = 4'-phenyl-2,2':6',2"-terpyridine).[55] For **XV^{2+}**, an overall $\pi^{10}(\delta^4)$-configuration arises, however degeneracy of the N_2-bonding orbital is lifted due to coupling with the redox active ligand (Figure 1.4). As expected, oxidation leads to stronger dinitrogen activation, however this effect is also observed upon reduction due to population of ligand-based orbitals.[55]

Up to this date, isolable terminal heavy transition metal pnictide complexes are still scarce and only known up to group 6.[60]–[65] This can partly be attributed to the synthetic problems associated with transferring single P or As atoms from P_4 and
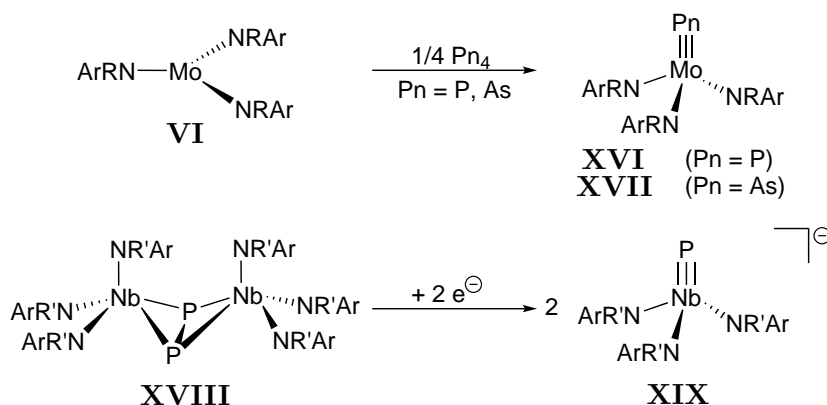
Scheme 1.7: Synthesis of phosphides and arsenides from the elements, Ar = 3,5-Me$_2$C$_6$H$_3$, R = C(CD$_3$)$_2$Me, R' = neopentyl.[23], [56]–[59]

As$_4$, respectively. Besides the terminal coordination of group 15 elements, various reports feature stabilization of the reactive triple bonds by metal coordination or metal-heterocumulene formation. However, a full coverage of this field is beyond the scope of this thesis.[63]

Cummins and co-workers showed that white phosphorus can be reacted with the Mo trisanilide complex **VI** to give [MoP(NRAr)$_3$] (**XVI**) representing the first isolable, terminal transition metal phosphide complex (Scheme 1.7).[23] Later, it was shown that yellow arsenic can be utilized in the same manner yielding [MoAs(NRAr)$_3$] (**XVII**).[56] The splitting of a P$_2^{4-}$ moiety towards a terminal phosphide complex was shown to be accessible upon reduction of the P$_4$-derived dimeric Nb^V complex [{Nb(NRAr)$_3$}$_2$($\mu-$P$_2$)] (**XVIII**, Ar = 3,5-Me$_2$C$_6$H$_3$, R = CH$_2^t$Bu) which gave the terminal Nb phosphide complex [NbP(NRAr)$_3$]$^-$ (**XIX**, Scheme 1.8).[58], [59]

1.2.3 Alternative Heavy Pnictide Sources

The first terminal arsenide **XX** and stibide **XXI** complexes were reported by Scheer and co-workers upon reacting trimethylsilyl substituted pnictide transfer reagents with the tungsten trisamido amine complex $[\text{WCl}(\text{N}\{\text{CH}_2\text{CH}_2\text{NSiMe}_3\}_3)]$ (**XXII**, Scheme 1.7).[57],[66] Additional examples have been reported for Ta and Nb.[63] A synthesis of terminal stibide complexes from antimony has not been reported so far.
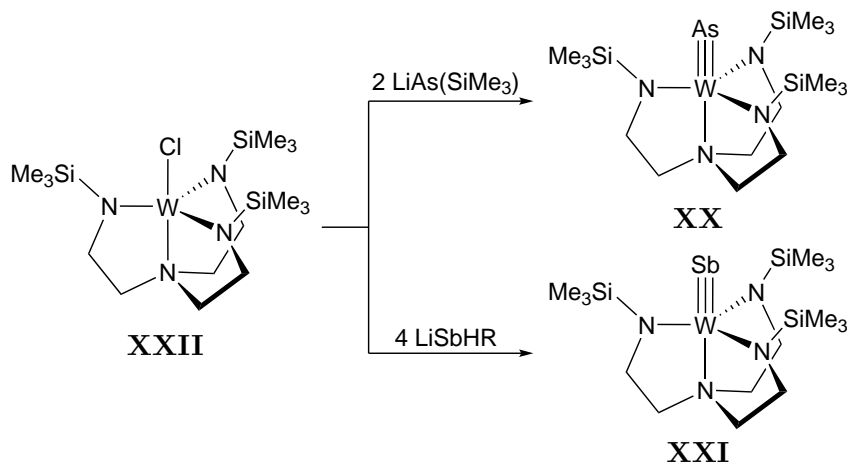
Scheme 1.8: Synthesis of the first arsenide (**XX**) and stibide (**XX**) complexes, R = $\text{CH}(\text{SiMe}_3)_2$.[57],[66]

The recently reported phosphorus transfer reagents ClP**A** (chloro-substituted dibenzo-$7\lambda^3$-phosphanorbornadiene, **A** = anthracene)[67] and $[\text{Na}(\text{diox})_x][\text{PnCO}]$ (diox = dioxane, Pn = P, As)[68],[69] offer the possibility to introduce single phosphorus atoms more conveniently and gave rise to the isolation of the first terminal pnictide complexes featuring d electrons. The PnCO$^-$ anions have extensively been used in organic and inorganic chemistry to synthesize phosphorus and arsenic containing heterocycles, Pn_2^{n-} (n = 2, 4) bridged transition metal complexes and new materials.[68],[70]–[74] Upon substitution of nitrogen for its heavier congeners, the carbon-pnictogen bond dissociation energy drops drastically, resulting in easier cleavage of the Pn-C bond.[75]

	$^{\ominus}$O−C≡Pn	O=C=Pn$^{\ominus}$
Pn = N	61%	30%
Pn = P	51%	38%
Pn = As	46%	36%
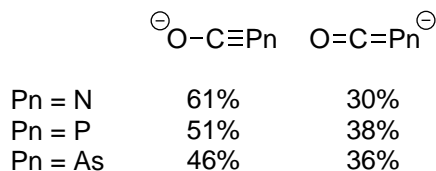
Figure 1.5: Resonance forms and their relative weights for NCO$^-$, PCO$^-$ and AsCO$^-$.[76]

Natural resonance theory of NCO$^-$, PCO$^-$ and AsCO$^-$ reveals two major resonance structure (Figure 1.5). The heavier analogues of isocyanate feature an increased contribution

to the HOMO, as expected for less electronegative molecules.[76] Therefore, orbital controlled reactions favor Pn-coordination to the metal center, whereas charged controlled processes result in O-coordination, e.g. in the case of f-block elements.[71]

Cummins and co-workers reported a series of terminal tungsten pnictide complexes upon decarbonylation of PnCO$^-$ (Pn = N, P, As) by reaction with [W(ODipp)$_4$] (**XXIII**) to give [WPn(ODipp)$_4$]$^-$ (**XXIV** (Pn = N), **XXV** (Pn = P), **XXVI** (Pn = As), Scheme 1.8).[65] Oxidative addition of a PCl moiety, stemming from ClP**A**, by the Mo^0 dinitrogen complex [Mo(N$_2$)(PCP)] (**XXVII**, PCP = 2,2"-bis(diisopropylphos-phaneyl)-1,1':4',1"-terphenyl) gave the Mo^{IV} phosphide [MoPCl(PCP)] (**XXVIII**, Scheme 1.9).
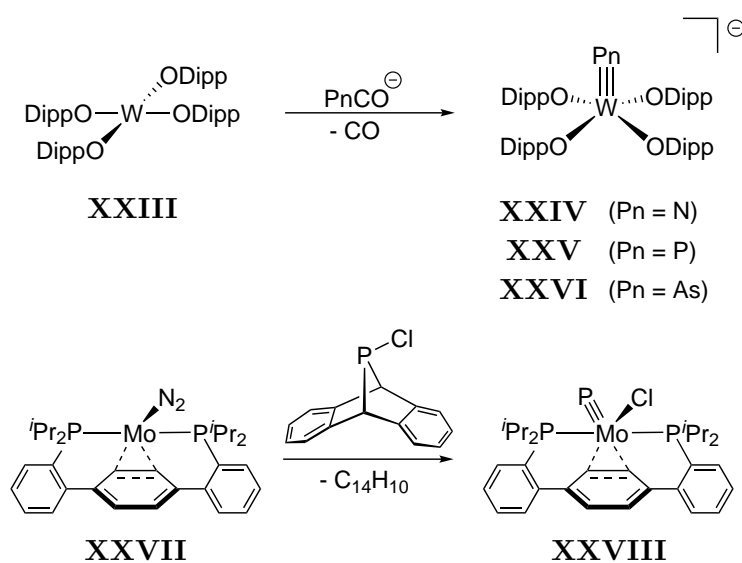
Scheme 1.9: Synthesis of the tungsten series **XXIV** - **XXVI** upon decarbonylation of PnCO$^-$ (Pn = N, P, As) and synthesis of **XXVIII** upon addition of ClP**A** to **XXVII**.[64], [65]

1.2.4 Transition Metal - Pnictogen Multiple Bonding

The Grey-Ballhausen (GB) model rationalizes transition metal oxo bonding in the prevalent octahedral and square-pyramidal geometries.[77],[78] These simple d orbital splitting considerations can be expanded to other two-faced, π-donating, six-electron donors, such as a terminal pnictides (Scheme 1.10, left). Only one d orbital remains σ- and π-nonbonding in character. Therefore, electronic configurations beyond d^2 are beyond the "oxo/nitrido wall" due to the destabilizing population of antibonding molecular orbitals. As a consequence, +VI is the dominating oxidation state for group 8 nitrido complexes.[22] In turn, isolable low-valent group 8 nitrides and terminal nitride complexes beyond group 8 are rare and generally exhibit lower coordination numbers, such as square-planar geometry, to evade π-bonding conflicts (Scheme 1.10, right).[79] Stabilization of this exotic coordination environment can be achieved upon utilization of meridionally coordinating pincer ligands, e.g. PNP pincer and PDI ligands, and was shown for Ru, Os, Rh (transient) and Ir.[80]–[86]

Nitride ligands bound to early-transition metal ions are generally susceptible to electrophilic attack. This nucleophilicity is attributed to the polarization of $M^{\delta+}N^{\delta-}$ π-bonding and is therefore attenuated along the transition series with dropping metal d orbital energies (Scheme 1.11).[54]
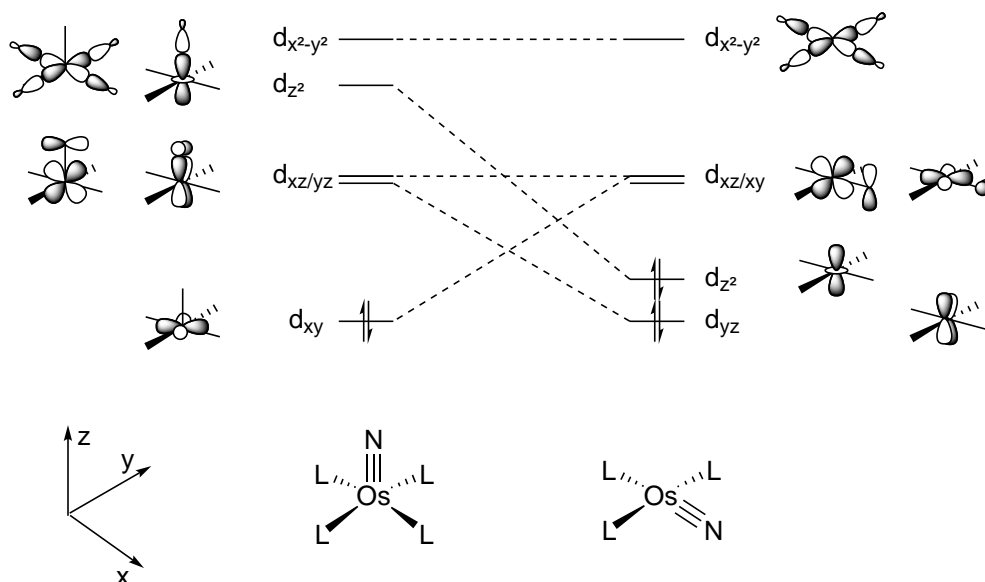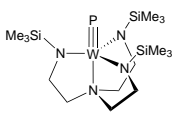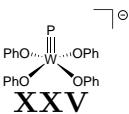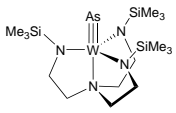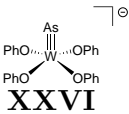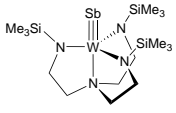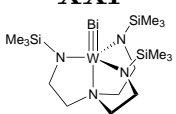
Scheme 1.10: Qualitative d orbital splitting for square-pyramidal Os^{VI} and square-planar Os^{IV} nitride complexes.[77],[78],[80]
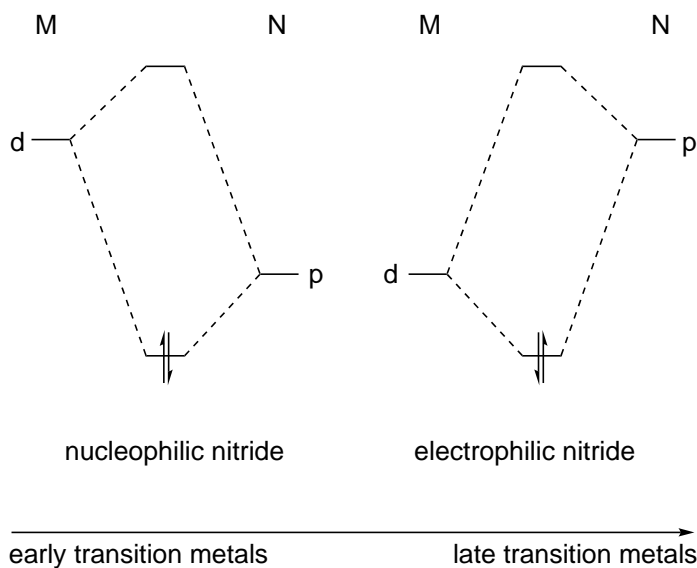
Scheme 1.11: Qualitative orbital interaction of transition metal d orbitals with nitrogen p orbitals resulting in either nucleophilic or electrophilic nitride reactivity.

Since the electronegativity of elements drops drastically when moving from the 2nd period to heavier elements, the transition metal pnictide triple bond is expected to become less polarized and should exhibit electrophilic reactivity.[87], [88] In fact, computations of the terminal pnictide series $[WPn(N\{CH_2CH_2NSiMe_3\}_3)]$ (**XXIX**: Pn = P, **XX**: Pn = As, **XXI**: Pn = Sb, **XXX**: Pn = Bi) reveal only weak polarization towards the pnictide ligand in all cases.[66] The σ-bond carries considerably s-character of the tungsten center which increases for the heavier pnictides while the group 15 elements construct the bond *via* p orbitals. The overall high covalency is reflected in the computed partial charges which render the pnictogen atoms almost neutral or slightly positive. NBO calculations of **XXV** and **XXVI** yield a similar s-character for the pnictide ligands while the s-character of the tungsten center is drastically reduced in a five-fold coordination environment. Frenking and co-workers perfomed EDA calculations on the series $[MPn(OH)_3]$ (M = Mo, W; Pn = N, P, As, Sb, Bi).[88] NBO analysis reveals that the σ-bonds are always polarized towards the pnictogen atoms as also described above. The π-bonds are slightly polarized towards the metal center for the heavier analogues of nitrides. While these bond are calculated to be highly covalent, the electrostatic contributions to the triple bond become dominant for the heavier pnictogens accompanied by severe weakening of the bond dissociaton energies. The tungsten species are predicted to be more stable than the molybdenum analogues.

Table 1.2: Natural bond orbital analysis of the pnictide series **XLV**, **XXV**-Ph, **XX**, **XXVI**-Ph, **XXI**, **XXX**, NBO partial charges, NBO occupancies (occ) % W/Pn: bond polarizations, % s: contribution of the s orbital, WBI: Wiberg bond index, D_e: Bond dissociation energies in kJ mol^{-1}.[65], [66]

Compound	Partial charge		occ	% W	% s	% Pn	% s	WBI	D_e
XLV	W: 0.84	σ:	1.917	42.2	43.5	57.8	23.2	2.38	481.9
	P: -0.03	π:	1.652	46.9		53.1			
		π:	1.664	47.3		52.7			
XXV					16.8		17.3		
XX	W: 0.81	σ:	1.913	42.8	44.6	57.2	20.1	2.35	429.0
	As: 0.01	π:	1.636	47.3		52.7			
		π:	1.636	48.2		51.8			
XXVI					18.6		14.3		
XXI	W: 0.73	σ:	1.890	45.8	47.6	54.2	17.4	2.28	333.4
	Sb: 0.11	π:	1.591	47.3		52.7			
		π:	1.643	48.2		50.6			
XXX	W: 0.71	σ:	1.887	46.0	47.8	54.0	14.2	2.27	293.3
	Bi: 0.15	π:	1.664	51.4		48.6			
		π:	1.555	47.2		52.8			

1.2.5 Reactivity of Transition Metal Pnictide Complexes

The reactivity of transition metal nitride complexes and their electronic structure has been extensively studied due to their relevance for important transformations, such as nitrogen fixation or nitrogen group transfer. Besides the above mentioned direct generation from gaseous dinitrogen, the synthesis *via* salt metathesis of halide ligands for azides or oxidative deprotonation of coordinated ammonia are typical synthetic approaches.[22],[89] As described above, the reactivity (nucleophilic/electrophilic) of the M≡N triple bond is dependent on the metal. In the case of group 9, electrophilic reacitivty was observed.[80],[84],[85],[90],[91] Group 8 nitrides apparently define a transition. Several high-valent Ru^{IV}, Os^{VI} and Fe^{IV} nitride complexes exhibit reactivity that is attributed to nucleophilic attack at the nitride ligand.[92]–[96] Mayer and co-workers demonstrated that the philicity of Os^{VI} nitrides can be tuned by subtle changes of the coordination environment, enabling ambiphilic nitride reactivity. The Os^{VI} nitrides **XXXI** and **XXXII** show different reactivity when reacted with the Lewis-acidic borane $B(C_6F_5)_3$. While **XXXII** forms the adduct **XXXIII**, substitution of the phenyl groups for chloride ligands allows for splitting of the boron carbon bond upon addition of $B(C_6F_5)_3$ to **XXXI** yielding the amide complex **XXXIV** (Scheme 1.12).[92],[93] This change in reactivity was rationalized by the different donor-properties of the ancillary ligands affecting the LUMO energy. This multifaceted reactivity renders group 8 nitrides particular attractive for nitride funtionalization.
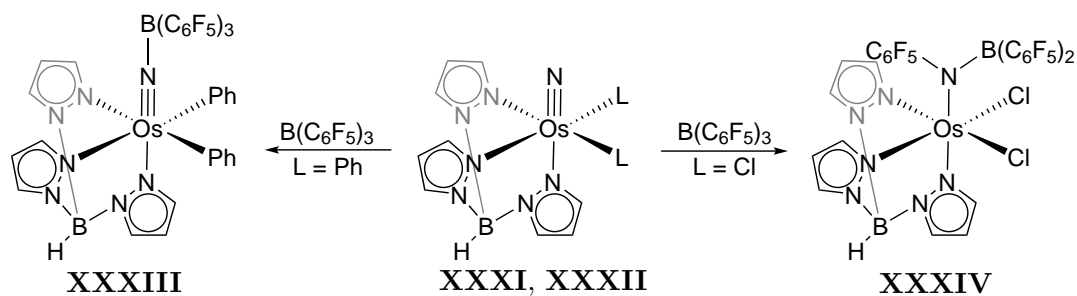
Scheme 1.12: Tuning of the reactivity of Os nitride complexes by variation of the ancillary ligands.[92],[93]

In the case of Os^{IV} nitrido complexes, only two examples have been reported so far. While $[OsN(L^1)]$ (**XXXV**,$L^1 = N(CH_2CH_2P^tBu_2)_2$) exhibits square-planar geometry, the reaction of the Os^{II} iodide complex $[OsI(L^{Si})]$ (**XXXVI**) with Me_3NO or pyridine-N-oxide affords the tetrahedral nitride complex $[OsNI(L^{SiO})]$ (**XXXVII**, Scheme 1.13, L^{SiO}: $O(SiMe_2CH_2P^tBu_2)_2$).[97] The nitride complex **XXXV** exhibits ambiphilic reactivity, as demonstrated by TMS^+ and PMe_3 addition to the nitride complex. However, the low coordination number gives rise to additional reaction patterns in comparison with
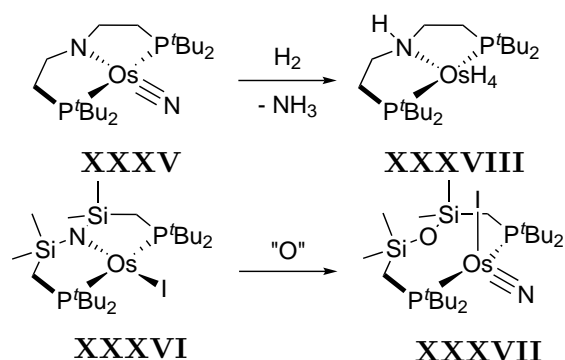
Scheme 1.13: Top: Hydrogenolysis of **XXXV** towards **XXXVIII**; Bottom: Synthesis of **XXXVII** from **XXXVI**.[83], [97]

"traditional" nitride chemistry. For example, the reaction with a Brønsted acid leads to reversible metal protonation and nitride hydrogenolysis affords the tetrahydride complex $[OsH_4(L^{1H})]$ (**XXXVIII**, Scheme 1.13) and ammonia in almost quantitative yield.[83] In analogy to the respective Ru^{IV} nitride, this reaction presumably proceeds via initial H_2 heterolysis facilitated by pincer ligand cooperativity.[81] These observations emphasize the relevance of low-valent group 8 nitrides for nitrogen fixation schemes.[98], [99] However, the reactivity of Os^{IV} nitrides in general remains scarcely examined.

The investigation of the reactivity of heavy terminal pnictide complexes is still at a nascent stage due to the limited number of isolated examples. **XIX** was reacted with Mes*NPCl to give $[Nb(NRAr)_3(P_2NMes^*)]$ (**XXXIX**, Ar = 3,5-Me$_2$C$_6$H$_3$, R= *neo*-pentyl) which releases diphosphorus at elevated temperatures (Scheme 1.14). Trapping experiments proved successful P_2 generation upon addition of 1,3-cyclohexadiene.[100]
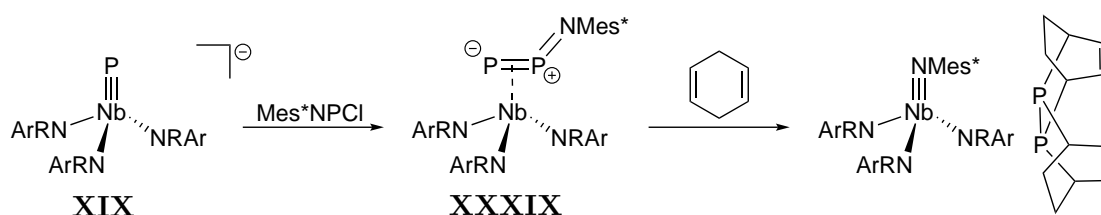
Scheme 1.14: P_2 generation by reaction of **XIX** and Mes*NPCl, Ar = 3,5-Me$_2$C$_6$H$_3$, R= *neo*-pentyl[100]

Due to the strong pnictogen-chalcogen bonds and the electrophilicity of heavy pnictide ligands, several reports feature the synthesis of heterocumulenes from heavy terminal transition metal pnictide complexes. The oxygenation of the terminal molybdenum phosphide **XVI** yielded the unprecedented terminal phosphorus monoxide complex $[Mo(PO)(NArR)_3]$ (**XL**, Scheme 1.15, Ar = 3,5-Me$_2$C$_6$H$_3$, R = *tert*-butyl) reminiscent

of known transition metal nitride reactivity.[22],[90],[101] **XL** could be further converted
to the diphosphenido complex [Mo(P$_2$SR$_3$")(NArR)$_3$] (**XLI**, R" = *iso*-propyl) upon re-
action with [Nb(PSiR$_3$")(NArR$_3$')] (**XLII**, Scheme 1.15, R' = *neo*-pentyl).[102] The
Mo≡P triple bond was also susceptible towards functionalization with elemental sul-
fur and N$_3$Mes* which yielded the phosphorous monosulfide complex [Mo(PS)(NArR)$_3$]
(**XLIII**) and [Mo(PNMes*)(NArR)$_3$] (**XLIV**), respectively (Scheme 1.15).[23]

Similar reactivity was reported for the terminal phosphide and arsenide complexes
[WPn(N{CH$_2$CH$_2$NSiMe$_3$}$_3$)] (Pn = P (**XLV**), Pn = As (**XX**)). The PS and AsS lig-
ated complexes [W(PnS)(N{CH$_2$CH$_2$NSiMe$_3$}$_3$)] (Pn = P, (**XLVI**), Pn = As (**XLVII**)
were obtained *via* reaction with cyclohexane sulfide (Scheme 1.15). A theoretical inves-
tigation of the bonding patterns indicate a suitable description as two 3c4e bonds.
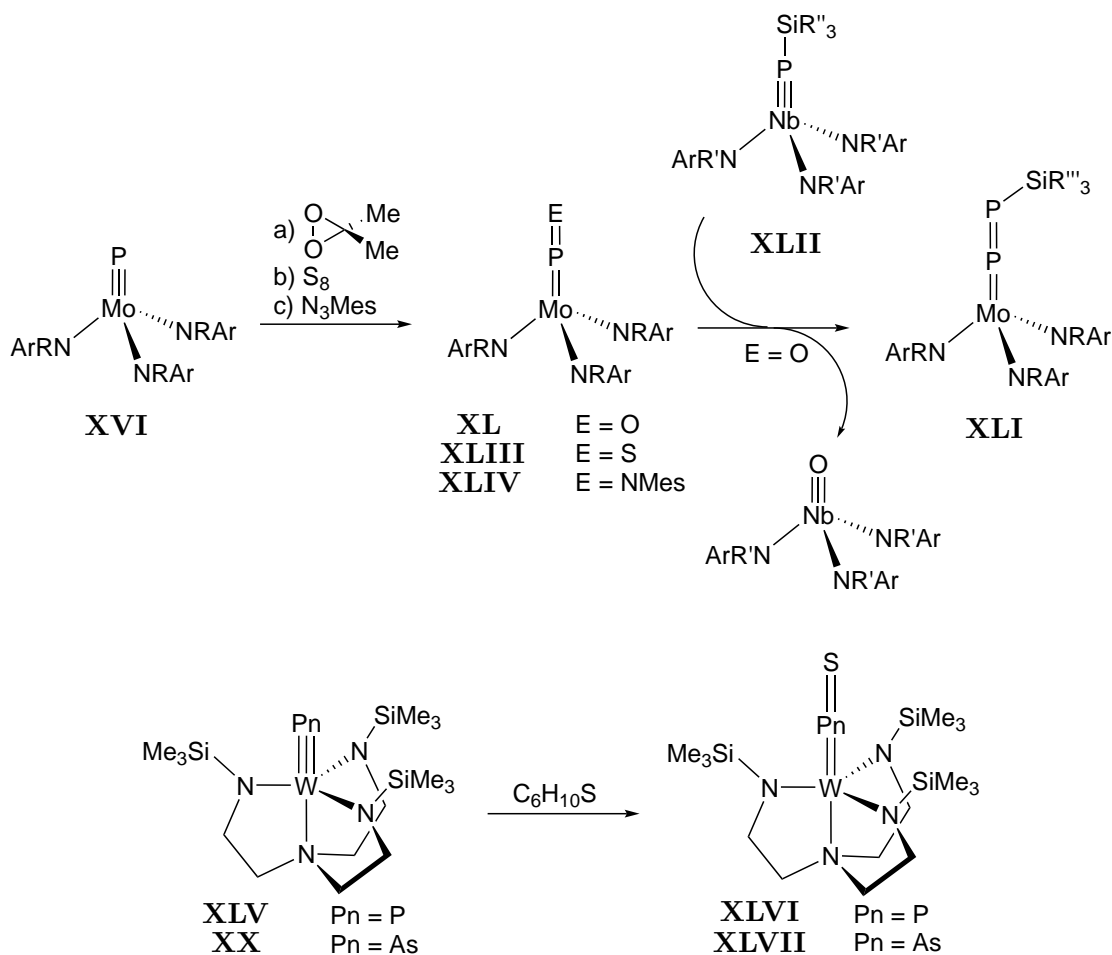
Scheme 1.15: Selected functionalization reaction of heavy terminal transition metal pnictide
complexes, Ar = 3,5-Me$_2$C$_6$H$_3$, R = *tert*-butyl, R' = *neo*-pentyl, R" = *iso*-propyl.[23],[101]–[103]

1.3 Generation of Dipnictogens in the Condensed Phase

The reverse reaction of dinitrogen splitting, the coupling of terminal transition nitrides towards dinitrogen complexes, is commonly observed for octahedral M^V nitrides (M = Fe, Ru, Os) which are accessible by photolysis of azides, reduction of stable M^{VI} nitrides or oxidation of ammine complexes.[104]–[108] This is easily understood by considering the amount of π-electrons within the {MNNM} unit as described above. However, detailed studies on the electronic structure and the associated coupling kinetics of these systems remain scarce and closed-shell nitrides are also known to perform coupling reactions indicating that the electronic configuration of such systems is not an axiomatic predictor.[94], [109]–[112]
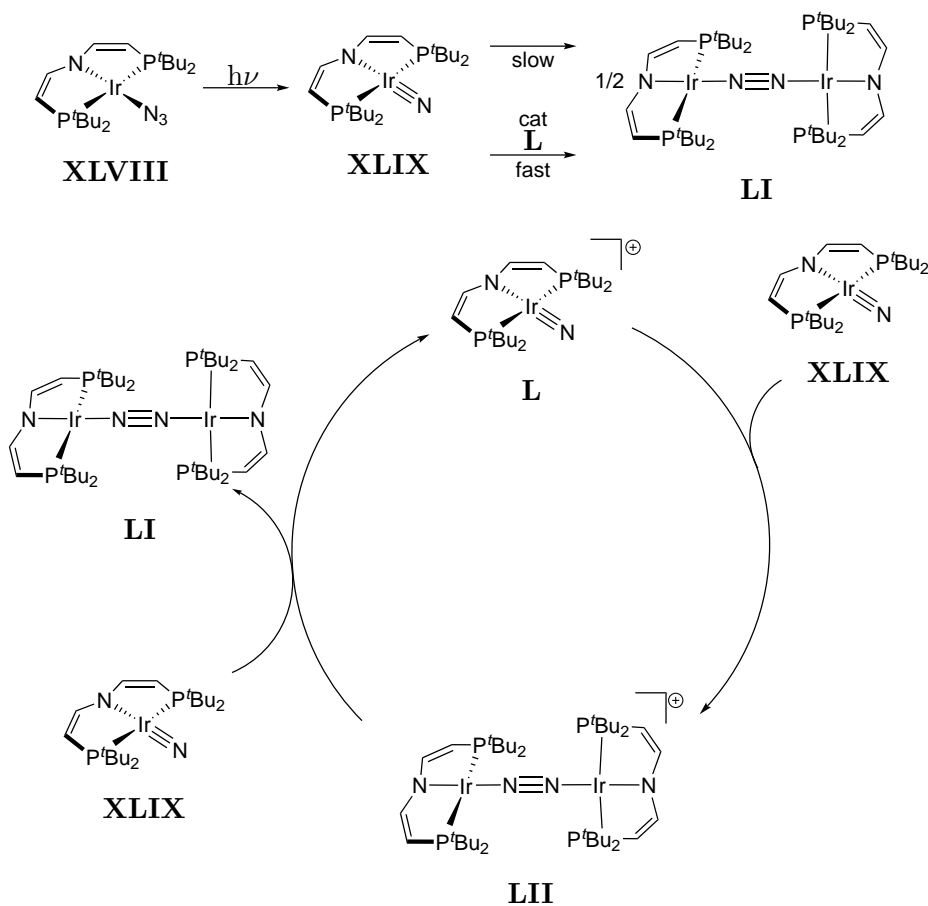
Scheme 1.16: Nitride-Coupling reactions of the {Ir(L^3)} pincer platform.[80], [113]

Studying the reverse reaction of dinitrogen splitting can give insights into the associated thermodynamic and kinetic parameters of this important reaction. The ligand platform L^3 (L^3 = N(CHCHP^{t}Bu$_2$)$_2$) has proven to be a suitable platform for the isolation of unusual coordination numbers and exotic bonding motifs. In the case of Ir, the square-

planar azide complex [Ir(L^3)(N$_3$)] (**XLVIII**) was isolated which could be photolyzed or oxidized yielding open shell Ir^{IV} (**XLIX**) and closed shell Ir^V (**L**) species, respectively (Scheme 1.16).[80] While **L** is an isolable species, radical homo-coupling of **XLIX** yields the dimeric dinitrogen complex [{Ir(L^3)}$_2$($\mu-$N$_2$)] (**LI**). In the case of Rh, similar reactivity was observed but no isolable nitride could be obtained.[82] A mechanistic study revealed that hetero-coupling of **XLIX** and **L** towards [{Ir(L^3)}$_2$($\mu-$N$_2$)]$^+$ (**LII**) is basically barrierless, allowing for redox catalytic nitride coupling (Scheme 1.16).[113] Additionally, the dicationic dimeric N$_2$ complex [{Ir(L^3)}$_2$($\mu-$N$_2$)]$^{2+}$ (**LIII**) could be isolated which features a $\pi^{10}(\delta^4)$ configuration. However, no splitting of dinitrogen was observed since the overall thermochemistry does not allow for nitride formation, as shown by computational analysis.[113]

As outlined in Chapter 1.1, the heavier homologues of dinitrogen exhibit significantly reduced bond dissociation energies which render them highly reactive. The homo-coupling of an isolable terminal heavy transition metal pnictide towards a well-defined Pn$_2$ complex is unknown. The generation of diphosphorus and diarsenic in the condensed phase has been shown by extrusion from the above described diphosphaazide complex **XXXIX**, white phosphorus, the P$_2$-bisanthracene adduct **LIV** and the Ni dipnictide complexes [{NiL(CO)}$_2$($\mu-$Pn$_2$)] (**LV**, **LVI**, L = 1,3-bis(2,4,6-trimethylphenyl)-imidazol-2-ylidene, Pn = P, As, Figure 1.6).[67], [73], [100], [114] Recent reports showcase different strategies to stabilize Pn$_2$ fragments, e.g. with N-heterocyclic carbene ligands upon reductive coupling of PCl$_3$ (**LVII**, Figure 1.7, left) and AsCl$_3$ or *via* extrusion from white phosphorus.[115]–[117] This area of research strongly benefited from the introduction of the previously mentioned pnictogen transfer reagents PCO$^-$, AsCO$^-$ and ClP**A**. The (photo)decarbonylative coupling of the heavier isocyanate analogues led to a variety of phosphanyl, germanyl, cyclopropenyl and stannyl stabilized diphosphene/diarsene (RPn=PnR) products.[118]–[122]

XXXIX   **LIV**   **LV/LVI**
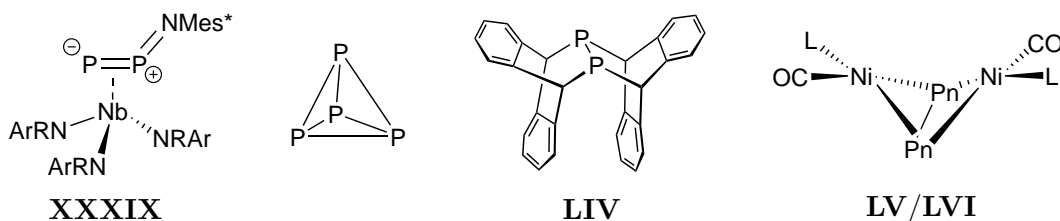
Figure 1.6: Isolable sources of Pn$_2$ in the condensed phase, Ar = 3,5-Me$_2$C$_6$H$_3$, L = 1,3-bis(2,4,6-trimethylphenyl)-imidazol-2-ylidene, Pn = P, As, R = *neo*-pentyl.[67], [73], [100], [114]

Transition metal coordination provides an alternative strategy to stablize dipnictide fragments. P$_4$ activation has led to several side-on bridged complexes with M$_2$P$_2$ butterfly-core (**XVIII**, Figure 1.7, middle) and in rare cases end-on bridging diphosphinidene

species M=P−P=M, contrasting the rich chemistry of end-on dinitrogen bridged coordination compounds.[31],[60],[123],[124] The decarbonylative coupling of PCO⁻ gave bridging P_2^{4-} and P_2^{2-} ligands, e.g. $[\{Ir(PDI)(CO)\}_2(\mu-P_2)]$ (**LVIII**, Figure 1.7, right).[70],[73],[74] Terminal phosphide complexes can be assumed as key intermediates for these P-P coupling reactions but direct observation of oxidative M≡P coupling or the reverse reduction remains scarcely examined.
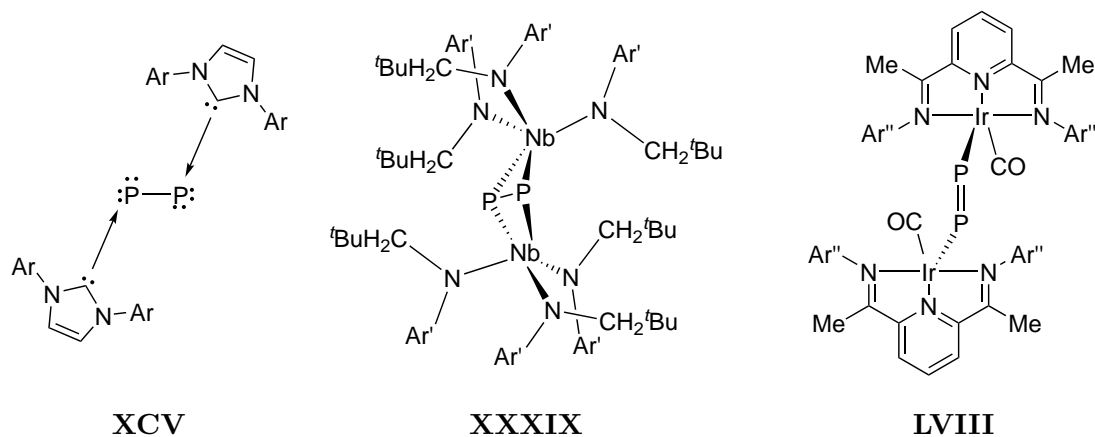
Figure 1.7: Examples for isolable diphosphene compounds generated by PCl₃ reduction (**XCV**, left), P₄ activation (**XXXIX**, middle) and PCO decarbonylation (**LVIII**, right), Ar = 2,6-$^iPr_2C_6H_3$, Ar' = 3,5-Me₂C₆H₃, Ar" = 2,6-Me₂C₆H₃.[58],[74],[115]

As mentionened above, heavy transition metal terminal pnictide complexes are restricted to group 5 and 6 and mostly feature a d⁰ electron configuration, preventing oxidative functionalization. One-electron oxidation of **XXVIII** (d² configuration) results in the formation of the isolable open-shell complex [MoPCl(PCP)]⁺ (**LIX**) which undergoes unprecedented oxidative phosphide coupling towards dimeric $[\{MoCl(PCP)\}_2(\mu-P_2)]$ (**LX**) at temperatures above −10°C (Scheme 1.17). Although **LX** could not be isolated, the generated P_2^{4-} fragment was trapped chemically.[64] The coupling reactivity of terminal arsenide complexes has not been investigated so far.
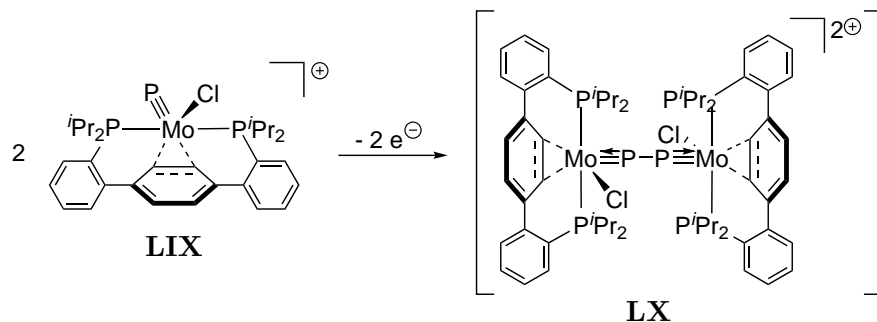
Scheme 1.17: Proposed coupling reactivity of **LIX** towards **LX**.[64]

1.4 Phosphinyl Radicals and Phosphinidenes

Parts of this chapter were adapted from: **J. Abbenseth**, D. Delony, M. C. Neben, C. Würtele, B. de Bruin, S. Schneider, *Angew. Chem. Int. Ed.* **2019**, *58*, 6338-6341, with permission from WILEY-VCH Verlag GmbH & Co. KGaA, Weinheim.

Phosphinyl radicals possess seven valence electrons and carry a lone-pair and an unpaired electron at the phosphorus center. Over the last 50 years phosphinyl radicals have been proposed to play a key role in $P-C$ bond formation reactions, like olefin phosphination.[125]–[129] Nevertheless, stabilization by metal coordination has only been scarcely examined and, so far, did not lead to isolable compounds. The PPh_2 radical was first observed in 1963 after photolysis of $HPPh_2$ or $(Ph_2P)_2$.[130] Further EPR studies afforded a full characterization of this radical.[131]–[136] Due to the forcing irradiation conditions, complex product mixture were generated. This was partly overcome by the utilization of spin traps.[137]–[140] Irradiation of metal carbonyl phosphine complex single-crystals to give phosphinyl radicals has also been reported. In all studied cases, the unpaired electron mainly resides at the phosphorus center with minor delocalization towards the metal center.[141] More recently, the PPh_2 radical was generated from $HPPh_2$ by proton coupled electron transfer (PCET) mediated by 2,2-diphenyl-1-picrylhydrazyl which represents the first non-irradiative method for the production of this species (Scheme 1.18).[142],[143]
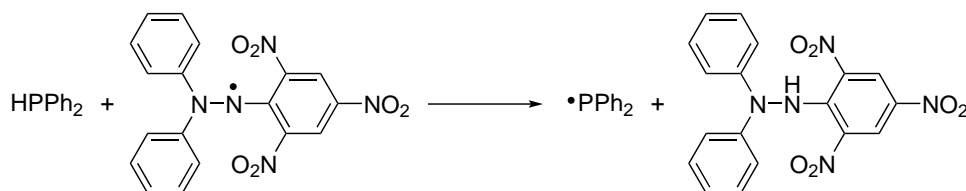
Scheme 1.18: Generation of the PPh_2 phosphinyl radical by PCET.[143]

Over the last years, several isolable phosphinyl radicals have been reported. Structural and spectroscopic characterization of free and coordinated phosphinyl radicals facilitated the examination of (electronic) structure/reactivity relationships.[141],[144]–[158] Isolable free phosphinyl radicals however require stabilization by bulky ligands and do not feature $P-H$ bonds. Stabilization of such highly reactive species by transition metal coordination offers an attractive pathway to investigate this class of compounds. A possible access consists of the generation of open shell species by redox-chemical conversion of terminal phosphanide complexes. Terminal phosphanide complexes are still scarce due to their high reactivity owing to their available lone pair and radicals generated this way undergo rapid follow-up reactivity.[157] In comparison, free phosphinidenes (PR)

could only very recently be sufficiently stabilized.[118],[159] A variety of transition metals form isolable phosphinidene complexes (M=PR) with promising stoichiometric reactivity, such as P−C bond formation.[160]–[163] However, catalytic phosphinidene transfer protocols remain exceedingly rare, compared to, e.g. nitrene transfer which has emerged as a powerful method for C−N bond formation.[164]–[168]

The scarcity of catalytic PR-transfer might in part be attributed to a lack of suitable oxidizing PR-transfer reagents, such as analogs of iminoiodane (ArI=NR) or azide (RN$_3$) nitrene sources. Primary phosphines are attractive precursors to phosphinyl radicals as well as phosphinidenes from a thermochemical point of view due to lower intrinsic P−H vs. N−H bond dissociation (free) energies (BD(F)Es, Scheme 1.19).[16],[169]–[172] Further chemical conversion represents an attractive strategy to utilize primary phosphines as P$_1$-building blocks.

BDFE(H-NH$_2$) = 45.8 kcal mol^{-1}
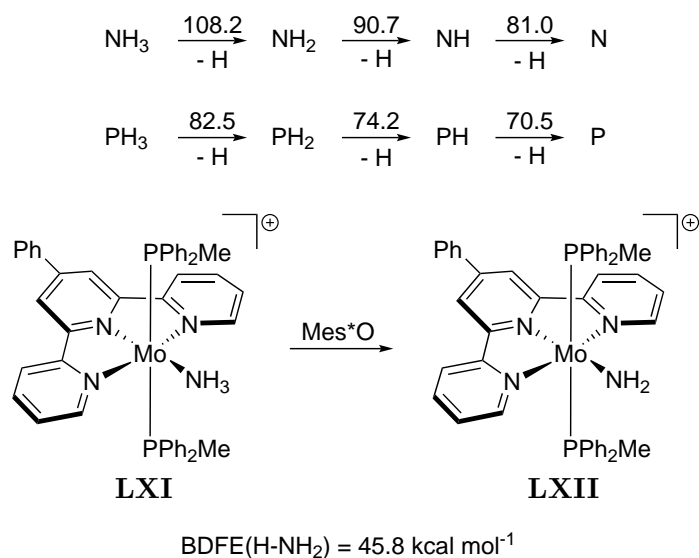
Scheme 1.19: Top: N−H and P−H bond dissociation energies (BDEs) in the gas phase (kcal · mol^{-1}), The BDE(NH$_2$) was calculated *via* a Hess cycle: BDE(NH$_2$) = $\Delta_f H^\circ_{gas}$(N)+2$\Delta_f H^\circ_{gas}$(H)− BDE(NH)−$\Delta_f H^\circ_{gas}$(NH$_2$);[16],[169]–[172] Bottom: Severe weakening of the N−H bond in ammonia by **LXI** and its PCET reactivity towards **LXII**, Mes* = 2,4,6-^{t}Bu$_3$C$_6$H$_2$.[173]

The P−H bonds might be further weakened upon coordination to a metal complex as was demonstrated for coordinated H$_2$O and NH$_3$ ligands.[174] The group of Chirik and co-workers showed that the bond dissociation free energy of ammonia is severely weakened when coordinated to the Mo^I complex [Mo(NNN)(PPh$_2$Me)$_2$(NH$_3$)]$^+$ (**LXI**) allowing for synthesis of the amido complex [Mo(NH$_2$)(^{Ph}Tpy)(PPh$_2$Me)$_2$]$^+$ (**LXII**, Scheme 1.19) by PCET.[173] Since the N-H BDFE of the coordinated ammonia molecule is smaller than the BDFE of dihydrogen, H$_2$ formation was observed when heating **LXI** to 60°C. However, while amide ligand N−H bond activation by PCET is an active

field of research, phosphide P−H homolysis was only reported by Hillhouse and co-workers.[79], [175]–[185]   The open-shell phosphanide complex **LXIII** reacts with Mes*O to form the phosphinidene **LXIV** (Scheme 1.20).[186], [187]   This result showcases the potential of transition metal complexes to stabilize open-shell phosphorus centers with decreased steric bulk, therefore allowing for generation of radicals possessing a P-H moiety that allows for interconversion of phosphinyl radicals and phosphinidene complexes *via* proton coupled electron transfer. Coordinatively unsaturated, electron-rich transition metal complexes, e.g. square-planar Os^{II}, represent privileged starting platforms to facilitate oxidative addition of phosphines to yield a phosphanide complex which might be further converted to the targeted species.
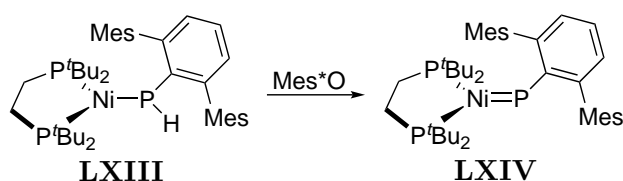
Scheme 1.20: Generation of a nickel phosphinidene complex by PCET reported by Hillhouse and co-workers.[186], [187]

1.5 Scope of this Work

The aim of this thesis is to investigate and develop suitable platforms capable of forming unprecedented M≡Pn species and to further elucidate the electronic and structural requirements to access these compounds.

- A low-valent, **square-planar Os halide pincer complex** with a d^6 configuration is targeted. This complex should feature an interesting electronic structure due to its isolobal-relationship with octahedral Re^{III} which is well-known to feature effects of temperature independent paramagnetism. The system will be further **derivatized by chelating neutral and anionic ligands** to tune the overall redox potentials. Additionally, prior reported $\mathbf{Re^{III}}$ **pincer complexes** will be characterized by magnetic measurements and the influence of the ancillary ligands on the magnetic behaviour will be evaluated by **derivatization**.

- Synthesis of **square-planar Os nitride complexes** will be targeted by reacting the prior obtained Os halide complex with azide salts. The reactivity will be examined upon addition of typical nucleophiles and electrophiles. Furthermore, possible **redox-mediated dinitrogen coupling reactions** will be evaluated.

- **Transition metal complexes featuring multiple bonds with heavy pnictogens** will be targeted by the following approaches:

  - The phosphorus and arsenic atom transfer reagents $PnCO^-$ (Pn = P, As) and ClP**A** will be reacted with the obtained Re PNP pincer complexes to access unprecedented **terminal Re pnictide complexes** and investigate their reactivity.

  - The low-valent Os halide complex should allow for the activation of electron rich, primary phosphines to access terminal Os phosphanide complexes which represent an interesting starting point to investigate the effect of metal-coordination on the P-H bond strength. The **interconversion of Os-PHR and Os-PR complexes** by proton coupled electron transfer will be investigated.

  - The possible formation of **terminal Os phosphide/phosphinidene complexes** by addition of PCO^- and ClP**A** to the low-valent Os halide complex will be evaluated.

- **Dimeric molybdenum dinitrogen complexes** will be investigated by spectroscopic methods to gain additional insights into the electronic structure of this class of compounds and how the degree of dinitrogen activation changes upon oxidation of the metal center.

Os(II/III) and Re(III) PNP Pincer Complexes

Author contributions

J.A.	Synthesis, spectroscopy, theoretical calculations (Chapter 2.4) and crystallography (**6**, **10**)
M.D.	Theoretical calculations (Chapter 2.2, supporting)
S.B.	Synthesis and spectroscopy (Chapter 2.2, supporting)
C.W.	Crystallography
C.V.	Crystallography (Chapter 2.2, scsupporting)
S.D.	SQUID
M.H.	Theoretical calculations (Chapter 2.2)

2 Os(II/III) and Re(III) PNP Pincer Complexes

2.1 Possible Platforms for the Stabilization of Low-Valent Os Complexes

A simple access to low-valent, square-planar Os nitride complexes featuring a d^4 electron configuration is a substitution reaction of a halide ligated d^6 complex with an azide salt and subsequent dinitrogen extrusion to yield a nitride complex. Utilization of tridentate, meridionally coordinating pincer ligands allows for the possible synthesis of suitable halide precursors. The control of pincer complex reactivity is often achieved by varying the substituents in their electronic and steric properties at the terminal donor positions. However, typical bond activation reactions occur *trans* to the central pincer donor so variations of the donor properties of this moieties have a significant higher impact on reactivity.[188]–[190] Slight variation can not only alter the reactivity but also offer the possibility to change the multiplicity of the studied system.
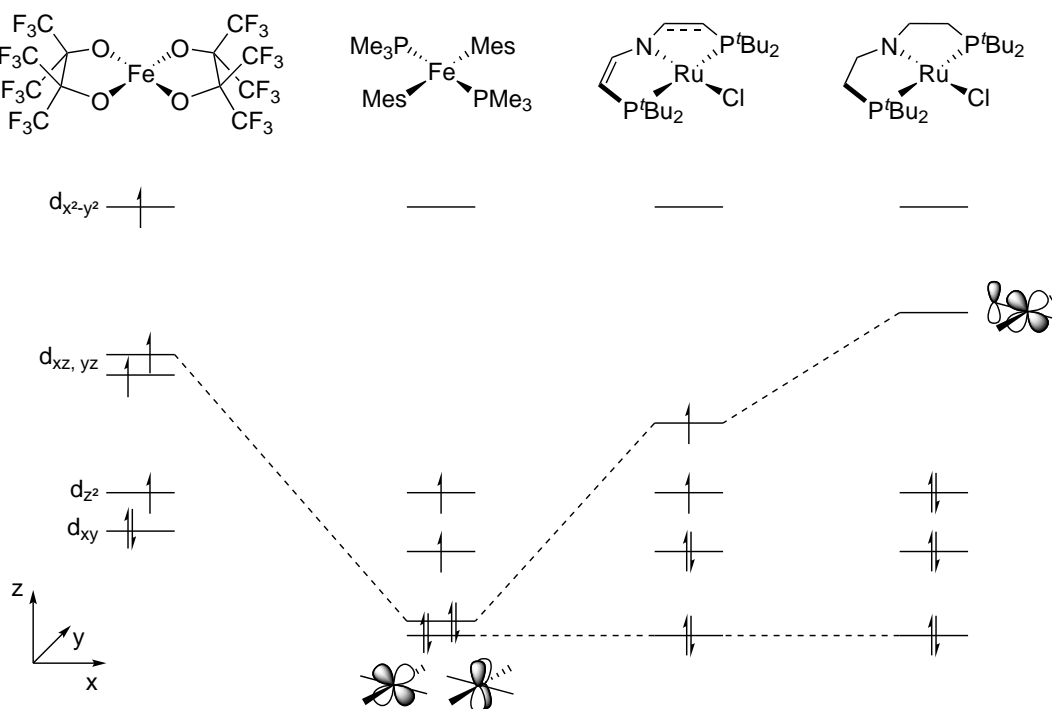
Figure 2.1: Qualitative d orbital splitting of square-planar d^6 complexes with strongly π-donating (left), pure σ-donating ligands (middle left) and Ru-pincer systems **LXV** - **LXVII** (right).[191]

For square-planar group 8 complexes with a d^6-configuration, three possible spin states have to be considered ($S = 0, 1, 2$). In ideal D_{4h}-symmetry, the d orbital manifold is split into a set of three non-bonding ($d_{xy,xz,yz}$, e_g and b_{2g}), a weakly antibonding (d_{z^2}, a_{1g})

and a strongly antibonding orbital ($d_{x^2-y^2}$, b_{1g}). For 1st row transition-metals usually the intermediate-spin configuration $(e_g)^4(b_{2g})^1(a_{1g})^1(b_{1g})^0$ arises (Figure 2.1, middle left). When strongly π-donating ligands are employed the e_g set is raised in energy which can result in a high-spin configuration (Figure 2.1, left). For heavier elements the ligand field splitting is increased significantly which favors intermediate- and low-spin configurations. Schneider and co-workers examined the reactivity of coordinatively unsaturated metal complexes with unusual electronic structures. The use of related diphosphineamido pincer ligands (Figure 2.2) enabled the isolation and characterization of square-planar d^6 complexes like $[CoCl(L^3)]^+$, $[IrCl(L^3)]^+$ and the Ru^{II} series $[RuCl(L^{1,2,3})]$ (**LXV**, **LXVI**, **LXVII**, Figure 2.2, L^2: $N(CHCHP^tBu_2)(CH_2CH_2P^tBu_2)$).[191]–[194] **LXV** exhibits a singlet ground-state due to the strong π-donation of the pincer ligands which raises the d_{xz} orbital in energy (Figure 2.1 right). Weakening this interaction by successive dehydrogenation of the pincer ligand results in **LXVI** and **LXVII** which are best described by an intermediate spin-state ($S = 1$, Figure 2.1 middle right). Both compounds exhibit sharp signals in the ^1H NMR spectrum which show a linear shift over a temperature range of $\Delta T = 140°C$, indicating the presence of an energetically well separated ground state.[191] The latter also exhibit large magnetic anisotropy as a consequence of mixing with excited state through spin-orbit coupling (SOC) resulting in unusual high D values (axial component of the magnetic dipole-dipole interaction) of over $200\,cm^{-1}$.
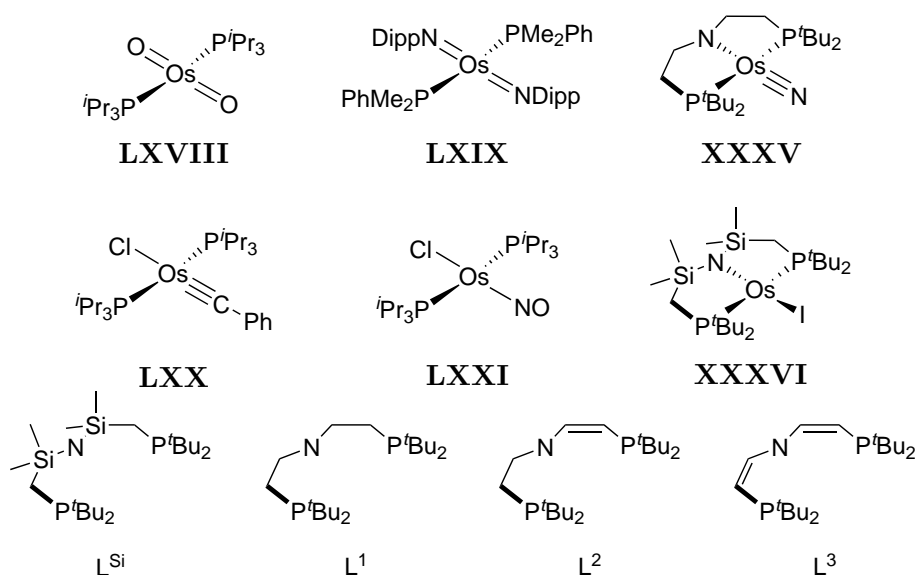
Figure 2.2: Square-planar osmium complexes reported in the literature and the anionic PNP ligands used by the Caulton and Schneider group.[83],[97],[195]–[198]

The coordination chemistry of osmium is strongly dominated by six-coordinate Os^{II}. While low-coordinate species are known for high valent osmium featuring strong π-donating ligands (e.g. OsO_4), square-planar species are rare. There are a number of Os^{IV} complexes reported in literature which feature oxo (**LXVIII**), imido (**LXIX**), nitrido (**XXXV**) or carbyne ligands (**LXX**) and for (formal) Os^0 with the π-acceptor ligand NO (**LXXI**) (Figure 2.2).[83],[195]–[198] The only square-planar d^6 system is represented by the Os^{II} halide complex $[OsI(L^{Si})]$ (**XXXVI**).[97] Although the pincer resonances in the ^{1}H NMR of **XXXVI** are sharp and coupling towards the phosphorus atoms is resolved, no ^{31}P NMR signal was detected and a non-magnetic triplet ground state was proposed which is unparalleled in osmium chemistry. Theoretical computations predict the singlet state to be $1.7 \, \text{kcal} \cdot \text{mol}^{-1}$ higher in energy than the assigned electronic ground state which lies in the error of the employed method.[199] The Ru analogue $[RuI(L^{Si})]$ (**LXXII**) was also reported, however no coupling patterns in the ^{1}H NMR were observed and the triplet state was calculated to be favored by an energetic difference of $12.8 \, \text{kcal} \cdot \text{mol}^{-1}$. These results indicate that 3rd row metal complexes like **XXXVI** could exhibit unique electronic structures and magnetic properties. Moreover, the electronic structure of square-planar Os^{II} might not be accurately described by DFT and should be investigated by more elaborate computational methods. Since a systematic study of the ligand set L^1 - L^3 is available in the case of ruthenium, the corresponding osmium analogues are attractive synthetic targets to gain further insight into the electronic structure of heavy group 8 square-planar halide complexes. Additionally, Schneider and co-workers recently reported the synthesis of the five-coordinate Re^{III} dichloride complex $[ReCl_2(L^1)]$ (**LXXIII**) which served as a starting platform for dinitrogen fixation.[52] In contrast to the targeted Os system, **LXXIII** features a saturated pincer ligand which is expected to result in stronger splitting of states due to its stronger π-donating properties.[191] Furthermore, the complex $[ReCl_2(L^3)]$ (**LXXIV**) has been synthesized.[1] The effect of successive PNP pincer desaturation or halide exchange has not been investigated thoroughly until this point.

---

[1]Unpublished results. See the Ph.D. thesis of Isabel Klopsch for additional details.

2.2 A Square-Planar Os(II) Complex

Schneider and co-workers reported the synthesis of the Os^{IV} complex [OsCl$_2$H(L^1)] (**LXXV**) upon coordination of ^{H}L^1 to [OsCl$_2$(PPh$_3$)].[83] All attempts to synthesize [OsCl(L^1)] by elimination of HCl resulted in unselective decomposition, even at low temperatures.[200] The divinylamide pincer ligand L^3 can be introduced by application of a template ligand dehydrogenation strategy which has been successfully employed in the case of Co and Ni.[192], [201]
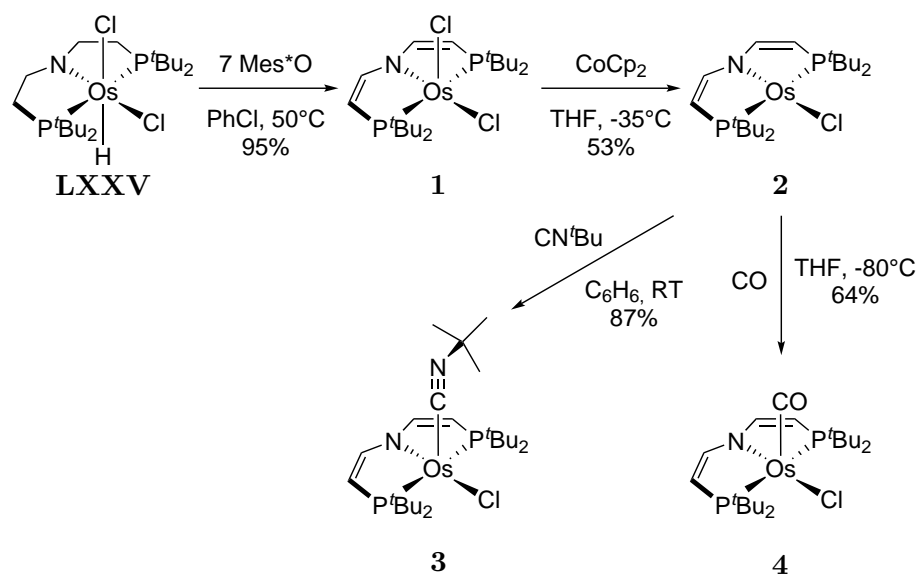
Scheme 2.1: Synthesis of **1** by five-fold H atom abstraction *via* Mes*O and reduction towards **2** followed by coordination of CN^{t}Bu (**3**) and CO (**4**).

Reaction of **LXXV** with excess Mes*O at 50°C in chlorobenzene affords the five-coordinate Os^{III} complex [OsCl$_2$(L^3)] (**1**, Scheme 2.1) in almost quantitative yield. Single-crystal X-ray analysis confirms complete ligand dehydrogenation (Figure 2.3, C1-C2: 1.323(9) Å). The coordination geometry is best described as square-pyramidal with the Cl1 ligand in apical position ($\tau = 0.02$).[202] In contrast to the solid state, C_{2v}-symmetry is observed on the NMR timescale in solution as indicated by three strongly paramagnetically shifted and broadened ^{1}H NMR resonances ($\delta_{t_{Bu}} = -0.06$ ppm; δ_{CH} = 43.9 ppm and -97.7 ppm). The magnetic moment of **1** derived by Evans' method at room temperature ($\mu_{eff} = 1.65\,\mu_B$) is close to the spin-only value for an $S = 1/2$ ground state. Furthermore, the broad, rhombic EPR powder spectrum with large g-anisotropy ($g_x = 1.215$, $g_y = 2.000$, $g_z = 2.220$, Appendix 8.1.1) is in agreement with a metal centered radical. The redox chemistry of **1** was examined by cyclic voltammetry (Appendix 8.1.2). Quasi-reversible oxidation was found at $E_{1/2} = 0.04$ V vs. Fc$^{+/0}$ besides two reduction waves at $E_{p.c.} \approx -1.28$ V and $E_{p.c.} \approx -2.05$ V that remained irreversible
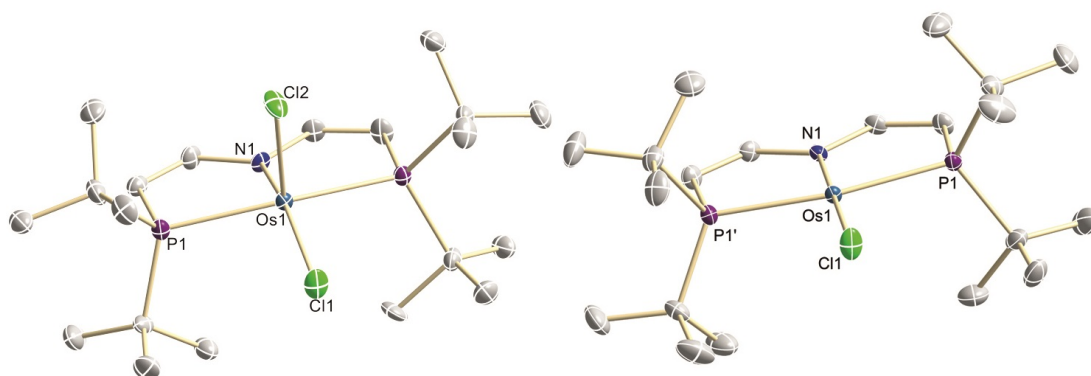
Figure 2.3: Molecular structure of complex **1** and **2** from single-crystal X-ray diffraction (thermal ellipsoids drawn at the 50% probability level); hydrogen atoms are omitted for clarity. Selected bond lengths [Å] and angles [°]: **1** Os1–N1 1.966(6), Os1–Cl1 2.380(3), Os1–Cl2 2.319(2), N1–C1 1.409(6), C1–C2 1.323(9), N1–Os1–Cl1 160.16(19), N1–Os1–Cl2 106.82(19), Cl1–Os1–Cl2 93.02(10); **2** Os1–N1 1.980(2), Os1–Cl1 2.3542(7), N1–C1 1.403(2), C1–C2 1.333(3)).

up to scan rates of $1\,\mathrm{V}\cdot\mathrm{s}^{-1}$, suggesting successive chloride elimination upon reduction. Accordingly, chemical reduction of **1** with $CoCp_2$, extraction with pentane at $-30°C$ and crystallization overnight at $-35°C$ allows for the isolation of dark purple, crystalline $[OsCl(L^3)]$ (Scheme 2.1, **2**) in isolated yield over 50%. **2** is temperature sensitive and decomposes unselectively over the course of 24 h. NMR spectroscopic detection of isobutene points towards intramolecular decomposition pathways, which also prevented reliable characterization by elemental analysis (Appendix 8.1.4). However, crystallographic, spectroscopic, and mass spectrometric data confirm the proposed structure.

In the solid state, the osmium ion exhibits square-planar coordination with some distortion due to the pincer bite angle (Figure 2.3). The bond lengths around the metal center are close to parent **1** and no indications for intermolecular interactions could be found. While no ^{31}P NMR signal was reported in the case of **XXXVI**, the $^{31}P\{^1H\}$ spectrum of **2** features a signal with an unusual chemical shift for a trialkylphosphine ($\delta_P = -978.2\,\mathrm{ppm}$). In addition, three strongly shifted ($\delta_{t\mathrm{Bu}} = -4.2\,\mathrm{ppm}$; $\delta_{\mathrm{CH}} = 18.4\,\mathrm{ppm}$ and $-35.3\,\mathrm{ppm}$), yet sharp signals with resolved ^1H and ^{31}P J-coupling are observed in the ^1H NMR spectrum (Appendix 8.1.3). Between -55 to $-15°C$ the chemical shifts exhibit non-Curie behavior, i.e. a linear ($\delta \propto T$) and very small ($\Delta\delta < 0.4\,\mathrm{ppm}$) temperature dependence (Appendix 8.1.5). This observation suggest temperature independent magnetism (TIP) indicating an energetically well separated ($\gg k_{\mathrm{B}T}$) ground state.[203] This interpretation is further supported by SQUID magnetometry of a powdered sample (Figure 2.4, top right). In the range of 2 - 295 K constant susceptibility $\chi_{\mathrm{M}}(\mathrm{TIP}) = 1030 \cdot 10^{-6}\,\mathrm{cm}^3\,\mathrm{mol}^{-1}$ is observed. Hence, the magnetic properties are in line with the exclusive thermal population of a ground state, which experiences only second order paramagnetism through mixing with excited states. In comparison, the

ruthenium analogue **LXVII** exhibits strongly temperature dependent NMR spectra and magnetic susceptibility in these temperature ranges as a consequence of smaller separations of the lowest spin-orbit states.[191] This reflects the significant higher spin-orbit coupling constant of osmium ($\zeta_{Os} \approx 3000 \, cm^{-1}$) compared to that of ruthenium ($\zeta_{Ru} \approx 1000 \, cm^{-1}$).[204]   Large TIP is typically found for (octahedrally coordinated) heavy d^4 ions like Re^{III} (*vide infra*) which share an isolobal relationship with **2**.[205] Further information is obtained from computational analysis of **2**. Correlated single reference *ab initio* calculations, ONIOM-(CCSD(T)-F12:PBE0D), predict a triplet ground state separated from the lowest singlet by merely $1.5 \, kcal \cdot mol^{-1}$. The singly occupied molecular orbitals are computed to be mainly metal centered with minor admixtures of the nitrogen pincer atom and the chloride ligand in the case of the d_{yz} orbital (Figure 2.4, left). Additional multireference computations were performed to get insights into state mixing through SOC. A state-averaged NEVPT2/CAS(16,10) approach (Figure 2.4, bottom right) also indicates a triplet ground state with a $(d_{z^2})^1 (d_{xz})^1$ configuration (94% weight). The first excited state lies $6.2 \, kcal \cdot mol^{-1}$ above the triplet and corresponds to the lowest singlet state $(d_{z^2})^2 (d_{xz})^0$ configuration (86% weight). Hence, these results qualitatively reflect the single reference ONIOM calculations. However, after QDPT/SOC treatment on the NEVPT2/CASSCF energies the ground-state triplet root is stabilized by $\Delta E(SOC) = -9.2 \, kcal \cdot mol^{-1}$. Furthermore, it splits into three sublevels, where the lowest eigenstate derives from a triplet contribution with significant admixtures (16%) of the lowest singlet state. The two eigenstates above originate directly from the lowest triplet state. This state-energy diagram supports the rationalization of the magnetic susceptibility measurements with an energetically isolated ground-state. In an effective spin-Hamiltonian picture this would translate to large positive axial zero field splitting with the corresponding three ground-state magnetic sublevels of a $S = 1$ spin system. However, this model breaks down and should not be applied if the spin-orbit coupling matrix elements approach the same order of magnitude of the associated non-relativistic excitation energies.[206] The Os^{II} pincer platform was further characterized by the coordination of spectroscopic probes. As was reported for Caulton's complex **XXXVI**, the coordinatively unsaturated, low-valent complex **2** undergoes facile coordination of additional π-acceptor ligands.[97] Addition of one equivalent of CN^tBu to *in situ* prepared **2** results in an immediate color change to dark blue and isolation of $[OsCl(L^3)(CN^tBu)]$ (**3**, Scheme 2.1) in high yield after column chromatography. The band at $\tilde{\nu}_{CN^tBu} = 1931 \, cm^{-1}$ in the IR spectrum (Appendix 8.1.6), assignable to the C=N stretching vibration, indicates strong back bonding. This is confirmed by single crystal X-Ray diffraction (Figure 2.5).
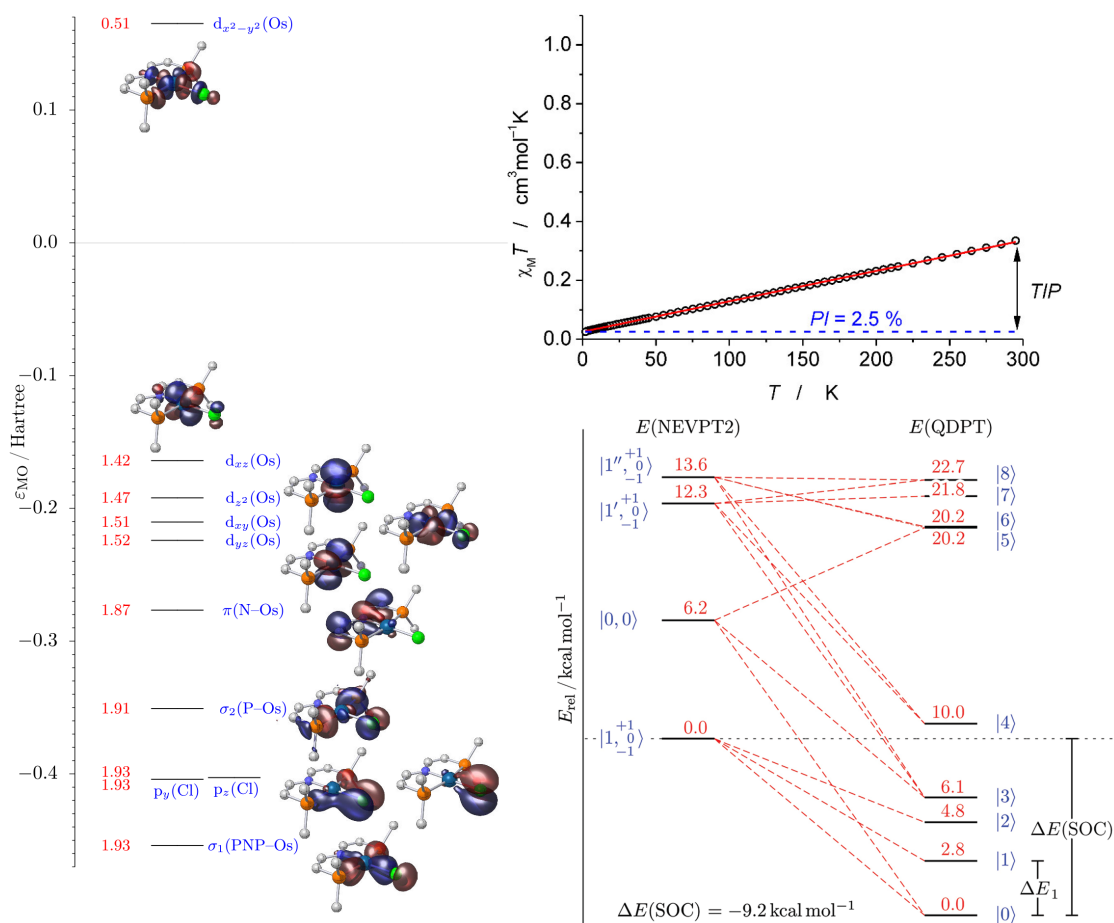
Figure 2.4: Left: Active MO scheme computed at the C_2-symmetric triplet geometry of **2** for a SA-CASSCF(16,10) wavefunction, state-averaged over the 5 quintet, 45 triplet, and 50 singlet CSFs, which arise from the local $5d^6$ configuration of the formal Os^{II} center; average occupation numbers are given in red. Top right: $\chi_M T$ versus T plot for **2**, PI = 2.5%, $S = 1$, $\chi_M(TIP) = 1030 \cdot 10^{-6}\,cm^3\,mol^{-1}$. Bottom right: State-energy diagram for **2** based on NEVPT2/SA-CASSCF(16,10) computations. Non-relativistic energies of the lowest four states are shown with their corresponding state labels (left). The lowest nine spin-orbit states (right) are complemented with selected contributions (weights > 10%) of the corresponding spin-free states (dashed red lines).

The isonitrile ligand of **3** is situated in the apical position of the square-pyramidal structure and features strong bending (C21-N2-C22: 144.4(4)°) to an extent which is rarely observed.[53],[207] Furthermore, the Os-N bond is slightly elongated with respect to parent **2** ($\Delta d = 0.07\,\text{Å}$) indicating reduced π-donation by the pincer ligand.

In analogy, exposure of *in situ* prepared **2** to one equivalent of CO gives the pink compound $[OsCl(L^3)(CO)]$ (**4**, Scheme 2.1). When treated with one atmosphere of carbon monoxide the formation of several side products is observed, e.g. a dicarbonyl complex which decomposes quickly. As in the case of complex **3**, the ^{1}H NMR spectrum is in agreement with C_S-symmetry on the NMR timescale. Complex **4** was fully characterized

Figure 2.5: Molecular structure of complex **3** from single-crystal X-ray diffraction (thermal ellipsoids drawn at the 50% probability level); hydrogen atoms are omitted for clarity. Selected bond lengths [Å] and angles [°]: **3** Os1–N2 2.050(3), Os1–C21 1.827(4), Os1–Cl1 2.4046(9), C21–N1 1.197(5), C21–N2–C22 144.4(4).

including single-crystal X-Ray diffraction (Due to significant disorder the bond lengths will not be discussed in detail). The CO ligand exhibits a rather unusual high-field shift in the ^{13}C NMR spectrum ($\delta_{CO} = 168.3$ ppm). The CO stretching vibration is observed at $\tilde{\nu}_{CO} = 1893$ cm^{-1} in the IR spectrum (Appendix 8.1.7), almost identical with Caulton's [OsI(L^{Si})(CO)] (**LXXVI**, 1892 cm^{-1}).[97] These values confirm the electron rich nature of the {OsX(PNP)} platform and increased back bonding in comparison with the Ru^{II} analogue [RuCl(L^3)(CO)] (**LXXVII**, $\tilde{\nu}_{CO} = 1916$ cm^{-1}).[191] Importantly, the NMR data of complexes **3** and **4** indicate the removal of the TIP experienced by parent **2** upon coordination of a fifth ligand (**3**: $\delta_P = 55.6$, $\delta_H = 7.04 - 1.19$ ppm; **4**: $\delta_P = 65.1$, $\delta_H = 6.92 - 1.16$ ppm).

2.3 Re(III) PNP Pincer Halide Complexes

Based on the results obtained for Os^{II}, a reinvestigation of isoelectronic **LXXIII** and **LXXIV** is promising. Furthermore, the influence of dehydrogenation of the ligand backbone and substitution of the halide ligands could provide additional insights into magnetic property - structure relationships. Stirring **LXXIII** with an excess of NaI results in the complete exchange of the chloride ligands resulting in the formation of $[ReI_2(L^1)]$ (**5**, Scheme 2.2) in 91% isolated yield. The NMR signals are unusually shifted with ^1H NMR signals in the range of $\delta_H = 3.31 - -0.71$ and a ^{31}P shift of $\delta_P = -164.2$ ppm. The complex can be further reacted with an excess of Mes*O at elevated temperatures to give the L^3 ligated system $[ReI_2(L^3)]$ (**6**, Scheme 2.2) in 70% yield.

Scheme 2.2: Synthesis of **5** by salt metathesis and its dehydrogenation towards **6**.
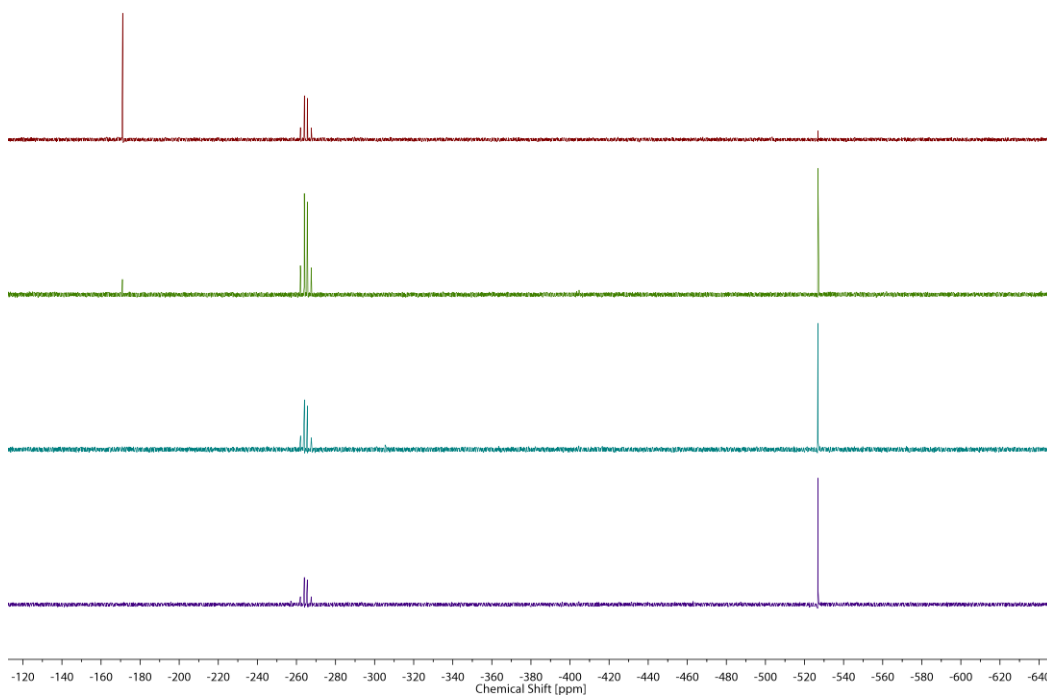
Figure 2.6: Dehydrogenation of **5** with Mes*O (5.0 eq.), C_6D_6, 50°C, after 30 min (red), 2 h (green), 18 h (turquoise), 24 h (purple).
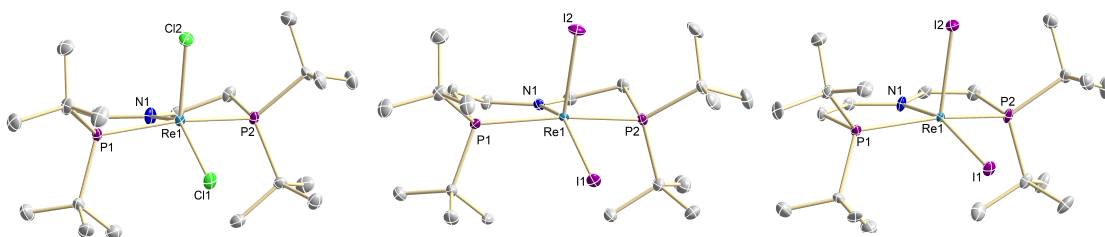
Figure 2.7: Molecular structure of complex **LXXIII**, **5** (middle) and **6** (right) from single-crystal X-ray diffraction (thermal ellipsoids drawn at the 50% probability level); hydrogen atoms are omitted for clarity. Selected bond lengths [Å] and angles [°]: **LXXIII**[52] Re1-Cl1 2.364(2), Re1-Cl2 2.331(2), Re1-N1 1.923(7), Re1-P1 2.402(2), Re1-P2 2.407(3), N1-Re1-Cl1 140.8(3), P1-Re1-P2 163.04(9), $\tau = 0.37$; **5** Re1-I1 2.7156(2), Re1-I2 2.6382(2), Re1-N1 1.926(2), Re1-P1 2.4277(8), Re1-P2 2.4172(8); N1-Re1-I1 151.09(7), N1-Re1-I2 107.70(7), P1-Re1-P2 161.62(3), $\tau = 0.18$; **6** Re1-I1 2.6336(3), Re1-I2 2.6898(3), Re1-N1 1.994(4), Re1-P1 2.4470(12), Re1-P2 2.4568(12), N1-Re1-I1 159.21(11), N1-Re1-I2 100.39(11), P1-Re1-P2 158.12(4), $\tau = 0.02$.

Over the course of the reaction, the half-saturated complex $[\text{ReI}_2(\text{L}^2)]$ can be observed as an intermediate by ^{31}P NMR, as indicates by the detection of two inequivalent phosphorus atoms ($\delta_\text{P} = -263.6, -266.5\,\text{ppm}$, $^2J_\text{PP} = 240\,\text{Hz}$, Figure 2.6), that cleanly convert to **6**. The ^1H and ^{31}P NMR values are further shifted with respect to **5** ($\delta_\text{H} = 4.30$ - -7.08, $\delta_\text{P} = -526.9\,\text{ppm}$). In the solid state, **LXXIII** and **5** exhibit almost identical bond lengths between the metal center and the PNP pincer scaffold, however **5** adopts a more square-pyramidal geometry as indicated by its τ-value (Figure 2.7). The molecular structure of **6** reveals a shortening of the Re1-I1 distance with respect to **5** due to the
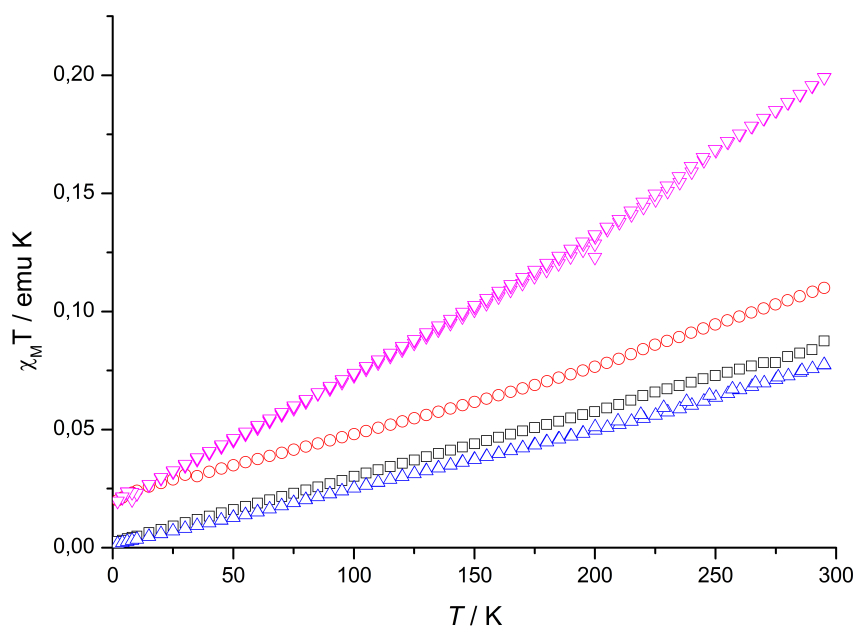
Figure 2.8: Top: $\chi_\text{M}T$ vs. T plot of **LXXIII** (black), **LXXIV** (red), **5** (blue) and **6** (pink).

reduced bite angle and the decreased π-donating properties of the pincer framework. The overall coordination mode is close to ideal square-pyramidal ($\tau = 0.02$). The Re-N1 bond is elongated by $\Delta d = 0.07$ Å which is close to the isoelectronic Os complex **2**. The observed ^{31}P NMR chemical shift values become more negative upon substitution of the chloride for iodide ($\Delta \delta_P = 112.7$ ppm) and ligand dehydrogenation ($\Delta \delta_P = 224.1$ (Cl), 251.9 ppm (I), Figure 2.8, Table 2.1). SQUID magnetometry reveals that the observed chemical shifts do not correlate with the magnetic moment of the substances (Figure 2.8, Table 2.1). All complexes feature linear behavior in the temperature region of $2 - 300$ K, indicating no thermal population of excited states, as observed for the square-planar Os^{II} complex **2**. For **LXXIII**, **LXXIV** and **5** similar $\chi_M T$ values are obtained whereas **6** differs significantly. A possible explanation lies in the reduced donor properties of iodide that lead to reduced ligand field splitting. Furthermore, L^3 also reduces the energetic gap between the ground state and excited states. A combination of both factors apparently leads to an increase in the magnetic moment suggesting that **6**, like **2**, can be described with a non-magnetic ground state which strongly mixes with excited states *via* SOC. Nevertheless, multi-reference computations are needed when such effects are observed since S is not a good quantum number and rather J should be used, as discussed above.

Table 2.1: ^{31}P NMR and SQUID values of **LXXIII**, **LXXIV**, **5** and **6**.

	LXXIII	**LXXIV**	**5**	**6**
δ / ppm	-51.5	-275.6	-164.2	-527.5
χ_M(TIP) / 10^{-6} cm^3 mol^{-1}	282.6	296.5	248.4	569.2

2.4 Five- and Six-Coordinate Os Bipyridine Complexes

A common strategy to vary the redox-potential of complexes is the exchange or attachment of ancillary ligands. 2,2'-bipyridine is particular attractive in case of **2** since it is a planar chelate ligand which should afford a sterically encumbered octahedral platform, without inducing too much steric strain on the PNP ligand. Additionally, this chelate is one of the most prominent ligands in photochemistry which could allow for light induced reactions.[208] For example, the Ir[III] hydride [Ir(Cp*)H(bipy)]$^+$ (**LXXVIII**, Scheme 2.3) is known to engage in multiple photochemical transformations.[209]–[214] A hypothetical isoelectronic, octahedral Os[II] hydride complex ligated by L^3 and bipy might exhibit rich photochemistry allowing for new transformations. For example, unprecedented photochemical CO_2 activation was reported for [NiH(L^3)] (**LXXIX**) to give a [Ni(COOH)(L^3)] (Scheme 2.3, **LXXX**).[215] Therefore, a six-coordinate Os[II] hydride complex is an attractive synthetic target.
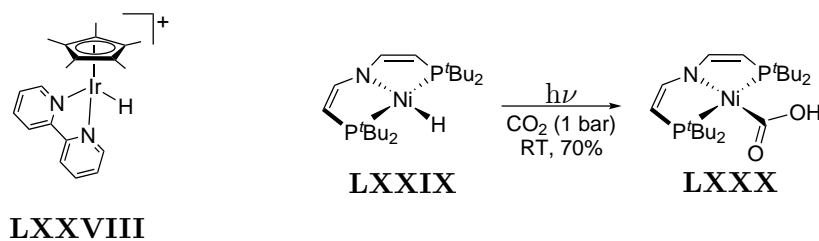
Scheme 2.3: Extensively studied Ir[III] photocatalyst **LXXVIII** and photochemical induced fixation of CO_2 by **LXXIX** to give **LXXX**.[209]–[215]

As described above, the square-planar halide **2** can be prepared *in situ* by addition of CoCp$_2$ to **1**. The addition of 2,2'-bipyridine in benzene allows for the isolation of [OsCl(L^3)(bipy)] (**7**, Scheme 2.4) in high yield. **7** does not show any signs of significant spin-orbit coupling contributions to the ^{1}H NMR signals as indicated by well-resolved coupling constants and shift values similar to complexes obtained by the addition of monodentate π-acceptors to **2** (Chapter 2).
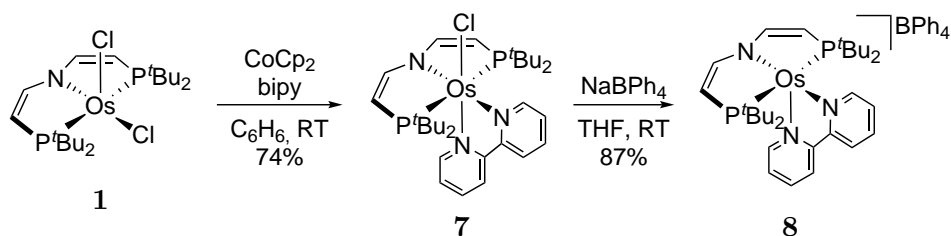
Scheme 2.4: Synthesis of **7** by addition of 2,2'-bipyridine to *in situ* generated **2** and successive chloride removal yielding **8**.

In the solid state, **7** exhibits a distorted octahedral coordination sphere (Figure 3.6). In comparison to **2**, the Os-N distance of the pincer ligand is significantly elongated due to the more electron rich Os^{II} center. The bipyridine ligand remains planar suggesting no significant charge transfer by the metal center. Furthermore, the metal-chloride distance is elongated by $\Delta d \approx 0.1\,\text{Å}$ with respect to **2**. Addition of NaBPh$_4$ results in the clean formation of [Os(L^3)(bipy)][BPh$_4$] (**8**, Scheme 2.4) in almost quantitative yield. The solid-state structure of **8** reveals a distorted square-pyramidal complex ($\tau = 0.30$) with a slightly shortened Os1-N1 distance due to increased π-donation of the pincer ligand. The ^{1}H NMR signals of **8** reveal C_{2v}-symmetry on the NMR timescale suggesting that the solid-state structure is not preserved in solution due to a flexible bipy ligand.
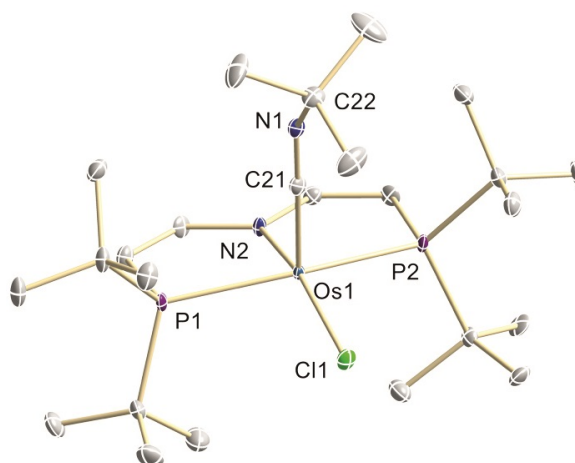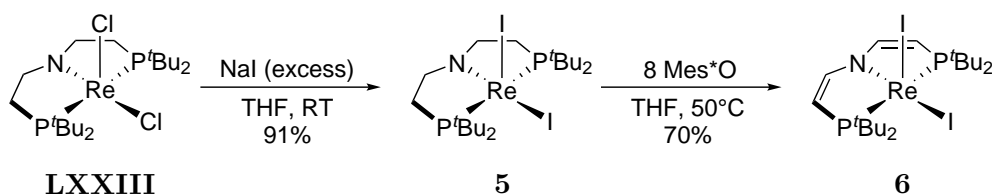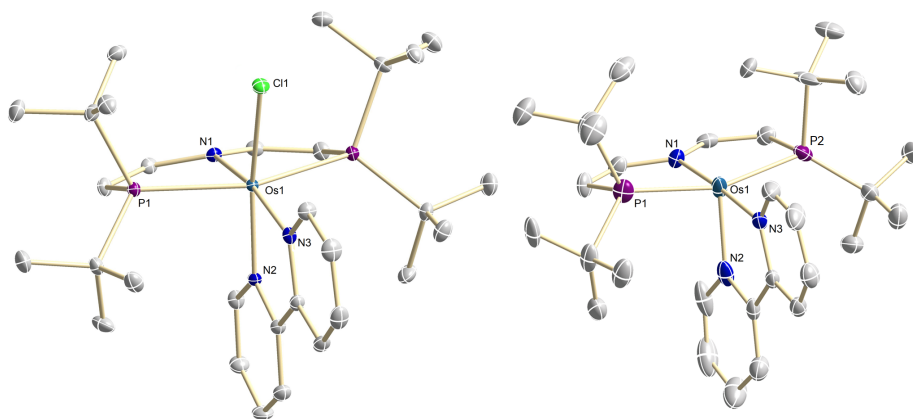

Figure 2.9: Molecular structure of **7** (left) and **8** from single-crystal X-ray diffraction (thermal ellipsoids at the 50% probability level); hydrogen atoms, solvent and anion molecules are omitted for clarity. Selected bond lengths [Å] and angles [°]: **7** Os1-Cl1 2.4557(6), Os1-N1 2.120(2), Os1-N2 2.031(2), Os1-N3 2.060(2), Os1-P1 2.4352(5), N1-Os1-Cl1 107.00(6), P1-Os1-P1# 156.05(2); **8** Os1-N1 2.015(4), Os1-N2 2.039(3), Os1-N3 2.036(2), Os1-P1 2.3676(7), Os1-P2 2.3852(7), N1-Os1-N3 178.02(16), P1-Os1-P2 160.29(2), $\tau = 0.30$.

With L^3 and bipy attached to the Os center, the question arises if electrons can be stored on either of the two ligands since L^3 exhibits redox non-innocent behavior in the case of 3d metals.[192],[201] Additionally, clearly defined bipy$^-$ ligand are scarce due to the difficult discrimination between strong back-bonding and electron transfer in such systems.[216],[217] The cyclic voltammogram of **8** features two reductive redox events (Figure 2.10). The first wave is reversible with $E_{1/2} = -1.83\,\text{V}$ while the second redox event at $E_{\text{p.c.}} \approx -2.59\,\text{V}$ vs. Fc$^{0/+}$ appears pseudo-reversible. When **8** is reacted with an excess of NaHg in THF a color change from brown to dark red can be observed. The ^{31}P NMR spectrum features no detectable signals indicating the formation of a paramagnetic species. Over the course of several minutes the formation of asymmetric diamagnetic products can be observed in the ^{31}P NMR which were not further investigated (Appendix 8.2.4).
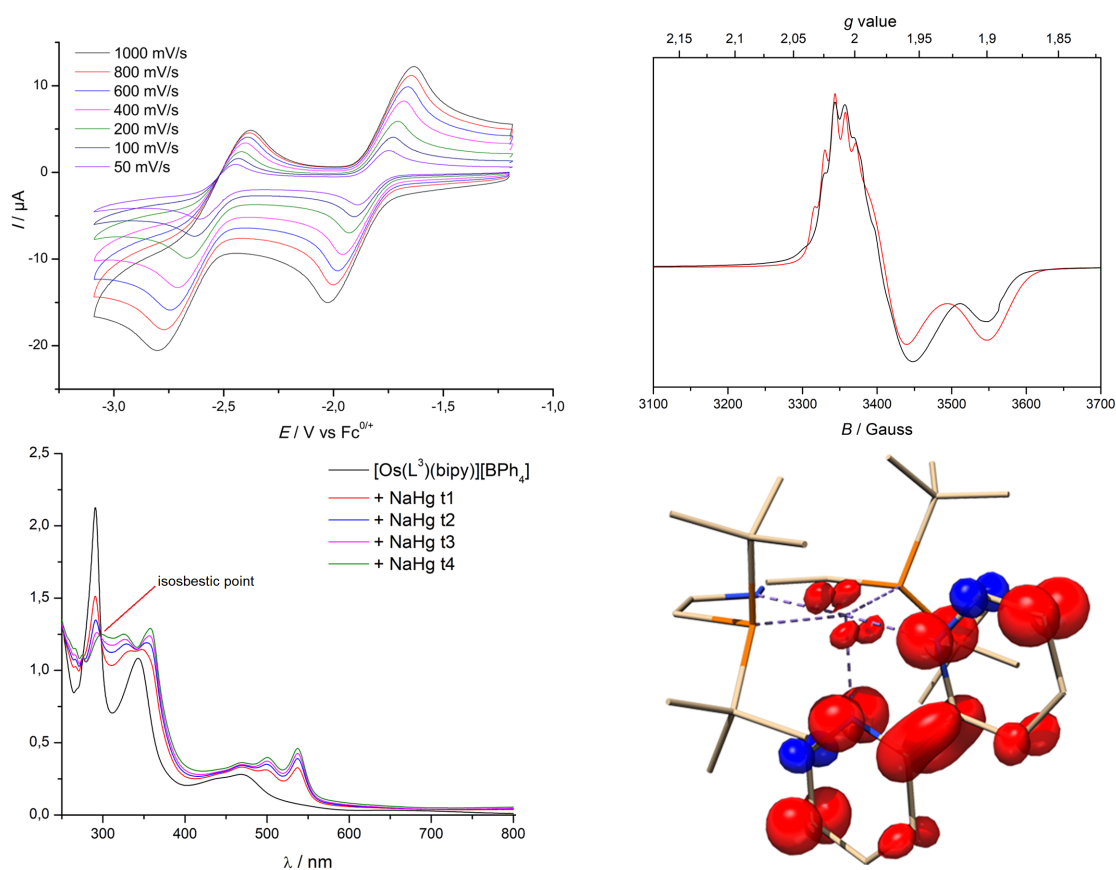
Figure 2.10: Top left: Cyclovoltammogramm of **8**, 0.1 mM, THF, 0.1 M NBu$_4$PF$_6$, RT; Top right: EPR spectrum of **9**, 140 K, 9.434 GHz, Simulation: $g_x = 1.898$, $g_y = 1.976$, $g_z = 2.015$, A$_{1/2}$(^{14}N)$= -, -, 40$ MHz; Bottom left: UV/vis spectrum of **8** and its reduction with NaHg, $5 \cdot 10^{-5}$ mM, THF, RT, 30 s intervals; Bottom right: Spin-density of **9**.

Keeping the reaction mixture at low temperatures did no lead to formation of single crystals suitable for X-ray diffraction. Following the reduction of **8** with NaHg by UV/vis spectroscopy reveals an isosbestic point at $\lambda = 298$ nm suggesting clean initial reduction (Figure 2.10). An EPR spectrum of the reaction mixture shows a narrow, rhombic EPR signal ($\Delta B = 300$ G) with resolved ^{14}N super-hyperfine interaction for one g-value. Based on this results, DFT calculations were performed to clarify if [Os(L^3)(bipy)] (**9**) is indeed formed as the initial reaction product. Theory predicts the electron to be mainly located at the bipy ligand with only minor contributions of the Os center which features a spin density of 4.1%. The computed EPR parameters reproduce the experimental findings and confirm that nitrogen hyperfine interaction, caused by spin polarization, is only observed at one of the principal axis which is in agreement with the observed spectrum (Appendix 8.1). Other orientations of the hyperfine interaction tensor could not be quantified due to significant line broadening. However, combination of spectroscopy and theory supports the assumption that **9** is observable and exhibits

a certain lifetime at room temperature. The two-electron reduction of **8** was extremely sluggish and produced multiple products which were not further investigated. **7** and **8** should exhibit a high tendency to bind anionic ligands such as azide or hydride due to the labile chloride ligand and the cationic charge, respectively.
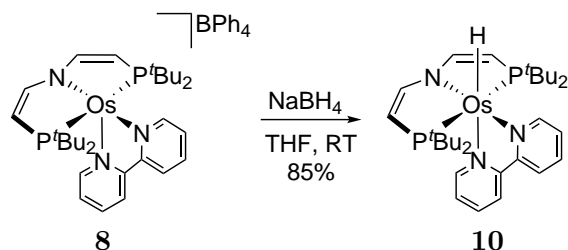
Scheme 2.5: Synthesis of **10** by addition of NaBH$_4$ to **8**.

By reacting **8** with an excess of NaBH$_4$ the hydride complex [OsH(L^3)(bipy)] (**10**, Scheme 2.5) can be isolated in 85% yield. Although confirmation of the existence of the hydride ligand was not accurately possible by X-ray crystallography (Figure 2.11), the complex is easily identified by its characteristic ^{1}H NMR and IR signals ($\delta_H = -11.0$ ppm, $\tilde{\nu}_{OsH} = 2074$ cm^{-1}). **10** is a dark powder which easily dissolves in polar and apolar solvents with a dark greenish color, hinting towards multiple electronic absorptions in the UV/vis region. In fact, the electronic absorption spectrum exhibits multiple intense absorptions in the visible range (Figure 2.11). Time-dependent functional theory is in good agreement with the experimental spectrum accompanied by a typical offset to higher energies.[218] The absorptions with the most prominent oscillator strengths were visualized by their difference densities (Figure 2.11). The highest energy absorption at $\lambda = 248$ nm (a) is caused by a $\pi \rightarrow \pi^*$ transition of the bipy ligand. The band at $\lambda = 290$ nm consists of multiple intense transitions. While (b) and (c) are bipy centered $\pi \rightarrow \pi^*$ transitions, band (d) is caused by an MLCT process of the Os-N$_{PNP}$ unit to the pincer backbone.

A similar process is found within the broad absorption at $\lambda = 386$ nm (e) with small admixtures of the bipy π-orbitals accompanied by an Os-bipy MLCT process (f). The shoulder at $\lambda = 435$ nm and the broad transition at $\lambda = 575$ nm are caused by transitions of the metal d orbitals into the π^*-orbitals of the bipy ligand (g,h). Since the transitions appear well-separated, **10** could represent an attractive compound for future band-selective hydride photochemistry.
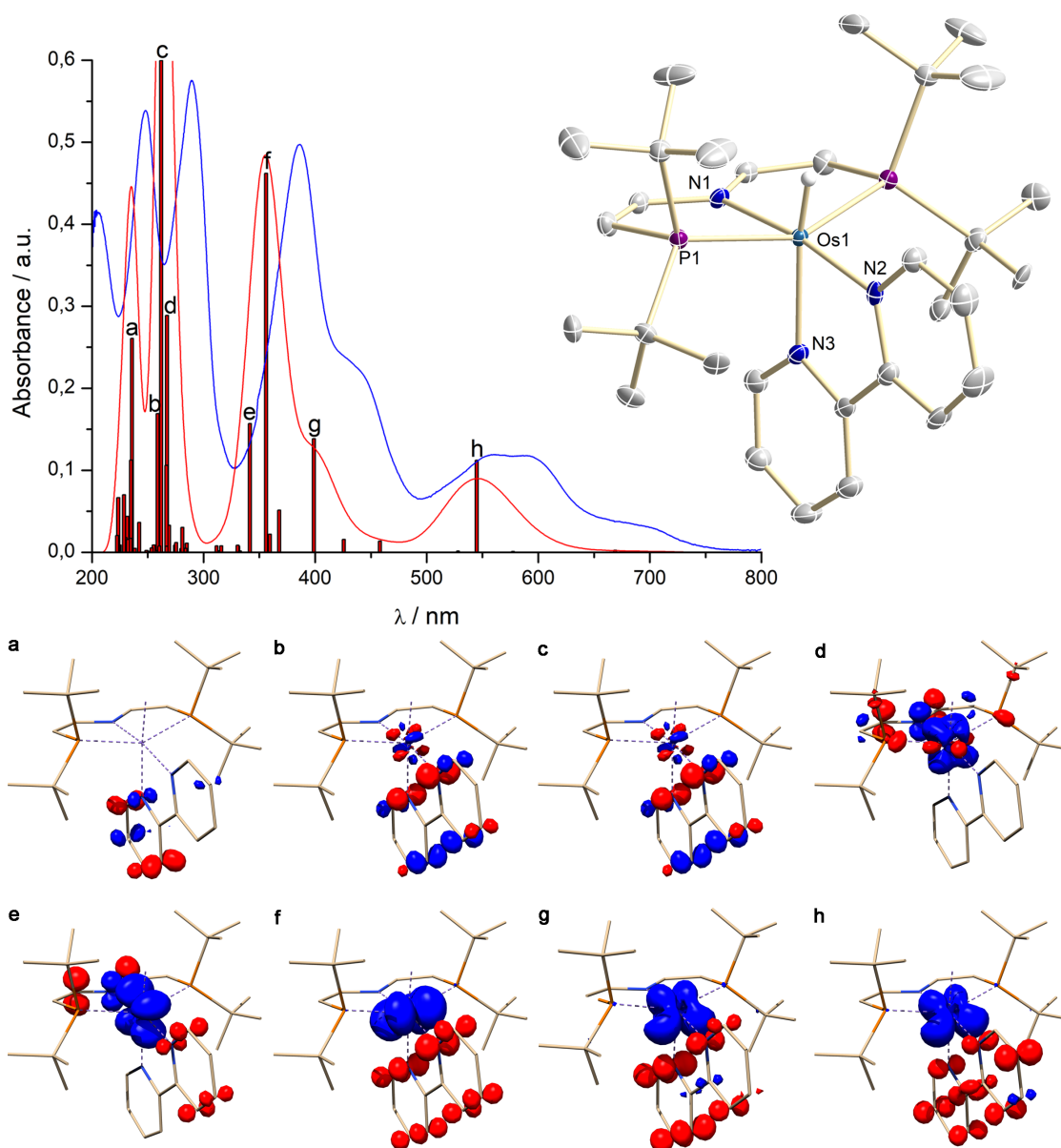
Figure 2.11: Top left: Experimental (blue) and computed (red, sticks and broadened by 2500 cm^{-1}) UV/vis spectrum of **10**, $3 \cdot 10^{-5}$ M, pentane, RT; Top right: Molecular structure of **10** from single-crystal X-ray diffraction (thermal ellipsoids at the 50% probability level); hydrogen atoms, except the hydride ligand, are omitted for clarity. Selected bond lengths [Å] and angles [°]: **10**: Os1-N1 2.103(5), Os1-N2 2.021(5), Os1-N3 2.096(5), Os1-P1 2.3621(11), N1-Os1-N2 170.1(2), P1-Os1-P1# 152.17(5); Bottom: Selected computed difference densities (loss and gain of electron density is depicted in blue and red, respectively).

2.5 Re and Os PNP Pincer Complexes Ligated by a Hemilabile Chelate

Heavy pnictide ligands presumably exhibit a strong *trans*-influence. The presence of a ligand in *trans*-position would therefore result in a destabilization of the multiple bond. The higher reactivity might lead to unwanted follow-up reactivity and thermal instability. However, the pnictide transfer reagents PnCO⁻ (Pn = P, As) also release carbon monoxide upon triple-bond formation which could also bind to the starting material, inhibiting further reactivity, or destabilize the reaction product. Consequently, a system is to be designed that does not react with carbon monoxide but also allows for the generation of isolable M≡Pn species. Linkage isomerism is an attractive strategy in this particular case. The system needs to be flexible enough to form stable compounds in monodentate and chelating coordination modes, preferably upon binding to different donor sites of the chelate ligand. Therefore, 3-(1*H*-pyrazol-3-yl)-pyridine (^{H}PyrPz) was introduced as a possible hemilabile ligand by reaction with **5** under basic conditions yielding [ReI(L^1)($\kappa^2 N^1, N^3$-PyrPz)] (**11**, Scheme 2.6). **11** exhibits an octahedral coordination mode in the solid state with the iodide in the apical position. The chelate ligand is fully coordinated with the pyrazole unit in *trans*-position to the iodide ligand which slightly elongates when compared to **5** (Figure 2.12, Table 2.2).
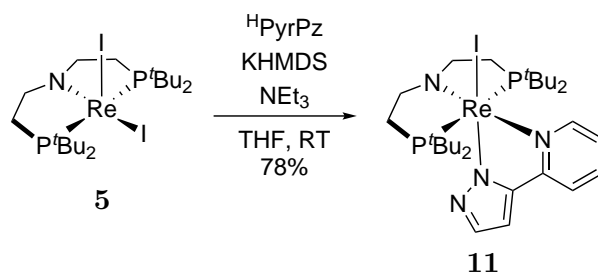
Scheme 2.6: Synthesis of **11** by reaction of **5** with ^{H}PyrPz.

In analogy to the Re^{III} iodide **11**, a six-coordinate Os complex featuring the PyrPz ligand could give rise to more selective Os≡P(R) chemistry. Stirring **1** with ^{H}PyrPz results in the clean formation of the octahedral Os^{III} complex [OsCl(L^3)($\kappa^2 N^1 N^3-$PyrPz)] (**12**, Scheme 4.13) in 90% isolated yield. **12** features a rhombic EPR signal with pronounced g-anisotropy ($g_x = 1.498$, $g_y = 2.095$, $g_z = 2.530$) and no resolved hyperfine coupling, in analogy to the values obtained for **1** (Scheme 2.13). In the solid state, **12** features a slightly distorted octahedral coordination geometry. In comparison with **11**, the Os-N$_{PNP}$ distance is slightly elongated ($\Delta d \approx 0.1$ Å) due to the higher d electron count with the remaining bonding parameters being almost identical (Table 2.2).

Figure 2.12: Solid state structure of **11** from single-crystal X-ray diffraction (thermal ellipsoids drawn at the 50% probability level); hydrogen atoms are omitted for clarity. Selected bond lengths [Å] and angles [°]: **11** Re1-I1 2.7966(4), Re1-N1 1.900(4), Re1-N2 2.213(4), Re1-N3 2.081(4), Re1-P1 2.4532(12), Re1-P2 2.4713(13), N1-Re1-N2 173.58(16), P1-Re1-P2 160.03(4).
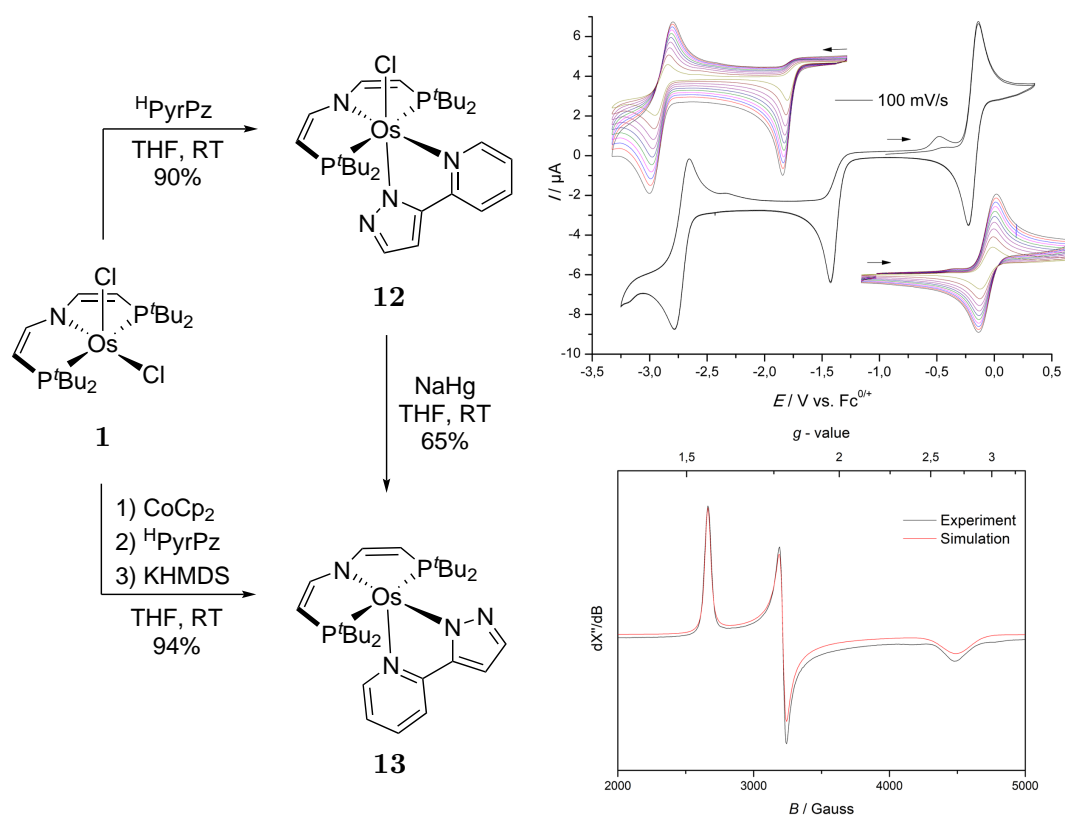
Figure 2.13: Left: Synthesis of **12** and **13** starting from **1**, respectively; Right: Cyclic voltammogram (top) of **12**, $100 \, \text{mV} \cdot \text{s}^{-1}$, $1 \, \text{mM}$, $0.1 \, \text{M} \, \text{NBu}_4\text{PF}_6$, THF, RT; Inset: Isolated scans of oxidative and reductive regions, $1 \, \text{V·s}^{-1}$ - $100 \, \text{mV·s}^{-1}$; EPR spectrum (bottom) of **12**, $g_x = 1.498$, $g_y = 2.095$, $g_z = 2.530$, toluene, $150 \, \text{K}$, $9.4324 \, \text{GHz}$

Figure 2.14: Molecular structure of complex **12** (left) and **13** (right) from single-crystal X-ray diffraction (thermal ellipsoids drawn at the 50% probability level); hydrogen atoms are omitted for clarity. Selected bond lengths [Å] and angles [°]: **12** Os1-N1 2.017(3), Os1-N2 2.161(3), Os1-N3 2.063(3), Os1-Cl1 2.3837(9), Os1-P1 2.4297(6), N1-Os1-N2 157.83(11), P1-Os1-P1# 157.74(3); **13**: Os1-N1 2.087(3), Os1-N2 2.041(3), Os1-N3 2.065(3), Os1-P1 2.3937(9), Os1-P2 2.3129(9), N1-Os1-N3 171.21(12), P1-Os1-P2 158.92(3).

Table 2.2: Comparison of the PyrPz ligated Re and Os Systems **11**, **12**, **13**, and the corresponding dihalide compounds **5** and **1**.

	$M-N_{PNP}$	$M-N_{pyrazole}$	$M-N_{pyridine}$	$M-X_{apical}$
5	1.926(2)			2.6382(2)
11	1.900(4)	2.081(4)	2.213(4)	2.7966(4)
1	1.980(2)			2.319(2)
12	2.017(3)	2.063(3)	2.161(3)	2.3837(9)
13	2.087(3)	2.065(3)	2.041(3)	

The six-fold coordination environment results in a minor elongation of the $Os-N_{PNP}$ and the $Os-Cl_{apical}$ bond distance. Cyclic voltammetry reveals a reversible oxidation at $E_{1/2} = -0.18\,V$ and an irreversible followed by a pseudo-reversible reductive redox event at $E_{p.c.} \approx -1.40$ and $E_{1/2} = -2.71\,V$ vs. $Fc^{0/+}$ suggesting initial chloride loss upon reduction (Figure 2.13). In fact, one-electron reduction of **12** with NaHg results in the clean formation of $[Os(L^1)(\kappa^2 N^1 N^3 - PyrPz)]$ (**13**, Figure 2.13). The complex can alternatively be synthesized in almost quantitative yield by successive addition of $CoCp_2$, ^{H}PyrPz and KHMDS to **1**. In the solid state, **13** features a slightly distorted square-pyramidal coordination sphere (Figure 4.16). The chelate ligand rearranged itself upon reduction with the pyrazole moiety in the equatorial position. The $Os-N_{PNP}$ distance is slightly elongated with respect to **12** due to the increase in oxidation state ($\Delta d \approx 0.07\,Å$). The NMR spectroscopic signals suggest no significant admixture of excited states ($\delta_P = 24.6$, $\delta_H = 8.42 - 0.64\,ppm$).

2.6 Conclusion

In summary, the isolation and full characterization of a square-planar Os^{II} species was presented. Spectroscopic, crystallographic and magnetic characterization of **2** indicates an energetically separated ground state, which is subject to large TIP. A correlated single-reference *ab initio* formalism on the basis of CCSD(T) expansions predicts a triplet ground state energetically close to an excited singlet state. Multi-reference computations corroborate the experimental picture and assign an electronic triplet ground state, which is strongly stabilized by mixing with excited states through SOC. Additionally, isoelectronic, five-coordinate Re^{III} complexes were investigated. The L^3 scaffold in combination with iodide ligands enforces strong TIP to occur in the case of Re. Moreover, SQUID measurements show that the observed NMR shifts give no direct indications of the magnitude of this effect.

The synthesis and characterization of a new PNP pincer bipy system was demonstrated. The complexes **7** and **8** can be isolated in high yield and represent suitable platforms for the synthesis of octahedral Os^{II} complexes by addition of anionic nucleophiles. Furthermore, one-electron reduction yields the neutral radical complex **9** with the electron density mainly located at the bipy ligand which possesses a limited live-time at room temperature. The hydride complex **10** could be isolated in high yield and represents a promising entry into Os hydride photochemistry based on multiple well-separated absorptions in the visible spectrum.

The hemilabile ligand 3-(1*H*-pyrazol-3-yl)-pyridine (^{H}PyrPz) was utilized to obtain the Re^{III} complex **11**. Additionally, the Os^{III} complex **12** was synthesized which can be cleanly converted to the five-coordinate Os^{II} species **13**. Both platforms represent interesting entries for the synthesis of multiply bonded pnictide species due to the possible linkage isomerism of the PyrPz ligand which accounts for the expected strong *trans*-influence of these ligands.

Os Nitride and Imide Complexes in Various Coordination Spheres

Parts of this chapter were adapted from:

J. Abbenseth, S. C. Bete, M. Finger, C. Volkmann, C. Würtele, S. Schneider*,
Organometallics **2018**, *37*, 802-811.

Author contributions

J.A.	Synthesis, spectroscopy and theoretical calculations
S.B.	Synthesis and spectroscopy (supporting)
M.F.	Relaxed surface scan calculation
C.V.	Crystallography (Chapter 3.1, supporting)
C.W.	Crystallography

3 Os Nitride and Imide Complexes in Various Coordination Spheres

3.1 Four-and Five-Coordinate Os(IV) Nitrides and Imide Complexes

Based on the successful isolation of **2**, the synthesis and follow-up chemistry of square-planar nitride complexes will be evaluated. The reaction of *in situ* generated **2** with $[N(PPh_3)_2]N_3$ ([PPN]N_3) at room temperature results in an immediate color change from purple to brown. From this mixture the square-planar Os^{IV} nitride $[OsN(L^3)]$ (**14**, Scheme 3.1) can be isolated in over 60% yield. No intermediate azide complex was detected by NMR or IR spectroscopy indicating rapid dinitrogen elimination after salt metathesis. Alternatively, **1** undergoes clean chloride-azide exchange by reacting with TMSN$_3$ to generate a putative open shell nitride which is subsequently oxidized by the trityl cation, which is not able to oxidize parent **1**, to generate the Os^{VI} nitride $[OsNCl(L^3)][PF_6]$ (**15**, Scheme 3.1). A characterization of intermediate $[OsNCl(L^3)]$ was not targeted since rapid dinitrogen coupling is expected to proceed without oxidant present as observed for group 9 nitrides ligated by L^3.[80],[82],[113] The spectroscopic and crystallographic characterization of **15** confirms the typical square-pyramidal ($\tau = 0.14$)[202] coordination geometry found for Os^{VI} with the nitride ligand in the apical position (Figure 3.1). Treatment of **15** with an excess of NaHg allows for the isolation of **14** in 95% yield. The cyclic voltammogram features an irreversible redox event at $E_{p.c.} \approx -1.48\,\text{V}$ (an oxidative event was not observed, Appendix 8.2.2).
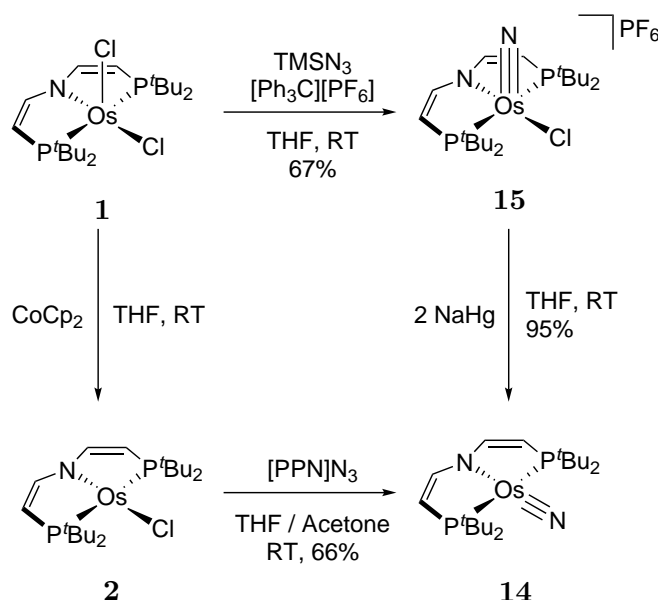
Scheme 3.1: Synthesis of square-planar Os^{IV} nitride **14**.
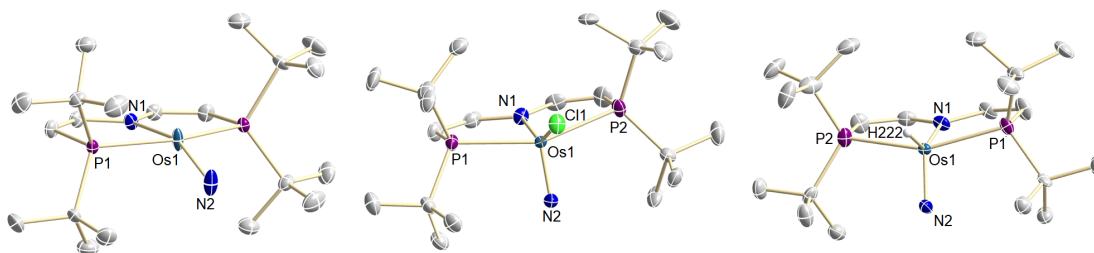
Figure 3.1: Molecular structure of complex **14** (left), **15** (middle) and **16** (right) derived by single-crystal X-ray diffraction (thermal ellipsoids drawn at the 50% probability level); hydrogen atoms except H222 and anions are omitted for clarity. Selected bond lengths [Å] and angles [°]: **14** Os1-N1 2.137(3), Os1-N2 1.735(5), Os1-P1 2.3697(7), N1-Os1-N2 152.8(2), P1-Os1-P1# 158.60(4); **15** Os1-Cl1 2.3277(18), Os1-N1 1.977(3), Os1-N2 1.629(4), Os1-P1 2.4400(12), Os1-P2 2.4408(11), N1-Os1-N2 107.55(19), P1-Os1-P2 155.35(4), $\tau = 0.14$; **16** Os1-H222 1.67(4), Os1-N1 2.029(3), Os1-N2 1.630(2), Os1-P1 2.4118(6), Os1-P2 2.4277(6), N2-Os1-H222 97.2(15), N1-Os1-H222 143.4(15), N1-Os1-N2 119.45(13), P1-Os1-P2 154.54(2), $\tau = 0.19$.

Multinuclear NMR characterization of diamagnetic **14** indicates C_{2v}-symmetry on the NMR timescale at room temperature ($\delta_{t\mathrm{Bu}} = 1.54$ ppm, 36H). However, the molecular structure in the solid state features a distinctively bent Os≡N unit with respect to the pincer backbone (N1-Os1-N2: 152.8(2)°). Such bending was also found for the previously reported nitride **XXXV**, albeit less pronounced (N1-Os1-N2: 168.02(11)°) as well as for the Ru^{IV} nitrides [RuN(L$^{Si/1}$)] (N1-Ru1-N2: 155.86(13)/165.3(3)°).[81],[83],[86] In fact, computational analysis of **XXXV** indicated very flat N-M-N bending potentials as a result of two mutually opposing effects. Bending of the strong donor ligand nitride out of the plane defined by the pincer ligand stabilizes the HOMO with mainly d$_{z^2}$ character (Scheme 3.3). In turn, the Os≡N triple bond length is slightly weakened due to reduced π-bonding, which is manifested by the longer nitride bond of **14** (Os1-N2: 1.735(5) Å) versus more planar **XXXV** (Os1-N2: 1.6832(18) Å).[83] The nitride bond length is also considerably longer in comparison with Os^{VI} nitrides such as **15** (Os1-N2: 1.629(4) Å, Figure 3.1) which is attributed to the lower formal oxidation state and *trans*-influence of the pincer ligand.

The electron rich Os^{IV} nitride **14** readily reacts with electrophiles, such as Brønsted acids and boranes. In analogy to **XXXV**, protonation results in electrophilic attack at the HOMO with mainly d$_{z^2}$ character (Figure 3.3). Using Brookhart's acid, [H(OEt$_2$)$_2$][BArF$_{24}$] (BarF$_{24}^-$ = B(C$_6$H$_3$-3,5-(CF$_3$)$_2$)$_4^-$), [OsNH(L^3)][BarF$_{24}$] (**16**, Scheme 3.2) can be isolated in over 80% yield. The hydride ligand of **16** is detected at $\delta_H = 0.47$ ppm by ^{1}H NMR spectroscopy. As expected for Os^{VI}, square-pyramidal osmium coordination ($\tau = 0.19$) is observed in the solid state with the strong donor ligand nitride in the apical position (Figure 3.1). The formal metal oxidation and the vacant site *trans* to the nitride results in decrease of the metal nitride bond length by more than 0.1 Å
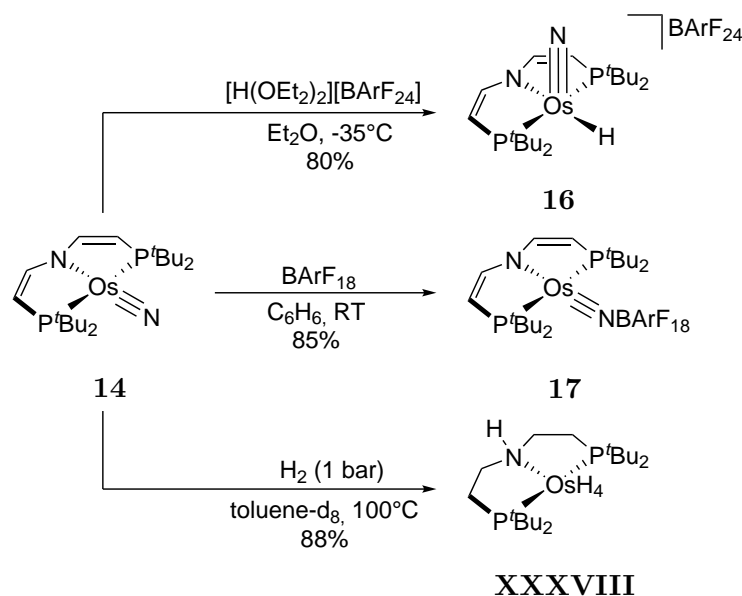
Scheme 3.2: Reactions of **14** with electrophiles to give **16** and **17** and hydrogenolysis of **14**.

(Os1-N2: 1.60(2) Å) in comparison to **14**. In contrast to Brønsted acids, the sterically demanding Lewis acid B(C$_6$H$_3$-3,5-(CF$_3$)$_2$)$_3$ (BArF$_{18}$) attacks the lone pair of the nitride ligand and the borane adduct [Os{NB(C$_6$H$_3$-3,5-(CF$_3$)$_2$)$_3$}(L^3)] (**17**, Scheme 3.2) was isolated in over 80% yield. Solution NMR characterization is in agreement with C_{2v}-symmetry. The structure is further confirmed by single-crystal X-ray analysis (Figure 3.2). The considerably reduced nitride bending of **17** (N1-Os1-N2: 174.6(2)/176.7(2)°) in comparison to parent **14** is accompanied by slight shortening of the osmium-nitride bond distance ($\Delta d = 0.03$ Å). In contrast to **XXXV**, which is selectively silylated at nitride lone pair with TMSBr, the reaction of **14** with trimethylsilyl halides is surprisingly sluggish, giving several products.

In previous work it was demonstrated that hydrogenolysis of [MN(L^1)] (M = Ru, Os) with dihydrogen yields ammonia and polyhydride complexes in high yield.[81],[83] Computational analysis of the Ru system suggests metal-ligand cooperative H$_2$ heterolysis across the metal-amide bond as the initial step of the reaction sequence. For the divinyl amide ligand L^3, not the amine nitrogen but the remote sp^2 carbon bound to phosphorus generally represents the basic pincer site.[192],[201] Exposure of **14** to H$_2$ (1 bar) at elevated temperatures results in clean conversion over 48h with release of NH$_3$ in about 88% yield as determined by indophenolic titration (Scheme 3.2, Figure 3.3). In addition to ammonia, the known tetrahydride **XXXVIII** is obtained as in the case of **XXXV** (Appendix 8.2.1). The full hydrogenation of the oxidized ligand L^3 to parent amine HL^1 suggests cooperative dihydrogen activation also for the unsaturated ligand L^3. The reaction was followed by NMR at 100°C to obtain further insights into the
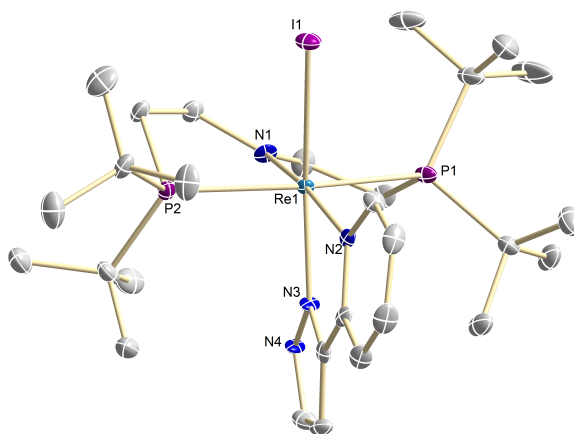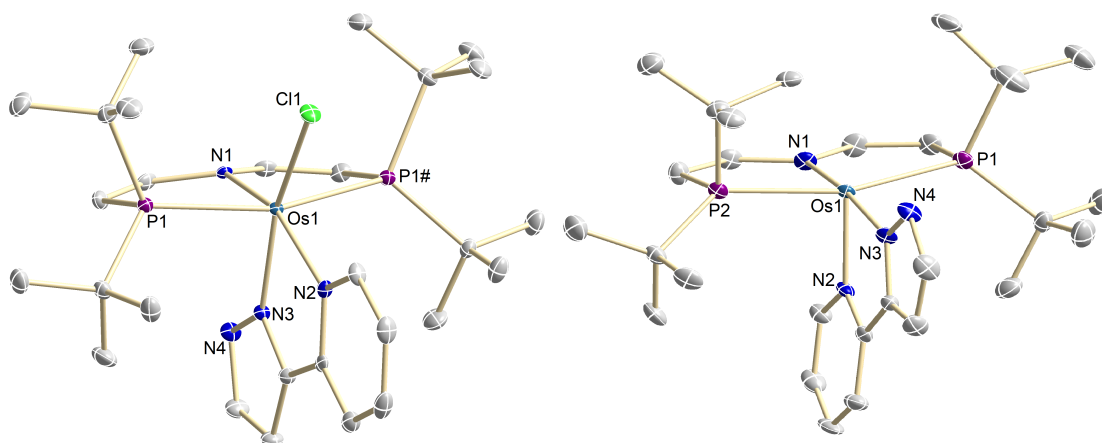
Figure 3.2: Molecular structure of complex **17** derived by single-crystal X-ray diffraction (thermal ellipsoids drawn at the 50% probability level); hydrogen atoms are omitted for clarity. Selected bond lengths [Å] and angles [°]: **17** (one of two independent molecules) B1-N2 1.593(9), Os1-N1 2.087(5), Os1-N2 1.700(5), Os1-P1 2.4282(16), Os1-P2 2.3991(17), B1-N2-Os1 173.6(4), N1-Os1-N2 174.6(2), P1-Os1-P2 156.07(6).

reaction mechanism. A fast 1st order decay of the starting material is observed with $k_{obs} = 0.353(3)\,h^{-1}$. Over the course of the reaction, two intermediates are observed which feature an asymmetric PNP pincer ligand due to the detected coupling patterns of the PNP phosphorus atoms (Figure 3.3). This can most likely be attributed to partial hydrogenation of the ligand backbone which occurs in several steps.[192] ^{1}H NMR spectroscopy did not give further insights into the structure of the intermediates due to broadened signals at 100°C. The formed product also exhibits broadened NMR signals at elevated temperatures, even in the ^{31}P{^{1}H} NMR, due to dynamic processes.[83]

Lewis acidic reactivity, such as the addition of a fifth ligand, might at first be anticipated for coordinatively unsaturated 16-valence-electron nitride complexes such as **XXXV** and **14**. However, five-coordinate d^4 nitrides are predicted to be unstable by the GB model.[77],[78],[219] In fact, both **XXXV** and **14** exhibit relatively high-lying LUMOs with mainly π*-antibonding character with respect to the metal nitride moiety, suggesting weak electrophilicity (Figure 3.3). Accordingly, PMe$_3$ attacks at the nitride ligand rather than the metal center of **XXXV**, forming an equilibrium with the corresponding phosphoraneiminato complex.[83] However, the addition of phosphines to nitrides is somewhat ambiguous due to synergistic donor/acceptor character of phosphines in the transition state.[220] In contrast to **XXXV**, complex **14** does not react with phosphines (PMe$_3$, PPh$_3$) or stronger nucleophiles such as Grignard reagents. The apparently reduced electrophilicity of **14** versus **XXXV** correlates with a longer osmium-nitride bond and stronger bending of the nitride ligand. This observation suggests that reduced covalency in metal-nitride bonding contributes to the shifted reactivity.
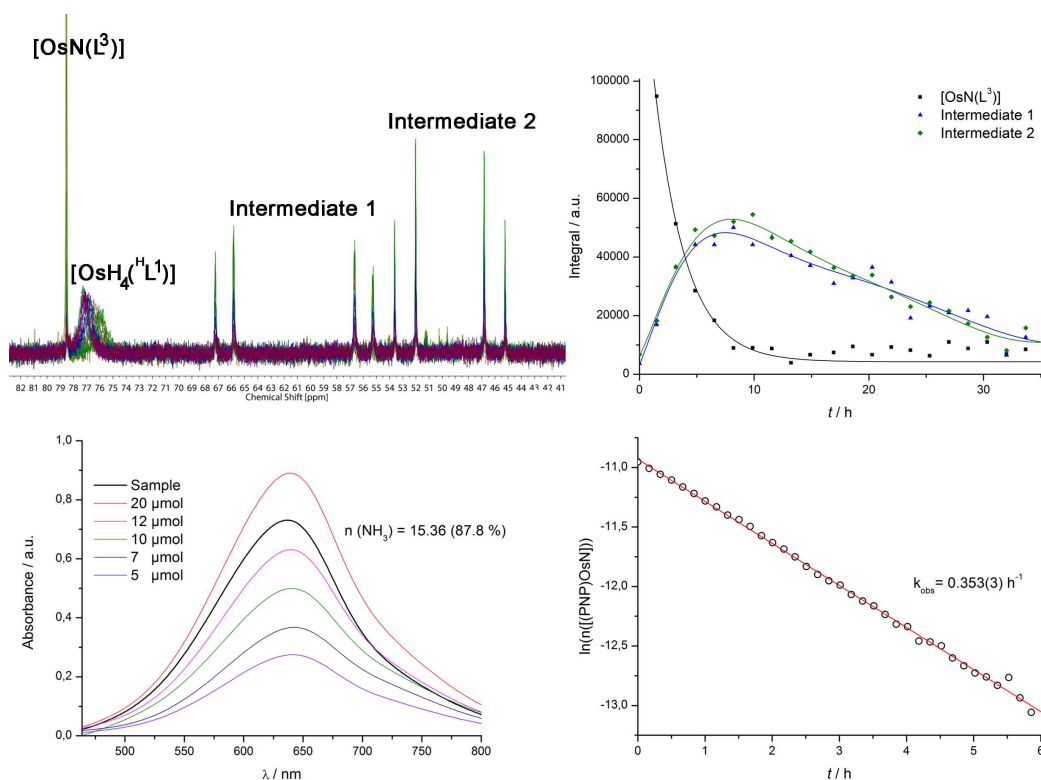
Figure 3.3: Top left: Stacked ^{31}P$\{^1$H$\}$ NMR spectra of the hydrogenation of **14** to **XXXVIII**, toluene-d_8, 100°C.; Top right: Integral-time plot of the decay of **14** and rise and fall of intermediate 1/2 over the course of the reaction; Bottom left: UV/vis spectrum of the indophenolic titration experiment to determine the amount of generated ammonia; Bottom right: 1st order plot of the decay of **14**.

In contrast to phosphines, **14** immediately reacts with CN^{t}Bu, even at low temperatures, as indicated by a color change from brown to bright green. Surprisingly, NMR spectroscopic characterization at −50°C and single-crystal X-ray analysis reveal the formation of an unprecedented five-coordinate Os$^{\text{IV}}$ nitride, the thermally unstable complex [OsN(L^3)(CN^{t}Bu)] (**18**, Scheme 3.3). A particular striking structural feature of square-pyramidal **18** ($\tau = 0.03$) is the basal coordination of the nitride ligand (Figure 3.2). This contrasts with all other square-pyramidal nitrides, which favor axial nitride coordination as a consequence of the strong *trans* influence. Furthermore, the isonitrile ligand exhibits an unusual tilt (Os1-C21-N3: 165.16(8)/164.27(18)°). Marked bending within the isonitrile ligand and the distinct bathochromic shift of the C≡N stretching vibration ($\tilde{\nu}_{\text{CN}^t\text{Bu}} = 2007\,\text{cm}^{-1}$) support significant back-donation by the {OsN(L^3)} platform. However, both values and the C≡N bond lengths (C21-N3: 1.175(3)/1.180(3) Å) still favor the isonitrile over the azavinylidene resonance representation.[53],[207] Interestingly, coordination of the isonitrile ligand keeps the nitride bond distance and angle almost unchanged (Os1-N2: 1.6995(18) Å, N1-Os1-N2: 152.69(8)°).
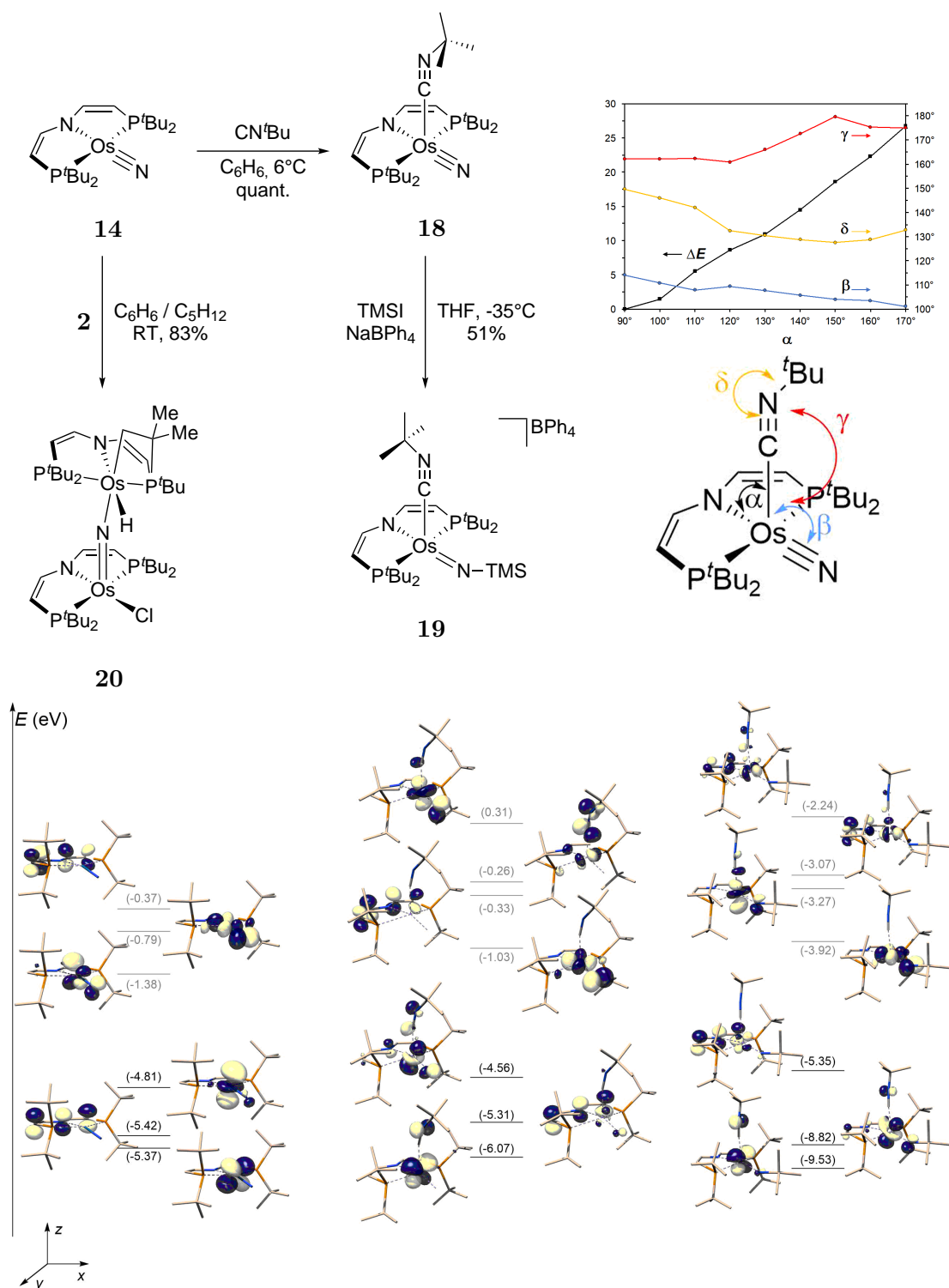
Scheme 3.3: Top left: Syntheses of five-coordinate Os^{IV} nitrido (**18**) and imido (**19**, **20**) complexes; Top-right: Relaxed surface scan for the (^{t}BuNC)-Os-N_{amide} angle (α) and selected structural parameters (y-axis right), energies given in units of $kcal \cdot mol^{-1}$ (y-axis left); Bottom: Computed MO scheme of **14** (left), **18** (middle) and **19** (right). Unoccupied MOs are drawn in grey and the MO energies are given in eV.
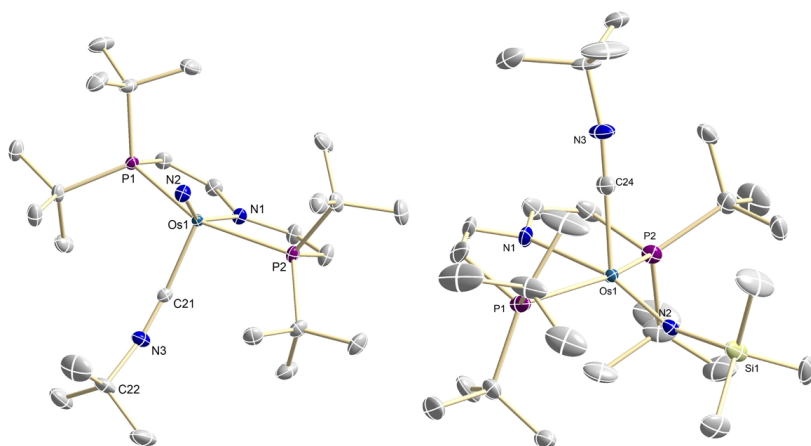
Figure 3.4: Molecular structure of complex **18** (left) and **19** (right) derived by single-crystal X-ray diffraction (thermal ellipsoids drawn at the 50% probability level); hydrogen atoms are omitted for clarity. Selected bond lengths [Å] and angles [°]: **18** (one of two independent molecules) C21-N3 1.175(3), Os1-C21 1.941(2), Os1-N1 2.2423(17), Os1-N2 1.6995(18), Os1-P1 2.4022(5), Os1-P2 2.4027(5), C21-N3-C22 160.7(2), N1-Os1-C21 91.25, N2-Os1-C21 116.05(9), N1-Os1-N2 152.69(8), P1-Os1-P2 150.970(18); **19** C24-N3 1.151(6), Os1-N1 2.237(4), Os1-N2 1.754(4), Os1-C24 1.933(5), Os1-P1 2.4169(12), Os1-P2 2.4232(13), C24-N3-C25 170.9(6), N1-Os1-C24 74.38(19), N2-Os1-C24 122.4(2), N1-Os1-N2 163.18(17), Os1-C24-N3 179.0(4), P1-Os1-P2 148.28(5), Os1-N2-Si1 156.8(3).

DFT computations were carried out to rationalize the stability and unusual structural features of complex **18**. The DFT model reproduces basal nitride and tilted isonitrile coordination (Os1-C21-N3: 162.1°). In fact, a local minimum for axial nitride coordination could not be found and a relaxed surface scan reveals a relatively steep energy surface that is around $25\,\text{kcal·mol}^{-1}$ above the ground state for such a structure (Scheme 3.3 right). The computed frontier orbital MO scheme of **18** indicates considerable mixing of the metal in-plane interactions with the nitride and the isonitrile (Figure 3.3). A more localized bonding picture is provided by natural bond orbital (NBO) analysis (Scheme 3.4). The natural localized molecular orbital (NLMO) that represents the isonitrile/metal σ-interaction reveals donation of the carbon lone pair into the metal d_{xz} orbital. The Os≡N antibonding character of this orbital results in a three-center/four-electron interaction of the metal with the isocyanide (σ) and the nitride (π) ligand, in addition to the two cleanly defined 2c2e σ- and π-Os≡N bonds. However, this geometry also enables back-donation from the high-lying d_{z^2} orbital into the isonitrile π^*-acceptor MO. Within this bonding picture, the isonitrile-tilt is a consequence of avoiding an unfavorable σ-overlap with the filled d_{z^2} orbital but instead favorable back-donation from this orbital. Consequently, weak multicenter isonitrile σ-bonding results, which is counterbalanced by strong back-donation. Therefore, it is fully consistent that the weakest σ-donor and strong π-acceptor isonitrile coordinates apically, rather than the nitride ligand as in case of d^2 nitride complexes. These considerations suggest that such a five-

coordinate d^4 nitrides that are formally situated beyond the "oxo wall" can be stabilized with a weak σ-donor/strong π-acceptor ligand.
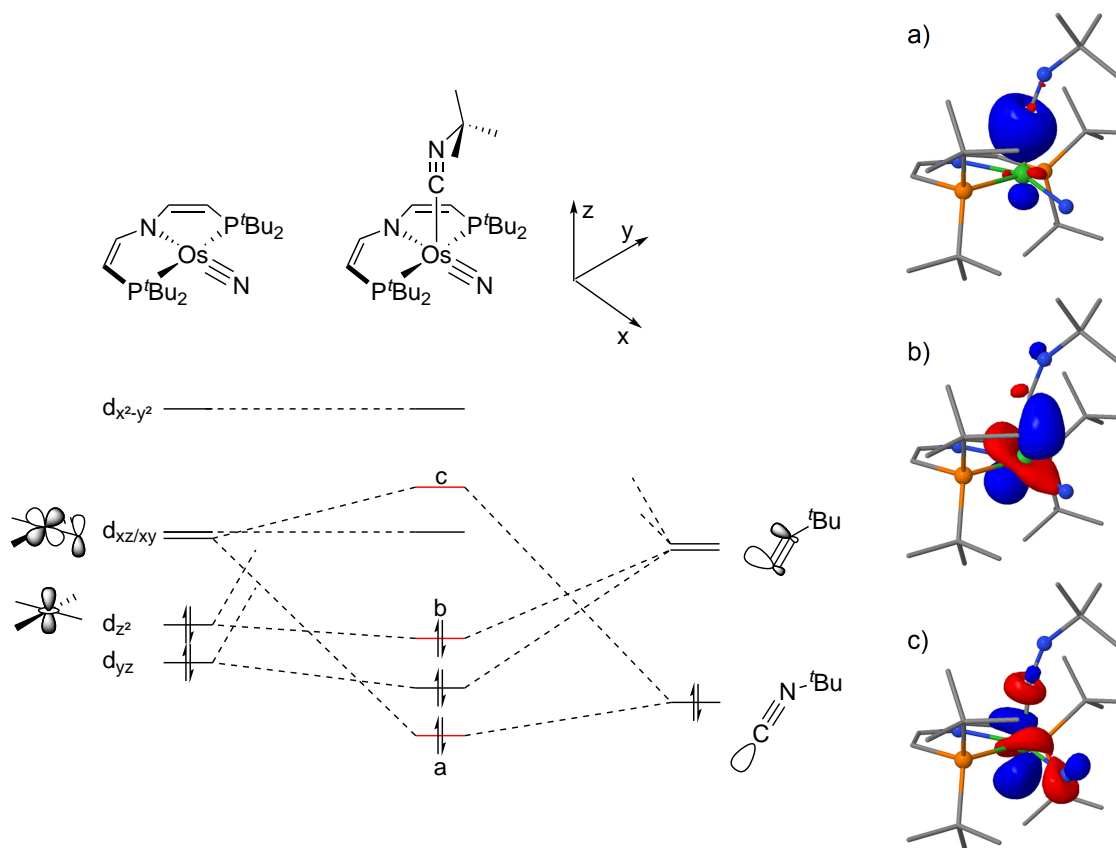
Scheme 3.4: Left: Qualitative MO interactive diagram of **14** with the isonitrile ligand; Right: NLMO representation of the σ- (top) and π-bonding (middle) interactions and the antibonding σ-interaction (bottom) of the metal with the isonitrile.

In comparison to parent **14**, five-coordinate **18** exhibits much cleaner reactivity with silyl halide electrophiles. NMR spectroscopic monitoring reveals selective in situ nitride silylation with TMSI. The silylimide complex $[Os(NTMS)(L^3)(CN^tBu)][BPh_4]$ (**19**, Scheme 3.3) can be isolated in around 50% yield after anion exchange with $NaBPh_4$. In contrast to nitride **18**, the five-coordinate Os^{IV} imido complex is thermally stable at room temperature in both solution and solid state. Monomeric d^4 imido complexes are rare, due to the same general considerations discussed for nitrides.[196],[221] Meyer and coworkers structurally characterized octahedral Os^{IV} imide complexes upon addition of cyanide, azide, amines or thiols to the respective Os^{VI} nitride.[222]–[225] Electron delocalization resulting from the heterocumulene character of these ligand probably contributes to their stability. Furthermore, they exhibit distinct bending of the M=N−R moiety, which evades the in-plane π-bonding conflict with the low-valent metal center.

In contrast, simple five- or six-coordinate d^4 alkyl-, aryl-, or silylimides have not been characterized to date, rendering **19** the first example, but might be intermediates in the addition of nucleophiles to electrophilic d^2 nitrides.[92],[93],[226],[227] NMR spectroscopic characterization of **19** is in agreement with a C_S- symmetric structure in solution. The molecular structure in the solid state confirms slightly more distorted square-pyramidal geometry in comparison with **18** (Figure 3.2, $\tau = 0.25$). However, the overall relatively small structural perturbations that result from nitride silylation are reflected in the similarities of the computed frontier molecular orbital scheme (Scheme 3.3). The distinct tilt of the isocyanide ligand is not observed for **19** (Os1-C24-N3: 179.0(4)°), suggesting reduced $d_{z^2} \rightarrow \pi^*(C\equiv N)$ back-donation. This interpretation is supported by enhanced linearity of the isonitrile ligand (C24-N3-C25: 170.9(6)°), a slightly shortened $C\equiv N$ bond (C24-N3: 1.151(6) Å) and a hypsochromic shift of the $C\equiv N^t Bu$ stretching vibration by about $\Delta\tilde{\nu} = 120\,\mathrm{cm}^{-1}$ in the IR spectrum. Instead, the isocyanide ligand of **19** exhibits an incline towards the amide ligand (N1-Os1-C24: 74.38(19)°) to maintain isonitrile σ-donation within the $^t\mathrm{BuNC}-\mathrm{Os}\equiv\mathrm{N}\ \sigma/\pi$ 3c4e interaction as detailed for **18**. Furthermore, bending of the imido moiety (Os1-N2-Si1: 156.8(3)°) reduces the in-plane π-interaction of the metal with the nitride accompanied by elongation of the metal nitride bond (Os1-N2: 1.754(4) Å). The unusual basal imide coordination is therefore again attributed to a preference for the weakest σ-donor and strongest π-acceptor to coordinate in the apical position.

Another way of avoiding π-bonding conflicts of low valent Os^{IV} in five-fold coordination geometry with a nitride ligand is represented by forming metalloimido species. The Schneider group recently reported the formation of nitride bridged ruthenium complexes featuring the ligands L^1 and L^3. In this report it was discussed that double bonding of the nitride ligand to both metal centers effectively prevents repulsive π-interactions which has also been proposed for a few other ruthenium and osmium μ-nitrido species.[228]–[230] However, a detailed bonding analysis of such species is yet to be done.

The reaction of a freshly prepared solution of **2** with either an equimolar amount of **14** or 0.5 equivalents of TMSN_3 allows for the isolation of the bright green bridging nitride $[(\mathrm{L}^3)\mathrm{ClOs}(\mu\text{-N})\mathrm{OsH}\{\mathrm{N}(\mathrm{CHCHP}^t\mathrm{Bu}_2)(\mathrm{CHCHP}^t\mathrm{BuCMeCH}_2)\}]$ (**20**, Scheme 3.3) in over 80% yield after column chromatography. In contrast to the analogous ruthenium platform,[228] spectroscopic and crystallographic characterization of **20** reveals cyclometallation of one of the $\mathrm{P}^t\mathrm{Bu}$ substituents, resulting in an $\{\mathrm{Os}^{IV}(\mu\text{-N})\mathrm{Os}^{IV}\}$ core that is close to linearity (Figure 3.5, Os1-N3-Os2: 170.11(16)°). The significant higher metal basicity of 5d over 4d metals is most likely responsible for the observed structural differences. The two Os-PNP fragments are twisted toward each other by about 90° as a result of the bulky phosphine substituents. Computational examination supports the $\mathrm{Os}^{IV/IV}$ redox state assignment.
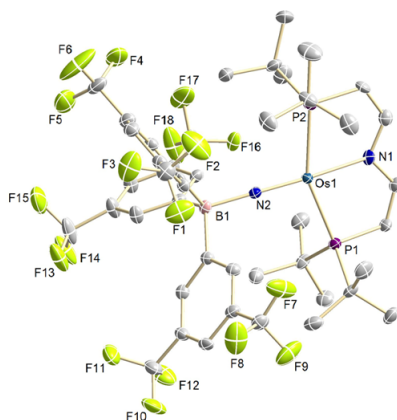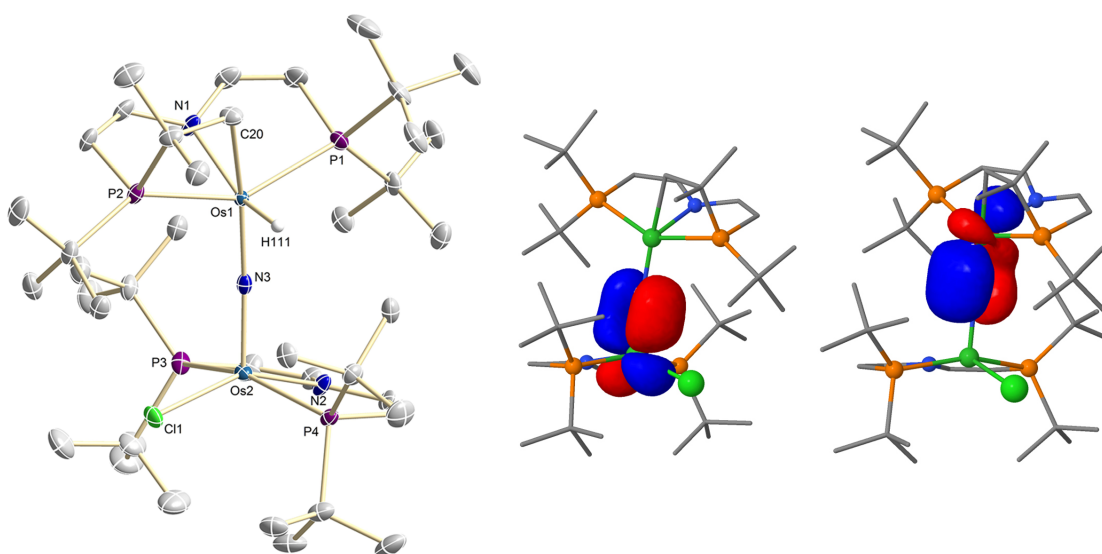
Figure 3.5: Left: Molecular structure of complex **20** from single-crystal X-ray diffraction (thermal ellipsoids drawn at the 50 % probability level); hydrogen atoms except the hydride ligand are omitted for clarity. Selected bond lengths [Å] and angles [°]: **20** Os1-H111 1.53(4), Os1-N1 2.126(3), Os1-N3 1.839(3), Os1-C20 2.220(3), Os1-P1 2.3778(8), Os1-P2 2.4502(8), Os2-N2 2.034(4), Os2-N3 1.796(3), Os2-Cl1 2.3648(9), Os2-P3 2.4271(19), Os2-P4 2.4404(9); Os1-N3-Os2 170.11(16), P2-Os1-P1 150.09(3), P3-Os2-P4 155.95(4); Right: NBO representation of the Osmium/nitride π-bonding interactions in **20**.

The computed frontier orbitals show a high degree of interaction between the metal center resulting in rather complex orbitals which cannot be easily assigned in terms of simple bonding considerations (Appendix 8.2.3). Therefore, NBO analysis was again employed to get insight into the bonding situation of the {OsNOs} core. NBO analysis features one π-bond of the bridging nitride with each osmium center, which are orthogonal to each other (Figure 3.5). Consequently, the nitride effectively serves as a single-faced π-donor or metalloimido four-electron donor ligand for both Os fragments. As a result, the d^4 configuration is easily sustained for five- and six-coordinate geometry and the μ-nitrido ligand occupies the apical site of the square-pyramidal fragment.

3.2 Bipyridine Ligated Os Nitride Complexes

Since square-planar **2** does not allow for the substitution of the chloride ligand to give stable azides and exhibited no discrete redox chemistry, 2,2'-bipyridine (bipy) is chosen as a spectator ligand with the potential of high π-backbonding or even charge transfer to stabilize open-shell nitrides. Reacting **7** with $TMSN_3$ results in the formation of $[Os(L^3)(N_3)(bipy)]$ (**21**, Scheme 3.5) in 85% isolated yield. The NMR resonances are in line with a C_S-symmetric species in solution and are only minorly shifted with respect to **7** as expected for a pseudohalogenide complex. Successful addition of azide is confirmed by IR spectroscopy ($\tilde{\nu}_{N_3} = 2072\,\mathrm{cm}^{-1}$) and single crystal X-ray crystallography (Figure 3.6)
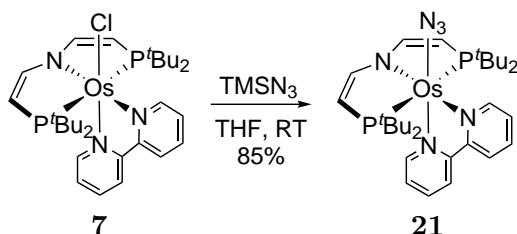
Scheme 3.5: Synthesis of **21** from **7** by ligand exchange.

The solid-state structure exhibits almost identical bonding parameters between metal and bipy/PNP ligand with respect to **7** and a slightly bent azide ligand which shows equivalent N-N distances (N4-N5: 1.179(4) Å, N5-N6: 1.177(4) Å, N4-N5-N6: 175.9(3)°). **21** is stable at room temperature and does not show any sign of decomposition when exposed to light in solution or in the solid state. Irradiation of **21** should lead to release
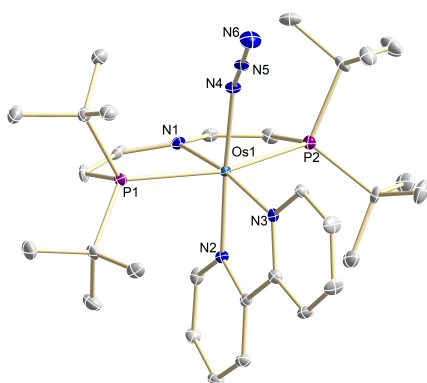
Figure 3.6: Molecular structure of **21** from single-crystal X-ray diffraction (thermal ellipsoids at the 50% probability level); hydrogen atoms are omitted for clarity. Selected bond lengths [Å] and angles [°]: **21** Os1-N1 2.110(2), Os1-N2 2.032(3), Os1-N3 2.064(2), Os1-N4 2.112(3), Os1-P1 2.4627(8), Os1-P2 2.4329(8), N4-N5 1.179(4), N5-N6 1.177(4), N1-Os1-N4 98.95(10), P1-Os1-P2 158.44(3), Os1-N4-N5 142.3(2), N4-N5-N6 175.9(3).

of dinitrogen and formation of an octahedral Os^{IV} nitrene complex which is not expected to be isolable due to the high d electron count. Nitride coupling and formation of **9** could be a possible follow-up reaction pathway. However, irradiation experiments yielded no isolable reaction products to be detected by NMR or EPR spectroscopy (Appendix 8.2.4). This indicates that the photo-product is too reactive to be accurately studied. The cyclic voltammogram of **21** shows a reversible oxidative wave at $E_{1/2} = -0.74\,\text{V}$ and a second irreversible oxidative wave at $E_{\text{p.a.}} \approx 0.21\,\text{V}$ vs. $Fc^{0/+}$ which suggest that $Os^{V/VI}$ nitride species could be isolable upon oxidation of **21** (Appendix 8.2.5).
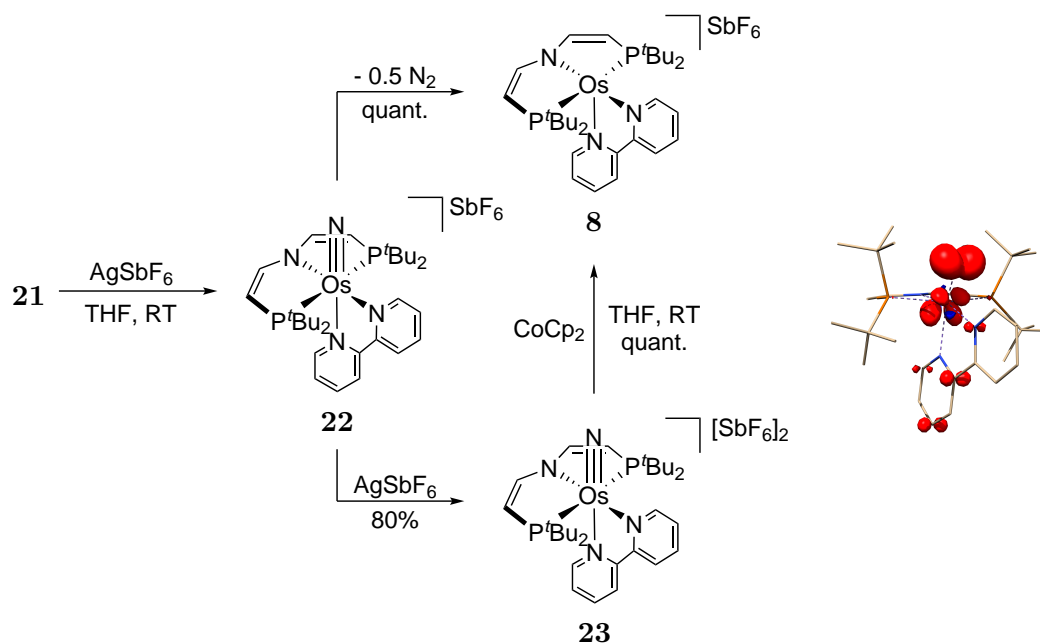
Scheme 3.6: Left: Fate of the transient open-shell nitride **22**; Right: Spin-density of **22**.

An instant color change from red to dark brown is detected accompanied by silver precipitation when **21** is oxidized by one equivalent of $AgSbF_6$. NMR spectroscopy reveals **8** to be the sole reaction product (Scheme 3.6, Appendix 8.2.7). Since the starting material is stable in solution, oxidation most likely triggers dinitrogen extrusion to yield the open-shell Os^V nitride species $[OsN(L^3)(bipy)][SbF_6]$ (**22**). As stated in the introduction, these species are prone to undergo oxidative nitride coupling towards dinitrogen complexes. Following the reaction at lower temperatures by NMR or EPR did not give any further information about possible intermediates of this reaction indicating rapid coupling reactivity of **22**. Reacting **21** with two equivalents of $AgSbF_6$ results in the formation of a C_S-symmetric species, accompanied by minor formation of an asymmetric side product and organic impurities, as indicated by NMR spectroscopy (Appendix 8.2.6). The procedure is highly sensitive to the scale of the reaction and could only be performed on a $6.7\,\mu\text{M}$ scale in acceptable purity which prevented full characteriza-

tion. However, mass-spectrometry suggests that $[OsN(L^3)(bipy)][SbF_6]_2$ (**23**, $\frac{m}{z} = 359.1$
$[M^{2+}]$) is formed. Prolonged standing in solution or heating did not result in any further
conversion of **23**. The addition of stochiometric amounts of $CoCp_2$ gives **8** quantitatively
(Appendix 8.2.7). This results reaffirms the presence of **22** prior to dinitrogen coupling.
DFT computations of **22** provide a possible explanation for the observed reactivity. The
SOMO is represented by an Os-N π*-orbital with 60% and 9.2% spin-density located at
the nitride nitrogen and the osmium center, respectively (Scheme 3.6). Although there
are reasonable arguments for the existence of **22**, the experimental results lack a direct
spectroscopic observation of the compound. The problems associated with isolating **23**
prevented an alternative access *via* reduction. Based on these results the system was not
further investigated in terms of kinetics of homo-/hetero- coupling reactions of **22/23**.

3.3 Conclusion

In summary, this chapter exemplarily showcases different strategies to stabilize low-valent transition-metal nitrido and imido complexes. Terminal nitrides of d^4 ions such as Os^{IV} in square-pyramidal or octahedral geometry are formally beyond the "nitrido wall" defined by the GB bonding model. Population of the M-N π^*-antibonding molecular orbitals renders them inherently unstable. This π-conflict can be avoided by reduction of the coordination number. In analogy to Os^{IV}, Ru^{IV} and Ir^{V} nitrides with bulky pincer ligands, the four-coordinate nitride complex **14** can be synthesized. Nucleophilic reactivity of the metal and the nitride is observed with Brønsted and Lewis acids. Nitride hydrogenolysis gives ammonia and the tetrahydride **XXXVIII** in high yield. Surprisingly, the addition of CN^tBu allows for the isolation of the five-coordinate, thermally labile Os^{IV} nitride **18**. The highly unusual preference of the isonitrile instead of the strong donor nitride for axial coordination is attributed to the high metal valence electron count and the unexpected binding mode of the isocyanide. On one hand, tilting about the Os-C-N angle allows for stabilization of the filled d_{z^2} orbital by π-backdonation. On the other hand, mixing of the isonitrile lone pair with the in-plane $Os{\equiv}N$ π-interaction results in an overall stabilizing 3c4e interaction. This synergistic binding mode explains why the strong π-acceptor and comparatively weak σ-donor isocyanide is placed in the axial position. Nitride silylation further stabilizes this compound and allows for the isolation of the first d^4 silylimido complex beyond four-coordination. Electrophilic attack of low-valent nitrides provides a new synthetic route to such electron-rich imidos. In analogy to the five-coordinate nitride **18**, 3c4e bonding of the isonitrile in combination with reduced in-plane π-donation by imide bending stabilizes silylimide **19**. Finally, stabilization arises from binding of two low-valent metal ions. The bridging nitride ligand within the $\{Os^{IV}{=}N{=}Os^{IV}\}$ core of dinuclear complex **20** forms one π-bond with each metal ion. The resulting $Os{-}N$ double bond character also avoids π-bonding conflicts. Accordingly, the metalloimido ligand is in the apical position of the OsCl(PNP) platform, as is usually observed for high-valent group 8 nitrido and imido complexes.

The azide complex **21** was obtained which could be oxidized by one and two electrons to give transient **22**, which exhibits rapid nitride coupling reactivity, and stable the nitride complex **23**, respectively. Kinetics of homo-/hetero-coupling reactions could not be obtained since clean complex synthesis was hampered by low selectivity at increased reaction scales.

Transition Metal Complexes with Metal-Pnictogen Multiple Bonds

Author contributions

J.A.	Synthesis, spectroscopy, crystallography (**25**, **31**, **34** and **44**) and theoretical caluclations (Chapter 4.2 and 4.4)
M.D.	Theoretical calculations (Chapter 4.1, supporting)
A.H.	Synthesis of [Na(diox)$_x$][PnCO]
L.A.	Crystallography (**24**, supporting)
C.W.	Crystallography
D.D.	Isothermal titration calorimetry
M.N.	Synthesis and spectroscopy (Chapter 4.3, supporting)
B.B.	Theoretical Calculations (Chapter 4.3)
M.H.	Theoretical Calculations (Chapter 4.1)

4 Transition Metal Complexes with Metal-Pnictogen Multiple Bonds

4.1 P_2 and As_2 Complexes from Coupling of Terminal Re Pnictides

LXXIII proved to be an efficient platform for nitrogen fixation to yield terminal nitrides upon dinitrogen splitting, indicating strong pnictide bonding.[52] Therefore, this complex provides a promising platform to also stabilize higher homologues. **LXXIII** was reacted with $[\mathrm{Na(diox)}_{1.39}][\mathrm{PCO}]$ yielding unselective conversion to multiple products as indicated by $^{31}\mathrm{P}$ NMR spectroscopy, but also afforded a Re≡P species suggested by signals above $\delta_\mathrm{P} = 1000\,\mathrm{ppm}$ (Figure 4.1). The reaction of **LXXIII** with PCO⁻ yields a C_S-symmetric species as the main product ($\delta_\mathrm{P} = 31.5\,\mathrm{ppm}$). IR spectroscopy gave an intense absorption at $\tilde{\nu}_\mathrm{CO} = 1875\,\mathrm{cm}^{-1}$ suggesting carbon monoxide coordination as the dominant side reaction. This was proven by independent synthesis of $[\mathrm{ReCl}_2(\mathrm{L}^1)(\mathrm{CO})]$ upon reaction of **LXXIII** with carbon monoxide (**24**, Scheme 4.1, $\delta_\mathrm{P} = 31.5\,\mathrm{ppm}$, Appendix 8.3.2). The different products could not be separated by crystallization or column chromatography. Therefore, **5** was reacted with $[\mathrm{Na(diox)}_{1.39}][\mathrm{PCO}]$ since the more electron withdrawing properties should hinder carbon monoxide coordination. In fact, no CO-complex is formed over the course of the reaction and a $^{31}\mathrm{P}$ NMR signals above $\delta_\mathrm{P} = 1000\,\mathrm{ppm}$ suggest phosphide complex formation (Figure 4.1), however the side products could not be removed by crystallization or other purification methods. To prevent CO trapping and increase selectivity the vacant coordination site was to be blocked as a synthetic strategy. Multiply bonded heavy pnictide ligands presumably exhibit a strong *trans*-influence. Therefore, 3-(1*H*-pyrazol-3-yl)-pyridine (^HPyrPz) was introduced as a possible hemilabile ligand (Chapter 2).
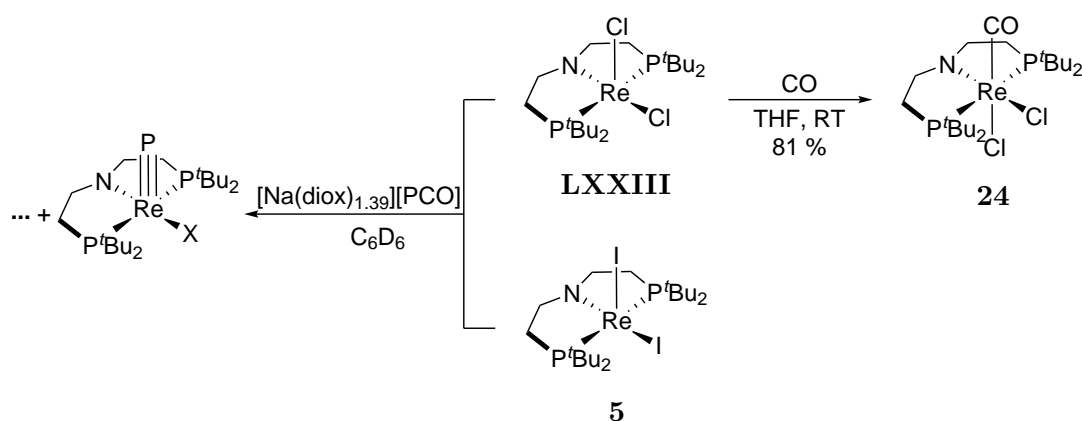
Scheme 4.1: Reactivity of **LXXIII** and **5** towards PCO⁻ and synthesis of **24** by addition of CO to **LXXIII**.
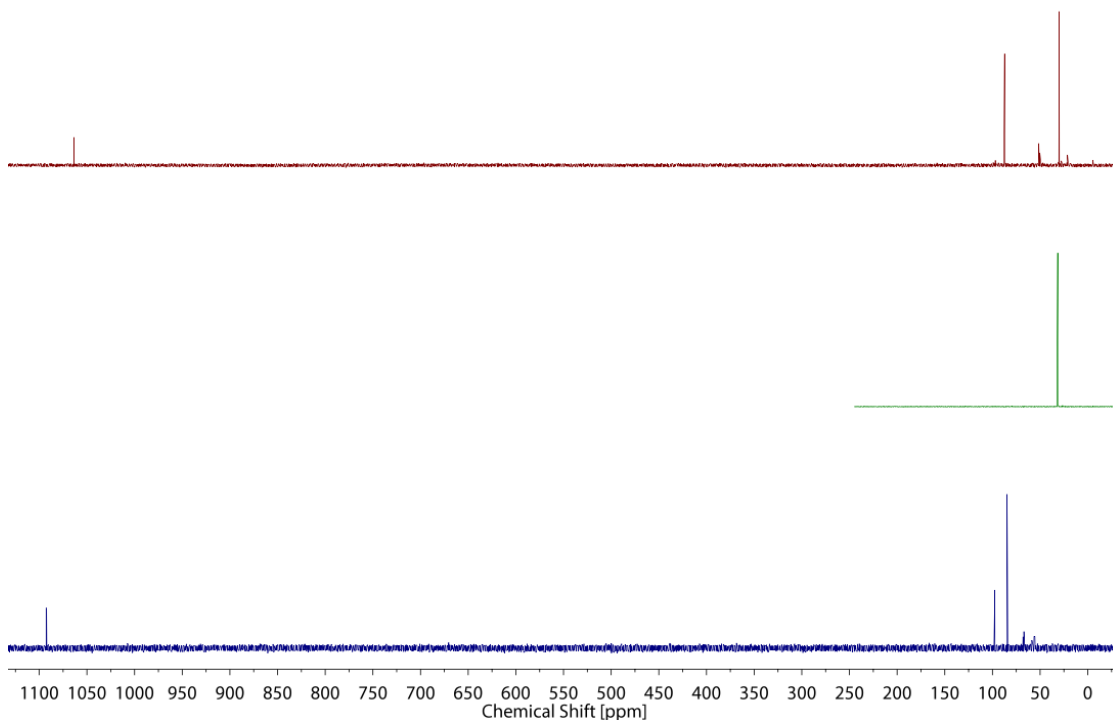
Figure 4.1: ^{31}P{^{1}H} NMR spectra of the reaction of **LXXIII** and [Na(diox)$_{1.39}$][PCO] (top), C$_6$D$_6$; pure **24** (middle), CD$_2$Cl$_2$; reaction of **5** and [Na(diox)$_{1.39}$][PCO] (bottom), C$_6$D$_6$, all RT.

Inspired by the work of Cummins and co-workers, **11** was reacted with NCO$^-$ to access a terminal nitride complex upon decarbonylation.[65] [Re(L^1)(NCO)($\kappa^2 N^1,N^3$-PyrPz)] (**25**, Scheme 4.2) can be isolated after salt metathesis as indicated by an intense IR absorption at $\tilde{\nu}_{NCO} = 2234\,\text{cm}^{-1}$ (Appendix 8.3.2) and a ^{13}C NMR resonance of $\delta_{NCO} = 159.6\,\text{ppm}$. The isocyanate ligand is slightly tilted due to the high d electron count of the Re center (see crystallographic details). **25** did not show any signs of decarbonylation after irradiation or heating to 80°C over an extended period of time, suggesting that nitride formation might be thermodynamically unfavorable.

Reaction of **11** with [Na(diox)$_{1.39}$][PCO] at low temperatures results in formation of transient [Re(L^1)(PCO)($\kappa^2 N^1,N^3$-PyrPz)] (**26**, Scheme 4.2) as indicated by its ^{31}P NMR signals ($\delta_P = 1.92, -268.8\,\text{ppm}$, Appendix 8.3.6). The characteristic proton resonance of the pyridine o-CH unit is in line with PyrPz ligand still acting as a chelate ligand ($\delta_H = 9.81\,\text{ppm}$, Appendix 8.3.6 - 8.3.9). Upon warming, a clean conversion towards the terminal phosphide complex [ReP(L^1)(κN^2-PyrPz)] (**27**, Scheme 4.2) is observed. The phosphide ligand exhibits a characteristic ^{31}P NMR shift of $\delta_P = 1069\,\text{ppm}$ that arises from second-order paramagnetic shielding contribution.[231]
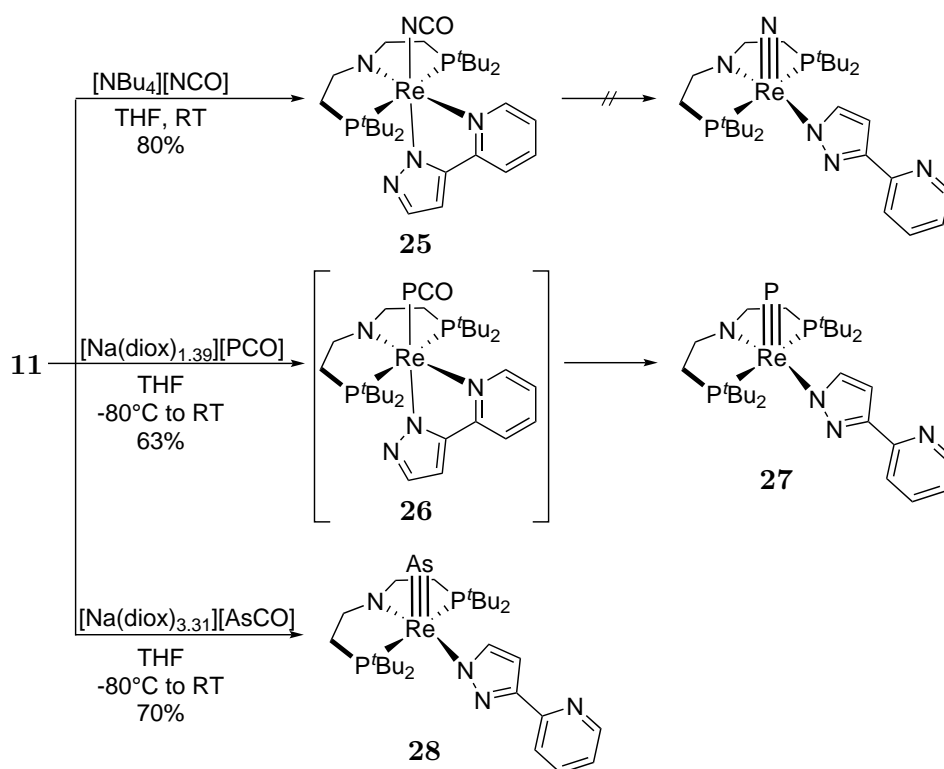
Scheme 4.2: Access to the isocyanate complex **25** by salt metathesis and synthesis of the terminal heavy pnictide complexes **27** and **28** upon decarbonylation of $[\text{Na(diox)}_{1.39}][\text{PnCO}]$.

When **11** is reacted with $[\text{Na(diox)}_{3.31}][\text{AsCO}]$, an AsCO^- ligated complex could not be identified but direct conversion to the terminal arsenide $[\text{ReAs(L}^1)(\kappa N^2\text{-PyrPz})]$ (**28**, Scheme 4.2) was observed. Both pnictide complexes could be fully characterized including X-ray diffraction studies (Figure 4.2). The ^{1}H NMR resonances of the PyrPz ligand are considerably broadened for both complexes at room temperature (Appendix 8.3.3), but sharpening of all signals is observed at 0°C which is readily explained by the solid state structure that reveals the PyrPz ligand to be partly decoordinated, most likely due to the *trans*-influence of the Re≡Pn bonds. The Re≡Pn bond distances (Re1-P3: 2.0939(6) Å, Re1-As1: 2.2021(3) Å) are in the range found for terminal group 6 pnictide complexes.[63]–[65]

A complementary quantum-chemical study of the electronic structure of **27** and **28** corroborates the notion of triply bound terminal rhenium pnictides. For both species a natural bond order (NBO) analysis reveals a set of three bonding, natural localized molecular orbitals (NLMOs) which correspond to $\sigma^2\pi^4$ triple bonds complemented by a lone-pair localized at the pnictide end in support of a genuine Re≡Pn| Lewis-picture (Figure 4.3; Wiberg bond index: 2.23 (**27**), 2.17 (**28**)).
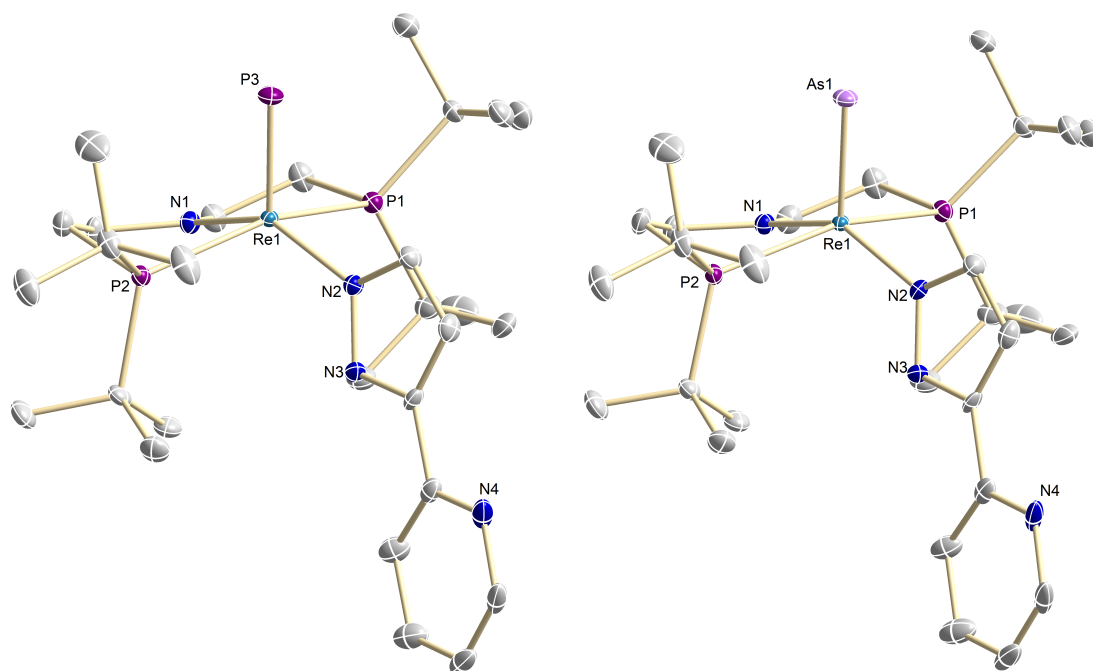
Figure 4.2: Solid state structure of **27** (left) and **28** (right) from single-crystal X-ray diffraction (thermal ellipsoids drawn at the 50% probability level); hydrogen atoms are omitted for clarity. Selected bond lengths [Å] and angles [°]: **27** Re1-N1 1.9894(17), Re1-N2 2.1208(17), Re1-P1 2.4223(6), Re1-P2 2.4280(6), Re1-P3 2.0939(6), N1-Re1-N2 148.29(7), N1-Re1-P3 110.66(5), P1-Re1-P2 154.820(19), τ = 0.11; **28** Re1-N1 1.986(2), Re1-N2 2.123(2), Re1-P1 2.4227(8), Re1-P2 2.4288(7), Re1-As1 2.2021(3), N1-Re1-N2 148.60(9), N1-Re1-As1 110.60(7), P1-Re1-P2 154.86(3), τ = 0.10.

In both cases, the σ- and one of the π-bonds are distributed almost equally while the other π-bond carries increased Re d orbital character. This is substantiated by topological analysis of the computed electron densities by means of Bader's quantum theory of atoms in molecules (QTAIM).

The Re≡P interaction classifies as a strong, covalent and polar bond with corresponding values at the bcp for the electron density $\rho(\mathbf{r}_b) = 1.07\,\mathrm{e\mathring{A}}^{-3}$, the relative total energy density $H(\mathbf{r}_b)/\rho(\mathbf{r}_b) = -0.68\,\mathrm{au}$ and the relative kinetic energy density $G(\mathbf{r}_b)/\rho(\mathbf{r}_b) = 0.56\,\mathrm{au}$, all slightly weaker but remarkably close to those for the homonuclear and lighter diatomic congener P≡P (Appendix 8.3.23, 8.3.22). Furthermore, the cylindrical electron density at the bcp with a bond ellipticity of $\epsilon = 0.04$, as well as a delocalization index of $\delta(\mathrm{Re,P}) = 2.47$, support the formulation as a triply bonded Re≡P moiety. The arsenide draws a close parallel to this description, however the bond exhibits reduced covalency due to the more diffuse electron density of arsenic ($\rho(\mathbf{r}_b) = 0.95\,\mathrm{e\mathring{A}}^{-3}$, $H(\mathbf{r}_b)/\rho(\mathbf{r}_b) = -0.61\,\mathrm{au}$, $G(\mathbf{r}_b)/\rho(\mathbf{r}_b) = 0.65\,\mathrm{au}$, $\epsilon = 0.06$, $\delta(\mathrm{Re,As}) = 2.40$).

(47%) Re1–P3 (50%)   (47%) Re1–P3 (51%)   (67%) Re1–P3 (31%)   (99%) P3 sp$^{0.28}$

(48%) Re1–As1 (50%)   (46%) Re1–As1 (51%)   (69%) Re1–As1 (28%)   (99%) As1 sp$^{0.23}$
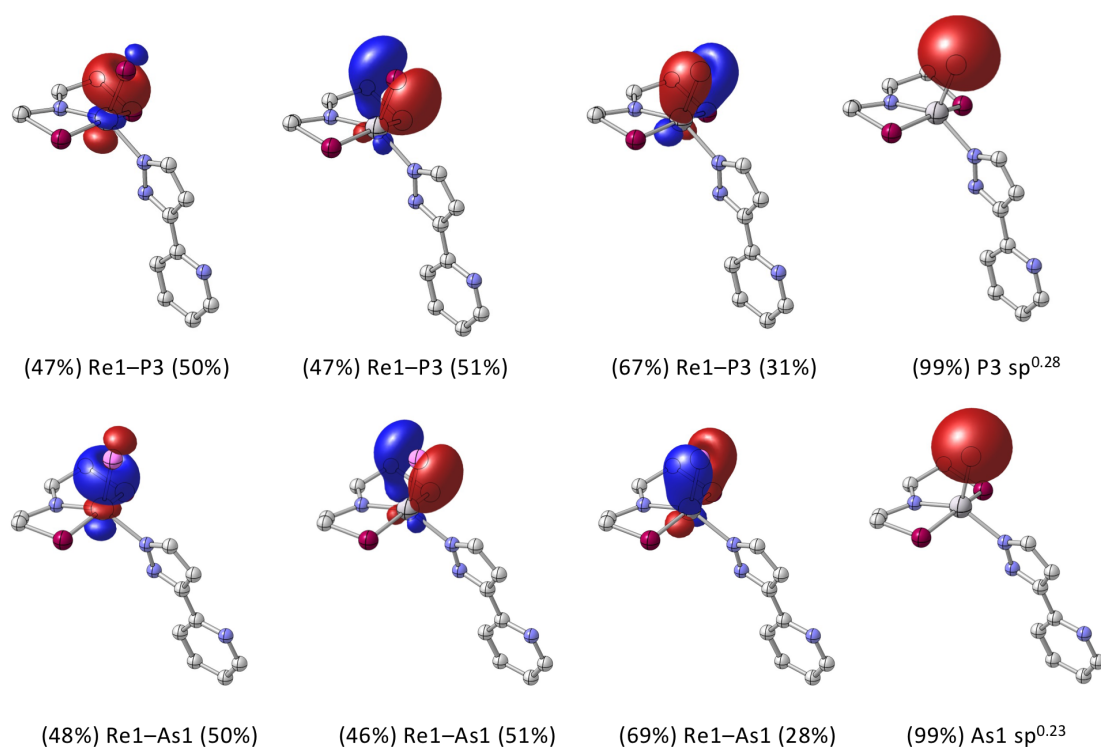
Figure 4.3: NLMOs (σ, π and lone-pairs) representing the bonding in **27** (top) and **28** (bottom).
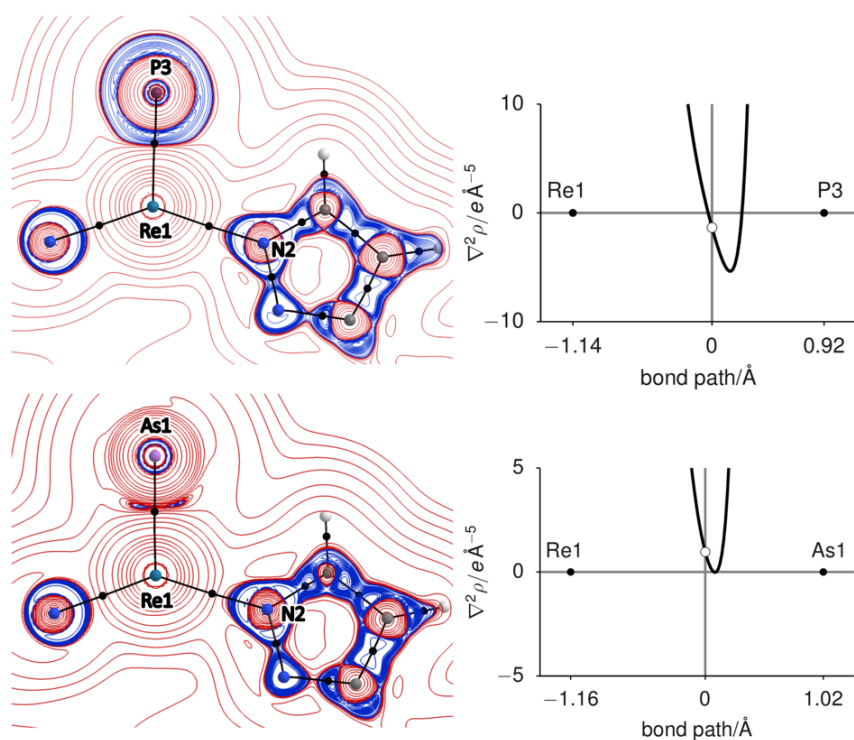
Figure 4.4: Bonding analysis of **27** (left) and **28**; Left: 2D plots of $\nabla^2\rho(r)$, charge concentrations
(blue) and depletion (red), bond paths (black lines), and bond critical points (black dots); Right:
1D Laplacian profiles along the bond paths.
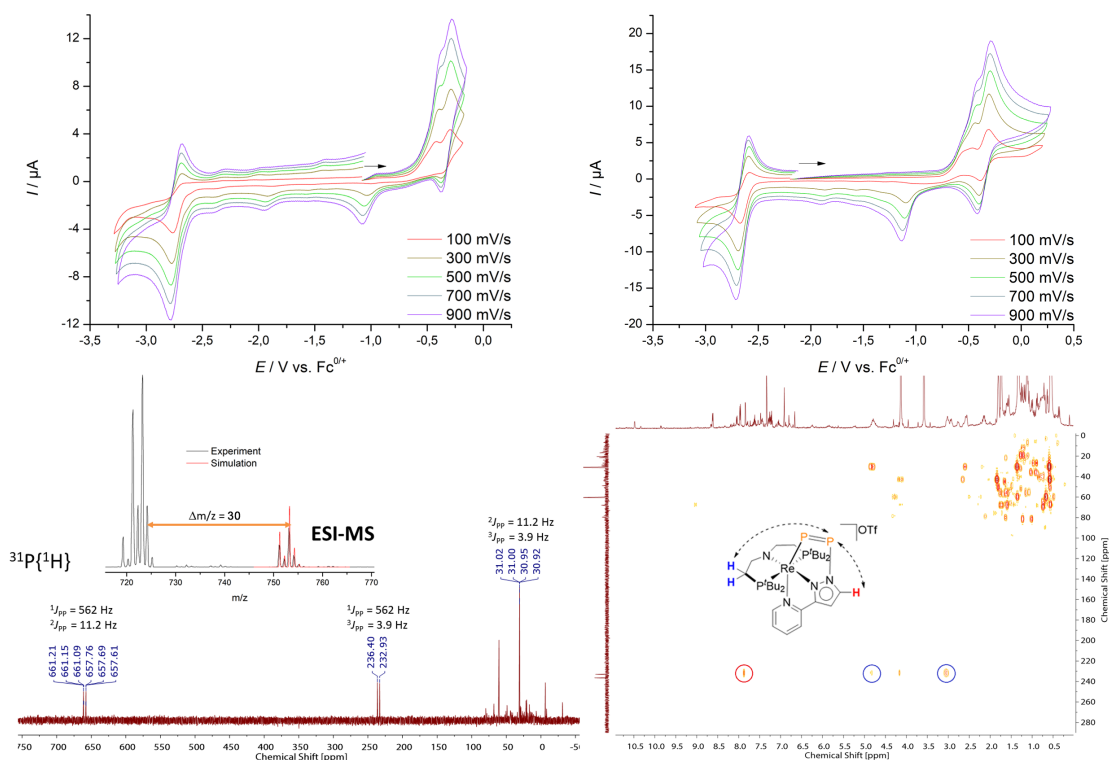
Figure 4.5: Top left: Cyclic voltammogram of **27**, 1 mM, 0.1 M NBu$_4$PF$_6$, THF, RT; Top right: Cyclic voltammogram of **28**, 1.3 mM, 0.1 M NBu$_4$PF$_6$, THF, RT; Bottom left: ^{31}P{^{1}H} NMR spectrum of the oxidation of **27** with [Fc][OTf], THF, RT; Inset: ESI spectrum of the oxidation of **27** with [Fc][OTf] (Main peak: **27**+H$^+$; Simulation: **29**); Bottom right: ^{31}P{^{1}H}-^{1}H HMBC NMR spectrum of the oxidation of **27** with [Fc][OTf], THF, -38°C.

The cyclic voltammogram of **27** features an irreversible oxidation at $E_{\text{p.a.}} \approx -0.42$ V vs. Fc$^{0/+}$ closely followed by a quasi-reversible wave at $E_{1/2} = -0.31$ V, indicating rapid reactivity that follows oxidation. For **28** a similar result is obtained with increased reversibility for the quasi-reversible redox event (Figure 4.5). Cathodic reverse scans reveal the same irreversible, reductive feature just below $E = -1.0$ V vs. Fc$^{0/+}$ for both pnictides, suggesting at least partial pnictide loss after initial oxidation (Appendix 8.3.4, 8.3.5). Chemical oxidation of **27** and **28** with [Fc][OTf] at room temperature lead to the formation of several products. Mass spectrometry of the reaction solution hints towards the formation of [Re(Pn$_2$)(L^1)(PyrPz)] (**29** (Pn = P), Figure 4.5, Appendix 8.3.14, **30** (Pn = As), Appendix 8.3.19) as major oxidation products. The respective yields are determined by NMR to be $33-44\%$. In addition, **27** exhibits two ^{31}P NMR signals at $\delta_{\text{P}} = 569, 235$ ppm which correspond to a single P atom, respectively, when compared to the pincer resonance ($\delta_{\text{P}} = 31.0$ ppm). The observed chemical shifts and their large mutual J-coupling ($^1J_{\text{PP}} = 560$ Hz) indicate phosphide radical coupling upon oxidation, yielding a product featuring a P-P multiple bonded moiety that is unsymmetrically

72

bound to the Re center, as suggested by the largely different P-P$_{PNP}$ coupling constants ($^2J_{PP} = 11.8\,\text{Hz}$, $^3J_{PP} = 3.9\,\text{Hz}$). The proton resonances are sharpened when compared to **27** indicating full coordination of the PyrPz chelate ligand. ^{31}P{^{1}H}-^{1}H HMBC spectroscopy reveals indicative cross peaks for the P atom at $\delta_P = 235\,\text{ppm}$ and the pincer PCH$_2$ unit as well as for a CH group of the pyrazole moiety suggesting the presence of a Re−P=P−N bonding motif (Figure 4.5). The oxidation of **28** yields almost identical NMR parameters (^{1}H, ^{13}C and ^{31}P) and ESI spectrometry further supports the formation of an isostructural As$_2$ complex (Appendix 8.3.16 - 8.3.19).

While **29** could not be isolated due to gradual degradation during workup, even at $-40°$C, the crystallographic characterization of **30** confirms the structural assignment (Scheme 4.3). The PyrPz ligand rearranges over the course of the reaction with the pyrazole ring in *trans*-position to the pincer backbone, since the Re−Pn bond strength is considerably lowered. The As$_2$ unit of **30** bridges the metal center and the pyrazole N4 atom. The As=As bond distance of 2.2422(7)\,Å suggests double bonding.[232] This structural assignment is in full agreement with the multinuclear NMR features of both pnictide oxidation products. Furthermore, spin-orbit relativistic NMR calculations ac-
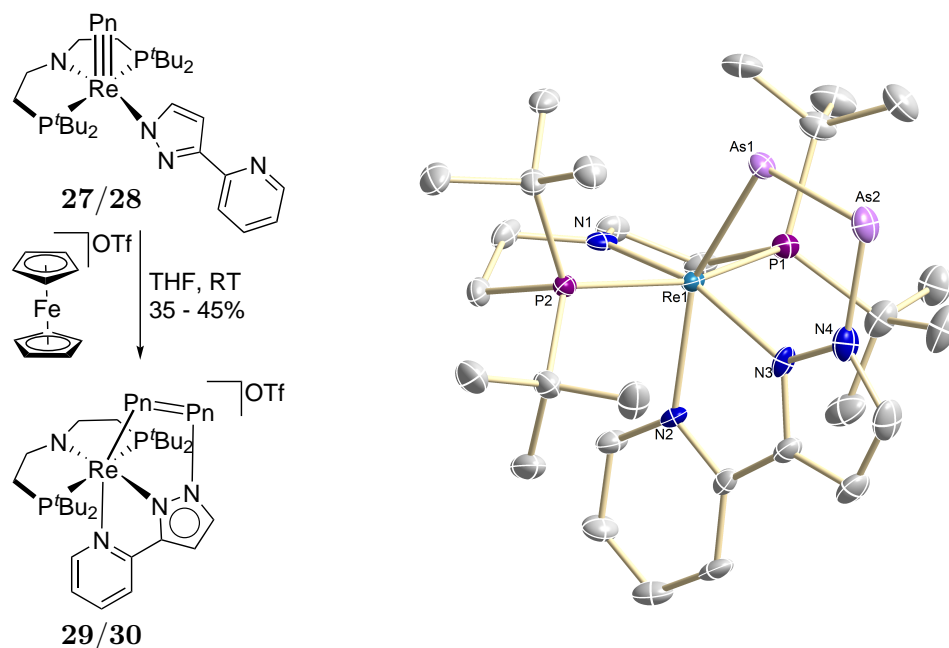
Scheme 4.3: Left: Synthesis of **29** (Pn = P) and **30** (Pn = As) by oxidation of **27** and **28**, respectively; Right: Solid state structure of **30** (one of the complexes in the asymmetric unit) from single-crystal X-ray diffraction (thermal ellipsoids drawn at the 50% probability level); solvent molecules, anions and hydrogen atoms are omitted for clarity. Selected bond lengths [Å] and angles [°]: **30** Re1-As1, 2.4421(5), Re1-N1 1.951(4), Re1-N2 2.173(3), Re1-N3 2.139(3), Re1-P1 2.4482(12), Re1-P2 2.4743(12), As1-As2 2.2422(7), As2-N4 1.943(4), Re1-As1-As2 109.83(2), As1-As2-N4 93.75(11), N1-Re1-N2 90.98(13), N1-Re1-As1 115.31(10), P1-Re1-P2 160.86(4).

curately reproduce the ^{31}P chemical shifts and coupling constants of **29** ($\delta_{\text{P1/2}}^{\text{DFT}} = 30\,\text{ppm}$, $\delta_{\text{P3}}^{\text{DFT}} = 664\,\text{ppm}$, $\delta_{\text{P4}}^{\text{DFT}} = 212\,\text{ppm}$, $^1J_{\text{P3/4}}^{\text{DFT}} = -400\,\text{Hz}$). Identification of **29** and **30** as the main reaction products involves the formal loss of a $[\text{Re}(\text{L}^1)(\text{PyrPz})]^+$ unit.

All attempts to synthesize this complex were unsuccessful and gave multiple products, as observed for the oxidation of **27/28**. Oxidizing **27** at $-80°$C and instant freezing led to the observation of a weak, rhombic EPR signal, suggesting that most of the immediate $S = \frac{1}{2}$ oxidation product has decayed, possibly by P-P coupling (Appendix 8.3.15). Interestingly, slow warming of the solution to room temperature did not give **29** in detectable amounts. The stabilization of a putative $\{\text{Re}_2\text{P}_2\}$ intermediate might be associated with the kinetic barrier for κ^1- to κ^2-rearrangement of the PyrPz ligand.

(37%) Re1–P3 (58%)   (49%) P3–P4 (48%)   (39%) P3–P4 (58%)

(94%) P3 sp$^{0.59}$ (98%) P4 sp$^{0.41}$ (20%) P4–N4 (79%)
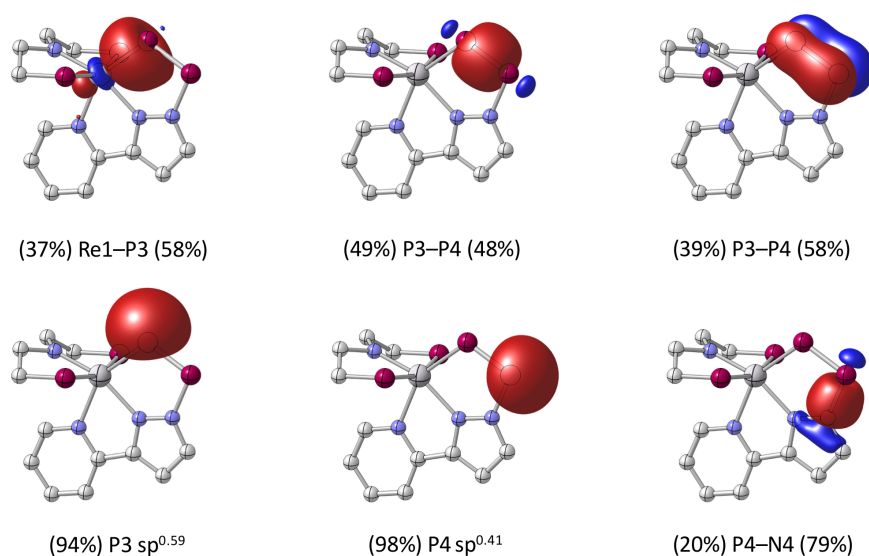
Figure 4.6: Bonding analysis of **29**: a) NLMOs representing the Re1–P3, P3=P4 and P4–N4 bonds and the two lone pairs at P3 and P4 (isosurfaces at $\pm 0.05\,\text{a}_0^{-3/2}$).

NBO analysis of the computed electron density of **29** yields four NLMOs, which correspond to a P=P double bond and a σ-type lone-pair at each phosphorus atom (Figure 4.6). Two additional NLMOs represent significantly polarized, localized 2c2e single bonds between Re1-P3 and P4-N4. Accordingly, alternating atomic charges are obtained by natural population analysis (Re1: 0.21, P3: -0.03, P4: 0.36, N4: -0.41). From this considerations it is not obvious if the dipnictide moiety is best described as a neutral Pn$_2$ unit, a *cis*-dipnictogene or a metalla-diazadipnictole (Scheme 4.4).
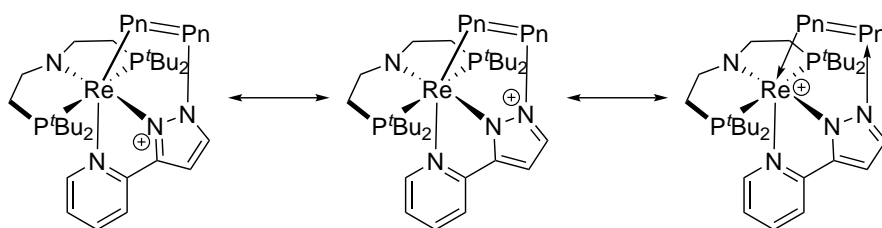
Scheme 4.4: Possible mesomeric structures of **29** and **30**.

Further insight is provided by QTAIM analysis of the computed electron density of
29. All topological criteria point towards an electron-sharing, covalent P-P interaction
that closely mirrors diphosphene, P_2H_2 (Appendix 8.3.23). The computed delocalization
index $\delta(P3,P4) = 1.71$ and the ellipticity $\epsilon = 0.36$ indicates the presence of a formal P=P
double bond. The symmetric, one-dimensional Laplacian distribution profile between
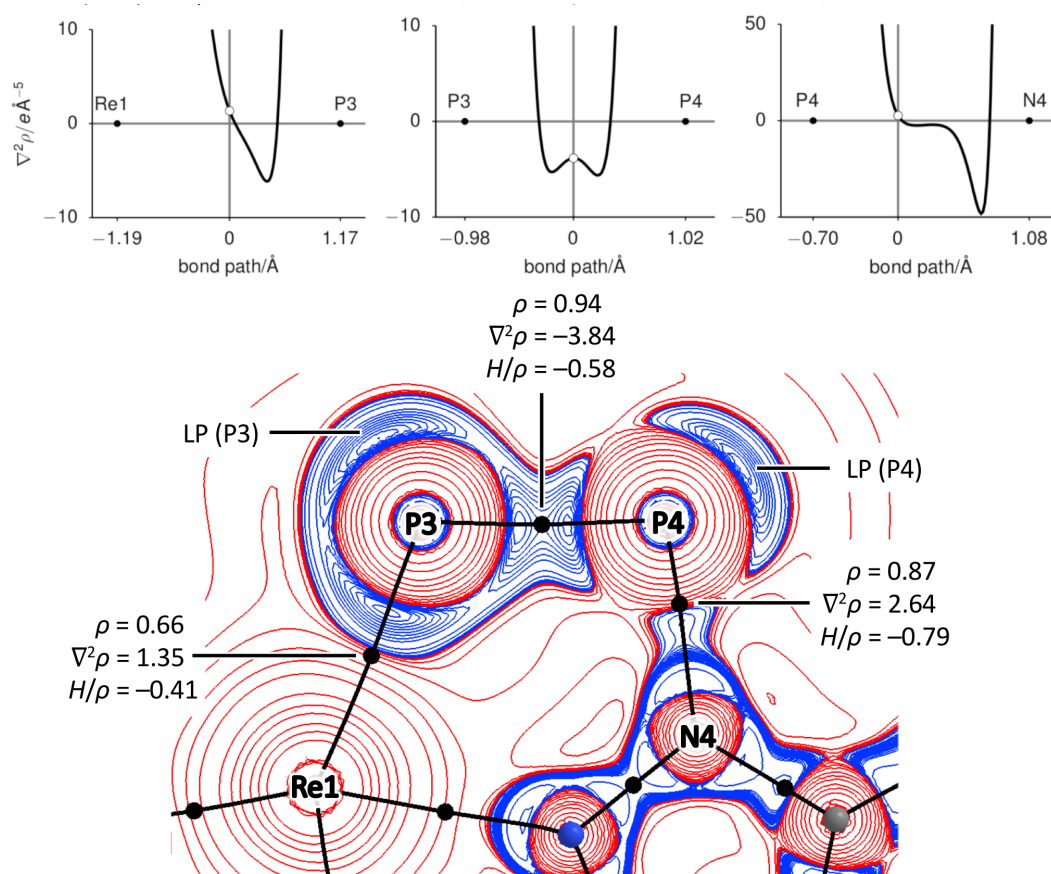
Figure 4.7: Top: 1D Laplacian profiles along the R1–P3 (left), the P3=P4 (middle) and the
P4–N4 (right) bond paths; Bottom: 2D plot of $\nabla^2\rho$; charge concentration (blue) and depletion
(red), bond paths (black lines), and bond critical points (black dots) with selected characteristic
properties at the bcp (ρ in eÅ^{-3}, $\nabla^2\rho$ in eÅ^{-5}, relative total energy density H/ρ in au).

P3 and P4 shows two valence shell charge concentrations (VSCC), originating from the overlapping valance shells of the interacting atoms, with two minima on both sides of the bcp, suggesting essentially homopolar covalent bonding (Figure 4.7). In contrast, the profiles along the Re1-P3 and the P4-N4 bond paths exhibit typical features of dative covalent interactions.[233]–[235] In both cases, the bcp resides close to the nodal surface in the Laplacian distribution such that the sign of $\nabla^2\rho$ at the bcp is unsuitable for a bond classification (Figure 4.7).[236],[237] As commonly found for transition metals, the diffuse outer valence shell of Re lies in a region of charge depletion and a VSCC is present only in the P3 donor atomic basin. Similarly, the profile along the P4-N4 bond path exhibits a pronounced VSCC in the vicinity of the more electronegative nitrogen donor atom and a shallow shoulder corresponding to the second VSCC near P4, both residing within the N4 atomic basin. The computed delocalization indices δ(Re1,P3) = 1.11 and δ(P4,N4) = 0.79 further document the covalent nature of these interactions. A very similar bonding situation is found for the arsenide analog **30** (Appendix 8.3.24). The covalency is slightly reduced by the more diffuse arsenic electron density (δ(Re1,As1) = 1.07; δ(As2,N4) = 0.77), however As=As double bonding is evident due to δ(As1,As2) = 1.70 and $\epsilon = 0.27$.

The NBO and QTAIM results for both complexes are therefore best represented by a formal Re←Pn=Pn←N bonding pattern corresponding to *push-pull* stabilized neutral P$_2^0$- and As$_2^0$-ligands with Pn=Pn double bonds.

4.2 Oxygenation of a Terminal Re Phosphide Complex

The aerobic oxidation of white phosphorus (P_4) was first performed by Brandt in 1680 in search of the Philosopher's stone. Upon burning, a greenish glow is observed which coined the term phosphorescence.[238] Until today, combustion of P_4 and organophosphorus compounds (OPCs) is still not well understood. Investigating these processes on a molecular level is of great interest in the context of chemical warfare agent disposal such as Sarin or VX.[239] Observed phosphorus containing species in these reaction are lower phosphorus oxides and hydroxides (PO, PO_2, HOPO and $HOPO_2$).[240]–[242] In general, lower (charged) phosphorus oxides can only be generated and studied under carefully controlled experimental conditions.[243],[244] However, several experimental and computational studies are available providing bond distances, ionization potentials and further characteristic data of $P_xO_y^{n+/-}$ species.[241]–[252]

While low molecular oxides of nitrogen are ubiquitous in nature, easily synthesized and well-studied ligands in coordination chemistry, preparing the phosphorus analogues is hindered by suitable precursors.[253]–[255] In this context, rare terminal phosphide transition metal complexes are particularly attractive since they represent P_1 building blocks which can be functionalized stoichiometrically, providing an entry into low-valent phosphorus chemistry.[63]

In the case of phosphorus monoxide, a molecule only found in interstellar clouds, several μ^3-type complexes have been described for various transition metals across the periodic table, however terminal phosphorus monoxide transition metal complexes remain extremely scarce.[243],[256] The oxygenation of the terminal molybdenum phosphide **XVI** gave the unprecedented terminal phosphorus monoxide complex **XL**, as described in the introduction of this thesis. The phosphorus monoxide ligand is coordinated almost linearly suggesting no antibonding interaction of the metal center and the π-system and a retention of the Mo^{VI} oxidation state.[257]

Other low-molecular phosphorus oxides are limited to three examples. The *push-push* stabilized diphosphorus compound **XCV** was oxygenated by molecular O_2 yielding an NHC stabilized neutral P_2O_4 compound **LXXXI**, while the oxygenation of the Fe-Co-P cluster **LXXXII** gave a P_2O ligand encumbered within the cluster **LXXXIII** (Scheme 4.5).[258],[259] A recent report features the preparation of PO_3^{2-} upon heating ReI_3 with red phosphorus and sodium cyanate and subsequent hydrolysis yielding the cluster $Na_8[\{Re_4(PO)_3(PO_2)\}(CN)_{12}]$ (**LXXXIV**, Scheme 4.5).

Oxygenation of **27** could enable access to new $P_xO_y^{n-}$ species and will be evaluated in the following.
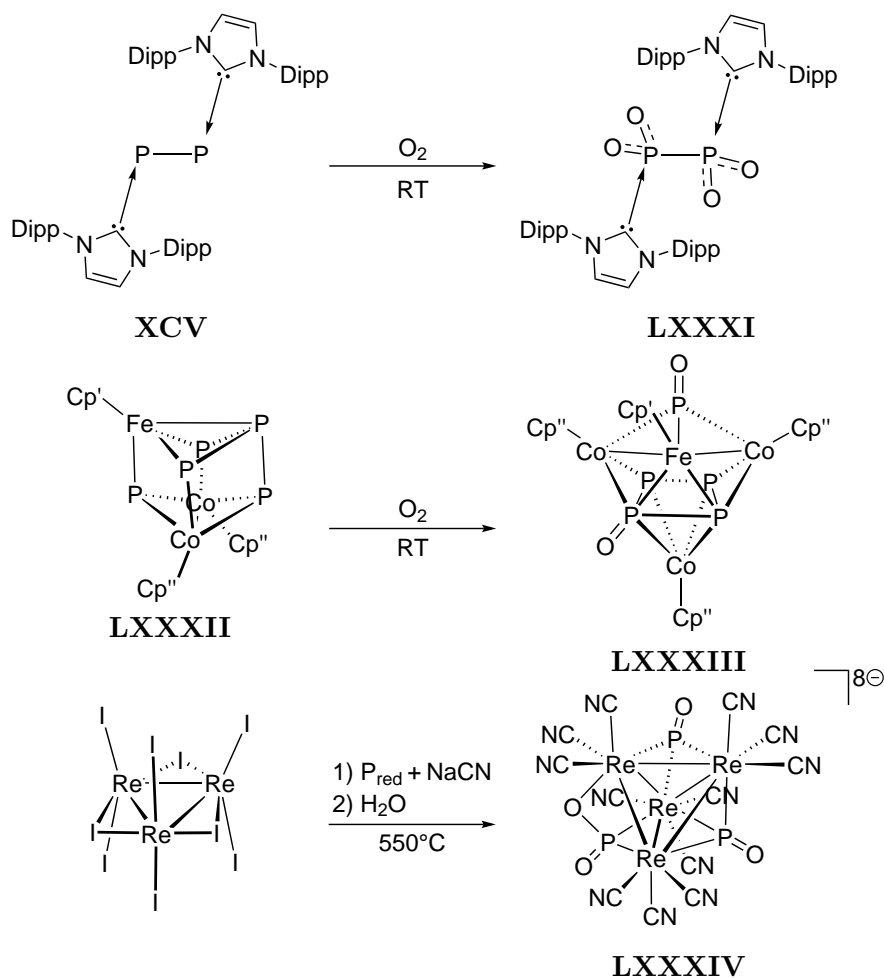
Scheme 4.5: Oxygenation of **XCV** and **LXXXII** to give **LXXXI** and **LXXXIII**, respectively, Cp' = C$_5$Me$_5$, Cp" = 1,3-^{t}Bu$_2$C$_5$H$_3$, and synthesis of the cluster compound **LXXXIV** from ReI$_3$.[258]–[260]

Table 4.1: P−O bond lengths in low-molecular phosphorus oxide ligands.

Compound	Ligand	Bond distance / Å
XL	PO	1.49(2)
LXXXI	P$_2$O$_4$	1.466(3) 1.470(3)
LXXXIII	P$_2$O	1.509(6)
LXXXIV	PO$_2^{3-}$	1.58(3) 1.50(3)

Heating **27** with two equivalents of pyridine-N-oxide in benzene at elevated temperatures results in the clean formation of dimeric $[\{Re(L^1)(\kappa^2 N^1 N^2\text{-PyrPz})\}_2\{\mu-P^1 P^2\text{-}P_2O_4\}]$ (**31**, Scheme 4.6) in 77% isolated yield. **31** features an unprecedented dianionic $P_2O_4^{2-}$ fragment with a planar P_2O_2 unit bridging both Re^{III} centers (Figure 4.8), in stark contrast to **LXXXI**. The oxygenation reaction results in a significant elongation of the Re−P bond by $\Delta d = 0.36\,\text{Å}$ with respect to **27**. The PyrPz ligand rearranges over the course of the reactions, reminiscent of the iodide complex **11**, since the strong *trans*-influence of the phosphide ligand is lost upon oxygenation, allowing for chelation, resulting in the overall observed octahedral coordination sphere. An intense band at $\tilde{\nu}_{PO} = 1112\,\text{cm}^{-1}$ is observed for the antisymmetric stretching vibration of the $P_2O_4^{2-}$ ligand, redshifted by $\Delta\tilde{\nu}_{PO} = 167\,\text{cm}^{-1}$ when compared to **LXXXI**. Two signals are detected by ^{31}P{^{1}H} NMR spectroscopy at $\delta_P = 245.7$ and 13.2 with a mutual coupling constant of $^2 J_{PP} = 20.7\,\text{Hz}$. When the reaction is carried out with equimolar amounts of oxygen atom transfer reagent, 50% conversion towards **31** is observed by ^{31}P NMR, suggesting that a putative phosphorus monoxide complex is too reactive to be isolated under this reaction conditions. A DFT geometry optimization of the hypothetical complex $[Re(PO)(L^1)(\kappa^2 N^1 N^2\text{-PyrPz})]$ (**32**) reveals a short Re−P bond distance and a highly bent Re-P-O unit, contrasting with linear **XL**, suggesting Re=P double bond character (Re-P: $2.16\,\text{Å}$, P-O: $1.52\,\text{Å}$, Re-P-O: $146.4°$; for an NBO analysis see: Appendix 8.3.25).
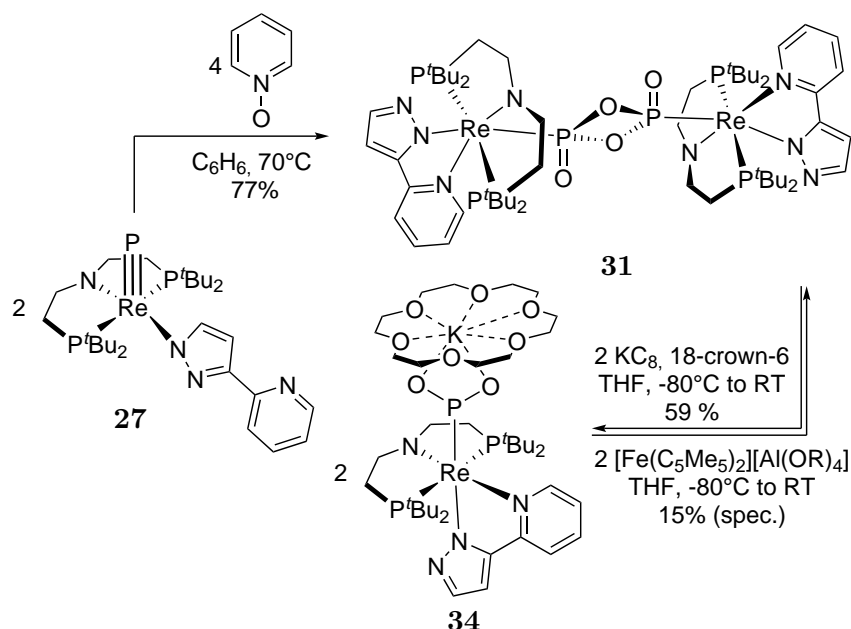
Scheme 4.6: Oxygenation of **27** to give **31** and its redox-chemical interconversion with **34**, R = $C(CF_3)_3$.
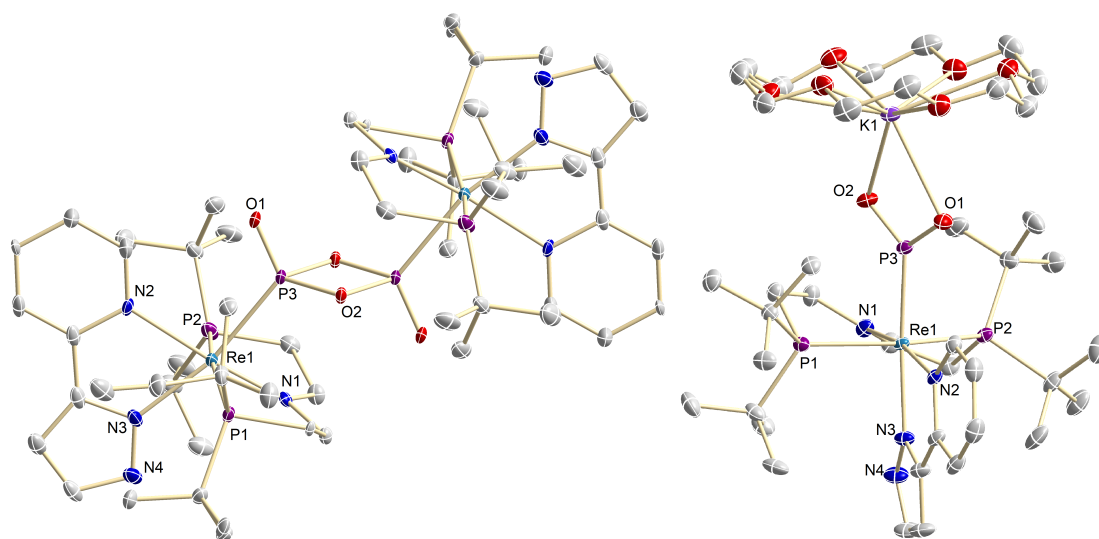
Figure 4.8: Solid state structure of **31** (left) and **34** (right) from single-crystal X-ray diffraction (thermal ellipsoids drawn at the 50% probability level); solvent molecules and hydrogen atoms are omitted for clarity. Selected bond lengths [Å] and angles [°]: **31** Re1-N1 1.900(5), Re1-N2 2.263(5), Re1-N3 2.143(6), Re1-P1 2.4457(19), Re1-P2 2.4528(18), Re1-P3 2.4564(18), P3-O1 1.484(5), P3-O2 1.685(5), N1-Re1-P3 82.75(16), P1-Re1-P2 163.84(16), O2-P3-O2# 82.8(2); **34** Re1-N1 2.082(2), Re1-N2 2.141(2), Re1-N3 2.162(2), Re1-P1 2.3977(7), Re1-P2 2.4332(7), Re1-P3 2.2545(7), P3-O1 1.517(2), P3-O2 1.512(2), O1-K1 2.730(2), O1-K2 2.731(2), N1-Re1-P3 94.31(9), P1-Re1-P2 155.70(2), O1-P3-O2 110.26(12).

The cyclic voltammogram of **31** features an irreversible oxidative wave at $E_{\text{p.a.}} \approx 0.23\,\text{V}$, a reversible reduction at $E_{1/2} = -1.92\,\text{V}$ and an irreversible reductive event at $E_{\text{p.c.}} \approx -3.02\,\text{V}$ vs. $\text{Fc}^{0/+}$ (Figure 4.10, Appendix 8.3.26). A new wave at $E_{\text{a.c.}} \approx 1.71\,\text{V}$ emerges from the irreversible reductive event, suggesting an overall *EEC* mechanism. The decrease of the peak current at $E_{\text{p.c.}} \approx 1.71\,\text{V}$ upon application of slower scan rates is indicative for a chemical follow-up reaction of the two-electron reduction product of **31**.[261] Stirring **31** with one equivalent of NaHg and 15-crown-5 in THF results in a slow color change from orange to red. The obtained product slowly decomposes at room temperature in THF and toluene, indicated by a color change to brown. The cyclic voltammogram suggests that the one-electron reduction of **31** towards $[\{\text{Re}(\text{L}^1)(\kappa^2 N^1 N^2\text{-PyrPz})\}_2\{\mu - P^1 P^2\text{-P}_2\text{O}_4\}]^-$ (**33**) is reversible on the timescale of the experiment, indicating a certain lifetime. The formation of a paramagnetic species is confirmed by EPR spectroscopy (Figure 4.10). The unpaired electron resides mainly on the metal center since only $^{185/187}$Re hyperfine splitting is detected ($A_{\text{iso}}(^{185/187}\text{Re}) = 756\,\text{MHz}$, Figure 4.10). No additional (super)-hyperfine interactions could be resolved. The sign of A_{iso} can be derived by the different broadenings of the observed transitions. For an $S = \frac{1}{2}$ systems, the peak-to-peak linewidths ΔB_{p-p} for the anisotropically splitted signal can be expressed as a polynome dependent on m_I:[262]

$$\Delta B_{p-p} = A + Bm_I + Cm_I^2 + Dm_I^3 \tag{4.1}$$

A, B, C and D are constant and positive. D is usually close to zero and therefore
neglected. From this equation it is obvious that signals with positive m_I values will
be splitted the most, while negative values lead to smaller splitting and thereby eas-
ier isotropic averaging at room temperature. The term Bm_I is usually dominant and
therefore allows to determine the sign of A_{iso}. Since the transition at higher fields are
broadened the most, a positive sign is derived for the hyperfine coupling constant (Figure
4.9). A possible rationalization of the positive value lies in electron-electron exchange
interactions at the Re center resulting in spin-polarization of the s orbitals.[263]–[266]
Nevertheless, spin-orbit coupling and other effects could also play an important role and
a more thorough theoretical analysis of the EPR spectrum would be required to fully
interpret this finding which is beyond the scope of this thesis.
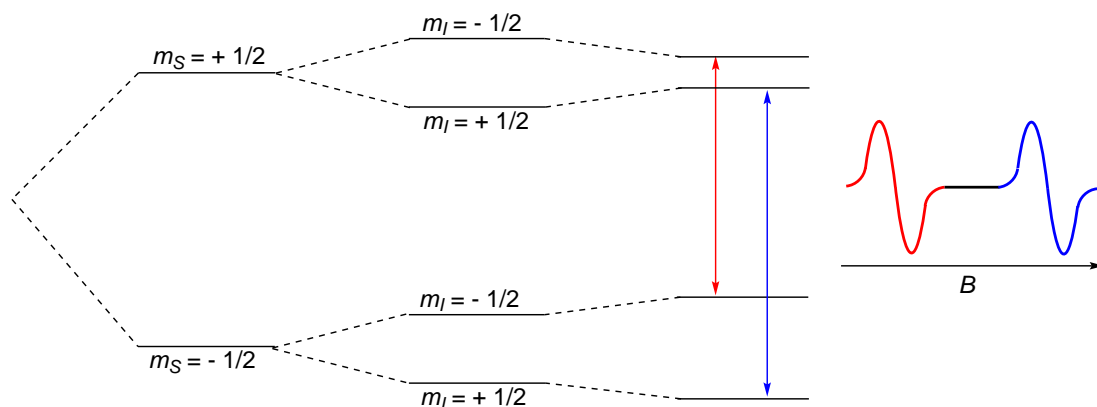
Figure 4.9: State-splitting for an $S = \frac{1}{2}$ system coupled with an $I = \frac{1}{2}$ nucleus and a positive
hyperfine splitting value A.

IR spectroscopy reveals an intense band at $\tilde{\nu}_{\mathrm{PO}} = 1124\,\mathrm{cm}^{-1}$. The minor shift of the
stretching vibration when compared to **31** suggests no significant alteration of the bond-
ing situation in the $P_2O_4^{2-}$ fragment upon reduction, in line with the results of the EPR
spectroscopy. Single-crystals suitable for X-ray diffraction experiments could not be
obtained.

When **31** is reacted with an excess of KC_8 in THF, at low temperatures in the pres-
ence of 18-crown-6, a color change from orange over red to deep purple can be ob-
served upon slow warming to room temperature. The disappearance of all ^{31}P NMR
signals suggests paramagnetism of the reaction product. Single crystal X-ray diffrac-
tion reveals that the $P_2O_4^{2-}$ ligand is split homolytically resulting in the formation of
$[K(C_{12}H_{24}O_6)][Re(L^1)(PO_2)(\kappa^2 N^1 N^3\text{-PyrPz})]$ (**34**, Scheme 4.6, Figure 4.8), which rep-

resents the first example of a PO_2^- ligand bound to a transition metal. **34** features an octahedral coordination mode with a twisted PNP ligand. The P–O bond lengths of the trigonal planar PO_2^- moiety are almost identical (P3-O1: 1.517(2) Å, P3-O2: 1.512(2) Å), close to the shorter bond in **LXXXIV** (P-O: 1.50(3) Å) and slightly elongated when compared to the experimental value of free PO_2^- (P-O: 1.50 ± 0.01 Å).[245], [260]
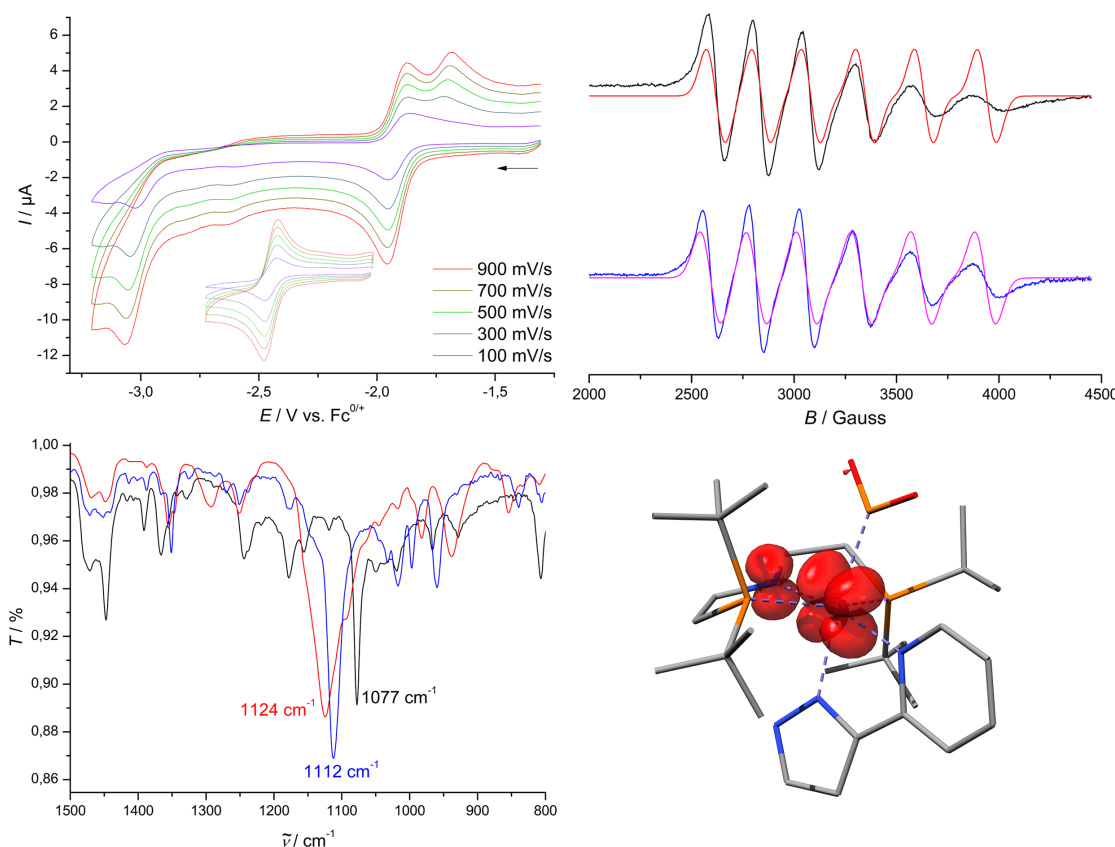
Figure 4.10: Top-Left: Cyclic voltammogram of **31**, 0.7 mM, 0.1 M NBu_4PF_6, THF, RT; Inset: First reduction; Top-right: EPR spectrum of **33**, Toluene, 260 K, 9.4277 GHz, g_{iso} = 2.038, $A_{iso}(^{185/187}Re)$ = 756 MHz (top, simulation in red), **34**, THF, 300 K, 9.4169 GHz, g_{iso} = 2.046, $A_{iso}(^{185/187}Re)$ = 770 MHz (bottom, simulation in pink); Bottom-left: IR spectra of **31** (blue), **33** (red), **34**, ATR, RT; Bottom-right: Computed spin-density of **34**.

The Re–P bond length of d_{ReP} = 2.4564(18) Å and its torsion angle (N1-Re1-P3-O2: 22.6(3)°) suggest no π-interaction between the metal center and the phosphorus atom. Interestingly, no pure compound can be obtained when no crown ether is added, in line with the cyclic voltammogram. An intense band for the asymmetric stretching vibration is detected at $\tilde{\nu}_{PO_2}$ = 1077 cm^{-1} (Figure 4.10). The EPR spectrum of **34** shows high similarities with **33**, accompanied by more effective isotropic averaging. While the hyperfine interaction value is almost identical, g_{iso} shows a minor shift of ca. 0.01. This suggests that the singly occupied molecular orbitals of **33** and **34** are highly similar in

shape with no significant participation of the $P_2O_4^{2-}$ and PO_2^- ligands, respectively. Chemical reversibility of the splitting reaction could be shown by reacting **34** with one equivalent of $[Fe(C_5Me_5)_2][Al(O(C(CF_3)_3)_4]$ at $-80°C$, which resulted in 33% conversion towards **31** accompanied by several dia- and paramagnetic side products (Scheme 4.6, Appendix 8.3.28). This result suggests that coupling of the neutral complex PO_2-complex $[Re(L^1)(PO_2)(\kappa^2N^1N^3\text{-PyrPz})]$ (**35**) towards **31** is feasible at low temperatures but unselective. Therefore, oxygenation of **27** towards **31** is likely to proceed *via* a different pathway, e.g. coupling of a phosphorus monoxide complex towards a dimeric $P_2O_2^{2-}$ complex which is further oxygenated towards **31**.

The electronic structure is further elucidated by DFT calculations. Spin-density calculations reveal a minor density of 1.3% at the PO_2^--phosphorus atom while 74.6% is located at the Re ion (Figure 4.10). The Re s orbital contribution is calculated to be 10%, in line with the observed sign of the hyperfine coupling constant. In accordance with the computed SOMO, which represents an antibonding N_{PNP}-Re π^*-orbital, the PNP-nitrogen atom exhibits a spin-density of 28.7% (Appendix 8.3.27). To clarify the bonding situation between the metal center and the PO_2^- ligand NBO/NLMO computations and Mayer bond orders were considered to obtain a representative Lewis-structure. The calculated bond order of 1.19 of the Re$-$P unit and the shape of the bonding Re-P NLMOs reveal only σ-bonding interactions while π-interactions seem to be small, as in nitrogen-bound NO_2^- ligands, in line with the molecular orbital diagram of free PO_2^- (Figure 4.11, Appendix 8.3.29).[253] The Re-P bond features 66% P character. However, an energy decomposition analysis of this bonding situation could provide a more detailed description of the Re-PO_2 interaction.[19] Bond analysis of the PO_2^- fragment reveals P$-$O bond order of 1.63 and 1.69. Three lone-pairs are found for each oxygen atom while the phosphorus atom features an unoccupied valence orbital. One of the lone pairs of each oxygen atoms is depleted of electron density which can be located at the phosphorus center (Figure 4.11). Based on this, the PO_2^- ligand is best described as an anionic σ-donor ligand which features a phosphorus atom that is resonance-stabilized by the oxygen lone-pairs, resulting in the Lewis-structure shown in Figure 4.11, in line with the computed NPA charges. Due to the identical contributions of α and β spin NLMOs to the fragments considered in the PO_2^- unit, it can be concluded that the unpaired electron has no significant influence on this bonding situation.

Fragment	Orbital	α occ.	β occ.	NPA charge
O$_1$	LP	0.99	0.99	
	LP	0.94	0.93	-0.57
	LP	0.86	0.86	
O$_2$	LP	0.99	0.99	
	LP	0.93	0.93	-0.57
	LP	0.87	0.87	
P	LV	0.33	0.33	0.88
Re	LP	0.94	0.86	
	LP	0.86	0.82	-0.11
	LP	0.82	/	
P−O$_1$	BD	0.99	0.99	
P−O$_2$	BD	0.99	0.99	
P−Re	BD	0.99	0.95	

Fragment	O / %	P / %	Re / %
O$_1 \xrightarrow{\pi}$ P	82.9	16.1	
O$_2 \xrightarrow{\pi}$ P	85.5	11.7	
P $\xrightarrow{\sigma}$ Re		62.5	34.0
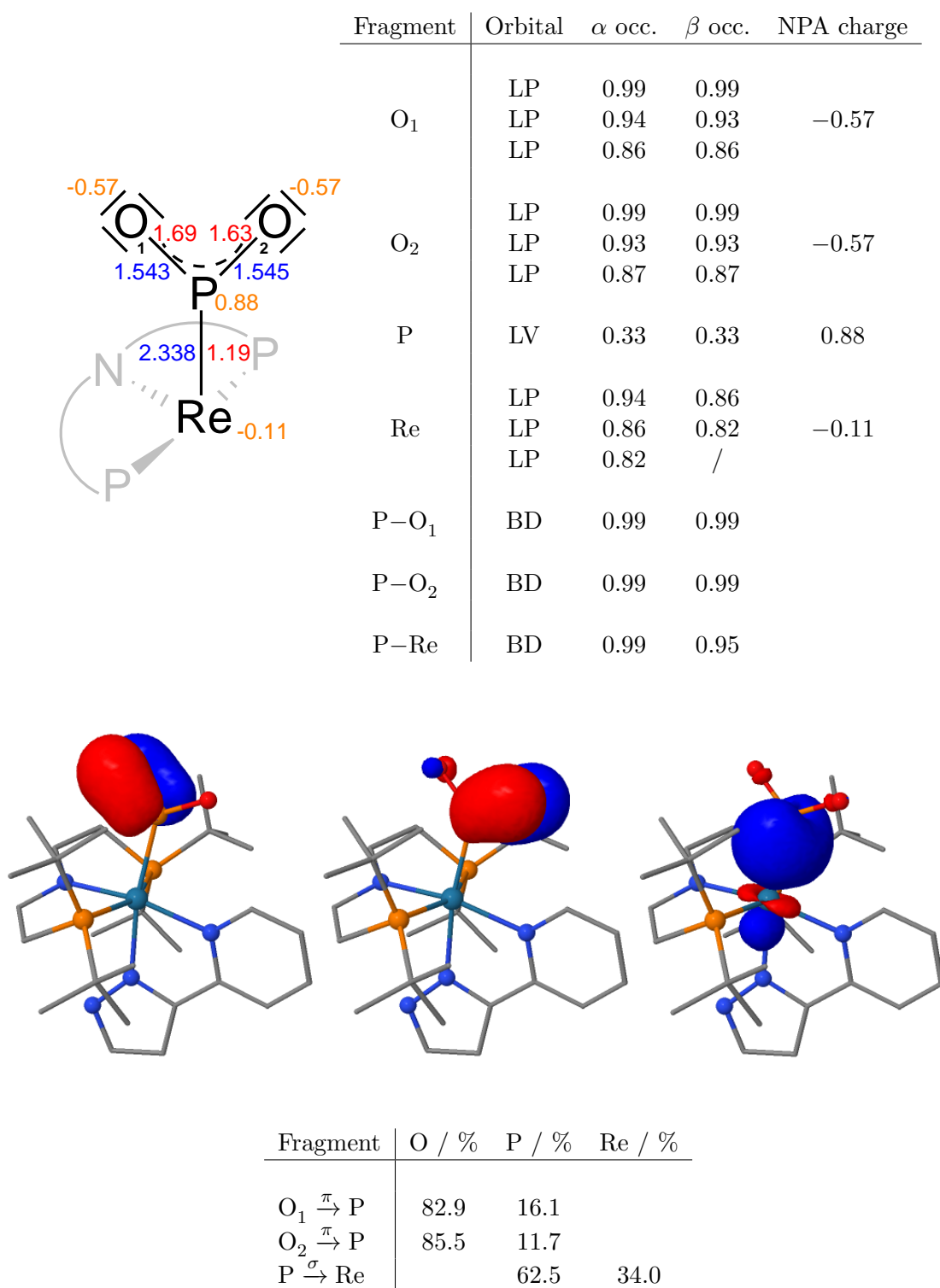
Figure 4.11: Top left: Lewis-structure of **34** derived by NBO/NLMO and Mayer bond order calculations (calculated bond distances in blue, bond orders in red, NPA charges in orange); Top right: NBO occupations for α and β spin orbitals, LP = lone pair, LV = lone vacancy, BD = 2c2e bond and calculated NPA charges; Middle: Computed α spin NLMOs representing the resonance stabilization of the phosphorus atom (left, middle) and σ-donation of the ligand to the Re d$_{z^2}$ orbital (right); Bottom: Atom contributions to the Re-P σ and π NLMOs.

4.3 Interconversion of Os PHMes* and PMes* Complexes by PCET

The reactivity of **2** towards oxidative addition of primary phosphines was initially probed
by reaction with PH_2Ph. When a freshly prepared solution of **2** is reacted with PH_2Ph,
clean formation of green phosphine complex $[OsCl(L^3)(PH_2Ph)]$ (**36**, Scheme 4.7) can
be accomplished in 80% isolated yield. **36** exhibits a distorted square-pyramidal co-
ordination sphere in the solid state with the phosphine ligand in the apical position
(Figure 4.12). Due to coordination, the ^{31}P NMR signal of PH_2Ph is downshifted to
$\delta_P = -62.2\,ppm$ with a coupling constant of $^2J_{PP} = 18.7\,Hz$. No conversion to an
Os^{IV} species was observed upon heating indicating that oxidative addition might be
thermodynamically unfavorable.
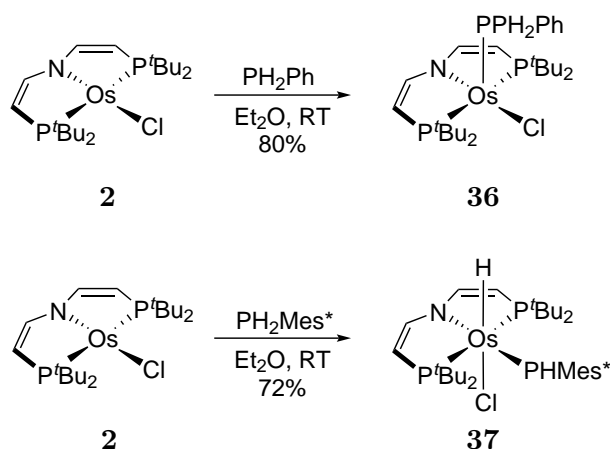
Scheme 4.7: Reaction of **2** with the primary phosphines PH_2Ph and PH_2Mes^* to yield **36** and
37, respectively.

Therefore, the more electron-rich phosphine PH_2Mes^* was utilized. Complex **2** reacts
readily with the primary phosphine to the dark-blue oxidative addition product [OsCl-
H(L^3)(PHMes*)] (**37**, Scheme 4.7). The ^{31}P signal of the PHMes* moiety is observed at
$\delta_P = 103.9\,ppm$ excluding simple phosphine coordination. Upon mixing an instant color
change to green is observed which is tentatively assigned to initial phosphine coordina-
tion. **37** decomposed over the course of a few hours in solution at room temperature
but could be fully characterized including single crystal X-ray diffraction. The NMR
signals at $-30°C$ are in agreement with C_1-symmetry, indicating phosphanide to Os^{IV}
π-donation. Accordingly, the phosphide P-atom exhibits trigonal-planar coordination in
the solid state (Figure 4.12).
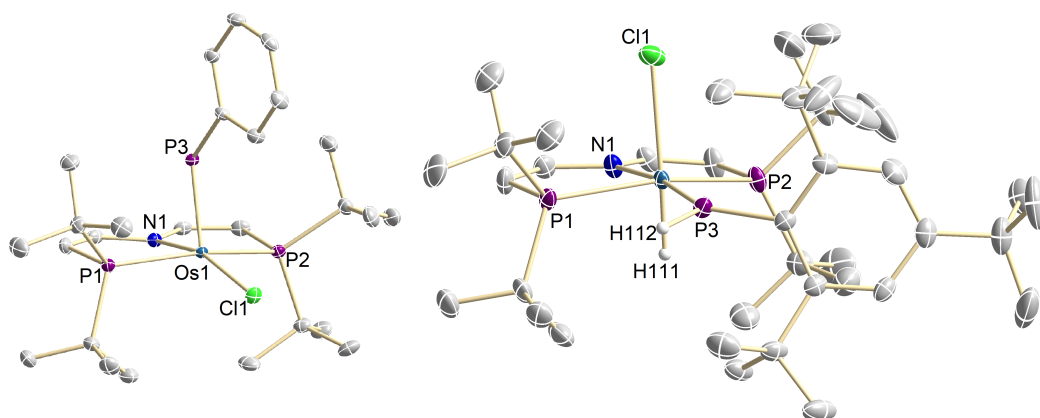
Figure 4.12: Molecular structure of complex **36** (left) and **37** (right) from single-crystal X-ray diffraction (thermal ellipsoids drawn at the 50% probability level); solvent molecules, hydrogen atoms, except hydrides and the P−H of **37** are omitted for clarity. Selected bond lengths [Å] and angles [°]: **36** Os1-Cl1 2.3865(5), Os1-N1 3.0754(18), Os1-P1 2.3604(6), Os1-P2 2.3602(6), Os1-P3 2.1928(6), N1-Os1-Cl1 162.89(6), P1-Os1-P2 160.39(2), τ = 0.04; **37** Os1-Cl1 2.4912(11), Os1-H111 1.54(2), Os1-N1 2.078(3), Os1-P1 2.4004(11), Os1-P2 2.4475(10), Os1-P3 2.1919(11), P3-H112, 1.35(3), N1-Os1-P3 171.59(8), P1-Os1-P2 156.14(5).
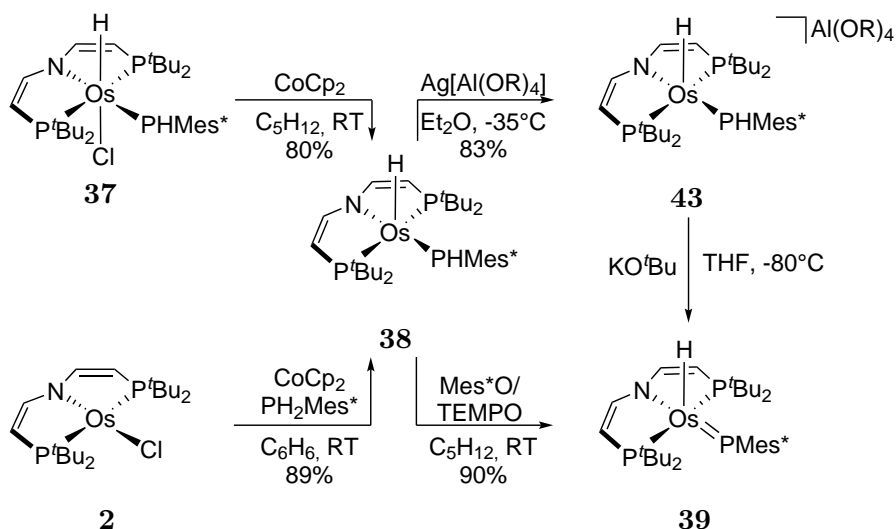
Scheme 4.8: Synthesis of **38** starting from **37** or **2** and its conversion towards **43** and **39**, R = C(CF$_3$)$_3$.

Reduction of **37** with CoCp$_2$ affords the radical complex [OsH(L^3)(PHMes*)] (**38**, Scheme 4.8) in 80% isolated yield after column chromatography. The magnetic moment in solution (μ_{eff} = 1.51 μ_{B}) derived by Evan's method is in agreement with an $S = \frac{1}{2}$ system with unquenched orbital momentum. **38** can also be directly synthesized from **2** by one-pot oxidative addition and subsequent reduction. Characteristic bands for the PHMes* and hydride ligands were detected in the IR spectrum ($\tilde{\nu}_{\mathrm{PH}}$ = 2345 cm^{-1};
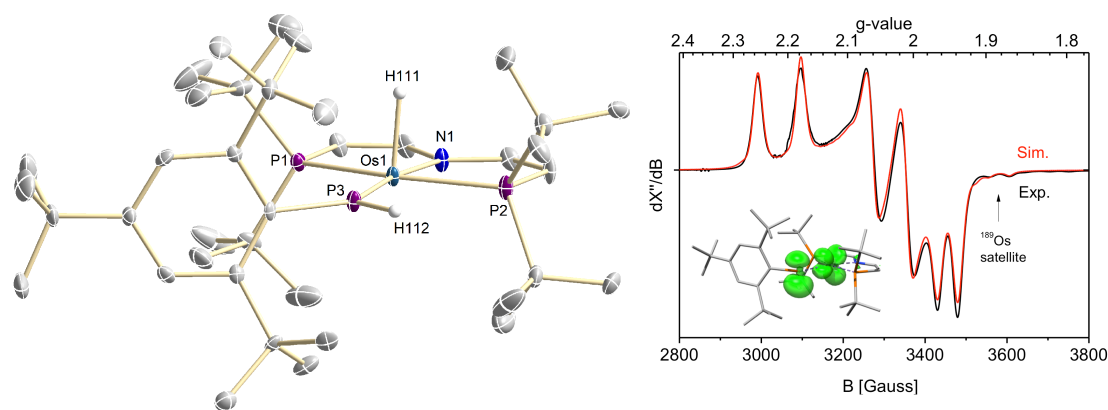
Figure 4.13: Left: Molecular structure of complex **38** (left) from single-crystal X-ray diffraction (thermal ellipsoids drawn at the 50% probability level); solvent molecules, hydrogen atoms, except hydrides and the PH protons of **38** are omitted for clarity. Selected bond lengths [Å] and angles [°]: **38** Os1-H111 1.96(6), Os1-N1 2.069(4), Os1-P1 2.3723(12), Os1-P22.3537(13), Os1-P3 2.2301(13), P3-H112 1.35(5), N1-Os1-P3 172.17(11), P1-Os1-P2 160.20(4), $\tau = 0.2$; Right: EPR spectrum of **38**, 9.4366 GHz, toluene, 148 K, simulation (red) with the following parameters (DFT computed values in brackets): $g_x = 1.952(1.951)$, $g_y = 2.033(2.024)$, $g_z = 2.214(2.230)$; $A_x(^{31}P) = +57$ Mhz(+58 MHz), $A_y(^{31}P) = +105$ MHz(+95 MHz), $A_z(^{31}P) = +440$ Mhz(+441 MHz); Euler angles: $\alpha = -73(-74.3)$, $\beta = +137(+142.7)$, $\gamma = -7.5(-7.5)$; $A_x(^{189}Os) = -240$ MHz(-277 MHz). Inset: Spin-density plot.

$\tilde{\nu}_{OsH} = 2180 \, cm^{-1}$, Appendix 8.3.36). In the solid state, complex **38** features a distorted square-pyramidal coordination geometry with the hydride in the apical position (Figure 4.12). The Os−P bond to the PHMes* ligand is slightly elongated by $\Delta d = 0.04 \, Å$ upon reduction from **37** to **38**.

The EPR spectrum of **38** in frozen toluene exhibits a rhombic signal that is in agreement with an $S = \frac{1}{2}$ low-spin configuration (Figure 4.13). The g-anisotropy ($g_x = 1.952$, $g_y = 2.033$, $g_z = 2.214$) is considerably smaller than that of typical Os^{III} complexes, e.g. **1** and **12**, in line with reduced spin-orbit interaction due to ligand redox non-innocence.[267] Accordingly, large and slightly rhombic hyperfine interaction (HFI) with one ^{31}P nucleus is observed in all principal directions of the g-tensor ($A_x = +57$ MHz, $A_y = +105$ MHz, $A_z = +440$ MHz), supporting considerable spin delocalization to the PHMes* ligand. Partially resolved ^{189}Os satellite HFIs are detected as well. The free phosphinyl radical PPh$_2$ exhibits axial ^{31}P-HFI with an isotropic coupling constant ($A_{iso}(^{31}P) = 260$ MHz) close to that of **38** ($A_{iso}(^{31}P) = 201$ MHz). The higher isotropic HFI ($A_{iso}(^{31}P) = 499$ MHz), yet reduced dipolar coupling, found for the transient phosphinyl radical complex $[W(PPh_2)(CO)_5]$ was attributed to p$_P$→d$_W$ spin delocalization ($\rho_P = 75\%$) and concomitant polarization of the P lone-pair.[141] For **38**, the higher g-anisotropy and smaller isotropic and anisotropic contributions of the HFI tensor are consistent with increased P→M spin delocalization. Comparing the isotropic ($A_{iso} = 201$ MHz) and anisotropic ($T_x = -144$ MHz, $T_y = -96$ MHz, $T_z = +239$ MHz)

contributions to the ^{31}P-HFI with atomic parameters allows for a rough estimate of phosphorus spin densities ($\rho_{3s} \approx 2\%$, $\rho_{3p} \approx 42\%$) when treating the HFI approximately axial ($T_\perp = (T_x + T_y)/2$).[267] DFT calculations fully support this interpretation. Both the experimental molecular structure and the EPR parameters were reproduced computationally ($g_x^{\mathrm{DFT}} = 1.951$, $g_y^{\mathrm{DFT}} = 2.024$, $g_z^{\mathrm{DFT}} = 2.230$; ^{31}P-HFI: $A_x^{\mathrm{DFT}} = +58\,\mathrm{MHz}$, $A_y^{\mathrm{DFT}} = +95\,\mathrm{MHz}$, $A_z^{\mathrm{DFT}} = +441\,\mathrm{MHz}$). The SOMO of **38** represents an antisymmetric (π^*) combination of the metal d_{yz} orbital and a phosphorus p orbital (Appendix 8.3.37). Reduced π-bonding is expressed by the Os$-$PHMes* Mayer bond index (1.46). In consequence, the computed spin density is almost equally distributed between the phosphorus ($\rho_P = 47\%$) and osmium atoms ($\rho_{Os} = 50\%$). The spectroscopic and computational evaluation supports considerable redox non-innocence of the PHMes* ligand. Complex **38** represents an unprecedented, isolable phosphanide complex with large phosphinyl radical-character (Os^{II}-•PR$_2$). Therefore, possible PCET reactivity of the radical ligand, specifically as an entry to phosphinidene chemistry, was examined. Two experimental methods are widely used to estimate E$-$H BD(F)Es of organometallic compounds, i.e. (a) bracketing based on hydrogen transfer reagents with reference H-donor/acceptor reagents and (b) quantification *via* the square-scheme formalism, i.e. a thermochemical redox/protonation cycle.[268]

Complex **38** shows no reactivity with the H-atom donor reagent TEMPO-H (TEMPO = 2,2,6,6-tetramethylpiperidinyloxyl; BDFE$_{OH} \approx 66\,\mathrm{kcal \cdot mol}^{-1\,[268]}$), indicating weak P$-$H bonds for the hypothetical Os^{II} phosphine complex [OsH(L^3)(PH$_2$Mes*)]. Kinetic reasons are unlikely for the lack of reactivity as **38** readily undergoes P$-$H transfer with TEMPO. In turn, **38** readily reacts with the H-atom acceptors Mes*O and TEMPO. The purple product that is obtained in high yields around 90% exhibits low thermal stability at room temperature even in the solid state but could be characterized by NMR spectroscopy at $-30°$C (Appendix 8.3.38). Retention of the hydride ligand is indicated by a ^{1}H NMR signal at $\delta_H = -15.9\,\mathrm{ppm}$. Formation of the phosphinidene complex [Os(PMes*)H((L^3)] (**39**, Scheme 4.8) is evidenced by the ^{31}P NMR signal at $\delta_P = 825\,\mathrm{ppm}$, assignable to the PMes* group. While suitable crystals for X-ray diffraction could not be obtained, the structural integrity of the osmium pincer phosphinidene framework is supported by derivatization (Scheme 4.9).

A solution of *in situ* prepared **39** in THF selectively converts over the course of some hours to a mixture of the two diastereomers of Os^{II} phosphine complex **40** as indicated by LIFDI-MS and NMR spectroscopy (Figure 4.14, Appendix 8.3.41). Electrophilic phosphinidene insertion into C$-$H bonds has previously been reported.[161], [269] Furthermore, addition of carbon monoxide to **39** gives the five-coordinate phosphanide complex [Os(L^3)(PHMes*)(CO)] (**41**, Scheme 4.9) after Os$-$H reductive elimination, which could be crystallographically characterized (Figure 4.15).

Figure 4.14: $^{31}P\{^1H\}$ NMR spectrum of the reaction of **39** with PhCCH yielding **42**, C_6D_6 (top), **41**, THF-d$_8$ (middle) and **40**, C_6D_6 (bottom).

Scheme 4.9: Conversion of **39** towards **40** and reaction with CO and PhCCH to give **41** and **42**, respectively.

The Os-PHMes* distance shows an elongation by $\Delta d = 0.034\,\text{Å}$ with respect to **38**, accompanied by a non-planar phosphorus atom which can be attributed by further population of the repelling Os d orbital. Considerable π^*-backbonding is indicated by $\tilde{\nu}_{CO} = 1888\,\text{cm}^{-1}$ (Appendix 8.3.42). Since the phosphinidene shows electrophilic reactivity, the terminal alkyne PhCCH was reacted with **39** to investigate if heterocycle formation occurs. Full conversion towards a C_1-symmetric species is observed by ^{31}P NMR. As for **41**, a PHMes* moiety is detected in the ^1H NMR ($\delta_H = 9.39\,\text{ppm}$, $^1J_{HP} = 308.7$, $^3J_{HP} = 12.3$, 5.3, $^4J_{HP} = 1.6\,\text{Hz}$) suggesting reductive elimination of the hydride ligand. This is further supported by the phosphorus NMR shift of the PHMes* moiety ($\delta_P = 3.52\,\text{ppm}$, Figure 4.14). ^{13}C NMR shows that the alkyne isomerized over the course of the reaction yielding a vinylidene ligand as commonly observed for the addition of alkynes to low-valent metal centers ($\delta_{Os=C=C} = 274.8, 113.2\,\text{ppm}$).[270] The reaction was accompanied by the formation of side products which could not be removed

by common purification techniques preventing characterization by combustion analysis. Due to high solubility in organic solvents, even at $-80°$C, no single crystals suitable for X-ray diffraction could be obtained. However, the indicative NMR signals suggest that the vinylidene complex $[Os(CCHPh)(L^3)(PHMes^*)]$ (**42**) was formed. The observed metal centered reactivity likely occurs due to the high Lewis-basicity of Os center in combination with the steric bulk shielding the phosphinidene phosphorus atom.
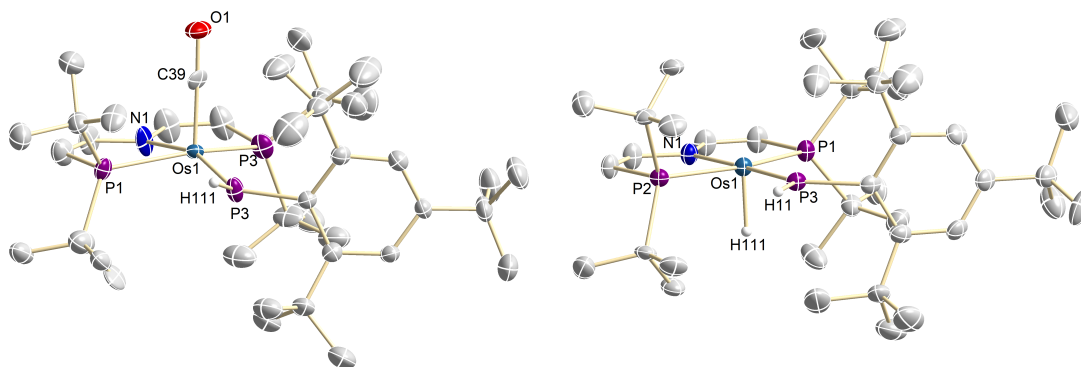
Figure 4.15: Molecular structure of complex **41** (left) and **43** (right) from single-crystal X-ray diffraction (thermal ellipsoids drawn at the 50% probability level); hydrogen atoms, except the PH protons and hydride ligands, and anions are omitted for clarity. Selected bond lengths [Å] and angles [°]: **41** Os1-C39 17.761(16), C39-O1 1.24(2), Os1-N1 2.141(9), Os1-P1 2.443(3), Os1-P2 2.372(3), Os1-P3 2.264(3), P3-H111 1.31(12), N1-Os1-P3 161.4(3), P1-Os1-P2 155.39(13), $\tau = 0.1$; **43** Os1-H111 1.59(2), Os1-N1 2.004(5), Os1-P1 2.4011(15), Os1-P2 2.3927(15), Os1-P3 2.1943(15), P3-H11 1.27(7), N1-Os1-P3 175.14(15), P1-Os1-P2 161.03(5), $\tau = 0.24$.

Parent **38** offers two potential sites for hydrogen atom abstraction. The generation of phosphinidene **39** therefore indicates higher Os$-$H over P$-$H bond strength if the reaction proceeds under thermodynamic control. BDE quantification was attempted by stepwise oxidation and deprotonation of **38**. The cyclic voltammogram of **38** reveals quasi-reversible reduction at $E_{p.c.} \approx -2.06$ V and reversible oxidation at $E_{1/2} = -0.88$ V vs. $FeCp_2^{+/0}$ (Appendix 8.3.31).

Chemical oxidation with $Ag[Al(OR)_4]$ (R = C(CF$_3$)$_3$) at $-35°$C immediately gives the deep blue Os^{IV} phosphanide complex $[OsH(L^3)(PHMes^*)][Al(OR)_4]$ (**43**, Scheme 4.8). Complex **43** readily decomposes at room temperature but could be fully characterized at low temperatures including crystallography which features square-pyramidal coordination and a shortening of the Os-PHMes* by $\Delta d = 0.036$ Å with respect to **38**. Retention of the hydride and PHMes* proton is indicated by their distinctive ^{1}H NMR signals ($\delta_H = 18.3, -21.7$ ppm). **38**, **41** and **43** represent an unprecedented series of five-coordinate Os complexes with a terminally bound phosphanide ligand in three oxidation states (Figure 4.15). Deprotonation of *in situ* prepared **43** with KO^{t}Bu at $-80°$C gives the phosphinidene complex **39** in almost quantitative yield. However, the low thermal stability of **43** severely hampered reliable pK_a derivation.

The P−H bond strength of **38** was therefore derived by isothermal titration calorimetry (ITC) using a PCET reagent. Titration of **38** with Mes*O in benzene or THF afforded the reaction enthalpies for HAT ($\Delta_r H^{C_6H_6} = -16.5 \, \text{kcal} \cdot \text{mol}^{-1}$, $\Delta_r H^{THF} = -17 \, \text{kcal} \cdot \text{mol}^{-1}$) and consequently the BDE_{PH} of **38** ($BDE^{C_6H_6} = 65.1 \pm 1 \, \text{kcal} \cdot \text{mol}^{-1}$, $BDE^{THF} = 67 \pm 1 \, \text{kcal} \cdot \text{mol}^{-1}$). Computational evaluation confirmed the calorimetric results. DFT analysis of **38** predicted a BDE of the phosphanide P−H bond (calibrated $BDE_{PH} = 67.5 \, \text{kcal} \cdot \text{mol}^{-1}$; non-calibrated: $64.0 \, \text{kcal} \cdot \text{mol}^{-1}$), i.e. considerably lower than the Os−H bond (calibrated $BDE_{OsH} = 74.2 \, \text{kcal} \cdot \text{mol}^{-1}$; non-calibrated: $70.1 \, \text{kcal} \cdot \text{mol}^{-1}$, for calibration details see experimental section), indicating that phosphinidene **39** is the thermodynamic PCET product.
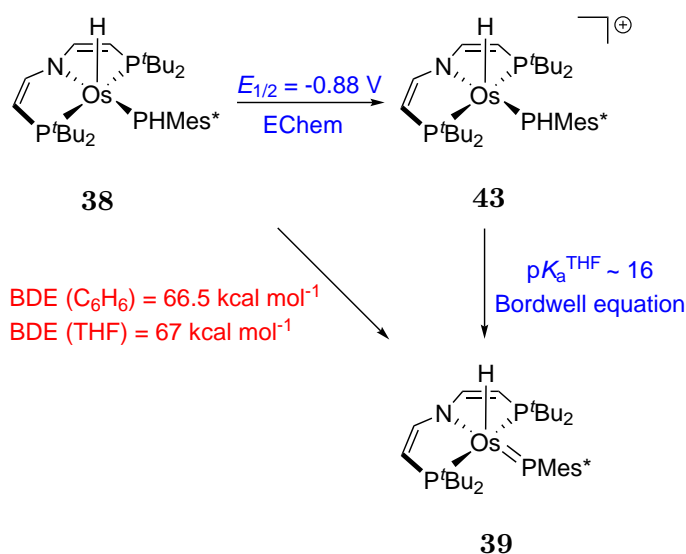
Scheme 4.10: Thermochemical square-scheme of **38**, **43** and **39**.

The calorimetric and electrochemical data also allows for calculation the pK_a of **43** ($pK_a^{THF} = 16$) from a thermochemical square-scheme by using the Bordwell equation (Scheme 4.10, Equation 4.2).

$$BDE_{THF}(\text{X-H}) = 1.37 pK_a + 23.06 E^\circ + C_{H,THF}, \quad \text{where } C_{H,THF} = 66 \, \text{kcal} \cdot \text{mol}^{-1}$$

(4.2)

4.4 An Isolable Terminal Chlorophosphinidene Complex

In Chapter 4.1 it was demonstrated that the phosphaethynolate anion is a competent phosphorus transfer reagent to access the terminal Re phosphide complex **27**. The question arises if this approach can be transferred to group 8 systems to further extend the realm of heavy pnictide multiple bonds. Besides this possible entry to low valent osmium phosphorus chemistry, utilization of the recently reported chloro-substituted 7-phospha-dibenzonorbornadiene (ClP**A**, Scheme 4.11), which has served as an attractive precursor for the synthesis of phosphorus transfer reagents, can be considered.[67], [271]–[273] A recent report features the transfer of a P−Cl unit to a Mo^0 complex resulting in a Mo^{IV} phosphide chloride complex (For details see the introduction of this thesis).[64] Additionally, it was demonstrated that ClP**A** can serve as a phosphorus atom source when reacted with the anionic vanadium nitride **LXXXV** yielding the transient unprecedented N≡P ligated complex **LXXXVI** which quickly aggregates towards the cyclo-P$_3$ trimeric complex **LXXXVII** (Scheme 4.11).[274]

The existence of **LXXXVI** was verified by addition of peri-1,8-naphthalene disulfide yielding compound **LXXXVIII** (Scheme 4.11). Addition of ClP**A** to low valent, coor-
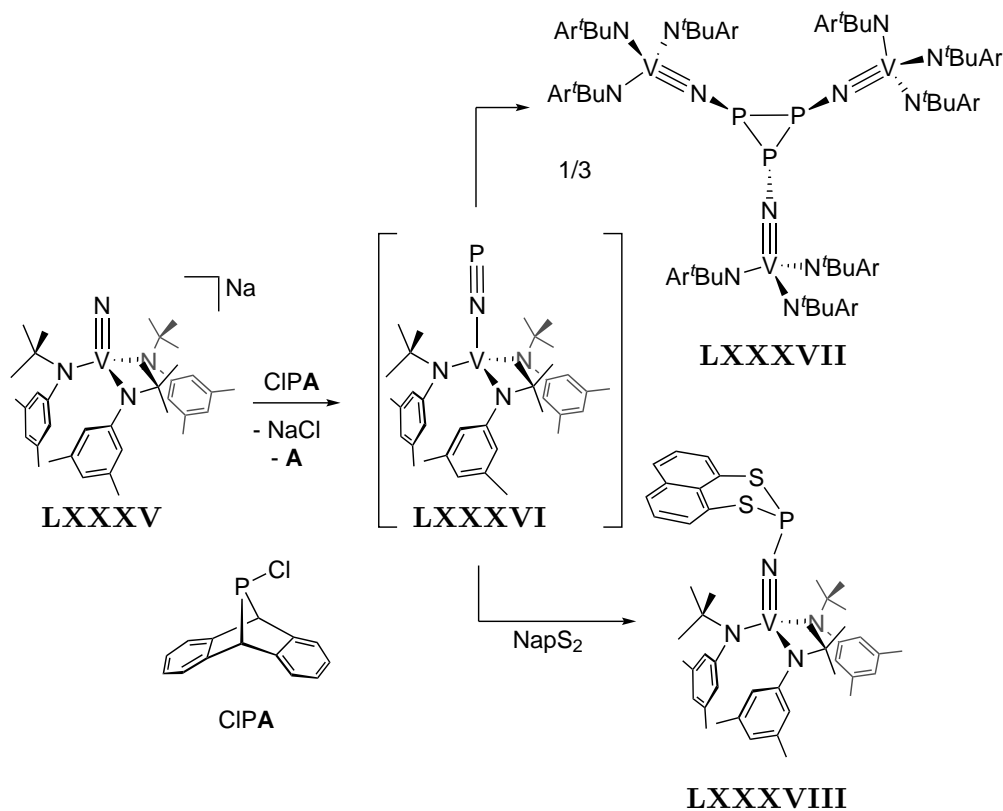
Scheme 4.11: Phosphorus atom transfer of ClP**A** towards **LXXXV**.[274]

dinatively unsaturated transition metal complexes could also give rise to unprecedented chlorophosphinidene complexes which lack a general synthetic procedure. Chlorophosphinidene complexes represent highly desired synthetic targets since they are expected to be strong electrophiles and therefore more reactive than the well-known alkyl- and aryl-substituted phosphinidenes in terms of follow-up P−C coupling reactions.[275], [276] In addition to this, the P−Cl moiety allows for diverse derivatization to access a variety of different phosphines, most desirable in a catalytic process, which are ubiquitous ligands in transition metal chemistry.[277]   Heating of the tungsten chlorophosphole complex **LXXXIX** and dimethyl acetylenedicarboxylate (DMAD) yielded the 7-phosphanorbornadiene complex **XC** which served as a source of the transient chlorophosphinidene **XCI**. Trapping by addition of tolane or cyclohexene gave **XCII** and, exclusively *cis*-configured, **XCIII**, respectively (Scheme 4.12).[275]   This observed reactivity was attributed to a phosphorus centered, low lying LUMO resulting in pronounced electrophilicity. Although no mechanistic or computational studies concerning the reaction pathway were presented that indicate the actual formation of the PCl-complex, this results nevertheless demonstrate the possible potential of chlorophosphinidenes in synthetic phosphorus chemistry. Employing transition metals beyond group 7 are particular attractive since the M≡P bond strength is expected to decrease successively along the periodic table, when going to more electron rich systems, which might favor transfer of the PCl moiety as a whole.[54]
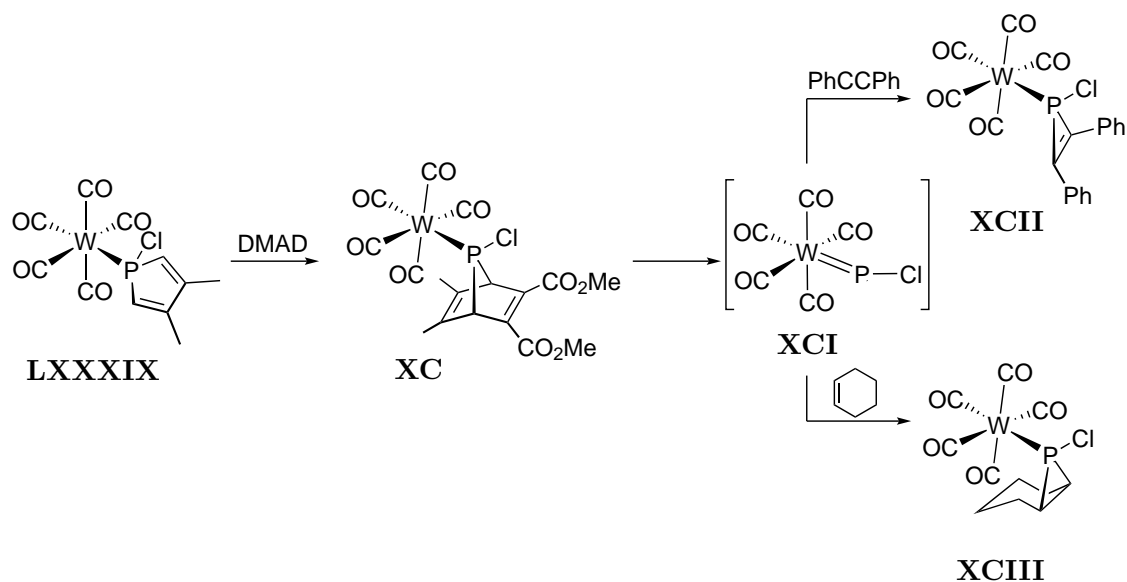
Scheme 4.12: Formation and follow-up reactivity of the proposed chlorophosphinidene complex **XCI**.[275]

Stirring **1** with one equivalent of $[Na(diox)_{1.39}][PCO]$ in THF results in an immediate color change to deep purple. Quantitative formation of **2** is confirmed by NMR spectroscopy (Scheme 4.13). If **7** is used instead, a color change towards deep red accompanied by no detectable ^{31}P NMR signals is observed, suggesting formation of **9** (Scheme 4.13). One-electron reduction is also observed for **12** (Scheme 4.13). The products obtained after the reduction reactions show no further reactivity towards PCO^{-} which renders the studied systems unsuitable as a whole.
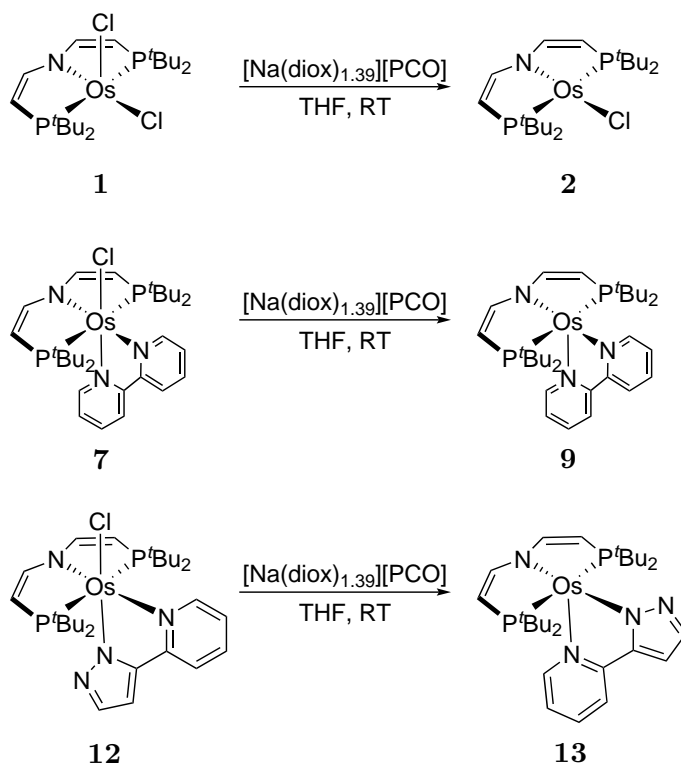
Scheme 4.13: Reduction of **1**, **7** and **12** with $[Na(diox)_{1.39}][PCO]$ towards **2**, **9** and **13**, respectively.

ClP**A** is another possible transfer reagent for phosphorus atoms. The square-planar Os^{II} complex **2** represents an ideal substrate since the low coordination number and high electron count should favor PCl extrusion from the sterically demanding 7-phosphanorbornadiene moiety. Furthermore, the four-electron oxidation upon formation of an $Os\equiv P$ and an $Os-Cl$ bond would result in an overall oxidation state of $+VI$ which is a suitable electron configuration for the stabilization of terminal pnictide complexes.
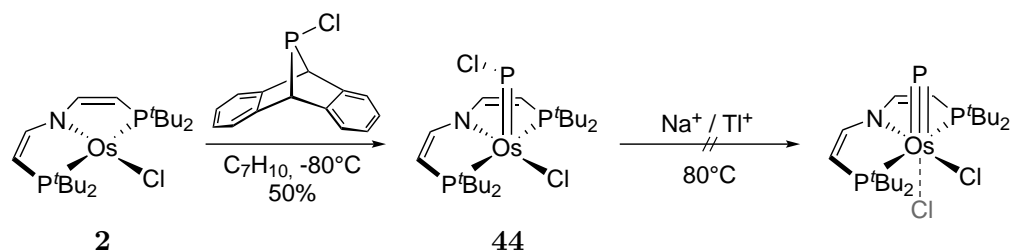
Scheme 4.14: Transfer of a PCl moiety to **2** upon addition of ClP**A** to yield **44**.

When a freshly prepared solution of **2** is reacted with one equivalent of ClP**A** at $-80°$C
and slowly warmed to room temperature, a slow color change from purple to reddish-
brown is observed. ^{31}P NMR spectroscopy indicates full and quantitative conversion
to a new diamagnetic species with phosphorus signals suggesting formation of a phos-
phinidene species over the course of the reaction ($\delta_P = 854.8, 70.4$ ppm). The ^{31}P NMR
signals are significantly broadened at room temperature hinting towards a flexible phos-
phorus substituent. The obtained molecular structure in the solid state shows that the
chlorophosphinidene complex [Os(PCl)Cl(L^3)] (**44**, Scheme 4.14) is indeed obtained. **44**
features a distorted square-pyramidal coordination sphere and an Os=P bond length
of $d_{OsP} = 2.1759(12)$ Å. This result is remarkable since it demonstrates the first ex-
ample of a transition metal chlorophosphinidene complex which is isolable and stable
at room temperature. Furthermore, this implies that the generation of the terminal
phosphide dichloride complex [OsPCl(L^3)] is associated with a high kinetic barrier or
thermodynamically unfeasible or both.
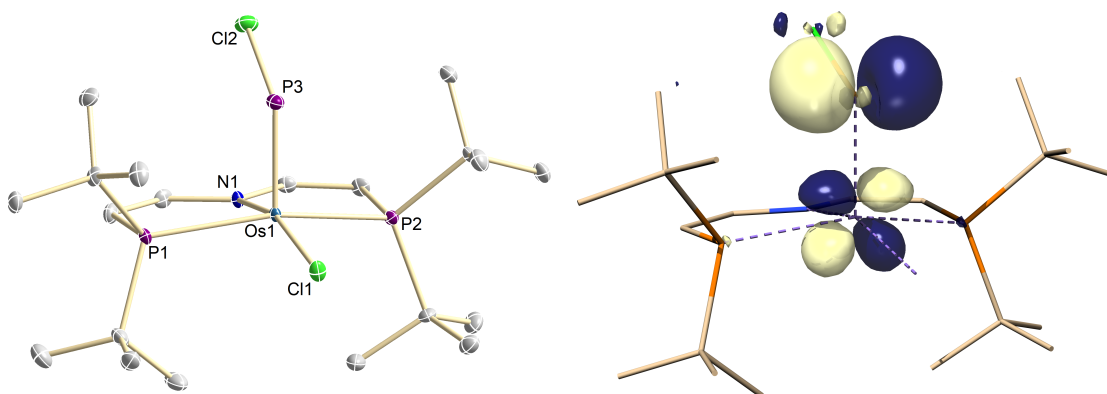
Figure 4.16: Left: Molecular structure of complex **44** from single-crystal X-ray diffraction
(thermal ellipsoids drawn at the 50% probability level); hydrogen atoms are omitted for clar-
ity. Selected bond lengths [Å] and angles [°]: **44** Os1-Cl1 2.387(3), Os1-N1 2.056(3), Os1-P1
2.3942(9), Os1-P2 2.4073(9), Os1-P3 2.1759(12), P3-Cl2 2.1759(12), N1-Os1-Cl1 162.46(8), P1-
Os1-P2 157.34(3), N1-Os1-P3 93.69(8); Right: Computed LUMO of **44**.

44 can be heated to 80°C in benzene without any signs of decomposition. Additionally, the addition of halide abstracting agents such as sodium or thallium salts did not result in any observed transformation of the compound. DFT computation show that the $P-Cl$ moiety can rotate easily on a relatively flat energy surface, in line with the broadened ^{31}P NMR signals, to a rotamer featuring *syn*-orientation of the chloride atoms ($\Delta G^{\ddagger}_{\text{Rot.}} = 9.85\,\text{kcal·mol}^{-1}$, $\Delta G_{\text{Rot.}} = 5.05\,\text{kcal·mol}^{-1}$, Figure 4.17). However, the computed kinetic and thermodynamic values for the further rearrangement towards a terminal phosphide dichloride complex are calculated to be highly unfavorable which can be explained by the successive weakening of the transition metal pnictide multiple bonds when moving right in the periodic table ($\Delta G^{\ddagger}_{\text{Ox.Ad.}} = 39.30\,\text{kcal·mol}^{-1}$, $\Delta G_{\text{Ox.Ad.}} = 35.38\,\text{kcal·mol}^{-1}$, Figure 4.17).
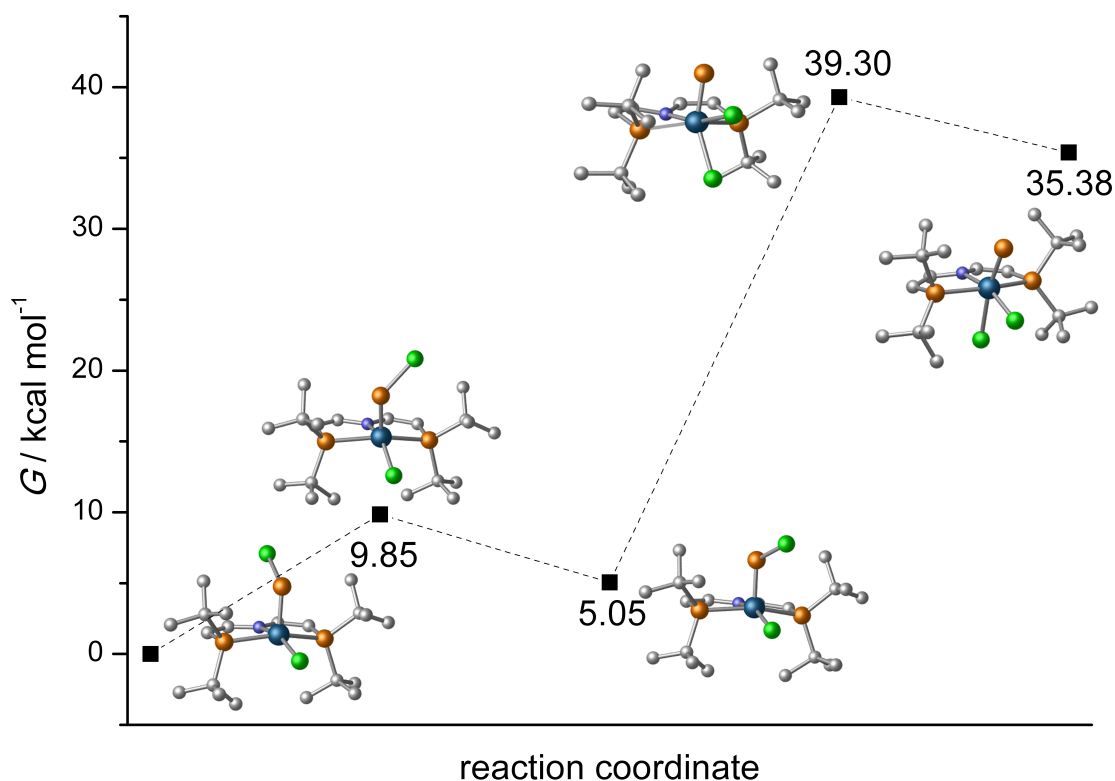
Figure 4.17: Computed reaction pathway of the isomerization of **44** towards the terminal phosphide $[\text{OsCl}_2(\text{L}^3)\text{P}]$.

Chlorophosphinidenes could serve as suitable species to perform $P-C$ coupling reactions with dienes and diynes yielding chloro-substituted cyclic phosphines. Theoretical calculations demonstrate that the LUMO of **44** is mainly P-centered and should therefore serve as an electrophilic attack site for nucleophilic unsaturated substrates as tolane, cyclohexene or dimethyl butadiene (Figure 4.16). However, no reactivity with any of the substrates was observed, even at elevated temperatures up to 80°C in benzene for

hours. Therefore, DFT computations of the hypothetical reaction of **44** and tolane to give the phosphirene complex [OsCl(L^3)(PClR$_2$)] (**45**, PClR$_2$ = 1-chloro-2,3-diphenyl-1H-phosphirene) were carried out to identify the main obstacles for this reaction. The overall reaction is calculated to be thermoneutral with a relative energetic difference of only $\Delta G = -0.67\,\text{kcal} \cdot \text{mol}^{-1}$. The kinetic barrier however is calculated to be $\Delta G^{\ddagger} = 33.5\,\text{kcal} \cdot \text{mol}^{-1}$. In the transition state **46$^{\text{tBu}}$**, significant steric repulsion of the *tert*-butyl groups of the phosphorus donor sites and the substrate is indicated by the short distance between one of the phenyl and the *tert*-butyl groups and a long P3-C2 bond distance (Figure 4.18, Table 4.2). To clarify if repulsive steric interactions are the main obstacle for the reaction to proceed, the *tert*-butyl groups were substituted by *iso*-propyl substituents and the reaction was again investigated by DFT. The transition state **46$^{\text{iPr}}$** exhibits almost identical bond distances around the metal center but the bond distances and angles of the P$-$Cl moiety and the tolane unit are strikingly different. While the chloride is situated almost directly above the nitrogen pincer atom in the sterically more demanding model, it shows a significant twist in the *iso*-propyl case preventing a Y-shaped phosphorus centrum in transition state. Additionally, the phenyl substituent of the tolane molecule can approach the P$-$Cl moiety more easily as indicated by the shortened P3-C2 distance and shows no direct hints for strong steric repulsion due to the long C3-C4 distance which leads to a computed activation barrier of $\Delta G^{\ddagger} = 14.9\,\text{kcal} \cdot \text{mol}^{-1}$ and by that renders the reaction to be feasible even at room temperature. The decreased steric bulk also results in a stabilization of the reaction product yielding an overall exergonic reaction ($\Delta G = -22.6\,\text{kcal} \cdot \text{mol}^{-1}$, Figure 4.18).

Table 4.2: Computed bond lengths of **46$^{\text{iPr}}$** and **46$^{\text{tBu}}$**.

	46$^{\text{iPr}}$	46$^{\text{tBu}}$	Δ
Os1-N1	2.065	2.092	0.027
Os1-Cl1	2.419	2.430	0.011
Os1-P1	2.358	2.413	0.055
Os1-P2	2.377	2.422	0.045
Os1-P3	2.155	2.155	0.000
P3-Cl2	2.151	2.157	0.006
P3-C1	1.844	1.856	0.012
P3-C2	2.258	2.342	0.084
P3-C3	4.639	5.435	0.796
C3-C4	3.848	3.162	0.686
C1-C2-C3	167.42	158.02	9.400
Cl2-P3-Os1-N1	55.02	7.09	47.93
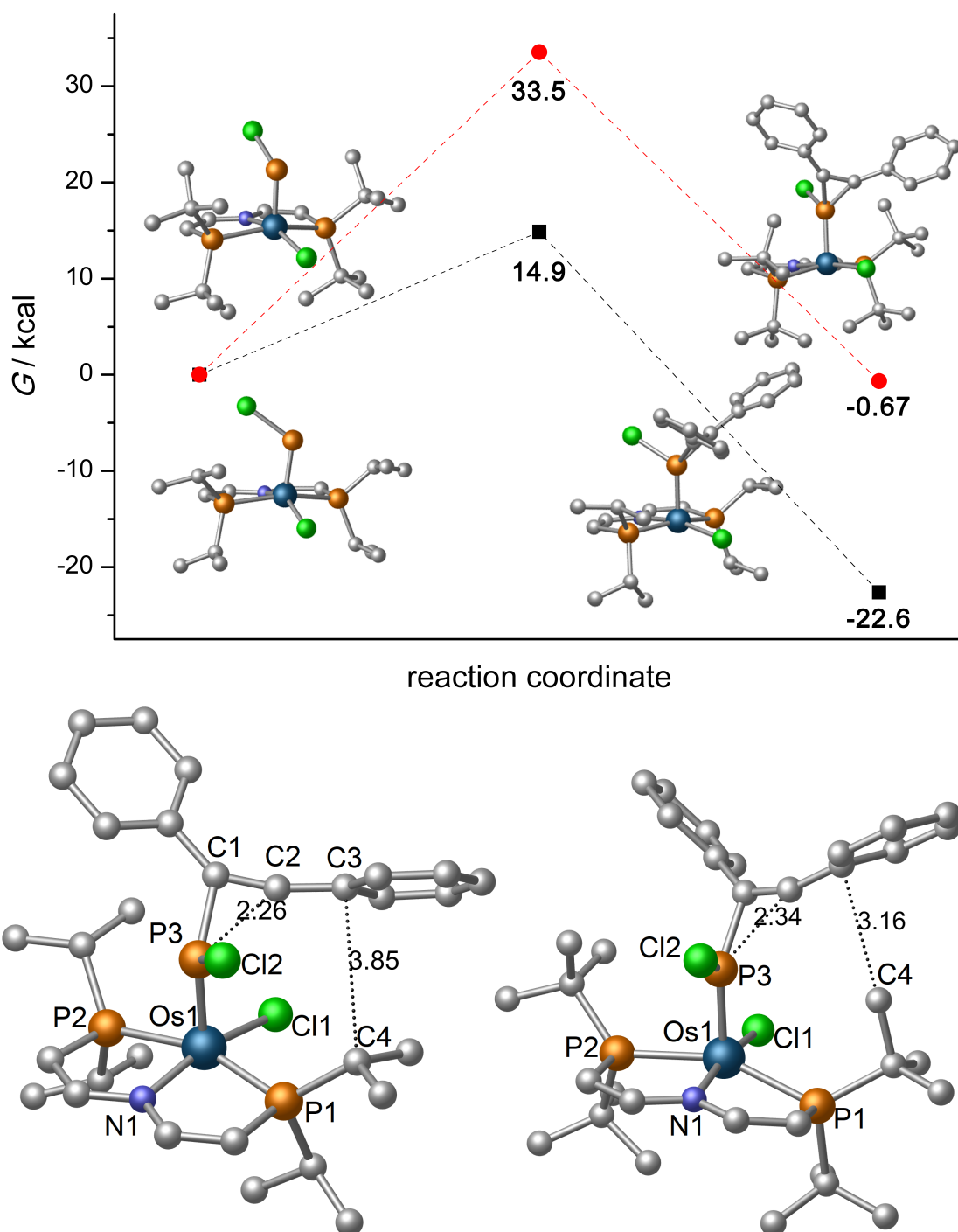
Figure 4.18: Top: Computed reaction pathway of the cyclization of tolane by **44** to yield **45** with differently substituted phosphorus donor sites (isopropyl in black; *tert*-butyl in red); Bottom: Computed structures of the transition states.

As outlined above, phosphorus atom transfer from ClP**A** can be realized when reacted with the anionic vanadium nitride complex **LXXXV** to give a transient N≡P ligated complex. Since **44** features a PCl ligand, the substitution of chloride for nitrogen is targeted to obtain a phosphorus-bound P≡N ligand. When **44** is reacted with azides such as TMSN$_3$ or TBAN$_3$ (TBA = NBu$_4$) slow reaction towards multiple products is observed which were not further investigated.
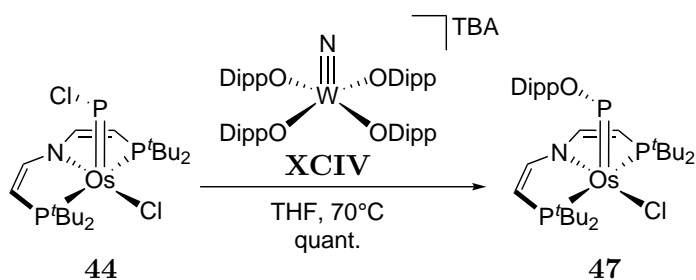
Scheme 4.15: Reaction of **44** and **XCIV** yielding **47**.

Figure 4.19: ^{1}H NMR spectrum of the reaction of **44** and **XCIV** after purification, C$_6$D$_6$, RT; Inset: ^{31}P\{^{1}H\} NMR spectrum, C$_6$D$_6$, RT (since **44** was prepared *in situ* anthracene is still present in the purified sample).
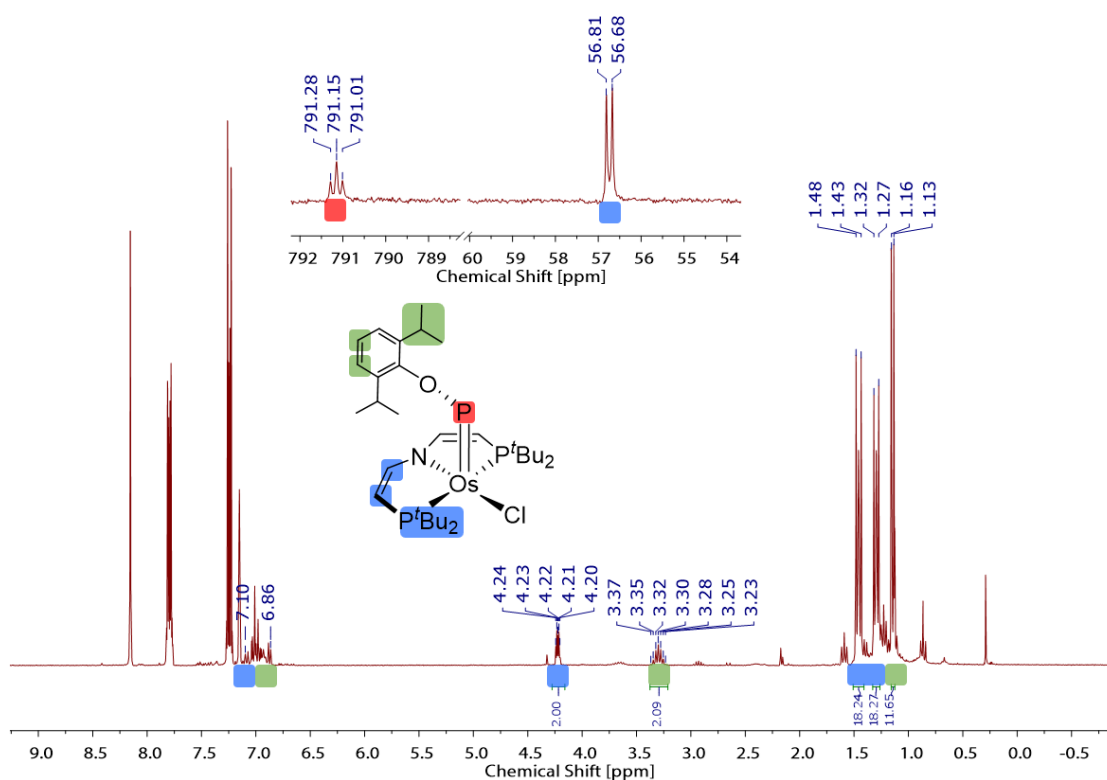
N≡P is expected to be a highly reactive molecule which may necessitate a more thorough steric protection. Therefore, synthesis by coupling of **44** with the anionic nitride complex [TBA][WN(ODipp)$_4$] (**XCIV**) was attempted. Upon mixing at room temperature, no conversion was detected over the course of days, however heating the solution to 70°C for 24 h gave complete conversion to a new diamagnetic phosphinidene complex (δ_P = 791.3, 56.7 ppm, Figure 4.19). The sharpened signals and observed mutual coupling ($^2J_{PP}$ = 16.8 Hz) suggest the formation of an Os=PR species which is not as flexible as **44**. Based on ^{1}H NMR spectroscopy it can be concluded that no P-N coupling occurs and rather an ODipp ligand is transferred yielding the phosphinidene complex [Os(PODipp)Cl(L^3)] (**47**, Figure 4.19, Scheme 4.15) quantitatively, accompanied by minor organic impurities stemming from the disassembly of **XCIV**. Although additional spectroscopy was not performed, the indicative NMR signatures sufficiently proof the formation of **47**.

4.5 Conclusion

This chapter demonstrated the synthesis of the first terminal heavy pnictide complexes beyond group 6 (**27** and **28**). The species were fully characterized and DFT calculations reveal a highly covalent bonding between the Re center and the Pn ligands. Upon one-electron oxidation, coupling reactivity towards the Pn_2-species **29** and **30** was observed and the products were characterized by NMR, mass spectrometry and XRD studies. QTAIM analysis reveals an unprecedented donor-acceptor interaction between diphosphorus and diarsenic with the Re^{III} ion and the PyrPz ligand, representing the first isolable example of neutral Pn_2^0 coordinated by a metal center. The *push-pull* interaction leads to a formal reduction of the bond order resulting in the observed double bond which contrasts with prior reported NHC stabilized Pn_2^0 compounds **XCV** and **XCVI** (Figure 4.20).[115],[116],[278],[279] In this case, the donation of the electron rich carbene results in the formation of a Pn−Pn single bond due to *push-push* stabilization (Figure 4.20).
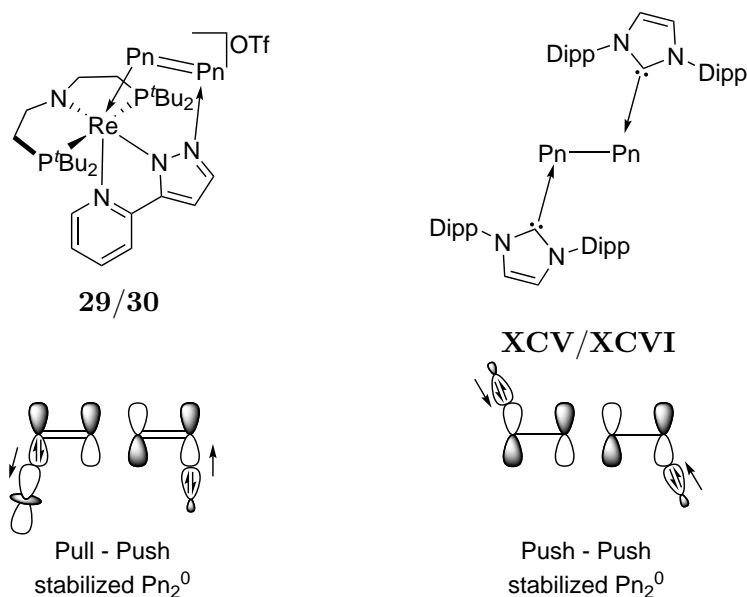
Figure 4.20: Left: *Push-pull* stabilization of Pn_2 by the $\{Re(L^1)(PyrPz)\}$ platform; Right: *Push-push* stabilization of Pn_2 by **XCV** and **XCVI** (Pn = P, As).[115],[116]

The oxygenation of the terminal Re phosphide **27** with pyridine-*N*-oxide was presented. Upon addition of two oxygen atoms the dinuclear species **31** is obtained which features an unprecedented bridging $P_2O_4^{2-}$ moiety. Single addition of an oxygen atom could not be accomplished. **31** was fully characterized and cyclic voltammetry revealed a possible two electron reduction which results in the formation of the open-shell complex **34**, representing the first example of a PO_2^- ligand coordinated to a transition metal.

PO$_2^-$ acts as a σ-donor ligand with delocalized P-O bonds, as shown by NBO analysis. One-electron oxidation of **34** results in the reformation of **31**.

The first spectroscopically and crystallographically characterized isolable phosphanide complex with large phosphinyl radical character was accomplished. The rhombic ^{31}P HFI tensor and the DFT model are in line with even spin delocalization over the Os$-$P core. Versatile access to an electrophilic phosphinidene complex that undergoes intramolecular C$-$H activation was demonstrated by P$-$H PCET. Thermochemical analysis by means of ITC was particularly useful as the thermal instability of **43** prevented experimental pK_a determination. The data indicates that concerted or stepwise ET/PT are both viable routes to access phosphinidenes from phosphanide complexes.

Several Os PNP platforms were tested towards possible substitution reactions with the PCO$^-$ anion which led to clean one-electron reduction chemistry. The obtained reduction products exhibited no further reactivity with the reagent. The reaction of ClP**A** with the square-planar Os^{II} chloride **2** gives the first isolable chlorophosphinidene complex **44** in 50% isolated yield. Attempts to substitute the chloride with nitrogen failed. The test reactions with unsaturated substrates were unsuccessful since no reactivity was observed even at elevated temperatures. A computational investigation of the reaction of **44** with tolane suggests that the steric demand of the *tert*-butyl substituents leads
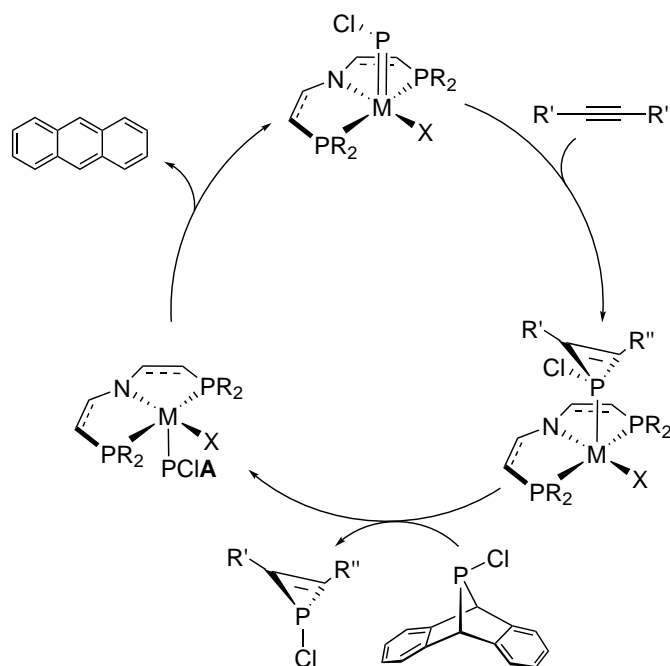
Scheme 4.16: Possible formation of chloro-substituted phospirenes by catalytic PCl transfer.

to an unfavorable transition state. Comparison with a computed *iso*-propyl substituted system yields a significantly lowered kinetic barrier and an overall exergonic reaction. These results show that PCl transfer from ClP**A** to mid- and late transition metals might offer a unique possibility to access chlorophosphinidene complexes. Increased reactivity towards unsaturated substrates, e.g. alkynes, could be realized by introduction of smaller substituents at the phosphorus donor atoms. In this context also catalytic PCl transfer might be possible. The choice of appropriate phosphorus substituents might however be challenging since the activation barrier for cyclization has to allow for heterocycle formation but thereby also facilitate the decoordination of the product to enable the metal to re-enter the catalytic cycle (Scheme 4.16).

Proton-Induced Splitting of Dinitrogen by Dimeric Mo PNP Pincer Complexes

J. Abbenseth, Serhiy Demeshko, Markus Finger, Maximilian Fritz, Christian Herwig, Jean-Pierre Oudsen, Bas Venderbosch, Christian Würtele, Moniek Tromp, Sven Schneider*

Author contributions

J.A.	Synthesis and spectroscopy
S.D.	SQUID
M.Fi.	Theoretical calculations
M.Fr.	Crystallography (supporting)
C.H.	rRaman
J.O.	XAS
B.V.	XAS
M.T.	XAS
C.W.	Crystallography

5   Proton-Induced Splitting of Dinitrogen by Dimeric Mo PNP Pincer Complexes

Dinitrogen functionalization is an active field of research in the Schneider group and dinitrogen splitting into terminal nitrides was demonstrated for Mo and Re systems which extended this process up to group 7.[33], [35], [40], [52], [53], [280]

The N_2-bridged Mo complex $[\{MoCl(L^1)\}_2(N_2)]$ (**XCVII**) is thermally stable and does not convert to nitride complexes upon heating or irradiation. Although this process was computed to be thermodynamically favored, the associated kinetic barrier of $\Delta G^\ddagger_{\mathrm{DFT}} = 37\,\mathrm{kcal \cdot mol^{-1}}$ rationalized the non-observed splitting. However, twofold protonation towards $[\{MoCl(^{H}L^1)\}_2(N_2)][OTf]_2$ (**XCVIII**) at low temperatures and successive warming to room temperature results in complete N≡N bond scission yielding the open-shell nitride $[MoNCl(^{H}L^1)][OTf]$ (**XCIX**, Scheme 5.1).[280] Due to C_2-symmetry of **XCVII**, a set of degenerate δ-bonding orbitals with respect to the dinitrogen bridge have to be taken into account which results in an overall $\pi^8(\delta^4)$-configuration (Scheme 5.1). When **XCVII** is protonated by two equivalents of triflic acid the π-donor capabilities of the L^1 ligands are switched off, resulting in a stabilization of the σ^*- and π_2-orbital, which allows for the generation of a $S = \frac{3}{2}$ state for **XCVIII**. Furthermore, mixing of the σ^*- and π_2-orbital in the zig-zag transition state becomes feasible, allowing for dinitrogen splitting.

XCVII was characterized electrochemically yielding no reductive but reversible oxidative waves at $E_{1/2} = -1.14$ and $-0.64\,\mathrm{V}$ vs. $Fc^{0/+}$. This chapter aims to provide a comprehensive study of one- and two-electron oxidized derivatives of **XCVII**. The effect of depopulation of δ-symmetric orbitals with respect to the N_2 bridge has not been investigated for any dimeric molybdenum dinitrogen systems. In addition, characterization of **XCVIII** was restricted to Evan's method and UV/vis spectroscopy in combination with DFT computations due to thermal instability. X-ray absorption spectroscopy will be utilized to validate the initial structural and electronic hypotheses concerning **XCVIII** and derive experimental structural parameters.

XCVII XCVIII XCVIII$^{\text{TS}}$

σ^*

π_2

α β β α

δ

α β β α

π_1

XCVII $\xrightarrow[-40°C]{2\ \text{HOTf}}$ XCVIII$^{\text{TS}}$ $\xrightarrow{\text{to RT}}$ 2 XCIX
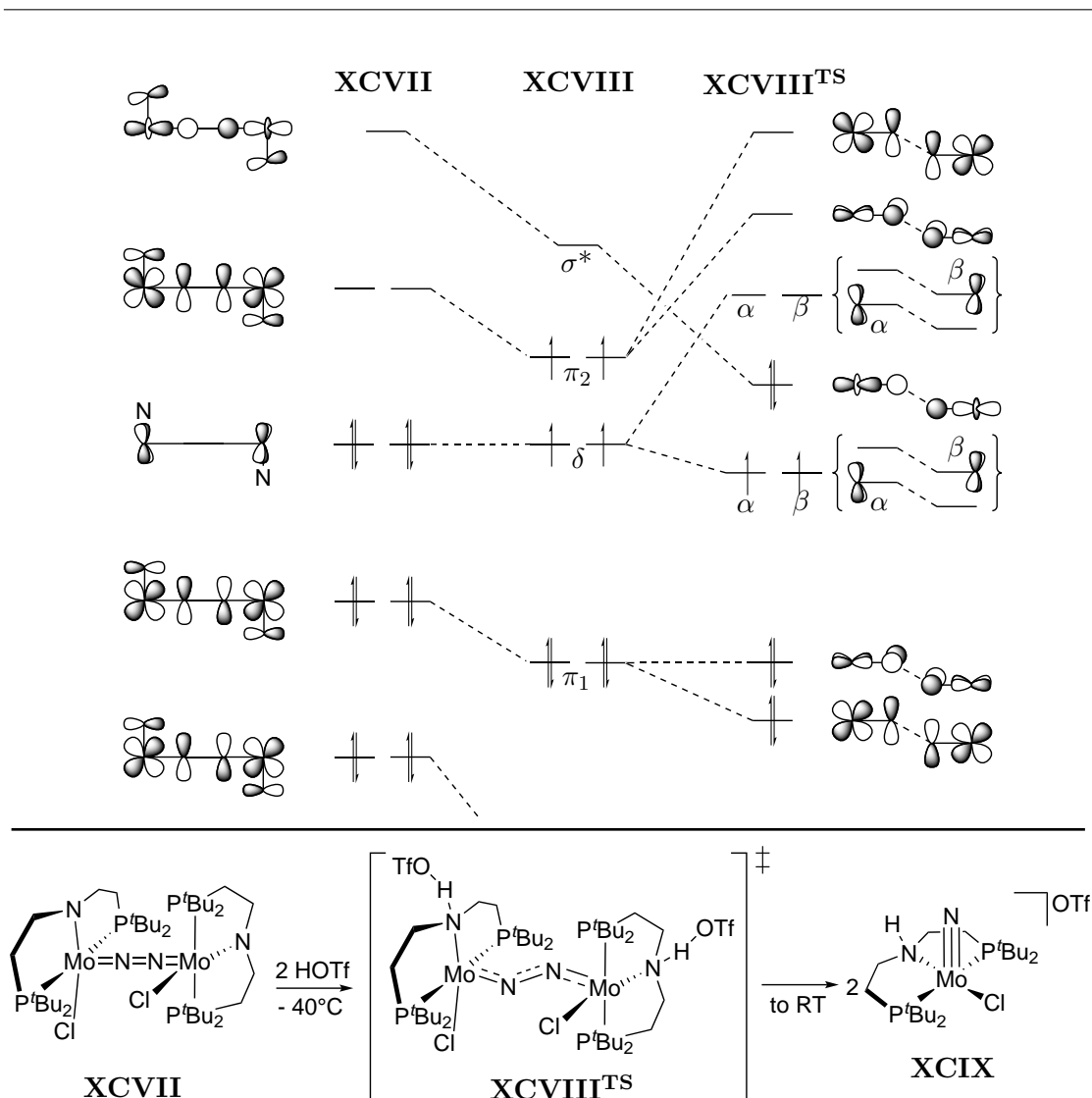
Scheme 5.1: MO scheme for the protonation of **XCVII** (left) to **XCVIII** (middle) and its zig-zag transition state (right) resulting in splitting towards **XCIX**.[280]

Based on electrochemical studies of **XCVII**, one- and two-electron oxidations towards dimeric species were targeted. Mixing **XCVII** with $Ag[Al(OR)_4]$ (R = $C(CF_3)_3$) in benzene results in the clean formation of $[\{MoCl(L^1)\}_2(N_2)][Al(OR)_4]_n$ (**48**, n = 1; **49**, n = 2) in 88% and 69% isolated yield, respectively (Scheme 5.2). This synthetic procedure allows for the clean separation of the mono- and dicationic species since **48** exhibits minor benzene solubility due to the large non-coordinating anion. Both complexes exhibit paramagnetically shifted ^{1}H NMR signals suggesting a $S = \frac{1}{2}$ state for **48** and a $S = 1$ state for **49**, respectively. The number of detected peaks and their corresponding integrals are in line with the preservation of the molecular structure upon oxidation with rapid electron transfer between the metal centers in the case of **48** (Appendix 8.4.1).
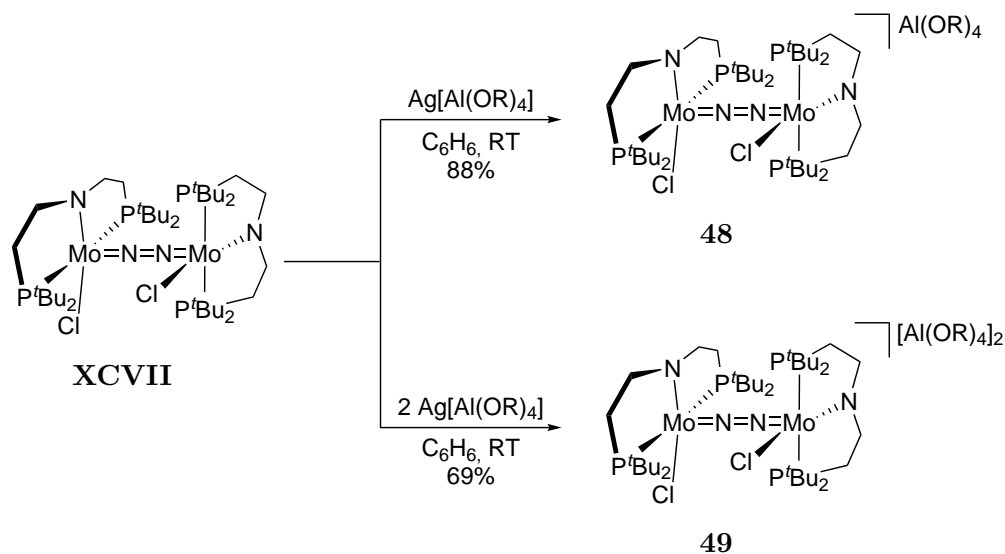
Scheme 5.2: Synthesis of **48** and **49** by oxidation of **XCVII**, R = $C(CF_3)_3$.

Species	$\tilde{\nu}(^{14}N_2)$	$\tilde{\nu}(^{15}N_2)$	$\Delta\tilde{\nu}(N_2)$	$\Delta\tilde{\nu}_{\text{theo.}}$
XCVII	1343	1300	43	45
48	1397	1350	47	47
49	1390	1343	47	47
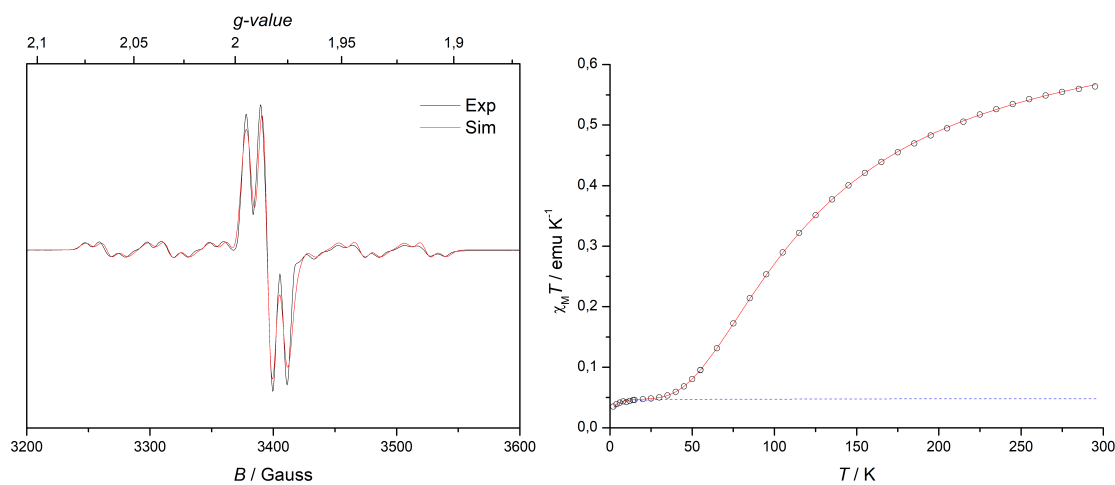
Figure 5.1: Top: EPR spectrum of **48** (left), 9.43087 GHz, THF, RT, $g = 1.9846$, $A(^{95/97}\text{Mo}) = 142$ MHz; $A(^{31}\text{P}) = 33.7$ MHz; SQUID data of **49** (right), $g_{1/2} = 1.921$, $J_{1/2} = -75.672$ cm^{-1}; Bottom: $^{14}N_2/^{15}N_2$ rRaman data of **XCVII**,[280] **48** and **49**; $\Delta\tilde{\nu}_{\text{theo.}}$: Expected shift of $\tilde{\nu}(N_2)$ in the harmonic oscillator approximation upon labelling.

EPR spectroscopy of **48** in PhCl reveals a Mo-centered radical with hyperfine interaction towards both phosphorus atoms of the PNP pincer ligand (Figure 5.1). According to the Robin-Day classification, **48** can be described as a class II/III system with a rate of inner sphere electron transfer between the timescales of NMR and EPR spectroscopy at room temperature ($10^{-4} - 10^{-7}\,\mathrm{s}^{-1}$).[281],[282] SQUID measurement reveals that **49** is best described as two antiferromagnetically coupled $S = \frac{1}{2}$ systems ($J = -75.672\,\mathrm{cm}^{-1}$, Figure 5.1) which is reasonable since the SOMOs consist of degenerate Mo-centered, δ-symmetric, non-bonding orbitals with respect to the dinitrogen bridge (Scheme 5.1). To probe the degree of activation of the bridging dinitrogen ligand vibrational spectroscopy was employed.

Resonance Raman measurements show that one-electron oxidation leads to a blue shift of the N=N stretching vibration by $\Delta\tilde{\nu}_{\mathrm{NN}} = 54\,\mathrm{cm}^{-1}$. Two-electron oxidation does not further strengthen the dinitrogen bond but leads to a minor weakening when compared to **48** ($\Delta\tilde{\nu} = 9\,\mathrm{cm}^{-1}$, Figure 5.1). Overall, these changes are significantly smaller when compared to the series **VII** - **XI** reported by Cummins and co-workers.

Although both dimers can be purified by crystallization, no suitable singe-crystals for X-ray diffraction could be obtained when $\mathrm{Ag[Al(OR)_4]}$ was used as the oxidant. The reaction of **XCVII** with silver salts containing more coordinating anions such as $\mathrm{PF_6^-}$, $\mathrm{BF_4^-}$, $\mathrm{SbF_6^-}$ and $\mathrm{BPh_4^-}$ gave sluggish reaction mixtures which prevented characterization by elemental analysis. However, single-crystals could be obtained for **48-BF$_4$** and **49-(SbF$_6$)$_2$** (Figure 5.2). The overall structural changes upon oxidation are minor since δ-symmetric orbitals with respect to the N=N bond are depopulated. Applying a confidence interval of 95% (2σ) shows that the data quality is not sufficient to discuss structural changes of the {MoNNMo} moiety upon oxidation since the error bars overlap in all selected bond lengths (Figure 5.2). Furthermore, the bond distances might be altered by packing effects.[283]–[285]

X-ray absorption spectroscopy is particularly useful in this case since it allows for the determination of bond distances in solution *via* extended X-ray absorption fine structure spectroscopy (EXAFS)).[286]–[288] As outlined in the introduction, the doubly protonated dimer **XCVIII** leads to dinitrogen splitting into the terminal nitride **XCIX**. XAS spectroscopy could allow to gain insight into the bond distances and overall electronic structure of **XCVIII** which are currently only accessible by theoretical calculations.[280]
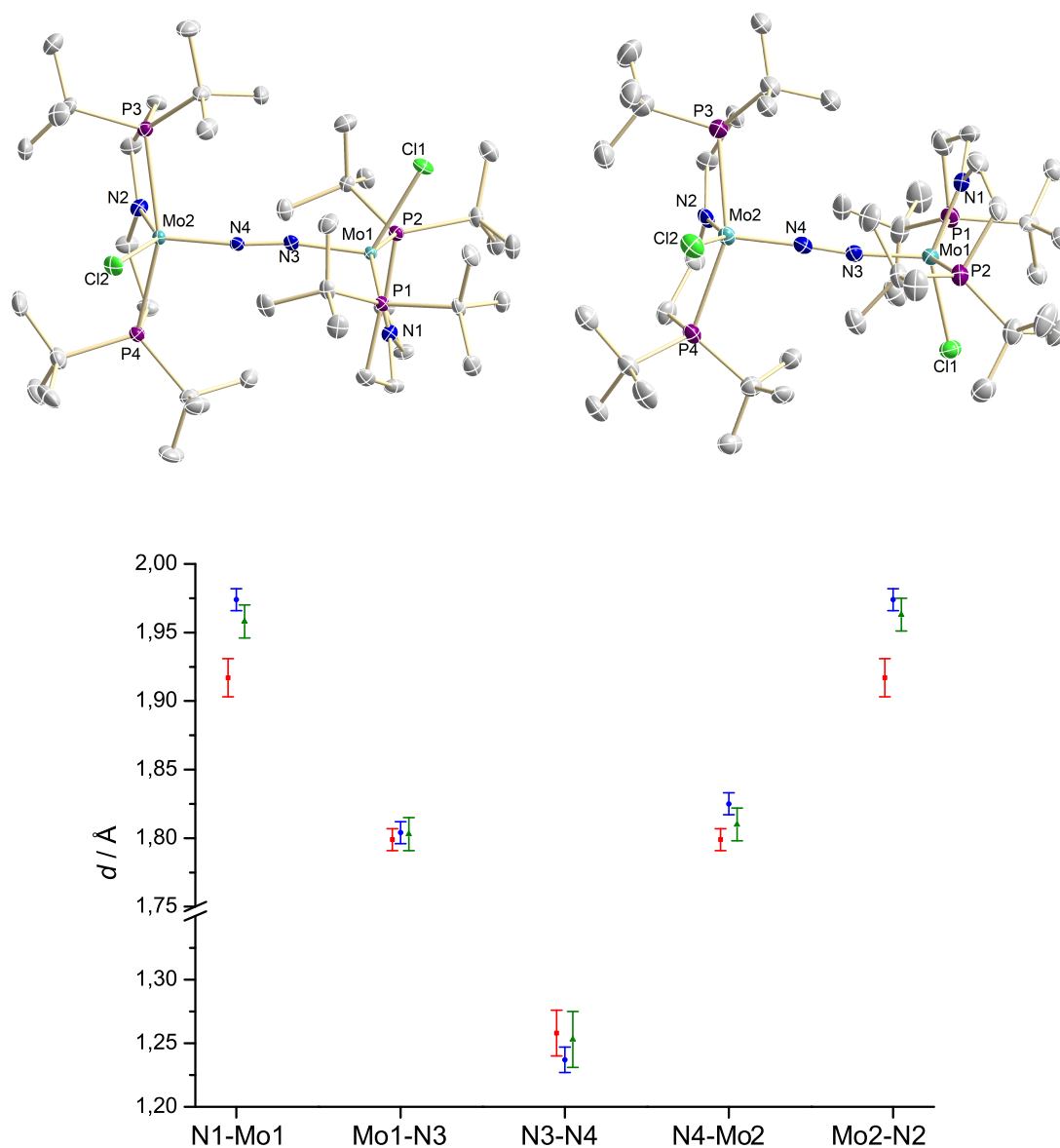
Figure 5.2: Top: Solid state structure of **48-BF₄** (left) and **49-(SbF₆)₂** (right) from single-crystal X-ray diffraction (thermal ellipsoids drawn at the 50% probability level); solvent molecules, anions and hydrogen atoms, are omitted for clarity. Selected bond lengths [Å] and angles [°]: **48** Mo1-Cl1 2.3519(11), Mo1-N1 1.974(4), Mo1-N3 1.804(4), Mo1-P1 2.5387(12), Mo1-P2 2.5387(12) Mo2-Cl2 2.4515(11) Mo2-N2 1.974(4), Mo2-N4 1.825(4), Mo2-P3 2.4966(12), Mo2-P4 2.4921(12), N3-N4 1.237(5), N1-Mo1-N3 113.24(17) P1-Mo1-P2 155.84(4), Mo1-N3-N4 169.6(3), N2-Mo2-N4 109.51(16), P3-Mo2-P4 154.34(4), Mo2-N4-N3 170.9(3); **49** Mo1-Cl1 2.352(3), Mo1-N1 1.958(8), Mo1-N3 1.803(8), Mo1-P1 2.532(3), Mo1-P2 2.583(3), Mo2-Cl2 2.349(3), Mo2-N2 1.963(8), Mo2-N4 1.810(8), Mo2-P3 2.534(3), Mo2-P4 2.574(3), N3-N4 1.253(11), N1-Mo1-N3 108.9(3), P1-Mo1-P2 151.29(9), Mo1-N3-N4 171.0(7), N2-Mo2-N4 108.1(3), P3-Mo2-P4 152.10(9), Mo2-N4-N3 168.7(7); Bottom: Selected bond lengths of **XCVII** (red),[280] **48** (blue) and **49** (green) from single-crystal X-ray diffraction, 2σ error bars.

Table 5.1: Experimental structural parameters of **XCIX**, **XCVII**, **48**, **49** and **XCVIII** in solution derived by Mo-K edge EXAFS spectroscopy and single crystal X-ray diffraction in Å, THF, 100°C, for **XCVIII** three set of computed bond lengths are given for the considered spin states, [a]: For **XCIX** the nitride bond length is given.[280]

	Mo-N$_{\text{PNP}}$		Mo-N$_2$[a]		Mo-Mo		N-N	
	XRD	XAS	XRD	XAS	XRD	XAS	XRD	XAS
XCIX	2.209(2)	2.11(3)	1.646(2)	1.62(1)				
XCVII	1.917(7)	1.99(2)	1.799(4)	1.80(1)	4.846(1)	4.74(2)	1.258(9)	1.27(4)
48	1.974(4) 1.974(4)	1.99(2)	1.804(4) 1.825(4)	1.82(3)	4.846(1)	4.74(1)	1.237(5)	1.22(4)
49	1.958(8) 1.963(8)	1.99(2)	1.803(8) 1.810(8)	1.82(3)	4.847(2)	4.74(8)	1.25(2)	1.20(1)
	DFT	XAS	DFT	XAS	DFT	XAS	DFT	XAS
XCVIII								
$S = 0$	2.30		1.82		4.88		1.27	
$S = 1$	2.34	2.30(9)	1.932	1.87(2)	5.05	5.17(3)	1.22	n.a.
$S = 2$	2.32		1.94		5.08		1.22	
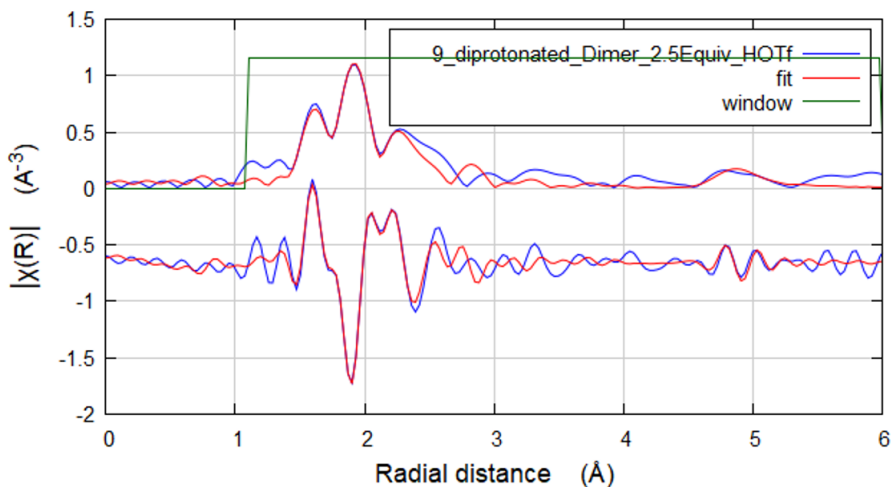
Figure 5.3: EXAFS spectrum of **XCVIII**, R space, fitted as mixture of **XCVIII** / **XCIX**: 75%/25% (refined with fixed nitride complex bond lengths).

The molecular geometries of **XCVII**, **48**, **49**, **XCIX** and **XCVIII** in THF solution were derived by Mo-K edge EXAFS spectroscopy (Table 5.1). The lower data resolution when compared to single-crystal X-ray diffraction prevents the discussion of trends within the dimer redox series, however both utilized techniques give similar results for the bond distances around the metal center. The Mo-Mo bond distances are consid-

erably shortened in solution, possibly owing to packing effect in the solid state. A
significantly shorter Mo-N$_{PNP}$ bond length is obtained for the nitride complex **XCIX**
by EXAFS spectroscopy which may be attributed to non-quantitative triflate coordi-
nation to the protonated pincer complex in solution. Structural information about the
proposed diprotonated dimer **XCVIII** were obtained *via* protonation of **XCVII** with
2.5 equivalents of triflic acid at −80°C and successive EXAFS spectroscopy. The re-
sulting spectrum could be satisfactory fitted as a mixture of a dimeric Mo dinitrogen
complex with small amount of the splitting product **XCIX** (Figure 5.3). Since no solid-
state structure could be obtained, Schneider and co-workers calculated different possible
spin states for **XCVIII** ($S = 0, 1, 2$) in a prior report as discussed in the introduction
to this chapter.[280] Although the resolution of the obtained data set was not as high
as for the isolable compounds, a Mo-Mo multiple scattering pathway could be identi-
fied resulting in Mo-Mo distance of 5.17(3) Å. The formation of a dimer in a quintet
state prior to dinitrogen splitting can be confirmed due to the computed Mo-Mo bond
length of $d_{MoMo} = 5.08$ Å that agrees well with the experimental value (experimental
and computed values show a decent agreement for **XCVII**, **48** and **49**: Table 8.3)
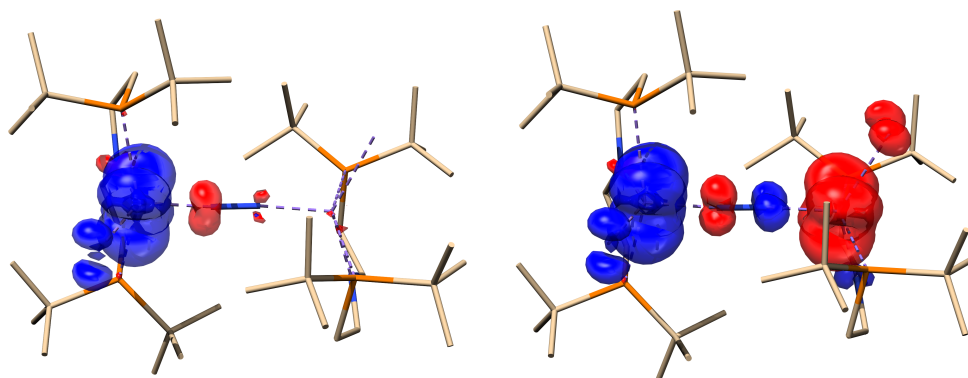
Figure 5.4: Spin-density plot of **48** (left) and **49** (right), positive densities given in blue.

Table 5.2: Selected bond orders of **XCVII**, **48** and **49**.

Bond	Bond order		
	XCVII	**48**	**49**
N1-Mo1	1.08	1.09	1.15
Mo1-N3	1.54	1.60	1.49
N3-N4	1.25	1.39	1.47
N4-Mo2	1.54	1.37	1.49
Mo2-N2	1.08	1.15	1.15

The results are further corroborated by DFT calculations. Spin-density calculations reveal the SOMO of **48** to be a metal centered δ-symmetric orbital with respect to the dinitrogen bridge without extensive delocalization, in line with the obtained EPR spectrum (Figure 5.4). An antiferromagnetically coupled singlet ground state is predicted for **49**. The calculated spin-density reveals similar localization features as for **48** per metal center. Since only non-bonding orbitals with respect to the bridging dinitrogen ligand are depopulated, the effect on the overall bonding situations are minor as shown by the computed bond orders (Table 5.2). Upon oxidation, an increase in the Mo-N_{N_2} bond order for one metal center is observed. The second oxidation re-symmetrizes the bonding situation, yielding identical values for both Mo atoms. The bond order of the dinitrogen ligands shows a gradual increase per oxidation step. The overall minor changes upon oxidation are in line with the MO considerations described in the introduction and the observed changes are likely to be attributed to electrostatic effect since the depopulated orbitals are not part of the π-core of the {MoNNMo} moiety.
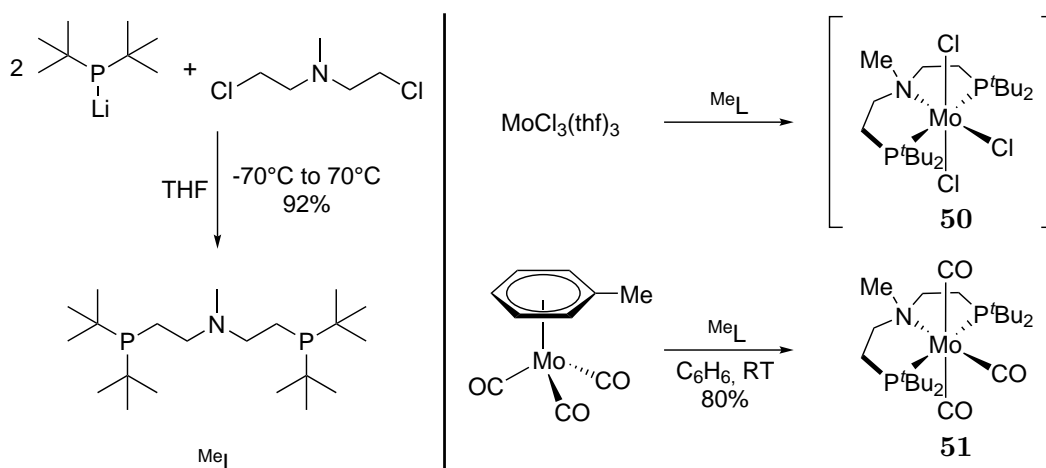
Scheme 5.3: Synthesis of ^{Me}L and its reaction towards [MoCl$_3$(THF)$_3$] and [Mo(CO)$_3$(toluene)] yielding **51** .

As outlined in the introduction, protonation of the pincer backbone is necessary to allow for splitting of dinitrogen. If the nitrogen atom of the pincer ligand was alkylated, the destabilization of the σ^* -and π_2-orbital would be prevented and direct splitting of N$_2$ by a suitable Mo halide complex upon reduction could be feasible. The methylated pincer ligand (Me)N(CH$_2$CH$_2$P^{t}Bu$_2$)$_2$ (^{Me}L) has been reported by Prechtl and co-workers by coupling of *in situ* generated LiP^{t}Bu$_2$ and (Me)N(CH$_2$CH$_2$Cl)$_2$. Besides a low yield, the published procedure does not allow for isolation of the pure ligand (69% yield, 67% purity). The authors claim that the lithiation of PH^{t}Bu$_2$ is unselective and produces impurities that cannot be removed.[289] Therefore, a new synthetic approach *via* lithiation of PCl^{t}Bu$_2$ and successive coupling with (Me)N(CH$_2$CH$_2$PCl)$_2$ was developed (Scheme
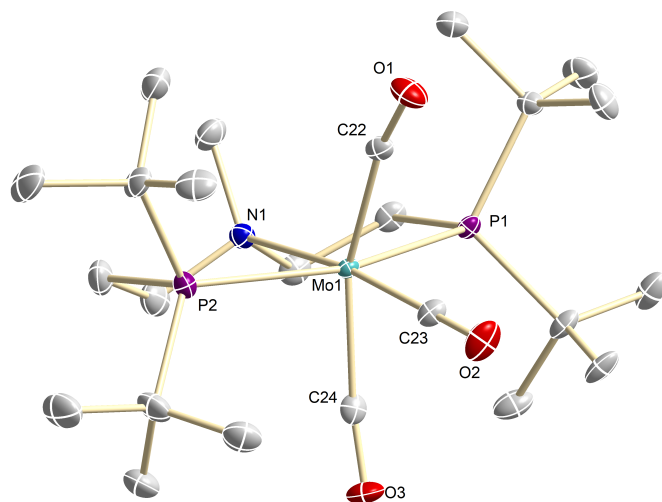
Figure 5.5: Solid state structure of **51** (one complex molecule of the asymmetric unit) from single-crystal X-ray diffraction (thermal ellipsoids drawn at the 50% probability level); hydrogen atoms are omitted for clarity. Selected bond lengths [Å] and angles [°]: **51** Mo1-C22 2.012(4), Mo1-C23 1.933(4), Mo1-C24 1.994(4), Mo1-N1 2.401(3), Mo1-P1 2.5154(10), Mo1-P2 2.4959(11), C22-Mo1-C24 156.06(17), C23-Mo1-N1 172.02(15), P1-Mo1-P2 157.00(4).

5.3) which gives $^{\text{Me}}$L in 92% isolated yield. Sivasankar and co-workers independently published an identical protocol and obtained a yield of 65%.[290]

Synthesis of [MoCl$_3$($^{\text{Me}}$L)] (**50**) was attempted by complexation of [MoCl$_3$(THF)$_3$]. In apolar solvents like pentane, benzene and diethyl ether, precipitation of solid and a complex mixture of dia- and paramagnetic products was observed. Stirring [MoCl$_3$(THF)$_3$] and $^{\text{Me}}$L in PhCl at 50°C and DCM/THF (1:2) at room temperature both yield a paramagnetic product, accompanied by organic and paramagnetic side products (Appendix 8.4.5). The number of signals and their relative intensity suggest the formation of a C_{S}-symmetric complex, however the complex proved to be unstable in solution for extended periods of time. Mass spectrometry gave no conclusive results and no single-crystals suitable for X-ray diffraction were obtained which prevented full characterization. Complexation by a Mo^0 carbonyl precursor was chosen as an alternative entry since the carbon monoxide ligand should be partly exchangeable upon oxidation/irradiation. Stirring [Mo(CO)$_3$(toluene)] and $^{\text{Me}}$L in benzene at room temperature gives the tricarbonyl complex [Mo(CO)$_3$($^{\text{Me}}$L)] in high yield (**51**, Scheme 5.3). Due to the low oxidation state, significant π^*-backdonation of the CO ligands is observed by three intense band in the IR spectrum, in line with the formation of a C_{S}-symmetric complex ($\tilde{\nu}_{\text{CO}} = 1911\,\text{cm}^{-1}$, $1805\,\text{cm}^{-1}$, $1784\,\text{cm}^{-1}$). In the solid state, **51** features an octahedral coordination geometry with a *mer*-coordinated $^{\text{Me}}$L ligand (Figure 5.5). The Mo-N bond distance is considerably elongated when compared to L^{1,2,3} ligated systems due to the absence of π-donating properties (Mo1-N1: 2.401(3) Å). Cyclic voltammetry shows that **51** can be

reversibly oxidized at $E_{1/2} = -0.33\,\text{V}$ vs. $\text{Fc}^{0/+}$ (Appendix 8.4.7). One-electron oxidation followed by ligand exchange could offer the possibility to access Mo^{III}, however further experiments are yet to be done.

Conclusion

The dinitrogen bridged molybdenum dimer **XCVII** could be successfully oxidized by one and two electrons to afford cationic **48** and **49**. Both species were completely characterized, including single-crystal X-ray diffraction and extended X-ray absorption fine structure spectroscopy. Upon oxidation, only minor changes in the bond distances and overall geometry are observed. The cationic complex features a $S = \frac{1}{2}$ ground-state with a high degree of charge localization on one metal center. The dinitrogen bond get strengthened by $\Delta\tilde{\nu} = 50\,\text{cm}^{-1}$ due to polarization effects. Further oxidation leads to a minor weakening of the N_2 bond and restores the overall symmetry of the complex. An $S = 1$ ground-state for **49** was derived by SQUID magnetometry. In general, the depopulation of δ-symmetric metal-based orbitals with respect to the dinitrogen bridge does not result in significant weakening of the dinitrogen bond. The prior postulated diprotonated dimer **XCVIII** was investigated by EXAFS spectroscopy. The acquired resolution was sufficient to identify a Mo-Mo multiple scattering pathway which yielded a bond distance of $d_{\text{MoMo}} = 5.17(3)\,\text{Å}$, confirming the predicted formation of a quintet ground-state prior to dinitrogen splitting.[280] Dinitrogen splitting without the need for protonation was attempted by synthesizing the methylated analogue of L^1. Coordination towards Mo(III) did not result in the formation of a pure compound. However, L^{Me} could be successfully coordinated to Mo(0) carbonyl precursor complexes which might represent an entry into dinitrogen chemistry upon oxidative removal of the carbonyl ligands.
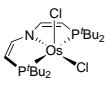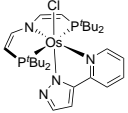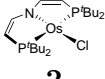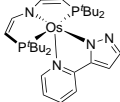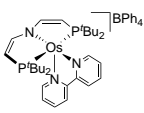
Summary

6   Summary and Outlook

The main goal of this thesis was to investigate the bonding between transition metals and pnictogen containing ligands as well as terminal pnictides in unprecedented coordination spheres and analyze their electronic structures. Therefore, several Os and Re starting platforms were synthesized.

The first well-defined, square-planar Os^{II} complex **2** with a triplet ground state could be synthesized and completely characterized. **2** exhibits large temperature-independent paramagnetism which was investigated by coupled-cluster calculations that yielded a suitable electronic structure description as a thermally isolated ground state which mixes with excited states through spin-orbit coupling. The platform was reacted with different π-accepting ligands which resulted in adduct formation and the negation of spin-orbit coupling effects, yielding classical singlet ground state systems. The addition of the chelating ligands 2,2'-bipyridine and 3-(1H-pyrazol-3-yl)-pyridine lead to octahedral
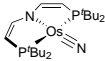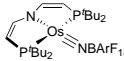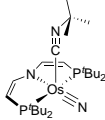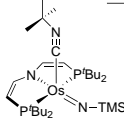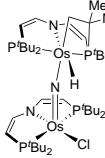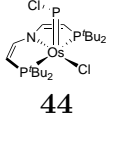
Table 6.1: Comparison of bond lengths and redox potentials of Os pincer platforms synthesized in this thesis, potentials given in V vs. $Fc^{0/+}$ and bond lengths in Å.

Complex	M-N$_{PNP}$	M-Cl$_{apical}$	E_{Red}
1	1.966(6)	2.380(3)	−1.28
12	2.120(2)	2.4557(6)	−1.40
2	1.980(2)		−2.05
13	2.017(3)	2.3837(9)	−2.71
8	2.015(4)		−1.83

platforms. In these cases, the M-N$_{\text{PNP}}$ and M-Cl$_{\text{apical}}$ bond distances elongated due to the increased electron density at the metal center (Table 6.1). This is also reflected in a negative shift of the reduction potentials. The synthesis of the cationic, five-coordinate bipy complex **8** allowed to shift the redox potential of Os$^{\text{II}}$ to more positive values. This results show that **2** represents an attractive platform to access a variety of L^3 ligated species with, dependent on the added ligand, tuneable redox potentials.

2 proved to be a competent platform for the synthesis of the Os$^{\text{VI}}$ nitrides **16**, **15** and the Os$^{\text{IV}}$ nitride **14** . In contrast to the prior reported system ligated by L^1, **14** did not exhibit ambiphilic reactivity. Upon addition of ^{t}BuCN, the five coordinate adduct **18** was obtained which represents the first d^4 configured nitride complex in a five-fold coordination sphere. Although the Gray-Ballhausen scheme predicts such compounds not to be stable, 3c4e bonding interactions circumvent this general rule. Additionally, stabilization of d^4 nitrides was shown upon silylation to give the first isolable d^4 configured silylimido complex **19** and heterocumulene formation with **2**, respectively. Interestingly, the Os≡N bond lengths changed only minorly upon adduct formation (**17**, **18**) with respect to parent **14** (Table 6.2). In contrast, imide complex formation results in an elongation up to $\Delta d \approx 0.06\,\text{Å}$ (**19**, **20**). Investigation of oxidative nitride coupling of bipy ligated systems was unsuccessful.

Table 6.2: Comparison of bond lengths of complexes with M≡Pn(R) bonds and a d^4 electron count synthesized in this thesis, bond lengths given in Å.
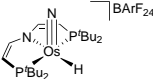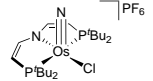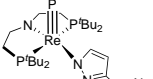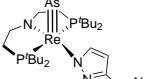
Complex	Os-N$_{\text{PNP}}$	Os≡Pn(R)	Complex	Os-N$_{\text{PNP}}$	Os≡Pn(R)
14	2.137(3)	1.735(5)	**17**	2.087(5)	1.700(5)
18	2.2423(17)	1.6995(18)	**19**	2.237(4)	1.754(4)
20	2.034(4)	1.796(3)	**44**	2.056(3)	2.1759(12)

Re PNP pincer complexes were investigated by means of magnetic measurements and significant contributions of temperature independent paramagnetism were observed by SQUID magnetometry. The combination of iodide substituents and the dehydrogenated pincer ligand L^3 exhibited the most prominent mixing of thermally non-accessible, excited electronic states to the ground state. An examination of the corresponding bromide compound could give valuable insight into the overall effect of halide ligands on spin-orbit coupling effect in these systems. Additionally, a comprehensive study on the dependencies of the redox potentials of the systems upon variation of halide ligands and degree of dehydrogenation of the pincer backbone is yet to be done.

The hemilabile ligand 3-(1*H*-pyrazol-3-yl)-pyridine was utilized to obtain the Re^{III} complex **11**. **11** showed selective formation of the terminal pnictide complexes **27** and **28** upon decarbonylation of PCO^- and $AsCO^-$, respectively, which represent the first examples of heavy transition metal pnictide complexes beyond group 6. Both species were completely characterized and resulted in the formation of donor-acceptor stabilized P_2 and As_2 complexes upon one-electron oxidation. This bonding description was substantiated by QTAIM analysis. Furthermore, the phosphide complex showed unprecedented reactivity towards pyridine-N-oxide which allowed for the isolation of the $P_2O_4^{2-}$ bridged dimeric compound **31**. Two-electron reduction gave the PO_2^--ligated complex **34** which represents the first transition metal complex of such kind. The bonding situation could be elucidated by quantum chemical calculation and revealed that this ligand is best described as a σ-donor with delocalized P-O bonds. The observed reactivity represents an attractive starting point to access low-valent phosphorus species from terminal phosphides as P_1 building blocks.

The triple bond distances of the isoelectronic complexes **15**, **16**, **27** and **28** show a significant change in bond lengths upon comparing nitride and phosphide/arsenide complexes (Table 6.3). These systems feature an occupied d orbital which is non-bonding with respect to the triple bond. However, this does not severely affect the observed bond distances when compared to d^0 systems.[22],[63] Theoretical calculations revealed that the heavy triple bonds show a high degree of covalency with minor polarization. As outlined in the introduction, the Pauli repulsion is likely to be the main factor to rationalize the increase in bond distance when moving from nitrogen to phosphorus and arsenic. While oxidation and reduction potentials of **15** are separated by at least 3 V, the heavier pnictides exhibit significantly decreased, similar spacing between the redox events ($\Delta = 2.32$ V (P), 2.30 V (As)). A smaller HOMO-LUMO gap for the heavy multiple bonds can be derived by this, owing to less effective orbital splitting.

Table 6.3: Comparison of bond lengths and redox potentials of five-coordinate transition metal pnictide complexes with a d^2 electron count synthesized in this thesis, potentials given in V vs. $Fc^{0/+}$ and bond lengths in Å.

Complex	M≡Pn	E_{Ox}	E_{Red}
16	1.629(4)		
15	1.630(2)	> 1.5	−1.48
27	2.0939(6)	−0.43	−2.75
28	2.2021(3)	−0.50	−2.70

The electron rich Os^{II} platform **2** allowed for the oxidative addition of the primary phosphine PH_2Mes^* which resulted in the formation of the first isolable transition metal phosphinyl radical complex **38**. EPR spectroscopy and theoretical calculation suggest an equal distribution of the unpaired electron along the Os-P bond. The P-H bond could be split homolytically *via* proton coupled electron transfer to give the corresponding phosphinidene complex **39**. The associated bond dissociation energy was derived by isothermal titration calorimetry which allowed to extract additional thermodynamic parameters of the system. The low BDE value of the P-H bond suggests that tailored systems could utilize primary phosphines as electrophilic P_1 building blocks.

Based on the results obtained for the Re system, the preparation of novel Os≡P(R) species was attempted upon reaction of PCO^- and ClP**A** with different platforms. The heavier analogue of isocyanate was not compatible with all examined systems and resulted in reduction of the metal complex or no reaction at all. The reaction of ClP**A** with the square-planar halide complex **2** resulted in the formation of the first isolable and remarkably stable chlorophosphinidene complex **44**. In comparison to other Os^{IV} systems covered in this thesis, the $Os-N_{PNP}$ bond length is comparable while the Os=P double bond distance features a value of over 2.1 Å (Table 6.2). Cyclization reactions with unsaturated organic substrates were examined but no reactivity was observed in all

cases. A DFT study revealed that the steric bulk of the *tert*-butyl substituents induced a high kinetic barrier which might be overcome upon substitution with sterically less demanding ^{i}Pr-groups. Further studies should focus on the preparation of such complexes to eventually allow for (catalytic) phosphinidene transfer to unsaturated substrates.

The prior reported dimeric molybdenum dinitrogen complex **XCVII** was successfully oxidized by one and two electrons to give the cationic species **48** and **49**, respectively. Both complexes were completely characterized to study the effect of depopulation of δ-symmetric, metal-centered orbitals with respect to the dinitrogen bridge. Beside polarization effects which slightly affect the N=N bond strength, no severe structural alterations were observed. This was further confirmed by EXAFS spectroscopy which also served as an experimental technique to investigate the prior postulated diprotonated molybdenum dimeric complex **XCVIII**. Based on the obtained Mo-Mo distance, a quintet ground state was derived upon comparison with quantum chemical calculations. Since protonation of **XCVII** is required to allow for dinitrogen splitting towards nitrides, the methylated PNP pincer ligand L^{Me} was synthesized to skip this reaction step and directly access a suitable orbital configuration in dimeric dinitrogen complexes to enable splitting of dinitrogen upon reduction of suitable precursors. However, complexation of Mo^{III} halide precursors proved to be difficult and a Mo^0 carbonyl complex was prepared instead. The compound exhibits promising redox chemistry which might allow for successive decarbonylation to access halide complexes.

In summary, this thesis demonstrated the synthesis of different Re and Os halide platforms which allowed for rich follow-up chemistry and featured unique magnetic properties. New ways of stabilizing nitride complexes beyond the "nitrido wall" were demonstrated. Heavier analogues of nitride complexes, namely phosphides and arsenides, were successfully synthesized and depict the first group 7 representatives of this compound class. Furthermore, different strategies to utilize terminal transition metal pnictides, primary phosphines and ClP**A** as Pn_1 building block were evaluated. New insight into the mechanism of dinitrogen splitting by Mo PNP pincer complexes were obtained.

Experimental Section

7   Experimental Section

7.1   General Comments

For all published computed structures the corresponding XYZ-Files can be obtained free of charge *via* the publisher. Therefore, this data will not be presented in this section.

If a transition metal compound could not be characterized by means of combustion analysis the full NMR characterization will be given in the Appendix.

7.2   Materials and Methods

All experiments were carried out using Schlenk (argon atmosphere) and glovebox (argon atmosphere) techniques. All solvents were dried by passing through columns packed with activated alumina. Deuterated solvents were obtained from Euriso-Top GmbH, dried over Na/K (THF, Toluene, Benzene) or CaH_2 (CD_2Cl_2), distilled by trap-to-trap transfer *in vacuo*, and degassed by three freeze–pump–thaw cycles, respectively. Silica gel 60 silanized and activated carbon were heated at 120°C *in vacuo* for 5 days prior to use.

Table 7.1: List of used chemicals.

Compound	Supplier	Purification
18-C-6	Sigma-Aldrich	Recrystallization
15-C-5	Sigma-Aldrich	
2,2'-Bipyridine	abcr	
$Ag[Al(OC(CF_3)_3)_4]$	Iolitec	
$AgBF_4$	Sigma-Aldrich	
$AgSbF_6$	Sigma-Aldrich	
$B(C_6H_3\text{-}3,5\text{-}(CF_3)_2)_3$	Sigma-Aldrich	
nBuli 2.5 M in hexane	Sigma-Aldrich	
C	Thermo-Fisher	
ClP**A**	[67]	
CN^tBu	Sigma-Aldrich	
CO	Linde	
$CoCp_2$	abcr	
Cyclohexene	TCI	
Dimethylbutadiene	Sigma-Aldrich	
$[Fe(C_5H_5)_2]$	Sigma-Aldrich	Sublimation
$[Fe(C_5Me_5)_2]$	Sigma-Aldrich	Sublimation
Hg	Sigma-Aldrich	
$[H(OEt_2)_2][B(C_6H_3\text{-}3,5\text{-}(CF_3)_2)_4]$	[291]	
HOTf	Sigma-Aldrich	
^{H}PNP	[292]	
^{H}PyrPz	TCI	
K	Sigma-Aldrich	
KO^tBu	Sigma-Aldrich	Sublimation

Li	abcr	
Mes*O	[293]	
[Mo(CO)$_3$(toluene)]	[294]	
[{MoCl(L^1)}$_2$(N$_2$)]	[280]	
[MoCl$_3$(THF)$_3$]	[295]	
[MoNCl(^{H}L^1)][OTf]	[280]	
N(CH$_2$CH$_2$Cl)$_2$Me · HCl	Sigma-Aldrich	
Na	Sigma-Aldrich	
NaBH$_4$	Sigma-Aldrich	
NaBPh$_4$	Sigma-Aldrich	
Na(diox)$_x$PnCO (Pn = P, As)	[119], [296]	
NaI	Sigma-Aldrich	dried at 100°C
[NBu$_4$][PF$_6$]	Sigma-Aldrich	
PhCCH	Sigma-Aldrich	
PH$_2$Ph	Sigma-Aldrich	
PH$_2$Mes*	Sigma-Aldrich	
PCl^{t}Bu$_2$	abr	
Pyr−N−O	TCI	Sublimation
[ReCl$_2$(L^1)]	[52]	
[ReCl$_2$(L^3)]	[297]	
TBP	[293]	
TEMPO	Sigma-Aldrich	
TlOTf	abcr	
Tolane	Sigma-Aldrich	
TMSI	Sigma-Aldrich	
TMSN$_3$	Sigma-Aldrich	
[OsCl$_2$(PPh$_3$)$_3$]	[298]	
[Ph$_3$C][PF$_6$]	Sigma-Aldrich	
[TBA][WN(ODipp)$_4$]	[65]	

Cyclic voltammograms were recorded with a Metrohm Autolab PGSTAT101 using Ag/Ag$^+$ reference-, glassy-carbon working- and Pt-wire counterelectrodes.

Experimental X-band **EPR spectra** were recorded on a Bruker ELEXSYS-II E500 CW-EPR. The spectra were simulated by iteration of the anisotropic g-values, (super)hyperfine coupling constants, and line widths using the EPR-simulation program W95EPR developed by Prof. Dr. Frank Neese and EasySpin.

IR spectra were recorded with a Thermo Scientific Nicolet iZ10 FT/IR spectrometer at room temperature.

Magnetic susceptibility measurements were performed with a Quantum Design MPMS-XL-5 SQUID magnetometer in the temperature range from 295 to 2 K at 0.5 T applied field. The powdered sample was contained in a Teflon bucket and fixed in a non-magnetic sample holder. Each raw data point for the measured magnetic moment of the sample was corrected for the diamagnetic contribution by subtraction of the experimentally de-

termined magnetic measurement of the Teflon bucket. The molar susceptibility data were corrected for the diamagnetic contribution using the Pascal constants and the increment method according to Haberditzl.[299] Experimental data were modelled with the *julX* program.[300]

Elemental analyses were obtained from the analytical laboratories at the Georg-August University on an Elementar Vario EL 3.

NMR spectra were recorded on Bruker Avance III 300, Bruker Avance III 300, Bruker Avance III 400 and Bruker Avance III HD 500 and were calibrated to the residual solvent proton resonance. (C_6D_6 = 7.16 ppm, THF-d_8 = 3.58 ppm, toluene-d_8 = 2.08 ppm, CD_2Cl_2 = 5.32 ppm).

LIFDI spectrometry was performed on a Joel AccuTOF spectrometer under inert conditions.

UV/vis spectra were recorded with an Agilent Technologies Cary 300 UV/vis spectrometer.

Indophenolic titration was used for the quantification of ammonia.[301]

Electrospray ionization (**ESI**) mass spectra were collected on a Bruker HCTultra instrument. The moisture and oxygen sensitive samples were prepared in a glovebox (MBRAUN UNIlab) under an argon atmosphere and injected into the Bruker HTCultra instrument via a direct Peek™ tubing connection to a syringe using dry and degassed solvents.

Suitable single crystals for **X-ray structure determination** were selected from the mother liquor under an inert gas atmosphere and transferred in protective perfluoro polyether oil on a microscope slide. The selected and mounted crystals were transferred to the cold gas stream on the diffractometer. The diffraction data were obtained at 100 K on a Bruker D8 three-circle diffractometer, equipped with a PHOTON 100 CMOS detector and an INCOATEC microfocus source with Quazar mirror optics (Mo-Kα radiation, λ = 0.71073 Å). The data obtained were integrated with SAINT and a semi-empirical absorption correction from equivalents with SADABS was applied. The structure was solved and refined using the Bruker SHELX 2014 software package.[2] All non-hydrogen atoms were refined with anisotropic displacement parameters. All C-H hydrogen atoms were refined isotropically on calculated positions by using a riding model with their Uiso values constrained to 1.5 U$_{eq.}$ of their pivot atoms for terminal sp^3 carbon atoms and 1.2 times for all other atoms.

Mo K-edge **XAS measurements** were performed at the B18 beamline at the Diamond Light Source in Didcot, United Kingdom. All measurements were performed in fluores-

---

[2]a) APEX3 v2016.9-0 (SAINT/SADABS/SHELXT/SHELXL), Bruker AXS Inc., Madison, WI, USA, **2016**. b) George M. Sheldrick, *Acta Cryst.*, **2015**, *A71*, 3. c) George M. Sheldrick, *Acta Cryst.*, **2015**, *C71*, 3. d) George M. Sheldrick, *Acta Cryst.*, **2008**, *A64*, 112.

cence mode, unless otherwise stated. Measurements at the Diamond Light Source were performed with a Si(311) double crystal monochromator in combination with a 9 element Ge Solid State detector. A typical measurement required around 90 minutes; a minimum of 20 scans were required to obtain good signal-to-noise in the data. All acquired spectra were calibrated to a Mo metal foil. EXAFS data processing and analysis was performed using the Demeter software package in Athena and Artemis respectively.[302] The amplitude reduction factor was determined using the Mo foil and was 0.95. Samples were prepared in J-Young NMR tubes and cooled (for setup see Appendix 8.4.3)

7.3 Os(II/III) and Re(III) PNP Pincer Complexes

Parts of this chapter were adapted from:
J. Abbenseth, M. Diefenbach, S. C. Bete, C. Würtele, C. Volkmann, S. Demeshko, M. C. Holthausen, S. Schneider *Chem. Commun.* **2017**, *53*, 5511-5514.
with permission from The Royal Society of Chemistry.

7.3.1 A Square-Planar Os(II) Complex - Computational Details

The molecular geometries of two singlet and two triplet isomers of **2** in C_2 and C_s symmetry were optimized under gas-phase conditions using the Gaussian09 program[303] with the PBE0 hybrid functional[304],[305] in conjunction with Grimme's 3rd generation atom-pairwise dispersion correction including Becke–Johnson damping (D3BJ).[306] The def2-TZVP orbital basis set[307] was employed with the quasi-relativistic ECP60MWB pseudopotential,[308] which replaces the 60 core electrons in osmium. This level of DFT is abbreviated as PBE0D/TZVP. The optimized geometries were identified as minima through analysis of the eigenvalues of the Hessian matrix. Further calculations were conducted on a smaller model system, in which the four *t*Bu groups of the pincer were replaced by methyl groups (**2,Me**). For each fully optimized electronic state of the real system **2**, the model systems **2,Me** were constructed in constrained geometries where only the C–H bond lenghts of the twelve newly added hydrogen atoms (which replace the twelve methyl fragments of the four *t*Bu groups) were allowed to relax, i.e., all angles and dihedrals are kept fixed and all remaining coordinates are unaltered.
Relative energies from correlated wavefunction theory were computed at the DFT molecular geometries for the electromers of the **2,Me** model system using the Molpro2015.1 program.[309] The explicitly correlated coupled-cluster ansatz with single and double excitations and perturbative triples, CCSD(T)-F12b,[310],[311] was employed in combination with the F12-optimized correlation-consistent polarized double- and triple-zeta orbital and auxiliary basis sets of the cc-pVnZ-F12 family[312]–[314] on non-metal atoms and the aug-cc-pVnZ-PP orbital basis set which includes the relativistic ECP60MDF pseudopotential on Os[315] in conjunction with the auxiliary def2-QZVPP/JKfit basis sets[?] for the many-electron integrals (CABS) as well as for the density-fitting of the Fock and exchange matrices (JKfit) and with the aug-cc-pV[316] for the remaining integrals. The CCSD(T)-F12 energies were extrapolated to the complete basis set limit CBS(D,T) according to the procedure of Hill *et al.*[317] Final energies given in the text are based on an ONIOM(CCSD(T)-F12:PBE0D) approach according to $E_{tot}(\mathbf{2}) = E_{\text{CCSD(T)-F12}}(\mathbf{2,Me})$ -$E_{\text{PBE0D}}(\mathbf{2,Me}) + E_{\text{PBE0D}}(\mathbf{2})$.
Quasi-degenerate perturbation theory (QDPT) was used to calculate spin-orbit eigenstates for the real system **2**. Computations were performed on the DFT-optimized geometry of the lowest-energy C_2-symmetric ^{3}B state based on a CASSCF wavefunction within the ORCA program.[318] The ZORA approximation[319] for all elements. The active space comprises the five Os-based 5d orbitals and five occupied ligand–metal based orbitals, giving rise to a CAS(16,10) expansion. In the CASSCF calculations the orbitals were optimized by the average of 5 quintet, 45 triplet and 50 singlet roots arising from the formal d^6 configuration of the osmium(II) center. The RI and RIJCOSX[320] approximations were used along with the corresponding def2TZVP/C auxiliary basis sets[321] and a fine grid (GridX6 in ORCA convention), respectively. The final energies

are obtained from NEVPT2 calculations,[322]–[324] and the energies that enter QDPT treatment via a full SOMF operator.[325]

For a complete list of all computed results see the originial publication.

7.3.2 Five- and Six-Coordinate Os Bipyridine Complexes - Computational Details

DFT calculations were carried out with the ORCA program package using the PBE and PBE0 functionals.[304],[318],[326] Ahlrichs' basis sets def2-SVP (for geometry optimization and frequency calculation) and def2-TZVPP (for single-point energies) were used with a full basis for all elements but Os for which the Stuttgart-Dresden 60 electron core potential was chosen to replace the inner shell 1s-4f orbitals.[307],[308] The RI-J (PBE) approximation in combination with the corresponding auxiliary basis sets of Alrichs was utilized to reduce computational costs in the geometry optimization and frequency calculations.[327]–[329] Grimme's model (D3) with Becke-Johnson damping was used to account for dispersion with the PBE or PBE0 functionals.[306],[330] No symmetry restraints were imposed and the optimized structures were defined as minima (no negative eigenvalues) by vibrational analyses. TDDFT/EPR calculations were performed with ORCA and the CPCM solvation model was used (pentane, THF).[331] Relativistic treatment was introduced by ZORA.[332] Geometries were analyzed and visualized with Avogadro and molecular orbitals, spin-densities and difference densities were visualized with Chimera.[333],[334]

Table 7.2: XYZ-coordinates of computed complex **9**.

Atom	x	y	z	Atom	x	y	z
C	-0.25646	2.68861	-1.70132	C	1.57293	2.24456	2.16366
C	-0.78199	1.66259	-2.44998	H	1.1423	2.03454	3.16711
N	-0.22282	0.40738	-2.48361	H	2.3253	1.45975	1.94644
H	-1.68978	1.81869	-3.06568	H	2.09951	3.216	2.23448
C	-0.7903	-0.57084	-3.26458	C	-0.53291	3.41432	1.3894
C	-0.26806	-1.83819	-3.36223	H	-0.99859	3.26451	2.38808
H	-1.70313	-0.29082	-3.82658	H	-1.34943	3.43222	0.64012
P	1.18605	-2.17453	-2.341	H	-0.04812	4.40657	1.3985
H	-0.74534	-2.58927	-4.00753	C	2.41662	3.71205	-0.86497
C	0.52491	-3.37571	-0.98223	C	1.92861	5.0117	-0.20697
C	2.41051	-3.12747	-3.47674	H	0.93371	5.32441	-0.58212
C	-0.21921	-2.44152	-0.01512	H	1.87908	4.93521	0.89609
H	0.4906	-1.72744	0.45515	H	2.64354	5.82758	-0.45028
H	-0.68658	-3.02385	0.80827	C	2.58529	3.96054	-2.37452
H	-1.01663	-1.86444	-0.52563	H	1.62436	4.22109	-2.86017
C	-0.47337	-4.41635	-1.50922	H	3.00405	3.08233	-2.89599
H	-0.89916	-4.97885	-0.6502	H	3.29196	4.80568	-2.52168
H	-0.00871	-5.15364	-2.18792	C	3.77344	3.29072	-0.2733
H	-1.315	-3.93361	-2.04421	H	4.52133	4.08939	-0.46802
C	1.68055	-4.05382	-0.23155	H	4.14823	2.36002	-0.74024
H	1.28416	-4.5651	0.67235	H	3.7311	3.13043	0.82011

Atom	x	y	z	Atom	x	y	z
H	2.44182	-3.31964	0.10135	Os	1.58283	0.01106	-1.41521
H	2.18567	-4.82429	-0.84601	N	2.90027	0.55229	-2.83916
C	1.92742	-4.54363	-3.82546	C	2.54372	1.01854	-4.06471
H	0.91944	-4.5425	-4.28733	C	3.46897	1.36989	-5.04324
H	1.90879	-5.21483	-2.94624	H	1.46058	1.10209	-4.22956
H	2.62704	-4.98968	-4.56568	C	4.85716	1.22612	-4.75329
C	2.53158	-2.3198	-4.78169	H	3.11155	1.74649	-6.01019
H	3.22686	-2.85081	-5.46701	C	5.23917	0.75027	-3.51121
H	2.94159	-1.30967	-4.60894	H	5.61598	1.48813	-5.50492
H	1.55538	-2.20873	-5.29243	C	4.27058	0.40661	-2.5206
C	3.79053	-3.18206	-2.79897	H	6.30323	0.62606	-3.26546
H	3.78607	-3.75578	-1.85438	C	4.54581	-0.08261	-1.21018
H	4.51581	-3.67053	-3.48515	N	3.40763	-0.35892	-0.43458
H	4.16929	-2.16601	-2.57761	C	3.57715	-0.81943	0.8244
P	1.17118	2.26188	-0.67566	C	4.82316	-1.05025	1.4097
H	-0.73234	3.67989	-1.70421	H	2.64678	-1.01029	1.3841
C	0.45062	2.26693	1.11655	C	5.98643	-0.78286	0.63501
C	-0.32892	0.94391	1.18699	H	4.88334	-1.42798	2.43842
H	-0.80805	0.83057	2.18343	C	5.8437	-0.30386	-0.65674
H	0.35495	0.07845	1.05511	H	6.98872	-0.95276	1.05552
H	-1.12315	0.88727	0.41535	H	6.72973	-0.08719	-1.26968

Table 7.3: XYZ-coordinates of computed complex **10**.

Atom	x	y	z	Atom	x	y	z
C	3.67567	12.2056	17.07189	C	4.72961	11.70545	10.62787
H	4.16669	13.11147	17.48067	H	5.66813	11.26421	10.22802
C	3.41457	11.12063	17.87501	H	4.91638	12.78665	10.7826
H	3.70878	11.12541	18.93438	H	3.95807	11.58527	9.84261
C	4.25603	8.41827	16.95894	C	1.5809	12.40904	11.61798
C	5.48783	9.23527	16.53131	C	2.07372	13.55979	10.7229
H	6.34252	8.54617	16.36069	H	2.8759	13.2686	10.02464
H	5.77582	9.97111	17.30636	H	2.42843	14.41835	11.32713
H	5.28841	9.78894	15.59381	H	1.21854	13.92468	10.11346
C	4.56497	7.76741	18.31536	C	1.09732	11.22188	10.77178
H	5.50719	7.18439	18.22493	H	0.21865	11.52767	10.16305
H	3.77794	7.06078	18.64173	H	0.78337	10.37115	11.41093
H	4.72277	8.52054	19.11319	H	1.87264	10.86259	10.06853
C	3.99021	7.33067	15.90551	C	0.40173	12.94938	12.4428
H	3.84674	7.79255	14.90967	H	-0.32095	13.44783	11.76156
H	3.10097	6.71349	16.13701	H	0.73529	13.69206	13.19473
H	4.86758	6.64978	15.84721	H	-0.13365	12.14011	12.96672
C	1.40283	8.96845	18.15634	C	0.26919	12.79207	15.94472
C	1.81297	8.9246	19.6384	H	1.21247	13.28271	16.22254
H	2.64387	8.23099	19.84798	C	-0.96876	13.36951	16.20448
H	0.94033	8.5906	20.24127	H	-1.01463	14.34798	16.70302

H	2.09477	9.93055	20.00709	C	-2.14368	12.68779	15.81952
C	0.21017	9.93163	18.04312	H	-3.13706	13.11757	16.01118
H	-0.26932	9.87922	17.05062	C	-2.01368	11.45176	15.1881
H	0.51363	10.98162	18.22793	H	-2.90718	10.8946	14.87556
H	-0.55432	9.65377	18.79975	C	-0.732	10.91222	14.94799
C	0.96976	7.57939	17.65997	C	-0.48002	9.63126	14.29925
H	0.71363	7.59933	16.5804	C	-1.49811	8.76655	13.84686
H	0.0638	7.25168	18.21383	H	-2.54769	9.06171	13.98185
H	1.74912	6.80842	17.81992	C	-1.1847	7.55179	13.24083
C	3.75925	13.284	14.97055	H	-1.97582	6.87489	12.88943
H	4.2541	14.12425	15.49788	C	0.18018	7.22282	13.09431
C	3.57369	13.3179	13.60858	H	0.49602	6.28089	12.6239
H	3.935	14.17082	13.01678	C	1.1504	8.10339	13.55324
C	4.36349	10.98495	11.93307	H	2.22008	7.88292	13.4518
C	4.03872	9.51094	11.6434	N	3.36816	12.2188	15.73713
H	3.14139	9.38255	11.008	N	0.41002	11.58759	15.32867
H	3.87368	8.96875	12.59411	N	0.86462	9.29968	14.15717
H	4.89612	9.03754	11.11746	H	3.54829	9.73307	14.44161
C	5.57931	11.04849	12.87289	P	2.77662	9.67929	17.00147
H	6.42541	10.49133	12.41663	P	2.89311	11.80612	12.90293
H	5.34478	10.58753	13.85069	Os	2.24379	10.63407	14.88051
H	5.90253	12.09117	13.05456				

7.3.3 Crystallographic Details

CCDC-1534960 (**1**), CCDC-1534959 (**2**), CCDC-1534961 (**3**) and CCDC-1534958 (**4**) contain the supplementary complete crystallographic data for this chapter. This data can be obtained free of charge *via* http://www.ccdc.cam.ac.uk/ products/csd/request/
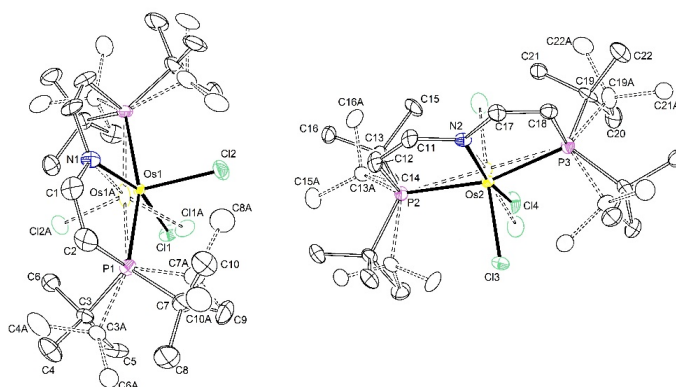
Figure 7.1: Thermal ellipsoid plot of **1** with the anisotropic displacement parameters drawn at the 50% probability level. The asymmetric unit contains two half complex molecules. Both complex molecules are disordered over two positions. The first disordered complex molecule was refined with population of 0.910(3) on the main domain using some restraints (SADI) and constraints (EADP). The second disordered complex molecule was refined with population of 0.502(6) on the main domain using some restraints (SADI, RIGU) and constraints (EADP).

Empirical formula	$C_{20}H_{40}Cl_2NOsP_2$
Formula weight	617.57
Temperature	102(2) K
Wavelength	0.71073 Å
Crystal system	Orthorhombic
Space group	Pnma
Unit cell dimensions	a = 16.8714(6) Å $\qquad \alpha = 90°$
	b = 16.9302(7) Å $\qquad \beta = 90°$
	c = 17.1112(6) Å $\qquad \gamma = 90°$
Volume	4887.6(3) Å^3
Z	8
Density (calculated)	1.679 Mg/m^3
Absorption coefficient	5.573 mm^{-1}
F(000)	2456
Crystal size	0.154 x 0.097 x 0.056 mm^3
Crystal shape and color	Block, clear intense green
Theta range for data collection	2.079 to 26.731°
Index ranges	-21<=h, k, l<=21
Reflections collected	70085
Independent reflections	5375 [R(int) = 0.0474]
Completeness to theta = 25.242°	99.9%
Max. and min. transmission	0.7454 and 0.5878
Refinement method	Full-matrix least-squares on F^2
Data / restraints / parameters	5375 / 64 / 357
Goodness-of-fit on F^2	1.549
Final R indices [I>2sigma(I)]	R1 = 0.0392, $\qquad$ wR2 = 0.0761
R indices (all data)	R1 = 0.0459, $\qquad$ wR2 = 0.0784
Largest diff. peak and hole	1.331 and -2.360 eÅ^{-3}
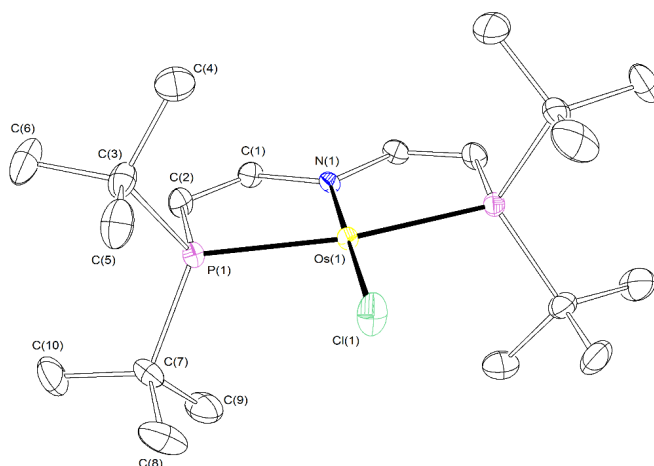
Figure 7.2: Thermal ellipsoid plot of **2** with the anisotropic displacement parameters drawn at the 50% probability level. The asymmetric unit contains a half complex molecule.

Empirical formula	$C_{20}H_{40}ClNOsP_2$	
Formula weight	582.12	
Temperature	112(2) K	
Wavelength	0.71073 Å	
Crystal system	Monoclinic	
Space group	P2/c	
Unit cell dimensions	a = 11.4519(6) Å	$\alpha = 90°$
	b = 8.5831(4) Å	$\beta = 113.000(2)°$
	c = 13.3683(6) Å	$\gamma = 90°$
Volume	1209.55(10) Å^3	
Z	2	
Density (calculated)	1.598 Mg/m^3	
Absorption coefficient	5.518 mm^{-1}	
F(000)	580	
Crystal size	0.187 x 0.157 x 0.072 mm^3	
Crystal shape and color	Block, clear intense purple	
Theta range for data collection	2.373 to 28.366°	
Index ranges	-15<=h<=15	
	-10<=k<=11	
	-17<=l<=17	
Reflections collected	36752	
Independent reflections	3027 [R(int) = 0.0469]	
Completeness to theta = 25.242°	100.0%	
Max. and min. transmission	0.7457 and 0.6334	
Refinement method	Full-matrix least-squares on F^2	
Data / restraints / parameters	3027 / 0 / 121	
Goodness-of-fit on F^2	1.122	
Final R indices [I>2sigma(I)]	R1 = 0.0161,	wR2 = 0.0301
R indices (all data)	R1 = 0.0269,	wR2 = 0.0329
Largest diff. peak and hole	0.484 and -0.634 eÅ^{-3}	
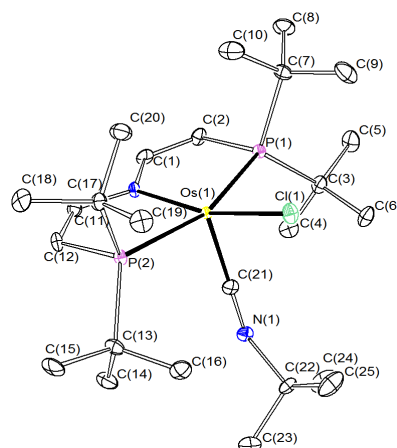
Figure 7.3: Thermal ellipsoid plot of **3** with the anisotropic displacement parameters drawn at the 50% probability level. The structure was refined using two constrains (EADP).

Empirical formula	$C_{25}H_{49}ClN_2OsP_2$
Formula weight	665.25
Temperature	100(2) K
Wavelength	0.71073 Å
Crystal system	Monoclinic
Space group	P21/c
Unit cell dimensions	a = 15.2391(7) Å $\quad\quad$ $\alpha = 90°$
	b = 10.9698(5) Å $\quad\quad$ $\beta = 96.832(2)°$
	c = 16.9742(8) Å $\quad\quad$ $\gamma = 90°$
Volume	2817.4(2) Å^3
Z	4
Density (calculated)	1.568 Mg/m^3
Absorption coefficient	4.750 mm^{-1}
F(000)	1344
Crystal size	0.947 x 0.766 x 0.556 mm^3
Crystal shape and color	Block, clear intense blue
Theta range for data collection	2.215 to 27.197°
Index ranges	-19<=h<=19
	-14<=k<=14
	-21<=l<=21
Reflections collected	76131
Independent reflections	6264 [R(int) = 0.0694]
Completeness to theta = 25.242°	100.0%
Max. and min. transmission	0.7455 and 0.1448
Refinement method	Full-matrix least-squares on F^2
Data / restraints / parameters	6264 / 0 / 283
Goodness-of-fit on F^2	1.067
Final R indices [I>2sigma(I)]	R1 = 0.0290, $\quad\quad$ wR2 = 0.0755
R indices (all data)	R1 = 0.0349, $\quad\quad$ wR2 = 0.0797
Largest diff. peak and hole	1.645 and -2.020 eÅ^{-3}
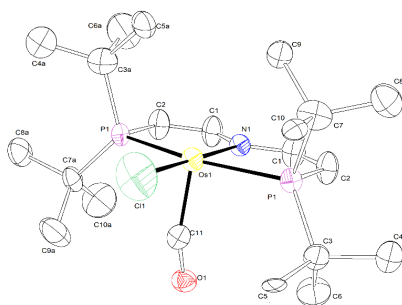
Figure 7.4: Thermal ellipsoid plot of **4** with the anisotropic displacement parameters drawn at the 50% probability level. The asymmetric unit contains a half disordered complex molecule. The disorder was refined with site occupation factors of 0.25 for both sites using PART commands and some restraints (SADI, RIGU) and constraints (EADP). The structure was refined as an inversion twin using the twin law -100 0-10 00-1 (BASF: 0.50(3)).

Empirical formula	$C_{21}H_{40}ClNOOsP_2$	
Formula weight	610.13	
Temperature	100(2) K	
Wavelength	0.71073 Å	
Crystal system	Tetragonal	
Space group	I4	
Unit cell dimensions	a = 12.0393(7) Å	$\alpha = 90°$
	b = 12.0393(7) Å	$\beta = 90°$
	c = 8.5145(5) Å	$\gamma = 90°$
Volume	1234.13(16) Å^3	
Z	2	
Density (calculated)	1.642 Mg/m^3	
Absorption coefficient	5.415 mm^{-1}	
F(000)	608	
Crystal size	0.309 x 0.180 x 0.142 mm^3	
Crystal shape and color	Block, dark brown	
Theta range for data collection	2.392 to 33.138°	
Index ranges	-17<=h<=18	
	-18<=k<=18	
	-13<=l<=12	
Reflections collected	28153	
Independent reflections	2296 [R(int) = 0.0545]	
Completeness to theta = 25.242°	100.0%	
Max. and min. transmission	0.7466 and 0.5604	
Refinement method	Full-matrix least-squares on F^2	
Data / restraints / parameters	2296 / 310 / 201	
Goodness-of-fit on F^2	1.066	
Final R indices [I>2sigma(I)]	R1 = 0.0355,	wR2 = 0.0641
R indices (all data)	R1 = 0.0520,	wR2 = 0.0685
Absolute structure parameter	0.50(3)	
Largest diff. peak and hole	1.354 and -1.026 eÅ^{-3}	
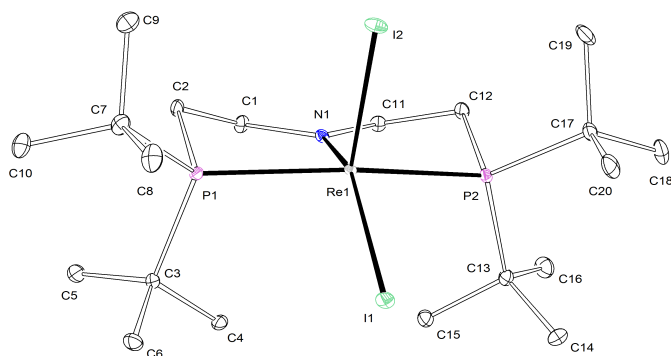
Figure 7.5: Thermal ellipsoid plot of **5** with the anisotropic displacement parameters drawn at the 50% probability level. The asymmetric unit contains one complex molecule.

Empirical formula	$C_{20}H_{44}I_2NP_2Re$
Formula weight	800.50
Temperature	100(2) K
Wavelength	0.71073 Å
Crystal system	Monoclinic
Space group	$P2_1/n$
Unit cell dimensions	a = 11.9420(6) Å $\qquad \alpha = 90°$
	b = 13.8096(6) Å $\qquad \beta = 105.337(2)°$
	c = 16.7699(7) Å $\qquad \gamma = 90°$
Volume	2667.1(2) Å^3
Z	4
Density (calculated)	1.994 Mg/m^3
Absorption coefficient	6.997 mm^{-1}
F(000)	1528
Crystal size	0.163 x 0.143 x 0.115 mm^3
Crystal shape and color	Block, clear intense red-brown
Theta range for data collection	2.303 to 28.391°
Index ranges	-15<=h<=15
	-18<=k<=18
	-22<=l<=22
Reflections collected	97793
Independent reflections	6666 [R(int) = 0.0755]
Completeness to theta = 25.242°	100.0%
Refinement method	Full-matrix least-squares on F^2
Data / restraints / parameters	6666 / 0 / 247
Goodness-of-fit on F^2	1.053
Final R indices [I>2sigma(I)]	R1 = 0.0237, $\qquad$ wR2 = 0.0349
R indices (all data)	R1 = 0.0342, $\qquad$ wR2 = 0.0367
Largest diff. peak and hole	0.874 and -0.880 eÅ^{-3}
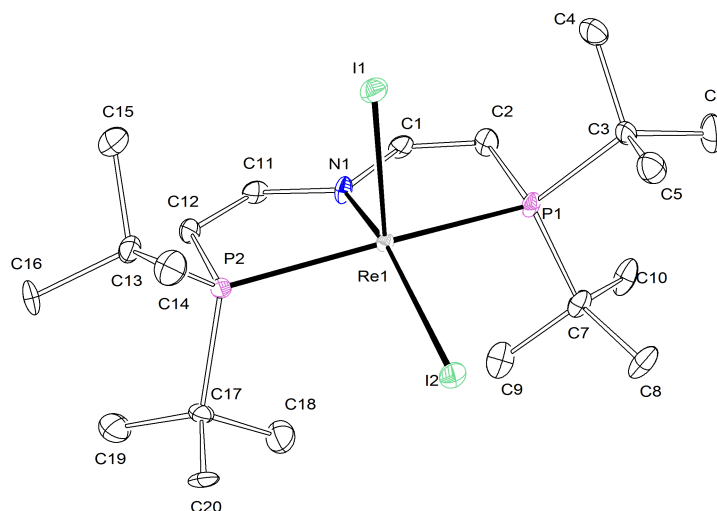
Figure 7.6: Thermal ellipsoid plot of **6** with the anisotropic displacement parameters drawn at the 50% probability level. The asymmetric unit contains one complex molecule.

Empirical formula	$C_{20}H_{40}I_2NP_2Re$
Formula weight	796.47
Temperature	100(2) K
Wavelength	0.71073 Å
Crystal system	Monoclinic
Space group	$P2_1/n$
Unit cell dimensions	a = 8.1344(2) Å $\alpha = 90°$
	b = 26.6172(7) Å $\beta = 108.4060(10)°$
	c = 12.6060(4) Å $\gamma = 90°$
Volume	2589.76(13) Å^3
Z	4
Density (calculated)	2.043 Mg/m^3
Absorption coefficient	7.206 mm^{-1}
F(000)	1512
Crystal size	0.333 x 0.206 x 0.170 mm^3
Crystal shape and color	Block, clear intense brown
Theta range for data collection	2.289 to 30.605°.
Index ranges	-11<=h<=11
	-38<=k<=37
	-18<=l<=17
Reflections collected	103794
Independent reflections	7942 [R(int) = 0.1614]
Completeness to theta = 25.242°	100.0%
Refinement method	Full-matrix least-squares on F^2
Data / restraints / parameters	7942 / 0 / 247
Goodness-of-fit on F^2	1.084
Final R indices [I>2sigma(I)]	R1 = 0.0456, wR2 = 0.0531
R indices (all data)	R1 = 0.0786, wR2 = 0.0576
Largest diff. peak and hole	1.188 and -1.544 eÅ^{-3}
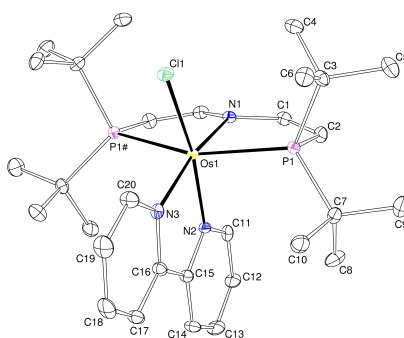
Figure 7.7: Thermal ellipsoid plot of **7** with the anisotropic displacement parameters drawn at the 50% probability level. The asymmetric unit contains only a half complex molecule. The reflections 2 0 0 and 0 4 0 are removed from the refinement using OMIT commands.

Empirical formula	$C_{30}H_{40}ClN_3OsP_2$	
Formula weight	738.30	
Temperature	100(2) K	
Wavelength	0.71073 Å	
Crystal system	Orthorhombic	
Space group	Pnma	
Unit cell dimensions	a = 14.1295(11) Å	$\alpha = 90°$
	b = 14.0882(11) Å	$\beta = 90°$
	c = 15.2802(11) Å	$\gamma = 90°$
Volume	3041.7(4) Å^3	
Z	4	
Density (calculated)	1.612 Mg/m^3	
Absorption coefficient	4.410 mm^{-1}	
F(000)	1488	
Crystal size	0.488 x 0.157 x 0.155 mm^3	
Crystal shape and color	Block, dark red	
Theta range for data collection	1.963 to 30.585°	
Index ranges	-20<=h<=20	
	-20<=k<=20	
	-21<=l<=21	
Reflections collected	64224	
Independent reflections	4830 [R(int) = 0.0743]	
Completeness to theta = 25.242°	99.9%	
Max. and min. transmission	0.7461 and 0.4071	
Refinement method	Full-matrix least-squares on F^2	
Data / restraints / parameters	4830 / 0 / 196	
Goodness-of-fit on F^2	1.066	
Final R indices [I>2sigma(I)]	R1 = 0.0191, wR2 = 0.0420	
R indices (all data)	R1 = 0.0250, wR2 = 0.0447	
Largest diff. peak and hole	0.981 and -1.545 eÅ^{-3}	
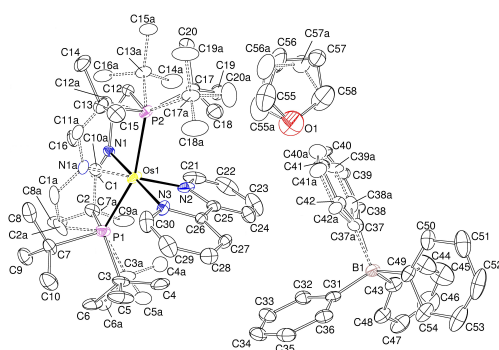
Figure 7.8: Thermal ellipsoid plot of **8** with the anisotropic displacement parameters drawn at the 50% probability level. The asymmetric unit contains one disordered complex molecule, one disordered THF solvent molecule and one disordered BPh4 anion. All disorders were refined with site occupation factors of 0.5 for both sites using PART commands and some restraints and constrains (SADI, RIGU, EADP).

Empirical formula	$C_{58}H_{76}BN_3OOsP_2$	
Formula weight	1094.16	
Temperature	100(2) K	
Wavelength	0.71073 Å	
Crystal system	Triclinic	
Space group	P-1	
Unit cell dimensions	a = 11.5963(6) Å	$\alpha = 93.881(2)°$
	b = 13.7010(7) Å	$\beta = 94.957(2)°$
	c = 16.6621(10) Å	$\gamma = 96.112(2)°$
Volume	2614.5(2) Å^3	
Z	2	
Density (calculated)	1.390 Mg/m^3	
Absorption coefficient	2.542 mm^{-1}	
F(000)	1128	
Crystal size	0.678 x 0.476 x 0.220 mm^3	
Crystal shape and color	Plate, clear pale brown-orange	
Theta range for data collection	2.062 to 30.637°	
Index ranges	-16<=h<=16	
	-19<=k<=19	
	-23<=l<=23	
Reflections collected	131156	
Independent reflections	16066 [R(int) = 0.0897]	
Completeness to theta = 25.242°	99.9%	
Max. and min. transmission	0.7461 and 0.5082	
Refinement method	Full-matrix least-squares on F^2	
Data / restraints / parameters	16066 / 89 / 847	
Goodness-of-fit on F^2	1.049	
Final R indices [I¿2sigma(I)]	R1 = 0.0368,	wR2 = 0.0649
R indices (all data)	R1 = 0.0622,	wR2 = 0.0736
Largest diff. peak and hole	1.769 and -2.988 eÅ^{-3}	
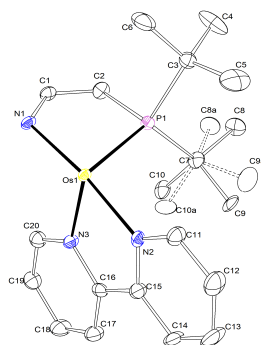
Figure 7.9: Thermal ellipsoid plot of **10** with the anisotropic displacement parameters drawn at the 50% probability level. The asymmetric unit contains one disordered complex molecule. The disordered complex molecule was refined with population of 0.60(1) on the main domain using some restraints and constraints (SADI, EADP). The hydride hydrogen atom could not be refined to give a stable solution and was therefore introduced by the DFIX command.

Empirical formula	$C_{30}H_{49}N_3OsP_2$	
Formula weight	703.86	
Temperature	100(2) K	
Wavelength	0.71073 Å	
Crystal system	Orthorhombic	
Space group	Pnma	
Unit cell dimensions	a = 14.5071(16) Å	$\alpha = 90°$
	b = 13.668(2) Å	$\beta = 90°$
	c = 15.2847(18) Å	$\gamma = 90°$
Volume	3030.6(7) Å^3	
Z	4	
Density (calculated)	1.543 Mg/m^3	
Absorption coefficient	4.336 mm^{-1}	
F(000)	1424	
Crystal size	0.470 x 0.060 x 0.050 mm^3	
Crystal shape and color	Plate, clear dark green	
Theta range for data collection	2.443 to 26.491°	
Index ranges	-18<=h<=18	
	-17<=k<=17	
	-19<=l<=19	
Reflections collected	38289	
Independent reflections	3212 [R(int) = 0.1007]	
Completeness to theta = 25.242°	98.2%	
Refinement method	Full-matrix least-squares on F^2	
Data / restraints / parameters	3212 / 16 / 218	
Goodness-of-fit on F^2	0.793	
Final R indices [I>2sigma(I)]	R1 = 0.0271,	wR2 = 0.0663
R indices (all data)	R1 = 0.0392,	wR2 = 0.0765
Largest diff. peak and hole	1.843 and -1.114 eÅ^{-3}	
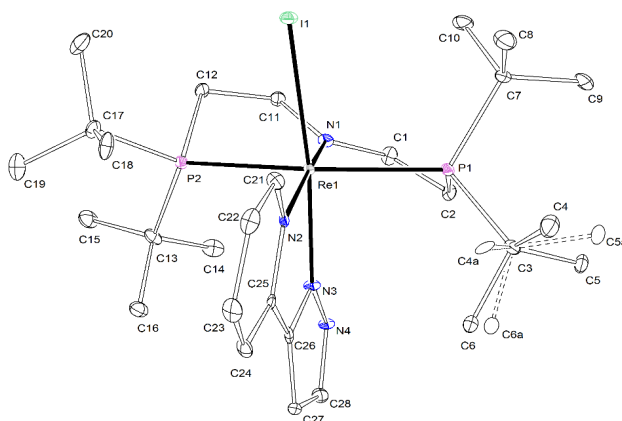
Figure 7.10: Thermal ellipsoid plot of **11** with the anisotropic displacement parameters drawn at the 50% probability level. The asymmetric unit contains one disordered complex molecule. The disordered complex molecule was refined with population of 0.63(7) on the main domain using some restraints and constraints (SADI, EADP).

|		
Empirical formula	$C_{28}H_{50}IN_4P_2Re$	
Formula weight	817.76	
Temperature	100(2) K	
Wavelength	0.71073 Å	
Crystal system	Monoclinic	
Space group	$P2_1/c$	
Unit cell dimensions	a = 9.5712(5) Å	$\alpha = 90°$
	b = 15.7700(8) Å	$\beta = 97.021(2)°$
	c = 20.5852(10) Å	$\gamma = 90°$
Volume	3083.8(3) $Å^3$	
Z	4	
Density (calculated)	1.761 Mg/m^3	
Absorption coefficient	5.069 mm^{-1}	
F(000)	1616	
Crystal size	0.242 x 0.137 x 0.115 mm^3	
Crystal shape and color	Block, clear intense red	
Theta range for data collection	2.375 to 28.414°	
Index ranges	-12<=h<=12	
	-21<=k<=21	
	-26<=l<=27	
Reflections collected	126695	
Independent reflections	7724 [R(int) = 0.1462]	
Completeness to theta = 25.242°	99.9%	
Refinement method	Full-matrix least-squares on F^2	
Data / restraints / parameters	7724 / 30 / 349	
Goodness-of-fit on F^2	1.070	
Final R indices [I>2sigma(I)]	R1 = 0.0417,	wR2 = 0.0606
R indices (all data)	R1 = 0.0689,	wR2 = 0.0659
Largest diff. peak and hole	2.042 and -1.126 $e Å^{-3}$	
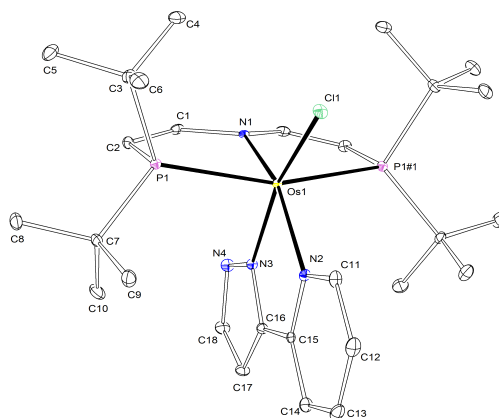
Figure 7.11: Thermal ellipsoid plot of **12** with the anisotropic displacement parameters drawn at the 50% probability level. The asymmetric unit contains only a half complex molecule.

|		
Empirical formula	$C_{28}H_{46}ClN_4OsP_2$	
Formula weight	726.28	
Temperature	102(2) K	
Wavelength	0.71073 Å	
Crystal system	Orthorhombic	
Space group	Pnma	
Unit cell dimensions	a = 12.6673(4) Å	$\alpha = 90°$
	b = 13.6362(4) Å	$\beta = 90°$
	c = 17.3873(5) Å	$\gamma = 90°$
Volume	3003.38(16) Å^3	
Z	4	
Density (calculated)	1.606 Mg/m^3	
Absorption coefficient	4.465 mm^{-1}	
F(000)	1460	
Crystal size	0.112 x 0.062 x 0.048 mm^3	
Crystal shape and color	Needle, clear intense red-brown	
Theta range for data collection	2.343 to 28.326°	
Index ranges	-16<=h<=16	
	-16<=k<=18	
	-23<=l<=21	
Reflections collected	28147	
Independent reflections	3876 [R(int) = 0.0642]	
Completeness to theta = 25.242°	99.9 %	
Refinement method	Full-matrix least-squares on F^2	
Data / restraints / parameters	3876 / 0 / 190	
Goodness-of-fit on F^2	1.039	
Final R indices [I>2sigma(I)]	R1 = 0.0240,	wR2 = 0.0394
R indices (all data)	R1 = 0.0369,	wR2 = 0.0423
Largest diff. peak and hole	0.573 and -1.272 eÅ^{-3}	
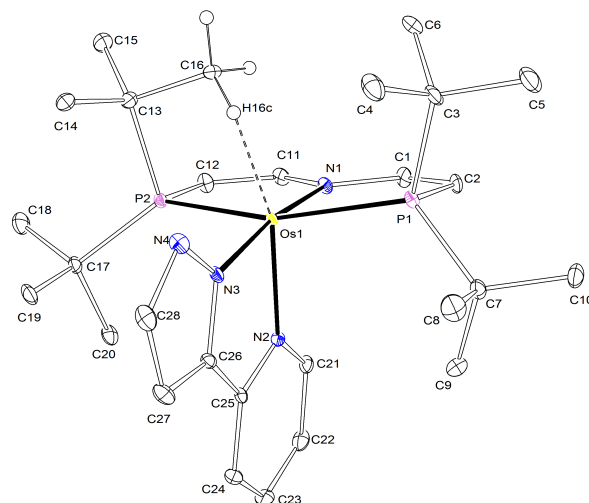
Figure 7.12: Thermal ellipsoid plot of **13** with the anisotropic displacement parameters drawn at the 50% probability level. The asymmetric unit contains one complex molecule.

Empirical formula	$C_{28}H_{46}N_4OsP_2$	
Formula weight	690.83	
Temperature	102(2) K	
Wavelength	0.71073 Å	
Crystal system	Monoclinic	
Space group	$P2_1/c$	
Unit cell dimensions	a = 16.6529(8) Å	$\alpha = 90°$
	b = 10.2535(4) Å	$\beta = 91.657(2)°$
	c = 17.6988(8) Å	$\gamma = 90°$
Volume	3020.8(2) Å^3	
Z	4	
Density (calculated)	1.519 Mg/m^3	
Absorption coefficient	4.350 mm^{-1}	
F(000)	1392	
Crystal size	0.353 x 0.191 x 0.184 mm^3	
Crystal shape and color	Block, clear intense red	
Theta range for data collection	2.296 to 28.396°	
Index ranges	-22<=h<=22	
	-13<=k<=13	
	-23<=l<=23	
Reflections collected	102457	
Independent reflections	7568 [R(int) = 0.1330]	
Completeness to theta = 25.242°	100.0 %	
Refinement method	Full-matrix least-squares on F^2	
Data / restraints / parameters	7568 / 0 / 328	
Goodness-of-fit on F^2	1.050	
Final R indices [I>2sigma(I)]	R1 = 0.0334,	wR2 = 0.0554
R indices (all data)	R1 = 0.0573,	wR2 = 0.0611
Largest diff. peak and hole	1.588 and -1.685 eÅ^{-3}	

7.3.4 Syntheses

Synthesis of LXXV

[OsCl$_2$(PPh$_3$)$_3$] (800 mg, 760 µmol, 1.00 eq.) is dissolved in C$_6$H$_6$/pentane (5:1, 30 mL) and ^{H}PNP (280 mg, 760 µmol, 1.00 eq.) in C$_6$H$_6$ (5 mL) is added to the solution. The mixture is stirred for 45 min at RT. The solvent is removed and the solid is washed with pentane at 0°C (4 x 10 mL). DCM (15 mL) is added to the solid and the solution is heated to 40°C for 16h. The solvent is removed and the crude product is purified by washing with Et$_2$O (4 x 10 mL) and EtOH (4 x 5 mL). The solid is extracted with DCM (5 x 2 mL) and the solvent is removed. **LXXV** (358 mg, 570 µmol, 75%) is isolated in form of a green solid. Spectroscopic characterization data was identical with the prior reported values.[83]

Synthesis of 1

LXXV (160 mg, 260 µmol, 1.00 eq.) and TBP (370 mg, 1.41 mmol, 7.00 eq.) are dissolved in PhCl (20 mL) and stirred at 50°C for 4.5 h. The solvent is removed and the residue is washed with pentanes (8 x 10 mL) and extracted with benzene (5 x 5 mL). Lyophilization yields **1** as a dark green powder (149 mg, 240 µmol, 95 %). Anal. Calcd for C$_{20}$H$_{40}$Cl$_2$N$_1$Os$_1$P$_2$ (617.62): C, 38.9; H, 6.53; N, 2.27 Found: C, 39.4; H, 6.36; N, 2.15. NMR (C$_6$D$_6$: ^{1}H (300 MHz, RT): δ = 43.9 (br, 2H, CH), −0.06 (br, 36H, P(C(CH_3)$_2$), −97.7 (br, 2H, CH). MS (LIFDI, toluene): m/z = 618.0 (100%, [M$^+$]). μ_{eff} $^{297\,\text{K}}$ = 1.65 μ_{B}.

Synthesis of 2

1 (20.0 mg, 32.4 µmol, 1.00 eq.) and CoCp$_2$ (6.1 mg, 32 µmol, 1.0 eq.) are dissolved in THF (2 mL) at -35°C and stirred for 1 min. The solvent is removed and the residue is extracted with pentane. Crystallization at -35°C yields **2** in form of dark purple crystals which are suitable for SQUID measurements (10.0 mg, 17.2 µmol, 53%). *Combustion analysis could not be obtained due to decomposition during drying in vacuo, presumably from loss of isobutene. However, SQUID data was reproduced with 3 independent samples.* NMR (C$_6$D$_6$): ^{1}H (300 MHz, RT): δ = 18.42 (ABXX'B'A', N = |$^3J_{\text{AX}}$ + $^4J_{\text{AX'}}$| = 17.0 Hz, $^3J_{\text{AB}}$ = 6.0 Hz. 2H, NCH), −4.20 (A$_{18}$XX'A'$_{18}$, N = |$^3J_{\text{AX}}$ + $^5J_{\text{AX'}}$| = 6.0 Hz, 36H, P(C(CH_3)$_2$), −35.28 (d, $^3J_{\text{AB}}$ = 6.1 Hz, 2H, PCH). ^{13}C (125.76 MHz): δ = 262.4 (d, $^1J_{\text{CH}}$ = 165.1 Hz, 2C, PCH), 77.1 (q, $^1J_{\text{CH}}$ = 125.5, 12C, P(C(CH$_3$)$_3$)$_2$), 34.3 (br, 4C, P(C(CH$_3$)$_3$)$_2$), 31.4 (d, $^1J_{\text{CH}}$ = 162.3 Hz, 2C, NCH). ^{31}P{^{1}H} (161.25 MHz): δ = −978.2 (s, 2P, P(C(CH$_3$)$_3$)$_2$). MS (LIFDI, toluene): m/z = 583.1 (100%, [M$^+$]).

Synthesis of 3

1 (25.0 mg, 40.5 µmol, 1.00 eq.) and CoCp$_2$ (7.7 mg, 42 µmol, 1.0 eq.) are dissolved in benzene (5 mL) and stirred for 1 min. CN^{t}Bu (4.6 µL, 41 µmol, 1.0 eq.) is added and the solution is stirred for an additional minute. After filtration the crude product is purified *via* column chromatography with silanized silica (benzene). Lyophilization yields **3** as a purple powder (18.3 mg, 27.5 µmol, 68%). Anal. Calcd for C$_{25}$H$_{49}$Cl$_1$N$_2$Os$_1$P$_2$ (665.30):

C, 45.1; H, 7.42; N, 4.21 Found: C, 45.4; H, 8.02; N, 4.10. NMR (C_6D_6, RT): ^{1}H (400 MHz): δ = 7.04 (ABXX'B'A', $N = |^3J_{AX} + {}^4J_{AX'}| = 17.0$ Hz, $^3J_{AB} = 5.9$ Hz. 2H, NCH), 4.33 (ABXX'B'A', $N = |^2J_{AX}+{}^4J_{AX'}| = 2.6$ Hz, $^3J_{AB} = 5.9$ Hz, 2H, PCH), 1.51 (A_9XX'A'$_9$, $N = |^3J_{AX} + {}^5J_{AX'}| = 6.6$ Hz, 18H, P(C(CH_3)$_3$)), 1.22 (A_9XX'A'$_9$, $N = |^3J_{AX} + {}^5J_{AX'}| = 6.6$ Hz, 18H, P(C(CH_3)$_3$)), 1.19 (s, 9H, CN(C(CH_3)$_3$)). ^{13}C$\{^1$H$\}$ (125.76 MHz): δ = 166.8 (AXX'A', $N = |^2J_{AX} + {}^3J_{AX'}| = 3.6$ Hz, 2C, NCH), 89.2 (AXX'A', $N = |^1J_{AX} + {}^3J_{AX'}| = 23.5$ Hz, 2C, PCH), 58.0 (s, 1C, CN(C(CH$_3$)$_3$), 39.3 (AXX'A', $N = |^1J_{AX} + {}^3J_{AX'}| = 11.2$ Hz, 2C, P(C(CH$_3$)$_3$), 36.3 (AXX'A', $N = |^1J_{AX} + {}^3J_{AX'}| = 11.8$ Hz, 2C, P(C(CH$_3$)$_3$), 33.3 (s, 3C, CN(CH_3)$_3$), 30.7 (A_3XX'A'$_3$, $N = |^2J_{AX} + {}^4J_{AX'}| = 2.7$ Hz, 6C, P(C(CH_3)$_3$), 28.9 (A_3XX'A'$_3$, $N = |^2J_{AX} + {}^4J_{AX'}| = 2.7$ Hz, 6C, P(C(CH_3)$_3$). *The isonitrile CN resonance was not detected.* ^{31}P$\{^1$H$\}$ (161.25 MHz): δ = 55.6 (s, 2P, P(C(CH$_3$)$_3$)$_2$). MS (LIFDI, toluene): m/z = 666.2 (100%, [M$^+$]). IR (KBr): $\tilde{\nu}$ = 1931 (C=N).

Synthesis of 4

1 (15.0 mg, 24.3 μmol, 1.00 eq.) and CoCp$_2$ (4.6 mg, 24 μmol, 1.0 eq.) are dissolved in THF (10 mL) in a 50 mL J-Young flask and stirred for 1 min at room temperature. The solution is degassed with three successive freeze-pump-thaw cycles and allowed to warm to room temperature. Upon melting, CO (600 μL, 1 bar, 24.3 μmol, 1.00 eq.) is slowly bubbled through the solution. The solution is stirred for 10 min at room temperature. After removal of the solvent the crude product is washed with pentanes (1 x 1 mL) and extracted with benzene (3 x 0.5 mL). The solution is concentrated and the product is further purified *via* column chromatography with silanized silica (benzene). The solvent is removed and the product is crystallized from Et$_2$O at -35°C. The crystals are washed with pentanes and dried. Lyophilization yields **4** (9.5 mg, 16 μmol, 64 %) as a purple powder. Anal. Calcd for $C_{21}H_{40}N_1O_1OsP_2$ (610.18): C, 41.3; H, 6.61; N, 2.30; Found: C, 41.0; H, 6.21; N, 2.12. NMR (C_6D_6): ^{1}H (400 MHz): δ = 6.92 (ABXX'B'A', $N = |^3J_{AX} + {}^4J_{AX'}| = 20.1$ Hz, $^3J_{AB} = 5.8$ Hz, 2H, NCH), 4.30 (ABXX'B'A', $N = |^2J_{AX}+{}^4J_{AX'}| = 2.8$ Hz, $^3J_{AB} = 5.8$ Hz, 2H, PCH), 1.41 (A_9XX'A'$_9$, $N = |^3J_{AX} + {}^5J_{AX'}| = 7.3$ Hz, 18H, P(C(CH_3)$_3$)), 1.16 (A_9XX'A'$_9$, $N = |^3J_{AX} + {}^5J_{AX'}| = 6.8$ Hz, 18H, P(C(CH_3)$_3$)). ^{13}C$\{^1$H$\}$ (125.76 MHz): δ = 168.4 (t, $^2J_{CP} = 7.9$ Hz, 1 C, CO), 166.8 (AXX'A', $N = |^2J_{AX} + {}^3J_{AX'}| = 6.6$ Hz, 2C, NCH), 89.7 (AXX'A', $N = |^1J_{AX} + {}^3J_{AX'}| = 21.7$ Hz, 2C, PCH), 39.2 (AXX'A', $N = |^1J_{AX} + {}^3J_{AX'}| = 11.8$ Hz, 2C, P(C(CH$_3$)$_3$), 37.0 (AXX'A', $N = |^1J_{AX} + {}^3J_{AX'}| = 12.4$ Hz, 2C, P(C(CH$_3$)$_3$), 30.0 (A_3XX'A'$_3$, $N = |^2J_{AX} + {}^4J_{AX'}| = 2.3$ Hz, 6C, P(C(CH_3)$_3$), 28.6 (A_3XX'A'$_3$, $N = |^2J_{AX} + {}^4J_{AX'}| = 2.7$ Hz, 6C, P(C(CH_3)$_3$). ^{31}P$\{^1$H$\}$ (161.25 MHz): δ = 65.1 (s, 2P, P(C(CH$_3$)$_3$)$_2$). IR (Nujol): $\tilde{\nu}$ = 1893 (C=O).

Synthesis of 5

LXXIII (250 mg, 405 μmol, 1.00 eq.) and NaI (1.25 g, 8.34 mmol, 20.6 eq.) are dissolved in THF and stirred for 90 minutes at room temperature under the exclusion of light. The solvent is evaporated and the residue is extracted with benzene (6 x 15 mL). After removal of the solvent the residue is again extracted with benzene (3 x 10 mL). Lyophilization yields **5** (295 mg, 369 μmol, 91%) in form of a green-brown powder. The product is sufficiently pure for further synthesis. A sample suitable for elemental anal-

ysis can be obtained by filtration of a benzene solution through a silica plug which is accompanied by decrease of the yield of 30%.

Anal. Calcd for $C_{20}H_{44}N_1I_2P_2Re_1$ (800.5): C, 30.0; H, 5.54; N, 1.75. Found: C, 30.55; H, 5.44; N, 1.69. NMR (C_6D_6, RT): ^{1}H (500 MHz): δ = 3.31 - 3.25 (m, 4H, PCH_2), 2.24 (36H, A_{18}XX'A'$_{18}$, $N = |^3J_{AX} + {}^5J_{AX'}|$ = 11.9 Hz), −0.65 - −0.71 (m, 4H, NCH_2). ^{13}C{^{1}H} (125.8 MHz): δ = 127.8 (superimposed with solvent, 2C, NCH$_2$), 69.3 (vt, $N = |^1J_{CP} + {}^3J_{CP}|$ = 7.9 Hz, 4C, P(C(CH$_3$)$_3$)$_2$), 49.1 (vt, $^1J_{PC}$ = 7.0 Hz, 2C, PCH$_2$), 36.0 (s br, 12C, P(C(CH$_3$)$_3$)$_2$). ^{31}P{^{1}H} (202.5 MHz): δ = −164.2 (s, 2P, P(C(CH$_3$)$_3$)$_2$. LIFDI-MS (Toluene): 801.1 (100 %, [M]$^+$).

Synthesis of 6

5 (50.0 mg, 62.5 µmol, 100 eq.) and Mes*O (130 mg, 500 µmol, 8.00 eq.) are dissolved in benzene (10 mL) and stirred at 50°C for 16 h. The solution is concentrated (3 mL) and after lyophilization the solid is sublimed at 70°C under reduced pressure for 12 h. The residue is extracted with pentane (10 x 3 mL), the solvent is removed and the crude product is washed with pentane (2 x 2 mL) at −50°C. The residue is dissolved in benzene and subjected to column chromatography (pentane/benzene 50:50). The solvent is removed and **6** (35.0 mg, 43.9 µmol, 70%) is obtained as a brown powder.

Anal. Calcd for $C_{20}H_{40}N_1I_2P_2Re_1$ (796.5): C, 30.2; H, 5.06; N, 1.76. Found: C, 30.5; H, 5.23; N, 1.73. NMR (C_6D_6, RT): ^{1}H (500 MHz): δ = 4.30 (36H, A_{18}XX'A'$_{18}$, $N = |^3J_{AX} + {}^5J_{AX'}|$ = 13.4 Hz), 0.94 (A_9BCXX'A'$_9$B'C', $N = |^3J_{CX} + {}^4J_{CX'}|$ = 33.4 Hz, $^3J_{BC}$ = 6.7 Hz, 2H, NCH), −7.08 (d br, $^3J_{HH}$ = 6.7 Hz, 2H, PCH). ^{13}C{^{1}H} (125.8 MHz): δ = 234.5 (vt, $^2J_{CP}$ = 7.9 Hz, 2C, P(C(CH$_3$)$_3$)$_2$), 185.1 - 184.4 (m, 2C, PCH$_2$), 67.5 (s, 2C, P(C(CH$_3$)$_3$)$_2$), 42.4 (s br, 12C, P(C(CH$_3$)$_3$)$_2$), 22.4 (s, 2C, P(C(CH$_3$)$_3$)$_2$). ^{31}P{^{1}H} (202.5 MHz): δ = −526.9 (s, 2P, P(C(CH$_3$)$_3$)$_2$. LIFDI-MS (Toluene): 797.1 (100 %, [M]$^+$).

Synthesis of 7

1 (5.0 mg, 8.1 µmol, 1.0 eq.) and CoCp$_2$ (1.5 µmol, 8.1 µmol, 1.0 eq.) are dissolved in benzene (2 mL) and stirred for 2 minutes at RT and filtered. 2,2'-Bipyridine (1.3 mg, 8.1 µmol, 1.0 eq) in benzene (2 mL) is added and stirring is continued for 5 minutes. The solvent is evaporated and the crude product is washed with pentane (2 x 2 mL) and extracted with benzene (3 x 1 mL). Lyophilization yields **7** (4.4 mg, 6.0 µmol, 74%) as a red powder.

Anal. Calcd. for $C_{30}H_{48}ClN_3OsP_2$ (738.36): C, 48.8; H, 6.55; N, 5.69 Found: C, 49.2; H, 7.00; N, 5.40. NMR (CD$_2$Cl$_2$, RT): ^{1}H NMR (400 MHz): δ = 11.4 (dd, $^3J_{HH}$ =

5.3 Hz, $^4J_{HH}$ = 2.4 Hz, 1H, A-H), 8.41 (dd, $^3J_{HH}$ = 6.3 Hz, $^4J_{HH}$ = 1.2 Hz, 1H, E-H), 7.59 (A$_9$BCXX'A'$_9$B'C', N = |$^3J_{CX}$+$^4J_{CX'}$| = 33.4 Hz, $^3J_{BC}$ = 6.0 Hz, 2H, NCHCHP), 7.20 (m, 1H, D-H), 7.03 (dd, $^3J_{HH}$ = 8.3 Hz, $^4J_{HH}$ = 1.6 Hz, 1H, H-H), 6.56 (m, 2H, B-H + C-H), 6.31 (ddd, $^3J_{HH}$ = 8.3 Hz, 7.2 Hz, $^4J_{HH}$ = 1.2 Hz, 1H, G-H), 6.15 (ddd, $^3J_{HH}$ = 7.2 Hz, 6.3 Hz, $^4J_{HH}$ = 1.2 Hz, 1H, F-H), 4.06 (A$_9$BCXX'A'$_9$B'C', N = |$^2J_{BX}$+$^4J_{BX'}$| = 4.1 Hz, $^3J_{BC}$ = 6.0 Hz, 2H, NCHCHP), 1.65 (A$_9$BCXX'A'$_9$B'C', $^3J_{AX}$ = 8.5 Hz, 18H, P(C(CH_3)$_3$)), 0.32 (A$_9$BCXX'A'$_9$B'C', $^3J_{AX}$ = 8.3 Hz, 18H, P(C(CH_3)$_3$)). ^{13}C{^{1}H}-NMR (101.25 MHz): δ = 168.9 (s, 1C, $C-$C$_E$), 165.1 (s, 1C, $C-$C$_A$), 163.8 (vt, $^2J_{CP}$ = 7.5 Hz, 2C, NCHCHP), 154.0 (s, 1C, C$_E$), 153.1 (s, 1C, C$_A$), 130.2 (s, 1C, C$_C$), 126.7 (s, 1C, C$_G$), 125.3 (s, 1C, C$_F$), 125.0 (s, 1C, C$_B$), 122.8 (s, 1C, C$_H$), 121.2 (s, 1C, C$_D$), 85.2 (vt, $^1J_{CP}$ = 18.7 Hz, 2C, NCHCHP), 42.0 (vt, $^1J_{CP}$ = 10.5 Hz, 2C, P(C(CH$_3$)$_3$)$_2$), 39.1 (vt, $^1J_{CP}$ = 8.5 Hz, 2C, P(C(CH$_3$)$_3$)$_2$), 31.8 (s br, 6C, P(C(CH$_3$)$_3$)$_2$). 30.3 (vt, $^2J_{CP}$ = 2.1 Hz, 6C, P(C(CH$_3$)$_3$)$_2$). ^{31}P{^{1}H}-NMR (161.25 MHz): δ = 19.5 (s, P(C(CH$_3$)$_3$)$_2$)). *All bipy NMR signals could be assigned to two chemically inequivalent ring systems. However, due to a lack of resolution in 2D NMR correlation experiments it might be possible that the position of the ring is not correctly assigned.* MS (LIFDI, toluene) m/z = 739.1 ([M$^+$]), 704.2 ([M-Cl$^+$])

Synthesis of 8

7 is prepared in situ according to the procedure described above and the solvent is removed after addition of 2,2'-bipyridine (**1**: 35.0 mg, 56.7 µmol, 1.00 eq.). An equimolar amount of NaBPh$_4$ in THF (5 mL) is added and the soution is stirred for 10 minutes at RT. The solvent is removed and the crude product is washed with pentane (3 x 5 mL) and extracted with DCM (3 x 3 mL). The solvent is evaporated and the compound is crystallized at −35°C from THF/pentane. The obtained crystals are washed with pentane (4 x 2 mL) and extracted with DCM (3 x 1 mL). **8** (50.6 mg, 49.5 µmol, 87%) is obtained as a brown powder.
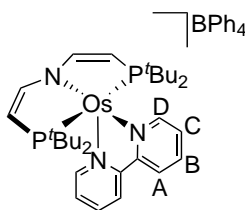
Anal. Calcd. for C$_{54}$H$_{68}$BClN$_3$OsP$_2$ (1057.6): C, 61.3; H, 6.48; N, 3.97 Found: C, 61.5; H, 6.53; N, 3.80. NMR (d_8-THF, RT): ^{1}H-NMR: (400 MHz): δ = 9.05 (s br, 2H, bipy:A-H), 7.82 (d, $^3J_{HH}$ = 8.3 Hz, 2H, bipy:B-H), 7.78 (A$_{18}$BXX'A'$_{18}$B'C', N = |$^3J_{CX}$+$^4J_{CX'}$| = 35.4 Hz, $^3J_{BC}$ = 5.8 Hz, 2H, NCHCHP), 7.49 (t, $^3J_{HH}$ = 7.5 Hz, 2H, bipy:C-H), 7.38 (t br, 8H, BPH$_4$: o-H), 7.14 (t br, $^3J_{HH}$ = 7.1 Hz, 2H, bipy:D-H), 7.04 (m br, 8H, BPH$_4$,: m-H), 6.87 (m br, 4H, BPH$_4$: p-H), 4.34 (A$_{18}$BXX'A'$_{18}$B'C', N = |$^2J_{BX}$+$^4J_{BX'}$| = 6.2 Hz, $^3J_{BC}$ = 5.8 Hz, 2H, NCHCHP), 0.49 (A$_{18}$XX'A'$_{18}$, N = |$^3J_{AX}$+$^5J_{AX'}$| = 6.8 Hz, 36H, P(C(CH_3)$_3$)$_2$). ^{13}C{^{1}H}-NMR (101.25 MHz): δ = 164.4 (vt, $^2J_{CP}$ = 7.5 Hz, NCHCHP), 164.0 (q, $^1J_{C^{11}B}$ = 49 Hz, 4C, BPh$_4$:C$_{ipso}$), 162.2 (s, 2C, bipy:NCCN), 156.4 (s, 2C, bipy:C$_A$), 135.9 (q, $^1J_{CB}$ = 1.6 Hz, 8C, BPh$_4$:C$_{ortho}$), 134.1

(s, 2C, bipy:C_C), 126.5 (s, 2C, bipy:C_D), 125.6 (q, $^1J_{CB} = 2.7$ Hz, 8C, BPh$_4$:C_{meta}), 123.5 (s, 2C, bipy:C_B), 121.7 (s, 4C, BPh$_4$:C_{para}), 85.2 (vt, $^1J_{CP} = 21.0$ Hz, NCHCHP), 42.6 (s br, 8C, P(C(CH$_3$)$_3$)$_2$), 27.4 (s, 24C, P(C(CH$_3$)$_3$)$_2$). ^{31}P{^{1}H}-NMR (161.25 MHz): $\delta = 26.9$ (s, P(C(CH$_3$)$_3$)$_2$)).

Reduction of 8

8 (5.0 mg, 4.9 μmol, 1.0 eq.) and NaHg (2 M, 0.33 g, 49 μmol, 10 eq) are dissolved in THF (1 mL) and stirred for 1 minute at RT. The solution is filtered and measured by EPR spectroscopy. For UV/vis measurements a stock solution of **8** in THF was diluted to appropriate concentrations and a tenfold excess of NaHg was added.

Synthesis of 10

8 (12.1 mg, 11.8 μmol, 1.00 eq.) and NaBH$_4$ (9.0 mg, 0.24 mmol, 20 eq.) are dissolved in THF (3 mL) and stirred for 24h at RT. The solvent is removed and the residue is extracted with pentane (4 x 1 mL). After evaporation of the solvent and lyophilization **21** (7.0 mg, 9.9 μmol, 84%) is obtained as a black powder.
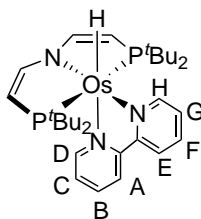
Anal. Calcd. for C$_{30}$H$_{49}$ClN$_3$OsP$_2$ (703.92): C, 51.2; H, 7.02; N, 5.97 Found: C, 51.4; H, 7.10; N, 5.90. NMR (C$_6$D$_6$, RT): ^{1}H NMR (400 MHz): $\delta = 10.27$ (d, $^3J_{HH} = 6.2$ Hz, 1H, A-H) 8.41 (d, $^3J_{HH} = 5.9$ Hz, 1H, E-H) 7.59 (A$_9$BCXX'A'$_9$B'C', $N = |^3J_{CX} + ^4J_{CX'}| = 34.0$ Hz, $^3J_{BC} = 5.5$ Hz, 2H, NCHCHP), 7.36 - 7.31 (m, 2H, D-H, H-H), 6.73 - 6.68 (m, 1H, G-H), 6.65 - 6.61 (m, 1H, C-H), 6.37 - 6.33 (m, 1H, H-F), 6.09 - 6.04 (m, 1H, B-H), 4.26 (A$_9$BCXX'A'$_9$B'C', $N = |^2J_{BX} + ^4J_{BX'}| = 5.5$ Hz, $^3J_{BC} = 5.5$ Hz, 2H, NCHCHP), 1.57 (A$_9$BCXX'A'$_9$B'C', $^3J_{AX} = 12.5$ Hz, 18H, P(C(CH_3)$_3$)), 0.45 (A$_9$BCXX'A'$_9$B'C', $^3J_{AX} = 12.2$ Hz, 18H, P(C(CH_3)$_3$)), -11.0 (t, $^3J_{HP} = 24.2$ Hz, Os-H). ^{13}C{^{1}H}-NMR (101.25 MHz): $\delta = 161.7$ (vt, $^2J_{CP} = 9.0$ Hz, 2C, NCHCHP), 161.6 (s, 1C, C−C$_A$), 160.2 (s, 1C, C$_A$), 159.4 (s, 1C, C−C$_E$), 149.3 (s, 1C, C$_E$), 125.7 (s, 1C, C$_G$), 124.8 (s, 1C, C$_B$), 124.6 (s, 1C, C$_C$), 123.9 (s, 1C, C$_F$), 122.8 (s, 1C, C$_{H/D}$), 122.4 (s, 1C, C$_{H/D}$), 85.3 (vt, $^1J_{CP} = 19.2$ Hz, 2C, NCHCHP), 41.0 (vt, $^1J_{CP} = 8.5$ Hz, 2C, P(C(CH$_3$)$_3$)$_2$), 39.7 (vt, $^1J_{CP} = 13.9$ Hz, 2C, P(C(CH$_3$)$_3$)$_2$), 30.1 (s br, 6C, P(C(CH$_3$)$_3$)$_2$). 29.5 (vt, $^2J_{CP} = 2.5$ Hz, 6C, P(C(CH$_3$)$_3$)$_2$). ^{31}P{^{1}H}-NMR (161.25 MHz): $\delta = 51.4$ (s, P(C(CH$_3$)$_3$)$_2$)). *All bipy NMR signals could be assigned to two chemically inequivalent ring systems. However, due to a lack of resolution in 2D NMR correlation experiments it might be possible that the position of the ring is not correctly assigned.* IR (ATR, RT) $\tilde{\nu} = 2074$ cm^{-1} (Os-H); MS (LIFDI, toluene) $\frac{m}{z} = 705.2$ ([M$^+$]).

Synthesis of 11

5 (100 mg, 125 µmol, 1.00 eq.) and HPyrPz (19.0 mg, 131 µmol, 1.05 eq.) are dissolved in THF (5 mL) and stirred for 30s. KHMDS (23.7 mg, 118.7 µmolm 0.95 eq.) is added in small portions over the period of 1 minute and stirring is continued for 5 minutes. After addition of NEt_3 (17.4 µL, 124.9 µmol, 1.0 eq.) the solution is stirred for 90 min. After evaporation of the solvent the residue is extracted with pentane (5 x 5 mL). Lyophilization yields **11** in form of a brown powder (80.0 mg, 97.8 µmol, 78%).

Anal. Calcd for $C_{28}H_{50}IN_4P_2Re$ (817.8): C, 41.1; H, 6.16; N 6.85. Found: C, 41.4; H, 6.06; N, 6.82. NMR (C_6D_6, RT): ^{1}H (500 MHz): $\delta = 10.4$ (ddd, $^3J_{HH} = 6.2\,Hz$, $^4J_{HH} = 1.4\,Hz$, $^5J_{HH} = 0.9\,Hz$, 1H, C_8H), 7.51 (d, $^3J_{HH} = 2.1\,Hz$, 1H, C_1H), 7.28 (ddd, $^3J_{HH} = 7.9\,Hz$, $^4J_{HH} = 1.6\,Hz$, $^5J_{HH} = 0.9\,Hz$, 1H, C_5H), 6.45 (ddd, $^3J_{HH} = 7.9\,Hz$, $^3J_{HH} = 7.2\,Hz$, $^4J_{HH} = 1.5\,Hz$, 1H, C_6H), 6.31 (ddd, $^3J_{HH} = 7.2\,Hz$, $^3J_{HH} = 6.2\,Hz$, $^4J_{HH} = 1.6\,Hz$, 1H, C_7H), 6.27 (d, $^3J_{HH} = 2.1\,Hz$, 1H, C_2H), 5.34 - 5.23 (m, 2H, NCH_2), 4.65 - 4.56 (m, 2H, NCH_2), 2.33 - 2.24 (m, 2H, PCH_2), 2.07 - 1.99 (m, 2H, PCH_2), 1.49 ($A_9XX'A_9'$, $N = |^3J_{AX} + {}^5J_{AX}| = 11.5\,Hz$, 18H, $P(C(CH_3)_3)_2$), 0.60 ($A_9XX'A_9'$, $N = |^3J_{AX} + {}^5J_{AX}| = 11.8\,Hz$, 18H, $P(C(CH_3)_3)_2$). $^{13}C\{^1H\}$ (125.8 MHz): $\delta = 156.1$ (s, 1C, C_8), 151.9 (s, 1C, C_4), 147.3 (s, 1C, C_3), 142.2 (s, 1C, C_1), 136.8 (s, 1C, C_5), 116.6 (s, 1C, C_7), 115.6 (s, 1C, C_5), 104.0 (s, 1C, C_2), 87.8 (vt, $N = |^2J_{PC} + {}^3J_{PC}| = 3.9\,Hz$, 2C, NCH_2), 46.7 (vt, $N = |^1J_{CP} + {}^3J_{CP}| = 7.8\,Hz$, 2C, $P(C(CH_3)_3)_2$), 40.6 (vt, $N = |^1J_{CP} + {}^3J_{CP}| = 6.4\,Hz$, 2C, $P(C(CH_3)_3)_2$), 30.1 (vt, $N = |^2J_{CP} + {}^4J_{CP}| = 1.6\,Hz$, 6C, $P(C(CH_3)_3)_2$), 30.9 (vt, $N = |^1J_{PC} + {}^3J_{PC}| = 6.9\,Hz$, 2C, PCH_2), 30.1 (vt, $N = |^2J_{CP} + {}^4J_{CP}| = 2.4\,Hz$, 6C, $P(C(CH_3)_3)_2$). $^{31}P\{^1H\}$ (202.5 MHz): $\delta = $ -27.8 (s, 2P, $P(C(CH_3)_3)_2$. LIFDI-MS (Toluene): 818.2 (100 %, $[M]^+$).

Synthesis of 12

1 (80.0 mg, 120 µmol, 1.00 eq.) and 2-(1H-pyrazol-5-yl)pyridine (19.9 mg, 137 µmol, 1.05 eq.) are dissolved in THF (20 mL). After addition of NEt_3 (80 µL, 574 µmol, 4.34 eq.) the solution is stirred for 36h at room temperature. After removal of the solvent the residue is washed with pentane (3 x 5 mL) at $-40°C$. Afterwards the residue is extracted with pentane (8 x 10 mL) at room temperature. The solvent is removed and lyophilization yields **12** in form of a yellow-brown powder (84.5 mg, 116 µmol, 90%).

Anal. Calcd. for $C_{28}H_{46}ClN_4OsP_2$ (726.3): C, 46.3; H, 6.38; N, 7.71. Found: C, 46.7; H, 6.46; N, 7.79.

NMR (THF-d_8, RT): ^{1}H (300 MHz) $\delta = 5.14$ (s br, 18H, $P(C(CH_3)_3)$), -1.24 (s br, 18H, $P(C(CH_3)_3)$) (other signals cannot be assigned due to paramagnetism).

Synthesis of 13

Route A:

12 (50.0 mg, 68.8 µmol, 1.00 eq.) and NaHg (1 w%, 1.66 g, 72.2 µmol, 1.05 eq.) are suspended in THF (10 mL) and stirred for 1h at room temperature. After removal of the solvent the residue is extracted with pentane (4 x 5 mL), the volume is reduced to ca. 3 mL and solution is stored at $-40°C$ for 2 days. The precipitate is filtered and washed with cold pentane. Dissolving of the red solid in benzene and lyophilization yields **13** (31.0 mg, 44.9 µmol, 65%) in form of a red powder.

Route B:

1 (200 mg, 323 μmol, 1.00 eq.) and CoCp$_2$ (42.2 mg, 323 μmol, 1.00 eq.) are dissolved in THF (15 mL) and stirred for 2 minutes. 2-(1H-pyrazol-5-yl)pyridine (47.0 mg, 323 μmol, 1.00 eq.) is added in small portions over the course of 3 minutes and stirring is continued for 5 minutes. After addition of KHMDS (64.6 mg, 323 μmol, 1.00 eq.) the solution is stirred for 90 minutes. The solvent removed and the solid is extracted with pentane (5 x 10 mL). The solvent is evaporated and the product is lyophilized to yield os$_2$pyrpzl$_3$ (210 mg, 304 μmol, 94%) in form of a red powder.

Anal. Calcd. for C$_{28}$H$_{46}$N$_4$OsP$_2$ (690.88): C, 48.7; H, 6.71; N, 8.11. Found: C, 48.9; H, 7.05; N, 7.95.

NMR (THF-d$_8$, RT): ^{1}H (500 MHz) δ = 8.42 (d, $^3J_{\text{HH}}$ = 2.1 Hz, 1H, C$_1$H), 7.98 (ddd, $^3J_{\text{HH}}$ = 6.1 Hz, $^4J_{\text{HH}}$ = 1.5 Hz, $^5J_{\text{HH}}$ = 0.7 Hz, 1H, C$_8$H), 7.64 (A$_{18}$BCXX'A'$_{18}$B'C', N = |$^3J_{\text{CX}}$+$^4J_{\text{CX'}}$| = 33.6 Hz, $^3J_{\text{BC}}$ = 5.5 Hz, 2H, NCH), 7.00 (ddd, $^3J_{\text{HH}}$ = 8.0 Hz, $^4J_{\text{HH}}$ = 1.5 Hz, $^5J_{\text{HH}}$ = 0.7 Hz, C$_5$H), 6.97 (d, $^3J_{\text{HH}}$ = 2.1 Hz, 1H, C$_2$H), 6.46 (m, $^3J_{\text{HH}}$ = 8.0 Hz, $^3J_{\text{HH}}$ = 7.3 Hz, 1H, C$_5$H), 5.87 (m, ^3J = 7.3 Hz, ^3J = 6.1 Hz, 1H, C$_6$H), 4.27 (A$_{18}$BCXX'A'$_{18}$B'C', N = |$^2J_{\text{BX}}$+$^4J_{\text{BX'}}$| = 5.6 Hz, $^3J_{\text{BC}}$ = 5.5 Hz, 2H, PCH), 0.64 (m, 18H, P(C(CH$_3$)$_3$)), 0.57 (m, 18H, P(C(CH$_3$)$_3$). ^{13}C{^{1}H} (128.8 MHz) δ = 163.7 (vt, N = |$^2J_{\text{CP}}$ + $^3J_{\text{CP}}$| = 7.8 Hz, 2C, NCH), 163.5 (t, $^3J_{\text{CP}}$ = 1.2 Hz, 1C, C_4), 153.9 (s, 1C, C_1), 148.3 (s, 1C, C_3), 139.3 (s, 1C, C_1), 131.2(s, 1C, C_6), 117.1 (s, 1C, C_7), 116.3(s, 1C, C_5), 102.9 (s, 1C, C_2), 86.0 (vt, N = |$^1J_{\text{CP}}$ + $^3J_{\text{CP}}$| = 19.3 Hz, 2C, PCH), 47.7 (vt, N = |$^1J_{\text{CP}}$ + $^2J_{\text{CP}}$| = 11.9 Hz, 2C, P(C(CH$_3$))), 35.4 (vt, N = |$^1J_{\text{CP}}$ + $^2J_{\text{CP}}$| = 10.5 Hz, 2C, P(C(CH$_3$))), 28.4 (vt, N = |$^2J_{\text{CP}}$ + $^4J_{\text{CP}}$| = 2.5 Hz, 6C, P(C(CH$_3$)$_3$)), 25.9 (vt, N = |$^2J_{\text{CP}}$ + $^4J_{\text{CP}}$| = 1.9 Hz, 6C, P(C(CH$_3$)$_3$)). ^{31}P{^{1}H} (202.5 MHz) δ= 24.6 (s, 2P, P(C(CH$_3$)$_3$)).

7.4 Os Nitride and Imide Complexes in Various Coordination Spheres

Parts of this chapter were adapted from:
J. Abbenseth, S. C. Bete, M. Finger, C. Volkmann, C. Würtele, S. Schneider, *Organometallics* **2018**, *37*, 802-811.
Copyright 2018 American Chemical Society.

7.4.1 Computational Details

DFT calculations were carried out with the ORCA program package using the PBE and PBE0 functionals.[304],[318],[326] Ahlrichs' basis sets def2-SVP (for geometry optimization and frequency calculation) and def2-TZVP (for single-point energies) were used with a full basis for all elements but Os for which the Stuttgart-Dresden 60 electron core potential was chosen to replace the inner shell 1s-4f orbitals.[307],[308] The RI-J (PBE) approximation in combination with the corresponding auxiliary basis sets of Alrichs was utilized to reduce computational costs in the geometry optimization and frequency calculations.[327]–[329] Grimme's model (D3) with Becke-Johnson damping was used to account for dispersion with the PBE or PBE0 functionals.[306],[330] No symmetry restraints were imposed and the optimized structures were defined as minima (no negative eigenvalues) by vibrational analyses. NBO analysis of **18**, **19** and **20** was carried out with NBO 6.0.[3] Geometries were analyzed and visualized with Avogadro, molecular orbitals were visualized with Chimera and for NBO/NLMO visualization, Jmol (http://www.jmol.org) was used.[333],[334] The XYZ-Files of all computed species can be obtained free of charge via the article page. TDDFT/EPR calculations were performed with ORCA and the CPCM solvation model was used (pentane, THF).[331] Relativistic treatment was introduced by ZORA.[332]

Table 7.4: XYZ-coordinates of computed complex **22**.

Atom	x	y	z	Atom	x	y	z
C	3.66137	12.13119	17.02107	H	5.92085	12.0675	12.85937
H	4.09274	13.07956	17.39171	C	4.67158	11.93939	10.44108
C	3.30445	11.14571	17.89122	H	5.60412	11.55532	9.97723
H	3.44708	11.28135	18.97274	H	4.84993	13.00028	10.70357
C	4.30489	8.44677	17.37213	H	3.88201	11.88635	9.66729
C	5.47575	9.07747	16.59453	C	1.50115	12.45277	11.58248
H	6.38785	8.48096	16.80258	C	1.94064	13.67806	10.75936
H	5.67343	10.11832	16.91678	H	2.7122	13.4525	10.00667
H	5.3041	9.06472	15.50217	H	2.30246	14.50336	11.40337
C	4.74567	8.3632	18.84732	H	1.05165	14.06262	10.217
H	5.72096	7.83539	18.87744	C	1.00594	11.32302	10.66574
H	4.05149	7.79944	19.48974	H	0.09699	11.66211	10.12623
H	4.90808	9.36603	19.28802	H	0.73298	10.41447	11.2413
C	3.97911	7.05576	16.80769	H	1.75551	11.04301	9.9026
H	3.65003	7.11786	15.75168	C	0.35277	12.90292	12.50032

---

[3]E. D. Glendening, J. K. Badenhoop, A. E. Reed, J. E. Carpenter, J. A. Bohmann, C. M. Morales, C. R. Landis, F. Weinhold, *NBO 6.0*, Theoretical Chemical Institute, University of Wisconsin, Madison, WI, USA, **2013**.

H	3.1996	6.53523	17.39826	H	-0.41016	13.41946	11.88189
H	4.89119	6.42395	16.8395	H	0.69132	13.61331	13.28025
C	1.24442	8.95161	18.13942	H	-0.14072	12.04684	12.98806
C	1.61052	8.27902	19.47197	C	0.47411	12.6519	15.94436
H	2.14157	7.31908	19.33018	H	1.41474	13.15941	16.18926
H	0.66738	8.05158	20.01155	C	-0.75048	13.21649	16.27638
H	2.21636	8.93211	20.12947	H	-0.77817	14.1887	16.78641
C	0.34511	10.16243	18.44393	C	-1.93876	12.51932	15.95422
H	0.01661	10.68617	17.53138	H	-2.92352	12.92907	16.21832
H	0.84708	10.89758	19.10255	C	-1.83326	11.30086	15.29082
H	-0.56374	9.80229	18.96924	H	-2.73759	10.7394	15.02276
C	0.48952	7.94597	17.25146	C	-0.55972	10.78613	14.95744
H	0.10353	8.42019	16.33257	C	-0.35044	9.55364	14.21673
H	-0.38085	7.54751	17.81307	C	-1.39699	8.75714	13.69427
H	1.11791	7.08459	16.954	H	-2.43809	9.07472	13.83551
C	3.8329	13.14633	14.86797	C	-1.11082	7.58284	13.0056
H	4.30321	13.98665	15.41229	H	-1.92247	6.96315	12.59879
C	3.59991	13.23834	13.52889	C	0.23822	7.20612	12.84448
H	3.89994	14.14262	12.98138	H	0.52319	6.28409	12.32038
C	4.35975	11.06492	11.66688	C	1.2323	8.02741	13.36862
C	4.0228	9.63429	11.21158	H	2.29988	7.77991	13.27578
H	3.09961	9.58201	10.60458	N	3.49863	12.04125	15.642
H	3.92426	8.95915	12.08159	N	0.5924	11.45461	15.30958
H	4.85584	9.25553	10.58272	N	0.96205	9.1804	14.03374
C	5.60363	11.04639	12.57375	N	3.66979	9.28501	14.28417
H	6.43608	10.57104	12.01471	P	2.76165	9.59285	17.15145
H	5.44479	10.45631	13.49538	P	2.90358	11.78878	12.71177
Os	2.51967	10.44596	14.80261				

7.4.2 Crystallographic Details

CCDC 1574571 (**14**), CCDC 1574572 (**15**), CCDC 1574573 (**??**), CCDC 1574574 (**17**), CCDC 1574575 (**18**), CCDC 1574576 (**19**) and CCDC 1574577 (**20**) contain the supplementary crystallographic data for this chapter. This data can be obtained free of charge via http://www.ccdc.cam.ac.uk/ products/csd/request/ (or from Cambridge Crystallographic Data Centre, 12 Union Road, Cambridge, CB2 1EZ, UK. Fax: +44-1223-336-033; e-mail: deposit@ccdc.cam.ac.uk).
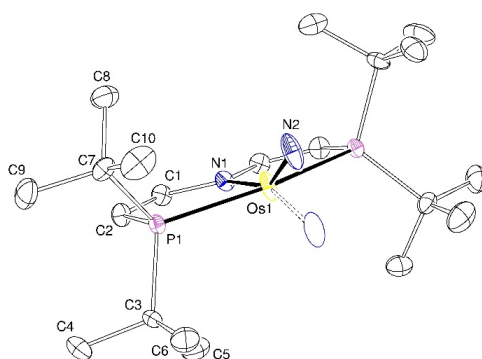
Figure 7.13: Thermal ellipsoid plot of **14** with the anisotropic displacement parameters drawn at the 50% probability level. The asymmetric unit contains a half complex molecule. The disorder was refined using PART -1 command.

Empirical formula	$C_{20}H_{40}N_2OsP_2$
Formula weight	560.68
Temperature	106(2) K
Wavelength	0.71073 Å
Crystal system	Monoclinic
Space group	C2/c
Unit cell dimensions	a = 22.3305(19) Å $\alpha = 90°$
	b = 7.5982(6) Å $\beta = 104.423(3)°$
	c = 14.0141(12) Å $\gamma = 90°$
Volume	2302.9(3) Å^3
Z	4
Density (calculated)	1.617 Mg/m^3
Absorption coefficient	5.682 mm^{-1}
F(000)	1120
Crystal size	0.349 x 0.324 x 0.122 mm^3
Crystal shape and color	Plate, clear intense brown
Theta range for data collection	2.841 to 27.222°
Index ranges	-28<=h<=28
	-9<=k<=9
	-18<=l<=17
Reflections collected	45860
Independent reflections	2565 [R(int) = 0.0548]
Completeness to theta = 25.242°	100.0%
Max. and min. transmission	0.7455 and 0.4678
Refinement method	Full-matrix least-squares on F^2
Data / restraints / parameters	2565 / 0 / 125
Goodness-of-fit on F^2	1.116
Final R indices [I>2sigma(I)]	R1 = 0.0207, wR2 = 0.0476
R indices (all data)	R1 = 0.0276, wR2 = 0.0527
Largest diff. peak and hole	0.925 and -2.005 eÅ^{-3}
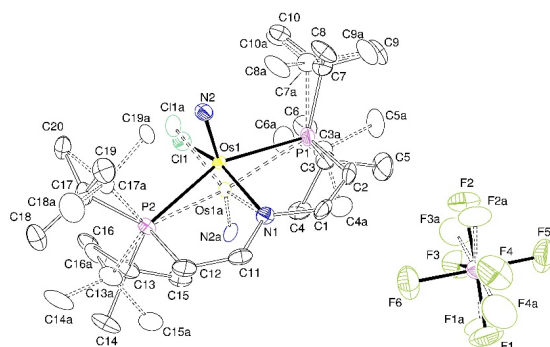
Figure 7.14: Thermal ellipsoid plot of **15** with the anisotropic displacement parameters drawn at the 50% probability level. The asymmetric unit contains one disordered complex molecule and one disordered PF6 anion. The disordered complex molecule was refined with population of 0.8345(8) on the main domain using some restraints (SADI) and constraints (EADP). The disordered PF6 anion was refined with population of 0.919(5) on the main domain using some restraints (SADI) and constraints (EADP).

Empirical formula	$C_{20}H_{40}ClF_6N_2OsP_3$	
Formula weight	741.10	
Temperature	100(2) K	
Wavelength	0.71073 Å	
Crystal system	Monoclinic	
Space group	P21/c	
Unit cell dimensions	a = 8.0653(5) Å	$\alpha = 90°$
	b = 12.9580(8) Å	$\beta = 97.546(2)°$
	c = 26.7808(17) Å	$\gamma = 90°$
Volume	2774.6(3) Å^3	
Z	4	
Density (calculated)	1.774 Mg/m^3	
Absorption coefficient	4.918 mm^{-1}	
F(000)	1464	
Crystal size	0.156 x 0.087 x 0.032 mm^3	
Crystal shape and color	Block, clear intense yellow	
Theta range for data collection	2.196 to 28.351°	
Index ranges	-10<=h<=10	
	-17<=k<=17	
	-35<=l<=35	
Reflections collected	119055	
Independent reflections	6919 [R(int) = 0.0745]	
Completeness to theta = 25.242°	100.0%	
Max. and min. transmission	0.7457 and 0.6217	
Refinement method	Full-matrix least-squares on F^2	
Data / restraints / parameters	6919 / 71 / 437	
Goodness-of-fit on F^2	1.286	
Final R indices [I>2sigma(I)]	R1 = 0.0402,	wR2 = 0.0681
R indices (all data)	R1 = 0.0506,	wR2 = 0.0700
Largest diff. peak and hole	0.956 and -2.530 eÅ^{-3}	
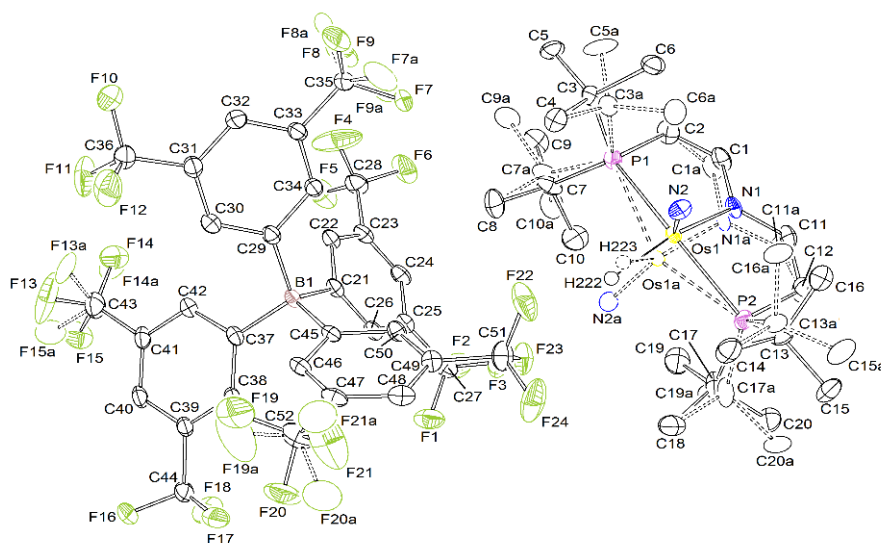
Figure 7.15: Thermal ellipsoid plot of **16** with the anisotropic displacement parameters drawn at the 50% probability level. The asymmetric unit contains one disordered complex molecule and one $BArF_{24}$ anion with three disordered CF_3 groups. The disordered complex molecule was refined with population of 0.7826(2) on the main domain using some restraints and constrains (SADI, EADP). The Os-H hydrogen atoms were found from the residual density map and isotropically refined. The disordered CF_3 groups were refined with populations of 0.735(7), 0.68(1) and 0.958(2) on their main domains using some restraints and constrains (SADI, RIGU, EADP).

Empirical formula	$C_{52}H_{53}BF_{24}N_2OsP_2$
Formula weight	1424.91
Temperature	100(2) K
Wavelength	0.71073 Å
Crystal system	Triclinic
Space group	P-1
Unit cell dimensions	a = 11.9297(5) Å $\alpha = 84.800(2)°$
	b = 15.5133(6) Å $\beta = 84.405(2)°$
	c = 15.6315(7) Å $\gamma = 84.611(2)°$
Volume	2856.7(2) Å^3
Z	2
Density (calculated)	1.657 Mg/m^3
Absorption coefficient	2.404 mm^{-1}
F(000)	1412
Crystal size	0.315 x 0.239 x 0.100 mm^3
Crystal shape and color	Plate, clear intense yellow
Theta range for data collection	2.257 to 30.508°
Index ranges	-17<=h<=17
	-22<=k<=22
	-22<=l<=22
Reflections collected	164409

Independent reflections	17419 [R(int) = 0.0447]
Completeness to theta = 25.242°	99.9%
Max. and min. transmission	0.7461 and 0.6166
Refinement method	Full-matrix least-squares on F^2
Data / restraints / parameters	17419 / 723 / 939
Goodness-of-fit on F^2	1.201
Final R indices [I>2sigma(I)]	R1 = 0.0307, $\qquad\qquad$ wR2 = 0.0672
R indices (all data)	R1 = 0.0354, $\qquad\qquad$ wR2 = 0.0689
Largest diff. peak and hole	1.011 and -1.921 eÅ^{-3}
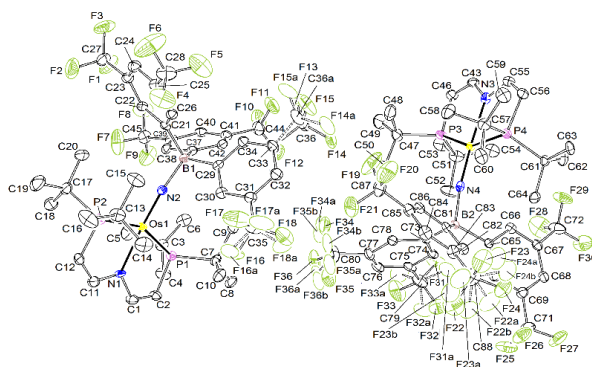
Figure 7.16: Thermal ellipsoid plot of **17** with the anisotropic displacement parameters drawn at the 50% probability level. The asymmetric unit contains two disordered complex molecules. Two disordered CF_3 groups were refined in three different positions with population of 0.42(2), 0.37(2) and 0.207(9) using PART/SUMP commands and some restraints (SADI, RIGU). Three other disordered CF_3 groups were refined in two different positions with population of 0.55(2), 0.64(2) and 0.74(3) on their main domains using PART commands and some restraints and constrains (SADI, RIGU, EADP). The structure was refined as twin using the twin law -100 0-10 101 (BASF: 0.0167(3)).

Empirical formula	$C_{44}H_{49}BF_{18}N_2OsP_2$	
Formula weight	1210.80	
Temperature	100(2) K	
Wavelength	0.71073 Å	
Crystal system	Monoclinic	
Space group	P21/c	
Unit cell dimensions	a = 22.3365(11) Å	$\alpha = 90°$
	b = 20.8614(11) Å	$\beta = 117.131(2)°$
	c = 23.8328(13) Å	$\gamma = 90°$
Volume	9883.4(9) Å^3	
Z	8	
Density (calculated)	1.627 Mg/m^3	
Absorption coefficient	2.746 mm^{-1}	
F(000)	4800	
Crystal size	0.374 x 0.175 x 0.080 mm^3	
Crystal shape and color	Block, clear intense brown	
Theta range for data collection	2.154 to 27.485°	
Index ranges	-24<=h<=29	
	-27<=k<=27	
	-30<=l<=30	
Reflections collected	370556	
Independent reflections	22952 [R(int) = 0.1118]	
Completeness to theta = 25.242°	99.9%	
Max. and min. transmission	0.7461 and 0.5790	
Refinement method	Full-matrix least-squares on F^2	
Data / restraints / parameters	22952 / 998 / 1439	
Goodness-of-fit on F^2	1.135	
Final R indices [I>2sigma(I)]	R1 = 0.0463,	wR2 = 0.1015
R indices (all data)	R1 = 0.0834,	wR2 = 0.1195
Largest diff. peak and hole	2.505 and -1.748 eÅ^{-3}	
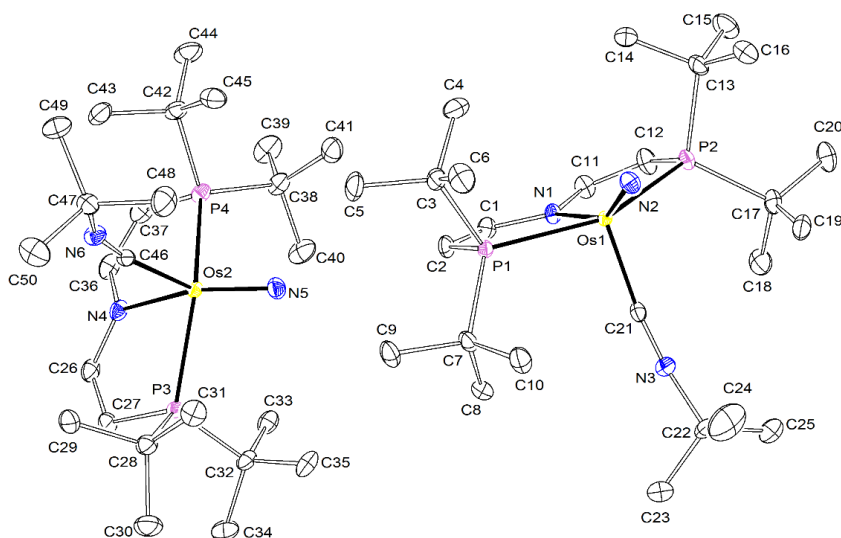
Figure 7.17: Thermal ellipsoid plot of **18** with the anisotropic displacement parameters drawn at the 50% probability level. The asymmetric unit contains two complex molecules.

Empirical formula	$C_{25}H_{49}N_3OsP_2$	
Formula weight	643.81	
Temperature	100(2) K	
Wavelength	0.71073 Å	
Crystal system	Monoclinic	
Space group	P21/c	
Unit cell dimensions	a = 11.8920(6) Å	$\alpha = 90°$
	b = 30.3897(15) Å	$\beta = 106.731(2)°$
	c = 16.5634(8) Å	$\gamma = 90°$
Volume	5732.5(5) Å^3	
Z	8	
Density (calculated)	1.492 Mg/m^3	
Absorption coefficient	4.577 mm^{-1}	
F(000)	2608	
Crystal size	0.575 x 0.339 x 0.262 mm^3	
Crystal shape and color	Block, clear dark green	
Theta range for data collection	2.235 to 28.366°	
Index ranges	-15<=h<=15	
	-40<=k<=40	
	-22<=l<=22	
Reflections collected	156514	
Independent reflections	14327 [R(int) = 0.0431]	
Completeness to theta = 25.242°	99.9%	
Max. and min. transmission	0.7457 and 0.4998	
Refinement method	Full-matrix least-squares on F^2	
Data / restraints / parameters	14327 / 0 / 589	
Goodness-of-fit on F^2	1.135	
Final R indices [I>2sigma(I)]	R1 = 0.0190,	wR2 = 0.0423
R indices (all data)	R1 = 0.0199,	wR2 = 0.0426
Largest diff. peak and hole	2.001 and -1.300 eÅ^{-3}	
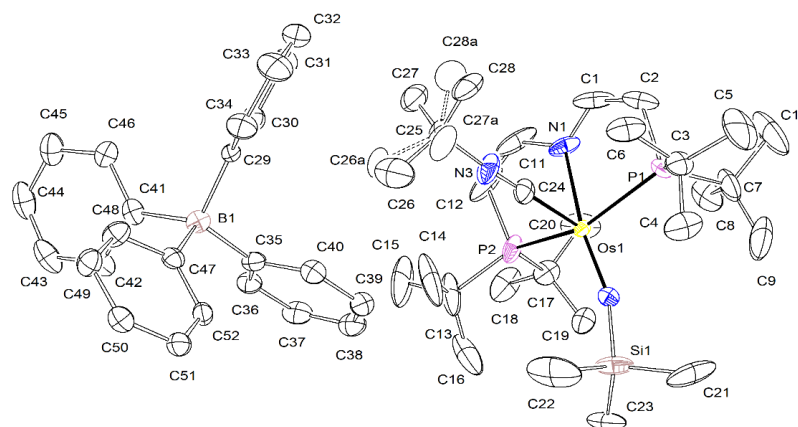
Figure 7.18: Thermal ellipsoid plot of **19** with the anisotropic displacement parameters drawn at the 50% probability level. The asymmetric unit contains one disordered complex molecule and one BPh4 anion. The disordered complex molecule was refined with population of 0.709(9) on the main domain using some restraints (SADI, RIGU).

|		
Empirical formula	$C_{52}H_{78}BN_3OsP_2Si$	
Formula weight	1036.21	
Temperature	129(2) KK	
Wavelength	1.54178 Å	
Crystal system	Monoclinic	
Space group	$P2_1$	
Unit cell dimensions	a = 11.5197(4) Å	$\alpha = 90°$
	b = 16.7973(6) Å	$\beta = 90.1691(19)°$
	c = 13.4774(5) Å	$\gamma = 90°$
Volume	2607.86(16) Å^3	
Z	2	
Density (calculated)	1.320 Mg/m^3	
Absorption coefficient	5.676 mm^{-1}	
F(000)	1072	
Crystal size	0.258 x 0.176 x 0.081 mm^3	
Crystal shape and color	Plate,	clear dark brown
Theta range for data collection	3.279 to 74.615°	
Index ranges	-14<=h<=14	
	-18<=k<=20	
	-16<=l<=16	
Reflections collected	94546	
Independent reflections	10499 [R(int) = 0.0554]	
Completeness to theta = 67.679°	99.9%	
Max. and min. transmission	0.7538 and 0.5666	
Refinement method	Full-matrix least-squares on F^2	
Data / restraints / parameters	10499 / 67 / 590	
Goodness-of-fit on F^2	1.088	
Final R indices [I>2sigma(I)]	R1 = 0.0248,	wR2 = 0.0486
R indices (all data)	R1 = 0.0284,	wR2 = 0.0496
Absolute structure parameter	0.003(3)	
Largest diff. peak and hole	0.384 and -0.675 eÅ^{-3}	
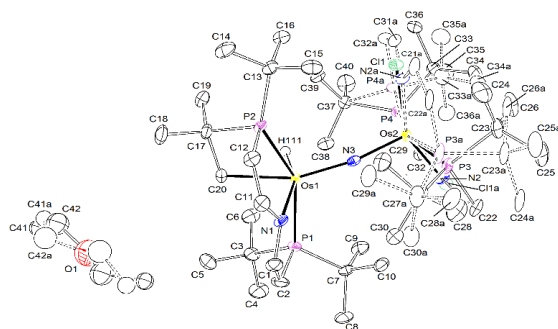
Figure 7.19: Thermal ellipsoid plot of **20** with the anisotropic displacement parameters drawn at the 50% probability level. The asymmetric unit contains one disordered complex molecule and a quarter of a disordered diethyl ether solvent molecule. The disordered complex molecule was refined with population of 0.933(2) on the main domain using some restraints and constraints (SADI, RIGU, EADP). The disordered diethyl ether solvent molecule was refined isotropically with population of 0.58(2) on the main domain using some restraints and constraints (SADI, RIGU, EADP). The N-H hydrogen atom was found from the residual density map and isotropically refined. The reflections -3 1 1, 5 1 0 and 44 8 9 are removed from the refinement using OMIT commands.

|		
Empirical formula	$C_{40}H_{80}ClN_3Os_2P_4$ x 0.25 $C_4H_{10}O$	
Formula weight	1161.33	
Temperature	100(2) K	
Wavelength	0.71073 Å	
Crystal system	Monoclinic	
Space group	C2/c	
Unit cell dimensions	a = 40.8402(17) Å	$\alpha = 90°$
	b = 19.2523(8) Å	$\beta = 92.098(2)°$
	c = 12.4764(5) Å	$\gamma = 90°$
Volume	9803.2(7) Å^3	
Z	8	
Density (calculated)	1.574 Mg/m^3	
Absorption coefficient	5.395 mm^{-1}	
F(000)	4644	
Crystal size	0.158 x 0.119 x 0.057 mm^3	
Crystal shape and color	Plate, clear dark brown	
Theta range for data collection	2.339 to 28.333°	
Index ranges	-54<=h<=54	
	-25<=k<=25	
	-16<=l<=16	
Reflections collected	158832	
Independent reflections	12204 [R(int) = 0.0678]	
Completeness to theta = 25.242°	99.9%	
Max. and min. transmission	0.7457 and 0.6157	
Refinement method	Full-matrix least-squares on F^2	
Data / restraints / parameters	12204 / 324 / 657	
Goodness-of-fit on F^2	1.051	
Final R indices [I>2sigma(I)]	R1 = 0.0253,	wR2 = 0.0488
R indices (all data)	R1 = 0.0369,	wR2 = 0.0519
Largest diff. peak and hole	2.242 and -1.627 eÅ^{-3}	
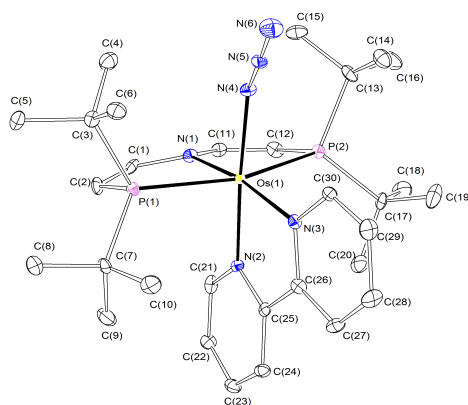
Figure 7.20: Thermal ellipsoid plot of **21** with the anisotropic displacement parameters drawn at the 50% probability level.

Empirical formula	$C_{30}H_{48}N_6OsP_2$	
Formula weight	744.88	
Temperature	100(2) K	
Wavelength	0.71073 Å	
Crystal system	Monoclinic	
Space group	$P2_1/n$	
Unit cell dimensions	a = 9.1148(3) Å	$\alpha = 90°$
	b = 16.6248(7) Å	$\beta = 95.383(2)°$
	c = 21.0265(8) Å	$\gamma = 90°$
Volume	3172.1(2) Å^3	
Z	4	
Density (calculated)	1.560 Mg/m^3	
Absorption coefficient	4.150 mm^{-1}	
F(000)	1504	
Crystal size	0.288 x 0.169 x 0.058 mm^3	
Crystal shape and color	Plate, dark purple	
Theta range for data collection	1.946 to 28.368°	
Index ranges	-12<=h<=12	
	-22<=k<=22	
	-28<=l<=28	
Reflections collected	124034	
Independent reflections	7925 [R(int) = 0.1149]	
Completeness to theta = 25.242°	100.0%	
Max. and min. transmission	0.7457 and 0.5574	
Refinement method	Full-matrix least-squares on F^2	
Data / restraints / parameters	7925 / 0 / 364	
Goodness-of-fit on F^2	1.049	
Final R indices [I>2sigma(I)]	R1 = 0.0299,	wR2 = 0.0439
R indices (all data)	R1 = 0.0490,	wR2 = 0.0472
Largest diff. peak and hole	0.665 and -1.204 eÅ^{-3}	

7.4.3 Synthesis

Synthesis of 14

Route A: **1** (85.5 mg, 138 μmol, 1.00 eq.) and CoCp$_2$ (26.2mg, 138 μmol, 1.00 eq.) are dissolved in THF (10 mL) and stirred for 1 minute under N$_2$ atmosphere. The solution is filtered into a solution of [PPN]N$_3$ (400 mg, 69 mmol, 5.0 eq.) and stirred for 10 min. The solvent is removed and the residue is extracted with benzene (3 x 10 mL) and pentanes (10 x 5 mL). The solution is concentrated and cooled at -90°C for 16 h. The solution is filtered at -90°C and the residue is washed with pentane (2 x 5 mL). The product is extracted with benzene (3 x 3 mL) and lyophilization yields **14** as a brown powder (48.0 mg, 85.4 μmol, 62%).

Route B: Complex **16** (10.0 mg, 13.5 μmol, 1.00 eq.) is dissolved in THF (5 mL). NaHg (620 mg, 0.1 w%, 27.0 μmol, 2.00 eq.) is added and the solution is stirred for 5 minutes. After evaporation of the solvent the crude product is extracted with pentane (4 x 2 mL). [OsN(L^3)] (7.2 mg, 12.8 μmol, 95%) is obtained as a brown solid.

Anal. Calcd for C$_{20}$H$_{40}$N$_2$OsP$_2$ (560.73): C, 42.8; H, 7.19; N, 5.00 Found: C, 42.7; H, 7.13; N, 4.90. NMR (C$_6$D$_6$, RT): ^{1}H (400 MHz): δ = 6.99 (ABXX'B'A', $N = |^3J_{AX} + ^4J_{AX'}| = 17.1$ Hz, $^3J_{AB} = 6.1$ Hz. 2H, NCH), 4.56 (ABXX'B'A', $N = |^2J_{AX} + ^4J_{AX'}| = 3.7$ Hz, $^3J_{AB} = 6.1$ Hz, 2H, PCH), 1.54 (A$_{18}$XX'A'$_{18}$, $N = |^3J_{AX} + ^5J_{AX'}| = 7.1$ Hz, 36H, P(C(CH_3)$_3$)). ^{13}C{^{1}H} (125.76 MHz): δ = 166.8 (AXX'A', $N = |^2J_{AX} + ^3J_{AX'}| = 9.0$ Hz, 2C, NCH), 89.2 (AXX'A', $^1J_{CP} = 24.3$ Hz. $^3J_{CP} = 22.6$ Hz, 2C, PCH), 37.8 (A$_2$XX'A'$_2$, $N = |^1J_{AX} + ^3J_{AX'}| = 12.7$ Hz, 4C, P(C(CH$_3$)$_3$)$_2$), 30.8 (A$_6$XX'A'$_6$, $N = |^2J_{AX} + ^4J_{AX'}| = 2.9$ Hz, 12C, P(C(CH$_3$)$_3$)$_2$). ^{31}P{^{1}H} (161.25 MHz): δ = 81.2 (s, 2P, P(C(CH$_3$)$_3$)$_2$). MS (LIFDI, toluene): m/z = 562.1 (100%, [M$^+$]). IR (KBr): $\tilde{\nu}$ = 1025 (Os≡N).

Synthesis of 15

1 (100 mg, 162 μM, 1.00 eq.) and [Ph$_3$C][PF$_6$] (62.0 mg, 160 μM, 0.99 eq.) are dissolved in THF (5 mL). TMSN$_3$ (21.2 μL, 160 μM, 0.99 eq.) in THF (5 mL) is slowly added and the reaction is stirred for 3h. After evaporation of the solvent the crude product is washed with Et$_2$O (4 x 10 mL) and extracted with DCM (2 x 5 mL). The solution is layered with Et$_2$O (100 mL) and stored at -35°C for 16h. After filtration the residue is washed with Et$_2$O (2 x 5 mL) and extracted with DCM (2 x 5 mL). Evaporation of the solvent gives **15** as an orange powder (80.0 mg, 108 μM, 67 %).

Anal. Calcd for C$_{20}$H$_{40}$ClF$_6$N$_2$OsP$_3$ (741.13): C, 32.4; H, 5.44; N, 3.77 Found: C, 32.6; H, 5.52; N, 3.70. NMR (CD$_2$Cl$_2$, RT): ^{1}H (500 MHz): δ = 7.76 (ABXX'B'A', $N = |^3J_{AX} + ^4J_{AX'}| = 19.0$ Hz, $^3J_{AB} = 6.4$ Hz. 2H, NCH), 5.09 (ABXX'B'A', $N = |^2J_{AX} + ^4J_{AX'}| = 5.1$ Hz, $^3J_{AB} = 6.4$ Hz, 2H, PCH), 1.59 (A$_9$XX'A'$_9$, $N = |^3J_{AX} + ^5J_{AX'}| = 8.5$ Hz, 18H, P(C(CH_3)$_3$)), 1.37 (A$_9$XX'A'$_9$, $N = |^3J_{AX} + ^5J_{AX'}| = 8.3$ Hz, 18H, P(C(CH_3)$_3$)). ^{13}C{^{1}H} (125.76 MHz): δ = 170.0 (AXX'A', $N = |^2J_{AX} + ^3J_{AX'}| = 3.6$ Hz, 2C, NCH), 93.0 (AXX'A', $N = |^1J_{AX} + ^3J_{AX'}| = 23.5$ Hz, 2C, PCH), 40.2 (AXX'A', $N = |^1J_{AX} + ^3J_{AX'}| = 12$ Hz, 6C, P(C(CH$_3$)$_3$), 38.9 (AXX'A', $N = |^1J_{AX} + ^3J_{AX'}| = 9.7$ Hz, 6C, P(C(CH$_3$)$_3$), 28.9 (A$_3$XX'A'$_3$, $N = |^2J_{AX} + ^4J_{AX'}| = 1.8$ Hz, 6C, P(C(CH$_3$)$_3$), 28.9 (s br, 6C, P(C(CH$_3$)$_3$). ^{31}P{^{1}H} (161.25 MHz): δ = 91.5 (s, 2P, P(C(CH$_3$)$_3$)$_2$), -145 (h, $^2J_{PF} = 711$ Hz, PF$_6$).

Synthesis of 16

14 (5.0 mg, 8.9 μmol, 1.0 eq.) is dissolved in Et$_2$O (2 mL) and cooled to $-35°$C. Brookhart's acid (9.0 mg, 8.9 μmol, 1.0 eq.) is added and the solution is stirred for 10 min. The solvent is removed and the residue washed with pentanes (5 x 1 mL) and extracted with Et$_2$O (2 x 1 mL). The solvent is removed and **16** is isolated in form of a yellow solid (10.0 mg, 7.00 μmol, 80%).

Anal. Calcd for C$_{52}$H$_{53}$BF$_{24}$N$_2$OsP$_2$ (1242.96): C, 43.8; H, 3.75; N, 1.97 Found: C, 43.7; H, 3.83; N, 1.93. NMR (CD$_2$Cl$_2$, RT): ^{1}H (500 MHz): δ = 7.74 - 7.71 (m, 8H, C$_{ortho}$$H$), 7.59 (ABXX'B'A', $N = |^3J_{AX} + {}^4J_{AX'}| = 19.0$ Hz, $^3J_{AB} = 6.3$ Hz. 2H, NCH), 7.58 – 7.55 (m, 4H, C$_{para}$$H$), 4.99 (ABXX'B'A', $N = |^2J_{AX}+{}^4J_{AX'}| = 5.3$ Hz, $^3J_{AB} = 6.3$ Hz, 2H, PCH), 1.49 (A$_9$XX'A'$_9$, $N = |^3J_{AX} + {}^5J_{AX'}| = 8.2$ Hz, 18H, P(C(CH_3)$_3$)), 1.26 (A$_9$XX'A'$_9$, $N = |^3J_{AX} + {}^5J_{AX'}| = 8.2$ Hz, 18H, P(C(CH_3)$_3$)), 0.47 (t, $^2J_{HP} = 13.5$ Hz, OsH). ^{13}C{^{1}H} (125.76 MHz): δ = 168.3 (AXX'A', $N = |^2J_{AX} + {}^3J_{AX'}| = 5.3$ Hz, 2C, NCH), 162.3 (q, $^1J_{CB} = 49.8$ Hz, 4C, C_{ipso}), 135.3 (s, 8C, C_{ortho}), 129.4 (qq, $^2J_{CF} = 31.5$ Hz, $^3J_{CB} = 2.8$ Hz, 8C, C_{meta}), 125.1 (q, $^1J_{CF} = 272.4$ Hz, 8C, CF$_3$), 118.0 (h, $^3J_{CF} = 4.0$ Hz, 4C, C_{para}), 90.5 (AXX'A', $N = |^1J_{AX} + {}^3J_{AX'}| = 23.9$ Hz, 2C, PCH), 38.4 - 38.0 (m, 2C, P(C(CH$_3$)$_3$), 29.1 (A$_3$XX'A'$_3$, $N = |^2J_{AX} + {}^4J_{AX'}| = 1.8$ Hz, 6C, P(C(CH$_3$)$_3$)), 28.9 (A$_3$XX'A'$_3$, $N = |^2J_{AX} + {}^4J_{AX'}| = 2.3$ Hz, 6C, P(C(CH$_3$)$_3$)). ^{31}P{^{1}H} (161.25 MHz): δ = 101.5 (s, 2P, P(C(CH$_3$)$_3$)$_2$).

Synthesis of 17

17 (5.0 mg, 8.9 μmol, 1.0 eq.) and BArF$_{18}$ (5.8 mg, 8.9 μmol, 1.0 eq.) are dissolved in benzene (2 mL) and stirred for 5 minutes. The crude product is purified *via* column chromatography over silanized silica (benzene). Lyophilization yields **17** as a red powder (9.1 mg, 7.5 μmol, 85%).

Anal. Calcd for C$_{44}$H$_{49}$BF$_{18}$N$_2$OsP$_2$ (1210.85): C, 43.7; H, 4.08; N, 2.31 Found: C, 43.4; H, 3.90; N, 2.35. NMR (d_6-benzene, RT): ^{1}H (500 MHz): δ = 8.31 – 8.29 (br, 6H, C$_{ortho}$$H$), 7.77 – 7.75 (br, 3H, C$_{para}$$H$), 5.69 (ABXX'B'A', $N = |^3J_{AX} + {}^4J_{AX'}| = 18.0$ Hz, $^3J_{AB} = 6.3$ Hz. 2H, NCH), 4.17 (ABXX'B'A', $N = |^2J_{AX}+{}^4J_{AX'}| = 4.4$ Hz, $^3J_{AB} = 6.3$ Hz, 2H, PCH), 1.04 (A$_{18}$XX'A'$_{18}$, $N = |^3J_{AX} + {}^5J_{AX'}| = 7.5$ Hz, 36H, P(C(CH_3)$_3$)). ^{13}C{^{1}H} (125.76 MHz): δ = 162.7 (AXX'A', $N = |^2J_{AX} + {}^3J_{AX'}| = 8.6$ Hz, 2C, NCH), 147.3 (br, 1C, C_{ipso}), 135.9 (s, 6C, C_{ortho}H), 130.2 (q, $^2J_{CF} = 32.14$ Hz, 6C, C_{meta}H), 124.5 (q, $^1J_{CF} = 273.4$ Hz, 6C, CF$_3$), 120.4 (h, $^3J_{CF} = 4.0$ Hz, 3C, C_{para}H), 94.2 (AXX'A', $N = |^1J_{AX} + {}^3J_{AX'}| = 24.2$ Hz, 2C, PCH), 38.3 (A$_2$XX'A'$_2$, $N = |^1J_{AX} + {}^3J_{AX'}| = 12.0$ Hz, 4C, P(C(CH$_3$)$_3$)$_2$), 30.4 (A$_6$XX'A'$_6$, $N = |^2J_{AX} + {}^4J_{AX'}| = 2.4$ Hz, 12C, P(C(CH$_3$)$_3$)$_2$). ^{31}P{^{1}H} (161.25 MHz): δ = 82.7 (s, 2P, P(C(CH$_3$)$_3$)$_2$.

Hydrogenolysis of 14

14 (9.8 mg, 17.5 mmol, 1.0 eq.) is dissolved in toluene-d$_8$ (0.5 mL) and heated to 100°C for 48 h under a dihydrogen atmosphere (1 bar). The reaction is followed by ^{31}P NMR spectroscopy with PPh$_3$O as internal standard (capillary). Ammonia was quantified by indophenolic titration.

Synthesis of 18

14 (20.4 mg, 36.1 μmol, 1.00 eq.) and CN^{t}Bu (4.3 mg, 38 μmol, 1.1 eq.) are dissolved in thawing benzene (5 mL) and stirred for 10 s. The solvent is evacuated and **18** is isolated in form of a green solid (23.1 mg, 36.1 μmol, quant.). *18 is only stable at low temperatures ($< -50°C$) and cannot be stored as a solid without decomposition over the course of a few hours which prevented reproducible characterization by combustion analysis. Small amounts of benzene are still visible in the NMR spectra.*

NMR (d_8-THF, -50°C): ^{1}H (400 MHz): δ = 6.94 (ABXX'B'A', $N = |^3J_{AX} + {}^4J_{AX'}|$ = 16.3 Hz, $^3J_{AB}$ = 5.7 Hz. 2H, NCH), 5.74 (ABXX'B'A', $N = |^2J_{AX} + {}^4J_{AX'}|$ = 4.2 Hz, $^3J_{AB}$ = 5.7 Hz, 2H, PCH), 1.51 (s, 9H, CN(C(CH_3)$_3$)), 1.40 (A$_9$XX'A'$_9$, $N = |^3J_{AX} + {}^5J_{AX'}|$ = 6.5 Hz, 18H, P(C(CH_3)$_3$)), 1.34 (A$_9$XX'A'$_9$, $N = |^3J_{AX} + {}^5J_{AX'}|$ = 7.2 Hz, 18H, P(C(CH_3)$_3$)). ^{13}C{^{1}H} (125.76 MHz): δ = 161.0 (AXX'A', $N = |^2J_{AX} + {}^3J_{AX'}|$ = 7.3 Hz, 2C, NCH), 155.9 (t, $^2J_{CP}$ = 3.2 Hz, 1C, OsC), 82.2 (AXX'A', $N = |^1J_{AX} + {}^3J_{AX'}|$ = 26.2 Hz, 2C, PCH), 57.4 (s, 1C, CN(C(CH$_3$)$_2$), 38.1 (AXX'A', $N = |^1J_{AX} + {}^3J_{AX'}|$ = 13.6 Hz, 2C, P(C(CH$_3$)$_3$), 37.9 (AXX'A', $N = |^1J_{AX} + {}^3J_{AX'}|$ = 11.3 Hz, 2C, P(C(CH$_3$)$_3$), 32.3 (s, 3C, CC(CH_3)$_3$)$_2$), 31.6 – 31.4 (br, 12C, P(C(CH_3)$_3$)$_2$). ^{31}P{^{1}H} (161.25 MHz): δ = 73.3 (s, 2P, P(C(CH$_3$)$_3$)$_2$). IR (nujol): $\tilde{\nu}$ = 2007 (C≡N).

Synthesis of 19

14 (21.3 mg, 38.0 μmol, 1.00 eq.) and NaBPh$_4$ (13.0 mg, 38.0 μmol, 1.00 eq.) are dissolved in THF and CNtBu (4.30 μL, 38.0 μmol, 1.00 eq.) is added. The solution is stirred for 30 seconds and SiMe$_3$I (4.92 μL, 38.0 μmol, 1.00 eq.) is added. The solution is stirred for 2 minutes and the solvent is removed. The residue is washed with Et$_2$O and extracted with DCM. The extract is layered with pentanes and stored at $-35°C$ for 16 h. After filtration the residue is washed with pentane (4 x 2 mL) and extracted with DCM (2 x 2 mL). **19** is isolated in form of an orange solid (20.1 mg, 19.4 μmol, 51%).

Anal. Calcd for C$_{52}$H$_{78}$ B$_1$ N$_3$Os$_1$P$_2$Si (1036.29): C, 60.27; H, 7.59; N, 4.05 Found: C, 59.97; H, 7.25; N, 4.01. NMR (d_8-THF, -50°C): ^{1}H (500 MHz): δ = 7.34 – 7.29 (m, 8H, C$_{meta}$$H$), 7.15 (ABXX'B'A', $N = |^3J_{AX} + {}^4J_{AX'}|$ = 18.3 Hz, $^3J_{AB}$ = 5.8 Hz. 2H, NCH), 7.05 – 7.00 (m, 8H, C$_{ortho}$$H$), 6.90 – 6.85 (m, 4H, C$_{para}$$H$), 4.33 (ABXX'B'A', $N = |^2J_{AX} + {}^4J_{AX'}|$ = 5.9 Hz, $^3J_{AB}$ = 5.8 Hz, 2H, PCH), 1.43 (s, 9H, CN(C(CH_3)$_3$)), 1.41 (A$_9$XX'A'$_9$, $N = |^3J_{AX} + {}^5J_{AX'}|$ = 7.7 Hz, 18H, P(C(CH_3)$_3$)), 1.24 (A$_9$XX'A'$_9$, $N = |^3J_{AX} + {}^5J_{AX'}|$ = 7.8 Hz, 18H, P(C(CH_3)$_3$)), 0.46 (s, 9H, Si(CH_3)$_3$). ^{13}C{^{1}H} (125.76 MHz): δ = 164.6 (q, $^1J_{CB}$ = 49.0 Hz, 4C, C_{ipso}), 161.1 (AXX'A', $N = |^2J_{AX} + {}^3J_{AX'}|$ = 5.5 Hz, 2C, NCH), 136.4 (s, 8C, C_{meta}), 132.3 (br, 1C, OsC), 126.2 (q, $^2J_{CB}$ = 2.9 Hz, 4C, C_{ortho}), 122.3 (s, 8C, C_{para}), 83.1 (AXX'A', $N = |^1J_{AX} + {}^3J_{AX'}|$ = 27.6 Hz, 2C, PCH), 59.8 (s, 1C, CN(C(CH$_3$)$_2$), 41.6 (AXX'A', $N = |^1J_{AX} + {}^3J_{AX'}|$ = 12.8 Hz, 2C, P(C(CH$_3$)$_3$), 41.2 (AXX'A', $N = |^1J_{AX} + {}^3J_{AX'}|$ = 12.1 Hz, 2C, P(C(CH$_3$)$_3$), 32.0 (s, 3C, CC(CH_3)$_3$)$_2$), 31.5 (A$_3$XX'A'$_3$, $N = |^2J_{AX} + {}^4J_{AX'}|$ = 1.7 Hz, 6C, P(C(CH_3)$_3$)), 29.5 (A$_3$XX'A'$_3$, $N = |^2J_{AX} + {}^4J_{AX'}|$ = 2.0 Hz, 6C, P(C(CH_3)$_3$)), 2.21 (s, 3C, Si(CH_3)$_3$). ^{31}P{^{1}H} (161.25 MHz): δ = 91.3 (s, 2P, P(C(CH$_3$)$_3$)$_2$). IR (nujol): $\tilde{\nu}$ = 2128 (C≡N).

Synthesis of 20

Route A: **2** (11.0 mg, 17.83 µmol, 1.00 eq.) and CoCp$_2$ (3.4 mg, 18 µmol, 1.0 eq.) are dissolved in benzene (5 mL) and stirred for 2 minutes at RT. A solution of **14** (10.0 mg, 17.83 µmol, 1.0 eq) in pentane (5 mL) is slowly added and the solution is stirred for 20 minutes at RT The solvent is removed and the residue extracted with pentanes (4 x 5 mL). The filtrate is concentrated and the crude product is purified *via* column chromatography with silanized silica (pentane). The solvent is removed and lyophilization yields **20** as a green powder (17.0 mg, 14.9 µmol, 83 %).

Route B: **2** (20.0 mg, 32.4 µmol, 1.00 eq.) and CoCp$_2$ (6.2 mg, 32 µmol, 1.0 eq.) are dissolved in benzene (5 mL) and stirred for 2 minutes. [TMS]N$_3$ (2.2 µL, 17 µmol, 0.50 eq.) in pentane (5 mL) is slowly added and the solution is stirred for additional 20 minutes. The solvent is removed and the residue extracted with pentanes (4 x 5 mL). The filtrate is concentrated and the crude product is purified *via* column chromatography with silanized silica (pentane). The solvent is removed and lyophilization yields **20** as a green powder (13.2 mg, 11.5 µmol, 71%).

Anal. Calcd for C$_{40}$H$_{80}$Cl$_1$N$_3$Os$_2$P$_4$ (1142.9): C, 42.0; H, 7.06; N, 3.67 Found: C, 41.9; H, 6.94; N, 3.48. NMR (toluene-d_8, RT): ^{1}H (500 MHz): δ = 6.99 (m, $^3J_{HH}$ = 6.1 Hz, 1H, NCH), 6.89 (m, $^3J_{HH}$ = 6.0 Hz, 1H, NCH), 6.67 (m, $^3J_{HH}$ = 6.3 Hz, 1H, NCH), 6.61 (m, $^3J_{HH}$ = 6.3 Hz, 1H, NCH), 4.44 (m, $^3J_{HH}$ = 6.0 Hz, 1H, PCH), 4.34 (m, $^3J_{HH}$ = 6.3 Hz, 1H, PCH), 4.31 (m, $^3J_{HH}$ = 6.1 Hz, 1H, PCH), 4.18 (m, $^3J_{HH}$ = 6.3 Hz, 1H, PCH), 1.93 – 1.07 (m, 69 H), 0.81 (m, 1H, OsCH_2), -0.56 (m, 1H, OsCH_2), -4.18 (m, 1H, OsH).^{13}C{^{1}H} (125.76 MHz) δ = 168.5 (dd, $^2J_{CP}$ = 10.3 Hz, $^3J_{CP}$ = 2.7 Hz, 1C, NCH), 168.4 (dd, $^2J_{CP}$ = 10.6 Hz, $^3J_{CP}$ = 2.9 Hz, 1C, NCH), 162.4 (dd, $^2J_{CP}$ = 12.4 Hz, $^3J_{CP}$ = 2.0 Hz, 1C, NCH), 161.2 (dd, $^2J_{CP}$ = 10.1 Hz, $^3J_{CP}$ = 2.4 Hz, 1C, NCH), 93.9 (dd, $^1J_{CP}$ = 35.0 Hz, $^3J_{CP}$ = 2.5 Hz, 1C, PCH), 93.6 (d, $^1J_{CP}$ = 39.3 Hz, 1C, PCH), 93.2 (dd, $^1J_{CP}$ = 35.2 Hz, $^3J_{CP}$ = 1.7 Hz, 1C, PCH), 90.6 (d, $^1J_{CP}$ = 38.8 Hz, 1C, PCH), 58.1 (dd, $^1J_{CP}$ = 35.2 Hz, $^3J_{CP}$ = 5.4 Hz, 1C, P(C(CH$_3$)$_2$CH$_2$Os)), 39.1 (dd, $^1J_{CP}$ = 18.7 Hz, $^3J_{CP}$ = 2.7 Hz, 1C, P(C(CH$_3$)$_3$)), 38.1 (m, 2C, P(C(CH$_3$)$_3$)), 37.5 (dd, $^1J_{CP}$ = 13.9 Hz, $^3J_{CP}$ = 4.0 Hz, 1C, P(C(CH$_3$)$_3$)), 37.3 (dd, $^1J_{CP}$ = 13.2 Hz, $^3J_{CP}$ = 4.0 Hz, 1C, P(C(CH$_3$)$_3$)), 36.0 (dd, $^1J_{CP}$ = 13.9 Hz, $^3J_{CP}$ = 5.1 Hz, 1C, P(C(CH$_3$)$_3$)), 34.5 (dd, $^1J_{CP}$ = 6.6 Hz, $^3J_{CP}$ = 2.7 Hz, 1C, P(C(CH$_3$)$_3$)), 33.2 – 29.8 (21C), 32.3 (d, $^2J_{CP}$ = 3.6 Hz, 1C, P(C(CH$_3$)$_2$CH$_2$Os)), 9.13 (dd, $^2J_{CP}$ = 30.4 Hz, $^2J_{CP}$ = 5.4 Hz, P(C(CH$_3$)$_2$$CH_2$Os)). ^{31}P{^{1}H} (202.46 MHz): δ = 38.0 (d, $^2J_{PP}$ = 250.2 Hz, 1P, P(C(CH$_3$)$_3$)), 19.7 (m, $^2J_{PP}$ = 291.6 Hz, N = |$^4J_{PP}$ + $^4J_{PP}$| = 2.5 Hz, 1P, P(C(CH$_3$)$_3$)$_2$), 16.6 (m, $^2J_{PP}$ = 291.6 Hz, N = |$^4J_{PP}$ + $^4J_{PP}$| = 2.5 Hz, 1P, P(C(CH$_3$)$_3$)$_2$), -15.5 (m, $^2J_{PP}$ = 250.1 Hz, N = |$^4J_{PP}$ + $^4J_{PP}$| = 2.5 Hz, 1P, P(C(CH$_3$)$_2$CH$_2$Os)). MS (LIFDI, toluene): m/z = 1143.5 (100%, [M$^+$]).

Synthesis of 21

Route A: **1** (30.0 mg, 48.6 µmol, 1.00 eq.) and CoCp$_2$ (9.2 mg, 49 µmol, 1.0 eq.) are dissolved in benzene (2 mL) and stirred for 2 minutes at RT. 2,2'-Bipyridine (7.6 mg, 48.6 µmol, 1.0 eq.) is added and stirring is continued for 5 minutes. TMSN$_3$ (64 µL, 486 µmol, 10 eq.) is added and the solution is filtered after 1 hour of stirring. The solvent is evaporated and the residue is washed with pentane (5 x 1 mL) at −20°C. The product is extracted with benzene (5 x 0.5 mL) and **21** (22.4 mg, 30.1 µmol, 62%) is

obtained in form of a red powder after lyophilization.

Route B: **7** (10.0 mg, 13.5 µmol, 1.00 eq.) is dissolved in benzene (2 mL), TMSN$_3$ (17.8 µL, 135 µmol, 10.0 eq.) is added and the solution is stirred for 1 hour at RT. The purification is identical with Route A.
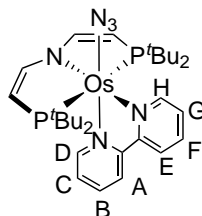
Anal. Calcd. for C$_{30}$H$_{48}$ClN$_6$OsP$_2$ (744.93): Route A: C, 48.4; H, 6.50; N, 11.3 Found: C, 48.8; H, 6.70; N, 10.7. Route B: C, 48.4; H, 6.50; N, 11.3 Found: C, 48.6; H, 6.38; N, 10.9. NMR (C$_6$D$_6$, RT): ^{1}H NMR (400 MHz): δ = 10.40 - 10.36 (m, 1H, A-H), 8.29 (dd, $^3J_{HH}$ = 6.2 Hz, $^4J_{HH}$ = 1.4 Hz, 1H, E-H), 7.48 (A$_9$BCXX'A'$_9$B'C', N = $|^3J_{CX}+^4J_{CX'}|$ = 34.0 Hz, $^3J_{BC}$ = 5.9 Hz, 2H, NCHCHP), 7.14 - 7.10 (m, 1H, D-H), 6.94 (dd, $^3J_{HH}$ = 8.3 Hz, $^4J_{HH}$ = 1.6 Hz, 1H, H-H), 6.59 - 6.52 (m, 2H, B-H, C-H) 6.24 (ddd, $^3J_{HH}$ = 8.3 Hz, 7.2 Hz, $^4J_{HH}$ = 1.4 Hz, 1H, G-H), 6.03 (ddd, $^3J_{HH}$ = 7.2 Hz, 6.2 Hz, $^4J_{HH}$ = 1.6 Hz, 1H, F-H), 4.00 (A$_9$BCXX'A'$_9$B'C', N = $|^2J_{BX}+^4J_{BX'}|$ = 6.0 Hz, $^3J_{BC}$ = 5.9 Hz, 2H, NCHCHP), 1.60 (A$_9$BCXX'A'$_9$B'C', $^3J_{AX}$ = 12.4 Hz, 18H, P(C(CH_3)$_3$)), 0.31 (A$_9$BCXX'A'$_9$B'C', $^3J_{AX}$ = 12.4 Hz, 18H, P(C(CH_3)$_3$)). ^{13}C{^{1}H}-NMR (101.25 MHz): δ = 163.7 (vt, $^2J_{CP}$ = 7.5 Hz, 2C, NCHCHP), 168.1 (s, 1C, C$_A$), 163.6 (s, 1C, C-C$_A$), 154.1 (s, 1C, C$_E$), 153.6 (s, 1C, C-C$_E$), 130.5 (s, 1C), 126.9 (s, 1C), 126.8 (s, 1C), 125.3 (s, 1C), 122.7 (s, 1C), 121.2 (s, 1C), 84.2 (vt, $^1J_{CP}$ = 19.2 Hz, 2C, NCHCHP), 38.3 (vt, $^1J_{CP}$ = 10.7 Hz, 2C, P(C(CH$_3$)$_3$)$_2$), 38.2 (vt, $^1J_{CP}$ = 9.5 Hz, 2C, P(C(CH$_3$)$_3$)$_2$), 30.5 (vt, $^2J_{CP}$ = 2.2 Hz, 6C, P(C(CH$_3$)$_3$)$_2$), 29.6 (vt, $^2J_{CP}$ = 2.3 Hz, 6C, P(C(CH$_3$)$_3$)$_2$). ^{31}P{^{1}H}-NMR (161.25 MHz): δ = 21.6 (s, P(C(CH$_3$)$_3$)$_2$)). *All bipy ^{1}H NMR signals could be assigned to two chemically inequivalent ring systems. However, due to a lack of resolution in 2D NMR correlatiokn experiments not all carbon signals could be assigned and it might be possible that the position of the ring is not correctly assigned..* IR (Nujol, RT) $\tilde{\nu}$ = 2072 (Os-N$_3$).

One-electron oxidation of 21

21 (5.0 mg, 6.7 µmol, 1.0 eq.) is dissolved in THF (1 mL) and AgSbF$_6$ (2.3 mg, 6.7 µmol, 2.0 eq.) is added. The solution is stirred for 1 minute at RT and filtered. The solvent evaporated, redisolved in THF-d$_8$ and measured by NMR which showed the formation of **8** as sole reaction product.

Two-electron oxidation of 21 and successive reduction

21 (5.0 mg, 6.7 µmol, 1.0 eq.) is dissolved in THF (1 mL) and AgSbF$_6$ (4.6 mg, 13 µmol, 2.0 eq.) is added in one portion under heavy stirring. The solution is stirred for 1 minute at RT and filtered. The solvent evaporated, redisolved in CD$_2$Cl$_2$ and measured by NMR which showed the formation of **23** accompanied by a minor asymmetric impurity

(^{31}P{^{1}H}-NMR (161.25 MHz): $\delta = 34.9$ (d, $^2J_{PP} = 223.4$ Hz, $P(C(CH_3)_3)_2$), 7.10 (d, $^2J_{PP} = 223.4$ Hz, $P(C(CH_3)_3)_2$)) and organic impurities.

NMR (CD$_2$Cl$_2$, RT): ^{1}H NMR (300 MHz): $\delta = 9.75 - 9.70$ (m, 1H), 8.92 - 8.87 (m, 1H), 8.70 - 8.60 (m, 1H), 8.43 - 8.35 (m, 1H), 8.16 - 7.87 (m, 2H), 8.05 (A$_9$BCXX'A'$_9$B'C', $N = |^3J_{CX} + {}^4J_{CX'}| = 38.6$ Hz, $^3J_{BC} = 6.0$ Hz, 2H, NCHCHP), 7.39 - 7.23 (m, 2H), 4.96 (A$_9$BCXX'A'$_9$B'C', $N = |^2J_{BX} + {}^4J_{BX'}| = 10.2$ Hz, $^3J_{BC} = 6.0$ Hz, 2H, NCHCHP), 1.50 (A$_9$BCXX'A'$_9$B'C', $^3J_{AX} = 16.4$ Hz, 18H, P(C(CH_3)$_3$)), 0.67 (A$_9$BCXX'A'$_9$B'C', $^3J_{AX} = 16.4$ Hz, 18H, P(C(CH_3)$_3$)). ^{31}P{^{1}H}-NMR (121.49 MHz): $\delta = 78.7$ (s, $P(C(CH_3)_3)_2$)).MS (LIFDI, THF) $\frac{m}{z} = 359.1$ ([M^{2+}]).)

This solvent is evaporated and the residue is redissolved in THF. To this solution CoCp$_2$ (1.2 mg, 6.4 μmol, 1.0 eq.) is added at RT. NMR spectroscopy shows exclusive formation of **8**.

7.5 Transition Metal Complexes with Metal-Pnictogen Multiple Bonds

Parts of this chapter were adapted from:

J. Abbenseth, M. Diefenbach, A. Hinz, L. Alig, C. Würtele, J. M. Goicoechea*, M. C. Holthausen*, S. Schneider*, **2019**, *58*, 10966-10970.

J. Abbenseth, D. Delony, M. C. Neben, C. Würtele, B. de Bruin, S. Schneider, *Angew. Chem. Int. Ed.* **2019**, *58*, 6338-6341.

with permission from WILEY-VCH Verlag GmbH & Co. KGaA, Weinheim

7.5.1 P_2 and As_2 Complexes from Coupling of Terminal Re Pnictides - Computational Details

Based on a detailed evaluation study of Minenkov et al. the ωB97XD meta-hybrid density functional as implemented in the Gaussian program along with the Stuttgart-Dresden effective core potentials (SDD ECP) to replace the innermost core electrons of all non-hydrogen atoms (C, N: 2 electrons; P: 10 electrons; As: 28 electrons, Re: 60 electrons) was employed.[308],[335]–[338] The corresponding standard [2s2p] SDD valence basis sets for C, N, P, As were augmented by a single d-polarization function, i.e., the 'HONDO 7 polarization' functions for C (0.72), N (0.98), and P (0.465) as well as the 'Huzinaga polarization' for As (0.293) as provided by the EMSL basis set library.[339],[340] The standard [6s5p3d] SDD valence basis set for Re and the D95 double-ζ basis set for H were used. This level of density functional theory, dubbed ωB97XD/BS1 was used for geometry optimizations and Hessian evaluations.[308],[335],[336],[341] Based on minimum structures optimized at this level subsequent single-point energy calculations were performed employing the 6-311++G(2d,2p) basis set for H, C, N, P,and As in combination with the SDD ECP/basis set representation of Re, all as implemented in the basis set library of the Gaussian program.[308],[335],[336],[342]–[345] Wave functions obtained at this level of theory, dubbed ωB97XD/BS2, were used for bonding analysis. Natural bond orbital (NBO) analysis was performed with the NBO 6.0 program interfaced with Gaussian 09. The programs AIMAll and Multiwfn were used for QTAIM analysis. Molecular graphics were rendered with the programs CylView and Chemcraft.

A refined molecular structure of **27** was optimized at the ωB97XD3/def2-TZVP level, applying the rijcosx approximation as implemented in the ORCA program.[318] Based on this structure, ^{31}P NMR chemical shift calculations were performed with the NMR module[346],[347] of the ADF program.[348] Relativistic spin-orbit contributions to nuclear magnetic shielding constants were accounted for by means of the two-component ZORA formalism implemented in ADF.[349]–[351] The PBE0 hybrid functional?,[326],[352] was employed in combination with the TZ2P Slater-orbital basis set.[353] 31P NMR chemical shifts were computed relative to the (bare) $[P(CH_3)_4]^+$ cation as standard and incremented for its experimentally determined 31P NMR chemical shift relative to 85% aqueous phosphoric acid (δ^{31}P($[PMe_4]$Br)$= 25.1$,[354] thus $\delta^{calc}(X) = \sigma^{calc}([PMe_4]^+) - \sigma^{calc}(X) + 25.1$). Solvent effects were taken into account with the COSMO model implemented in ADF (solvent tetrahydrofuran).[355],[356] The appendix lists several relevant characteristics derived from the electron density at the bcp, located at $\mathbf{r}_b$ along the bond path connecting two interacting atoms, which are customarily used for the classification of bonds. In homopolar bonding situations, a covalent interaction is characterized by a

negative Laplacian at the corresponding bcp. The magnitudes of the electron density $\rho\mathbf{r}_b$ and its Laplacian $\nabla^2\mathbf{r}_b$, and the relative total energy density $H\mathbf{r}_b/\rho\mathbf{r}_b$ relate to the strength of a covalent bond. The total energy density $H = V + G$ is the sum of the potential energy density V (always negative) and the kinetic energy density G (always positive). Covalent, electron-sharing bonding situations are indicated by the ratios $H(\mathbf{r}_b)/\rho(\mathbf{r}_b) < 0$ and $G(\mathbf{r}_b)/\rho(\mathbf{r}_b) < 1$. Further, the ellipticity ϵ of the density at the bcp serves as indicator for π-double bond character, and the delocalization index $\delta(A,B)$ is a measure for the number of electron pairs shared between two nuclei A and B. Compared to homonuclear bonds, the degree of covalency is generally reduced with increasing polarity of the interaction. As a consequence, in polar bonds the delocalization index is smaller than the formal bond order. Also, the bcp usually resides close to a nodal surface in the Laplacian distribution, an effect which further amplifies with diffuseness of valence electron density in heavy atoms. Thus, the sign of $\nabla^2\rho(\mathbf{r}_b)$ is unsuitable for a bond classification.

Table 7.6: XYZ-coordinates of computed complex **27**.

Atom	x	y	z	Atom	x	y	z
C	-4.08824	-1.96221	0.84562	H	2.40229	3.10119	2.26253
C	-3.71229	-2.2656	-0.47151	H	-6.19948	-4.10404	-1.47485
N	-4.46868	-3.02268	-1.27316	H	-7.02538	-3.65781	0.83226
C	-5.61383	-3.49171	-0.79082	H	-3.43796	-1.34987	1.46123
C	-6.07889	-3.24526	0.49598	H	-5.60133	-2.23982	2.34646
C	-5.28715	-2.45894	1.32924	H	-2.29583	-2.60329	-3.08673
C	-2.45491	-1.75769	-1.0274	H	0.0609	-1.15235	-3.00839
N	-1.66805	-0.93912	-0.31263	H	2.31506	-1.58352	-2.64559
N	-0.60392	-0.65735	-1.06251	H	1.83378	-3.13993	-1.96464
C	-0.70677	-1.28056	-2.25891	H	3.34438	-3.01009	-2.8798
C	-1.88959	-2.00092	-2.28748	H	5.35511	-1.03928	-0.51545
Re	0.95484	0.58056	-0.2498	H	4.21305	-0.16445	-1.55918
N	1.71126	1.2794	1.47635	H	5.11592	-1.54479	-2.19005
C	2.68135	0.58655	2.32372	H	4.92348	-3.74629	-1.11587
C	3.45792	-0.49007	1.56861	H	3.50364	-4.23005	-0.19081
P	2.33508	-1.32993	0.36383	H	4.74708	-3.20133	0.55541
C	3.49679	-2.14661	-0.90588	H	3.16515	-3.8949	1.9245
C	4.60272	-1.15502	-1.30246	H	1.69995	-4.17334	2.8648
P	2.04586	1.31811	-1.88568	H	2.6581	-2.72132	3.1521
P	-0.56826	2.45751	0.18418	H	-0.1759	-2.71515	2.81447
C	-1.19968	3.51107	-1.26418	H	-0.49411	-1.60526	1.4812
C	-0.01377	4.17526	-1.97912	H	0.64291	-1.15086	2.77523
C	1.40976	-2.66598	1.35678	H	1.44135	-4.31728	-0.10736
C	0.28696	-1.97392	2.14883	H	0.11569	-3.15365	-0.34449
C	0.73015	-3.66335	0.40538	H	0.06205	-4.3067	0.9921
C	2.30102	-3.39988	2.36967	H	-1.65404	5.32771	-0.1254
C	-1.98406	2.17654	1.4413	H	-3.07333	4.29659	-0.39754
C	-3.28925	1.75513	0.74725	H	-2.40109	5.23922	-1.72392
C	0.65078	3.50257	1.09399	H	-0.38605	4.66097	-2.8896

Atom	x	y	z	Atom	x	y	z
C	1.44501	2.60354	2.03985	H	0.74982	3.45503	-2.28606
C	-1.5888	1.01449	2.36815	H	0.46218	4.9482	-1.36642
C	-2.22888	3.41594	2.31659	H	-1.21397	1.78633	-2.60464
C	4.19559	-3.40382	-0.3693	H	-2.2319	3.14573	-3.1297
C	2.69009	-2.49213	-2.16645	H	-2.77336	2.07408	-1.83045
C	-1.89761	2.56779	-2.25803	H	-1.38088	3.61707	2.9803
C	-2.1387	4.64904	-0.83661	H	-3.09881	3.22079	2.95691
H	4.21062	0.01237	0.95546	H	-2.44077	4.32317	1.74633
H	3.97665	-1.17011	2.2515	H	-3.75182	2.55918	0.16979
H	3.40952	1.31194	2.7181	H	-4.01101	1.45916	1.52012
H	2.18641	0.15281	3.20883	H	-3.12915	0.88953	0.09972
H	0.21453	4.35627	1.6213	H	-1.56576	0.08075	1.8063
H	1.33173	3.88316	0.32767	H	-2.35078	0.92351	3.15459
H	0.92104	2.5183	3.00772	H	-0.62196	1.15786	2.85713

Table 7.7: XYZ-coordinates of computed complex **28**.

Atom	x	y	z	Atom	x	y	z
C	-4.3902	-1.72852	0.68012	H	2.39011	2.83389	2.50015
C	-3.95146	-2.04633	-0.61382	H	-6.49985	-3.67487	-1.80819
N	-4.70853	-2.73484	-1.47469	H	-7.44592	-3.18167	0.44293
C	-5.91689	-3.1163	-1.0774	H	-3.73695	-1.17622	1.34716
C	-6.44815	-2.84464	0.17836	H	-6.02048	-1.89806	2.0709
C	-5.6552	-2.13214	1.0743	H	-2.38985	-2.50984	-3.1207
C	-2.62529	-1.63287	-1.08165	H	0.05693	-1.23939	-2.88861
N	-1.83228	-0.86508	-0.32011	H	2.29748	-1.70771	-2.52845
N	-0.69998	-0.6715	-0.99561	H	1.66446	-3.23322	-1.90491
C	-0.7669	-1.30099	-2.19254	H	3.23023	-3.20384	-2.73303
C	-1.99478	-1.93122	-2.29867	H	5.23673	-1.41681	-0.21991
Re	0.89401	0.46156	-0.1079	H	4.20504	-0.42766	-1.2733
N	1.61822	1.07197	1.65709	H	5.04482	-1.83847	-1.92385
C	2.50831	0.3024	2.5275	H	4.67193	-4.05966	-0.92459
C	3.25955	-0.79584	1.77829	H	3.18403	-4.48351	-0.08114
P	2.15224	-1.53135	0.49368	H	4.447	-3.5486	0.75115
C	3.33277	-2.38412	-0.73646	H	2.78466	-4.16551	2.02875
C	4.51637	-1.45246	-1.0437	H	1.25972	-4.40553	2.88136
As	2.14395	1.22159	-1.7567	H	2.26309	-3.00691	3.26421
P	-0.54732	2.40109	0.32784	H	-0.53146	-2.84781	2.79689
C	-1.10576	3.52212	-1.10099	H	-0.7449	-1.7034	1.47284
C	0.11867	4.13441	-1.795	H	0.35616	-1.32065	2.81863
C	1.11574	-2.84509	1.40713	H	1.13532	-4.46415	-0.0935
C	-0.00867	-2.11773	2.16424	H	-0.12366	-3.23501	-0.36003
C	0.43348	-3.78839	0.40358	H	-0.28832	-4.4124	0.94606
C	1.91969	-3.6459	2.44304	H	-1.45494	5.3428	0.06675
C	-2.00175	2.16687	1.5551	H	-2.9313	4.39927	-0.21597
C	-3.32377	1.85679	0.83469	H	-2.2104	5.32211	-1.53006

C	0.69884	3.36212	1.29282	H	-0.22116	4.67797	-2.68518
C	1.41184	2.39927	2.24031	H	0.83124	3.37733	-2.13456
C	-1.69657	0.95086	2.44578	H	0.64849	4.84856	-1.15602
C	-2.17728	3.38989	2.46997	H	-1.21154	1.81961	-2.46575
C	3.92958	-3.69469	-0.20323	H	-2.12952	3.25038	-2.98787
C	2.57698	-2.64924	-2.04685	H	-2.76042	2.20043	-1.71151
C	-1.84786	2.64073	-2.11916	H	-1.33723	3.49983	3.16429
C	-1.97941	4.70397	-0.65317	H	-3.07923	3.24122	3.0776
H	4.07485	-0.32512	1.2227	H	-2.30034	4.33115	1.92911
H	3.69369	-1.52927	2.46465	H	-3.73018	2.7105	0.28743
H	3.25376	0.97619	2.97643	H	-4.06969	1.57709	1.59055
H	1.94681	-0.12614	3.37453	H	-3.21245	1.00988	0.15345
H	0.29382	4.22544	1.82917	H	-1.72984	0.03722	1.85228
H	1.42206	3.72236	0.55606	H	-2.47056	0.88587	3.22305
H	0.85627	2.32388	3.19101	H	-0.72691	1.0117	2.94595

Table 7.8: XYZ-coordinates of computed complex **29**.

Atom	x	y	z	Atom	x	y	z
Re	-0.19434	-0.11397	0	H	-4.34273	-0.1177	2.51529
P	-0.53782	-0.40157	2.42575	H	-3.32217	-1.19921	1.56945
P	-0.53782	-0.40157	-2.42575	H	-3.32399	0.53884	1.23971
N	-1.01178	-1.91397	0	C	-2.6669	-0.90421	4.29185
C	-0.515	-2.24688	2.43237	H	-3.58328	-0.50893	4.74759
H	-0.92173	-2.6992	3.34153	H	-1.9146	-0.9645	5.07975
H	0.53502	-2.55019	2.35436	H	-2.89557	-1.9224	3.95662
C	-1.26065	-2.74142	1.19784	C	0.42023	-0.09792	5.15183
H	-2.34233	-2.79445	1.38364	H	-0.43128	0.49435	5.49598
H	-0.95178	-3.77605	0.99162	H	1.2798	0.18888	5.77154
C	-0.515	-2.24688	-2.43237	H	0.21687	-1.15605	5.35442
H	0.53502	-2.55019	-2.35436	C	2.07284	-0.62756	3.39443
H	-0.92173	-2.6992	-3.34153	H	2.87605	-0.20277	4.0095
C	-1.26065	-2.74142	-1.19784	H	2.3851	-0.54941	2.35143
H	-0.95178	-3.77605	-0.99162	H	1.99386	-1.68779	3.65816
H	-2.34233	-2.79445	-1.38364	C	1.06504	1.643	3.45551
C	-2.28327	0.00882	3.11229	H	0.18749	2.27663	3.61189
C	0.77945	0.15096	3.68113	H	1.44241	1.82918	2.44516
C	-2.28327	0.00882	-3.11229	H	1.83626	1.96877	4.16519
C	0.77945	0.15096	-3.68113	C	-2.6669	-0.90421	-4.29185
N	1.78402	-1.00735	0	H	-2.89557	-1.9224	-3.95662
C	4.34541	-2.16298	0	H	-1.9146	-0.9645	-5.07975
C	2.91143	-0.24172	0	H	-3.58328	-0.50893	-4.74759
C	1.95641	-2.34846	0	C	-3.36098	-0.20987	-2.03319
C	3.19687	-2.9553	0	H	-3.32399	0.53884	-1.23971
C	4.19379	-0.78921	0	H	-3.32217	-1.19921	-1.56945
H	1.05335	-2.94561	0	H	-4.34273	-0.1177	-2.51529

Atom	x	y	z	Atom	x	y	z
H	3.25731	-4.03899	0	C	-2.3634	1.47919	-3.54572
H	5.05184	-0.12388	0	H	-2.03876	2.16406	-2.75356
H	5.3335	-2.61383	0	H	-3.4096	1.71994	-3.77339
C	2.62916	1.16407	0	H	-1.78035	1.69033	-4.44687
C	3.37995	2.35359	0	C	0.42023	-0.09792	-5.15183
C	2.43361	3.35403	0	H	0.21687	-1.15605	-5.35442
N	1.19865	2.77801	0	H	1.2798	0.18888	-5.77154
N	1.31505	1.44436	0	H	-0.43128	0.49435	-5.49598
H	4.45464	2.47122	0	C	1.06504	1.643	-3.45551
H	2.53231	4.43087	0	H	1.44241	1.82918	-2.44516
P	-1.55495	1.85284	0	H	0.18749	2.27663	-3.61189
P	-0.43787	3.55582	0	H	1.83626	1.96877	-4.16519
C	-2.3634	1.47919	3.54572	C	2.07284	-0.62756	-3.39443
H	-3.4096	1.71994	3.77339	H	2.3851	-0.54941	-2.35143
H	-2.03876	2.16406	2.75356	H	2.87605	-0.20277	-4.0095
H	-1.78035	1.69033	4.44687	H	1.99386	-1.68779	-3.65816
C	-3.36098	-0.20987	2.03319				

Table 7.9: XYZ-coordinates of computed complex **29** for NMR calculations.

Atom	x	y	z	Atom	x	y	z
Re	-0.27778	-0.07896	0.00014	H	-4.31155	0.10372	2.79774
P	-0.54519	-0.41368	2.45822	H	-3.45761	-1.01454	1.73701
P	-0.54504	-0.41415	-2.45782	H	-3.32275	0.72691	1.49773
N	-1.06454	-1.86069	0.00032	C	-2.61044	-1.00114	4.36631
C	-0.55891	-2.23865	2.42030	H	-3.47004	-0.5996	4.90830
H	-0.96742	-2.68664	3.32432	H	-1.8319	-1.20048	5.09663
H	0.47859	-2.56577	2.34019	H	-2.9277	-1.95404	3.93833
C	-1.32241	-2.69681	1.19103	C	0.50606	-0.3207	5.15853
H	-2.39889	-2.72983	1.38958	H	-0.34938	0.21058	5.56596
H	-1.03015	-3.72753	0.96622	H	1.36953	-0.04848	5.76960
C	-0.55891	-2.23912	-2.41968	H	0.34591	-1.39237	5.29496
H	0.47862	-2.5662	-2.33973	C	2.1116	-0.71713	3.34683
H	-0.96754	-2.68728	-3.32357	H	2.89702	-0.37235	4.02185
C	-1.32217	-2.69716	-1.19020	H	2.45114	-0.51861	2.33461
H	-1.02966	-3.72776	-0.96517	H	2.02725	-1.79522	3.48839
H	-2.39864	-2.73055	-1.38870	C	1.10961	1.53748	3.58328
C	-2.22994	0.00451	3.26554	H	0.24676	2.15243	3.82700
C	0.81996	0.03548	3.69857	H	1.44897	1.80794	2.58236
C	-2.22957	0.00448	-3.26527	H	1.90552	1.80268	4.28297
C	0.81986	0.03486	-3.69843	C	-2.60957	-1.00054	-4.36675
N	1.76168	-0.89195	0.00013	H	-2.92703	-1.95366	-3.93940
C	4.35749	-1.91028	-0.00032	H	-1.83063	-1.19954	-5.09679
C	2.83483	-0.06746	-0.00023	H	-3.46888	-0.59872	-4.90898
C	1.9961	-2.21712	0.00038	C	-3.37982	-0.05607	-2.24915
C	3.25811	-2.75945	0.00010	H	-3.32292	0.72624	-1.49759

Atom	x	y	z	Atom	x	y	z
C	4.13651	-0.55075	-0.00043	H	-3.4578	-1.0151	-1.73749
H	1.12704	-2.8549	0.00082	H	-4.31131	0.10354	-2.79815
H	3.37298	-3.83463	0.00023	C	-2.23225	1.42957	-3.83161
H	4.95727	0.15369	-0.00067	H	-1.95877	2.16552	-3.07371
H	5.36468	-2.30574	-0.00049	H	-3.24507	1.66779	-4.16670
C	2.47737	1.32804	-0.00041	H	-1.57745	1.55584	-4.69089
C	3.1593	2.55583	-0.00098	C	0.50528	-0.32134	-5.15824
C	2.1632	3.4989	-0.00100	H	0.34526	-1.39304	-5.29458
N	0.96866	2.85809	-0.00054	H	1.36839	-0.049	-5.76976
N	1.16008	1.53884	-0.00018	H	-0.3505	0.20978	-5.56523
H	4.21985	2.74056	-0.00133	C	1.10945	1.53685	-3.58323
H	2.20719	4.57579	-0.00136	H	1.44907	1.80734	-2.58239
P	-1.69907	1.81838	-0.00034	H	0.24648	2.15178	-3.82670
P	-0.67936	3.53012	-0.00055	H	1.90516	1.80212	-4.28311
C	-2.23298	1.42929	3.83261	C	2.11164	-0.71775	-3.34712
H	-3.24596	1.66723	4.16742	H	2.45153	-0.51919	-2.33502
H	-1.95927	2.16568	3.07523	H	2.89681	-0.37294	-4.02241
H	-1.57859	1.55516	4.69223	H	2.02729	-1.79584	-3.48863
C	-3.37986	-0.05565	2.24901				

Table 7.10: XYZ-coordinates of computed complex **30**.

Atom	x	y	z	Atom	x	y	z
Re	0.03197	0.36729	0	C	0.71418	2.40038	-2.42855
As	-2.16449	-0.81827	0	H	1.78587	2.20033	-2.33896
As	-1.78426	-3.01211	0	H	0.56716	2.98194	-3.34166
P	-0.13183	0.76235	2.42344	C	-1.86163	1.19072	-3.14576
P	-0.13183	0.76235	-2.42344	C	-2.77014	1.8275	-2.07487
N	0.09386	2.32838	0	H	-3.65212	2.24156	-2.57827
N	2.26294	0.38003	0	H	-2.29718	2.64429	-1.52595
N	0.77983	-1.69716	0	H	-3.13539	1.10227	-1.34703
N	0.15831	-2.8757	0	C	-1.76182	2.22107	-4.28718
C	0.25517	3.18094	1.20194	H	-2.74447	2.30265	-4.7672
H	-0.68495	3.71072	1.39831	H	-1.04354	1.96064	-5.06437
H	0.99398	3.96505	0.99056	H	-1.51365	3.21843	-3.90863
C	0.71418	2.40038	2.42855	C	-2.57417	-0.07319	-3.65148
H	0.56716	2.98194	3.34166	H	-2.60564	-0.86311	-2.89299
H	1.78587	2.20033	2.33896	H	-2.12039	-0.4846	-4.5562
C	-1.86163	1.19072	3.14576	H	-3.61266	0.18053	-3.89678
C	-2.77014	1.8275	2.07487	C	0.81163	-0.31838	-3.67216
H	-3.13539	1.10227	1.34703	C	0.64488	0.08482	-5.14308
H	-2.29718	2.64429	1.52595	H	-0.37054	-0.05657	-5.51864
H	-3.65212	2.24156	2.57827	H	1.30134	-0.54783	-5.75347
C	-1.76182	2.22107	4.28718	H	0.9433	1.12395	-5.31948
H	-2.74447	2.30265	4.7672	C	0.37529	-1.77973	-3.47465
H	-1.51365	3.21843	3.90863	H	-0.68681	-1.93941	-3.6725

Atom	x	y	z	Atom	x	y	z
H	-1.04354	1.96064	5.06437	H	0.5838	-2.12568	-2.45895
C	-2.57417	-0.07319	3.65148	H	0.93895	-2.41721	-4.16713
H	-3.61266	0.18053	3.89678	C	2.31219	-0.22512	-3.35184
H	-2.12039	-0.4846	4.5562	H	2.5276	-0.45462	-2.30899
H	-2.60564	-0.86311	2.89299	H	2.73251	0.75744	-3.58924
C	0.81163	-0.31838	3.67216	H	2.84655	-0.96	-3.96571
C	2.31219	-0.22512	3.35184	C	2.99498	1.5117	0
H	2.84655	-0.96	3.96571	H	2.44368	2.43968	0
H	2.73251	0.75744	3.58924	C	4.3747	1.52655	0
H	2.5276	-0.45462	2.30899	H	4.89506	2.47767	0
C	0.37529	-1.77973	3.47465	C	5.06614	0.31711	0
H	-0.68681	-1.93941	3.6725	H	6.15039	0.29451	0
H	0.93895	-2.41721	4.16713	C	4.33463	-0.85408	0
H	0.5838	-2.12568	2.45895	H	4.82041	-1.82353	0
C	0.64488	0.08482	5.14308	C	2.94292	-0.7915	0
H	-0.37054	-0.05657	5.51864	C	2.09701	-1.95278	0
H	0.9433	1.12395	5.31948	C	2.32893	-3.33629	0
H	1.30134	-0.54783	5.75347	H	3.27291	-3.86128	0
C	0.25517	3.18094	-1.20194	C	1.06528	-3.88225	0
H	0.99398	3.96505	-0.99056	H	0.73654	-4.91122	0
H	-0.68495	3.71072	-1.39831				

Table 7.11: XYZ-coordinates of computed compound P_2.

Atom	x	y	z	Atom	x	y	z
P	0	0	0.9478	P	0	0	-0.9478

Table 7.12: XYZ-coordinates of computed compound P_2H_2.

Atom	x	y	z	Atom	x	y	z
P	0	1.02017	0	P	0	-1.02017	0
H	1.42934	1.1292	0	H	-1.42934	-1.1292	0

Table 7.13: XYZ-coordinates of computed compound P_2H_4.

Atom	x	y	z	Atom	x	y	z
P	0	1.3155	0	P	0	-1.13155	0
H	0.98088	1.23025	1.03186	H	0.98088	1.23025	-1.03186
H	-0.98088	-1.23025	1.03186	H	-0.9888	-1.23025	-1.03186

7.5.2 Oxygenation of a Terminal Re Phosphide Complex - Computational Details

DFT calculations were carried out with the ORCA program package using the PBE and PBE0 functionals.[304],[318],[326] Ahlrichs' basis sets def2-SVP (for geometry optimization

and frequency calculation) and def2-TZVP (for single-point energies) were used with a full basis for all elements but Os for which the Stuttgart-Dresden 60 electron core potential was chosen to replace the inner shell 1s-4f orbitals.[307],[308] The RI-J (PBE) approximation in combination with the corresponding auxiliary basis sets of Alrichs was utilized to reduce computational costs in the geometry optimization and frequency calculations.[327]–[329] Grimme's model (D3) with Becke-Johnson damping was used to account for dispersion with the PBE or PBE0 functionals.[306],[330] No symmetry restraints were imposed and the optimized structures were defined as minima (no negative eigenvalues) by vibrational analyses. NBO analysis of **18**, **19** and **20** was carried out with NBO 6.0.[4] Geometries were analyzed and visualized with Avogadro, molecular orbitals were visualized with Chimera and for NBO/NLMO visualization, Jmol (http://www.jmol.org) was used. **34** was computed with and without the $[K(C_{12}H_{24}O_6)]$ cation. No significant structural changes were observed. Therefore, the smaller model was utlized to reduce computational costs.

Table 7.14: XYZ-coordinates of computed complex $[Re(L^1)(\kappa N^2\text{-PyrPz})(PO)]$.

Atom	x	y	z	Atom	x	y	z
C	-4.02244	-2.23688	1.06678	H	-6.10793	-4.46189	-1.27152
C	-3.68536	-2.45207	-0.29462	H	-6.84313	-4.17901	1.119
N	-4.43525	-3.24214	-1.10074	H	-3.38526	-1.58379	1.68
C	-5.52112	-3.82701	-0.5813	H	-5.4427	-2.70159	2.64284
C	-5.93692	-3.67474	0.75232	H	-2.49915	-2.47226	-3.0411
C	-5.15987	-2.85626	1.58967	H	-0.1893	-0.87845	-3.04419
C	-2.50537	-1.82333	-0.88872	H	2.12375	-1.5301	-2.63196
N	-1.6796	-1.02105	-0.16059	H	1.75343	-3.15808	-2.00539
N	-0.70005	-0.60349	-0.97677	H	3.23011	-2.8966	-2.98909
C	-0.88589	-1.1207	-2.23446	H	5.24612	-0.9476	-0.55195
C	-2.03775	-1.91214	-2.22282	H	4.07642	-0.10579	-1.62442
Re	0.88808	0.58375	-0.16496	H	5.03683	-1.47036	-2.24438
N	1.74369	1.29855	1.46305	H	4.84754	-3.7314	-1.25126
C	2.67852	0.55254	2.33237	H	3.43293	-4.23258	-0.28689
C	3.41907	-0.55352	1.58844	H	4.71714	-3.21595	0.4551
P	2.26199	-1.3487	0.36024	H	3.09342	-4.04589	1.78788
C	3.41878	-2.12824	-0.96502	H	1.66288	-4.27166	2.83077
C	4.4939	-1.09445	-1.3518	H	2.72079	-2.86134	3.08171
P	1.86296	1.19457	-1.98774	H	-0.23026	-2.75961	2.83301
P	-0.53195	2.53204	0.1667	H	-0.48099	-1.53466	1.55496
C	-1.01878	3.64499	-1.32194	H	0.71519	-1.24597	2.88185
C	0.25724	4.29301	-1.8912	H	1.33983	-4.32629	-0.17423
C	1.35683	-2.72343	1.35363	H	0.01532	-3.11995	-0.3533
C	0.28683	-2.00612	2.20012	H	-0.04223	-4.33348	0.95589
C	0.6376	-3.67181	0.37796	H	-1.58201	5.44413	-0.16546
C	2.27575	-3.51097	2.30167	H	-2.98082	4.41844	-0.63919

---

[4]E. D. Glendening, J. K. Badenhoop, A. E. Reed, J. E. Carpenter, J. A. Bohmann, C. M. Morales, C. R. Landis, F. Weinhold, *NBO 6.0*, Theoretical Chemical Institute, University of Wisconsin, Madison, WI, USA, **2013**.

Atom	x	y	z	Atom	x	y	z
C	-2.05075	2.28779	1.33099	H	-2.14713	5.41268	-1.85945
C	-3.27423	1.84293	0.51013	H	0.00509	4.7782	-2.85722
C	0.6607	3.53859	1.17944	H	1.0697	3.5698	-2.09791
C	1.42612	2.59465	2.10137	H	0.65952	5.08126	-1.22449
C	-1.70338	1.13769	2.29787	H	-0.94957	1.91315	-2.67767
C	-2.37588	3.5451	2.15541	H	-1.86807	3.32762	-3.29992
C	4.13322	-3.39673	-0.46946	H	-2.58494	2.26134	-2.0528
C	2.57542	-2.44931	-2.21166	H	-1.56137	3.8006	2.86191
C	-1.64252	2.72897	-2.39234	H	-3.28038	3.3403	2.76703
C	-1.98813	4.78319	-0.95796	H	-2.59106	4.43563	1.53807
H	4.22059	-0.09699	0.97695	H	-3.66376	2.64283	-0.146
H	3.89342	-1.26973	2.28805	H	-4.08967	1.56685	1.21215
H	3.41562	1.27018	2.75882	H	-3.04388	0.94386	-0.09451
H	2.12224	0.14223	3.2095	H	-1.55698	0.1975	1.73412
H	0.19169	4.36676	1.74566	H	-2.56086	0.98856	2.98968
H	1.36621	3.97776	0.44751	H	-0.8121	1.34412	2.92018
H	0.86367	2.42478	3.05058	O	3.00486	1.98731	-2.61105
H	2.3863	3.06893	2.40889				

Table 7.15: XYZ-coordinates of computed complex **34**+K($C_{12}H_{24}O_6$).

Atom	x	y	z	Atom	x	y	z
C	-1.75406	0.10323	-1.49309	H	4.92202	-0.36076	1.24084
C	-1.46407	-1.29578	-0.93455	Re	1.47914	-0.22992	-1.02839
N	-0.04567	-1.57465	-0.77371	N	3.19076	0.94199	-1.67028
H	-1.9287	-2.07588	-1.58644	C	3.68959	2.05589	-1.05682
H	-1.97773	-1.39965	0.05665	C	4.75604	2.79779	-1.55968
C	0.16138	-2.9853	-0.4783	H	3.1654	2.34606	-0.13186
C	1.59826	-3.32783	-0.06574	C	5.37075	2.40951	-2.76664
H	-0.10539	-3.59688	-1.37682	H	5.09296	3.68553	-1.00471
H	-0.55287	-3.30369	0.32129	C	4.90106	1.25343	-3.39123
P	2.48244	-1.81581	0.55877	H	6.20205	2.98667	-3.19753
H	2.166	-3.60454	-0.97826	C	3.83878	0.52054	-2.82565
H	1.63168	-4.17678	0.64626	H	5.3542	0.88041	-4.32035
P	-0.28709	0.71027	-2.47127	N	2.1619	-2.59954	-3.09446
H	-1.84361	0.80541	-0.64462	N	2.38527	-1.36279	-2.61895
H	-2.69949	0.12259	-2.07255	C	3.02084	-2.7772	-4.13504
C	-0.48814	2.65229	-2.57109	C	3.82016	-1.63897	-4.33877
C	-1.3023	3.16556	-1.37055	H	3.01896	-3.72555	-4.68892
H	-0.93454	2.80228	-0.39396	C	3.38398	-0.74785	-3.3324
H	-1.23234	4.27452	-1.3447	H	4.60822	-1.48312	-5.08333
H	-2.37421	2.89325	-1.45182	P	0.76526	1.22596	0.58605
C	0.93821	3.22482	-2.49212	O	1.58712	2.45605	1.10362
H	1.60191	2.81387	-3.27956	O	-0.60879	1.15126	1.32543
H	0.90192	4.32985	-2.6136	K	-0.18661	3.14797	3.07879
H	1.39862	3.00091	-1.51346	O	-0.22834	5.21579	1.2163

C	-1.16575	3.20667	-3.83385	O	-2.54271	4.35526	2.36299
H	-2.22211	2.89114	-3.92271	O	-0.20087	1.26469	5.18798
H	-1.15869	4.31652	-3.76512	O	1.85348	5.42319	3.34419
H	-0.63309	2.93507	-4.76449	O	1.79894	3.1169	4.93656
C	-0.60142	-0.02829	-4.23201	O	-2.71568	2.00843	3.89614
C	-0.68	-1.55963	-4.06441	C	1.09131	5.69199	0.99036
H	-1.65131	-1.85999	-3.62477	C	1.76579	6.29231	2.22851
H	-0.62259	-2.02594	-5.0714	H	1.0988	6.4633	0.17969
H	0.13901	-1.98909	-3.46002	H	1.64173	4.79822	0.63085
C	-1.92159	0.39616	-4.90735	H	1.20184	7.18093	2.58389
H	-2.14063	-0.32653	-5.7219	H	2.77902	6.65432	1.92525
H	-1.88738	1.3977	-5.36592	C	2.88427	4.44162	3.25491
H	-2.78333	0.35997	-4.20917	C	3.02424	3.7484	4.59722
C	0.59849	0.33983	-5.12003	H	3.86121	4.92875	3.01305
H	0.46805	-0.10463	-6.12991	H	2.66044	3.68845	2.46319
H	1.54421	-0.05055	-4.70179	H	3.30567	4.48131	5.39173
H	0.70824	1.43563	-5.24999	H	3.84576	2.99731	4.511
C	1.95864	-1.6933	2.42574	C	-1.20972	6.16578	1.57868
C	0.41867	-1.74789	2.47967	C	-2.56612	5.48214	1.50961
H	0.03923	-2.7567	2.22861	H	-1.04476	6.55355	2.61316
H	-0.06457	-1.00484	1.82014	H	-1.21032	7.04284	0.88572
H	0.10184	-1.52927	3.52241	H	-2.77333	5.16621	0.45874
C	2.43895	-0.35894	3.02994	H	-3.35583	6.21287	1.81254
H	3.50564	-0.3895	3.31898	C	-3.72656	3.57088	2.37816
H	2.30885	0.50109	2.34478	C	-3.3761	2.11783	2.64073
H	1.84082	-0.13724	3.93856	H	-4.24623	3.62189	1.39284
C	2.47785	-2.852	3.29386	H	-4.42994	3.95619	3.15575
H	3.5758	-2.83467	3.42868	H	-2.71286	1.73028	1.83152
H	2.02461	-2.76789	4.30501	H	-4.32198	1.52132	2.64126
H	2.1867	-3.84175	2.8894	C	-2.301	0.67881	4.18513
C	4.33822	-2.35785	0.53277	C	-1.47452	0.69225	5.45544
C	4.55702	-3.83336	0.9124	H	-1.69893	0.26921	3.341
H	4.05032	-4.51272	0.19998	H	-3.18763	0.01507	4.33777
H	4.21729	-4.08658	1.93109	H	-1.35977	-0.3501	5.83879
H	5.64427	-4.05896	0.8591	H	-2.01271	1.28707	6.23171
C	4.85595	-2.1608	-0.90015	C	1.89801	2.13566	5.94745
H	5.91829	-2.48527	-0.94185	C	0.50176	1.68512	6.34186
H	4.8156	-1.10002	-1.2001	H	2.40553	2.53805	6.85849
H	4.2953	-2.75424	-1.64598	H	2.49732	1.26683	5.58322
C	5.14998	-1.42643	1.44874	H	-0.04356	2.52546	6.83898
H	6.23426	-1.58308	1.2593	H	0.59695	0.85775	7.08744
H	4.97092	-1.61852	2.52374				

Table 7.16: XYZ-coordinates of computed complex **34**.

Atom	x	y	z	Atom	x	y	z
C	-0.9394	1.51121	-2.05382	H	-0.67582	-0.13011	1.48768
C	-1.40362	0.11101	-1.63422	H	-1.19297	-0.79297	3.06399
N	-0.3199	-0.74823	-1.18994	C	1.48625	-0.74943	3.19649
H	-1.95957	-0.38336	-2.47116	H	2.37391	-1.24604	3.62978
H	-2.15357	0.22018	-0.80709	H	1.84305	0.13114	2.62665
C	-0.80779	-2.1011	-0.98776	H	0.87353	-0.36688	4.04118
C	0.21221	-3.02867	-0.31623	C	0.37251	-2.99495	3.16146
H	-1.10219	-2.54752	-1.97355	H	1.30347	-3.47678	3.51627
H	-1.75111	-2.07336	-0.38376	H	-0.22085	-2.72958	4.06404
P	1.47204	-2.03116	0.6288	H	-0.21752	-3.74261	2.59302
H	0.80957	-3.52559	-1.10925	C	2.87352	-3.34442	0.93543
H	-0.28569	-3.80716	0.29805	C	2.34727	-4.7703	1.17936
P	0.84237	1.45079	-2.59438	H	1.78822	-5.14924	0.30156
H	-0.93322	2.14506	-1.14663	H	1.69662	-4.85924	2.06676
H	-1.61277	1.95936	-2.81394	H	3.21441	-5.45147	1.33135
C	1.47788	3.30483	-2.50028	C	3.74618	-3.38243	-0.32772
C	0.61869	4.11191	-1.50851	H	4.54146	-4.14805	-0.189
H	0.4983	3.62925	-0.51957	H	4.23817	-2.41059	-0.50471
H	1.10651	5.09777	-1.34385	H	3.17469	-3.65006	-1.23602
H	-0.39531	4.30506	-1.9143	C	3.77238	-2.89081	2.09746
C	2.9245	3.23066	-1.98001	H	4.68719	-3.52337	2.11792
H	3.56189	2.57156	-2.60309	H	3.28421	-2.98658	3.0858
H	3.37051	4.24967	-1.98615	H	4.09568	-1.83797	1.96801
H	2.95686	2.85422	-0.94176	Re	1.64418	-0.18896	-0.96111
C	1.48212	4.09197	-3.82054	N	3.77719	0.139	-1.08667
H	0.46357	4.26023	-4.21737	C	4.52258	0.93048	-0.25428
H	1.92397	5.09294	-3.61981	C	5.88893	1.14395	-0.42338
H	2.09946	3.61765	-4.60696	H	3.94549	1.41647	0.55624
C	0.70501	0.95059	-4.46772	C	6.57156	0.53309	-1.49585
C	-0.03927	-0.39942	-4.50967	H	6.40956	1.80172	0.28854
H	-1.12376	-0.26068	-4.33064	C	5.83655	-0.30806	-2.33388
H	0.07074	-0.82752	-5.53078	H	7.64678	0.69979	-1.66209
H	0.34814	-1.14752	-3.79483	C	4.46147	-0.51484	-2.10825
C	-0.10085	1.91158	-5.36516	H	6.31099	-0.83926	-3.17217
H	-0.39385	1.36468	-6.28853	N	1.76758	-2.6134	-3.09113
H	0.46718	2.80091	-5.68425	N	2.3573	-1.59119	-2.44475
H	-1.03972	2.25152	-4.88124	C	2.70601	-3.13801	-3.92687
C	2.12781	0.77204	-5.02202	C	3.92827	-2.45249	-3.82068
H	2.07861	0.44083	-6.08303	H	2.44838	-3.99113	-4.57001
H	2.68859	0.0053	-4.45578	C	3.66402	-1.46273	-2.84388
H	2.7126	1.71378	-4.99366	H	4.86856	-2.64641	-4.34838
C	0.62985	-1.71276	2.35117	P	1.2292	1.4653	0.63862
C	-0.74198	-1.06089	2.0833	O	2.36905	2.16053	1.41552

| H | -1.43735 | -1.76379 | 1.58461 | O | -0.19227 | 1.9805 | 0.946 |

Table 7.17: XYZ-coordinates of computed compound PO_2^-.

Atom	x	y	z	Atom	x	y	z
P	1.0000	0.96031	0.96031	O	1.00000	2.45798	0.58170
O	1.00000	0.58170	2.457982				

7.5.3 Interconversion of Os PHMes* and PMes* Complexes by PCET - Computational Details

DFT calculations were carried out with the ORCA program package using the PBE and PBE0 functionals.[304],[318],[326] Ahlrichs' basis sets def2-SVP (for geometry optimization and frequency calculation) and def2-TZVP (for single-point energies) were used with a full basis for all elements but Os for which the Stuttgart-Dresden 60 electron core potential was chosen to replace the inner shell 1s-4f orbitals.[307],[308] The RI-J (PBE) approximation in combination with the corresponding auxiliary basis sets of Alrichs was utilized to reduce computational costs in the geometry optimization and frequency calculations.[327]–[329] Grimme's model (D3) with Becke-Johnson damping was used to account for dispersion with the PBE or PBE0 functionals.[306],[330] No symmetry restraints were imposed and the optimized structures were defined as minima (no negative eigenvalues) by vibrational analyses. Geometries were analyzed and visualized with Avogadro, molecular orbitals were visualized with Chimera.[333],[334]

BDE Calculations

Geometry optimizations were carried out with the Turbomole program package coupled to the PQS Baker optimizer via the BOpt package, at the spin unrestricted ri-DFT level using the BP86 functional and the resolution-of-identity (ri) method.[357]–[362] The def2-TZVP basis set (small-core pseudopotentials on Os) and Grimme's version 3 dispersion corrections (disp3, "zero damping") for all geometry optimizations was used.[307],[308],[363],[364] Scalar relativistic effects were included implicitly through the use of the Os ECPs. All minima (no imaginary frequencies) were characterized by calculating the Hessian matrix. ZPE and gas-phase thermal corrections (entropy and enthalpy, 298 K, 1 bar) from these analyses were calculated. Spectroscopic properties and BDEs were evaluated using the full atom model of the complexes. The calculated BDEs were calibrated (taking advantage of internal error cancelation) against the know experimental BDE of propene, using the Hess cycle shown in Scheme 7.1.

EPR Property Calculations

EPR parameters of **38** were calculated with the ADF program system at the B3LYP / ZORA / QZ4P level, using the coordinates from the structure optimized in Turbomole as input.[365]–[370] Unrestricted SPINORBIT ZORA COLLINEAR calculations were used to compute the SOC corrected HFI-tensors and Zeeman corrected g-tensors.

Scheme 7.1: Calibration of the calculated BDE values.

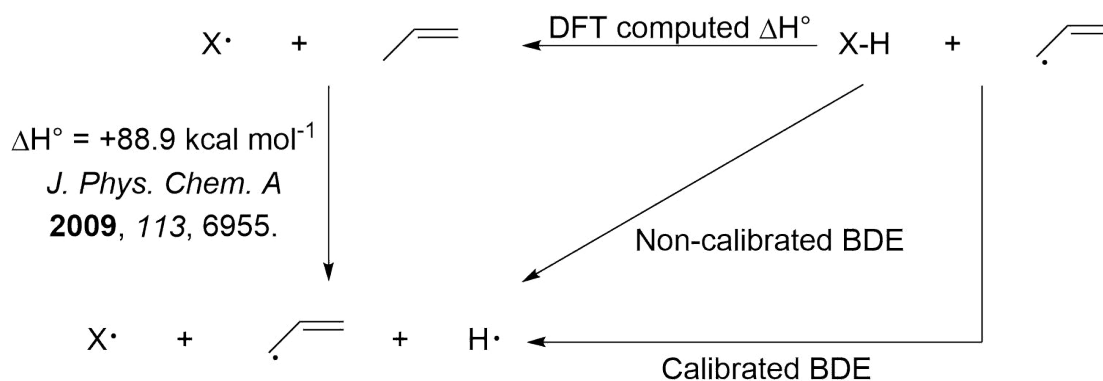## An Isolable Terminal Chlorophosphinidene Complex - Computational Details

DFT calculations were carried out with the ORCA program package using the PBE and PBE0 functionals.[304],[318],[326] Ahlrichs' basis sets def2-SVP (for geometry optimization and frequency calculation) and def2-TZVP (for single-point energies) were used with a full basis for all elements but Os for which the Stuttgart-Dresden 60 electron core potential was chosen to replace the inner shell 1s-4f orbitals.[307],[308] The RI-J (PBE) approximation in combination with the corresponding auxiliary basis sets of Alrichs was utilized to reduce computational costs in the geometry optimization and frequency calculations.[327]–[329] Grimme's model (D3) with Becke-Johnson damping was used to account for dispersion with the PBE or PBE0 functionals.[306],[330] No symmetry restraints were imposed and the optimized structures were defined as minima (no negative eigenvalues, one negative eigenvalue for transition states) by vibrational analyses. Geometries were analyzed and visualized with Cylview[5] and molecular orbitals, spindensities and difference densities were visualized with Chimera.[333],[334]

Table 7.18: XYZ-coordinates of computed complex **44$^{\text{tBu}}$**.

Atom	x	y	z	Atom	x	y	z
Os	3.12227	8.55294	10.92059	C	1.75915	9.69305	7.88058
Cl	3.73634	10.85463	11.32611	H	1.69428	10.27049	6.93455
Cl	2.11686	5.62267	12.96935	H	1.70109	8.61494	7.63061
P	0.81745	8.97699	10.34799	H	2.74925	9.89711	8.32569
P	5.38653	7.76907	10.61123	C	3.70984	5.89521	9.63594
P	2.77429	7.73151	12.82215	H	3.40991	4.93885	9.16651
N	2.69586	6.76738	9.93482	C	5.03423	6.16606	9.87697
C	1.40069	6.46141	9.60048	H	5.80751	5.42397	9.63316
H	1.23019	5.45651	9.17095	C	6.46714	7.46089	12.1678
C	0.35875	7.33878	9.76412	C	6.4132	8.70222	13.07373
H	-0.66523	7.04976	9.48996	H	6.81552	9.60715	12.58424

---

[5]Cylview, V 1.0b (build 562), C. Y. Legault, Université de Sherbrooke, Canada, 2009 (http://www.cylview.org).

C	-0.38267	9.48592	11.75557	H	7.01127	8.51299	13.98984
C	-1.73478	9.98795	11.2195	H	5.37335	8.9294	13.37826
H	-1.64172	10.93511	10.65537	C	7.92006	7.11803	11.793
H	-2.40588	10.1838	12.08261	H	8.44899	7.9582	11.30593
H	-2.23565	9.23633	10.57653	H	7.97884	6.22864	11.13349
C	0.29439	10.57626	12.60364	H	8.4762	6.87453	12.72281
H	0.57395	11.46663	12.01097	C	5.87733	6.25369	12.91053
H	1.22279	10.19958	13.07279	H	4.81217	6.39275	13.18292
H	-0.39936	10.8983	13.4093	H	6.43734	6.10357	13.85728
C	-0.64316	8.24046	12.61348	H	5.93751	5.32439	12.31178
H	-1.2062	7.46406	12.06074	C	6.37309	8.76242	9.29861
H	-1.23259	8.5345	13.50732	C	5.3139	9.22418	8.28301
H	0.28923	7.76673	12.98006	H	5.81595	9.70179	7.41468
C	0.6232	10.12536	8.82345	H	4.64554	9.9792	8.74107
C	-0.71074	9.91265	8.08895	H	4.70705	8.37818	7.90092
H	-0.67983	10.47448	7.13161	C	7.02655	10.00752	9.91879
H	-1.58547	10.27745	8.65407	H	7.43191	10.64114	9.10048
H	-0.87071	8.84477	7.84044	H	7.8703	9.75928	10.59015
C	0.82689	11.59239	9.22816	H	6.28153	10.60918	10.4788
H	0.88306	12.21957	8.3132	C	7.39979	7.88269	8.56805
H	1.77179	11.72207	9.79601	H	6.91349	7.01564	8.07906
H	-0.01084	11.98054	9.84088	H	8.20092	7.505	9.22765
H	7.88317	8.48782	7.7712				

Table 7.19: XYZ-coordinates of computed complex **44^{iPr}**.

Atom	x	y	z	Atom	x	y	z
Os	3.14555	8.47126	10.82874	C	3.70073	5.84781	9.49445
Cl	3.83829	10.74839	10.9717	H	3.36691	4.92239	8.98864
Cl	3.77012	6.21721	13.70386	C	5.00479	6.02942	9.85072
P	0.86735	8.991	10.30698	H	5.75248	5.24604	9.66161
P	5.37418	7.64054	10.58959	C	6.54009	7.32758	12.01785
P	2.57548	7.78329	12.75991	C	6.59778	8.52235	12.97695
N	2.71608	6.79302	9.74135	C	7.92344	6.80728	11.6127
C	1.40857	6.52907	9.37497	H	8.53562	7.59002	11.12166
H	1.23467	5.55861	8.87364	H	7.86245	5.93535	10.93109
C	0.37569	7.39423	9.61026	H	8.47609	6.48098	12.51868
H	-0.64519	7.14334	9.29123	H	5.99007	6.51344	12.53598
C	-0.34945	9.39478	11.67186	C	6.27032	8.60483	9.22522
C	-1.79814	9.56677	11.20766	H	5.40554	8.9622	8.62188
H	-1.93157	10.5079	10.63726	C	7.00629	9.83908	9.75855
H	-2.47099	9.61997	12.08894	H	7.34085	10.4673	8.90654
H	-2.14479	8.72563	10.57428	H	7.91261	9.55847	10.33196
C	0.13357	10.55351	12.55468	H	6.34693	10.45821	10.39844
H	-0.27177	8.45608	12.26679	C	7.15063	7.74102	8.31422
C	0.70042	10.215	8.87585	H	6.58955	6.88709	7.88821

C	-0.49376	9.95679	7.94987	H	8.03448	7.34113	8.84773
H	-0.4292	10.62436	7.06537	H	7.52615	8.35663	7.4699
H	-1.45969	10.1646	8.45074	H	0.1355	11.5175	12.01169
H	-0.5142	8.9127	7.58318	H	1.1616	10.37862	12.92669
C	0.78733	11.67397	9.33612	H	-0.53856	10.65868	13.43085
H	0.90531	12.33572	8.45318	H	7.12389	9.39085	12.53713
H	1.65513	11.83839	10.00639	H	7.13611	8.23267	13.90285
H	-0.13893	11.98846	9.85864	H	5.58111	8.85332	13.26284
H	1.63003	9.98146	8.30918				

Table 7.20: XYZ-coordinates of computed tolane.

Atom	x	y	z	Atom	x	y	z
C	-6.05987	2.49433	0.03129	C	-1.22817	1.50396	0.05189
C	-4.66256	2.56505	0.03318	C	0.19432	1.57197	0.05535
C	-6.70788	1.24771	0.0437	C	0.85903	2.82621	0.04121
H	-6.65099	3.42265	0.01981	C	2.25663	2.88744	0.04522
C	-5.94634	0.06701	0.05819	H	0.25925	3.7477	0.02695
H	-7.8075	1.1957	0.04199	C	3.02001	1.70791	0.06322
C	-4.54857	0.12612	0.06028	H	2.75789	3.86732	0.03408
H	-6.44926	-0.91208	0.06812	C	2.37386	0.46044	0.07721
C	-3.88197	1.37934	0.04769	H	4.11955	1.76158	0.06648
H	-3.94984	-0.79612	0.07171	C	0.97665	0.38754	0.07341
H	-4.15176	3.53887	0.02327	H	2.96642	-0.46695	0.09141
C	-2.45943	1.44573	0.04953	H	0.46693	-0.58683	0.0846

Table 7.21: XYZ-coordinates of computed complex **46ᵗᴮᵘ**.

Atom	x	y	z	Atom	x	y	z
C	-3.28673	3.00663	1.21724	H	-0.08081	5.68081	-1.79696
C	-3.91743	1.79105	1.29631	H	0.25102	3.92341	-1.61885
P	-1.71479	2.98676	0.33577	H	0.59731	5.05863	-0.26491
H	-3.67586	3.87621	1.76425	C	-0.37036	2.90069	1.72827
N	-3.46161	0.67251	0.64016	C	-0.18523	4.23198	2.47145
H	-4.82894	1.66204	1.91045	H	-1.14063	4.61795	2.87882
C	-4.07602	-0.53871	0.82794	H	0.2766	5.01484	1.84097
C	-3.67528	-1.69069	0.19554	H	0.49604	4.06295	3.3335
P	-2.25005	-1.53552	-0.8958	C	0.97251	2.44905	1.12873
H	-4.2125	-2.63335	0.37183	H	1.69317	2.24885	1.95051
C	-0.77583	-2.3026	0.06982	H	0.87796	1.53292	0.51448
C	-2.62919	-2.57559	-2.45258	H	1.41497	3.22104	0.47182
C	-0.48439	-1.23425	1.13539	C	-0.87279	1.86498	2.75057
H	0.36745	-1.54327	1.77911	H	-1.7438	2.24756	3.31568
H	-0.17895	-0.26917	0.66849	H	-1.18242	0.91837	2.27527
H	-1.36287	-1.05981	1.78698	H	-0.0589	1.63796	3.47152
C	-1.13142	-3.61139	0.78937	Os	-1.94793	0.85634	-0.79148
H	-0.30376	-3.88095	1.48063	Cl	0.09973	1.02313	-2.08926
H	-2.05202	-3.49782	1.39609	P	-3.40765	1.09573	-2.35923
H	-1.2723	-4.46069	0.09696	Cl	-5.49215	1.28229	-1.83877
C	0.45486	-2.46339	-0.8321	C	-0.9152	-0.10723	-6.56181
H	1.34117	-2.69042	-0.20137	C	-1.41153	0.70924	-5.5358
H	0.66743	-1.5331	-1.39863	C	-1.78262	-0.94483	-7.28215
H	0.34008	-3.30096	-1.54686	H	0.15982	-0.09221	-6.7977
C	-1.61584	-2.19857	-3.54431	C	-3.15281	-0.97077	-6.9721
H	-1.55022	-1.10412	-3.67851	H	-1.38861	-1.58201	-8.08879
H	-1.92377	-2.64152	-4.51423	C	-3.65607	-0.16026	-5.94485

H	-0.59875	-2.56398	-3.31278	H	-3.83419	-1.62575	-7.53665
C	-4.0533	-2.20929	-2.90262	C	-2.78912	0.69016	-5.22758
H	-4.81475	-2.51067	-2.15788	H	-4.72708	-0.17498	-5.69181
H	-4.27212	-2.71641	-3.86569	H	-0.73717	1.34221	-4.93995
H	-4.17336	-1.11952	-3.06937	C	-3.31178	1.55756	-4.15433
C	-2.58539	-4.08659	-2.17557	C	-3.84006	2.73313	-3.97719
H	-2.92353	-4.62641	-3.08613	C	-4.32781	4.0169	-4.31683
H	-3.25831	-4.38551	-1.34663	C	-3.47913	5.00344	-4.89897
H	-1.56426	-4.44313	-1.94672	C	-3.97512	6.2755	-5.19629
C	-1.55222	4.64119	-0.58704	H	-2.42994	4.74855	-5.10521
C	-2.47618	4.48697	-1.79733	C	-5.32232	6.59493	-4.94485
H	-2.52171	5.44232	-2.35877	H	-3.30547	7.02759	-5.64153
H	-2.10021	3.70076	-2.47833	C	-6.17192	5.62684	-4.37986
H	-3.51055	4.21851	-1.50266	H	-5.70783	7.59563	-5.19024
C	-2.02925	5.85095	0.23326	C	-5.68643	4.35705	-4.05339
H	-1.98659	6.75342	-0.41432	H	-7.22577	5.87167	-4.17713
H	-1.41057	6.05332	1.12386	H	-6.33663	3.60368	-3.58618
H	-3.08326	5.73444	0.55379	H	-4.93015	-0.55098	1.53181
C	-0.10957	4.82735	-1.08561				

Table 7.22: XYZ-coordinates of computed complex **46^{iPr}**.

Atom	x	y	z	Atom	x	y	z
C	-3.51603	2.33248	0.5367	C	-0.59328	2.64652	0.72523
C	-3.98879	1.04675	0.4438	C	-0.71536	3.60109	1.91216
P	-2.05293	2.66912	-0.46187	H	-1.6164	3.36661	2.51642
H	-4.00447	3.06288	1.19573	H	-0.78181	4.65983	1.59312
N	-3.43098	0.10517	-0.38993	H	0.16936	3.5089	2.57864
H	-4.85572	0.7149	1.04729	H	0.27006	2.9294	0.08502
C	-3.95406	-1.16518	-0.46486	C	-0.39988	1.18858	1.16896
C	-3.42871	-2.14086	-1.27605	H	-1.29782	0.79763	1.69003
P	-1.91038	-1.67928	-2.14145	H	-0.17631	0.52567	0.29911
H	-3.88808	-3.13949	-1.31293	H	0.46575	1.09686	1.85915
C	-0.52227	-2.58377	-1.23718	Os	-1.87205	0.64844	-1.66357
C	-2.06942	-2.28358	-3.90547	Cl	0.27284	1.17438	-2.65112
H	-0.50595	-2.0057	-0.28431	P	-3.18107	1.13746	-3.30463
C	-0.8204	-4.04469	-0.88579	Cl	-4.76091	2.5624	-2.98811
H	-0.02292	-4.44353	-0.22287	C	-3.05572	-0.43932	-8.45475
H	-1.78654	-4.14999	-0.35413	C	-2.64293	0.42292	-7.43157
H	-0.85001	-4.68789	-1.78741	C	-4.11882	-1.335	-8.24198
C	0.83094	-2.39883	-1.93225	H	-2.54006	-0.41786	-9.42682
H	1.00222	-1.34369	-2.22848	C	-4.77445	-1.3601	-6.99975
H	0.90312	-3.03164	-2.83914	H	-4.4379	-2.01222	-9.04864
H	1.65172	-2.70767	-1.25098	C	-4.3635	-0.50041	-5.97184
C	-0.9493	-1.74862	-4.80566	H	-5.61464	-2.05071	-6.83171
H	-0.70283	-0.69239	-4.57562	C	-3.29421	0.39393	-6.17867

Atom	x	y	z	Atom	x	y	z
H	-0.01854	-2.33738	-4.68711	H	-4.8739	-0.50137	-4.99464
H	-1.2585	-1.81339	-5.86926	H	-1.80541	1.12043	-7.5833
H	-3.00633	-1.75185	-4.18309	C	-2.85215	1.29577	-5.11192
C	-2.31065	-3.78441	-4.08467	C	-2.21708	2.40929	-4.90265
H	-2.61882	-3.99007	-5.13169	C	-1.6078	3.67817	-4.9677
H	-3.11068	-4.16766	-3.42051	C	-0.19186	3.8315	-5.00069
H	-1.3912	-4.37316	-3.89371	C	0.36922	5.10586	-5.10634
C	-2.15504	4.37416	-1.22329	H	0.43855	2.93646	-4.90961
H	-2.71307	4.16255	-2.1597	C	-0.4461	6.25183	-5.15616
C	-2.97114	5.38418	-0.41149	H	1.46496	5.21016	-5.13807
H	-3.02934	6.34497	-0.96465	C	-1.84393	6.11135	-5.09313
H	-2.51486	5.59928	0.57633	H	0.00719	7.25119	-5.23562
H	-4.0071	5.02994	-0.24489	C	-2.42913	4.84521	-4.99858
C	-0.75611	4.87379	-1.59797	H	-2.48937	7.00271	-5.12162
H	-0.83883	5.74534	-2.27909	H	-3.52133	4.72709	-4.94886
H	-0.17441	4.09067	-2.12488	H	-4.83665	-1.3694	0.17197
H	-0.18294	5.19701	-0.70383				

Table 7.23: XYZ-coordinates of computed complex **45$^{\text{tBu}}$**.

Atom	x	y	z	Atom	x	y	z
C	-3.33994	2.98349	1.31192	H	-0.06498	5.79189	-1.53245
C	-3.95223	1.75297	1.37551	H	0.28376	4.03466	-1.39727
P	-1.75547	2.99943	0.44636	H	0.55643	5.13097	0.00571
H	-3.73276	3.8278	1.89594	C	-0.42683	2.91369	1.86088
N	-3.48933	0.65223	0.69802	C	-0.26583	4.23085	2.63602
H	-4.85605	1.60271	1.99712	H	-1.22943	4.58836	3.05027
C	-4.09068	-0.57093	0.84881	H	0.18308	5.03857	2.02863
C	-3.68424	-1.69338	0.16675	H	0.41572	4.05331	3.49619
P	-2.28791	-1.46489	-0.94978	C	0.93094	2.49437	1.26738
H	-4.20981	-2.6482	0.30992	H	1.63395	2.24431	2.09099
C	-0.76516	-2.15875	-0.00214	H	0.85475	1.61907	0.59403
C	-2.61755	-2.52445	-2.49851	H	1.38864	3.30601	0.67253
C	-0.52506	-1.04124	1.02457	C	-0.9257	1.86006	2.86664
H	0.37739	-1.24453	1.6412	H	-1.80501	2.22883	3.42813
H	-0.29827	-0.06347	0.51886	H	-1.22378	0.91438	2.38432
H	-1.39072	-0.91847	1.70174	H	-0.11572	1.63619	3.59303
C	-1.04281	-3.46132	0.75788	Os	-1.97959	0.89006	-0.72594
H	-0.1943	-3.67562	1.44401	Cl	-0.00842	1.15923	-2.15711
H	-1.96234	-3.37899	1.37134	P	-3.43119	1.35871	-2.27907
H	-1.15015	-4.33226	0.08536	Cl	-5.48215	0.83169	-1.84376
C	0.46343	-2.28291	-0.91159	C	-1.04363	-0.11322	-6.79511
H	1.36738	-2.43992	-0.28407	C	-1.44026	0.57005	-5.63804
H	0.62043	-1.36402	-1.51391	C	-1.99377	-0.77271	-7.59312
H	0.3855	-3.15193	-1.59256	H	0.02156	-0.13799	-7.07194
C	-1.55856	-2.18257	-3.56357	C	-3.35086	-0.74459	-7.23202

Atom	x	y	z	Atom	x	y	z
H	-1.33394	-1.10008	-3.58669	H	-1.67515	-1.30951	-8.49941
H	-1.92404	-2.47731	-4.56943	C	-3.76051	-0.05813	-6.08034
H	-0.60652	-2.71444	-3.38589	H	-4.09883	-1.25839	-7.8548
C	-4.01648	-2.1388	-3.00736	C	-2.80672	0.6037	-5.27617
H	-4.80209	-2.32636	-2.25002	H	-4.82173	-0.03183	-5.79083
H	-4.24835	-2.734	-3.91563	H	-0.70412	1.0535	-4.97754
H	-4.08014	-1.07379	-3.28931	C	-3.20746	1.2988	-4.05771
C	-2.61015	-4.02876	-2.1863	C	-3.69447	2.49328	-3.63665
H	-2.91471	-4.58757	-3.09759	C	-4.1671	3.75466	-4.18125
H	-3.32477	-4.29567	-1.38147	C	-3.61763	4.27677	-5.37512
H	-1.60606	-4.39406	-1.90117	C	-4.09457	5.48646	-5.89506
C	-1.57182	4.69241	-0.42516	H	-2.80854	3.72815	-5.87991
C	-2.42555	4.57895	-1.68918	C	-5.12862	6.17793	-5.24047
H	-2.46098	5.55593	-2.21514	H	-3.65871	5.89361	-6.81942
H	-2.00017	3.82969	-2.38207	C	-5.68955	5.65505	-4.06255
H	-3.46565	4.28792	-1.44545	H	-5.49996	7.12859	-5.65115
C	-2.11037	5.86392	0.4124	C	-5.21025	4.45232	-3.53018
H	-2.03651	6.79564	-0.18983	H	-6.50571	6.19118	-3.55538
H	-1.55246	6.03156	1.34901	H	-5.64307	4.02336	-2.61476
H	-3.18075	5.723	0.66207	H	-4.93827	-0.61917	1.55922
C	-0.11099	4.9156	-0.85027				

Table 7.24: XYZ-coordinates of computed complex **45^iPr**.

Atom	x	y	z	Atom	x	y	z
C	-3.4394	2.33839	0.64607	H	-0.00696	5.02836	-0.9378
C	-3.98467	1.08471	0.49507	C	-0.49374	2.63929	0.83824
P	-1.96117	2.63717	-0.33577	C	-0.60663	3.60343	2.0185
H	-3.89545	3.06732	1.33035	H	-1.51198	3.38384	2.62213
N	-3.46772	0.14229	-0.35787	H	-0.65841	4.66118	1.69399
H	-4.88356	0.78642	1.06813	H	0.27457	3.50387	2.68852
C	-4.06256	-1.08895	-0.48924	H	0.36411	2.91565	0.18758
C	-3.56234	-2.07154	-1.30941	C	-0.30099	1.1848	1.29346
P	-1.99053	-1.66785	-2.1043	H	-1.20154	0.80071	1.81606
H	-4.07263	-3.04259	-1.38908	H	-0.08013	0.51836	0.42758
C	-0.67803	-2.64714	-1.16127	H	0.56277	1.09797	1.9865
C	-2.09836	-2.25025	-3.87847	Os	-1.8376	0.63135	-1.56302
H	-0.66355	-2.0689	-0.20799	Cl	0.35174	1.08828	-2.51299
C	-1.06243	-4.08921	-0.81655	P	-3.06349	1.38618	-3.16215
H	-0.31696	-4.52335	-0.11618	Cl	-5.10081	1.89492	-2.73986
H	-2.05576	-4.14135	-0.32879	C	-2.51664	-0.11371	-8.43129
H	-1.08523	-4.73649	-1.71556	C	-2.34591	0.6758	-7.28786
C	0.70569	-2.53145	-1.80988	C	-3.48546	-1.1322	-8.4495
H	0.93711	-1.48718	-2.10431	H	-1.88719	0.06289	-9.31676
H	0.77918	-3.17162	-2.71187	C	-4.29352	-1.35485	-7.32125
H	1.48775	-2.87501	-1.10021	H	-3.61348	-1.75283	-9.34949

C	-0.92486	-1.74627	-4.72687	C	-4.1246	-0.57226	-6.17255
H	-0.65078	-0.70266	-4.47152	H	-5.06083	-2.14393	-7.33895
H	-0.02131	-2.36918	-4.57684	C	-3.14318	0.44556	-6.14195
H	-1.19065	-1.78979	-5.80361	H	-4.75848	-0.72403	-5.28519
H	-3.00458	-1.68839	-4.19159	H	-1.58446	1.46962	-7.26217
C	-2.38031	-3.7414	-4.08036	C	-2.96837	1.2342	-4.93778
H	-2.64201	-3.93334	-5.14286	C	-2.55325	2.45371	-4.49916
H	-3.2247	-4.10069	-3.45891	C	-1.97754	3.72363	-4.91253
H	-1.49151	-4.36125	-3.84636	C	-0.644	3.78192	-5.37821
C	-2.06866	4.31351	-1.15911	C	-0.07637	5.01641	-5.72137
H	-2.75554	4.08803	-2.00526	H	-0.05158	2.85571	-5.41777
C	-2.71507	5.42322	-0.32616	C	-0.82709	6.19814	-5.60671
H	-2.83766	6.33448	-0.94893	H	0.96492	5.05666	-6.07408
H	-2.09736	5.7063	0.55013	C	-2.15101	6.14471	-5.13722
H	-3.71884	5.13048	0.03916	H	-0.37783	7.16513	-5.87816
C	-0.70118	4.69631	-1.73776	C	-2.72508	4.91696	-4.78343
H	-0.80939	5.53325	-2.45847	H	-2.74	7.06968	-5.04282
H	-0.23137	3.84229	-2.26726	H	-3.75736	4.86386	-4.40729
H	-4.97947	-1.25759	0.10787				

Table 7.25: XYZ-coordinates of computed complex **44**-rotamere.

Atom	x	y	z	Atom	x	y	z
Os	3.14508	8.4993	10.89374	C	1.97158	10.19876	8.11838
Cl	3.73986	10.77975	11.41308	H	1.90915	10.82616	7.20406
Cl	2.61078	9.0572	14.52932	H	2.14852	9.15231	7.79557
P	0.84258	9.02113	10.32055	H	2.83662	10.55366	8.71188
P	5.38295	7.63493	10.62408	C	3.67773	5.84189	9.55659
P	2.92834	7.68049	12.82295	H	3.35917	4.92149	9.02977
N	2.69327	6.76749	9.81754	C	4.98986	6.02506	9.91023
C	1.41064	6.55352	9.36624	H	5.738	5.24726	9.70094
H	1.22991	5.59438	8.84371	C	6.50949	7.35187	12.14765
C	0.39652	7.46128	9.52552	C	6.44611	8.59822	13.04848
H	-0.61201	7.23769	9.15079	H	6.78214	9.5145	12.52959
C	-0.44874	9.31643	11.70038	H	7.10311	8.44168	13.92983
C	-1.83976	9.57729	11.09756	H	5.4212	8.7946	13.41755
H	-1.87845	10.52847	10.53392	C	7.96625	7.05475	11.75307
H	-2.5763	9.65518	11.92518	H	8.46292	7.92171	11.27811
H	-2.17501	8.7545	10.43378	H	8.04894	6.18022	11.07673
C	-0.00833	10.49887	12.58094	H	8.53813	6.81437	12.67429
H	-0.07234	11.46601	12.05113	C	5.96161	6.13068	12.90275
H	1.02643	10.37559	12.94998	H	4.89092	6.25006	13.17242
H	-0.6771	10.55459	13.46549	H	6.52529	6.01015	13.85148
C	-0.51913	8.03603	12.54575	H	6.05877	5.19788	12.31418
H	-0.81042	7.15262	11.94508	C	6.32541	8.56993	9.23938
H	-1.26749	8.18258	13.35259	C	5.23792	8.88416	8.19849

Atom	x	y	z	Atom	x	y	z
H	0.44257	7.81329	13.04839	H	5.69649	9.38637	7.32047
C	0.67655	10.33994	8.93549	H	4.48533	9.57726	8.61795
C	-0.5214	10.06672	8.01137	H	4.7267	7.96784	7.84108
H	-0.52527	10.82699	7.20035	C	6.89641	9.89034	9.77885
H	-1.4964	10.13102	8.52738	H	7.2723	10.49482	8.92531
H	-0.44455	9.07014	7.53425	H	7.74912	9.73094	10.46689
C	0.61984	11.75756	9.52328	H	6.11445	10.48015	10.30168
H	0.7363	12.49148	8.69709	C	7.4072	7.71423	8.56116
H	1.44338	11.92542	10.24693	H	6.99559	6.75414	8.19228
H	-0.34895	11.97072	10.01463	H	8.2692	7.50091	9.21571
H	7.79205	8.26977	7.67922				

Table 7.26: XYZ-coordinates of computed complex **44**-rotamere-transition state.

Atom	x	y	z	Atom	x	y	z
Os	3.1267	8.55419	10.98028	C	1.85274	9.8046	8.01917
Cl	3.72874	10.87068	11.07946	H	1.79197	10.37582	7.06896
Cl	1.54851	7.49272	14.36916	H	1.88473	8.72648	7.76328
P	0.78414	8.98043	10.43107	H	2.79759	10.0887	8.51261
P	5.43597	7.7719	10.67256	C	3.73707	5.93883	9.65363
P	3.21747	7.93176	13.01012	H	3.4227	5.00563	9.14884
N	2.72077	6.82894	9.95365	C	5.05372	6.16659	9.93479
C	1.42787	6.51656	9.56056	H	5.81414	5.41812	9.6712
H	1.29631	5.5295	9.07986	C	6.6389	7.40878	12.13176
C	0.37434	7.36367	9.73008	C	6.68036	8.64273	13.05081
H	-0.63616	7.06812	9.41696	H	7.06417	9.54068	12.53302
C	-0.58638	9.39901	11.70528	H	7.34733	8.4355	13.914
C	-1.84479	10.05385	11.10922	H	5.67614	8.88794	13.44812
H	-1.65285	11.04869	10.66812	C	8.05943	7.05877	11.65658
H	-2.57417	10.19858	11.9349	H	8.56611	7.90328	11.15378
H	-2.33351	9.41278	10.34983	H	8.07173	6.17914	10.98188
C	0.04603	10.35158	12.73682	H	8.66885	6.79572	12.54736
H	0.43223	11.27435	12.26194	C	6.10032	6.19102	12.90415
H	0.88137	9.87069	13.27636	H	5.07767	6.35928	13.29569
H	-0.72162	10.64363	13.48438	H	6.76303	5.99983	13.77455
C	-1.03264	8.07157	12.34717	H	6.0746	5.28033	12.27444
H	-1.67	7.4897	11.65277	C	6.38101	8.70817	9.27917
H	-1.6332	8.29489	13.25444	C	5.29511	9.15117	8.28411
H	-0.18684	7.43674	12.66141	H	5.77739	9.54711	7.36537
C	0.64605	10.15542	8.90437	H	4.68224	9.96241	8.71714
C	-0.62847	9.90622	8.08018	H	4.63726	8.31041	7.9826
H	-0.5696	10.51494	7.15295	C	7.07235	9.9617	9.83891
H	-1.55411	10.19948	8.60286	H	7.44417	10.57378	8.98891
H	-0.71602	8.84586	7.77275	H	7.9453	9.7223	10.47592
C	0.75214	11.62704	9.33612	H	6.35898	10.58349	10.41707
H	0.84154	12.26258	8.42919	C	7.37101	7.80346	8.52575

H	1.65096	11.79808	9.96184	H	6.85809	6.93499	8.06784
H	-0.14116	11.97422	9.88971	H	8.19759	7.42853	9.1527
H	7.82354	8.39309	7.7				

Table 7.27: XYZ-coordinates of computed complex **44**-oxidative addition.

Atom	x	y	z	Atom	x	y	z
Os	3.13635	8.6355	10.70109	C	0.68874	10.17801	7.59878
Cl	3.69332	10.09514	8.73895	H	0.51991	11.07409	6.96393
Cl	3.66169	10.5851	11.99842	H	0.1018	9.34296	7.16878
P	0.73834	9.05628	10.18376	H	1.76035	9.9236	7.55647
P	5.47491	7.81353	10.60769	C	3.84571	6.1494	9.20368
P	2.64253	7.40395	12.33133	H	3.6012	5.27135	8.57473
N	2.8487	7.08147	9.35068	C	5.07739	6.24173	9.80511
C	1.58333	6.8185	8.87798	H	5.83403	5.46714	9.60971
H	1.48402	5.92583	8.23053	C	6.3502	7.44097	12.29307
C	0.479	7.56613	9.19271	C	7.05312	8.7188	12.78535
H	-0.5012	7.2929	8.77421	H	7.93709	8.9865	12.17983
C	-0.42434	8.92183	11.74491	H	7.40446	8.55667	13.82618
C	-1.88111	9.38367	11.56321	H	6.34948	9.57688	12.78902
H	-1.96819	10.48024	11.47604	C	7.31122	6.24214	12.18499
H	-2.44533	9.08728	12.47323	H	8.1555	6.4131	11.49818
H	-2.38315	8.91354	10.69713	H	6.77758	5.32681	11.86036
C	0.21213	9.76276	12.86783	H	7.73932	6.03531	13.18894
H	0.34216	10.82159	12.5683	C	5.30157	7.0708	13.34538
H	1.21851	9.40008	13.15386	H	4.66296	7.94228	13.60228
H	-0.44151	9.73526	13.76553	H	5.80777	6.7529	14.28129
C	-0.4989	7.43834	12.13151	H	4.67173	6.21271	13.02117
H	-1.08543	6.8493	11.40058	C	6.8003	8.61227	9.4285
H	-0.96995	7.3423	13.13254	C	6.34551	8.35364	7.97798
H	0.49762	6.9443	12.20419	H	7.04484	8.8898	7.3023
C	0.20036	10.51645	9.02343	H	5.32759	8.73318	7.78285
C	-1.32153	10.71736	8.89607	H	6.38403	7.27602	7.72569
H	-1.48979	11.38593	8.02488	C	6.89465	10.12327	9.70791
H	-1.77578	11.21329	9.76958	H	7.56945	10.5799	8.95246
H	-1.86838	9.776	8.68933	H	7.31588	10.34145	10.70567
C	0.84441	11.80018	9.57512	H	5.90714	10.61348	9.63044
H	0.60464	12.64773	8.89782	C	8.19087	7.96579	9.56498
H	1.9443	11.7089	9.65115	H	8.16571	6.8712	9.39387
H	0.44121	12.05269	10.57721	H	8.68619	8.16641	10.5331
H	8.84078	8.40285	8.77668				

Table 7.28: XYZ-coordinates of computed complex **44**-oxidative addition-transition state.

Atom	x	y	z	Atom	x	y	z
Os	3.1085	8.50577	10.97573	H	1.33815	10.67102	6.9961
Cl	3.72209	10.81229	10.26271	H	1.55269	8.97022	7.51182
Cl	3.49304	9.73267	13.2883	H	2.55062	10.27622	8.25676
P	0.78133	9.0015	10.36564	C	3.80819	6.16051	9.24635
P	5.44782	7.77277	10.66046	H	3.52601	5.30975	8.5974
P	2.62603	7.27461	12.60065	C	5.07188	6.25322	9.75943
N	2.80572	7.06952	9.50706	H	5.8298	5.50405	9.49073
C	1.51725	6.72351	9.15742	C	6.46239	7.26658	12.21516
H	1.41315	5.80698	8.5474	C	6.89572	8.5239	12.98725
C	0.41699	7.42777	9.56113	H	7.67032	9.09915	12.44906
H	-0.58987	7.11785	9.24861	H	7.33005	8.21323	13.96112
C	-0.47707	9.26806	11.79	H	6.03089	9.18539	13.1926
C	-1.89898	9.58748	11.29513	C	7.68301	6.40327	11.84605
H	-1.95432	10.57331	10.79827	H	8.46709	6.98561	11.33283
H	-2.57455	9.62716	12.17559	H	7.41686	5.53446	11.21209
H	-2.29708	8.81578	10.60597	H	8.13147	6.00702	12.78134
C	0.04133	10.40842	12.68484	C	5.54639	6.42555	13.11546
H	0.09192	11.37242	12.14507	H	4.76754	7.05884	13.59292
H	1.05347	10.19496	13.08164	H	6.1456	5.99533	13.94511
H	-0.65343	10.5366	13.54181	H	5.06726	5.58724	12.56934
C	-0.55258	7.96857	12.59977	C	6.54345	8.73442	9.3863
H	-0.921	7.11296	12.00098	C	5.63549	8.96193	8.16019
H	-1.22955	8.11791	13.4668	H	6.22325	9.50606	7.39081
H	0.4345	7.68472	13.03221	H	4.75595	9.57911	8.41436
C	0.45207	10.25348	8.9243	H	5.29963	8.0045	7.71682
C	-0.89433	9.96756	8.22978	C	7.02192	10.08183	9.95046
H	-0.97021	10.64636	7.3547	H	7.45022	10.67964	9.11755
H	-1.77589	10.15358	8.86459	H	7.82133	9.95517	10.70474
H	-0.94555	8.93138	7.84349	H	6.18754	10.66162	10.3884
C	0.49394	11.70018	9.43853	C	7.75138	7.90212	8.91933
H	0.42453	12.39176	8.57182	H	7.46968	6.87572	8.61523
H	1.44295	11.91026	9.96898	H	8.55659	7.84057	9.67375
H	-0.35899	11.92652	10.10816	H	8.1849	8.40043	8.02651
C	1.55055	10.01843	7.86956				

7.5.4 Crystallographic Details

CCDC-1894136 (**37**), CCDC-1894134 (**38**), CCDC-1894133 (**41**) and CCDC-1894135 (**43**) contain the supplementary crystallographic data for this chapter. This data can be obtained free of charge via http://www.ccdc.cam.ac.uk/ products/csd/request/ (or from Cambridge Crystallographic Data Centre, 12 Union Road, Cambridge, CB2 1EZ, UK. Fax: +44-1223- 336-033; e-mail: deposit@ccdc.cam.ac.uk).
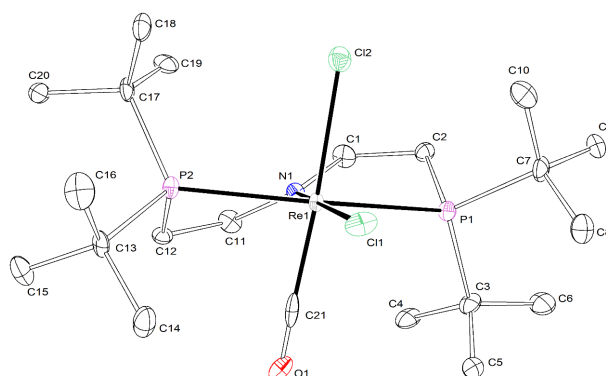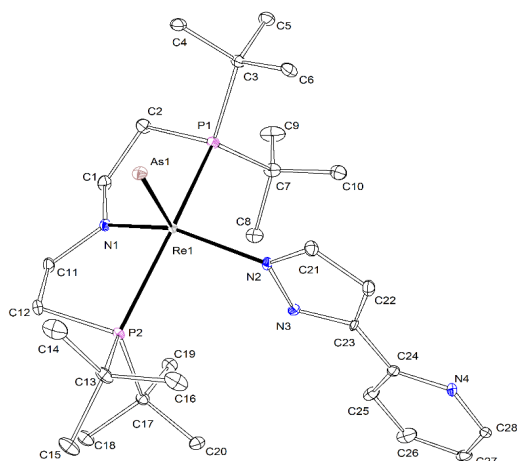
Figure 7.21: Thermal ellipsoid plot of **24** with the anisotropic displacement parameters drawn at the 50% probability level. The asymmetric unit contains one complex molecule.

|	
Empirical formula	$C_{21}H_{44}Cl_2NOP_2Re$
Formula weight	645.61
Temperature	100(2) K
Wavelength	0.71073 Å
Crystal system	Monoclinic
Space group	C2/c
Unit cell dimensions	a = 30.7099(14) Å $\quad\quad\quad$ $\alpha = 90°$
	b = 12.8064(6) Å $\quad\quad\quad$ $\beta = 111.463(2)°$
	c = 14.2870(6) Å $\quad\quad\quad$ $\gamma = 90°$
Volume	5229.2(4) Å^3
Z	8
Density (calculated)	1.640 Mg/m^3
Absorption coefficient	4.987 mm^{-1}
F(000)	2592
Crystal size	0.180 x 0.120 x 0.052 mm^3
Crystal shape and color	Plate, clear intense green
Theta range for data collection	2.486 to 26.450°
Index ranges	-38<=h<=38
	-16<=k<=16
	-17<=l<=17
Reflections collected	88105
Independent reflections	5382 [R(int) = 0.1671]
Completeness to theta = 25.242°	99.9%
Refinement method	Full-matrix least-squares on F^2
Data / restraints / parameters	5382 / 0 / 265
Goodness-of-fit on F^2	1.037
Final R indices [I>2sigma(I)]	R1 = 0.0371, $\quad\quad\quad$ wR2 = 0.0626
R indices (all data)	R1 = 0.0607, $\quad\quad\quad$ wR2 = 0.0681
Largest diff. peak and hole	1.436 and -1.305 eÅ^{-3}
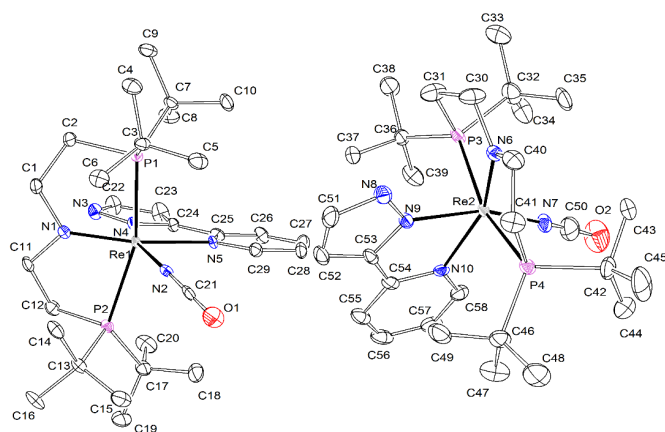
Figure 7.22: Thermal ellipsoid plot of **25** with the anisotropic displacement parameters drawn at the 50% probability level. The asymmetric unit contains two complex molecules.

|		
Empirical formula	$C_{29}H_{50}N_5OP_2Re$	
Formula weight	732.88	
Temperature	100(2) K	
Wavelength	0.71073 Å	
Crystal system	Monoclinic	
Space group	$P2_1/n$	
Unit cell dimensions	a = 18.0402(6) Å	$\alpha = 90°$
	b = 10.1427(4) Å	$\beta = 100.5570(10)°$
	c = 34.6876(12) Å	$\gamma = 90°$
Volume	6239.6(4) Å^3	
Z	8	
Density (calculated)	1.560 Mg/m^3	
Absorption coefficient	4.028 mm^{-1}	
F(000)	2976	
Crystal size	0.206 x 0.120 x 0.114 mm^3	
Crystal shape and color	Block, clear intense brown	
Theta range for data collection	2.297 to 28.282°	
Index ranges	-24<=h<=24	
	-13<=k<=13	
	-46<=l<=46	
Reflections collected	194220	
Independent reflections	15482 [R(int) = 0.0752]	
Completeness to theta = 25.242°	100.0%	
Refinement method	Full-matrix least-squares on F^2	
Data / restraints / parameters	15482 / 0 / 709	
Goodness-of-fit on F^2	1.117	
Final R indices [I>2sigma(I)]	R1 = 0.0370,	wR2 = 0.0588
R indices (all data)	R1 = 0.0533,	wR2 = 0.0621
Largest diff. peak and hole	1.539 and -1.729 eÅ^{-3}	
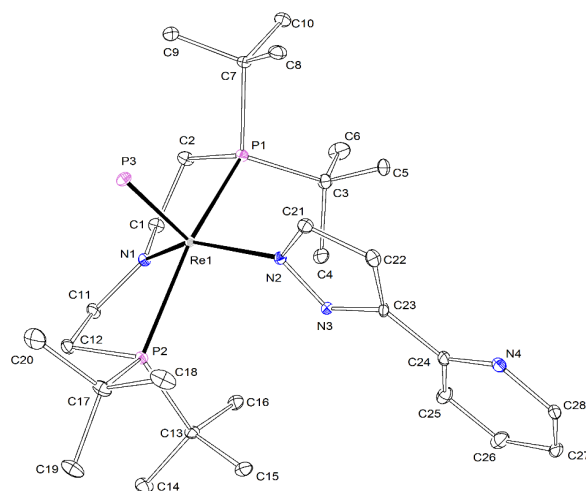
Figure 7.23: Thermal ellipsoid plot of **27** with the anisotropic displacement parameters drawn at the 50% probability level. The asymmetric unit contains one complex molecule.

|		
Empirical formula	$C_{28}H_{50}N_4P_3Re$	
Formula weight	721.83	
Temperature	101(2) K	
Wavelength	0.71073 Å	
Crystal system	Monoclinic	
Space group	P2$_1$/n	
Unit cell dimensions	a = 10.8199(4) Å	$\alpha = 90°$
	b = 20.3333(7) Å	$\beta = 104.6830(10)°$
	c = 14.7109(5) Å	$\gamma = 90°$
Volume	3130.77(19) Å^3	
Z	4	
Density (calculated)	1.531 Mg/m^3	
Absorption coefficient	4.058 mm^{-1}	
F(000)	1464	
Crystal size	0.247 x 0.137 x 0.128 mm^3	
Crystal shape and color	Plate, clear intense yellow-brown	
Theta range for data collection	2.188 to 30.625°	
Index ranges	-14<=h<=15	
	-29<=k<=29	
	-21<=l<=21	
Reflections collected	98300	
Independent reflections	9626 [R(int) = 0.0611]	
Completeness to theta = 25.242°	99.9%	
Refinement method	Full-matrix least-squares on F^2	
Data / restraints / parameters	9626 / 0 / 337	
Goodness-of-fit on F^2	1.018	
Final R indices [I>2sigma(I)]	R1 = 0.0248,	wR2 = 0.0382
R indices (all data)	R1 = 0.0380,	wR2 = 0.0406
Largest diff. peak and hole	0.733 and -0.742 eÅ^{-3}	

Figure 7.24: Thermal ellipsoid plot of **28** with the anisotropic displacement parameters drawn at the 50% probability level. The asymmetric unit contains one complex molecule.

|		
Empirical formula	$C_{28}H_{50}AsN_4P_2Re$	
Formula weight	765.78	
Temperature	100(2) K	
Wavelength	0.71073 Å	
Crystal system	Monoclinic	
Space group	$P2_1/n$	
Unit cell dimensions	a = 10.7835(4) Å	$\alpha = 90°$
	b = 20.3684(6) Å	$\beta = 104.465(2)°$
	c = 14.7721(5) Å	$\gamma = 90°$
Volume	3141.73(18) Å^3	
Z	4	
Density (calculated)	1.619 Mg/m^3	
Absorption coefficient	5.038 mm^{-1}	
F(000)	1536	
Crystal size	0.279 x 0.085 x 0.042 mm^3	
Crystal shape and color	Plate, clear intense yellow	
Theta range for data collection	2.192 to 30.572°	
Index ranges	-15<=h<=15	
	-29<=k<=29	
	-21<=l<=21	
Reflections collected	136063	
Independent reflections	9617 [R(int) = 0.1195]	
Completeness to theta = 25.242°	99.9%	
Refinement method	Full-matrix least-squares on F^2	
Data / restraints / parameters	9617 / 0 / 337	
Goodness-of-fit on F^2	1.064	
Final R indices [I>2sigma(I)]	R1 = 0.0370,	wR2 = 0.0435
R indices (all data)	R1 = 0.0630,	wR2 = 0.0472
Largest diff. peak and hole	0.816 and -1.145 eÅ^{-3}	
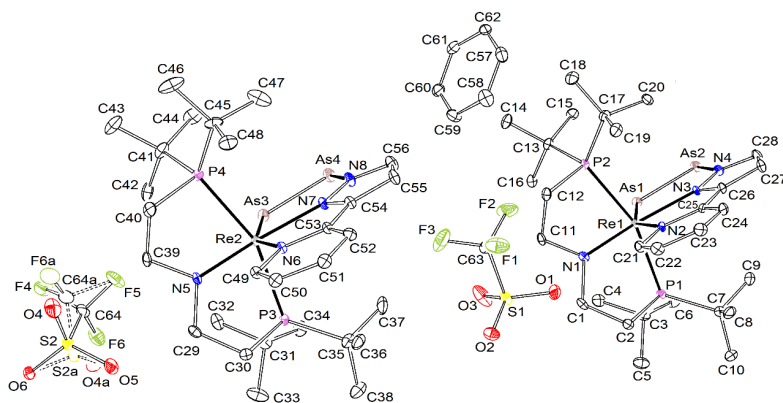
Figure 7.25: Thermal ellipsoid plot of **30** with the anisotropic displacement parameters drawn at the 50% probability level. The asymmetric unit contains two complex molecules, two CF_3SO_3- anions and one benzene solvent molecule. One disordered CF_3SO_3- anions was refined with population of 0.858(6) on the main domain using some restraints (RIGU).

|		
Empirical formula	$C_{64}H_{106}As_4F_6N_8O_6P_4Re_2S_2$	
Formula weight	2057.64	
Temperature	105(2) K	
Wavelength	0.71073 Å	
Crystal system	Monoclinic	
Space group	$P2_1/n$	
Unit cell dimensions	a = 10.8124(5) Å	$\alpha = 90°$
	b = 21.0452(10) Å	$\beta = 95.9810(10)°$
	c = 34.0720(15) Å	$\gamma = 90°$
Volume	7710.8(6) Å^3	
Z	4	
Density (calculated)	1.772 Mg/m^3	
Absorption coefficient	5.045 mm^{-1}	
F(000)	4088	
Crystal size	0.246 x 0.142 x 0.078 mm^3	
Crystal shape and color	Block,	dark red-brown
Theta range for data collection	2.263 to 28.383°	
Index ranges	-14<=h<=14	
	-28<=k<=28	
	-45<=l<=45	
Reflections collected	181199	
Independent reflections	19313 [R(int) = 0.0758]	
Completeness to theta = 25.242°	99.9%	
Refinement method	Full-matrix least-squares on F^2	
Data / restraints / parameters	19313 / 108 / 926	
Goodness-of-fit on F^2	1.059	
Final R indices [I>2sigma(I)]	R1 = 0.0393,	wR2 = 0.0703
R indices (all data)	R1 = 0.0601,	wR2 = 0.0755
Largest diff. peak and hole	1.601 and -1.677 eÅ^{-3}	
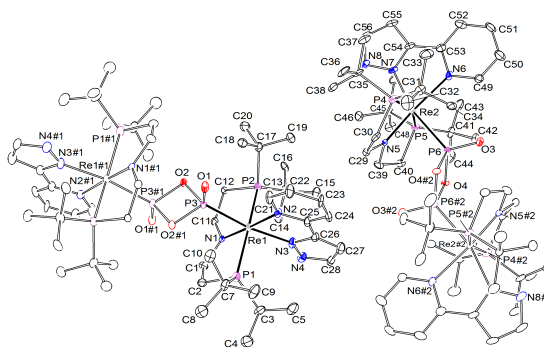
Figure 7.26: Thermal ellipsoid plot of **31** with the anisotropic displacement parameters drawn at the 50% probability level. The asymmetric unit contains two half complex molecules and was refined using some restraints and constraints (RIGU, EADP). The SQUEEZE algorithm was used to omit three disordered Et_2O solvent molecules.[371]

|	
Empirical formula	$C_{56}H_{100}N_8O_4P_6Re_2$ (+ 3 Et_2O)
Formula weight	1507.65
Temperature	101(2) K
Wavelength	0.71073 Å
Crystal system	Triclinic
Space group	P-1
Unit cell dimensions	a = 15.3409(15) Å $\alpha = 113.168(2)°$
	b = 15.4611(14) Å $\beta = 91.184(3)°$
	c = 17.6625(15) Å $\gamma = 103.670(3)°$
Volume	3712.0(6) Å^3
Z	2
Density (calculated)	1.349 Mg/m^3
Absorption coefficient	3.430 mm^{-1}
F(000)	1528
Crystal size	0.296 x 0.165 x 0.150 mm^3
Crystal shape and color	Block, clear intense green/brown
Theta range for data collection	2.193 to 25.407°
Index ranges	-18<=h<=18
	-18<=k<=18
	-20<=l<=21
Reflections collected	97135
Independent reflections	13625 [R(int) = 0.1572]
Completeness to theta = 25.242°	99.9%
Refinement method	Full-matrix least-squares on F^2
Data / restraints / parameters	13625 / 732 / 697
Goodness-of-fit on F^2	1.026
Final R indices [I>2sigma(I)]	R1 = 0.0432, wR2 = 0.0907
R indices (all data)	R1 = 0.0816, wR2 = 0.1031
Largest diff. peak and hole	1.852 and -1.154 eÅ^{-3}
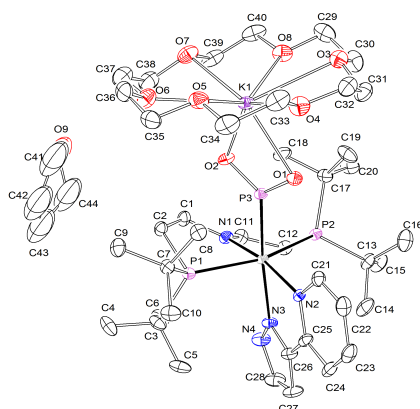
Figure 7.27: Thermal ellipsoid plot of **34** with the anisotropic displacement parameters drawn at the 50% probability level. The asymmetric unit contains one complex a disordered THF molecule. THF was set to a population of 0.5 and refined using some restraints and constraints (SADI, EADP).

|	
Empirical formula	$C_{40}H_{73}KN_4O_8P_3Rex0 \cdot 5\,(C_4H_8O)$
Formula weight	1092.28
Temperature	100(2) K
Wavelength	0.71073 Å
Crystal system	Monoclinic
Space group	P2$_1$/c
Unit cell dimensions	a = 12.8339(4) Å $\qquad \alpha = 90°$
	b = 23.5174(8) Å $\qquad \beta = 100.086(2)°$
	c = 16.6688(5) Å $\qquad \gamma = 90°$
Volume	4953.2(3) Å^3
Z	4
Density (calculated)	1.465 Mg/m^3
Absorption coefficient	2.686 mm^{-1}
F(000)	2256
Crystal size	0.454 x 0.162 x 0.100 mm^3
Crystal shape and color	Plate, clear intense purple
Theta range for data collection	2.364 to 28.369°
Index ranges	-17<=h<=17
	-31<=k<=31
	-22<=l<=22
Reflections collected	215272
Independent reflections	12383 [R(int) = 0.0992]
Completeness to theta = 25.242°	99.9%
Refinement method	Full-matrix least-squares on F^2
Data / restraints / parameters	12383 / 4 / 558
Goodness-of-fit on F^2	1.048
Final R indices [I>2sigma(I)]	R1 = 0.0291, $\qquad$ wR2 = 0.0519
R indices (all data)	R1 = 0.0454, $\qquad$ wR2 = 0.0566
Largest diff. peak and hole	1.743 and -0.934 eÅ^{-3}
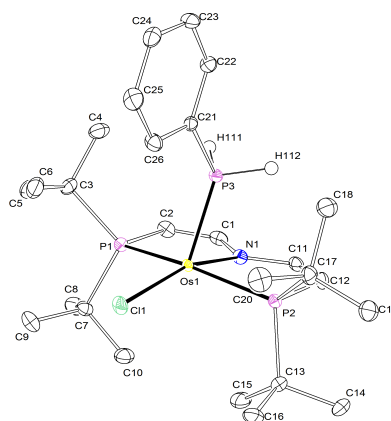
Figure 7.28: Thermal ellipsoid plot of **36** with the anisotropic displacement parameters drawn at the 50% probability level. The asymmetric unit contains one complex molecule. The P-H hydrogen atoms were found from the residual density map and isotropically refined.

|		
Empirical formula	$C_{26}H_{47}ClNOsP_3$	
Formula weight	692.20	
Temperature	100(2) K	
Wavelength	0.71073 Å	
Crystal system	Monoclinic	
Space group	$P2_1/c$	
Unit cell dimensions	a = 18.2079(6) Å	$\alpha = 90°$
	b = 8.1419(3) Å	$\beta = 113.0890(10)°$
	c = 21.6350(8) Å	$\gamma = 90°$
Volume	2950.40(18) $Å^3$	
Z	4	
Density (calculated)	1.558 Mg/m^3	
Absorption coefficient	4.590 mm^{-1}	
F(000)	1392	
Crystal size	0.193 x 0.103 x 0.065 mm^3	
Crystal shape and color	Block, clear intense blue	
Theta range for data collection	2.432 to 30.594○	
Index ranges	-26<=h<=26	
	-11<=k<=11	
	-28<=l<=30	
Reflections collected	106188	
Independent reflections	9079 [R(int) = 0.0735]	
Completeness to theta = 25.242°	99.9%	
Max. and min. transmission	0.7461 and 0.5601	
Refinement method	Full-matrix least-squares on F^2	
Data / restraints / parameters	9079 / 0 / 309	
Goodness-of-fit on F^2	1.056	
Final R indices [I>2sigma(I)]	R1 = 0.0273,	wR2 = 0.0423
R indices (all data)	R1 = 0.0407,	wR2 = 0.0448
Largest diff. peak and hole	0.704 and -0.997 e$Å^{-3}$	
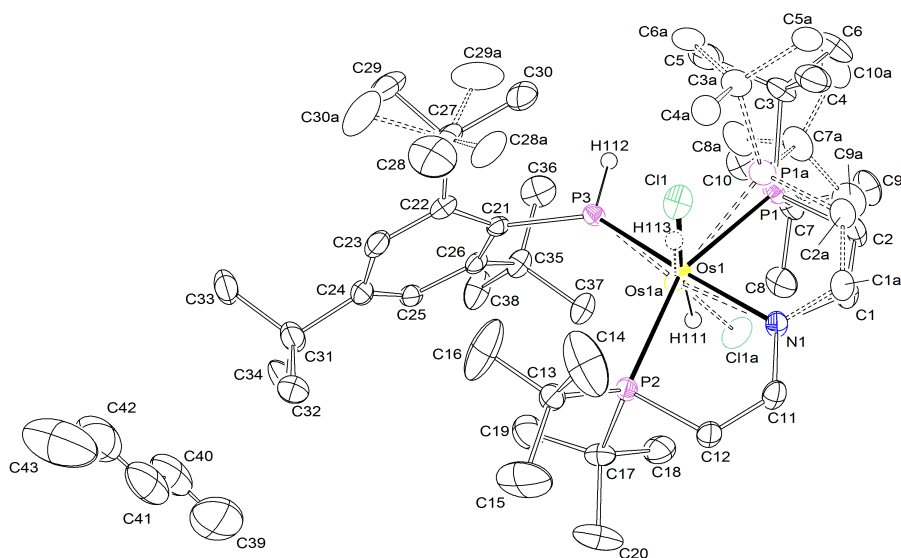
Figure 7.29: Thermal ellipsoid plot of **37** with the anisotropic displacement parameters drawn at the 50% probability level. The asymmetric unit contains one disordered complex molecule and one disordered pentane solvent molecule. The disordered Os(PNP)-part of the complex molecule was refined with population of 0.915(2) on the main domain using some restraints and constraints (SADI, RIGU, EADP). The disordered -C(CH$_3$)$_3$-part of the complex molecule was refined with population of 0.737(7) on the main domain using some restraints (SADI, RIGU). The disordered solvent molecule was refined using PART-1 command and some restraints (SADI, RIGU) and constraints (EADP). The Os-H and P-H hydrogen atoms were found from the residual density map and isotropically refined.

Empirical formula	C$_{39}$H$_{71}$ClNOsP$_3$·0.5C$_5$H$_{12}$	
Formula weight	896.59	
Temperature	100(2) K	
Wavelength	0.71073 Å	
Crystal system	Monoclinic	
Space group	C2/c	
Unit cell dimensions	a = 28.7206(11) Å	$\alpha = 90°$
	b = 12.8908(5) Å	$\beta = 99.050(2)°$
	c = 23.8342(9) Å	$\gamma = 90°$
Volume	8714.3(6) Å^3	
Z	8	
Density (calculated)	1.367 Mg/m^3	
Absorption coefficient	3.125 mm^{-1}	
F(000)	3720	
Crystal size	0.163 x 0.105 x 0.054 mm^3	
Crystal shape and color	Plate, clear intense blue-green	
Theta range for data collection	2.370 to 28.352°	
Index ranges	-38<=h<=38	
	-17<=k<=17	
	-31<=l<=31	

|	
Reflections collected	152470
Independent reflections	10862 [R(int) = 0.0597]
Completeness to theta = 25.242°	99.9%
Refinement method	Full-matrix least-squares on F^2
Data / restraints / parameters	10862 / 619 / 612
Goodness-of-fit on F^2	1.201
Final R indices [I>2sigma(I)]	R1 = 0.0332, wR2 = 0.0546
R indices (all data)	R1 = 0.0420, wR2 = 0.0564
Largest diff. peak and hole	1.000 and -1.522 e$\mathrm{\AA}^{-3}$
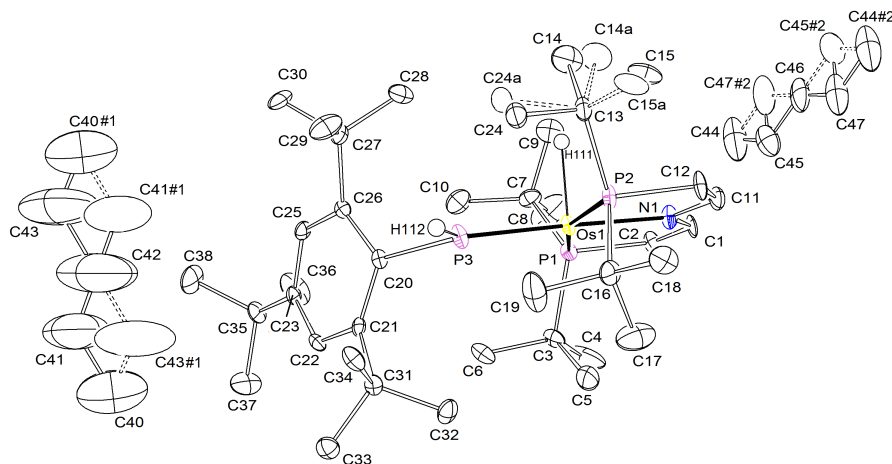
Figure 7.30: Thermal ellipsoid plot of **38** with the anisotropic displacement parameters drawn at the 50% probability level. The asymmetric unit contains one disordered complex molecule and two half pentane solvent molecules located at special positions. The disordered complex molecule was refined with population of 0.71(1) on the main domain using some restraints (SADI) and constraints (EADP). The Os-H and P-H hydrogen atoms were found from the residual density map and isotropically refined.

Empirical formula	$C_{43}H_{83}NOsP_3$	
Formula weight	897.21	
Temperature	100(2) K	
Wavelength	0.71073 Å	
Crystal system	Monoclinic	
Space group	P2$_1$/n	
Unit cell dimensions	a = 14.2026(6) Å	$\alpha = 90°$
	b = 15.4095(7) Å	$\beta = 97.2097(18)°$
	c = 21.0809(10) Å	$\gamma = 90°$
Volume	4577.2(4) Å^3	
Z	4	
Density (calculated)	1.302 Mg/m^3	
Absorption coefficient	2.918 mm^{-1}	
F(000)	1876	
Crystal size	0.238 x 0.211 x 0.162 mm^3	

Crystal shape and color	Block, dark green
Theta range for data collection	2.267 to 27.976°
Index ranges	-18<=h<=18
	-20<=k<=20
	-27<=l<=27
Reflections collected	124611
Independent reflections	11010 [R(int) = 0.1202]
Completeness to theta = 25.242°	99.9%
Refinement method	Full-matrix least-squares on F^2
Data / restraints / parameters	11010 / 45 / 498
Goodness-of-fit on F^2	1.053
Final R indices [I>2sigma(I)]	R1 = 0.0416, wR2 = 0.0531
R indices (all data)	R1 = 0.1021, wR2 = 0.0636
Largest diff. peak and hole	0.695 and -0.830 eÅ^{-3}
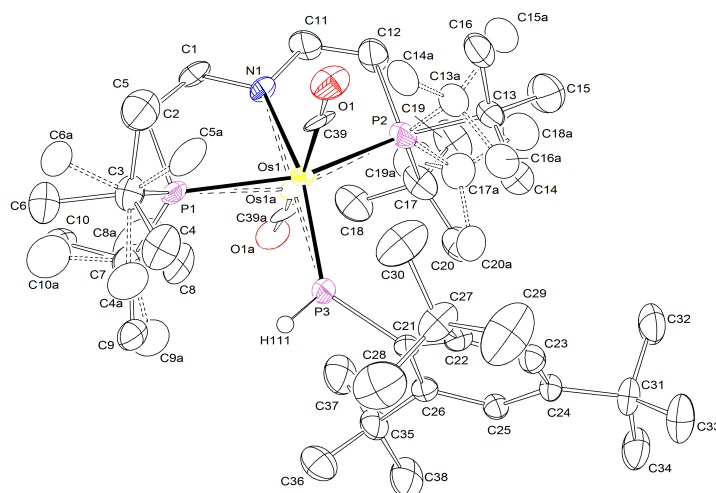
Figure 7.31: Thermal ellipsoid plot of **41** with the anisotropic displacement parameters drawn at the 50% probability level. The asymmetric unit contains one disordered complex molecule. The disordered complex molecule was refined with population of 0.682(7) on the main domain using some restraints and constraints (RIGU, SADI, EADP). The P-H hydrogen atom was found from the residual density map and isotropically refined. The structure was refined as an inversion twin using the twin law -100 0-10 00-1 (BASF: 0.061(16)). The reflections -2 2 4, 1 4 4, 0 1 9 and -2 1 10 are removed from the refinement using OMIT commands.

Empirical formula	$C_{39}H_{70}NOOsP_3$	
Formula weight	852.07	
Temperature	100(2) K	
Wavelength	0.71073 Å	
Crystal system	Orthorhombic	
Space group	$P2_12_12_1$	
Unit cell dimensions	a = 20.1894(14) Å	$\alpha = 90°$
	b = 11.4930(8) Å	$\beta = 90°$
	c = 17.4542(14) Å	$\gamma = 90°$
Volume	4050.0(5) Å^3	
Z	4	
Density (calculated)	1.397 Mg/m^3	
Absorption coefficient	3.296 mm^{-1}	
F(000)	1760	
Crystal size	0.265 x 0.178 x 0.120 mm^3	
Crystal shape and color	Block, clear intense red	
Theta range for data collection	2.331 to 28.424°	
Index ranges	-26<=h<=26	
	-15<=k<=15	
	-23<=l<=23	
Reflections collected	79045	
Independent reflections	10098 [R(int) = 0.1626]	
Completeness to theta = 25.242°	99.9%	
Refinement method	Full-matrix least-squares on F^2	

Data / restraints / parameters	10098 / 396 / 559
Goodness-of-fit on F^2	1.155
Final R indices [I>2sigma(I)]	R1 = 0.0588,
R indices (all data)	R1 = 0.0762,
Absolute structure parameter	0.061(16)
Largest diff. peak and hole	1.550 and -2.048 e$\text{\AA}^{-3}$

Final R indices [I>2sigma(I)]   wR2 = 0.1161

R indices (all data)   wR2 = 0.1245
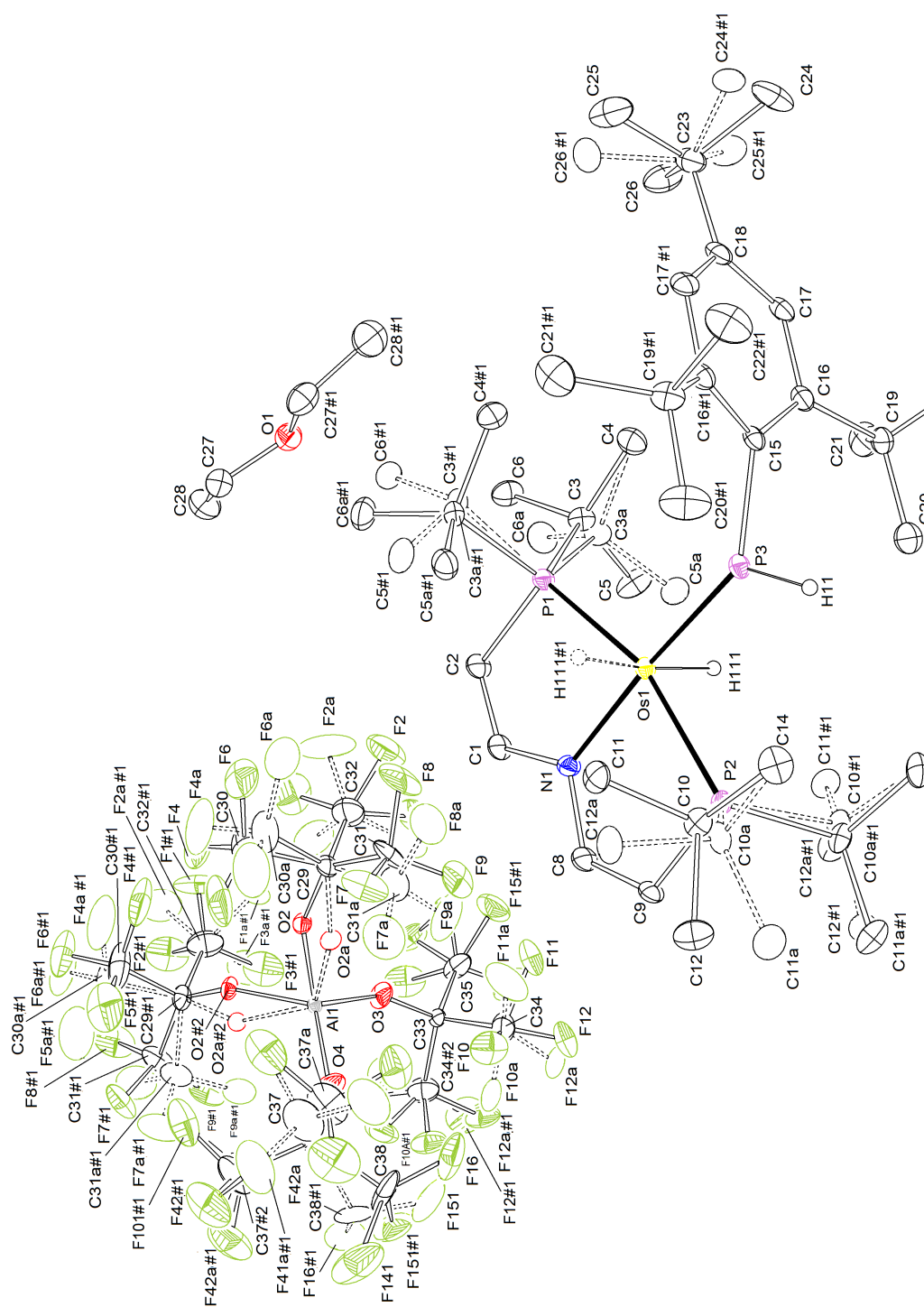
Figure 7.32: Thermal ellipsoid plot of **43** with the anisotropic displacement parameters drawn at the 50% probability level. The asymmetric unit contains a half disordered complex molecule, a half disordered $[Al\{OC(CF_3)_3\}_4]^-$ anion and a half diethyl ether solvent molecule. The disorder was refined with site occupation factors of 0.5 for both sites using PART commands and some restraints and constraints (SADI, RIGU, EADP). The Os-H hydrogen atom was found from the residual density map and isotropically refined using DFIX.

Empirical formula	$C_{58}H_{81}AlF_{36}NO_5OsP_3$	
Formula weight	1866.32	
Temperature	100(2) K	
Wavelength	0.71073 Å	
Crystal system	Monoclinic	
Space group	$P2_1/m$	
Unit cell dimensions	a = 14.9152(8) Å	$\alpha = 90°$
	b = 15.4377(8) Å	$\beta = 107.823(2)°$
	c = 16.7109(9) Å	$\gamma = 90°$
Volume	3663.1(3) Å^3	
Z	2	
Density (calculated)	1.692 Mg/m^3	
Absorption coefficient	1.955 mm^{-1}	
F(000)	1868	
Crystal size	0.513 x 0.242 x 0.128 mm^3	
Crystal shape and color	Plate, clear intense green-blue	
Theta range for data collection	2.195 to 28.443°	
Index ranges	-19<=h<=19	
	-20<=k<=20	
	-22<=l<=22	
Reflections collected	99819	
Independent reflections	9531 [R(int) = 0.0648]	
Completeness to theta = 25.242°	99.9%	
Refinement method	Full-matrix least-squares on F^2	
Data / restraints / parameters	9531 / 301 / 741	
Goodness-of-fit on F^2	1.086	
Final R indices [I>2sigma(I)]	R1 = 0.0508,	wR2 = 0.1312
R indices (all data)	R1 = 0.0573,	wR2 = 0.1378
Largest diff. peak and hole	1.562 and -1.653 eÅ^{-3}	
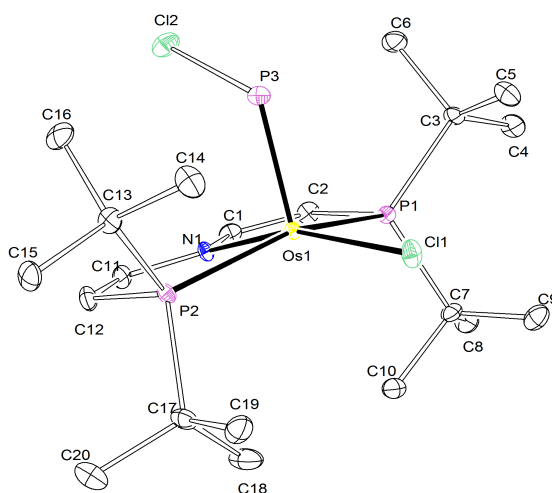
Figure 7.33: Thermal ellipsoid plot of **44** with the anisotropic displacement parameters drawn at the 50% probability level. The asymmetric unit contains one complex molecule.

Empirical formula	$C_{20}H_{40}Cl_2NOsP_3$
Formula weight	648.54
Temperature	293(2) K
Wavelength	0.71073 Å
Crystal system	Monoclinic
Space group	$P2_1/n$
Unit cell dimensions	a = 12.2910(7) Å $\qquad \alpha = 90°$
	b = 14.2611(7) Å $\qquad \beta = 107.780(2)°$
	c = 15.1564(8) Å $\qquad \gamma = 90°$
Volume	2529.8(2) Å^3
Z	4
Density (calculated)	1.703 Mg/m^3
Absorption coefficient	5.449 mm^{-1}
F(000)	1288
Crystal size	0.541 x 0.370 x 0.215 mm^3
Crystal shape and color	Block, clear intense purple
Theta range for data collection	2.251 to 28.362°.
Index ranges	-16<=h<=16
	-18<=k<=19
	-20<=l<=20
Reflections collected	99312
Independent reflections	6305 [R(int) = 0.1252]
Completeness to theta = 25.242°	100.0 %
Refinement method	Full-matrix least-squares on F^2
Data / restraints / parameters	6305 / 0 / 256
Goodness-of-fit on F^2	1.019
Final R indices [I>2sigma(I)]	R1 = 0.0268, $\qquad\qquad$ wR2 = 0.0458
R indices (all data)	R1 = 0.0454, $\qquad\qquad$ wR2 = 0.0504
Largest diff. peak and hole	1.081 and -1.328 eÅ^{-3}

7.5.5 Isothermal Titration Calorimetry

The bond dissociation energy (BDE) of **38** was determined by ITC using a TA INSTRU-MENTS NanoITC equipped with a 24 K gold cell (1 mL sampe volume) and a 250 µL titration syringe operated in overfill mode. The instrument was run under an indert atmosphere inside an argon filled glove box. The syringe concentration was chosen to be 6.4 times higher than the cell concentration to obtain a titration range from 0 - 2 eq.. Mes*O was used as a titrant. Both reactant solutions were prepared with Na/K dried benzene with a sample mass of more than 10.0 mg for sufficient accuracy. Titrations were carried out at 10°C to suppress decay of **39** to **40** and corrected vs. addition of Mes*O to pure benzene in the sampe cell. Further experimental conditions are detailed in Table 7.29. The data were evaluated using the implemented NanoAnalyze software.[6]

Table 7.29: Experimental details of ITC in benzene.

Concentration / volume of **38**	1.02 mM	950 µL
Concentration / volume of Mes*O	9.18 mM	250 µL
Injection Steps / Injected Volume	33	7.5 µL
Waiting time	350-650 s	
Stirring rate	350 rpm	
Equilibration time before start of the experiment	1514 s	
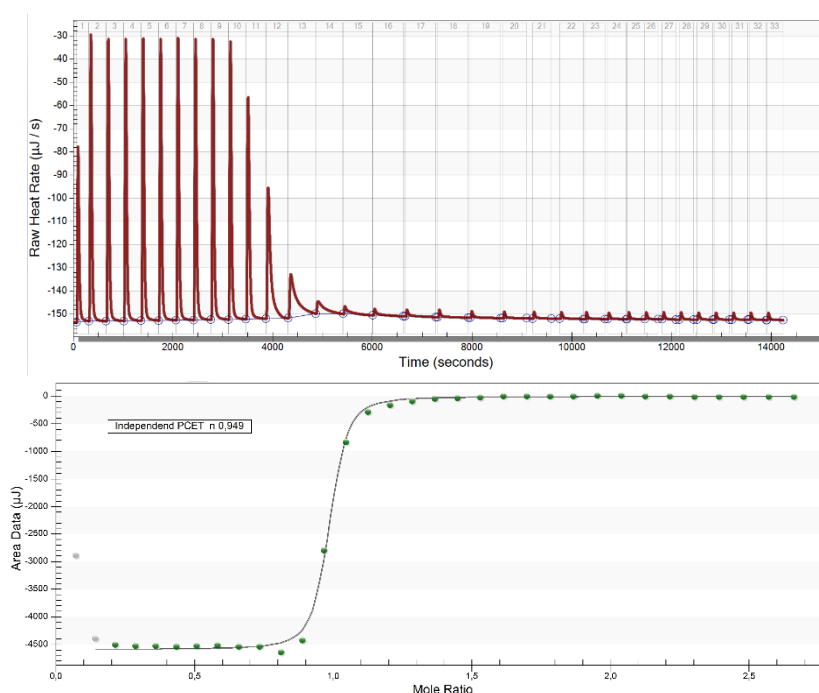
Figure 7.34: Top: Representative thermogram of calorimetric titration of **38** with Mes*O in benzene; Bottom: Integrated titration curve.

---

[6]a) Measurment by ITCRun Version 3.4.6.0, TA Instruments, **2017**; b) Evaluation by NanoAnalyze Version 3.7.5 TA Instruments, **2015**.

A representative thermogram is shown in Figure 7.34. The first two peaks of each titration were generally neglected due to diffusion of reactant solution into the cell during equilibration of the instrument. Around the addition of one equivalent of Mes*O, the peaks show increased tailing, which is tentatively attributed to follow-up reactivity of **39**. The P–H BDE was therefore determined at an early titration stage from the average of injections 3-6 (Tables 7.30, 7.31) while reliable BDFE determination was not possible. A cumulative error of 5% for stock solution concentrations was estimated from the fitted n-value (0.95) which gives rise to an error in ΔH of $\pm 0.8\,\text{kcal} \cdot \text{mol}^{-1}$.

Table 7.30: Integrated heats of the injections 3-6 for the BDE determination of **38** in benzene.

Injection	Heats / μJ 1^{st}run	Heats / μJ 2^{nd}run	Added moles / nmol
3	4682	4678	68.2
4	4708	4678	68.2
5	4703	4711	68.2
6	4716	4711	68.2
Mean	4702	4694	

Table 7.31: Results of the calorimetric BDE determination of **38** in benzene.

	Δ H / kJ$\cdot$mol^{-1}	Δ H / kcal$\cdot$mol^{-1}
Mean 1st run	-68.9	-16.5
Mean 2nd run	-68.8	-16.4
Mean	-68.9	-16.5
Mes*O		81.6
BDE(P$-$H) of **38**		65.1 ± 0.8

The BDE measurement was also performed in THF to allow to construct a thermochemical square-scheme of **38** (Table 7.32).

Table 7.32: Experimental details of ITC in THF.

Concentration / volume of **38**	1.40 mM	950 μL
Concentration / volume of Mes*O	11.17 mM	250 μL
Injection Steps / Injected Volume	49	5 μL
Waiting time	300 s	
Stirring rate	350 rpm	
Equilibration time before start of the experiment	1671 s	

The P$-$H BDE of **38** was calculated from the mean heat evolved at the peaks 2-5 (Figure 7.35). The O$-$H BDE of Mes*OH in THF was determined by a square-scheme using the oxidation potential of the Mes*O/Mes*O$^-$ redox couple ($E^\circ = -0.955$ V vs. Fc$^{0/+}$, Figure 7.35). The pK_a of Mes*OH was calculated from the reported value in DMSO according to Ding (pK_a^{THF}(Mes*OH)$= 1.03 \cdot 17.8 + 11.3 = 29.6$). This results in a BDE of 84.5 kcal $\cdot$ mol^{-1}.
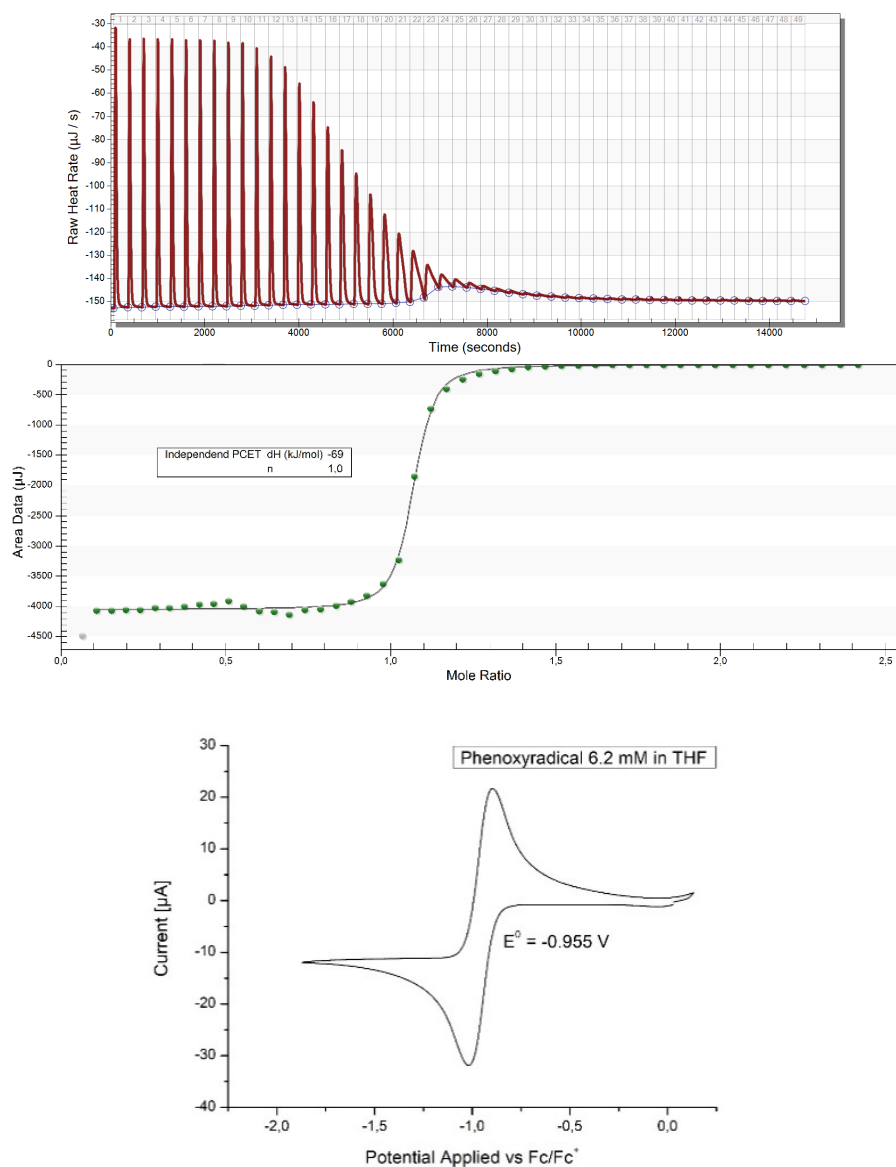
Figure 7.35: Top: Thermogram of calorimetric titration of **38** with Mes*O in THF; Middle: Integrated titration curve; Bottom: Cyclic voltammogram of Mes*O, $100\,\mathrm{Vm \cdot s^{-1}}$, $0.1\,\mathrm{M}$ NBu_4PF_6, THF, RT.

Table 7.33: Integrated heats of the injections 2-5 for the BDE determination of **38** in THF.

Injection	Heats / μJ 1strun	Added moles / nmol
2	4069	56.9
3	4066	56.9
4	4050	56.9
5	4049	56.9
Mean	4059	

Table 7.34: Results of the calorimetric BDE determination of **38** in THF.

	ΔH / kJ·mol^{-1}	ΔH / kcal·mol^{-1}
Mean	-71	-17
Mes*O		84.5
BDE(P−H) of **38**		67 ± 1

7.5.6 Syntheses

Reaction of LXXIII with [Na(diox)$_{1.39}$][PCO]

LXXIII (5.0 mg, 8.1 µmol, 1.0 eq.) and [Na(diox)$_{1.39}$][PCO] (1.6 mg, 8.1 µmol, 1.0 eq.) are dissolved in C$_6$D$_6$ (0.5 mL) and stirred for 1h at room temperature. Longer reaction times lead to no further consumption of the starting material and precipitation of a black solid.

NMR (C$_6$D$_6$, RT): ^{31}P{^{1}H} (162.1 MHz) = 1063.6 (br, 1P, Re≡P), 87.2 (br, 2P, P(C(CH$_3$)$_3$)$_2$), 30.0 (s, 2P, P(C(CH$_3$)$_3$)$_2$, (PNP)ReCl$_2$(CO)), -51.6 (s, 2P, P(C(CH$_3$)$_3$)$_2$, **1a**).

Synthesis of 24

LXXIII (123 mg, 198 µmol, 1.00 eq.) is dissolved in benzene and degassed *via* two freeze-pump-thaw cycles. CO (1.2 bar) is applied and the solution stirred for 1 minute. The green solution is degassed *via* two freeze-pump-thaw cycles and lyophilized overnight. The residue is washed with pentane (3 x 5 mL) and Et$_2$O (3 x 5 mL) and extracted with benzene. Lyophilization yields **24** (104 mg, 161 µmol, 81%) as a green powder.

Anal. Calcd for C$_{21}$H$_{44}$N$_1$I$_2$OP$_2$Re$_1$ (645.6): C, 39.1; H, 6.87; N, 2.17. Found: C, 39.4; H, 6.27; N, 2.22. NMR (CD$_2$Cl$_2$, RT): ^{1}H (300 MHz): δ = 4.11 - 3.85 (m, 4H, NCH$_2$), 2.74 - 2.60 (m, 2H, PCH_2), 2.34 - 2.30 (m, 2H, PCH_2), 1.43 (A$_9$XX'A$_9$', $N = |^3J_{AX} + {}^5J_{AX}'| = 12.7$ Hz, P(C(CH_3)$_3$)$_2$), 1.31 (A$_9$XX'A$_9$', $N = |^3J_{AX} + {}^5J_{AX}'| = 12.9$ Hz, P(C(CH_3)$_3$)$_2$). ^{13}C{^{1}H} (75.5 MHz) δ = 195.8 (t, $^3J_{PC} = 7.6$ Hz, 1C, CO), 93.4 (vt, $N = |^2J_{PC} + {}^3J_{PC}| = 3.0$ Hz, 2C, NCH$_2$), 42.2 (vt, $N = |^1J_{CP} + {}^3J_{CP}| = 7.7$ Hz, 2C, P(C(CH$_3$)$_3$)$_2$), 41.2 (vt, $N = |^1J_{CP} + {}^3J_{CP}| = 8.5$ Hz, 2C, P(C(CH$_3$)$_3$)$_2$), 31.6 (vt, $N = |^1J_{PC} + {}^3J_{PC}| = 9.3$ Hz, 2C, PCH$_2$), 30.9 (vt, $N = |^2J_{CP} + {}^4J_{CP}| = 1.5$ Hz, 6C, P(C(CH$_3$)$_3$)$_2$), 30.4 (vt, $N = |^2J_{CP} + {}^4J_{CP}| = 2.0$ Hz, 6C, P(C(CH$_3$)$_3$)$_2$).^{31}P{^{1}H} (121.5 MHz) δ = 31.5 (s, 2P, P(C(CH$_3$)$_3$)$_2$). LIFDI-MS (THF): 645.1 (100%, [M]$^+$).

Reaction of 5 with [Na(diox)$_{1.39}$][PCO]

5 (5.0 mg, 8.1 µmol, 1.0 eq.) and [Na(diox)$_{1.39}$][PCO] (1.6 mg, 8.1 µmol, 1.0 eq.) are dissolved in THF-d$_8$ (0.5 mL) and stirred for 1h at room temperature.

NMR (THF, RT): ^{31}P{^{1}H} (162.1 MHz) = 1092.4 (br, 1P, Re≡P), 84.7 (br, 2P, P(C(CH$_3$)$_3$)$_2$).

Synthesis of 25

11 (25.0 mg, 30.6 µmol, 1.00 eq.) and [NBu$_4$][NCO] (49.5 mg, 153 µmol, 5.00 eq.) are dissolved in THF (10 mL) and stirred for 90 min at room temperature. After evaporation

of the solvent the residue is extracted with benzene (3 x 5 mL). After removal of the solvent the residue is extracted with pentane (15 x 5 mL). The volume of the pentane solution is reduced until product starts to precipitate (ca. 5 mL). The solution is stored at -35°C for 2 days. After filtration the precipitate is washed with cold pentane (2 mL). Lyophilization yields **25** in form of a brown powder (18.0 mg, 24.6 µmol, 80%).

Anal. Calcd for $C_{29}H_{50}N_5OP_2Re$ (732.9): C, 47.5; H, 6.88; N 9.56. Found: C, 48.0; H, 6.90; N, 9.40. NMR (C_6D_6, RT): ^{1}H (500 MHz): $\delta = 9.82$ (ddd, $^3J_{HH} = 6.1$ Hz, $^4J_{HH} = 1.4$ Hz, $^5J_{HH} = 0.9$ Hz, 1H, C_8H), 7.68 (d, $^3J_{HH} = 2.1$ Hz, 1H, C_1H), 7.27 (ddd, $^3J_{HH} = 8.0$ Hz, $^4J_{HH} = 1.5$ Hz, $^5J_{HH} = 0.9$ Hz, 1H, C_5H), 6.56 (ddd, $^3J_{HH} = 8.0$ Hz, $^3J_{HH} = 7.2$ Hz, $^5J_{HH} = 1.5$ Hz, 1H, C_6H), 6.34 (d, $^3J_{HH} = 2.1$ Hz, 1H, C_2H), 6.32 (ddd, $^3J_{HH} = 7.2$ Hz, $^3J_{HH} = 6.1$ Hz, $^4J_{HH} = 1.5$ Hz, 1H, C_7H), 4.39 - 4.25 (m, 2H, NCH_2), 3.46 - 3.37 (m, 2H, NCH_2), 2.07 - 1.96 (m, 2H, PCH_2), 1.81 - 1.71 (m, 2H, PCH_2), 1.28 ($A_9XX'A_9'$, $N = |^3J_{AX} + {}^5J_{AX'}| = 11.4$ Hz, 18H, $P(C(CH_3)_3)_2)$, 0.39 ($A_9XX'A_9'$, $N = |^3J_{AX} + {}^5J_{AX'}| = 12.1$ Hz, 18H, $P(C(CH_3)_3)_2)$. $^{13}C\{^1H\}$ (125.8 MHz): $\delta = 159.6$ (br, 1C, NCO), 150.9 (s, 1C, C_4), 147.9 (s, 1C, C_8), 145.4 (s, 1C, C_3), 142.8 (s, 1C, C_1), 135.2 (s, 1C, C_6), 117.4 (s, 1C, C_5), 117.4 (s, 1C, C_7), 104.3 (s, 1C, C_2), 83.6 (vt, $N = |^2J_{PC} + {}^3J_{PC}| = 4.3$ Hz, 2C, NCH_2), 41.8 (vt, $N = |^1J_{CP} + {}^3J_{CP}| = 8.0$ Hz, 2C, $P(C(CH_3)_3)_2)$, 38.3 (vt, $N = |^1J_{CP} + {}^3J_{CP}| = 7.0$ Hz, 2C, $P(C(CH_3)_3)_2)$, 30.9 (vt, $N = |^2J_{CP} + {}^4J_{CP}| = 1.8$ Hz, 6C, $P(C(CH_3)_3)_2)$, 29.3 (vt, $N = |^1J_{PC} + {}^3J_{PC}| = 2.5$ Hz, 2C, PCH_2), 28.7 (vt, $N = |^2J_{CP} + {}^4J_{CP}| = 7.3$ Hz, 6C, $P(C(CH_3)_3)_2)$.. $^{31}P\{^1H\}$ (202.5 MHz) $\delta = 8.0$ (s, 2P, $P(C(CH_3)_3)_2)$. LIFDI-MS (Toluene): 733.2 (100 %, $[M]^+$). IR (ATR, cm^{-1}): $\tilde{\nu} = 2234$ (NCO).

Irradiation and heating of 25

Heating: **4a** (5.0 mg, 6.8 µmol, 1.0 eq.) are dissolved in C_6D_6 (0.5 mL) in a Y-Joung NMR tube and heated to 80°C for 4 hours. The $^{31}P\{^1H\}$ and ^{1}H NMR spectra indicated no conversion of the starting material.

Irradiation: **4a** (5 mg, 6.82 µmol, 1.0 eq.) are dissolved in C_6D_6 (0.5 mL) in a Y-Joung NMR tube and irradiated at room temperature overnight. The $^{31}P\{^1H\}$ and ^{1}H NMR spectra indicated no conversion of the starting material.

Synthesis of 27

11 (58.0 mg, 70.9 µmol, 1.00 eq.) and $[Na(diox)_{1.39}][PCO]$ (15.3 mg, 74.5 µmol, 1.05 eq.) are dissolved in THF at $-80°C$. The solution is warmed to $-10°C$ and stirred for 1h. After warming to room temperature the solvent is evaporated. The residue is washed with pentane (4 x 1 mL) and extracted with benzene (3 x 1 mL). Lyophilization yields **27** in form of a brown powder (32.5 mg, 42.0 µmol, 63%).

Anal. Calcd for $C_{28}H_{50}IN_4P_2Re$ (817.8): C, 46.6; H, 6.98; N 7.76. Found: C, 46.6; H, 6.88; N, 7.55. NMR (THF-d$_8$, 0°C): ^{1}H (500 MHz): $\delta = 8.37$ (ddd, $^3J_{HH} = 4.8$ Hz, $^4J_{HH} = 1.8$ Hz, $^5J_{HH} = 0.9$ Hz, 1H, C_8H), 8.31 (d, $^3J_{HH} = 1.8$ Hz, 1H, C_1H), 7.60 (m, 1H, C_5H), 7.42 (ddd, $^3J_{HH} = 8.0$ Hz, $^3J_{HH} = 7.3$ Hz, $^4J_{HH} = 1.8$ Hz, 1H, C_6H), 6.83 (m, 1H, C_2H), 6.81 (m, 1H, C_7H), 3.63 - 3.55 (m, 2H, NCH_2, superimposed with solvent), 3.40 - 3.28 (m, 2H, NCH_2), 2.51 - 2.43 (m, 2H, PCH_2), 1.94 - 1.86 (m, 2H, PCH_2), 1.42 ($A_9XX'A_9'$, $N = |^3J_{AX} + {}^5J_{AX'}| = 13.0$ Hz, 18H, $P(C(CH_3)_3)_2)$, 1.10 ($A_9XX'A_9'$, $N = |^3J_{AX} + {}^5J_{AX'}| = 13.0$ Hz, 18H, $P(C(CH_3)_3)_2)$. $^{13}C\{^1H\}$ (125.8 MHz):

δ = 155.7 (s, 1C, C_4), 152.2 (s, 1C, C_3), 150.5 (s, 1C, C_1H), 149.6 (s, 1C, C_8H), 135.6 (s, 1C, C_6H), 120.2 (s, 1C, C_7H), 119.3 (s, 1C, C_5H), 105.8 (s, 1C, C_2H), 75.0 (vt, $N = |^2J_{PC} + {}^3J_{PC}|$ = 3.5 Hz, 2C, NCH_2), 38.4 (vt, $N = |^1J_{CP} + {}^3J_{CP}|$ = 9.0 Hz, 2C, P(C(CH$_3$)$_3$)$_2$), 34.3 (vt, $N = |^1J_{CP} + {}^3J_{CP}|$ = 8.8 Hz, 2C, P(C(CH$_3$)$_3$)$_2$), 31.7 (vt, $N = |^1J_{PC} + {}^3J_{PC}|$ = 10.4 Hz, 2C, PCH_2), 30.4 (br, 6C, P(C(CH_3)$_3$)$_2$), 29.0 (br, 6C, P(C(CH_3)$_3$)$_2$). ^{31}P$\{^1$H$\}$ (204.5 MHz) δ = 1069.4 (s br, 1P; Re$\equiv$P), 91.0 (s, 2P, P(C(CH$_3$)$_3$)$_2$). LIFDI-MS (Toluene): 722.2 (100 %, [M]$^+$).

Synthesis of 28

11 (20.0 mg, 24.5 µmol, 1.00 eq.) and [Na(diox)$_{3.31}$][AsCO] (10.7 mg, 25.7 µmol, 1.05 eq.) are dissolved in THF at $-80°$C and the solution is allowed to warm to room temperature over the course of 90 minutes. The solvent is evaporated and the residue is washed with pentane (3 x 1 mL) and extracted with benzene (3 x 2 mL). Lyophilization yields **28** in form of a brown powder (13.2 mg, 17.2 µmol, 70%).

Anal. Calcd for C$_{28}$H$_{50}$AsN$_4$P$_2$Re (765.8): C, 43.9; H, 6.58; N 7.32. Found: C, 43.7; H, 6.17; N, 6.91. NMR (THF-d$_8$, 0°C): ^{1}H (500 MHz): δ = 8.41 (d, $^3J_{HH}$ = 1.8 Hz, 1H, C$_1$H), 8.37 (ddd, $^3J_{HH}$ = 4.8 Hz, $^4J_{HH}$ = 1.8 Hz, $^5J_{HH}$ = 0.9 Hz, 1H, C$_8$H), 7.58 (m, 1H, C$_5$H), 7.41 (ddd, $^3J_{HH}$ = 8.0 Hz, $^3J_{HH}$ = 7.4 Hz, $^4J_{HH}$ = 1.9 Hz, 1H, C$_6$H), 6.82 (m, 2H, C$_2$H, C$_7$H, superimposed), 3.55 - 3.47 (m, 2H, NCH_2), 3.41 - 3.31 (m, 2H, NCH_2), 2.53 - 2.46 (m, 2H, PCH_2), 1.94 - 1.84 (m, 2H, PCH_2), 1.40 (A$_9$XX'A$_9$', $N = |^3J_{AX} + {}^5J_{AX'}|$ = 13.0 Hz, 18H, P(C(CH_3)$_3$)$_2$), 1.08 (A$_9$XX'A$_9$', $N = |^3J_{AX} + {}^5J_{AX'}|$ = 12.9 Hz, 18H, P(C(CH_3)$_3$)$_2$).^{13}C$\{^1$H$\}$ (125.8 MHz): δ = 155.6 (s, 1C, C_4), 152.1 (s, 1C, C_3), 151.0 (s, 1C, C_1H), 149.5 (s, 1C, C_8H), 135.5 (s, 1C, C_6H), 120.1 (s, 1C, C_7H), 119.2 (s, 1C, C_5H), 105.6 (s, 1C, C_2H), 75.6 (vt, $N = |^2J_{PC} + {}^3J_{PC}|$ = 3.5 Hz, 2C, NCH_2), 38.6 (vt, $N = |^1J_{CP} + {}^3J_{CP}|$ = 8.8 Hz, 2C, P(C(CH$_3$)$_3$)$_2$), 33.5 (vt, $N = |^1J_{CP} + {}^3J_{CP}|$ = 8.7 Hz, 2C, P(C(CH$_3$)$_3$)$_2$), 32.3 (vt, $N = |^1J_{PC} + {}^3J_{PC}|$ = 10.2 Hz, 2C, PCH_2), 30.5 (br, 6C, P(C(CH_3)$_3$)$_2$), 28.6 (br, 6C, P(C(CH_3)$_3$)$_2$). ^{31}P$\{^1$H$\}$ (204.5 MHz) δ = 89.9 (s, 2P, P(C(CH$_3$)$_3$)$_2$). LIFDI-MS (Toluene): 766.2 (100 %, [M]$^+$).

Synthesis of 26

When followed by variable-temperature NMR, the transient species **26** can be observed by ^{31}P$\{^1$H$\}$ and ^{1}H NMR. NMR (THF-d$_8$, $-20°$C): ^{1}H (400 MHz) δ = 9.81 (d br, $^3J_{HH}$ = 5.9 Hz, 1H, C$_8$H), 7.92 - 7.90 (m, 1H, PyrPz), 7.46 - 7.37 (m, 1H, PyrPz, superimposed with **5**), 7.22 - 7.18 (m, 1H, PyrPz), 6.96 (br, 1H, PyrPz), 6.29 (br, 1H, PyrPz), 4.87 - 4.74 (m, 2H, NCH_2), 4.40 - 4.29 (m ,2H, NCH_2), 2.32 - 2.28 (m, 2H, PCH_2), 1.99 - 1.89 (m, 2H, PCH_2, superimposed with **5**), 1.33 (A$_9$XXA$_9$', $N = |^3J_{AX} + {}^5J_{AX'}|$ = 10.6 Hz, 18 H, P(C(CH_3)$_3$)$_2$), 0.38 (A$_9$XXA$_9$', $N = |^3J_{AX} + {}^5J_{AX'}|$ = 11.6 Hz, 18 H, P(C(CH_3)$_3$)$_2$). ^{31}P$\{^1$H$\}$ (204.5 MHz) δ = 1.92 (br, 2P, P(C(CH$_3$)$_3$)$_2$), -268.8 (br, 1P, PCO).

Oxidation of 27 to 29

27 (16.0 mg, 22.2 µmol, 1.00 eq.) and [FeCp$_2$]OTf (7.5 mg, 22 µmol, 1.0 eq.) are dissolved in THF-d$_8$ (0.5 mL) in a J-Young NMR tube and shaken for 1 minute at room temperature. The solution is directly transferred to the NMR machine and measured at $-38°$C.

The spectroscopic yield was determined to be 44%.

NMR (THF-d$_8$, −38°C) : ^{1}H (500 MHz): δ = 8.62 (d, $^3J_{HH}$ = 5.6 Hz, 1H, C$_8$H), 7.96 (d, $^3J_{HH}$ = 7.7 Hz, 1H, C$_5$H), 7.84 (d, $^3J_{HH}$ = 2.7 Hz, 1H, C$_1$H), 7.28 - 7.24 (m, 1H, C$_6$H), 7.24 - 7.19 (m, 1H, C$_7$H), 6.91 (d, $^3J_{HH}$ = 2.7 Hz, 1H, C$_2$H), 4.86 - 4.68 (m, 2H, NCH$_2$), 3.08 - 2.97 (m, 2H, NCH$_2$), 2.61 - 2.52 (m, 2H, PCH$_2$), 2.20 - 2.09 (m, 2H, PCH$_2$), 1.39 - 1.26 (br, 18H, P(C(CH$_3$)$_3$)$_2$), 0.59 - 0.50 (br, 18H, P(C(CH$_3$)$_3$)$_2$). ^{13}C{^{1}H} (125.8 MHz): δ = 157.9 (s, 1C, C$_4$), 156.2 (s, 1C, C$_8$), 147.1 (s, 1C, C$_3$), 140.6 (s, 1C, C$_7$), 135.2 (s, 1C, C$_1$), 123.8 (s, 1C, C$_5$), 123.6 (s, 1C, C$_6$), 106.6 (s, 1C. C$_2$), 82.4 (vt, N = $|^2J_{PC}$ + $^3J_{PC}|$ = 5.0 Hz, 2C, NCH$_2$), 42.8 (vt, N = $|^1J_{CP}$ + $^3J_{CP}|$ = 7.6 Hz, 2C, P(C(CH$_3$)$_3$)$_2$), 41.5 (vt, N = $|^1J_{CP}$ + $^3J_{CP}|$ = 11.3 Hz, 2C, P(C(CH$_3$)$_3$)$_2$), 29.7 (br, 6C, P(C(CH$_3$)$_3$)$_2$), 29.3 (br, 6C, P(C(CH$_3$)$_3$)$_2$), 26.5 (vt, N = $|^1J_{PC}$ + $^3J_{PC}|$ = 8.1 Hz, 2C, PCH$_2$), ^{31}P{^{1}H} (204.5 MHz) δ = 656.7 (d, $^1J_{PP}$ = 560 Hz, 1P, P$_1$), 231.6 (d, $^1J_{PP}$ = 560 Hz, 1P, P$_2$), 30.3 (br, 2P, P(C(CH$_3$)$_3$)$_2$). ^{31}P{^{1}H} (162.0 MHz) δ = 659.4 (dt, $^1J_{PP}$ = 562 Hz, $^2J_{PP}$ = 11.8 Hz, 1P, P$_1$), 234.7 (dt, $^1J_{PP}$ = 562 Hz, $^3J_{PP}$ = 3.9 Hz, 1P, P$_2$), 31.0 (dd, $^2J_{PP}$ = 11.8 Hz, $^3J_{PP}$ = 3.9 Hz, 1P, P(C(CH$_3$)$_3$)$_2$).

Oxidation of 28 to 30

3b (20.0 mg, 26.1 µmol, 1.00 eq.) and [FeCp$_2$]OTf (8.7 mg, 26 µmol, 1.0 eq.) are dissolved in THF-d$_8$ (0.5 mL) in a J-Young NMR tube and shaken for 1 minute at room temperature. The solution is directly transferred to the NMR machine and measured at −38°C. The spectroscopic yield was determined to be 33 %.

NMR (THF-d$_8$, −38°C) : ^{1}H (500 MHz): δ = 8.44 (d, $^3J_{HH}$ = 6.03 Hz, 1H, C$_8$H), 7.86 (d, $^3J_{HH}$ = 2.7 Hz, 1H, C$_1$H), 7.85 - 7.83 (m, 1H, C$_5$H), 7.31 - 7.25 (m ,1H, C$_7$H), 7.21 - 7.16 (m, 1H, C$_6$H), 6.83 (d, $^3J_{HH}$ = 2.7 Hz, 1H, C$_2$H), 4.92 - 4.81 (m, 2H, NCH$_2$), 3.13 - 3.08 (m, 2H, NCH$_2$), 2.61 - 2.52 (m, 2H, PCH$_2$), 2.15 - 2.08 (m, 2H, PCH$_2$), 1.30 - 1.28 (m, 18H, P(C(CH$_3$)$_3$)$_2$), 0.62 - 0.61 (m, 18H, P(C(CH$_3$)$_3$)$_2$). ^{13}C{^{1}H} (125.8 MHz): δ = 158.7 (s, 1C, C$_4$), 155.7 (s, 1C, C$_8$), 148.0 (s, 1C, C$_3$), 140.8 (s, 1C, C$_6$), 139.6 (s, 1C, C$_1$), 123.4 (s, 1C, C$_5$), 123.3 (s, 1C, C$_7$), 106.9 (s, 1C, C$_2$), 84.8 (vt, N = $|^2J_{PC}$ + $^3J_{PC}|$ = 4.6 Hz, 2C, NCH$_2$), 44.1 (vt, N = $|^1J_{CP}$ + $^3J_{CP}|$ = 7.3 Hz, 2C, P(C(CH$_3$)$_3$)$_2$), 41.5 (vt, N = $|^1J_{CP}$ + $^3J_{CP}|$ = 11.2 Hz, 2C, P(C(CH$_3$)$_3$)$_2$), 30.3 (br, 6C, P(C(CH$_3$)$_3$)$_2$), 29.5 (br, 6C, P(C(CH$_3$)$_3$)$_2$), 26.7 (vt, N = $|^1J_{PC}$ + $^3J_{PC}|$ = 8.1 Hz, 2C, PCH$_2$). ^{31}P{^{1}H} (162.0 MHz) δ = 26.5 (s, 2P, P(C(CH$_3$)$_3$)$_2$).

Synthesis of 31

27 (10.0 mg, 13.9 µmol, 1.00 eq.) and pyridine-N-oxide (2.6 mg, 28 µmol, 2.0 eq.) are dissolved in benzene (0.5 mL) and heated to 70°C for 2h. After cooling to room temperature the solution is filtered and the residue is extracted with benzene (2 x 0.5 mL). The volume is reduced to 0.5 mL and the crude product is purified by column chromatography over silanized silica (C$_6$H$_6$/THF). The solvent is removed, the residue is extracted with benzene and subsequent lyophilization yields **31** in form of a red powder (8.1 mg, 5.4 µmol, 77%).

Anal. Calcd for C$_{56}$H$_{100}$N$_8$O$_4$P$_6$Re$_2$ (1507.7): C, 44.6; H, 6.69; N, 7.43. Found: C, 44.8; H, 6.80; N, 7.33. NMR (C$_6$D$_6$, 25°C): ^{1}H (500 MHz): δ = 11.3 (d, $^3J_{HH}$ = 5.9 Hz, 2H, C$_8$H), 7.77 (d, $^3J_{HH}$ = 1.6 Hz, 2H, C$_1$H), 7.33 (ddd, $^3J_{HH}$ = 8.0 Hz, $^4J_{HH}$ = 1.5 Hz, $^5J_{HH}$ = 0.8 Hz, 2H, C$_5$H), 6.81 (ddd, $^3J_{HH}$ = 7.5 Hz, $^3J_{HH}$ = 6.0 Hz, $^4J_{HH}$ = 1.5 Hz,
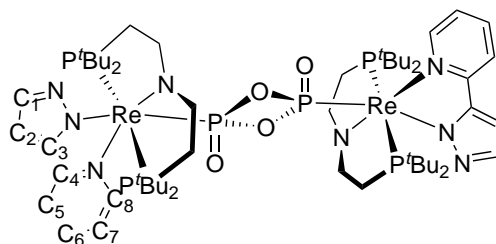
2H, C$_7$$H$), 6.42 (ddd, $^3J_{HH} = 7.5$ Hz, $^3J_{HH} = 6.0$ Hz, $^4J_{HH} = 1.5$ Hz, 2H, C$_6$$H$), 6.36 (m, $^3J_{HH} = 1.8$ Hz, 2H, C$_2$$H$), 3.74 - 3.38 (m, 8H, NCH_2), 2.28 - 2.08 (m, 8H, PCH_2), 1.23 (A$_9$XX'A$_9$', $N = |^2J_{AX} + ^4J_{AX}| = 12.6$ Hz, 18H, P(C(CH_3)$_3$)$_2$), 0.51 (A$_9$XX'A$_9$', $N = |^2J_{AX} + ^4J_{AX}| = 12.1$ Hz, 18H, P(C(CH_3)$_3$)$_2$). ^{13}C{^{1}H} (125.8 MHz): $\delta = 155.8$ (s, 2C, C_8), 150.7 (d, $^3J_{CP} = 2.8$ Hz, 2C, C_4), 149.1 (d, $^3J_{CP} = 4.3$ Hz, 2C, C_3), 143.1 (d, $^4J_{CP} = 4.1$ Hz, 2C, C_1), 138.6 (s, 2C, C_6), 117.9 (s, 2C, C_7), 115.9 (s, 2C, C_5), 104.4 (d, $^4J_{CP} = 1.2$ Hz, 2C, C_2), 96.6 (vt, $N = |^2J_{PC} + ^3J_{PC}| = 7.6$ Hz, $^3J_{CP} = 1.0$ Hz, 4C, NCH$_2$), 41.5 (vt, $N = |^1J_{CP} + ^3J_{CP}| = 18.9$ Hz, 4C, P(C(CH$_3$)$_3$)$_2$), 40.7 (vt, $N = |^1J_{CP} + ^3J_{CP}| = 14.2$ Hz, 4C, P(C(CH$_3$)$_3$)$_2$), 31.1 (vt, $N = |^2J_{CP} + ^4J_{CP}| = 3.9$ Hz, 12C, P(C(CH$_3$)$_3$)$_2$), 29.6 (vt, $N = |^2J_{CP} + ^4J_{CP}| = 4.5$ Hz, 12C, P(C(CH$_3$)$_3$)$_2$), 28.2 (vt, $N = |^1J_{PC} + ^3J_{PC}| = 15.3$ Hz, 4C, PCH$_2$). ^{31}P{^{1}H} (204.5 MHz) $\delta = 245.7$ (t, $^2J_{PP} = 20.7$ Hz, 2P; P_2O$_4$), 13.2 (d, $^2J_{PP} = 20.7$ Hz, 4P, P(C(CH$_3$)$_3$)$_2$).

One-electron reduction of 31

31 (5.0 mg, 3.3 μmol, 1.0 eq.) and $C_{10}H_{20}O_5$ (790 μL, 4.0 μmol, 1.0 eq.) are dissolved in THF (1 mL) and cooled to −35°C. NaHg (0.1 w%, 76 mg, 3.3 μmol, 1.0 eq.) is added and the reaction is stirred for 10 minutes while warming to room temperature. The obtained dark red solution is filtered and analyzed.

Synthesis of 34

31 (10.0 mg, 6.63 μmol, 1.00 eq.) and $C_{12}H_{24}O_6$ (3.5 mg, 13 μmol, 2.0 eq.) are dissolved in THF and cooled to −80°C. KC_8 (2.0 mg, 15 μmol, 2.2 eq.) is added in one portion and the solution is slowly allowed to warm to room temperature. After stirring for 30 minutes at room temperature the formed carbon is removed by filtration. The solvent is removed *in vacuo* and the residue is extracted with benzene (3 x 1 mL). The solvent is removed *in vacuo* and the product is crystallized from THF/pentane at −80°C for 3 days. The supernatant is decanted off and the residue is extracted with benzene. Lyophilization affords **34** in form of a purple powder (8.3 mg, 7.9 μmol, 59%).
Anal. Calcd for $C_{40}H_{74}KN_4O_8P_3Re$ (1057.3): C, 45.4; H, 7.06; N, 5.30. Found: C, 45.8; H, 7.23; N, 5.28.

Synthesis of $[Fe(C_5Me_5)_2][Al(O(C(CF_3)_3)_4]$

$[Fe(C_5Me_5)_2]$ (25.0 mg, 76.9 μmol, 1.00 eq.) and $Ag[Al(O(C(CF_3)_3)_4]$ (80.0 mg, 74.2 μmol, 0.97 eq.) are dissolved in DCM (3 mL) at 0°C and stirred for 30 minutes. The solution is filtered, concentrated and layered with pentane (10 mL). The solution is kept at −35°C for 1 day. The precipitate is filtered off, washed with pentane (3 x 1 mL) and extracted with THF (3 x 1 mL). The product is dried in vacuo. $[Fe(C_5Me_5)_2][Al(O(C(CF_3)_3)_4]$ is obtained in form of a turquoise powder(78 mg, 59.7 μmol, 78%).
Anal. Calcd for $C_{36}H_{30}AlF_{36}FeO_4$ (1293.4): C, 33.4; H, 2.34. Found: C, 33.6; H, 2.16.

Oxidation of 34 with $[Fe(C_5Me_5)_2][Al(O(C(CF_3)_3)_4]$

34 (5.0 mg, 4.7 μmol, 1.0 eq.) and $[Fe(C_5Me_5)_2][Al(O(C(CF_3)_3)_4]$ (6.1 mg, 4.7 μmol, 1.0 eq.) are placed in a J-Young NMR tube. THF-d_8 is added *via* vacuum condensation and the solvent is thawed at −90°C. The sample is gradually warmed to room temperature in the NMR machine.

Synthesis of 36

1 (30.0 mg, 48.6 μmol, 1.00 eq.) and $CoCp_2$ (9.6 mg, 51 μmol, 1.0 eq.) are dissolved in Et_2O (5 mL) and stirred for one minute at room temperature. PH_2Ph (77.3 μL, 47.1 μmol, 0.97 eq., 10 w% in hexane) is added and stirring is continued for 30 minutes. The solvent is evaporated and the residue is extracted with pentane (3 x 2 mL). The solution is concentrated and purified by column chromatography (pentane). **36** (26.1 mg, 37.8 μmol, 80%) is obtained as a green solid.
Anal. Calcd for $C_{26}H_{47}ClNOsP_3$ (692.27): C, 45.1; H, 6.84; N, 2.02 Found: C, 45.6; H, 6.39; N, 1.84. NMR (THF-d_8, -30°): ^{1}H (300 MHz): δ = 7.83 - 7.71 (m, 2H, $C_{ortho}H$), 7.36 ($A_{18}BCXX'A'_{18}B'C'$, $N = |^3J_{CX} + ^4J_{CX'}| = 33.6$ Hz, $^3J_{BC} = 5.7$ Hz, 2H, NCH), 7.30

- 7.21 (m, 3H, $C_{meta}H$, $C_{para}H$), 4.96 (dt, $^1J_{HP} = 337\,\text{Hz}$, $^2J_{HP} = 8.9\,\text{Hz}$, 2H, PH_2Ph), 4.49 ($A_{18}BCXX'A'_{18}B'C'$, $N = |^2J_{BX} +^4 J_{BX'}| = 8.0\,\text{Hz}$, $^3J_{BC} = 5.7\,\text{Hz}$, 2H, PCH), 1.21 ($A_{18}BCXX'A'_{18}B'C'$, $^3J_{AX} = 13.0\,\text{Hz}$, 18H, $PC(CH_3)_3$), 1.17 ($A_{18}BCXX'A'_{18}B'C'$, $^3J_{AX} = 12.6\,\text{Hz}$, 18H, $PC(CH_3)_3$). $^{13}C\{^1H\}$ (125.76 MHz): $\delta = 164.7$ (vt, $^2J_{CP} = 6.6\,\text{Hz}$, 2C, NCH), 135.8 (d, $^2J_{CP} = 10.4\,\text{Hz}$, 2C, $C_{ortho}H$), 132.8 (d, $^2J_{CP} = 61.6\,\text{Hz}$, 1C, $C_{ipso}H$), 130.7 (d, $^4J_{CP} = 2.7\,\text{Hz}$, 1C, $C_{para}H$), 129.0 (d, $^3J_{CP} = 11.2\,\text{Hz}$, 2C, $C_{meta}H$), 90.0 (vt, $^1J_{CP} = 19.5\,\text{Hz}$, 2C, PCH), 42.5 (vt, $^1J_{CP} = 10.3\,\text{Hz}$, 2C, $PC(CH_3)_3$), 37.7 (vt, $^1J_{CP} = 11.4\,\text{Hz}$, 2C, $PC(CH_3)_3$), 31.0 (vt, $^1J_{CP} = 2.8\,\text{Hz}$, 6C, $PC(CH_3)_3$), 30.3 (vt, $^1J_{CP} = 2.6\,\text{Hz}$, 6C, $PC(CH_3)_3$). $^{31}P\{^1H\}$ (161.25 MHz): $\delta = 51.0$ (d, $^2J_{PP} = 18.7\,\text{Hz}$, 2P, $PC(CH_3)_3$), -62.2 (t, $^2J_{PP} = 18.7\,\text{Hz}$, 1P, PH_2Ph). IR (Nujol, cm^{-1}): 2320, 2292 ($\tilde{\nu}_{PH_2}$). LIFDI-MS (Toluene): 693.1 (100%, M$^+$).

Synthesis of 37

1 (42.5 mg, 68.8 μmol, 1.00 eq.) and CoCp$_2$ (13.1 mg, 69.3 μmol, 1.00 eq.) are dissolved in Et$_2$O (5 mL) and stirred for 1 min at room temperature. PH$_2$Mes* (19.2 mg, 68.8 μmol, 1.00 eq.) is added and stirring is continued for 2h. After filtration the solvent is evaporated and the crude product is extracted with pentane (10 x 3 mL). The solution is concentrated and stored at -40° for 3 days. The solvent is decanted off and the solid is washed with cold pentane. After extraction with benzene (3 x 5 mL) Lyophilization yields **37** in form of a blue powder (42.8 mg, 49.7 μmol, 72%).

Anal. Calcd for $C_{38}H_{71}ClNOsP_3$ (860.58): C, 53.04; H, 8.32; N, 1.63 Found: C, 53.54; H, 7.82; N, 1.45. NMR (THF-d$_8$, -30°): ^1H (500 MHz): $\delta = 18.5$ (d, $^1J_{HP} = 337.2\,\text{Hz}$, 1H, PHMes*), 7.34 (d, $^4J_{HH} = 1.93\,\text{Hz}$, 1H, $C_{meta}H$, Mes*), 7.26 (d, $^4J_{HH} = 1.93\,\text{Hz}$, 1H, $C_{meta}H$, Mes*), 6.82 – 6.70 (m, 2 H, $NCHCHP$), 4.35 (m, $^3J_{HH} = 6.0\,\text{Hz}$, 1H, $NCHCHP$), 4.14 (m, $^3J_{HH} = 6.0\,\text{Hz}$, 1H, $NCHCHP$), 1.64 (d, $^3J_{HP} = 10.5\,\text{Hz}$, 9H, $PC(CH_3)_3$), 1.45 (d, $^3J_{HP} = 9.8\,\text{Hz}$, 9H, $PC(CH_3)_3$), 1.36 (s, 9H, $C_{ortho}C(CH_3)_3$, Mes*), 1.34 (s, 9H, $C_{ortho}C(CH_3)_3$, Mes*), 1.30 (s, 9H, $C_{para}C(CH_3)_3$, Mes*), 1.17 (d, $^3J_{HP} = 10.7\,\text{Hz}$, 9H, $PC(CH_3)_3$), 1.00 (d, $^3J_{HP} = 9.7\,\text{Hz}$, 9H, $PC(CH_3)_3$), -5.37 (m, 1H, OsH). $^{13}C\{^1H\}$ (125.76 MHz): $\delta = 162.8$ (dd, $^2J_{CP} = 11.5\,\text{Hz}$, $^3J_{CP} = 4.7\,\text{Hz}$, 1C, $NCHCHP$), 162.1 (dd, $^2J_{CP} = 10.4\,\text{Hz}$, $^3J_{CP} = 3.8\,\text{Hz}$, 1C, $NCHCHP$), 153.9 (s, 1C, C_{ortho}, Mes*), 152.6 (s, 1C, C_{ortho}, Mes*), 148.9 (s, 1C, C_{para}, Mes*), 146.4 (br, 1C, C_{ipso}, Mes*), 125.5 (s, 1C, C_{meta}, Mes*), 123.1 (s, 1C, C_{meta}, Mes*), 93.9 (m, $^1J_{CP} = 31.5\,\text{Hz}$, $^3J_{CP} = 7.3\,\text{Hz}$, 1C, $NCHCHP$), 92.6 (m, $^1J_{CP} = 34.5\,\text{Hz}$, $^3J_{CP} = 4.9\,\text{Hz}$, 1C, $NCHCHP$), 42.8 (dd, $^1J_{CP} = 14.3\,\text{Hz}$, $^3J_{CP} = 7.7\,\text{Hz}$ 1C, $PC(CH_3)_3$), 40.7 (s, 1C, $C_{para}C(CH_3)_3$, Mes*) 40.0 (s, 1C, $C_{ortho}C(CH_3)_3$, Mes*), 39.6 (dd, $^1J_{CP} = 13.6\,\text{Hz}$, $^3J_{CP} = 6.5\,\text{Hz}$ 1C, $PC(CH_3)_3$), 38.8 (dd, $^1J_{CP} = 21.4\,\text{Hz}$, $^3J_{CP} = 6.1\,\text{Hz}$, 1C, $PC(CH_3)_3$), 35.9 (dd, $^1J_{CP} = 19.0\,\text{Hz}$, $^3J_{CP} = 6.0\,\text{Hz}$, 1C, $PC(CH_3)_3$), 35.6 (s, 1C, $C_{ortho}C(CH_3)_3$, Mes*), 33.7 (br, 3C, $PC(CH_3)_3$), 33.5 (br, 3C, $PC(CH_3)_3$), 33.2 (s, 3C, $C_{ortho}C(CH_3)_3$), 32.8 (s, 3C, $C_{para}C(CH_3)_3$), 31.6 (s, 3C $C_{ortho}C(CH_3)_3$), 31.5-30.8 (br, 6C, $PC(CH_3)_3$). $^{31}P\{^1H\}$ (161.25 MHz): $\delta = 103.9$ (m, 1P, PHMes*), 31.6 (dd, $^2J_{PP} = 259.8\,\text{Hz}$, $^2J_{PP} = 20.1\,\text{Hz}$, 1P, $PC(CH_3)_3$), 30.0 (dd, $^2J_{PP} = 259.8\,\text{Hz}$, $^2J_{PP} = 18.3\,\text{Hz}$, 1P, $PC(CH_3)_3$). IR (Nujol, cm^{-1}): 2349 ($\tilde{\nu}_{PH}$, partially superimposed with the absorbance of CO$_2$ in the atmosphere). LIFDI-MS (Toluene): 861.5 (39%, [M]$^+$, 825.5 (100%, [M-HCl]$^+$).

Synthesis of 38

Route A: **37** (30 mg, 34.9 µmol, 1.00 eq.) and CoCp$_2$ (6.6 mg, 35 µmol, 1.0 eq.) are dissolved in pentane (3 mL) and stirred for 5 minutes at room temperature. After filtration and extraction of the residue with pentane (3 x 1 mL) the solvent is evaporated. After column chromatography (silanized silica, pentane), the solvent is evaporated. **38** is obtained after lyophilization as a dark green powder (23.0 mg, 27.9 µmol, 80%).
Anal. Calcd for C$_{38}$H$_{71}$NOsP$_3$ (825.1): C, 55.1; H, 8.53; N, 1.68 Found: C, 54.9; H, 8.65; N, 1.65. IR (Nujol, cm^{-1}): 2345 ($\tilde{\nu}_{PH}$) 2180 ($\tilde{\nu}_{OsH}$). LIFDI-MS (Toluene): 826.4 (100%, [M]$^+$).
Route B: **1** (35.0 mg, 56.7 µmol, 1.00 eq) and CoCp$_2$ (21.4 mg, 113 µmol, 2.00 eq.) are dissolved in C$_6$H$_6$ (3 mL) and stirred for 2 minutes at room temperature. PH$_2$Mes* (15.8 mg, 56.7 µmol, 1.00 eq.) is added and stirring is continued for additional 4 hours. The solvent is removed and the crude product is extracted with pentane (5 x 1 mL) and the solvent is evaporated. After column chromatography (silanized silica, pentane) the solvent is evaporated. Lyophilization yields **38** as a dark green powder (41.8 mg, 50.7 µmol, 89%)
Anal. Calcd for C$_{38}$H$_{71}$NOsP$_3$ (825.1): C, 55.3; H, 8.67; N, 1.70 Found: C, 54.9; H, 8.65; N, 1.65. IR (Nujol, cm^{-1}): 2345 ($\tilde{\nu}_{PH}$) 2180 ($\tilde{\nu}_{OsH}$). LIFDI-MS (Toluene): 826.4 (100%, [M]$^+$). $\mu_{eff}^{298K} = 1.51\ \mu_B$

Synthesis of 39

Route A: **38** (10.0 mg, 12.1 µmol, 1.00 eq.) and TEMPO (5.7 mg, 38 µmol, 3.0 eq.) are dissolved in pentane and stirred for 10 minutes at room temperature. After column chromatography (silanized silica, pentane) and removal of the solvent **39** is obtained in form of a violet powder (9.0 mg, 11 µmol, 90%).
NMR (THF-d$_8$, -30°): ^{1}H (500 MHz): δ =7.36 (d, $^4J_{HH}$ = 1.8 Hz, 1H, C$_{meta}$H), 7.23 (m, $^3J_{HH}$ = 6.1 Hz, 2H, NCH), 7.03 (d, $^4J_{HH}$ = 1.8 Hz, 1H, C$_{meta}$H), 4.63 (m, $^3J_{HH}$ = 5.0 Hz, 2H, PCH), 1.55 (s, 9H, C$_{ortho}$C(CH$_3$)$_3$), 1.35 (s, 9H, C$_{ortho}$C(CH$_3$)$_3$), 1.34 (s, 9H, C$_{para}$C(CH$_3$)$_3$), 1.22 (br, 18H, PC(CH$_3$)$_3$), 1.20 (br, 18H, PC(CH$_3$)$_3$), -15.91 (t, $^2J_{HP}$ = 14.5 Hz, 1H, OsH). ^{31}P{^{1}H} (161.25 MHz): δ = 825.1 (t, $^2J_{PP}$ = 36.6 Hz, 1P, PH), 43.2 (d, $^2J_{PP}$ = 36.6 Hz, 2P, PC(CH$_3$)$_3$). LIFDI-MS (Toluene): 825.5 (100%, [M]$^+$).
Route B: **38** (10 mg, 12.1 µmol, 1.0 eq.) is dissolved in THF (1 mL) and cooled to -80°. Ag[Al(O-^{t}Bu-F$_9$)$_4$] (13.0 mg, 12.1 µmol, 1.00 eq.) is added and the solution is stirred for 30 seconds. KOtBu (1.4 mg, 1.0 µmol, 1.0 eq.) is added and stirring is continued for 3 minutes. After evaporation of the solvent the crude product is extracted with pentane and purified by chromatography (silanized silica, pentane). NMR spectra (-30°) were identical with spectra of the product obtained by route A.

Synthesis of 40

Complex **39** is prepared by route A and dissolved in benzene-d$_6$ (0.5 mL), transferred to a J-Young NMR tube and stirred at room temperature until complete conversion of **6** is detected by NMR. Lyophilization yields a brown powder as a mixture of the two diastereomers of **7** in a ratio about 60 (**A**) : 40 (**B**) according to NMR spectroscopy.

Anal. Calcd for $C_{39}H_{70}NOOsP_3$ (825.1):C, 55.4; H, 8.56; N, 1.70 Found: C, 55.5; H, 8.63, N, 1.68. LIFDI-MS (Toluene): 825.5 (100%, $[M]^+$).

NMR (**A**, C_6D_6, RT): ^{1}H (500 MHz): δ = 8.34 (m,$^1J_{HP}$ = 308.7 Hz, $^3J_{HP}$ = 9.14, $^3J_{HP}$ = 4.67, P*H*), 7.55 -7.40 (m, 3H, NC*H*, $C_{meta}H$), 7.18-7.15 (m, 1H, $C_{meta}H$), 4.52-4.44 (m, 2H, PC*H*), 2.92-2.85 (m, 1H, PC*H*$_2$C(CH$_3$)$_2$), 2.69-2.63 (m, 1H, PC*H*$_2$C(CH$_3$)$_2$), 1.71 (s, 9H, C_{ortho}C(C*H*$_3$)$_3$), 1.64 (m, 3H, PCH$_2$C(C*H*$_3$)$_2$), 1.49 (d, $^2J_{HP}$ = 12.4 Hz, 9H, PC(C*H*$_3$)$_3$), 1.32 (s, 9H, C_{para}C(C*H*$_3$)$_3$), 1.25 (d, $^2J_{HP}$ = 12.1 Hz, 9H, PC(C*H*$_3$)$_3$), 1.14 (m, 3H, PCH$_2$C(C*H*$_3$)$_2$), 0.96 (d, $^2J_{HP}$ = 12.7 Hz, 9H, PC(C*H*$_3$)$_3$), 0.93 (d, $^2J_{HP}$ = 11.0 Hz, 9H, PC(C*H*$_3$)$_3$), -44.7 (ddd, $^2J_{HP}$ = 18.4 Hz, $^2J_{HP}$ = 13.1 Hz, $^2J_{HP}$ = 13.0 Hz, Os*H*). ^{31}P{^{1}H} (161.25 MHz): δ = 64.9 (dd, $^2J_{PP}$ = 234.4 Hz, $^2J_{PP}$ = 11.5 Hz), 53.0 (dd, $^2J_{PP}$ = 234.4 Hz, $^2J_{PP}$ = 10.9 Hz), -54.6 (dd, $^2J_{PP}$ = 11.5 Hz, $^2J_{PP}$ = 10.9 Hz)

NMR (**B**, C_6D_6, RT): ^{1}H (500 MHz): δ = 8.43 (m,$^1J_{HP}$ = 300.7 Hz, $^3J_{HP}$ = 8.7, $^3J_{HP}$ = 4.8, P*H*), 7.55 -7.40 (m, 3H, NC*H*, $C_{meta}H$), 7.18-7.15 (m, 1H, $C_{meta}H$), 4.57-4.52 (m, 2H, PC*H*), 2.53-2.41 (m, 2H, PC*H*$_2$C(CH$_3$)$_2$), 1.51(s, 9H, C_{ortho}C(C*H*$_3$)$_3$), 1.50 (m, 3H, PCH$_2$C(C*H*$_3$)$_2$), 1.43 (d, $^2J_{HP}$ = 11.4 Hz, 9H, PC(C*H*$_3$)$_3$), 1.41 (d, $^2J_{HP}$ = 12.43 Hz, 9H, PC(C*H*$_3$)$_3$), 1.33 (s, 9H, C_{para}C(C*H*$_3$)$_3$), 1.11 (d, $^2J_{HP}$ = 12.6 Hz, 9H, PC(C*H*$_3$)$_3$), 1.11 (m, 3H, PCH$_2$C(C*H*$_3$)$_2$), 0.91 (d, $^2J_{HP}$ = 12.5 Hz, 9H, PC(C*H*$_3$)$_3$), -45.7 (ddd, $^2J_{HP}$ = 21.4 Hz, $^2J_{HP}$ = 14.4 Hz, $^2J_{HP}$ = 14.4 Hz, Os*H*). ^{31}P{^{1}H} (161.25 MHz): δ = 68.0 (dd, $^2J_{PP}$ = 234.8 Hz, $^2J_{PP}$ = 10.5 Hz), 58.0 (dd, $^2J_{PP}$ = 234.8 Hz, $^2J_{PP}$ = 10.8 Hz), -55.4 (dd, $^2J_{PP}$ = 10.8 Hz, $^2J_{PP}$ = 10.5 Hz).

Synthesis of 41

38 (20.0 mg, 24.2 µmol, 1.00 eq.) and TEMPO (11.4 mg, 72.7 µmol, 3.00 eq) are dissolved in pentane and stirred for 10 min at room temperature. The solution is degassed by three freeze-pump-thaw cycles and one atmosphere of CO is added. The solution is stirred at -80° for 5 minutes and the solvent is removed *i. vac.* The crude product is purified *via* column chromatography (silanized silica, pentane) and crystalized at -80° to give **41** (16.5 mg, 19.4 µmol, 80 %) as dark red crystals.

Anal. Calcd for $C_{39}H_{70}NOOsP_3$ (825.1): C, 54.9; H, 8.28; N, 1.64 Found: C, 54.6; H, 8.34; N, 1.55. NMR (THF-d$_8$): ^{1}H (500 MHz): δ = 9.79 (ddd, $^1J_{PH}$ = 308.9 Hz, $^3J_{PH}$ = 13.3 Hz, $^3J_{PH}$ = 4.9 Hz, 1H, P*H*Mes*), 7.44 (ddd, $^3J_{PH}$ = 36.6 Hz, $^3J_{HH}$ = 6.0 Hz, $^4J_{PH}$ = 1.4 Hz, 1H, NC*H*), 7.33 (ddd, $^3J_{PH}$ = 34.6 Hz, $^3J_{HH}$ = 5.9 Hz, $^4J_{PH}$ = 2.2 Hz, 1H, NC*H*), 7.24 (m, 2H, C$_{meta}$*H*) , 4.44 (m, $^2J_{PH}$ = 5.1 Hz, $^3J_{HH}$ = 6.0 Hz, $^4J_{PH}$ = 1.7 Hz, 1H, PC*H*), 4.33 (m, $^2J_{PH}$ = 5.0 Hz, $^3J_{HH}$ = 5.8 Hz, $^4J_{PH}$ = 1.8 Hz, 1H, PC*H*), 1.62 (s, 9H, C_{ortho}(C*H*$_3$)$_3$)), 1.61 (s, 9H, C_{ortho}(C*H*$_3$)$_3$)), 1.51 (d, $^3J_{PH}$ = 13.5 Hz, 9H, PC(C*H*$_3$)$_3$)), 1.31 (d, $^3J_{PH}$ = 13.0 Hz, 9H, PC(C*H*$_3$)$_3$)) ,1.31 (s, 9H, C_{para}(C*H*$_3$)$_3$)), 1.03 (d, $^3J_{PH}$ = 13.8 Hz, 9H, PC(C*H*$_3$)$_3$)), 0.81 (d, $^3J_{PH}$ = 13.4 Hz, 9H, PC(C*H*$_3$)$_3$)). ^{13}C{^{1}H} (125.76 MHz): δ = 181.7 (ddd, $^2J_{CP}$ = 48.3 Hz, $^2J_{CP}$ = 6.0, $^2J_{CP}$ = 5.6, 1C, Os-*C*O), 164.9 (d, $^2J_{CP}$ = 12.0 Hz, 1C, N*C*H), 163.7 (d, $^2J_{CP}$ = 11.0 Hz, 1C, N*C*H), 155.7 (br, 1C, C_{ortho}), 155.6 (d, $^2J_{CP}$ = 4.1 Hz, 1C, C^{ortho}), 148.8 (d, $^4J_{CP}$ = 2.2 Hz, 1C, C^{para}), 140.2 (d, $^1J_{CP}$ = 6.1 Hz, 1C, C_{ipso}), 123.0 (d, $^3J_{CP}$ = 5.1 Hz, 1C, C_{meta}), 122.2 (d, $^3J_{CP}$ = 10.2 Hz, 1C, C_{meta}), 88.4 (dd, $^1J_{CP}$ = 45.5 Hz, $^3J_{CP}$ = 3.7 Hz, 1C, P*C*H), 86.7 (dd, $^1J_{CP}$ = 46.8 Hz, $^3J_{CP}$ = 5.0 Hz, 1C, P*C*H), 41.9 (ddd, $^1J_{CP}$ = 22.0 Hz, $^3J_{CP}$ = 7.4, $^3J_{CP}$ = 3.1 Hz, 1C, P*C*(CH$_3$)$_3$), 40.8 (ddd, $^1J_{CP}$ = 21.1 Hz, $^3J_{CP}$ = 7.5, $^3J_{CP}$ = 2.9 Hz, 1C, P*C*(CH$_3$)$_3$), 40.7 (s, 1C, C_{ortho}*C*(CH$_3$)$_3$), 40.0 (s, 1C, C_{ortho}*C*(CH$_3$)$_3$),

39.9 (dd, $^1J_{CP} = 23.5\,\text{Hz}$, $^3J_{CP} = 2.2$, 1C, PC(CH$_3$)$_3$), 37.5 (dd, $^1J_{CP} = 24.2\,\text{Hz}$, $^3J_{CP} = 2.0$, 1C, PC(CH$_3$)$_3$), 35.3 (s, 1C, C$_{para}C$(CH$_3$)$_3$), 35.1 (s, 3C, C$_{ortho}$C(CH$_3$)$_3$), 33.6 (s, 3C, C$_{ortho}$C(CH$_3$)$_3$), 31.9 (s, 3C, C$_{para}$C(CH$_3$)$_3$), 31.4 (d, $^2J_{CP} = 4.9\,\text{Hz}$, 3C, PC($CH_3$)$_3$), 31.3 (d, $^2J_{CP} = 3.8\,\text{Hz}$, 3C, PC($CH_3$)$_3$), 30.5 (br, 3C, PC($CH_3$)$_3$), 30.2 (br, 3C, PC($CH_3$)$_3$). ^{31}P$\{^1H\}$ (161.25 MHz): $\delta = 66.9$ (dd, $^2J_{PP} = 197{,}1\,\text{Hz}$, $^2J_{PP} = 35.4$, 1P, PC(CH$_3$)$_3$), 53.5 (dd, $^2J_{PP} = 197{,}1\,\text{Hz}$, $^2J_{PP} = 35.3$, 1P, PC(CH$_3$)$_3$), 17.7 (dd, $^2J_{PP} = 35.4\,\text{Hz}$, $^2J_{PP} = 35.3$, 1P, PHMes*). IR (KBr, cm^{-1}): 2333 ($\tilde{\nu}_{PH}$), 1888 ($\tilde{\nu}_{CO}$). LIFDI-MS (Toluene): 853.4 (100%, [M]$^+$).

Reaction of 39 with PhCCH

38 (20.0 mg, 24.2 µmol, 1.00 eq.) and TEMPO (11.4 mg, 72.7 µmol, 3.00 eq) are dissolved in pentane and stirred for 10 min at room temperature. TEMPOH is removed by column chromatography (pentane, silanized silica), PhCCH (2.7 µL, 24 µmol, 1.0 eq.) is added and stirring is continued for 16 h.

NMR (C$_6$D$_6$, RT): ^{1}H (500 MHz): $\delta = 9.39$ (dddd, $^1J_{HP} = 308.7\,\text{Hz}$, $^3J_{HP} = 12.3\,\text{Hz}$, $^3J_{HP} = 5.3\,\text{Hz}$, $^4J_{HH} = 1.6\,\text{Hz}$, 1H, HPMes*), 7.41 (d, $^4J_{HH} = 2.3\,\text{Hz}$, C$_{meta}$H, HPMes*), 7.40 (d, $^4J_{HH} = 2.3\,\text{Hz}$, C$_{meta}$H, HPMes*), 7.29 (m, $^3J_{HH} = 6.2\,\text{Hz}$, 1H, NC$H$CHP), 7.21 (m, 2H, C$_{meta}$H, Ph), 7.20 (m, $^3J_{HH} = 6.5\,\text{Hz}$, 1H, NC$H$CHP), 6.87 (d, $^3J_{HH} = 7.4\,\text{Hz}$, 2H, C$_{ortho}$H, Ph), 6.76 (tt, $^3J_{HH} = 7.3\,\text{Hz}$, $^4J_{HH} = 1.2\,\text{Hz}$, 1H, C$_{para}$H, Ph), 4.37 (m, $^3J_{HH} = 6.2\,\text{Hz}$, 1H, NCHC$H$P), 4.36 (m, 1H, $^3J_{HH} = 6.5\,\text{Hz}$ NCHCHP), 2.68 (m, $^4J_{HH} = 1.6\,\text{Hz}$, Os=C=C$H$Ph), 1.81 (s, 9H, C$_{ortho}$C(CH$_3$)$_3$, HPMes*), 1.79 (s, 9H, C$_{ortho}$C(CH$_3$)$_3$, HPMes*), 1.46 (d, $^3J_{HP} = 13.8\,\text{Hz}$, 9H, PC(CH$_3$)$_3$), 1.36 (s, 9H, C$_{para}$C(CH$_3$)$_3$, HPMes*), 1.34 (br, 9H, PC(CH$_3$)$_3$), 1.12 (d, $^3J_{HP} = 14.0\,\text{Hz}$, PC(CH$_3$)$_3$), 0.84 (d, $^3J_{HP} = 13.2\,\text{Hz}$, 9H, PC(CH$_3$)$_3$). ^{13}C$\{^1H\}$ (125.76 MHz): $\delta = 274.8$ (ddd, $^2J_{CP} = 37.0\,\text{Hz}$, $^2J_{CP} = 8.7\,\text{Hz}$, $^2J_{CP} = 8.2\,\text{Hz}$, 1C, Os=$C$=CHPh), 164.9 (d, $^2J_{CP} = 12.0\,\text{Hz}$, 1C, N$C$HCHP), 163.7 (d, $^2J_{CP} = 11.2\,\text{Hz}$, 1C, N$C$HCHP), 156.7 (d, $^2J_{CP} = 15.9\,\text{Hz}$, 1C, C_{ortho}C(CH$_3$)$_3$, HPMes*), 156.0 (d, $^2J_{CP} = 6.4\,\text{Hz}$, 1C, C_{ortho}C(CH$_3$)$_3$, HPMes*), 148.3 (s, 1C, C_{para}C(CH$_3$)$_3$, HPMes*), 140.0 (s, 1C, C_{ipso}C(CH$_3$)$_3$, HPMes*), 133.7 (s, 1C, C_{ipso}, Ph), 124.4 (s, 2C, C_{ortho}, Ph), 122.7 (s, 1C, C_{para}, Ph), 122.3 (d, $^3J_{CP} = 4.8\,\text{Hz}$, 1C, $C_{meta}C$(CH3)3, HPMes*), 121.6 (d, $^3J_{CP} = 11.3\,\text{Hz}$, 1C, $C_{meta}C$(CH3)3, HPMes*), 113.2 (s, 1C, Os=C=CHPh), 92.2 (d, $^1J_{CP} = 42.6\,\text{Hz}$, 1C, NCH$C$HP), 90.3 (dd, $^1J_{CP} = 43.5\,\text{Hz}$, $^3J_{CP} = 4.5\,\text{Hz}$, 1C, NCH$C$HP), 40.8 (d, $^3J_{CP} = 21.16\,\text{Hz}$, 1C, PC(CH$_3$)$_3$), 40.6 (s, 1C, C$_{ortho}$C(CH$_3$)$_3$, HPMes*), 40.0 (d, $^3J_{CP} = 20.8\,\text{Hz}$, 1C, PC(CH$_3$)$_3$), 39.4 (s, 1C, C$_{ortho}$C(CH$_3$)$_3$, HPMes*), 37.8 (dd, $^3J_{CP} = 19.0\,\text{Hz}$, $^5J_{CP} = 3.2\,\text{Hz}$, 1C,PC(CH$_3$)$_3$), 35.9 (dd, $^3J_{CP} = 20.3\,\text{Hz}$, $^5J_{CP} = 3.1\,\text{Hz}$, 1C,PC(CH$_3$)$_3$), 35.0 (s, 3C, C$_{ortho}$C(CH$_3$)$_3$, HPMes*), 33.5 (s, 3C, C$_{ortho}$C(CH$_3$)$_3$, HPMes*), 31.7 (s, 3C, C$_{para}$C(CH$_3$)$_3$, HPMes*), 31.2 (s, 3C, PC(CH$_3$)$_3$), 31.0 (s, 3C, PC(CH$_3$)$_3$), 30.0 (br, 6C, PC(CH$_3$)$_3$). ^{31}P$\{^1$H$\}$ (161.25 MHz): $\delta = 50.0$ (dd, $^2J_{PP} = 242.3\,\text{Hz}$, $^2J_{PP} = 24.6\,\text{Hz}$ 1P, PC(CH3)3), 36.5 (dd, $^2J_{PP} = 242.3\,\text{Hz}$, $^2J_{PP} = 18.2\,\text{Hz}$ 1P, PC(CH3)3), 3.52 (dd, $^2J_{PP} = 24.6\,\text{Hz}$, $^2J_{PP} = 18.2\,\text{Hz}$, 1P, PMes*).

Synthesis of 43

38 (10.0 mg, 12.1 µmol, 1.00 eq.) is dissolved in Et$_2$O (1 mL) and cooled to -35°. Ag[Al(O-^{t}Bu-F$_9$)$_4$] (13.0 mg, 12.1 µmol, 1.00 eq.) is added and the solution is stirred for 30 seconds. After filtration the solvent is removed and the residue is extracted with Et$_2$O

(5 x 0.5 mL) at -35°. After concentration the solution is layered with pentane (5 mL) and stored at -85° for 24h. The solution is decanted off and the solid is washed with pentane at -30° (5 x 1 mL). After drying *in* vacuo at -30° **43** is obtained as a blue solid (18.0 mg, 10.0 μmol, 83%) NMR spectroscopic characterization shows minor decomposition products and some residual solvent (Et$_2$O/pentane). Elemental analysis did not give reproducible data due to high reactivity.

NMR (THF-d$_8$, -30°C): ^{1}H (500 MHz): δ = 18.3 (d, $^1J_{HP}$ = 345.5 Hz, 1H, P*H*Mes*), 7.86 – 7.68 (m, 2 H, NC*H*CHP), 7.50 (d, $^4J_{HH}$ = 1.83 Hz, 1H, C$_{meta}$*H*, Mes*), 7.42 (d, $^4J_{HH}$ = 1.893 Hz, 1H, C$_{meta}$*H*, Mes*), 5.79 (m, 1H, NCHC*H*P), 5.55 (m, 1H, NCHC*H*P), 1.58 (d, $^3J_{HP}$ = 14.0 Hz, 9H, PC(C*H$_3$*)$_3$), 1.52 (d, $^3J_{HP}$ = 13.9 Hz, 9H, PC(C*H$_3$*)$_3$), 1.46 (s, 9H, C$_{ortho}$C(C*H$_3$*)$_3$, Mes*), 1.40 (s, 9H, C$_{ortho}$C(C*H$_3$*)$_3$, Mes*), 1.36 (s, 9H, C$_{para}$C(C*H$_3$*)$_3$, Mes*), 1.10-1.00 (m, 18H, PC(C*H$_3$*)$_3$), -21.7 (m, 1H, Os*H*). ^{13}C{^{1}H} (125.76 MHz): δ = 168.2 (m, 1C, N*C*HCHP), 167.4 (m, 1C, N*C*HCHP), 154.5 (s, 1C, *C*$_{para}$, Mes*), 151.6 (s, 1C, *C*$_{ortho}$, Mes*), 151.9 (s, 1C, *C*$_{ortho}$, Mes*), 143.7 (br, 1C, *C*$_{ipso}$, Mes*), 125.16 (br, 2C, *C*$_{meta}$, Mes*), 122.3 (q, $^1J_{CF}$ = 291.8 Hz, 12C, *C*F$_3$), 110.0-108.9 (m, 2C, NCH*C*HP), 79.9 (br, 4C, *C*CF$_3$), 40.8 (s, 1C, C$_{ortho}$*C*(CH$_3$)$_3$), 40.3 (d, $^1J_{CP}$ = 21.6 Hz, 1C, P*C*(CH$_3$)$_3$), 40.1 (s, 1C, C$_{ortho}$*C*(CH$_3$)$_3$), 38.2 (d, $^1J_{CP}$ = 21.3 Hz, 1C, P*C*(CH$_3$)$_3$), 37.73 (d, $^1J_{CP}$ = 22.7 Hz, 1C, P*C*(CH$_3$)$_3$), 35.8 (s, 1C, C$_{para}$*C*(CH$_3$)$_3$), 34.7 (d, $^1J_{CP}$ = 22.4 Hz, 1C, P*C*(CH$_3$)$_3$), 33.8 (s, 3C, C$_{ortho}$C(*C*H$_3$)$_3$), 33.6 (s, 3C, C$_{ortho}$C(*C*H$_3$)$_3$), 31.4 (s, 3C, C$_{para}$C(*C*H$_3$)$_3$), 30.9 (br, 3C, PC(*C*H$_3$)$_3$), 30.7 (br, 3C, PC(*C*H$_3$)$_3$), 30.0 (br, 3C, PC(*C*H$_3$)$_3$), 29.3 (br, 3C, PC(*C*H$_3$)$_3$). ^{31}P{^{1}H} (161.25 MHz): δ = 169.2 (m, 1P, P*H* Mes*), 61.5 (dd, $^2J_{PP}$ = 224.0 Hz, $^2J_{PP}$ = 18.0 Hz, 1P, *P*C(CH$_3$)$_3$), 52.28 (dd, $^2J_{PP}$ = 224.0 Hz, $^2J_{PP}$ = 14.2 Hz, 1P, *P*C(CH$_3$)$_3$). IR (Nujol, cm^{-1}): 2350 ($\tilde{\nu}_{PH}$). LIFDI-MS (THF): 826.4 (100%, [M]$^+$).

Synthesis of 44

1 (15.0 mg, 24.3 μmol, 1.00 eq.) and CoCp$_2$ (4.6 mg, 24 μmol, 1.0 eq.) are dissolved in toluene (1 mL) stirred for 1 minutes and filtered. The residue is extracted with toluene (0.5 mL) and the combined filtrates are cooled to −80°C. ClP**A** (**A**/ClP**A**: 75/25, 18.4 mg, 94.8 μmol, 3.9 eq.) is added and the solution is warmed to room temperature over 1h. The solution is filtered and the solvent is removed. DCM (1 mL) is added and the solution is cooled to −80°C for 4h. The anthracene is decanted and more anthracene is crystallized from DCM/pentane (0.5 mL/5 mL) at −80°C. The anthracene is decanted and the obtained solution is subjected to filtration through an activated charcoal column. The solvent is removed the crude product is layered with pentane (3 mL) and stored at −30°C for 2 days. The solution is decanted and the solid is dried in vacuo. **44** (8.0 mg, 13 μmol, 50%) is obtained as a purple solid.

Anal. Calcd. for C$_{20}$H$_{40}$Cl$_2$NOsP$_3$ (648,6): C, 37.0; H, 6.22; N, 2.16. Found: C, 37.4; H, 6.53; N, 2.03.

NMR (CD$_2$Cl$_2$, RT): ^{1}H (400 MHz) δ = 7.36 (A$_{18}$BCXX'A'$_{18}$B'C', N = $|^3J_{CX}+^4J_{CX'}|$ = 35.7 Hz, $^3J_{BC}$ = 6.1 Hz, 2H, NC*H*), 4.32 (A$_{18}$BCXX'A'$_{18}$B'C', N = $|^2J_{BX}+^4J_{BX'}|$ = 6.6 Hz, $^3J_{BC}$ = 6.1 Hz, 2H, PC*H*), 1.37 (A$_{18}$BCXX'A'$_{18}$B'C', $^3J_{AX}$ = 14.7 Hz, 18H, P(C(C*H$_3$*)$_3$)), 1.24 (A$_{18}$BCXX'A'$_{18}$B'C', $^3J_{AX}$ = 14.3 Hz, 18H, P(C(C*H$_3$*)$_3$)). ^{13}C{^{1}H} (128.8 MHz) δ = 168.1 (vt, N = $|^2J_{CP}$ + $^3J_{CP}|$ = 5.6 Hz, 2C, N*C*H), 87.2 (vt, N = $|^1J_{CP}$ + $^3J_{CP}|$= 23.4 Hz, 2C, P*C*H), 40.1 (vt, N = $|^1J_{CP}$ + $^2J_{CP}|$ = 12.5 Hz, 2C,

P(C(CH$_3$))), 35.9 (vt, $N = |^1J_{CP} + {}^2J_{CP}| = 11.0$ Hz, 2C, P(C(CH$_3$))), 29.8 (vt, $N = |^2J_{CP} + {}^4J_{CP}| = 2.3$ Hz, 6C, P(C(CH$_3$)$_3$)), 29.4 (br, 6C, P(C(CH$_3$)$_3$)). ^{31}P{^{1}H} (202.5 MHz) $\delta = 858.4$ (s br, 1P, PCl), 70.4 (s br, 2P, P(C(CH_3)$_3$)). LIFDI-MS (Toluol): 649.2 ([M$^+$]).

Reaction of 1, 7 and 12 with PCO$^-$

7 µmol of the chosen complex and 14 µmol of [Na(diox)$_{1.33}$][PCO] are dissolved in THF (0.5 mL) and stirred for 5 minutes at room temperature. NMR spectroscopy reveals quantiative reduction without any detectable follow-up reactions in all cases.

Reaction of 44 with Na$^+$ and Tl$^+$

7 µmol of **44** and 7 µmol of NaBPh$_4$ or TlOTf are dissolved in THF (0.5 mL) and stirred for one hour at room temperature. No conversion was detected by NMR spectroscopy.

Reaction of 44 with unsaturated substrates

44 (5.0 mg, 7.72 µmol, 1.0 eq.) and cyclohexane/tolane/dimethyl butadiene (5.0 eq.) are dissolved in C$_6$D$_6$ and heated to 80°C for 3h. No conversion was observed by ^{31}P NMR spectroscopy.

Reaction of 44 with [TBA][WN(ODipp)$_4$]

44 (5.0 mg, 7.7 µmol, 1.0 eq., prepared *in situ*) and [TBA][WN(ODipp)$_4$] (9.3 mg, 7.7 µmol, 1.0 eq.) are dissolved in THF (0.5 mL) and heated to 70°C for 24h. The solvent is removed, the residue extracted with benzene and characterized by NMR spectroscopy. NMR (C$_6$D$_6$, RT): ^{1}H (400 MHz) $\delta = 7.10 - 6.86$ (m, 5H, NHH, C$_{\text{ortho/meta}}H$), 4.22 (A$_{18}$BCXX'A'$_{18}$B'C', $N = |^2J_{BX} + {}^4J_{BX'}| = 5.9$ Hz, $^3J_{BC} = 5.7$ Hz, 2H, PCH), 3.30 (h, $^3J_{HH} = 6.8$ Hz, 2H, CH(CH$_3$)$_2$) 1.46 (A$_{18}$BCXX'A'$_{18}$B'C', $^3J_{AX} = 14.0$ Hz, 18H, P(C(CH$_3$)$_3$)), 1.30 (A$_{18}$BCXX'A'$_{18}$B'C', $^3J_{AX} = 13.6$ Hz, 18H, P(C(CH$_3$)$_3$)), 1.15 (d, $^3J_{HH} = 6.8$ Hz, 12H, CH(CH_3)$_3$)). ^{31}P{^{1}H} (202.5 MHz) $\delta = 791.2$ (t, $^2J_{PP} = 16.8$ Hz, 1P, PODipp), 56.7 (d, $^2J_{PP} = 16.8$ Hz, 2P, P(C(CH_3)$_3$)).

7.6 Proton-Induced Splitting of Dinitrogen by Dimeric Mo PNP Pincer Complexes

7.6.1 Computational Details

DFT calculations were carried out with the ORCA program package using the PBE0 functional.[304], [318], [326]   Ahlrichs' basis sets def2-SVP (for geometry optimization and frequency calculation) and def2-TZVPP (for single-point energies) were used with a full basis for all elements but Mo for which the Stuttgart-Dresden electron core potential was chosen to replace the inner shell orbitals.[307], [308]   The RI-J (PBE) approximation in combination with the corresponding auxiliary basis sets of Alrichs was utilized to reduce computational costs in the geometry optimization and frequency calculations.[327]–[329]   Grimme's model (D3) with Becke-Johnson damping was used to account for dispersion with the PBE0 functional.[306], [330] No symmetry restraints were imposed and the optimized structures were defined as minima (no negative eigenvalues) by vibrational analyses. The CPCM solvation model was used (THF).[331] Relativistic treatment was introduced by ZORA.[332] Geometries were analyzed and visualized with Avogadro and molecular orbitals, spin-densities and difference densities were visualized with Chimera.[333], [334]

Table 7.35: XYZ-coordinates of computed complex **XCVII**.

Atom	x	y	z	Atom	x	y	z
Mo	-0.00633	2.40204	-0.03111	Mo	-0.05531	-2.39797	0.03397
C	-2.15749	4.67282	1.96298	C	-2.09258	-4.60745	-2.14174
P	-1.57741	2.86697	1.81326	P	-1.50367	-2.81035	-1.91947
N	1.27879	3.02406	1.35695	N	1.30474	-3.04065	-1.27255
P	1.96682	2.76214	-1.45507	P	1.81131	-2.80799	1.58292
C	2.14217	4.47674	-2.25717	C	1.88464	-4.51989	2.40402
Cl	-1.52543	3.46674	-1.65147	Cl	-1.70938	-3.4405	1.53141
C	-3.00928	1.67908	2.15373	C	-2.88918	-1.59927	-2.34986
C	2.45788	1.40481	-2.68281	C	2.25097	-1.45425	2.83523
N	-0.08572	0.6191	-0.04511	N	-0.10246	-0.6138	0.06309
C	3.25505	2.73353	-0.13315	C	3.18453	-2.8218	0.34868
H	4.21089	3.1972	-0.41813	H	4.10288	-3.31889	0.69475
H	3.44405	1.66853	0.05664	H	3.42254	-1.76388	0.17521
C	2.68586	3.35105	1.13602	C	2.68145	-3.41654	-0.959
H	2.83532	4.45138	1.12911	H	2.79272	-4.52123	-0.94851
H	3.28512	2.9894	1.99509	H	3.34903	-3.07274	-1.77379
C	0.96724	3.23579	2.7687	C	1.08434	-3.22845	-2.70427
H	1.7614	2.77132	3.38775	H	1.93502	-2.78767	-3.26254
H	1.00768	4.3163	3.02373	H	1.10258	-4.30718	-2.96957
C	-0.3716	2.64564	3.18769	C	-0.20153	-2.58658	-3.2016
H	-0.25841	1.55696	3.28741	H	-0.0515	-1.49953	-3.26157
H	-0.7029	3.04134	4.1597	H	-0.47421	-2.94678	-4.20497
C	1.42497	4.50395	-3.60858	C	1.0515	-4.51713	3.68765
H	1.38247	5.54669	-3.96506	H	0.95843	-5.55362	4.05288
H	0.39043	4.14137	-3.51027	H	0.03668	-4.13739	3.49359

H	1.94491	3.91813	-4.37927	H	1.51207	-3.92817	4.49289
C	3.59605	4.92607	-2.40593	C	3.30901	-5.00232	2.67937
H	3.61607	5.89984	-2.92354	H	3.26028	-5.97971	3.1883
H	4.20904	4.22901	-2.99093	H	3.88219	-4.32398	3.32326
H	4.07965	5.0723	-1.42892	H	3.87607	-5.15382	1.7491
C	1.41688	5.46658	-1.33775	C	1.22042	-5.49964	1.42939
H	1.57715	6.49058	-1.71494	H	1.29677	-6.52013	1.84074
H	1.77926	5.43453	-0.30078	H	1.69625	-5.50541	0.43889
H	0.33687	5.27172	-1.34035	H	0.1552	-5.264	1.31123
C	-1.08768	5.55304	1.30629	C	-1.10863	-5.51089	-1.38951
H	-1.37015	6.61189	1.43172	H	-1.38026	-6.56469	-1.57007
H	-1.02812	5.34861	0.22993	H	-1.17049	-5.32854	-0.30903
H	-0.0903	5.42004	1.74557	H	-0.06653	-5.37511	-1.70769
C	-3.4532	4.88384	1.17675	C	-3.46419	-4.80984	-1.49363
H	-3.67522	5.96376	1.14702	H	-3.70036	-5.88712	-1.5016
H	-4.31617	4.38605	1.63917	H	-4.27136	-4.29574	-2.03272
H	-3.34515	4.53368	0.13924	H	-3.45717	-4.47479	-0.44563
C	-2.33415	5.11402	3.41613	C	-2.12619	-5.02846	-3.61107
H	-2.71676	6.14853	3.43112	H	-2.52795	-6.05336	-3.68082
H	-1.37948	5.1157	3.96242	H	-1.11977	-5.04574	-4.05427
H	-3.04601	4.49044	3.97209	H	-2.76147	-4.38108	-4.22944
C	3.68811	1.73382	-3.5254	C	3.3961	-1.81661	3.77823
H	3.93904	0.85887	-4.14865	H	3.62394	-0.94456	4.41421
H	4.56662	1.95056	-2.89813	H	4.31574	-2.06942	3.22839
H	3.52712	2.58155	-4.2042	H	3.15014	-2.65158	4.44734
C	1.23888	1.1352	-3.56856	C	0.97667	-1.13393	3.62079
H	1.44284	0.26757	-4.21827	H	1.16529	-0.27614	4.28811
H	0.98462	1.98521	-4.21325	H	0.63551	-1.97293	4.23935
H	0.35732	0.91478	-2.95124	H	0.15826	-0.87534	2.93566
C	2.75119	0.1313	-1.88651	C	2.65163	-0.19799	2.05806
H	2.87544	-0.70237	-2.59652	H	2.76117	0.63287	2.77406
H	1.93454	-0.1431	-1.20811	H	1.89459	0.10637	1.3248
H	3.68569	0.20489	-1.31105	H	3.62051	-0.31285	1.5504
C	-2.40655	0.30179	2.44429	C	-2.24806	-0.22453	-2.55681
H	-3.21113	-0.45043	2.45745	H	-3.03923	0.5394	-2.61604
H	-1.91431	0.26143	3.42663	H	-1.67752	-0.16794	-3.49496
H	-1.68806	-0.01536	1.67914	H	-1.58909	0.06418	-1.72968
C	-3.89105	2.07603	3.33615	C	-3.66723	-1.96057	-3.61366
H	-4.64381	1.28683	3.49987	H	-4.39782	-1.16161	-3.82366
H	-4.4349	3.01543	3.16913	H	-4.22912	-2.89929	-3.51837
H	-3.3096	2.16991	4.26643	H	-3.00678	-2.03674	-4.49152
C	-3.83104	1.5791	0.86499	C	-3.81758	-1.515	-1.13454
H	-4.58068	0.77873	0.97364	H	-4.5364	-0.69332	-1.28431
H	-3.18641	1.33787	0.00831	H	-3.24562	-1.31374	-0.21748
H	-4.36205	2.5085	0.62722	H	-4.38867	-2.4369	-0.97234

Table 7.36: XYZ-coordinates of computed complex **48**.

Atom	x	y	z	Atom	x	y	z
Mo	0.00426	2.45656	-0.03567	Mo	-0.03754	-2.34801	0.0077
C	-2.16825	4.68443	1.99836	C	-2.08498	-4.63382	-2.12369
P	-1.60786	2.87930	1.86028	P	-1.51066	-2.8327	-1.93329
N	1.28752	3.06338	1.35297	N	1.30142	-3.00495	-1.28115
P	2.03423	2.80816	-1.49581	P	1.81465	-2.83953	1.58399
C	2.15611	4.52932	-2.27672	C	1.8447	-4.54159	2.41878
Cl	-1.4979	3.3327	-1.64247	Cl	-1.68268	-3.34417	1.49426
C	-3.02171	1.66987	2.16058	C	-2.90317	-1.62624	-2.35186
C	2.504	1.44257	-2.71069	C	2.25324	-1.47277	2.82389
N	-0.0717	0.68578	-0.09122	N	-0.05322	-0.5349	5.67E-04
C	3.26581	2.76664	-0.13372	C	3.18392	-2.87371	0.35032
H	4.23063	3.21574	-0.40998	H	4.08175	-3.4075	0.69326
H	3.43967	1.70104	0.06751	H	3.46319	-1.8237	0.18933
C	2.68835	3.40636	1.12005	C	2.66352	-3.43977	-0.96058
H	2.81359	4.50639	1.0897	H	2.71898	-4.54634	-0.95692
H	3.29019	3.07054	1.98474	H	3.34284	-3.12243	-1.7742
C	0.97007	3.23579	2.76883	C	1.07723	-3.21924	-2.71271
H	1.7703	2.7699	3.37481	H	1.92622	-2.7824	-3.27342
H	0.99581	4.31102	3.03485	H	1.10672	-4.30155	-2.95106
C	-0.35845	2.61846	3.17907	C	-0.21405	-2.59944	-3.21594
H	-0.23821	1.52807	3.24828	H	-0.07999	-1.51145	-3.29543
H	-0.68252	2.98207	4.16533	H	-0.48539	-2.98025	-4.21129
C	1.46205	4.54889	-3.6408	C	1.00388	-4.5115	3.69749
H	1.41253	5.59213	-3.99121	H	0.89472	-5.54253	4.07102
H	0.43035	4.17377	-3.57403	H	-0.00509	-4.12037	3.49872
H	2.0042	3.97667	-4.40523	H	1.46971	-3.92451	4.50068
C	3.60797	4.99438	-2.40091	C	3.26256	-5.03636	2.70866
H	3.62288	5.97111	-2.91073	H	3.19491	-6.00316	3.23351
H	4.23357	4.30899	-2.98633	H	3.84226	-4.35797	3.34593
H	4.07888	5.13984	-1.41782	H	3.83316	-5.21533	1.7857
C	1.39998	5.49706	-1.35889	C	1.17737	-5.5222	1.44802
H	1.54287	6.52418	-1.73114	H	1.23832	-6.53748	1.87212
H	1.75432	5.47476	-0.31917	H	1.66509	-5.54993	0.46356
H	0.32205	5.29034	-1.37112	H	0.11626	-5.27947	1.31539
C	-1.10156	5.55854	1.32922	C	-1.09281	-5.52134	-1.36455
H	-1.38546	6.61657	1.4483	H	-1.35547	-6.57769	-1.53778
H	-1.04424	5.35559	0.25177	H	-1.1555	-5.33554	-0.28547
H	-0.10223	5.43586	1.76662	H	-0.05173	-5.38397	-1.68596
C	-3.47704	4.90017	1.23479	C	-3.45594	-4.8376	-1.47395
H	-3.69956	5.97915	1.22447	H	-3.68354	-5.91587	-1.47442
H	-4.33211	4.39698	1.70435	H	-4.26653	-4.33596	-2.01884
H	-3.39564	4.56861	0.18938	H	-3.45637	-4.49677	-0.42822
C	-2.32346	5.11029	3.45895	C	-2.11591	-5.06533	-3.59049

Atom	x	y	z	Atom	x	y	z
H	-2.69667	6.1468	3.48781	H	-2.51509	-6.091	-3.64898
H	-1.36438	5.09973	3.99695	H	-1.1101	-5.0872	-4.03456
H	-3.03762	4.48856	4.01379	H	-2.75449	-4.42787	-4.21528
C	3.72302	1.78746	-3.56496	C	3.3808	-1.84708	3.78395
H	3.97066	0.91715	-4.19413	H	3.61354	-0.97458	4.41674
H	4.60784	2.00524	-2.94778	H	4.30376	-2.11856	3.24975
H	3.55017	2.6357	-4.23932	H	3.11189	-2.6715	4.45609
C	1.27628	1.16148	-3.5822	C	0.97463	-1.12754	3.59161
H	1.49569	0.3127	-4.24985	H	1.17521	-0.28268	4.27156
H	0.99409	2.01383	-4.21188	H	0.60261	-1.96209	4.19762
H	0.40617	0.89867	-2.96461	H	0.17208	-0.84355	2.89769
C	2.82078	0.17825	-1.90741	C	2.68664	-0.22964	2.04287
H	2.93941	-0.65628	-2.61652	H	2.79344	0.60552	2.75422
H	2.01847	-0.10411	-1.21507	H	1.94736	0.06958	1.28984
H	3.76566	0.26131	-1.35113	H	3.66422	-0.36134	1.55685
C	-2.4065	0.29474	2.43154	C	-2.27548	-0.2485	-2.57725
H	-3.20789	-0.45999	2.43653	H	-3.07766	0.50321	-2.64248
H	-1.91293	0.24139	3.41211	H	-1.70984	-0.19475	-3.51863
H	-1.69149	-0.01123	1.65863	H	-1.61675	0.05212	-1.75483
C	-3.90052	2.05254	3.3509	C	-3.6835	-2.00683	-3.60939
H	-4.65074	1.25975	3.50202	H	-4.42438	-1.21833	-3.82025
H	-4.44797	2.99178	3.19837	H	-4.23498	-2.94973	-3.50328
H	-3.31984	2.13216	4.28252	H	-3.0288	-2.08227	-4.49116
C	-3.84331	1.58664	0.87019	C	-3.82619	-1.53992	-1.13263
H	-4.60743	0.80188	0.98375	H	-4.56046	-0.7342	-1.2925
H	-3.21074	1.32242	0.01129	H	-3.25602	-1.31714	-0.21942
H	-4.36007	2.5236	0.63162	H	-4.38217	-2.46777	-0.95555

Table 7.37: XYZ-coordinates of computed complex **49**.

Atom	x	y	z	Atom	x	y	z
Mo	0.01909	2.40383	-0.00396	H	-4.31468	2.55294	0.60752
C	-2.14320	4.72541	1.97812	Mo	-0.03942	-2.39508	0.01086
P	-1.60184	2.91341	1.88275	C	-2.0923	-4.65216	-2.15898
N	1.29330	3.01893	1.36081	P	-1.54086	-2.84688	-1.98542
P	2.03531	2.82714	-1.49605	N	1.30366	-3.03695	-1.27495
C	2.12693	4.54634	-2.28426	P	1.86478	-2.88358	1.62639
Cl	-1.46550	3.25865	-1.59593	C	1.84275	-4.596	2.43104
C	-3.02380	1.71231	2.18472	Cl	-1.65461	-3.21618	1.48833
C	2.49267	1.45327	-2.70839	C	-2.91882	-1.62302	-2.37516
N	-0.04737	0.61427	-0.03284	C	2.27975	-1.51199	2.85844
C	3.27242	2.79115	-0.14114	N	-0.06603	-0.60458	0.05207
H	4.22285	3.2692	-0.41742	C	3.18826	-2.90053	0.35465
H	3.47818	1.72914	0.04989	H	4.09583	-3.42245	0.68988
C	2.68472	3.40851	1.11582	H	3.455	-1.84888	0.18344
H	2.76382	4.51116	1.08865	C	2.65841	-3.4863	-0.9427

H	3.29642	3.09421	1.98004	H	2.68921	-4.59123	-0.92007
C	0.97856	3.23362	2.77630	H	3.33792	-3.19301	-1.76242
H	1.77710	2.77161	3.38517	C	1.07651	-3.2218	-2.7107
H	1.02754	4.31452	3.00591	H	1.93206	-2.78702	-3.259
C	-0.35745	2.65238	3.20422	H	1.09412	-4.30102	-2.9535
H	-0.25997	1.56241	3.30802	C	-0.20407	-2.5801	-3.21122
H	-0.67326	3.05257	4.17865	H	-0.06642	-1.49113	-3.26882
C	1.42949	4.55316	-3.64678	H	-0.46395	-2.93729	-4.21811
H	1.37535	5.59462	-4.00029	C	1.01708	-4.56454	3.71964
H	0.39848	4.17667	-3.58030	H	0.9096	-5.59683	4.08768
H	1.97347	3.98358	-4.41147	H	0.00504	-4.17141	3.54569
C	3.57770	5.01591	-2.41377	H	1.49466	-3.98604	4.52112
H	3.58362	5.98585	-2.93562	C	3.26084	-5.10281	2.70291
H	4.20814	4.33048	-2.99352	H	3.18831	-6.07596	3.21373
H	4.04906	5.18013	-1.43406	H	3.84623	-4.43881	3.35012
C	1.36955	5.51251	-1.36721	H	3.826	-5.27394	1.77534
H	1.51346	6.53856	-1.74050	C	1.15432	-5.55322	1.45269
H	1.72490	5.49592	-0.32761	H	1.19459	-6.57102	1.8712
H	0.29151	5.30975	-1.38055	H	1.64189	-5.59169	0.46901
C	-1.06040	5.57689	1.30769	H	0.09559	-5.29858	1.32075
H	-1.33791	6.63835	1.40426	C	-1.10796	-5.52732	-1.37697
H	-0.98944	5.3585	0.23482	H	-1.36819	-6.58489	-1.54158
H	-0.06856	5.46041	1.76385	H	-1.18348	-5.33944	-0.29837
C	-3.44428	4.93909	1.20061	H	-0.06286	-5.39901	-1.68885
H	-3.65781	6.01916	1.17738	C	-3.47786	-4.86005	-1.54188
H	-4.30793	4.45051	1.66937	H	-3.70349	-5.93775	-1.56169
H	-3.36023	4.59853	0.15848	H	-4.27701	-4.35453	-2.09871
C	-2.30575	5.17089	3.43273	H	-3.51154	-4.53724	-0.49121
H	-2.66960	6.21062	3.44048	C	-2.08882	-5.07483	-3.62925
H	-1.35193	5.16351	3.97989	H	-2.47151	-6.10541	-3.69793
H	-3.03224	4.56768	3.99135	H	-1.07631	-5.08153	-4.05795
C	3.70403	1.80754	-3.57113	H	-2.72976	-4.44622	-4.2605
H	3.95209	0.93983	-4.20328	C	3.3933	-1.90287	3.83026
H	4.59266	2.03037	-2.96188	H	3.62289	-1.03466	4.46862
H	3.52034	2.65373	-4.24426	H	4.3219	-2.17751	3.3084
C	1.26061	1.16607	-3.57114	H	3.10986	-2.72619	4.4972
H	1.48619	0.32993	-4.25245	C	0.99329	-1.15942	3.61117
H	0.96182	2.02045	-4.18982	H	1.20326	-0.33577	4.31253
H	0.39810	0.88636	-2.94984	H	0.59614	-1.9968	4.19734
C	2.82693	0.19201	-1.90792	H	0.20529	-0.83395	2.91807
H	2.94316	-0.64092	-2.61931	C	2.73508	-0.27848	2.07405
H	2.03450	-0.08852	-1.20331	H	2.82343	0.56126	2.78159
H	3.77862	0.27984	-1.36451	H	2.01812	0.02036	1.29894
C	-2.42452	0.33876	2.49443	H	3.72617	-0.41465	1.6182
H	-3.23700	-0.40404	2.50738	C	-2.27996	-0.24869	-2.58551
H	-1.94416	0.30109	3.48237	H	-3.07977	0.50541	-2.64337

H	-1.70363	0.0121	1.73526	H	-1.71523	-0.1857	-3.52647
C	-3.90763	2.13285	3.35963	H	-1.623	0.04301	-1.75766
H	-4.66698	1.35147	3.52247	C	-3.68874	-1.99927	-3.64179
H	-4.44574	3.07188	3.17953	H	-4.4273	-1.20887	-3.8501
H	-3.33561	2.2288	4.29464	H	-4.24351	-2.94085	-3.54584
C	-3.83638	1.6081	0.89039	H	-3.0303	-2.06726	-4.52094
H	-4.63342	0.86131	1.03052	C	-3.84849	-1.54665	-1.16016
H	-3.20939	1.28237	0.04840	H	-4.6077	-0.77049	-1.34364
H	-4.31468	2.55294	0.60752	H	-3.29799	-1.27552	-0.24782
Mo	-0.03942	-2.39508	0.01086	H	-4.3781	-2.48663	-0.96709

7.6.2 Crystallographic Details
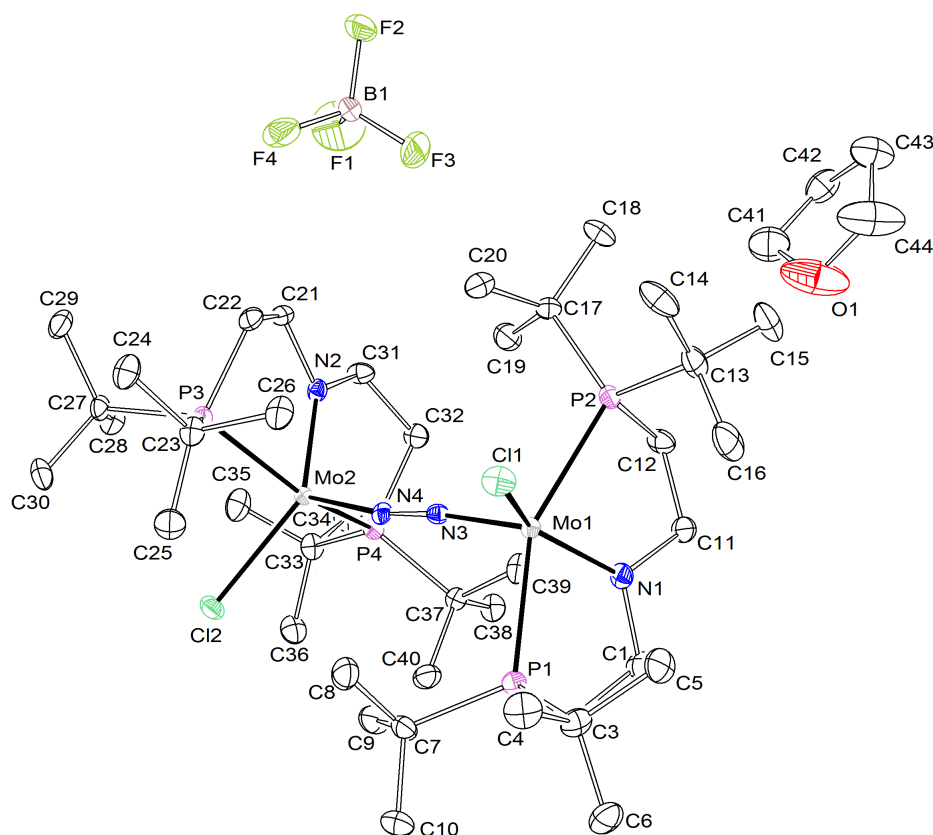
Figure 7.36: Thermal ellipsoid plot of **48** with the anisotropic displacement parameters drawn
at the 50% probability level. The asymmetric unit contains one complex molecule, one BF_4^-
anion and one THF solvent molecule. The structure was refined as an inversion twin using the
twin law -100 0-10 00-1 (BASF: 0.49(3)). The reflections 10 5 3, 10 4 2, -8 3 5, 6 3 1, -10 2 1, 6 4
3, 5 5 2, 5 4 1, 5 1 0, 10 3 6 and 10 0 4 are removed from the refinement using OMIT commands.

Empirical formula	$C_{44}H_{96}BCl_2F_4Mo_2N_4OP_4$	
Formula weight	1170.71	
Temperature	102(2) K	
Wavelength	0.71073 Å	
Crystal system	Monoclinic	
Space group	$P2_1$	
Unit cell dimensions	a = 12.3704(6) Å	$\alpha = 90°$
	b = 13.7799(7) Å	$\beta = 95.233(2)°$
	c = 16.8847(8) Å	$\gamma = 90°$
Volume	2866.2(2) Å^3	
Z	2	
Density (calculated)	1.357 Mg/m^3	
Absorption coefficient	0.690 mm^{-1}	
F(000)	1230	

Crystal size	0.373 x 0.165 x 0.118 mm^3
Crystal shape and color	Plate, clear intense brown
Theta range for data collection	2.218 to 28.389°
Index ranges	-16<=h<=16
	-18<=k<=18
	-22<=l<=22
Reflections collected	109664
Independent reflections	14315 [R(int) = 0.0528]
Completeness to theta = 25.242°	99.9%
Refinement method	Full-matrix least-squares on F^2
Data / restraints / parameters	14315 / 1 / 584
Goodness-of-fit on F^2	1.088
Final R indices [I>2sigma(I)]	R1 = 0.0334, wR2 = 0.0737
R indices (all data)	R1 = 0.0390, wR2 = 0.0775
Absolute structure parameter	0.49(3)
Largest diff. peak and hole	1.034 and -0.787 eÅ^{-3}
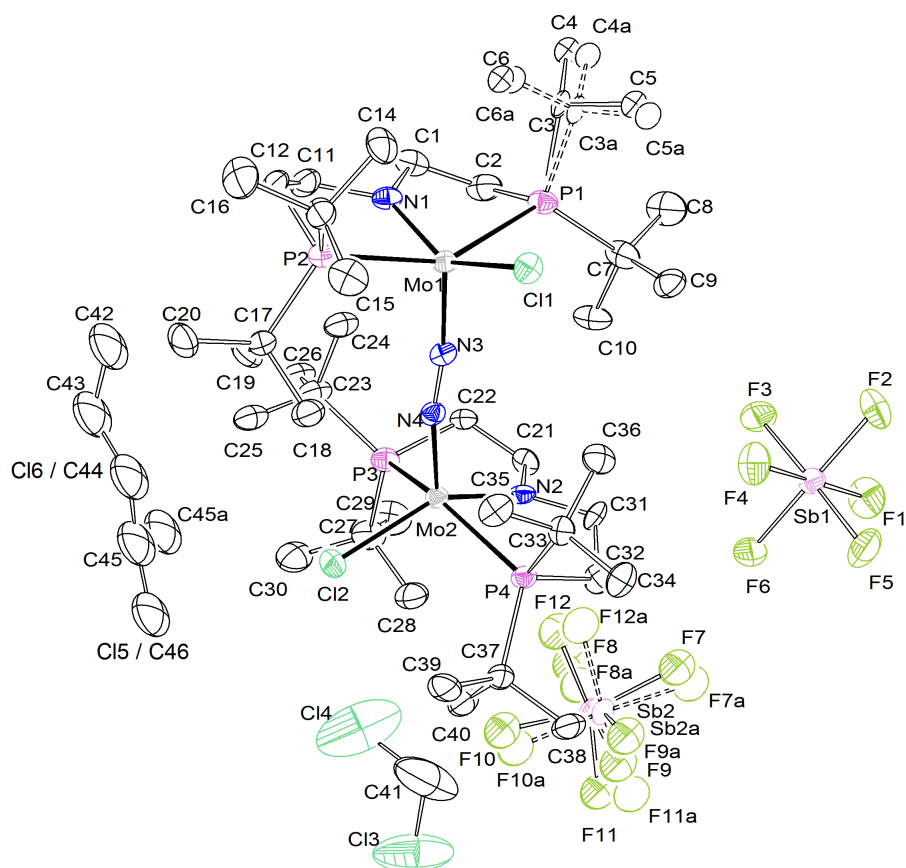
Figure 7.37: Thermal ellipsoid plot of **49** with the anisotropic displacement parameters drawn at the 50% probability level. The asymmetric unit contains one disordered complex molecule, two SbF_6^- anions, one and a half dichloromethane and half a pentane molecule. The disordered complex molecule was set to a population of 0.5 using some restraints and constraints (SADI, EADP). The solvent molecules were set to a population of 0.5 for one of the dichloromethane and pentane molecules using some restraints and constrains (SADI, EADP, EXYZ). One of the SbF_6^- anions was disordered and refined with a population of 0.73(1) for the main domain using some restraints and constraints (SADI, EADP).

Empirical formula	$C_{44}H_{97}Cl_5F_{12}Mo_2N_4P_4Sb_2$	
Formula weight	1646.76	
Temperature	100(2) K	
Wavelength	0.71073 Å	
Crystal system	Triclinic	
Space group	P-1	
Unit cell dimensions	a = 13.9158(14) Å	$\alpha = 108.380(3)°$
	b = 15.9147(17) Å	$\beta = 95.891(3)°$
	c = 17.1828(19) Å	$\gamma = 110.746(3)°$
Volume	3277.1(6) Å^3	
Z	2	
Density (calculated)	1.669 Mg/m^3	

Absorption coefficient	$1.558\,\text{mm}^{-1}$
F(000)	1656
Crystal size	$0.248 \times 0.240 \times 0.216\,\text{mm}^3$
Crystal shape and color	Block, clear intense brown
Theta range for data collection	2.219 to 25.815°
Index ranges	-16<=h<=17
	-19<=k<=19
	-21<=l<=21
Reflections collected	92374
Independent reflections	12553 [R(int) = 0.1037]
Completeness to theta = 25.242°	99.9%
Refinement method	Full-matrix least-squares on F^2
Data / restraints / parameters	12553 / 58 / 650
Goodness-of-fit on F^2	1.095
Final R indices [I>2sigma(I)]	R1 = 0.0744 wR2 = 0.1659
R indices (all data)	R1 = 0.1104 wR2 = 0.1863
Largest diff. peak and hole	1.985 and -1.643 eÅ^{-3}
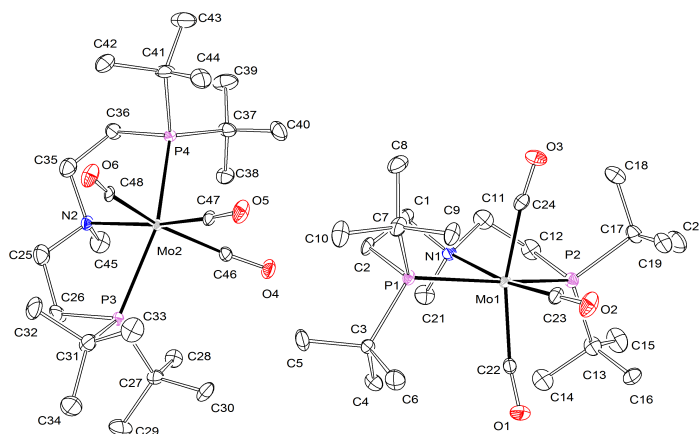
Figure 7.38: Thermal ellipsoid plot of **51** with the anisotropic displacement parameters drawn
at the 50% probability level. The asymmetric unit contains two complex molecules. The reflec-
tions 0 13 7, 1 15 7 and 73 0 -3 are removed from the refinement using OMIT commands.

Empirical formula	$C_{24}H_{47}MoNO_3P_2$	
Formula weight	555.50	
Temperature	100(2) K	
Wavelength	0.71073 Å	
Crystal system	Triclinic	
Space group	P-1	
Unit cell dimensions	a = 8.8455(4) Å	$\alpha = 85.608(2)°$
	b = 16.6139(8) Å	$\beta = 89.431(2)°$
	c = 18.8544(8) Å	$\gamma = 83.812(3)°$
Volume	2746.6(2) Å^3	
Z	4	
Density (calculated)	1.343 Mg/m^3	
Absorption coefficient	0.618 mm^{-1}	
F(000)	1176	
Crystal size	0.222 x 0.182 x 0.090 mm^3	
Crystal shape and color	Block, clear intense yellow	
Theta range for data collection	2.316 to 28.351°	
Index ranges	-11<=h<=11	
	-22<=k<=22	
	-25<=l<=25	
Reflections collected	190382	
Independent reflections	13695 [R(int) = 0.0935]	
Completeness to theta = 25.242°	99.9%	
Refinement method	Full-matrix least-squares on F^2	
Data / restraints / parameters	13695 / 0 / 585	
Goodness-of-fit on F^2	1.162	
Final R indices [I>2sigma(I)]	R1 = 0.0529,	wR2 = 0.1162
R indices (all data)	R1 = 0.0674,	wR2 = 0.1211
Largest diff. peak and hole	1.549 and -1.186 eÅ^{-3}	

7.6.3 Syntheses

Synthesis of 48

XCVII (10.2 mg, 10.1 μmol, 1.00 eq.) and Ag[Al(OR)$_4$] (10.8, 10.1 μmol, 1.00 eq.) are dissolved in benzene and stirred for 16 at room temperature. The solution is filtered and the residue is extracted with benzene (15 x 2 mL). The solvent is removed and the residue is dissolved in chlorobenzene (2 mL), layered with pentane and stored at -35°C for 2 days. The precipitate is washed with benzene/pentane (1:1) and extracted with chlorobenzene (4 x 2 mL). After removal of the solvent P is obtained as a dark brown powder (17.5 mg, 8.84 μmol, 88%)

Anal. Cald for C$_{56}$H$_{88}$AlCl$_2$F$_{36}$Mo$_2$N$_4$O$_4$P$_4$ (1978.98): C, 40.0; H, 4.48; N, 2.83. Found: C, 34.0; H, 4.68; N, 1.44.

Like parent **XCVII**, **48** most likely loses dinitrogen during combustion leading to:[280]

Anal. Cald for C$_{56}$H$_{88}$AlCl$_2$F$_{36}$Mo$_2$N$_2$O$_4$P$_4$ (1950.97): C, 34.5; H, 4.55; N, 1.44. Found: C, 34.0; H, 4.68; N, 1.44.

NMR (THF-d$_8$, RT): ^{1}H (300 MHz) δ = 2.66 (br, 18H, PC(CH_3)$_3$), 2.41 - 1.98 (br, 54H, PC(CH_3)$_3$), -2.59 (br, 2H), -4.02 (br, 4H), -4.71 (br, 2H), -24.08 (br, 2H), -30.97 (br, 2H), -32.32 (br, 2H), -35.37 (br, 2H).

Single-crystals suitable for X-ray diffraction were obtained upon reacting **XCVII** with one equivalent of AgBF$_4$ in THF and successive vapor diffusion of pentane at -35°C.

Synthesis of 49

XCVII (12.5 mg, 12.4 μmol, 1.00 eq.) and Ag[Al(OR)$_4$] (25.2 mg, 23.5 μmol, 1.90 eq.) are dissolved in benzene and stirred for 16h at room temperature. The solution is filtered, washed with benzene (5 x 2 mL) and the residue is extracted with DCM (3 x 2 mL). The solution is concentrated, layered with toluene and stored at -80°C for 2 days. The crude product is filtered, washed with benzene (2 x 2 mL) and extracted with DCM. The solution Is pushed through a celite pad and dried. P is obtained as a brown powder (25.0 mg, 8.48 μmol, 69%).

Anal. Cald for C$_{72}$H$_{88}$Al$_2$Cl$_2$F$_{72}$Mo$_2$N$_4$O$_8$P$_4$ (2946.08): C, 29.4; H, 3.01; N, 1.90. Found: C, 29.2; H, 3.30; N, 1.66.

NMR (CD$_2$Cl$_2$, RT): ^{1}H (300 MHz) δ = 3.81 (br, 18H, PC(CH_3)$_3$), 3.58 - 2.88 (br, 54H, PC(CH_3)$_3$), -5.46 (br, 4H), -13.08 (br, 2H), -15.8 (br, 2H), -58.93 (br, 2H), -71.26 (br, 2H), -83.05 (br, 2H), -88.56 (br, 2H).

Single-crystals suitable for X-ray diffraction were obtained upon reacting **XCVII** with two equivalents of AgSbF$_6$ in DCM and successive vapor diffusion of pentane at -35°C.

Protonation of XCVII to XCVIII

A J-Young NMR tube is filled with **XCVII** (11.1 mg, 10.9 μmol, 1.00 eq.) and THF (0.3 mL) is added carfully. HOTf (2.0 μL, 23 μmol, 2.1 eq.) is placed on top of the tube. After cooling to -40°C the tube is shaken for 2 minutes at -40°C. The tube is transferred to the spectrometer and emerged in liquid nitrogen.

Synthesis of ^{Me}L

^{t}Bu$_2$PCl (3.80 g, 21.0 mmol, 1.0 eq.) is dissolved in THF (20 mL) and added slowly to a suspension of Li (439 mg, 63.1 mmol, 3.0 eq.) in THF (20 mL) at 0°C. The suspension is allowed to warm to room temperature and stirred for 4 d. In a separate flask N(CH$_2$CH$_2$Cl)$_2$Me · HCl (1.94 g, 10.1 mmol, 0.48 eq.) is deprotonated in THF (10 mL) by slow addition of n-butyllithium (2.5 M in n-hexane, 4.21 mL, 10.5 mmol, 0.5 eq.) at −70°C and subsequent warming to room temperature. To this flask the greenish solution of ^{t}Bu$_2$PLi is added to slowly at −70°C. The solution is heated to 70°C for 16 h and after cooling to room temperature, the solution is filtered, and the volume is reduced to 10 mL. Impurities are extracted upon addition of degassed water (3 x 20 mL) and stirring for 30 minutes before removing the aqueous phase. After evaporation of the solvent ^{Me}L (3.8 g, 9.60 mmol, 92%) is obtained in form of a colorless oil. NMR (C$_6$D$_6$, RT): ^{1}H (500 MHz): δ = 2.81 - 2.74 (m, 4H, NCH_2), 2.30 (s, 3H, Me), 1.71 - 1.64 (m, 4H, PCH_2), 1.11 (d, $^3J_{HP}$ = 10.7 Hz, 36H, PC(CH_3)$_3$). ^{13}C{^{1}H} (125.8 MHz): δ = 58.8 (d, $^2J_{CP}$ = 37.2 Hz, 2C, NCH_2), 41.9 (s, 1C, Me), 31.1 (d, $^1J_{CP}$ = 22.6 Hz, 4C, PC(CH$_3$)$_3$), 29.7 (d, $^2J_{CP}$ = 14.1 Hz, 12C, PC(CH$_3$)$_3$), 19.9 (d, $^1J_{CP}$ = 22.5 Hz, 2C, PCH$_2$). ^{31}P{^{1}H} (202.5 MHz): δ = 24.5 (s, 2P, PC(CH$_3$)$_3$). HR-ESI ($\frac{m}{z}$): 376.3268 ([M+H]$^+$, calcd.: 376.3256).

Attempted complexation of [MoCl$_3$(thf)$_3$] by ^{Me}L

PhCl, elevated temperatures: [MoCl$_3$(thf)$_3$] (64.0 mg, 154 µmol, 1.00 eq.) and ^{Me}L (80.0 mg, 213 µmol, 1.38 eq.) are dissolved in PhCl (10 mL) and heated to 50°C for 16h. The solvent is removed, the residue is washed with pentane (5 x 5 mL) and extracted with benzene (3 x 5 mL). Lyophilization yields and orange powder.
NMR (C$_6$D$_6$, RT): ^{1}H (300 MHz): δ = 25.39, 16.76, 10.9, 5.99, 1.12, -7.69, -20.66, -63.26.
DCM, THF (1:2): [MoCl$_3$(thf)$_3$] (10.0 mg, 24.1 µmol, 1.00 eq.) and ^{Me}L (8.9 mg, 24 µmol, 1.0 eq.) are dissolved in DMC/THF (10 mL, 1:2) and heated stirred at room temperature for 16h. The solvent is removed, the residue is washed with pentane (5 x 5 mL) and extracted with benzene (3 x 5 mL). Lyophilization yields and orange powder.
NMR (C$_6$D$_6$, RT): ^{1}H (300 MHz): δ = 25.57, 16.84, 10.14, 9.50, 6.01, 1.12, -8.00, -63.73.

Synthesis of 51

[Mo(CO)$_3$(toluene)] (121 mg, 470 µmol, 1.00 eq.) and ^{Me}L (180 mg, 480 µmol, 1.02 eq.) are dissolved in benzene (5 mL) in the dark and stirred for 16 h at room temperature. The solvent is removed and the product is crystallized from pentane at −80°C. **51** (210 mg, 378 µmol, 80%) is obtained in form of a yellow powder.
Anal. Cald for C$_{24}$H$_{47}$MoNO$_3$P$_2$ (555.55): C, 51.9; H, 8.53; N, 2.52. Found: C, 51.8; H, 8.17; N, 2.40. NMR (C$_6$D$_6$, RT): ^{1}H (500 MHz): δ = 2.34 - 2.29 (m, 2H, NCH_2), 2.01 - 1.61(m, 2H, NCH_2), 1.86 (s, 3H, Me), 1.57 - 1.50 (m, 2H, PCH_2), 1.36 (18H, A$_{18}$XX'A'$_{18}$, N = |$^3J_{AX}$ + $^5J_{AX'}$| = 12.5 Hz), 1.31 (18H, A$_{18}$XX'A'$_{18}$, N = |$^3J_{AX}$ + $^5J_{AX'}$| = 12.3 Hz), 1.31 - 1.27 (m, 2H, PCH_2). ^{13}C{^{1}H} (125.8 MHz): δ = 232.1 (t, $^2J_{PP}$ = 5.8 Hz, 1C, CO), 226.9 (t, $^2J_{PP}$ = 9.5 Hz, 1C, CO), 225.1 (t, $^2J_{PP}$ = 8.7 Hz, 1C, CO), 65.2 (vt, N = |$^1J_{CP}$ + $^3J_{CP}$| = 5.3 Hz, 2C, NCH_2), 47.3 (s, 1C, Me), 37.8

(vt, $^1J_{PC}$ = 4.4 Hz, 2C, PC(CH$_3$)$_3$), 36.3 (vt, $^1J_{PC}$ = 4.4 Hz, 2C, PC(CH$_3$)$_3$), 30.8 (vt, $^2J_{PC}$ = 3.0 Hz, 6C, PC(CH$_3$)$_3$), 30.3 (br, 6C, PC(CH$_3$)$_3$), 22.3 (vt, $N = |^2J_{CP} + {}^3J_{CP}|$ = 3.6 Hz, 2C, NCH$_2$. ^{31}P$\{^1$H$\}$ (202.5 MHz): δ = 99.3 (s, 2P, P(C(CH$_3$)$_3$)$_2$. IR (ATR, cm^{-1}): $\tilde{\nu}_{CO}$= 1911, 1805, 1784.

Appendix

8   Appendix

8.1 Os(II) and Re(III) PNP Halide Complexes
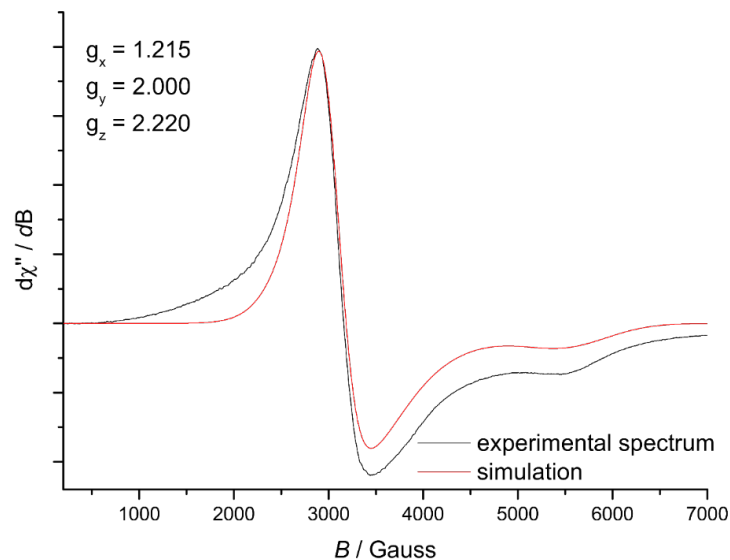
Appendix 8.1.1: EPR powder spectrum of **1**, 140 K, Freq.: 9.448 GHz.
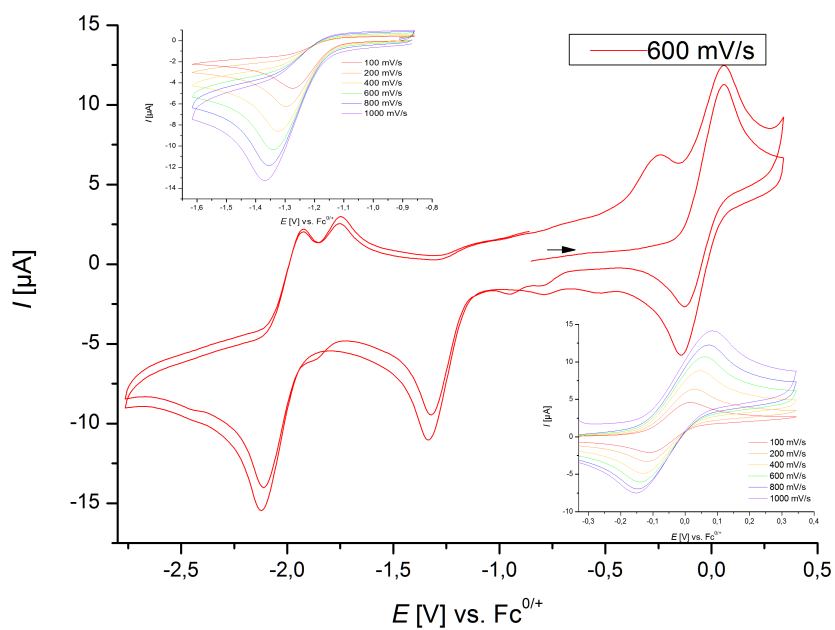
Appendix 8.1.2: Cyclovoltammogramm of **1**, 0.1 mM, 0.1 M NBu$_4$PF$_6$, THF, RT; Inset: First reduction and oxidation event.
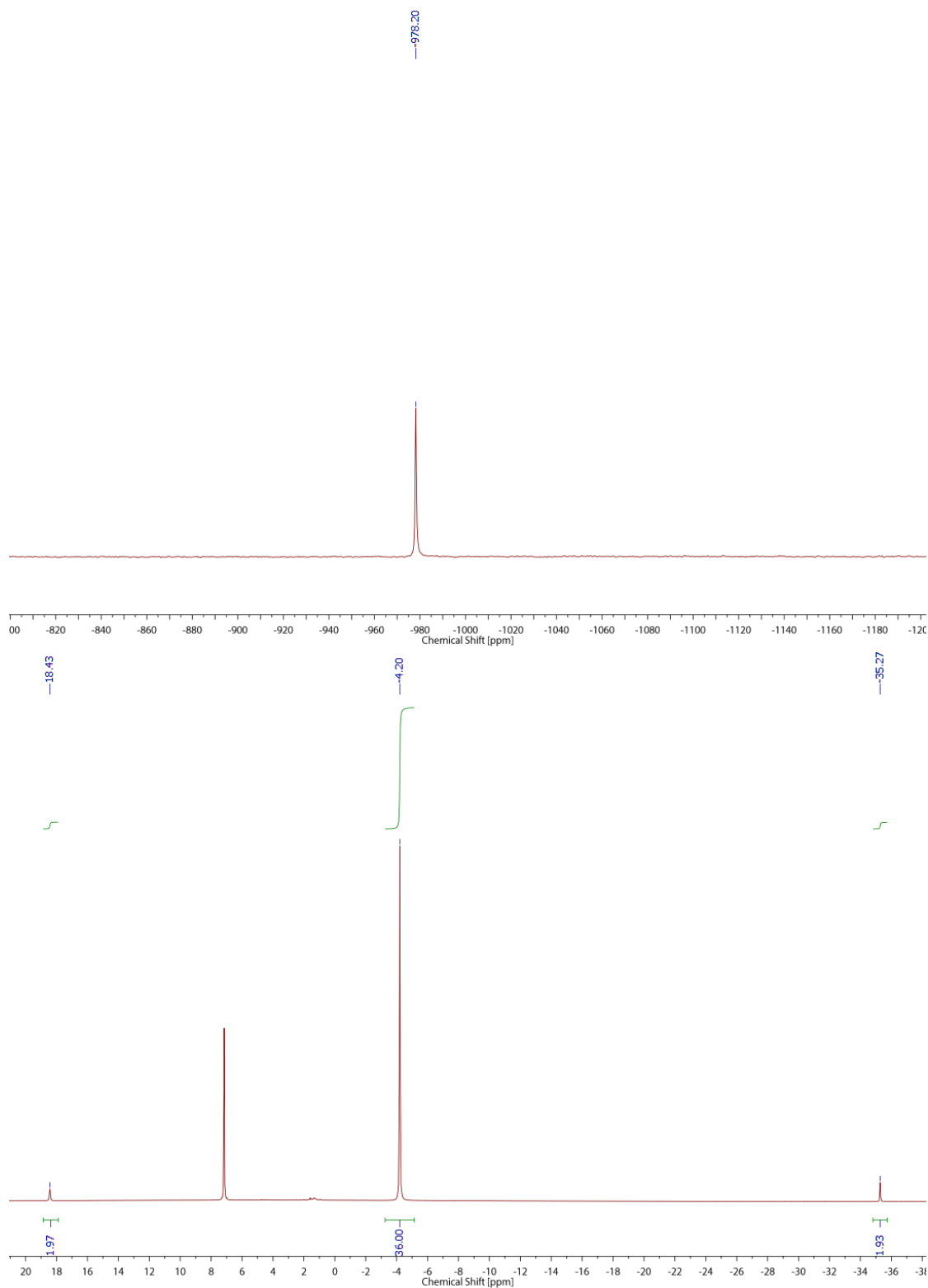
Appendix 8.1.3: Top: $^{31}P\{^1H\}$ NMR spectrum of **2**, C_6D_6, RT; Bottom: ^1H NMR spectrum of **2**, C_6D_6, RT.
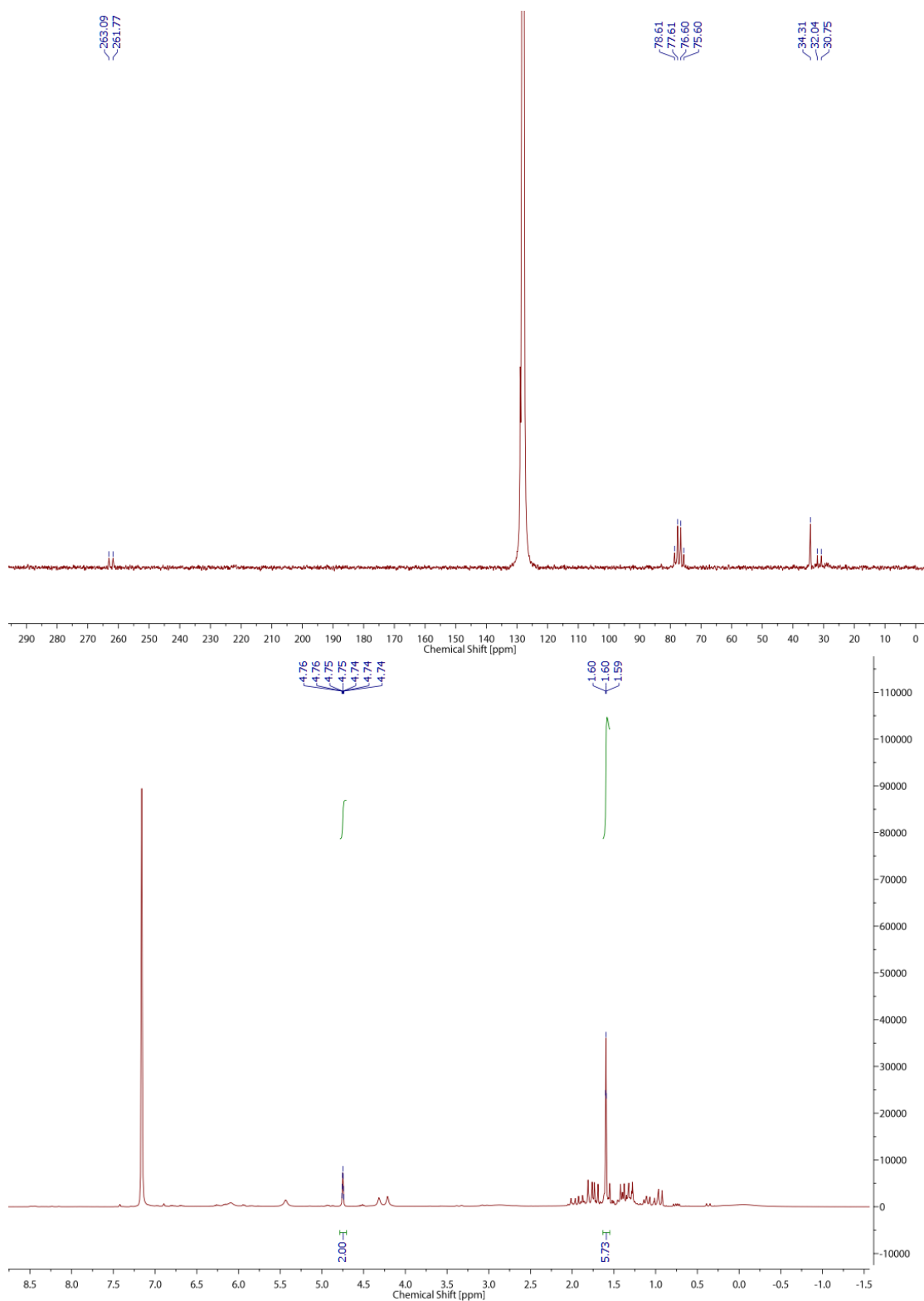
Appendix 8.1.4: Top: $^{13}\text{C}\{^1\text{H}\}$ NMR spectrum of **2**, C_6D_6, RT; Bottom: ^1H NMR spectrum of **2** after 24h at room temperature showing formation of isobutene, C_6D_6, RT.
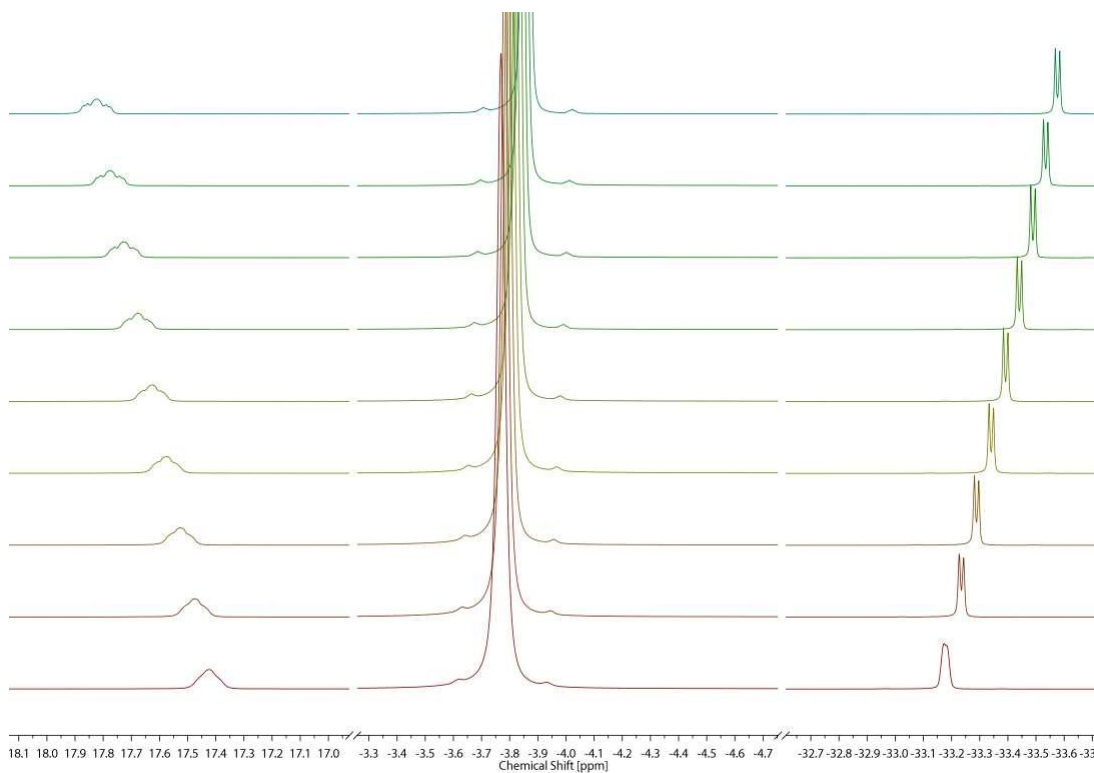
Appendix 8.1.5: VT ^{1}H NMR spectrum of **2**, Toluene-d_8, -55°C (red) to -15°C (green), 5°C steps.
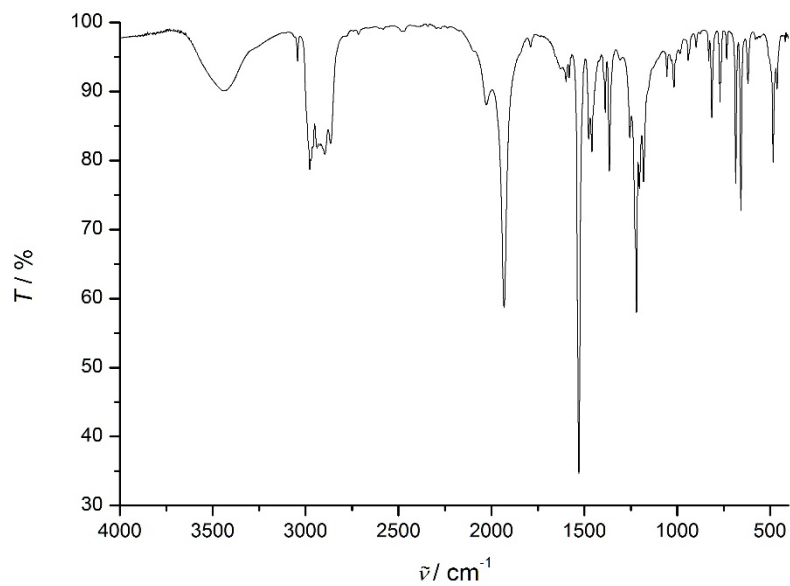
Appendix 8.1.6: VT ^{1}H NMR spectrum of **2**, Toluene-d_8, -55°C (red) to -15°C (green), 5°C steps.
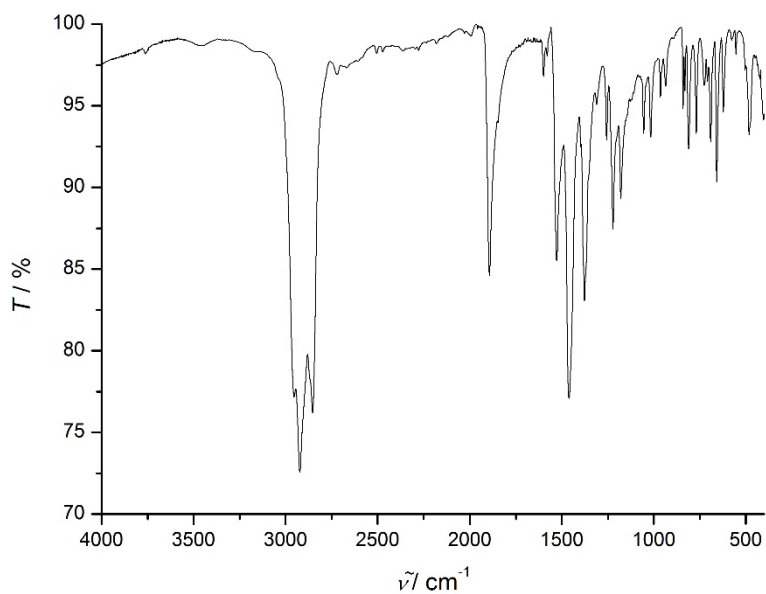
Appendix 8.1.7: Top: $^{13}C\{^1H\}$ NMR spectrum of **2**, C_6D_6, RT; Bottom: ^1H NMR spectrum of **2** after 24h at room temperature showing formation of isobutene, C_6D_6, RT.

Table 8.1: Experimental and computed EPR parameters (Hyperfine coupling constants are given in MHz).

Orientation	Parameter	Exp.	DFT
x	g	1.8980	1.9118
	$A_1(^{14}N)$		2.06
	$A_2(^{14}N)$		1.53
y	g	1.9756	1.9723
	$A_1(^{14}N)$		1.82
	$A_2(^{14}N)$		1.70
z	g	2.015	2.008
	$A_1(^{14}N)$	40	30.0
	$A_2(^{14}N)$	40	27.0

8.2 Os Nitride and Imide Complexes in Various Coordination Spheres
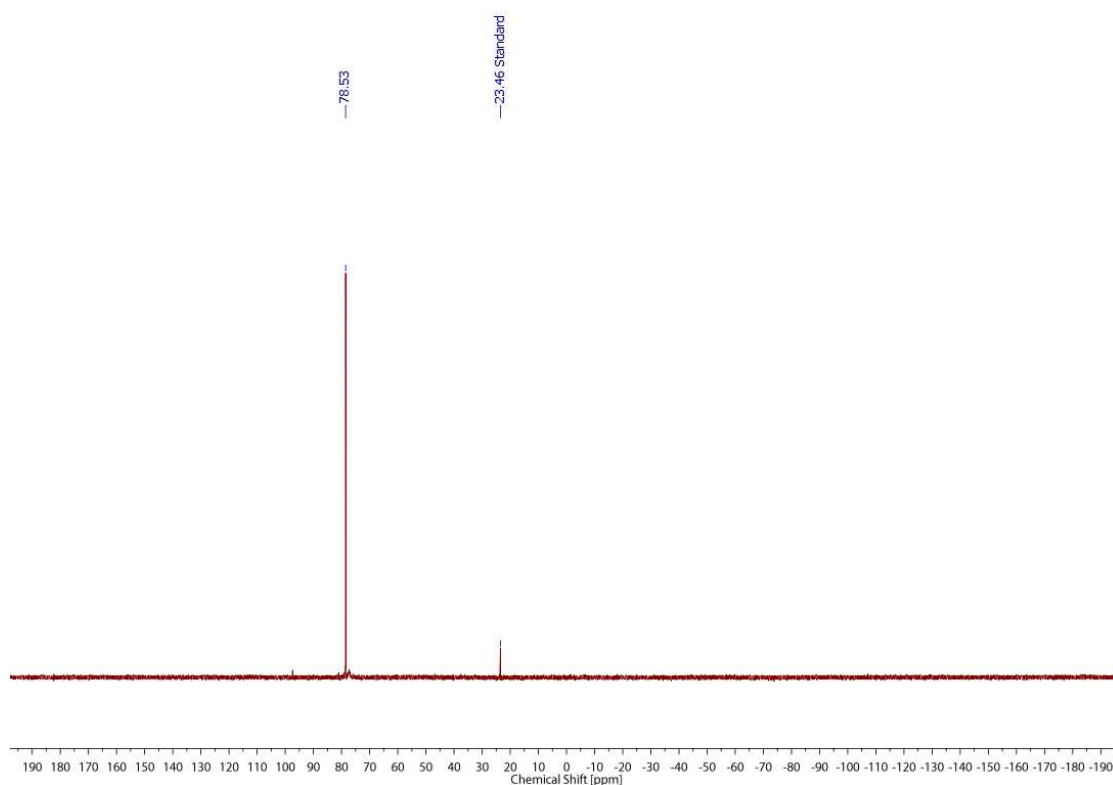
Appendix 8.2.1: ^{31}P{^{1}H} NMR spectrum of the reaction mixture after hydrogenolysis of **14**, toluene-d$_8$, RT.
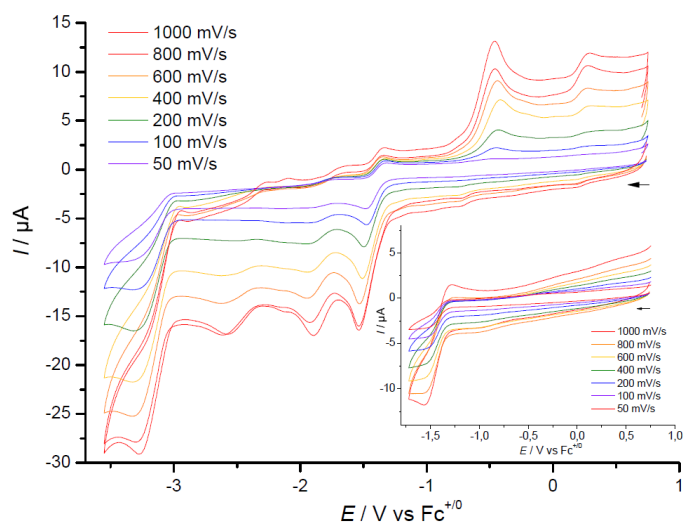
Appendix 8.2.2: Cyclic voltammogram of **15**, 1 mM, 0.1 M NBu$_4$PF$_6$, THF, RT.

E (eV)

0.06

-0.10

-0.41

-0.86

-1.08

-1.61

-4.73

-5.13

-5.50

-5.81

-5.87

-5.91

-6.41
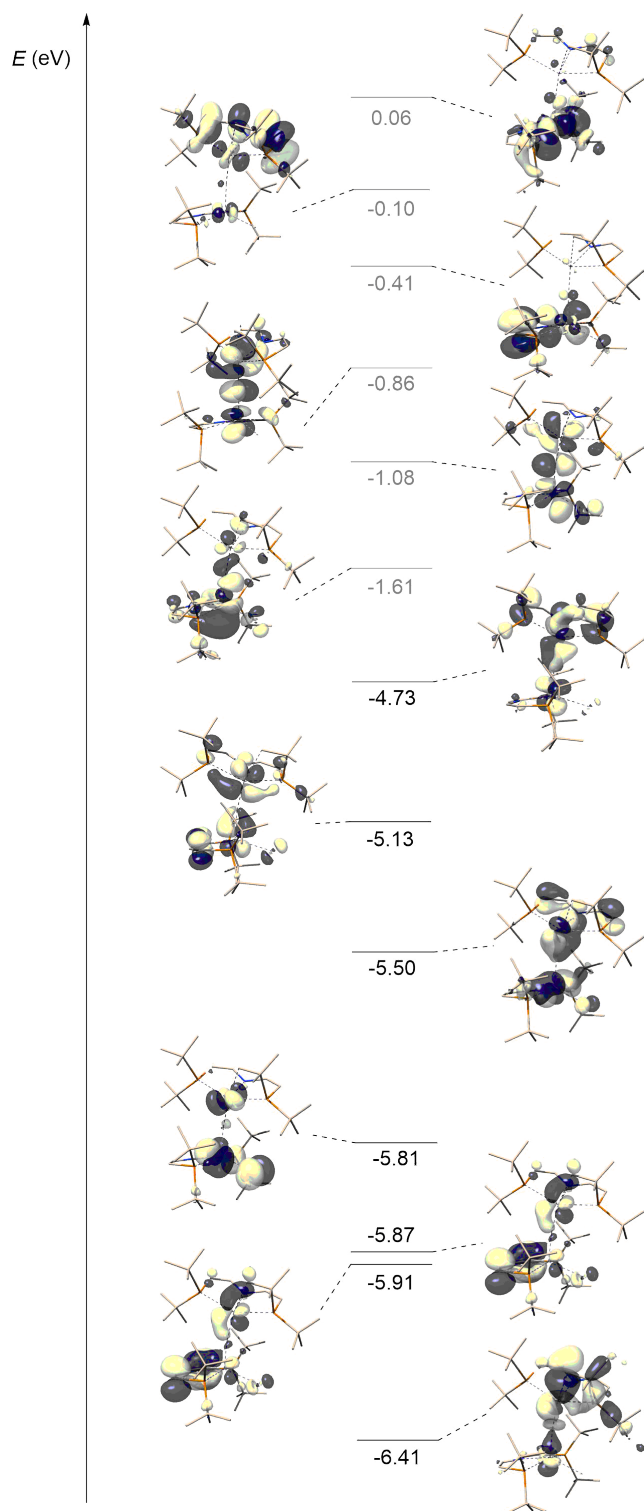
Appendix 8.2.3: Computed molecular orbital scheme of **20**. Unoccupied molecular orbitals are drawn in grey and energies are given in eV.
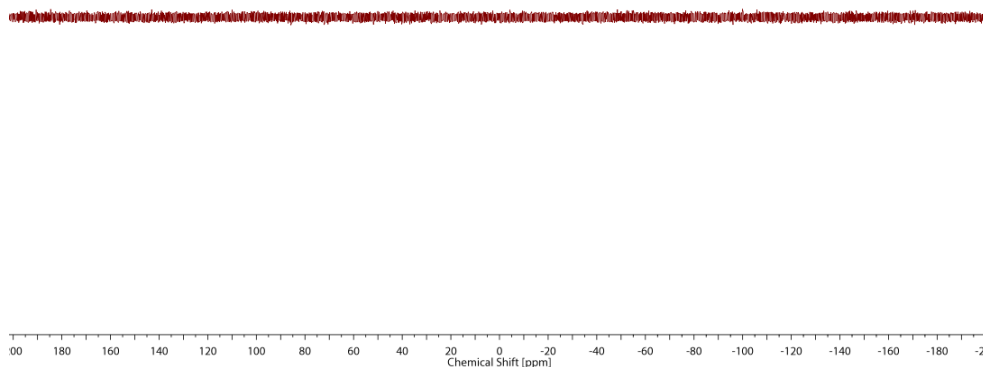
Appendix 8.2.4: $^{31}P\{^1H\}$ NMR spectrum of **21** after irradiation, THF-d$_8$, RT, after 1h of irradiation.
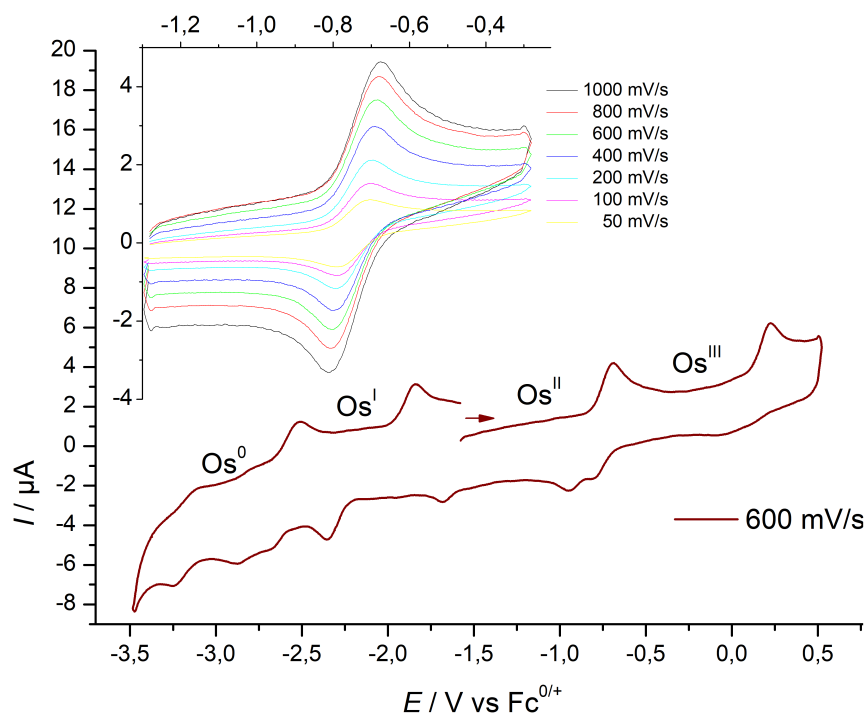
Appendix 8.2.5: Cyclic voltammogram of **21**, $200\,mV \cdot s^{-1}$, $1\,mM$, $0.1\,M$ NBu$_4$PF$_6$, THF, RT. Inset: Isolated 1st oxidative wave.
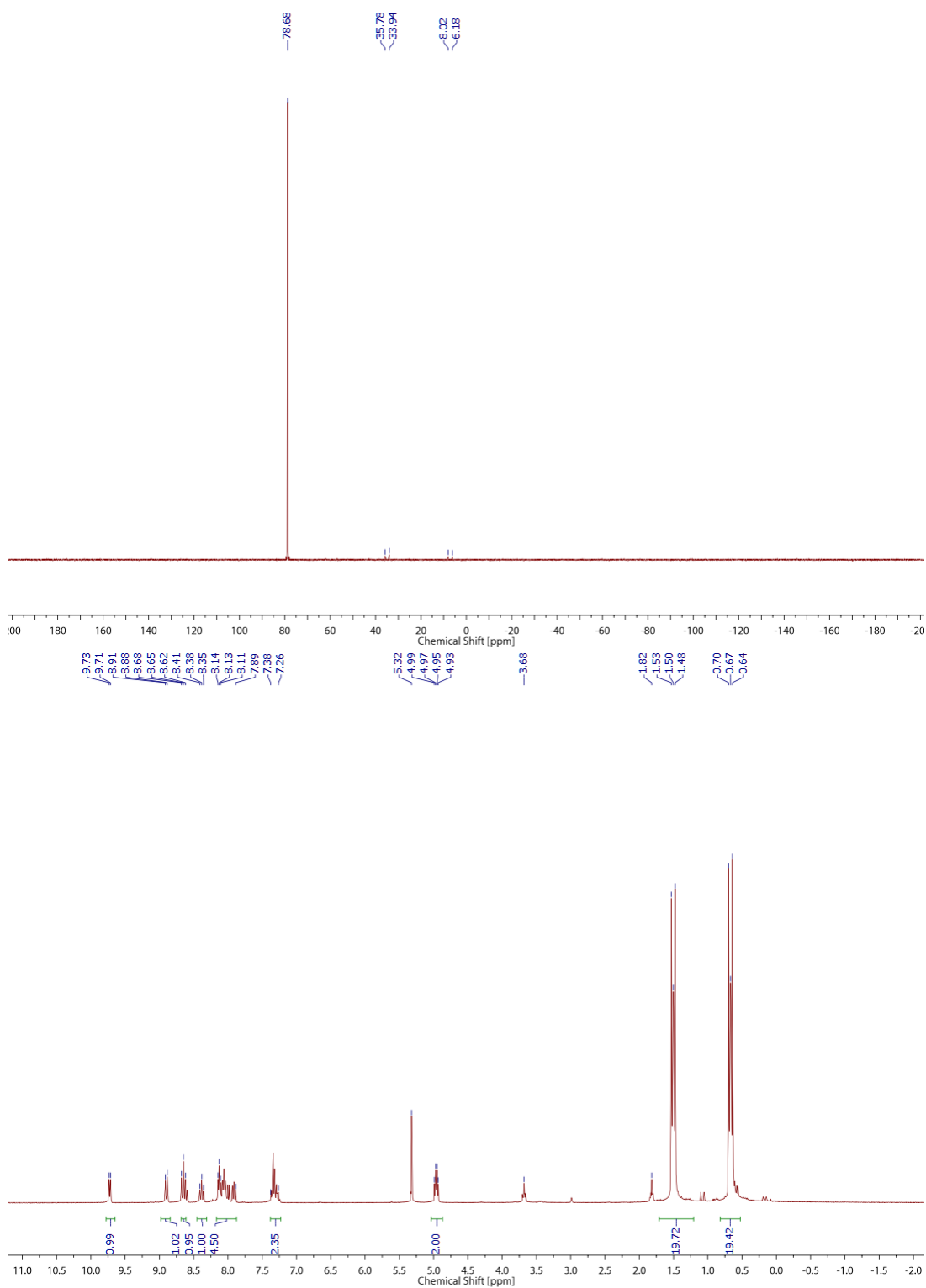
Appendix 8.2.6: Top: $^{31}P\{^{1}H\}$ NMR spectrum of the two-electron oxidation of **21**, CD_2Cl_2, RT; Bottom: ^{1}H NMR spectrum of the two-electron oxidation of **21**, CD_2Cl_2, RT.
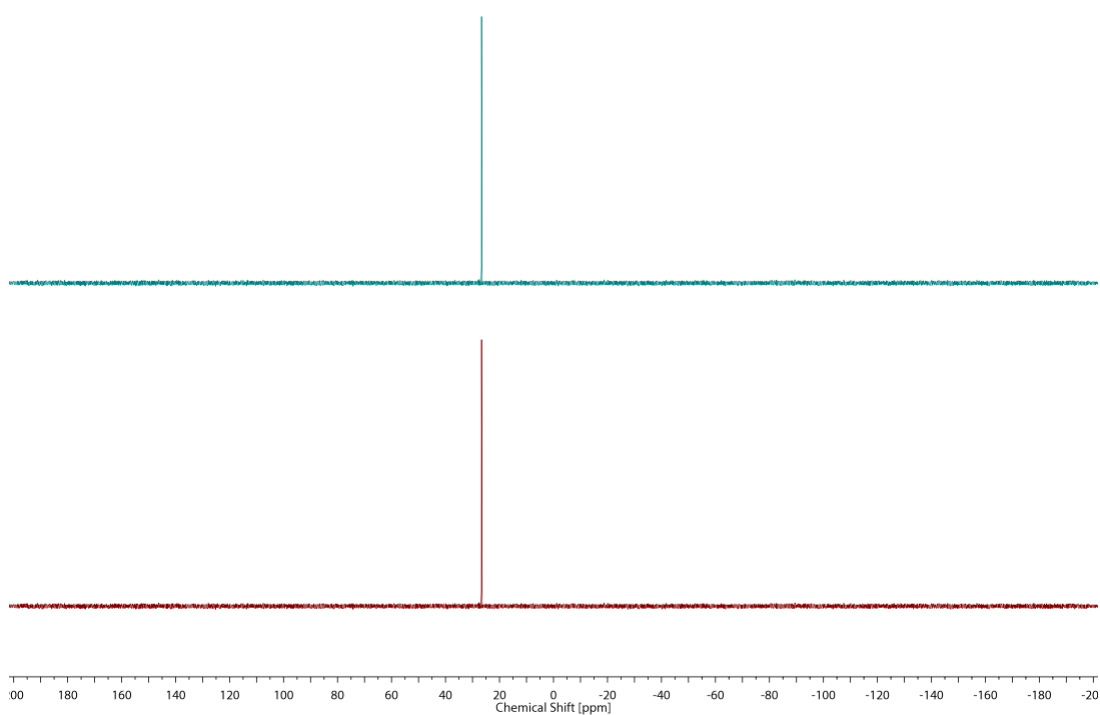
Appendix 8.2.7: Top: ^{31}P{^{1}H} NMR spectrum of the two-electron oxidation of **21** and successive reduction, CD_2Cl_2, RT; Bottom: ^{31}P{^{1}H} NMR spectrum of the one-electron oxidation of **21**, CD_2Cl_2, RT.

8.3 Transition Metal Complexes with Metal-Pnictogen Multiple Bonds
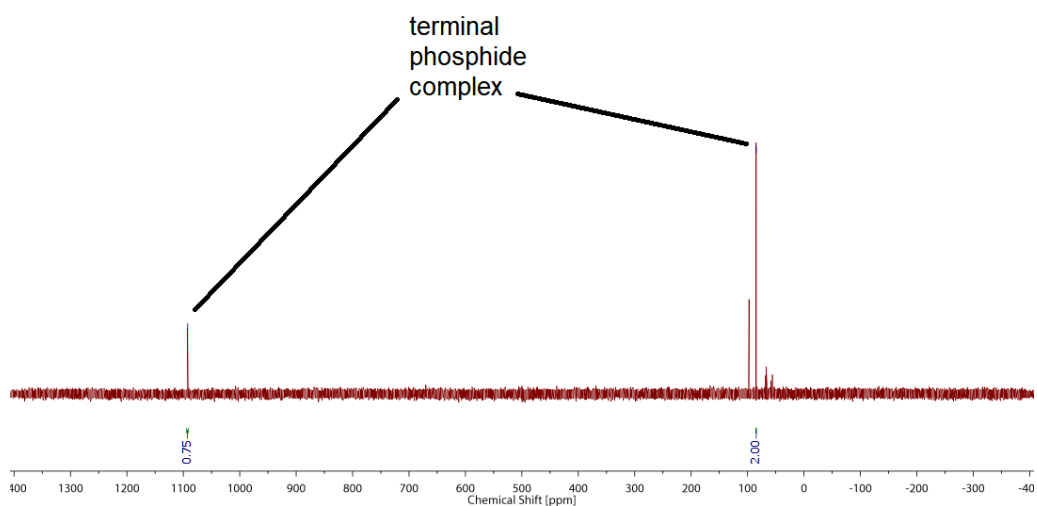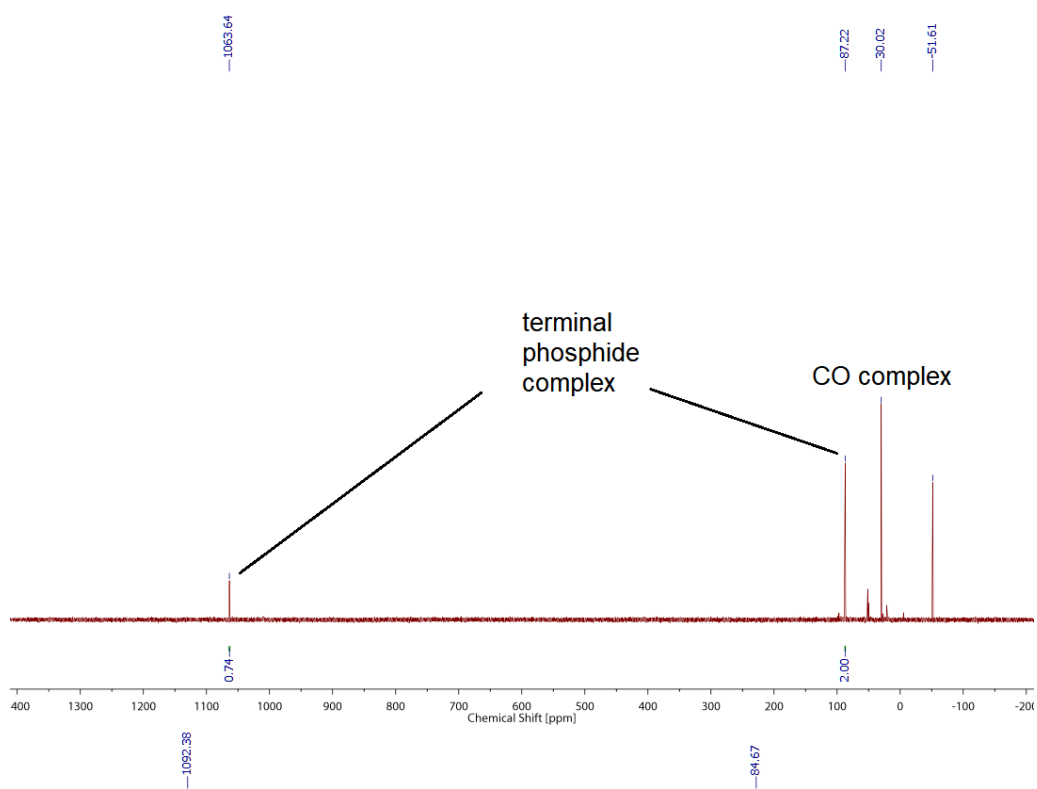
Appendix 8.3.1: Top: ^{31}P{^{1}H} NMR spectrum of the reaction of **LXXIII** with Na(diox)$_{1.39}$PCO; Bottom: ^{31}P{^{1}H} NMR spectrum of the reaction of **5** with Na(diox)$_{1.39}$PCO, C$_6$D$_6$, RT
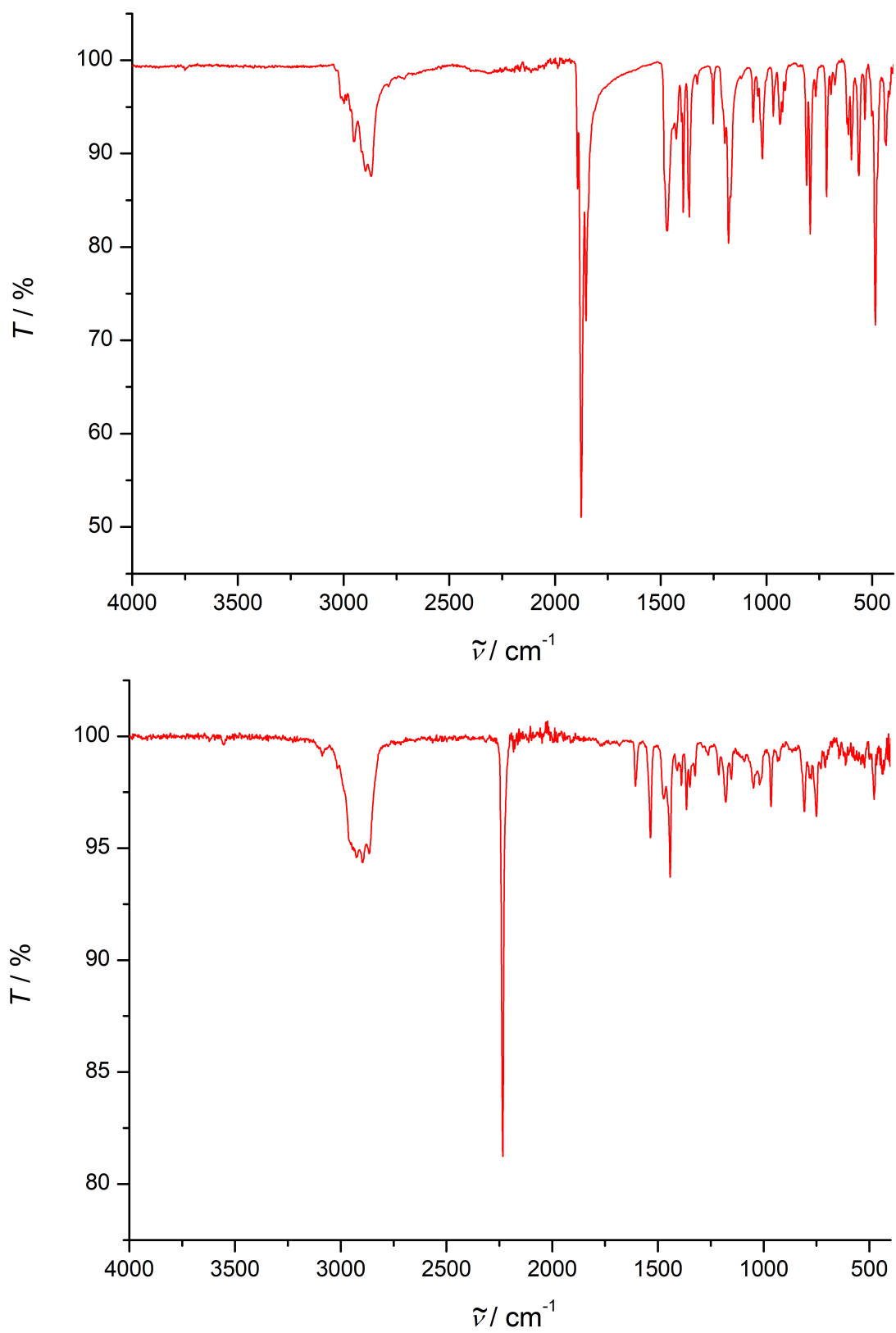
Appendix 8.3.2: Top: IR spectrum of **24**, RT; Bottom: IR spectrum of **25**, RT..
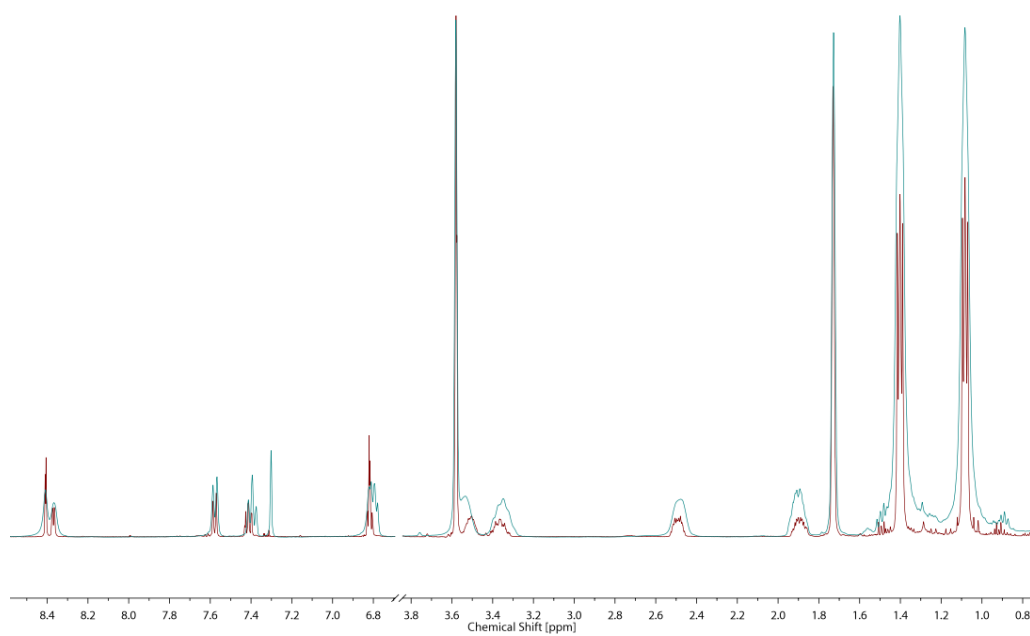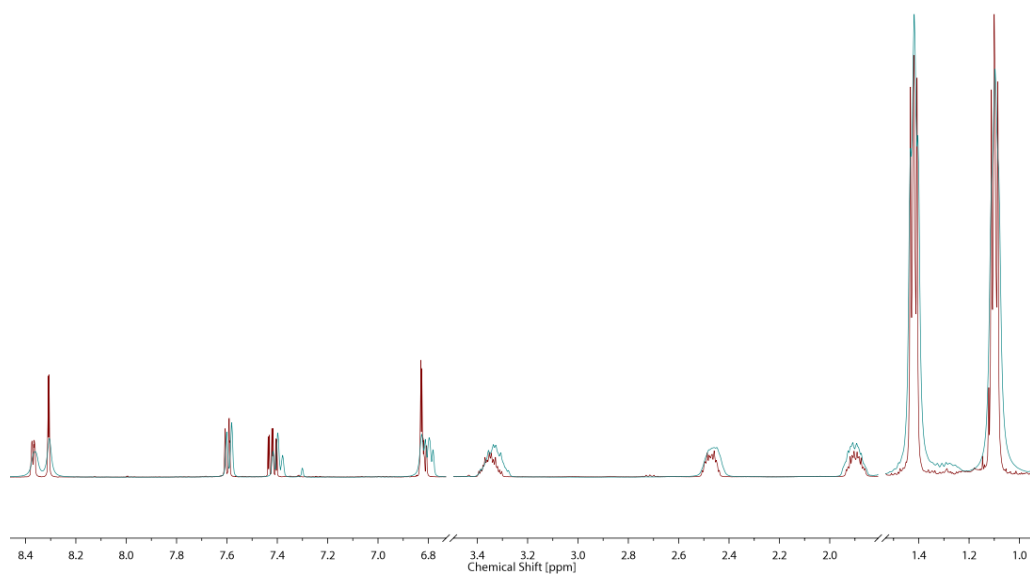
Appendix 8.3.3: Top: ^{1}H NMR spectrum of **27**; Bottom: ^{1}H NMR spectrum of **??**, THF-d$_8$, RT (turquoise), 0°C (red).
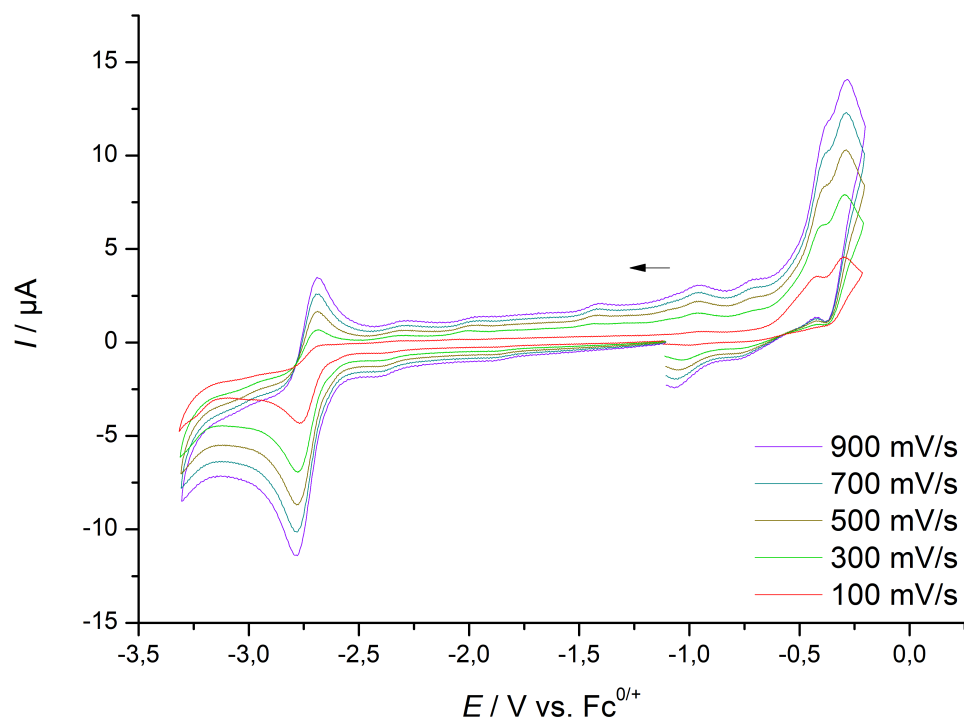
Appendix 8.3.4: Cyclic voltammogram of **27**, 1 mM, 0.1 M NBu$_4$PF$_6$, THF, RT.
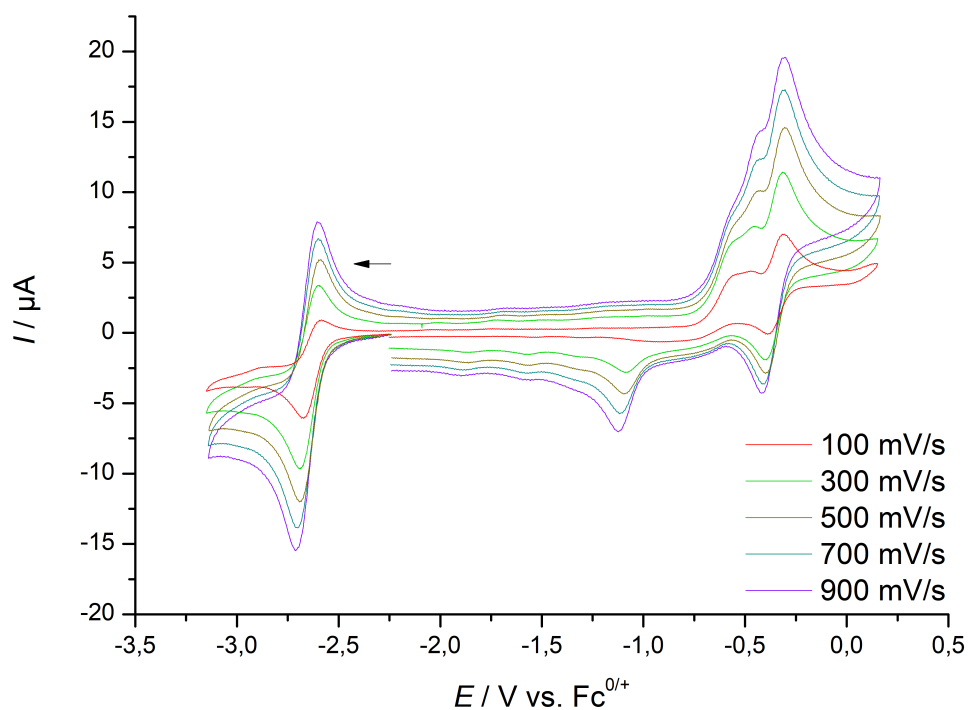
Appendix 8.3.5: Cyclic voltammogram of **28**, 1 mM, 0.1 M NBu$_4$PF$_6$, THF, RT.
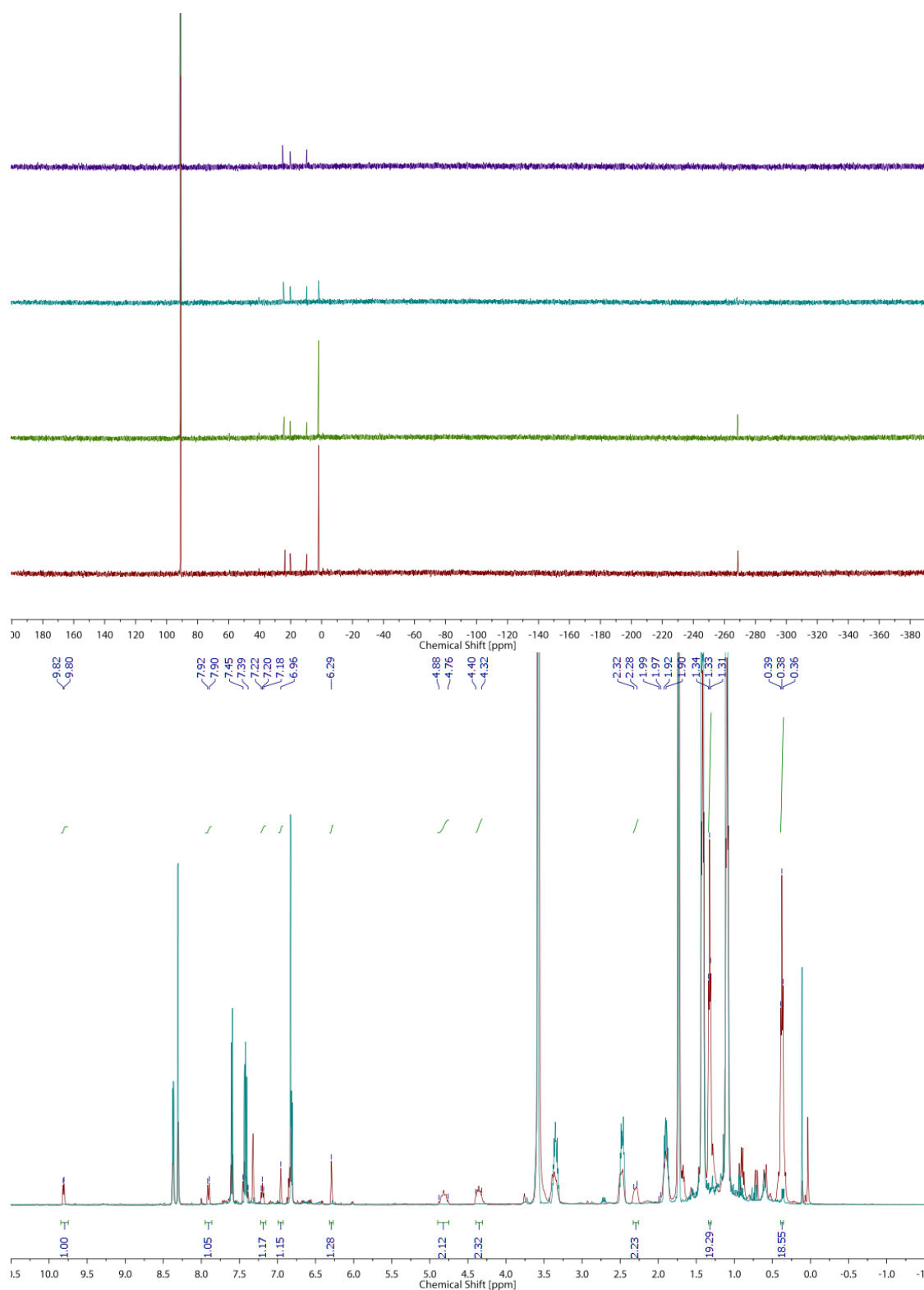
Appendix 8.3.6: Top: VT ^{31}P{^{1}H} NMR spectra of the reaction of **11** with Na(diox)$_{1.39}$PCO, THF-d$_8$, −20°C (red), −10°C (green), 0°C (teal), 10°C (purple); Bottom: ^{1}H NMR spectra of the reaction of **11** with Na(diox)$_{1.39}$PCO, THF-d$_8$, −20°C (red), pure **27**, THF-d$_8$, 0°C (teal), peaks belonging to **26** are marked in blue.
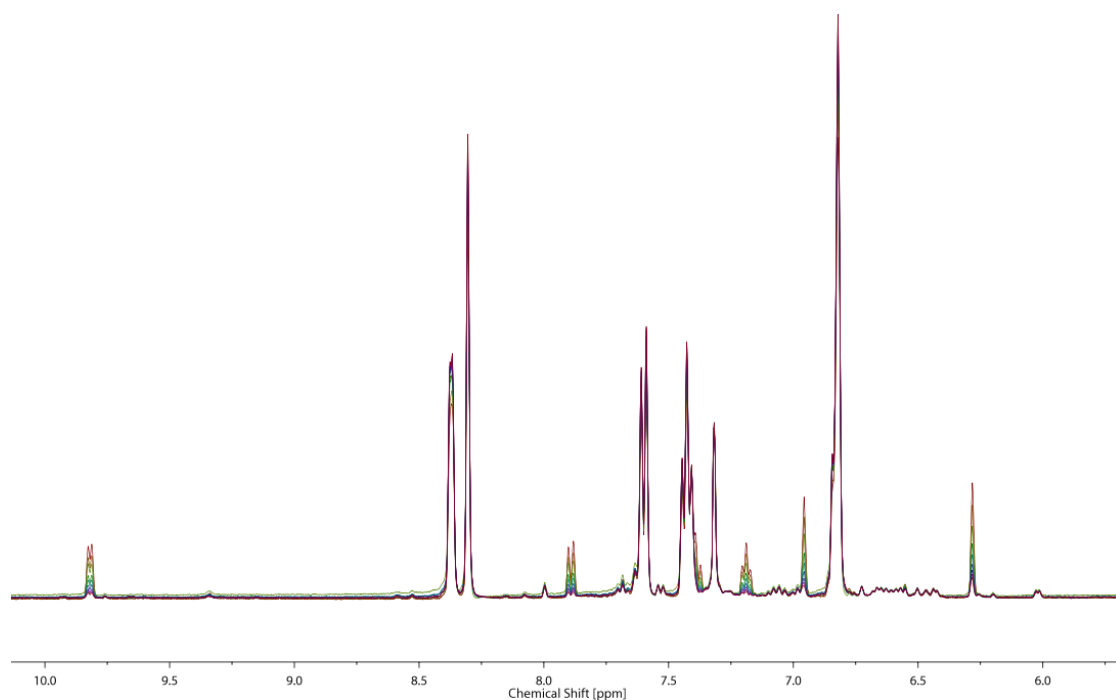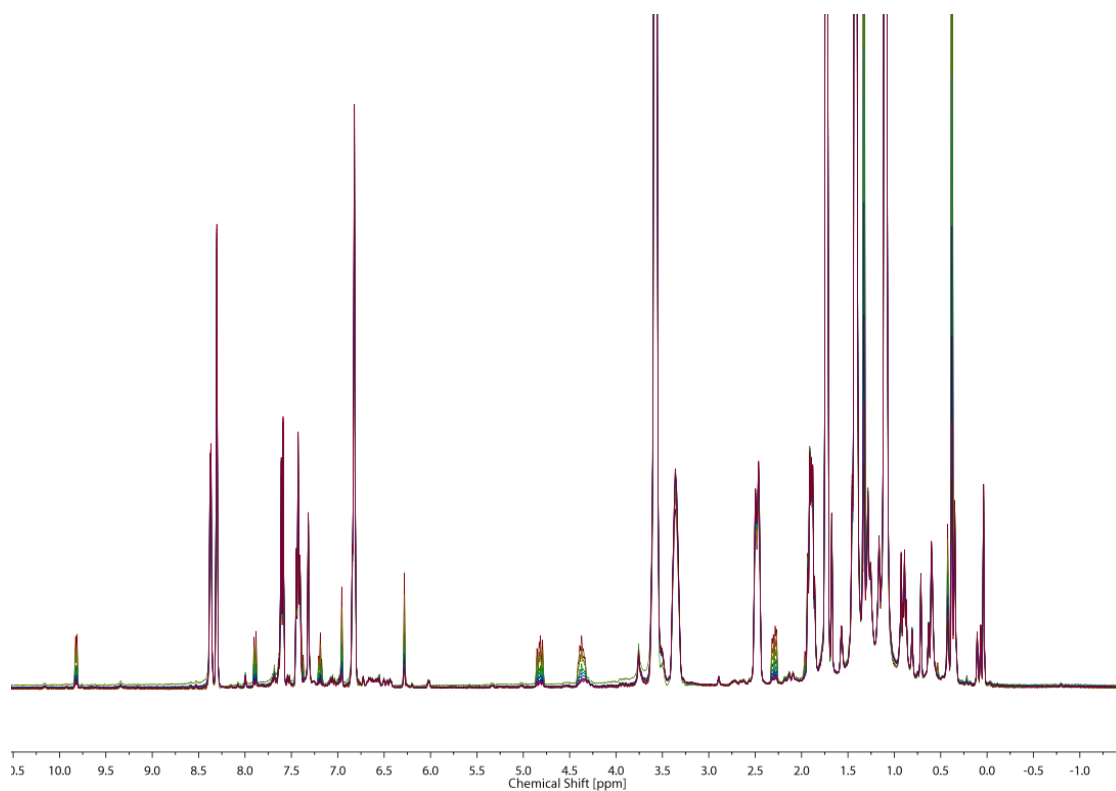
Appendix 8.3.7: Top: $^1\text{H}\{^{31}\text{P}\}$ NMR spectra of the reaction of **11** with $\text{Na(diox)}_{1.39}\text{PCO}$, THF-d$_8$, $-10°$C, the reaction was followed for 50 min; Bottom: $^1\text{H}\{^{31}\text{P}\}$ NMR spectra of the aromatic region of the reaction of **11** with $\text{Na(diox)}_{1.39}\text{PCO}$, THF-d$_8$, $-10°$C, the reaction was followed for 50 min.
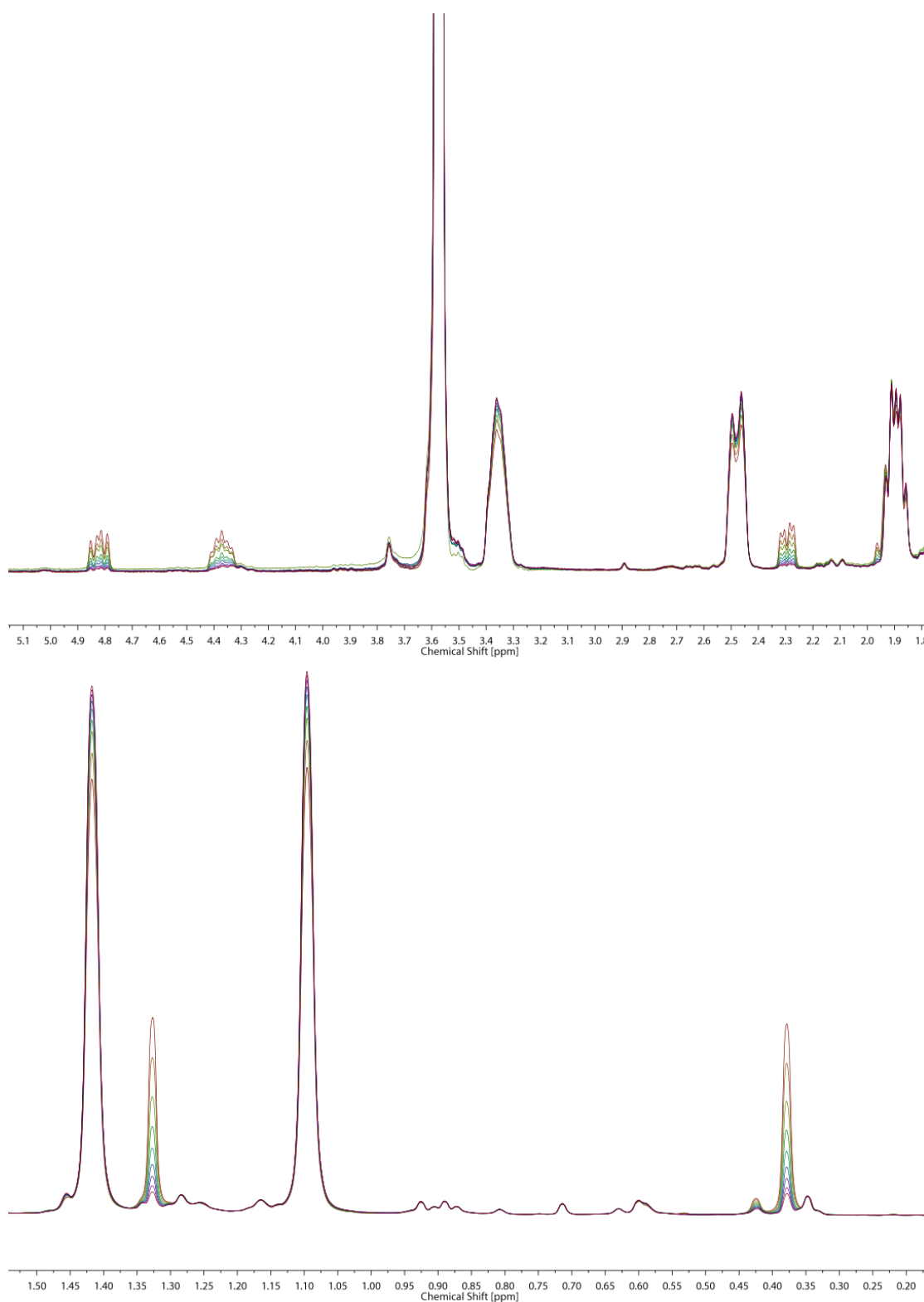
Appendix 8.3.8: Top: ^{1}H{^{31}P} NMR spectra of the PNP-aliphatic region of the reaction of **11** with Na(diox)$_{1.39}$PCO, THF-d$_8$, -10°C, the reaction was followed for 50 min; Bottom: ^{1}H{^{31}P} NMR spectra of the PNP-^{t}Bu region of the reaction of **11** with Na(diox)$_{1.39}$PCO, THF-d$_8$, -10°C, the reaction was followed for 50 min.
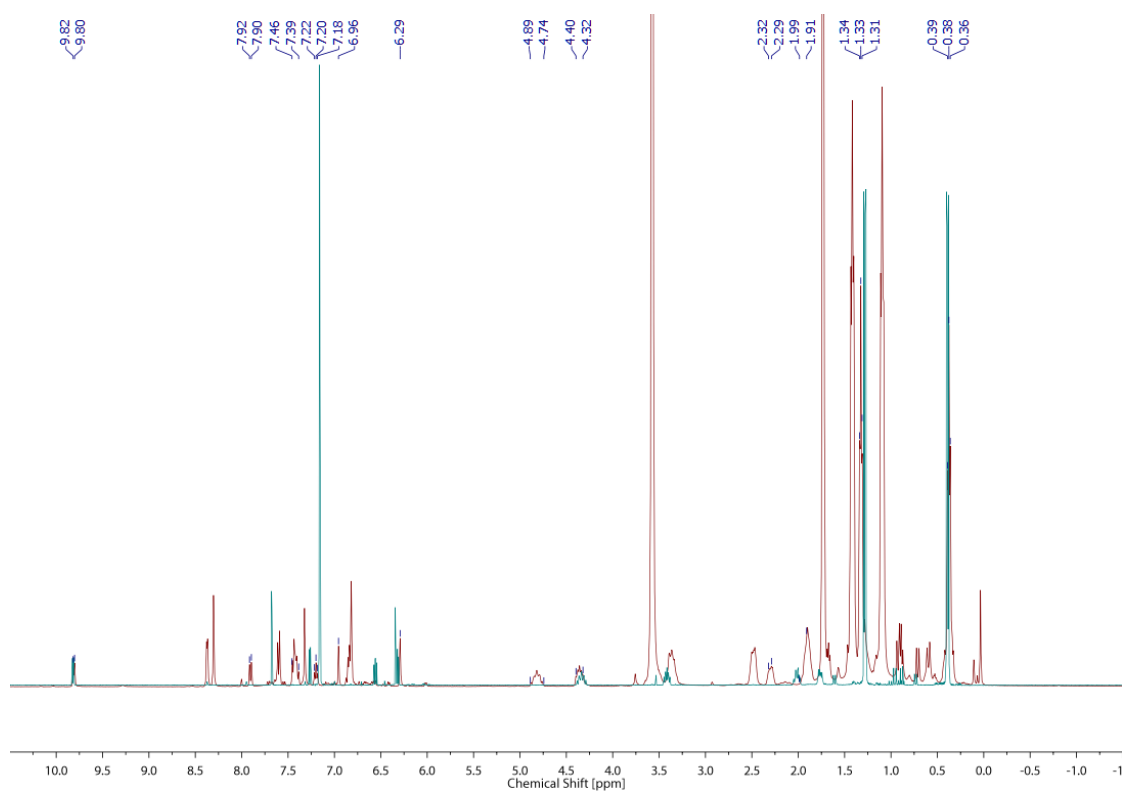
Appendix 8.3.9: Top: ^{1}H{^{31}P} NMR spectra of the reaction of **11** with Na(diox)$_{1.39}$PCO, THF-d$_8$, $-20°$C (red), pure **25** (teal), C$_6$D$_6$, RT.
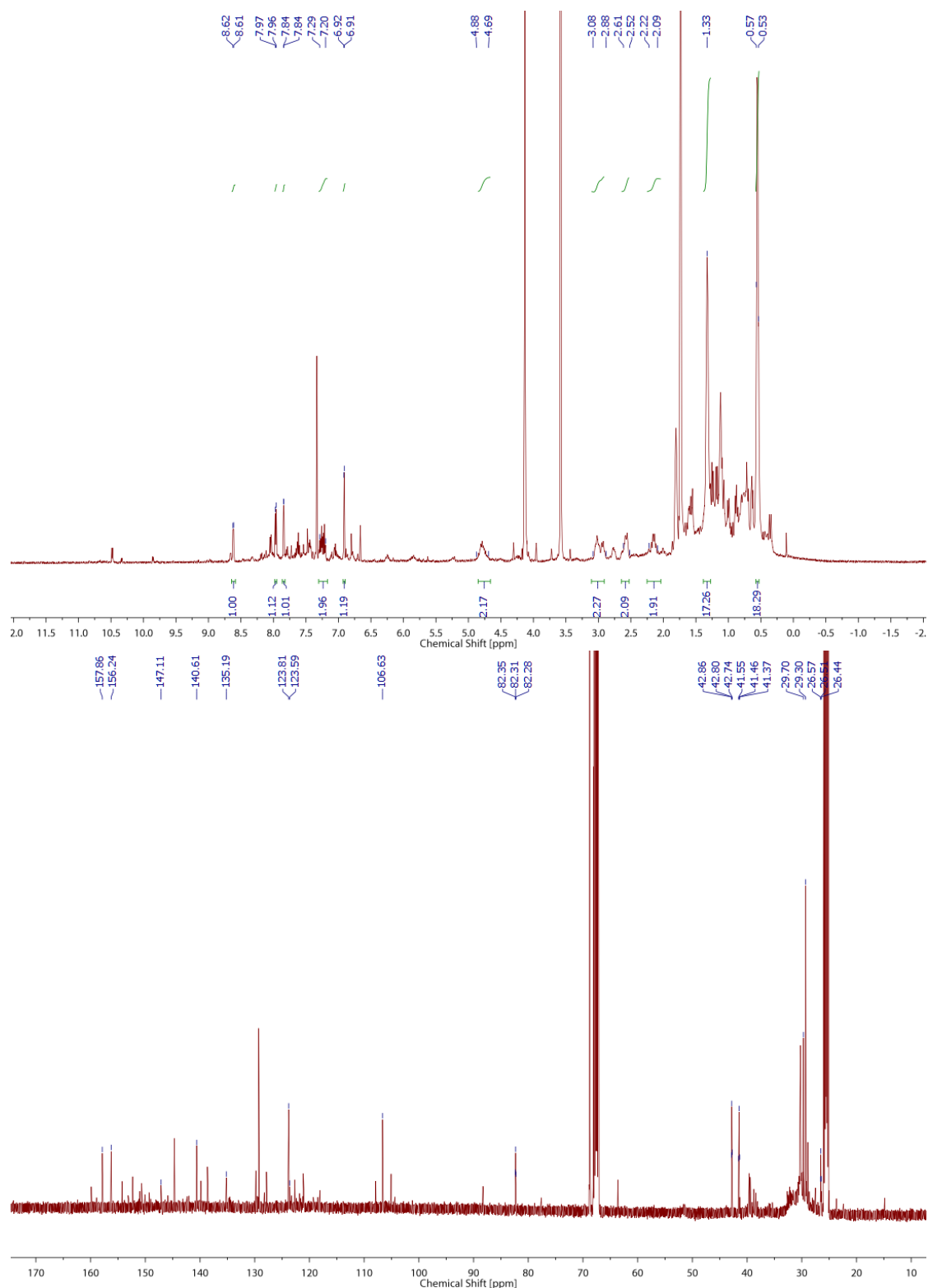
Appendix 8.3.10: Top: ^{1}H NMR spectrum of the oxidation of **27** with [Fc][OTf], THF-d$_8$, $-38°$C; Bottom: ^{13}C{^{1}H} NMR spectrum of the oxidation of **27** with [Fc][OTf], THF-d$_8$, $-38°$C.
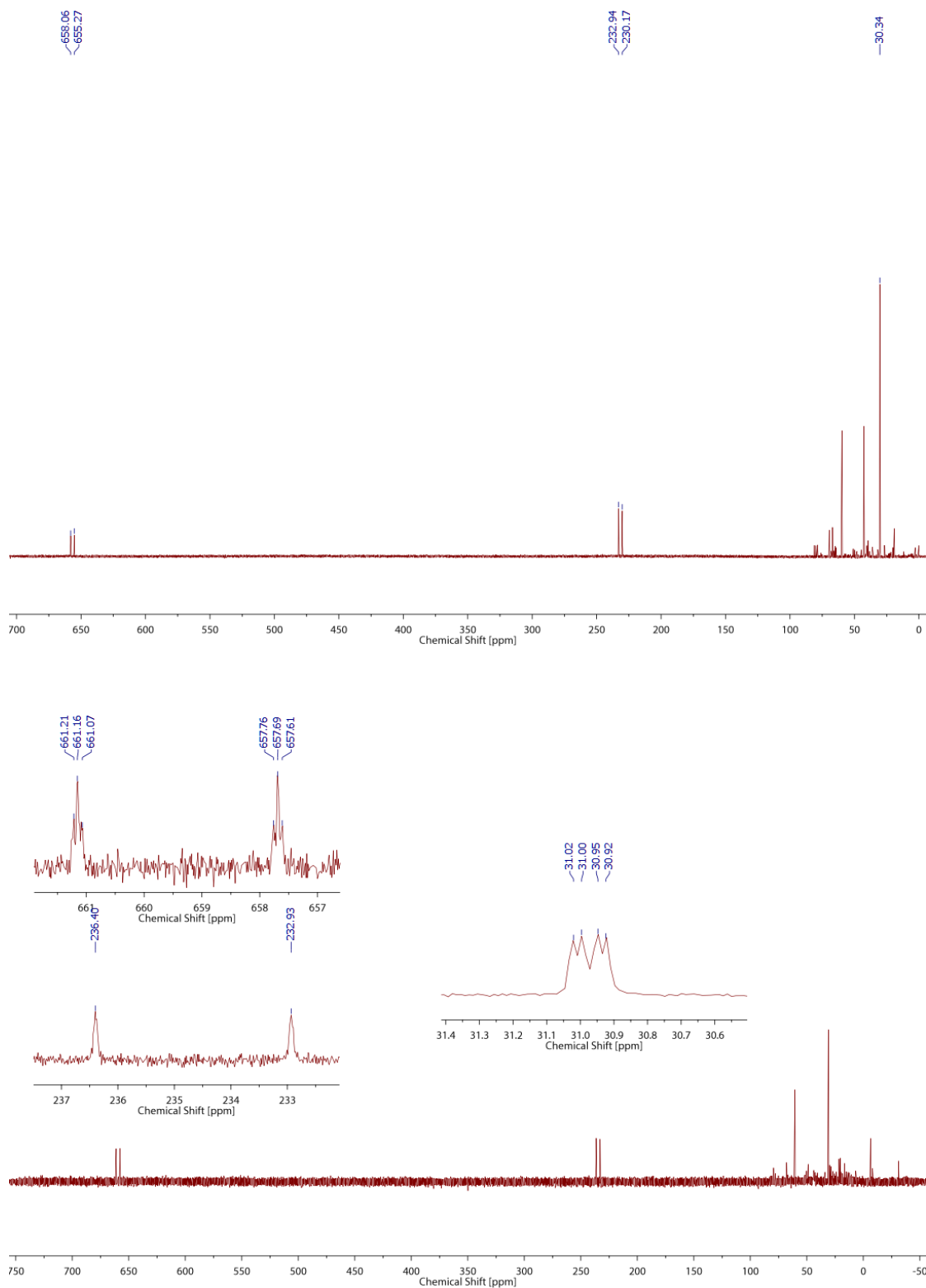
Appendix 8.3.11: Top: $^{31}P\{^1H\}$ NMR spectrum of the oxidation of **27** with [Fc][OTf], THF-$_8$, −38°C; Bottom: $^{31}P\{^1\}$ NMR spectrum of the oxidation of **27** with [Fc][OTf], THF-$_8$, RT.
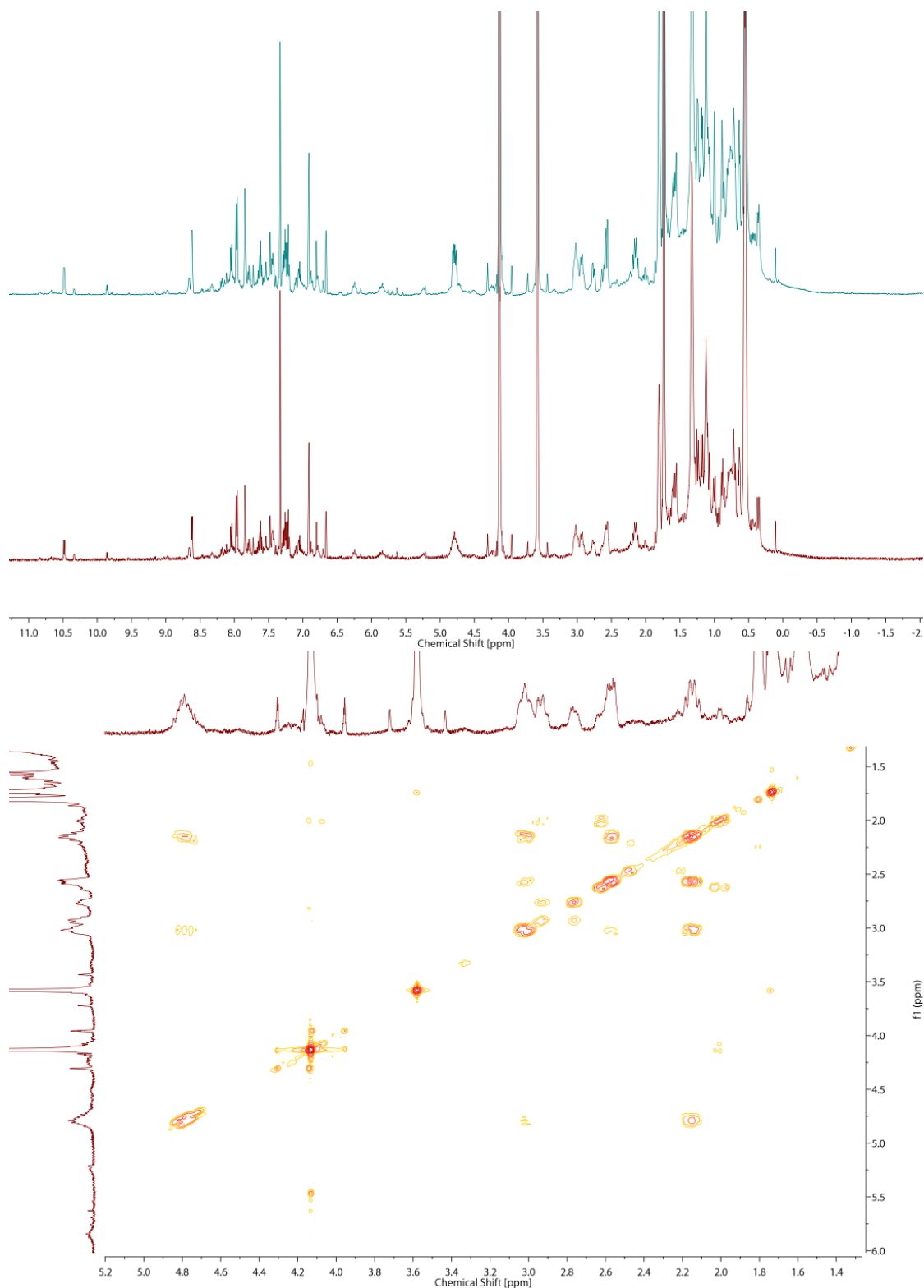
Appendix 8.3.12: Top: ^{1}H{^{31}P} NMR spectrum of the oxidation of **27** with [Fc][OTf], THF-d$_8$, $-38°$C, decoupled at 31 ppm (top) and without decoupling (bottom); Bottom: COSY NMR spectrum of the PNP pincer region of the oxidation of **27** with [Fc][OTf], THF-d$_8$, $-38°$C.
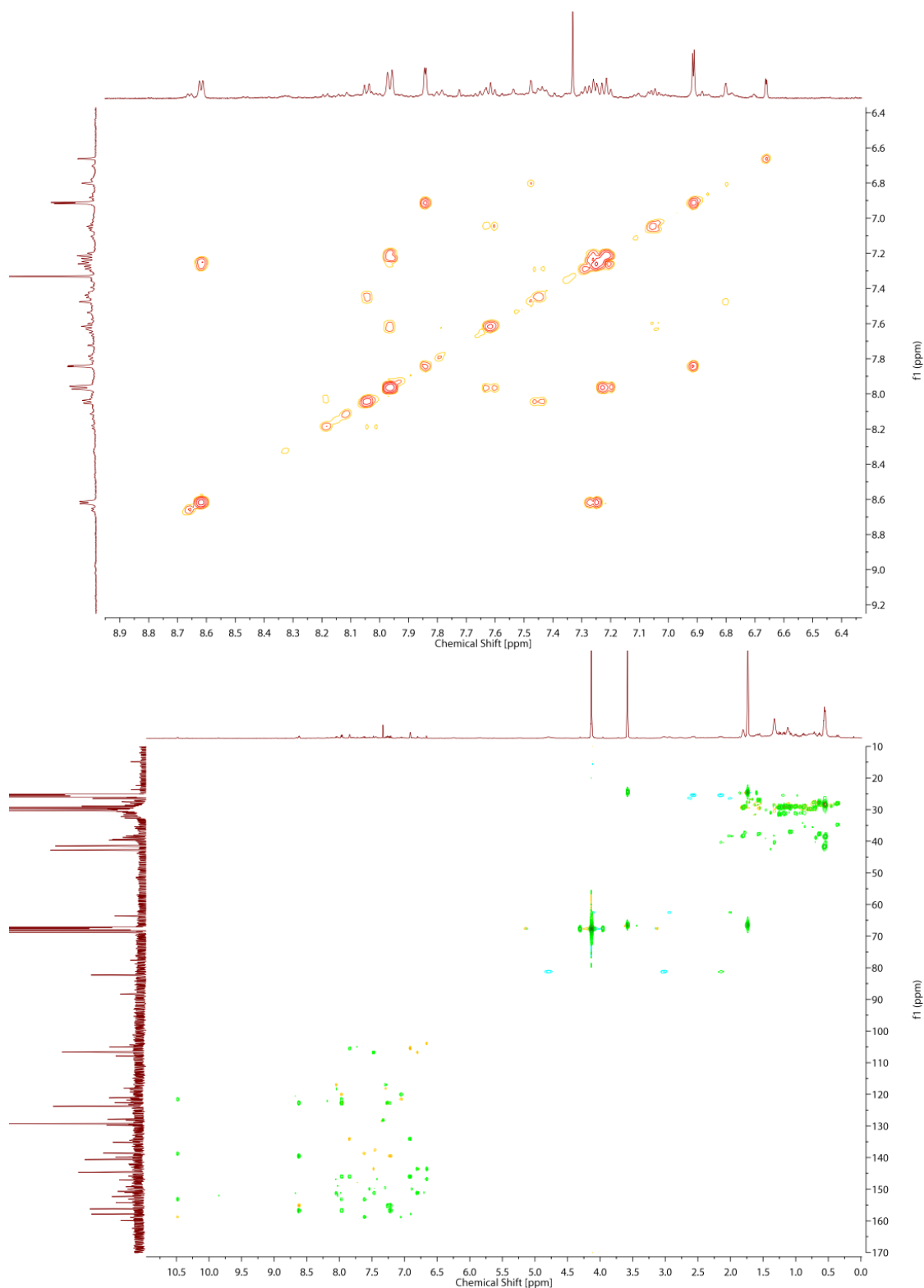
Appendix 8.3.13: Top: COSY NMR spectrum of the PNP pincer region of the oxidation of **27** with [Fc][OTf], THF-d$_8$, −38°C; Bottom: HSQC (green/yellow) and HMBC (blue) spectra of the oxidation of **27** with [Fc][OTf], THF-d$_8$, −38°C.
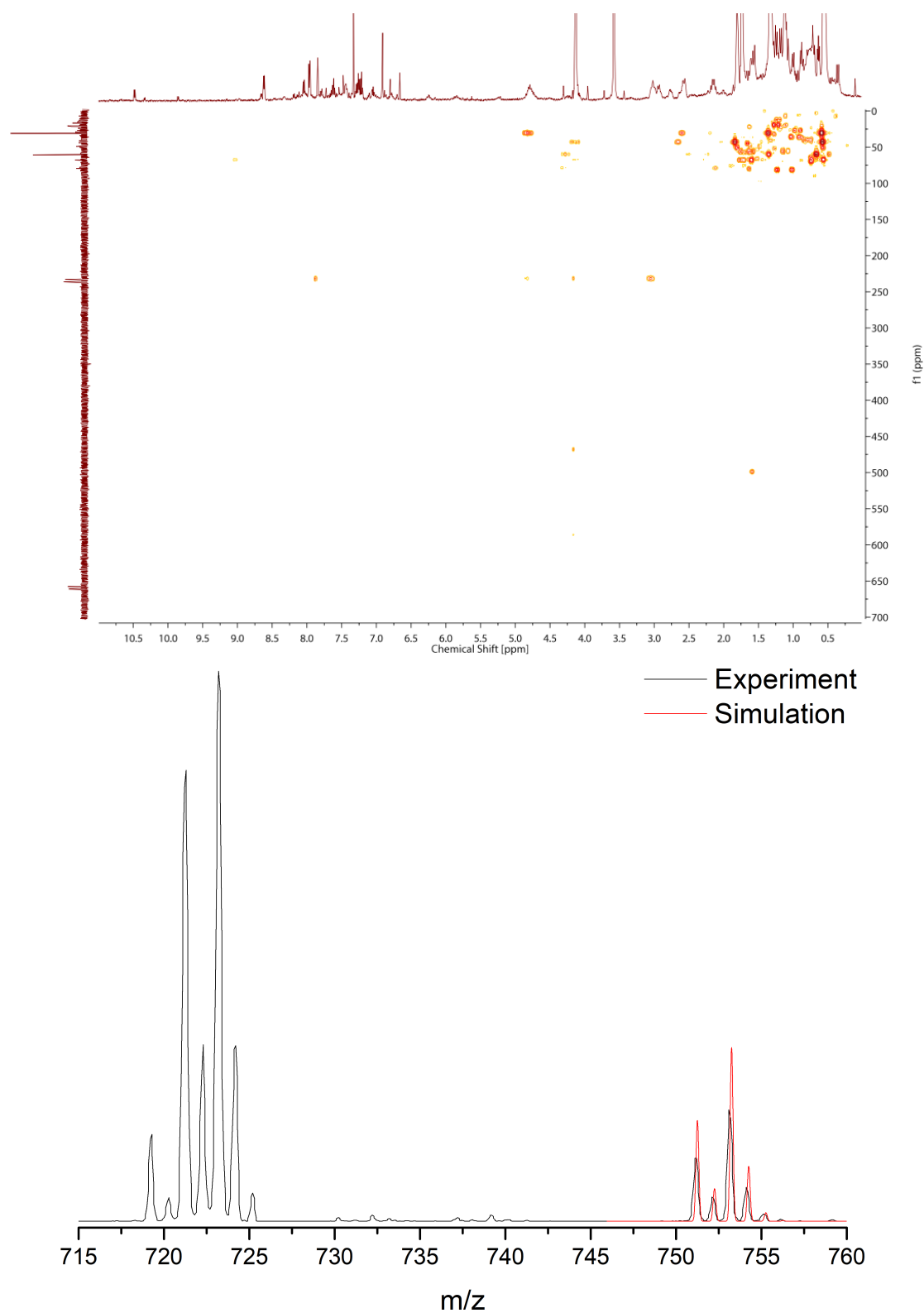
Appendix 8.3.14: Top: $^{31}P\{^1H\}$ NMR spectrum of the oxidation of **27** with [Fc][OTf], THF-d_8, $-38°C$; Bottom: ESI spectrum of the oxidation of **27** with [Fc][OTf], THF, RT.
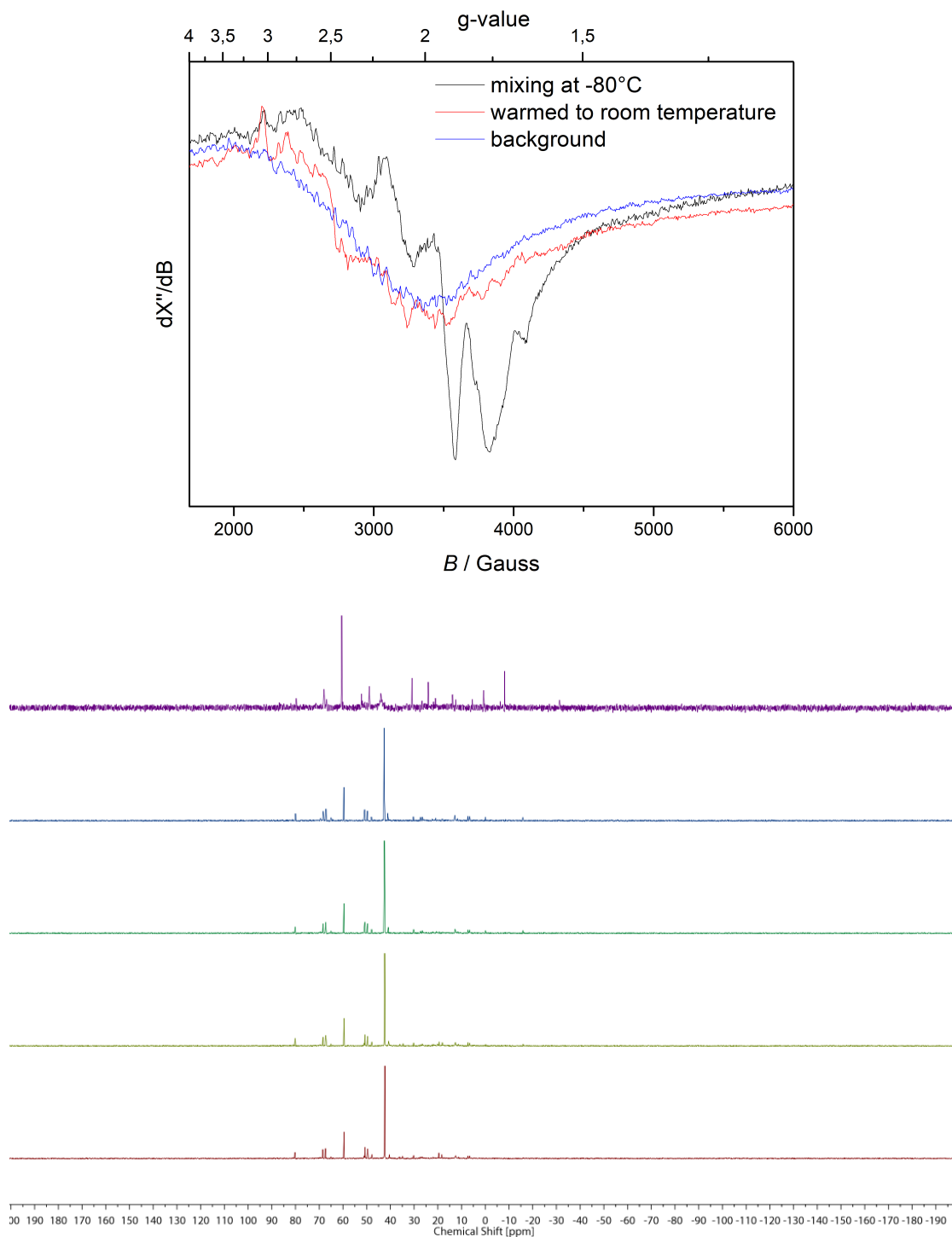
Appendix 8.3.15: Top: EPR spectra of the oxidation of **27** with [Fc][OTf], THF; Bottom: $^{31}P\{^{1}H\}$ NMR spectra of the oxidation of **27** with [Fc][OTf], THF-d$_8$, $-80°C$ (red), $-70°C$ (yellow), $-60°C$ (green), $-50°C$ (blue), RT (purple).
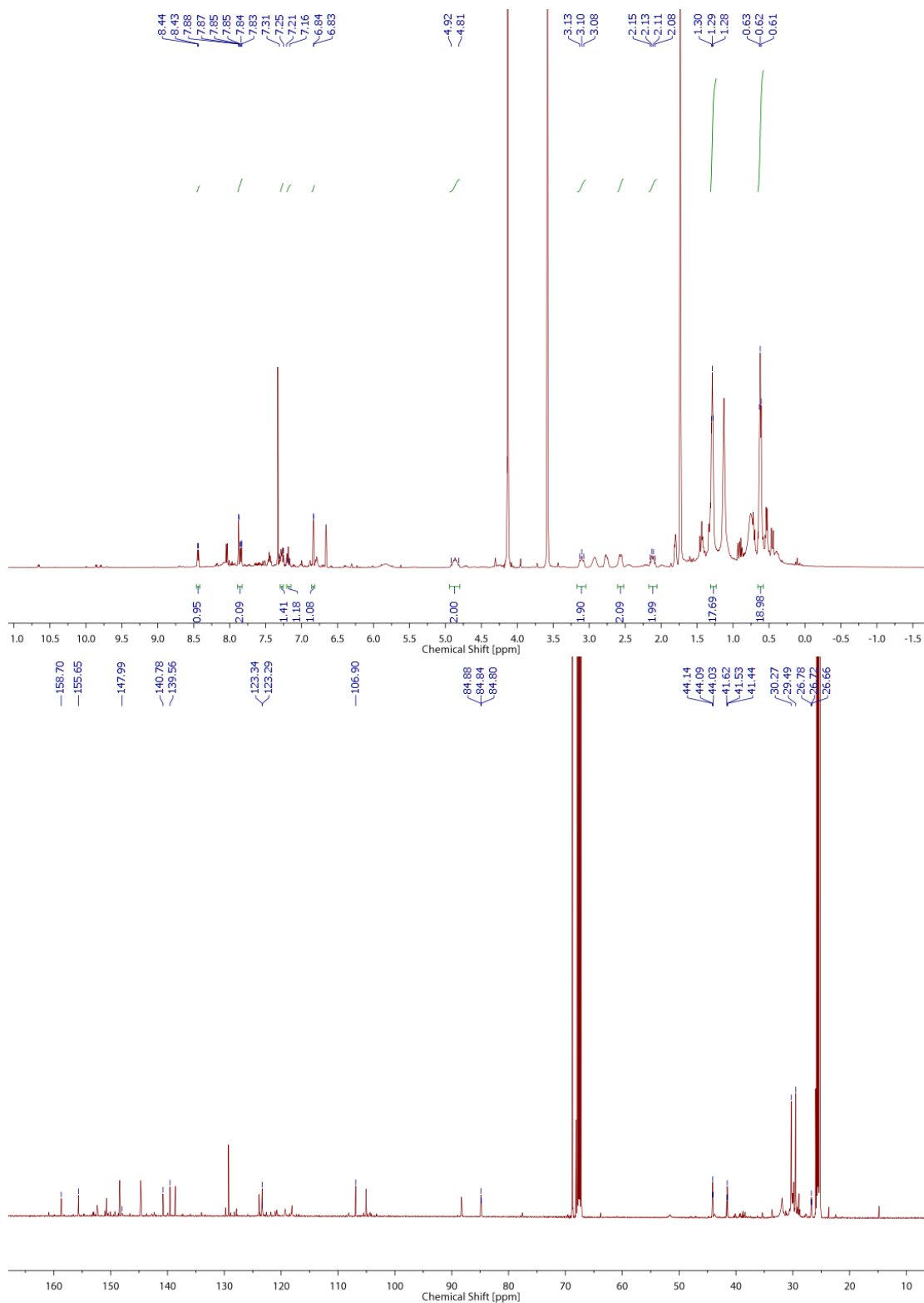
Appendix 8.3.16: Top: ^{1}H NMR spectrum of the oxidation of **28** with [Fc][OTf], THF-d$_8$, $-38°$C; Bottom: ^{13}C{^{1}H} NMR spectrum of the oxidation of **28** with [Fc][OTf], THF-d$_8$, $-38°$C.

—26.47
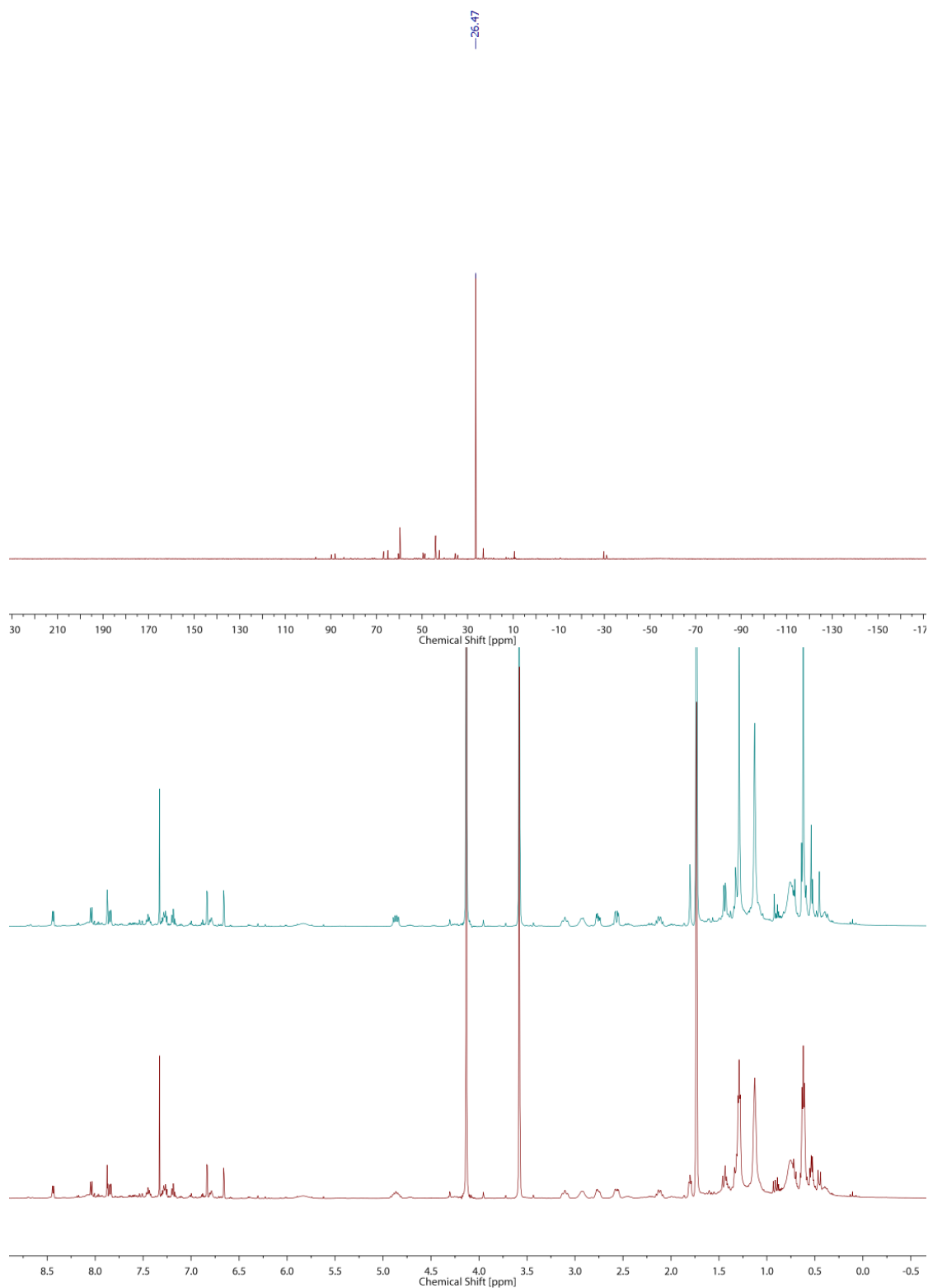
Appendix 8.3.17: Top: $^{31}P\{^{1}H\}$ NMR spectrum of the oxidation of **28** with [Fc][OTf], THF-$_8$, −38°C; Bottom: $^{31}P\{^{1}H\}$ NMR spectrum of the oxidation of **28** with [Fc][OTf], THF-$_8$, RT.
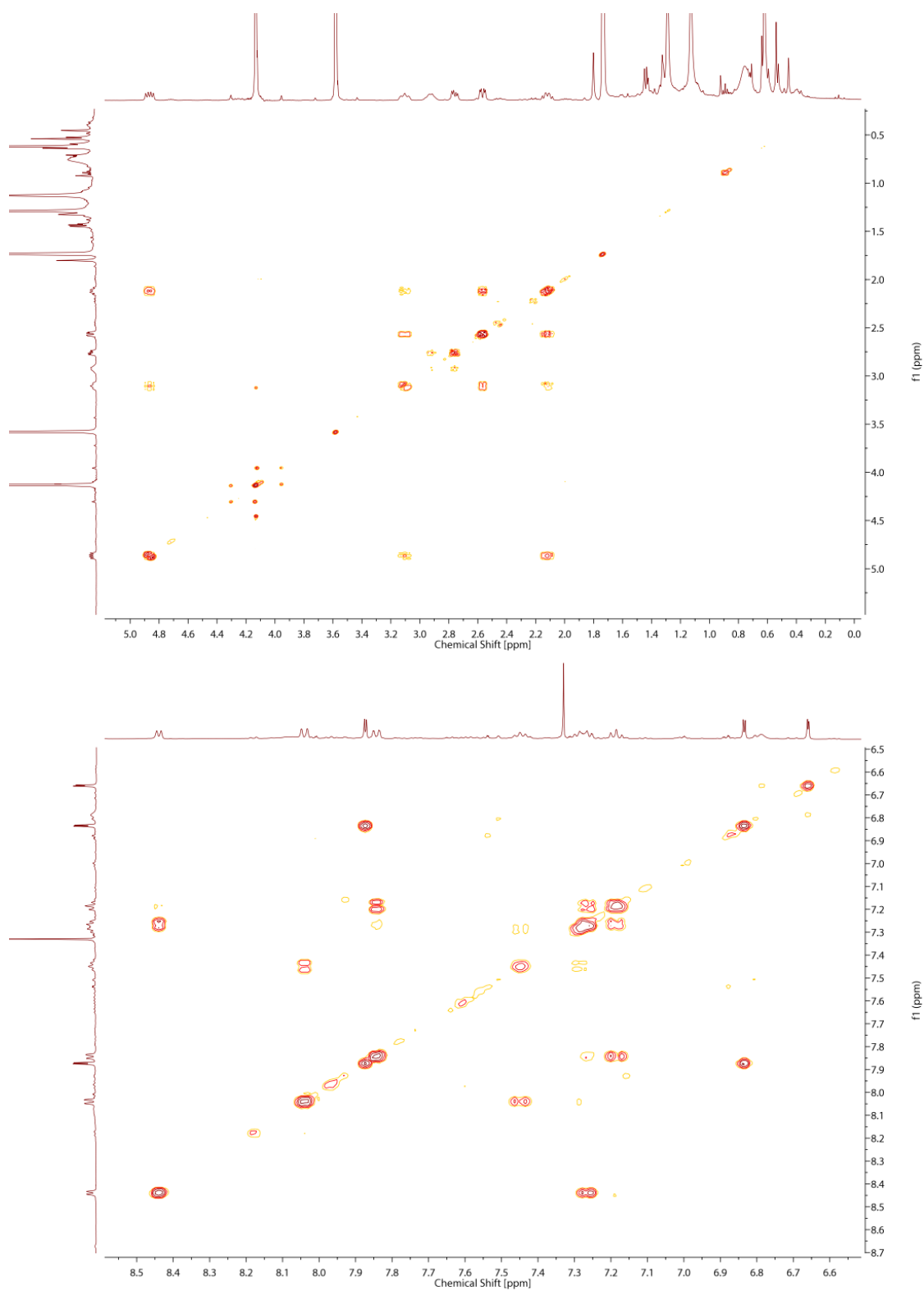
Appendix 8.3.18: Top: COSY NMR spectrum of the PNP pincer region of the oxidation of **28** with [Fc][OTf], THF-d$_8$, −38°C: Bottom: COSY NMR spectrum of the aromatic region of the oxidation of **28** with [Fc][OTf], THF-d$_8$, −38°C.
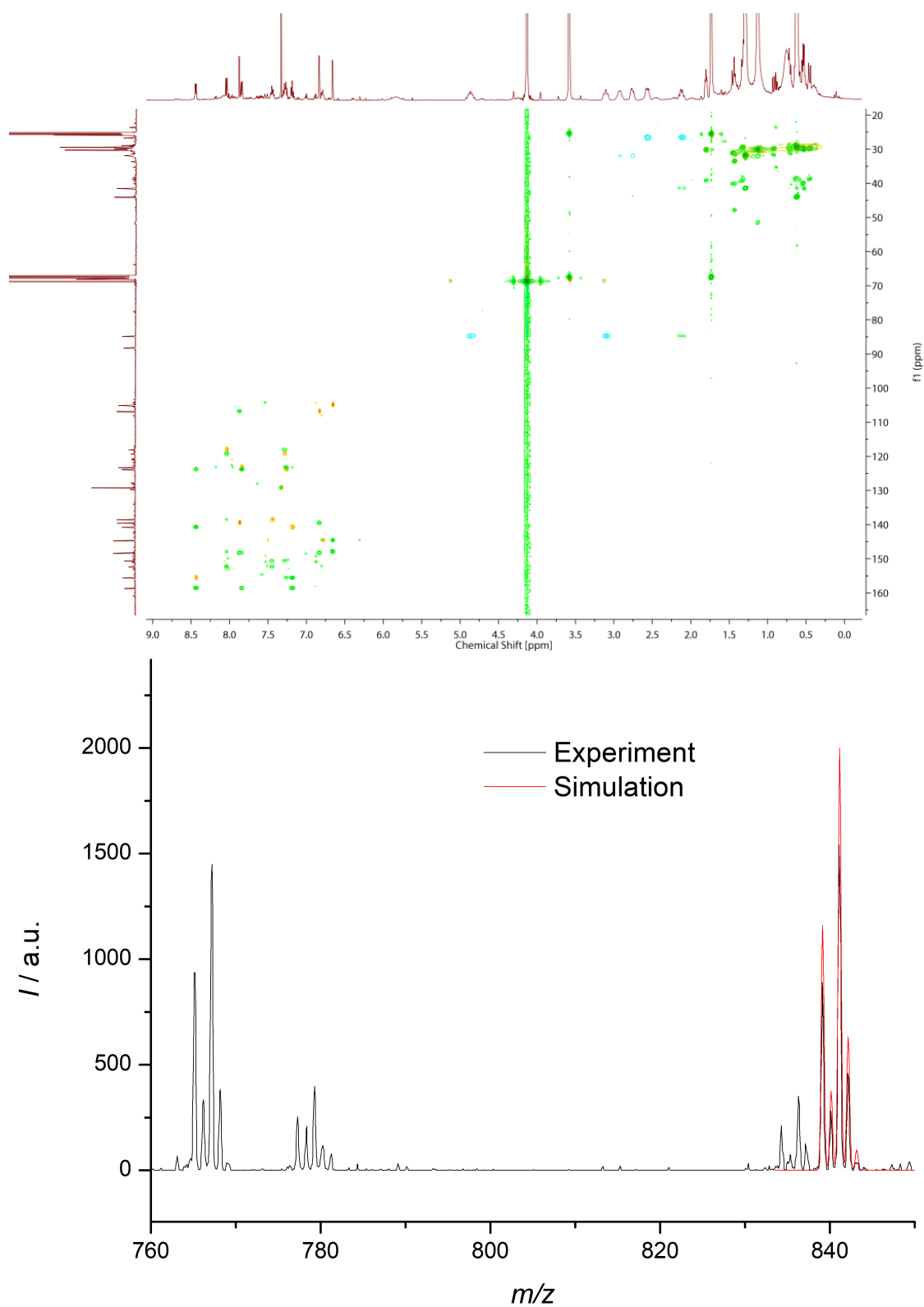
Appendix 8.3.19: Top: HSQC (green/yellow) and HMBC (blue) spectra of the oxidation of **28** with [Fc][OTf], THF-d$_8$, −38°C; Bottom: ESI spectrum of the oxidation of **28** with [Fc][OTf], THF, RT.
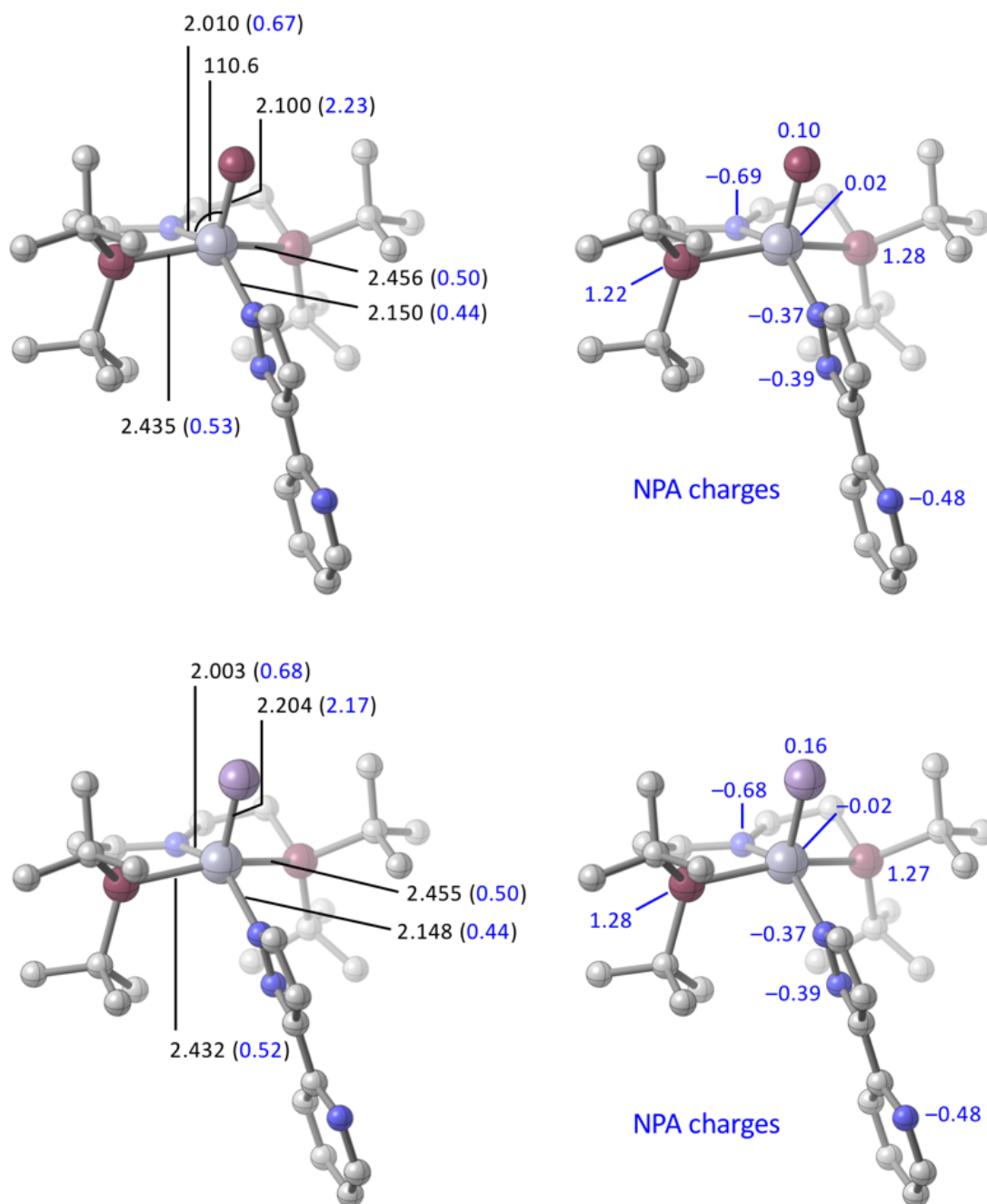
Appendix 8.3.20: Computed structures and properties of **27** (top) and **28** (bottom, ωB97XD/BS2//ωB97XD/BS1. Left: Selected bond lengths in Å(Wiberg bond indices in blue); Right: NPA charges.
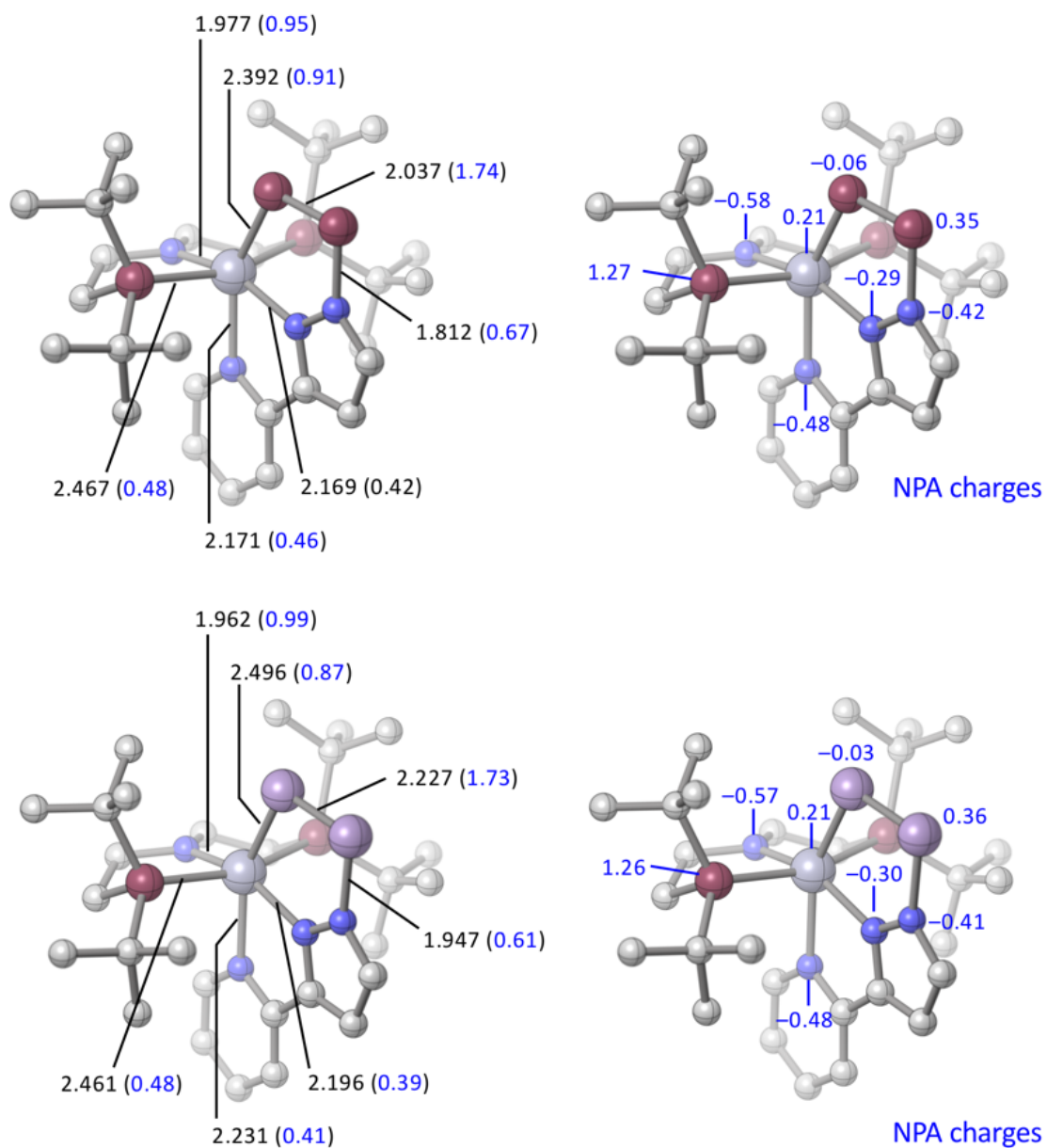
Appendix 8.3.21: Computed structures and properties of **29** (top) and **30** (bottom, ωB97XD/BS2//ωB97XD/BS1. Left: Selected bond lengths in Å(Wiberg bond indices in blue); Right: NPA charges.

Species	Bond	$\rho(\mathbf{r}_b)$ / eÅ^{-3}	$\nabla^2\rho(\mathbf{r}_b)$ / eÅ^{-5}	$H(\mathbf{r}_b)/\rho(\mathbf{r}_b)$ / Hartree/e	$G(\mathbf{r}_b)/\rho(\mathbf{r}_b)$ / Hartree/e	ϵ	$\delta(A,B)$
P_2	P - P	1.15	-5.74	-0.74	0.39	0.00	3.04
P_2H_2	P $-$ P	0.95	-4.07	-0.59	0.29	0.40	1.96
P_2H_4	P $-$ P	0.71	-2.48	-0.44	0.19	0.07	0.99
27	Re1 $-$ P3	1.07	-1.34	-0.68	0.56	0.04	2.47
	Re1 - P1	0.58	2.71	-0.35	0.63	0.57	0.78
	Re1 - P2	0.60	2.76	-0.36	0.63	0.57	0.81
	Re1 - N1	0.88	10.94	-0.36	1.14	0.37	0.95
	Re1 - N2	0.65	8.49	-0.25	1.07	0.90	0.63
	N2 - N3	2.54	-14.66	-0.93	0.53	0.13	1.41
28	Re1 $-$ As1	0.95	0.96	-0.61	0.65	0.06	2.40
	Re1 - P1	0.58	2.76	-0.35	0.64	0.56	0.79
	Re1 - P2	0.60	2.80	-0.36	0.64	0.54	0.83
	Re1 - N1	0.90	11.09	-0.37	1.15	0.37	0.97
	Re1 - N2	0.65	8.54	-0.25	1.07	0.88	0.64
	N2 - N3	2.53	-14.61	-0.93	0.53	0.13	1.41
29	Re1 $-$ P3	0.66	1.35	-0.41	0.51	0.80	1.11
	Re1 - P1	0.57	2.78	-0.35	0.65	0.23	0.81
	Re1 - P2	0.57	2.78	-0.35	0.65	0.23	0.81
	Re1 - N1	0.93	12.45	-0.38	1.22	0.21	1.10
	Re1 - N3	0.58	8.95	-0.18	1.17	1.38	0.57
	N3 - N4	2.49	-14.28	-0.91	0.51	0.16	1.32
	P3 - P4	0.94	-3.84	-0.58	0.30	0.36	1.71
	P4 - N4	0.87	2.64	-0.79	1.00	0.11	0.79
30	Re1 $-$ As1	0.59	1.14	-0.38	0.48	0.76	1.07
	Re1 - P1	0.57	2.91	-0.35	0.66	0.23	0.83
	Re1 - P2	0.57	2.91	-0.35	0.66	0.23	0.83
	Re1 - N1	0.97	12.75	-0.39	1.22	0.25	1.14
	Re1 - N3	0.54	8.42	-0.17	1.15	1.56	0.55
	N3 - N4	2.53	-14.78	-0.93	0.52	0.16	1.34
	As1 - As2	0.77	-1.46	-0.53	0.40	0.27	1.70
	As2 - N4	0.79	4.03	-0.55	0.91	0.09	0.77

Appendix 8.3.22: Topological characteristics computed at the bond critical points (Atom numbering as in the XRD structures).
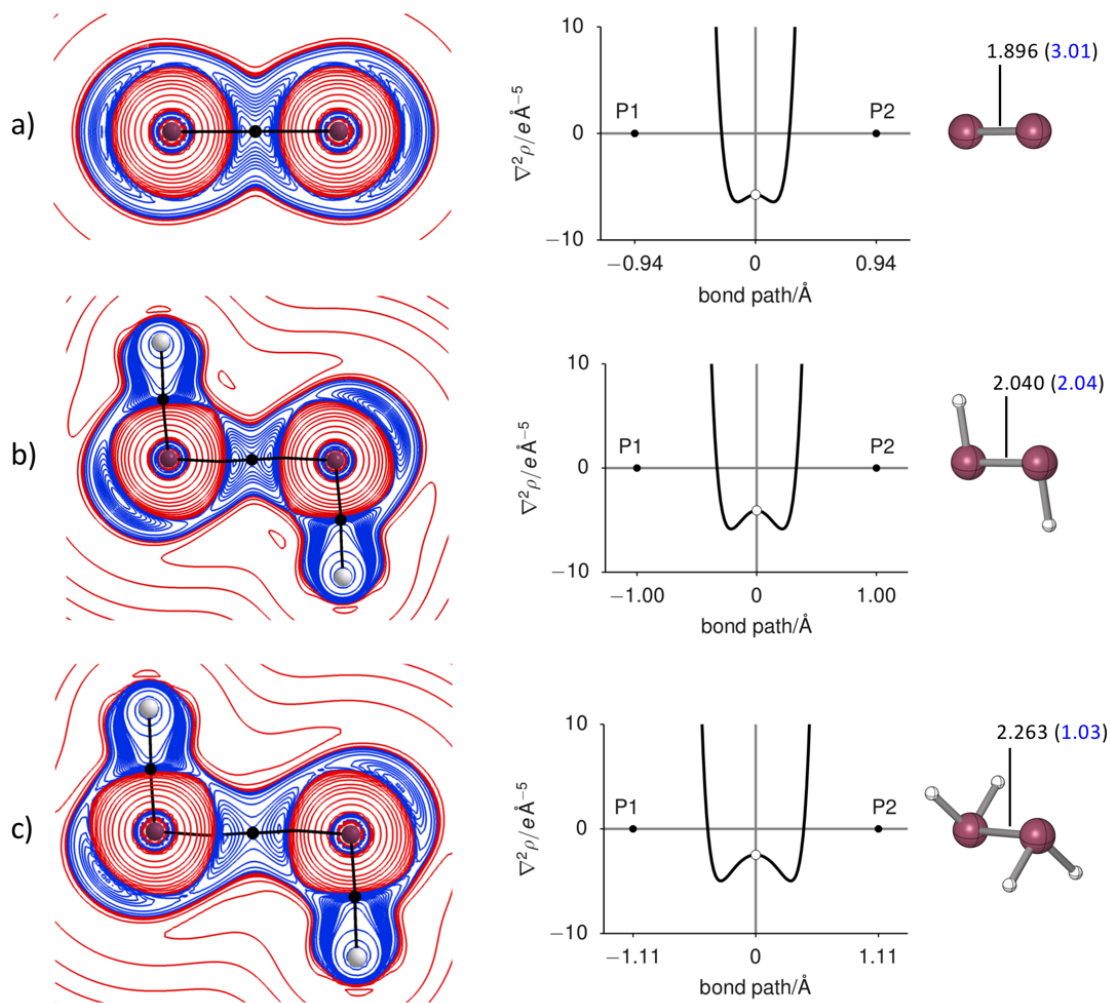
Appendix 8.3.23: Bonding analysis of P_2 (a), P_2H_2 (b) and P_2H_4 (c, ωB97XD/BS2//ωB97XD/BS1). Left: 2D plots of $\nabla^2\rho(r)$; charge concentration (blue) and depletion (red), bond paths (black lines), and bond critical points (black dots). Middle: 1D Laplacian profiles along the P–P bond paths. Right: P–P bond lenghts and Wiberg bond indices (in blue).

(37%) Re1–As1 (58%)

(49%) As1–As2 (48%)

(37%) As1–As2 (61%)

(95%) As1 sp$^{0.43}$

(99%) As2 sp$^{0.27}$

(18%) As2 − N4 (80%)
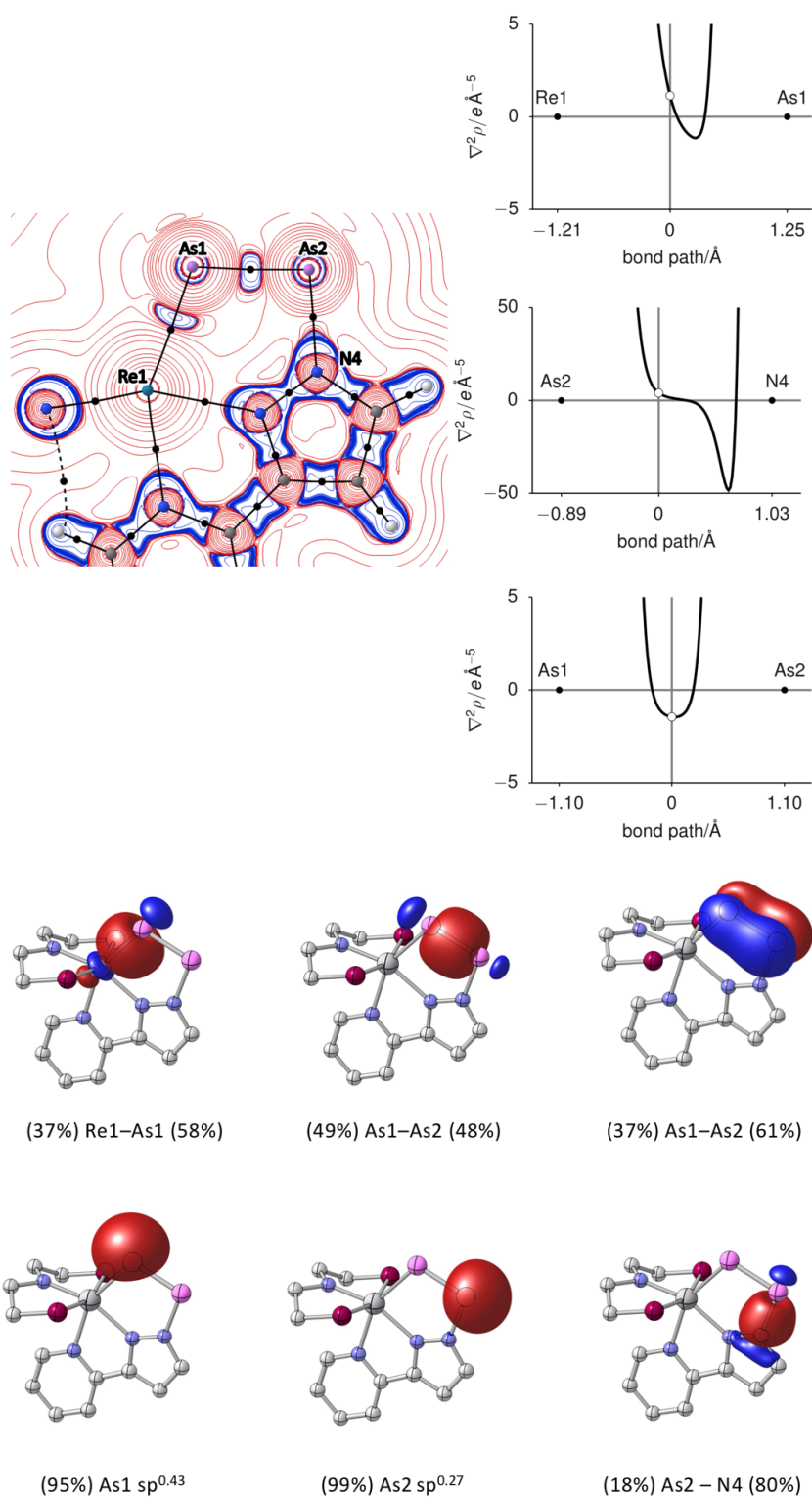
Appendix 8.3.24: Top: Bonding analysis of **30** (ωB97XD/BS2//ωB97XD/BS1). Left: 2D plots of $\nabla^2\rho(\mathrm{r})$; charge concentration (blue) and depletion (red), bond paths (black lines), and bond critical points (black dots). Right: 1D Laplacian profiles along the Re1–As1 (top), As1–As2 (middle) and As2–N4 (bottom) bond paths; Bottom: NLMOs representing the Re1–As1, As1=As2 and As2–N4 bonds and the two lone pairs at As1 and As2 (isosurfaces at $\pm 0.05\,\mathrm{a}_0^{3/2}$
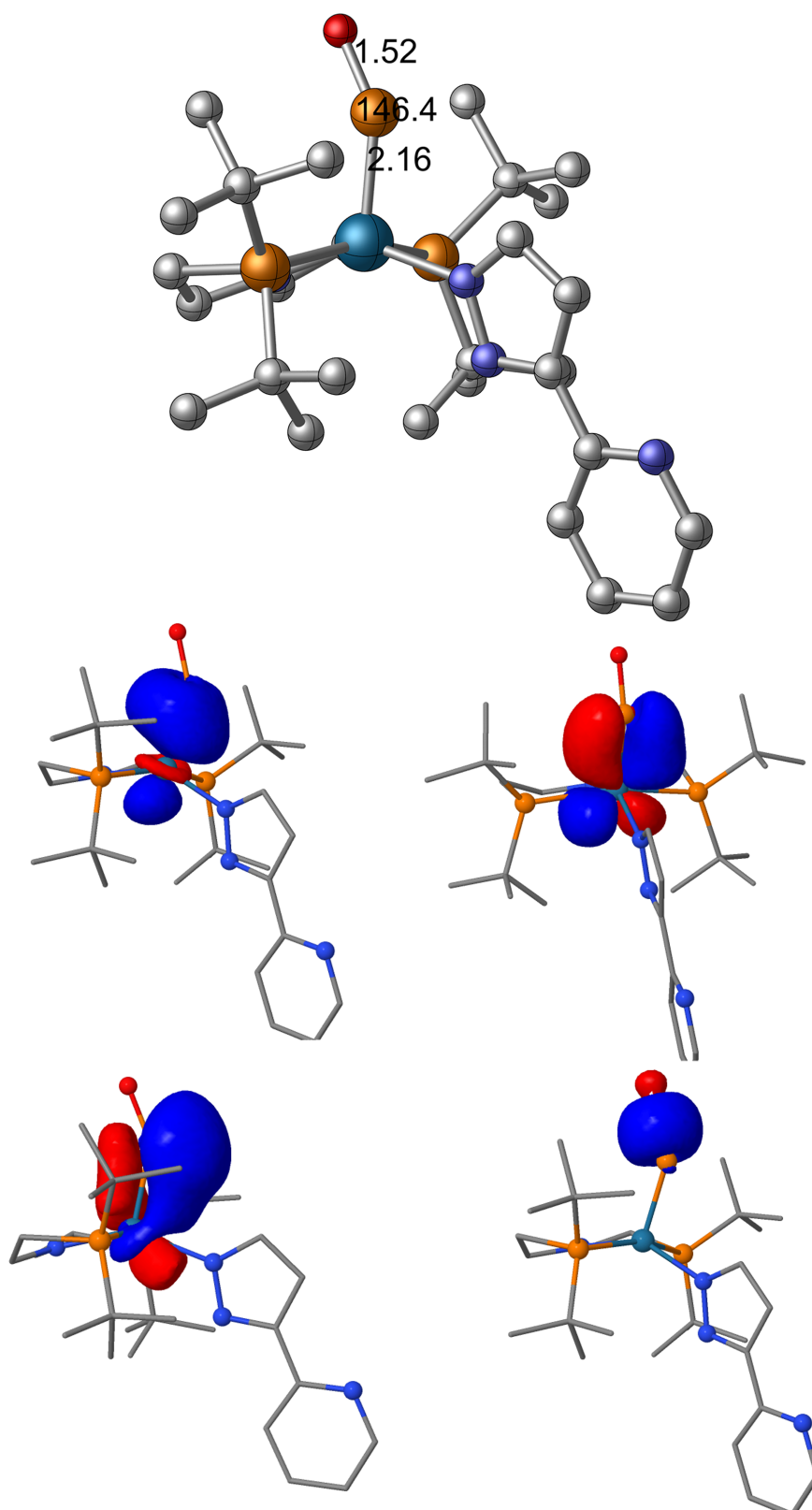
Appendix 8.3.25: Computed structure of **32** and the computed NBOs of the $^{+}$Re=P−O^{-} unit.
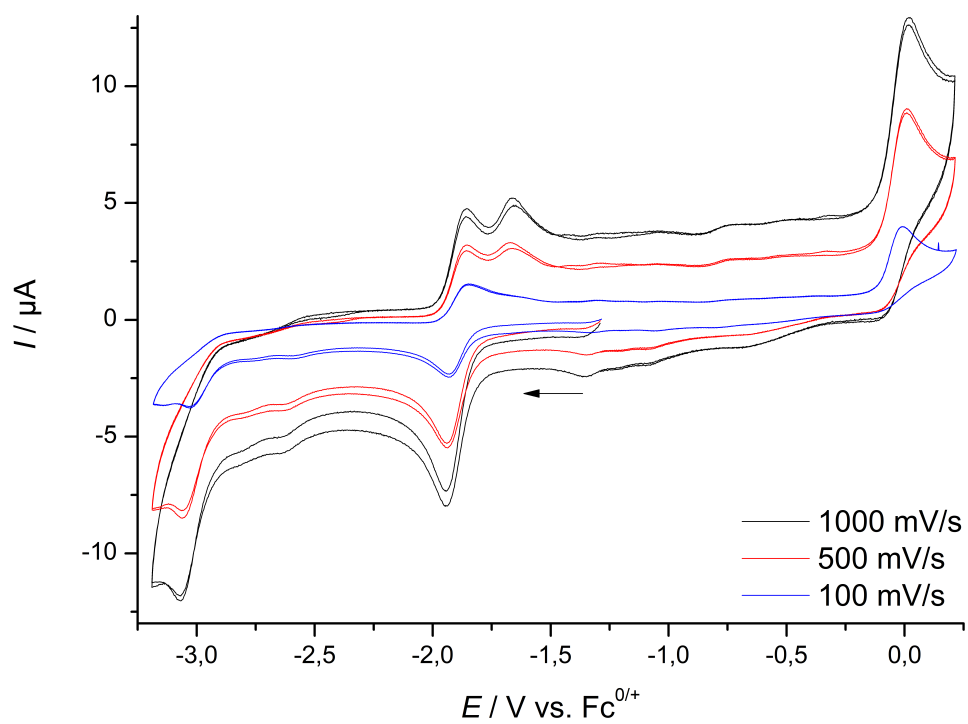
Appendix 8.3.26: Cyclic voltammogram of **31**, $0.7\,\text{mM}$, $0.1\,\text{M}$ NBu$_4$PH$_6$, 2 scans, THF, RT.
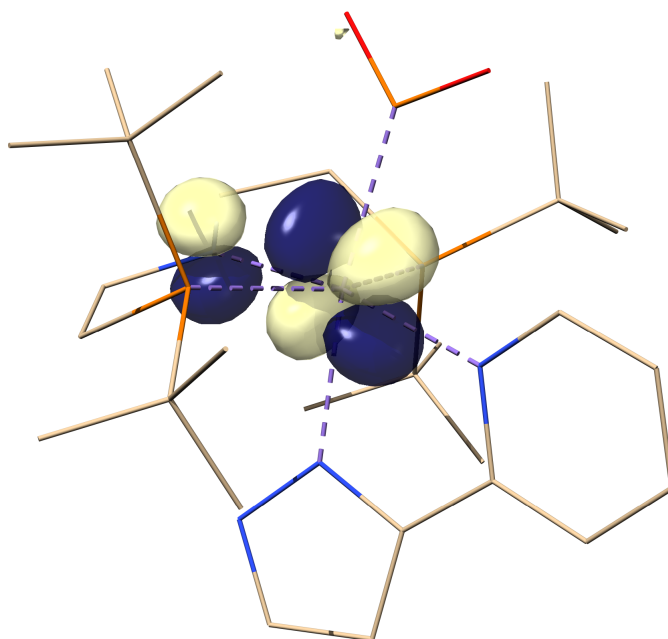
Appendix 8.3.27: Computed SOMO of **34**.
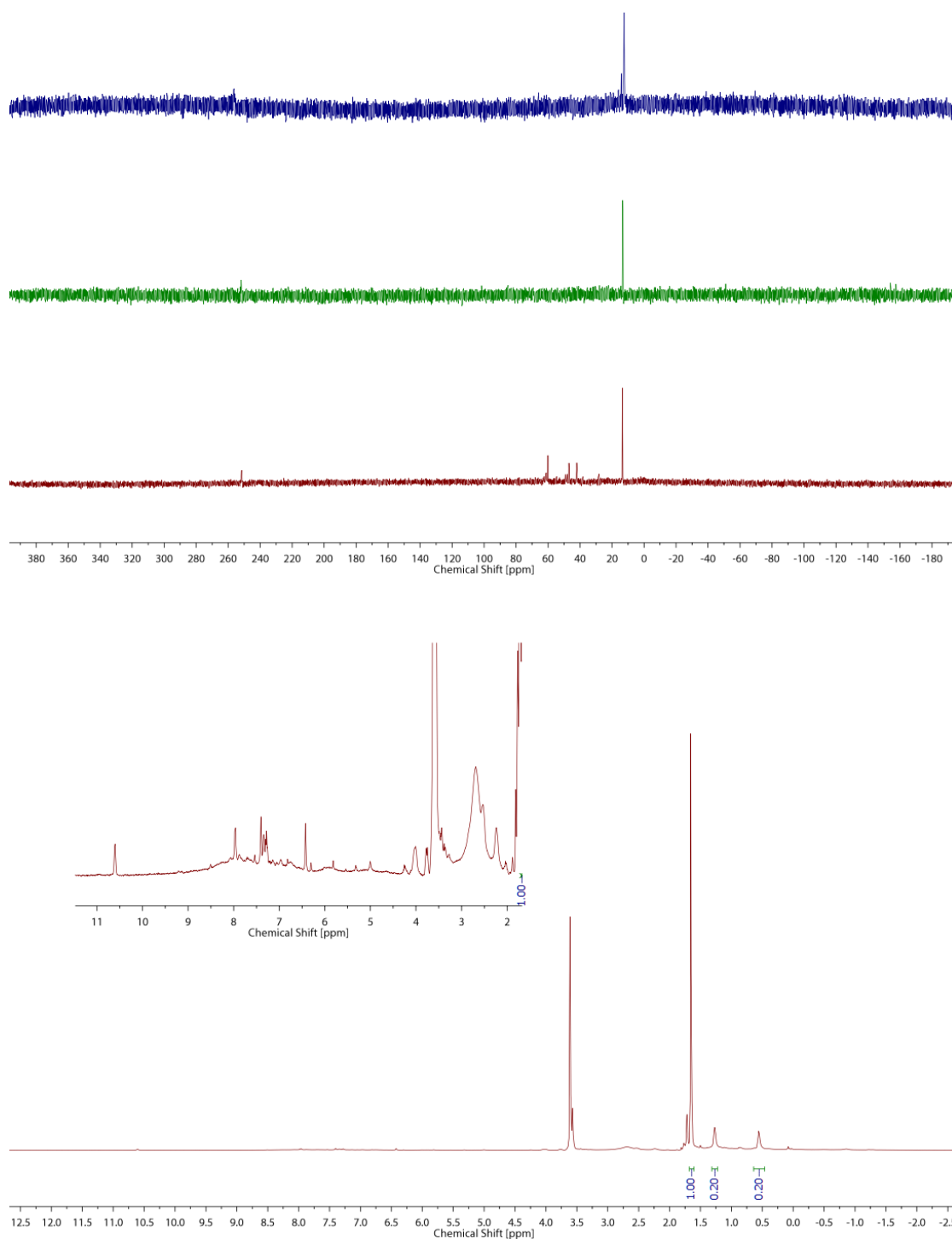
Appendix 8.3.28: Top: ^{31}P{^{1}H} NMR spectra of the oxidation of **34** with [Fe(C$_5$Me$_5$)$_2$][Al(O(C(CF$_3$)$_3$)$_4$], THF-d$_8$, -85°C (blue), 0°C (green), 25°C (red); Bottom: ^{1}H NMR spectrum of the oxidation of **34** with [Fe(C$_5$Me$_5$)$_2$][Al(O(C(CF$_3$)$_3$)$_4$], THF-d$_8$, 0°C.

E (eV)

(4.61)

- 0.91

- 2.05

- 2.37

- 4.36

- 4.40

- 4.90

-8.11
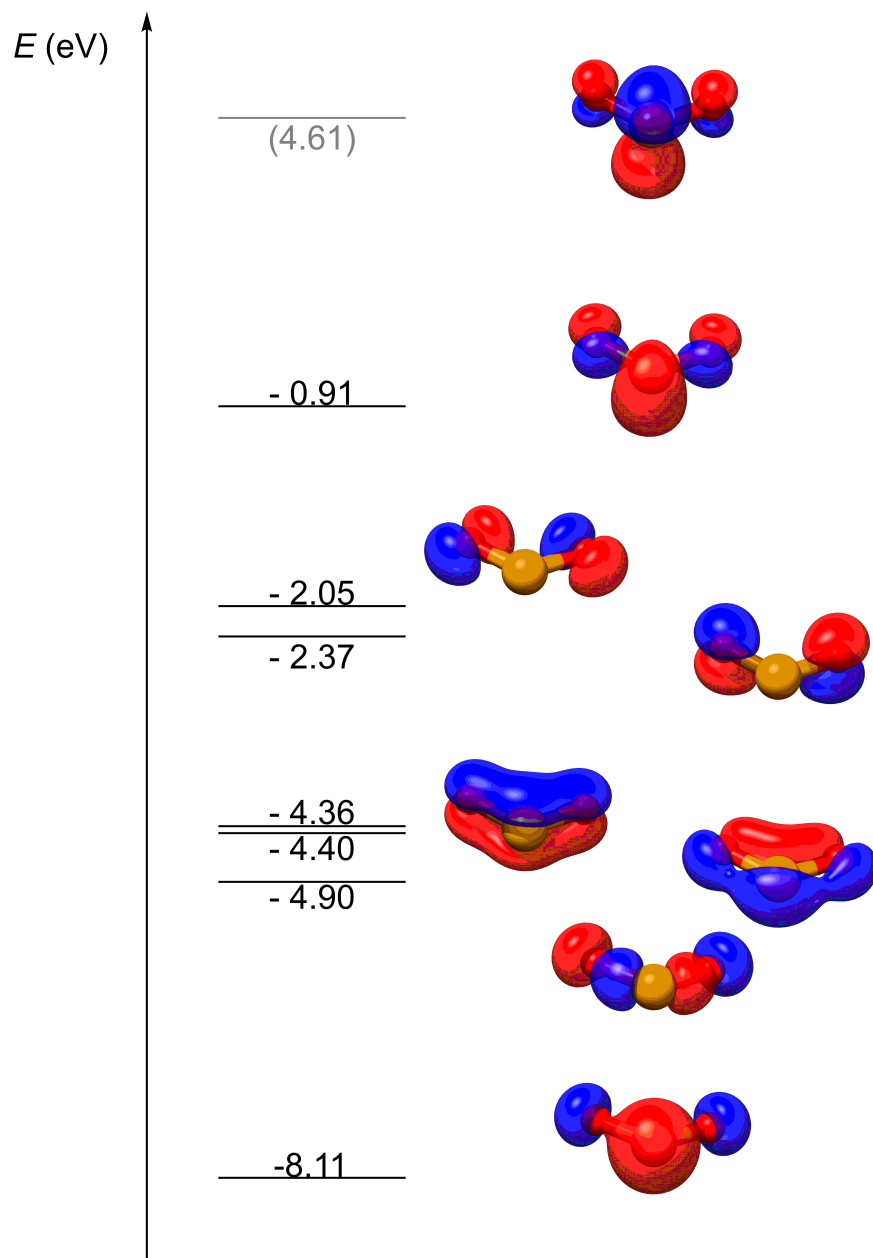
Appendix 8.3.29: Molecular orbital diagram of free PO_2^-, unoccupied orbitals in grey.
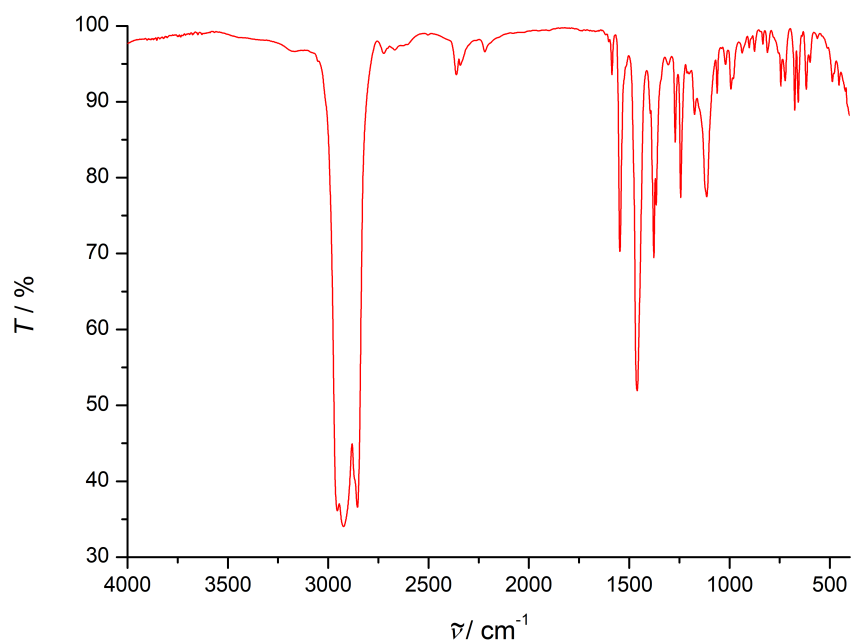
Appendix 8.3.30: IR spectrum of **37**, Nujol, RT.
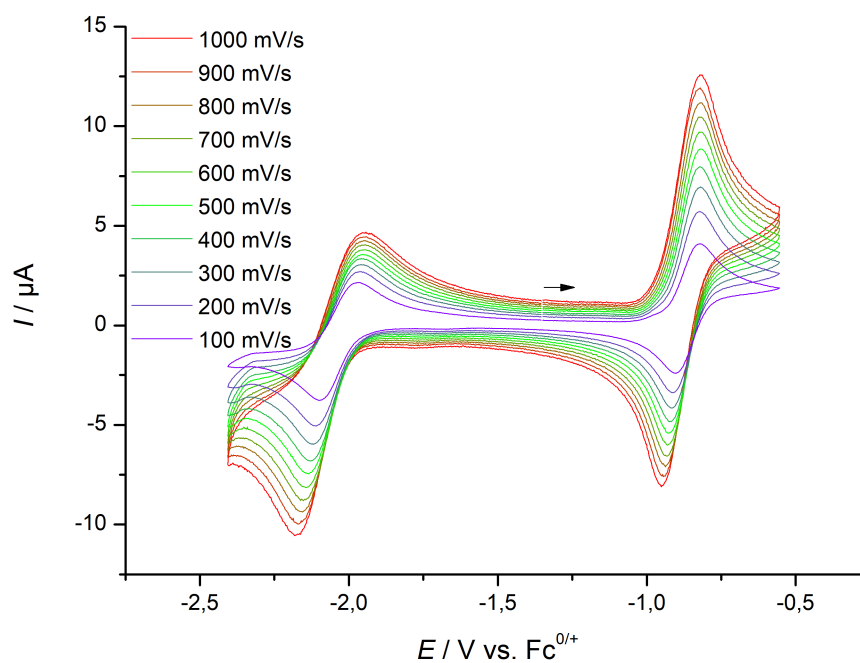
Appendix 8.3.31: Cyclovoltammogram of **38**, 2nd scan, $1\,\text{mM}$, $0.1\,\text{M}$ NBu_4PF_6, THF, RT.
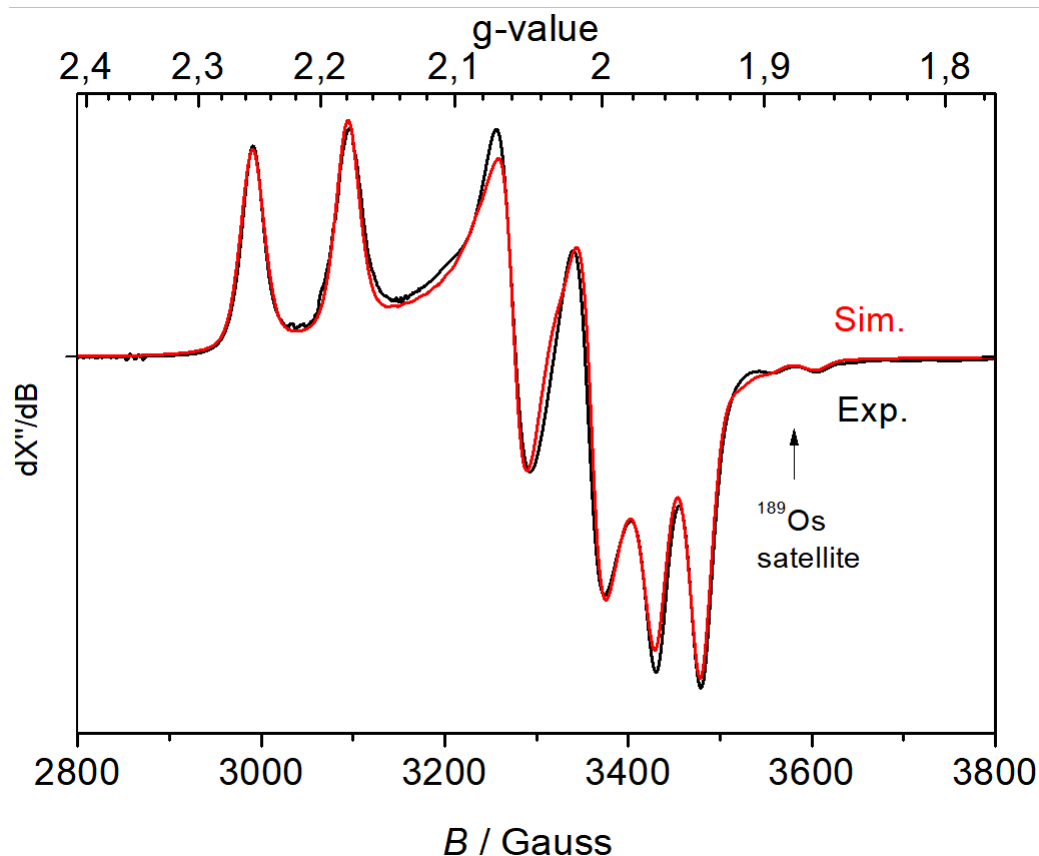
Appendix 8.3.32: EPR spectrum of complex **38**, toluene, 148 K, 9.436620 GHz, simulation assuming coaxial g- and ^{31}P A-tensors (blue): g_{11} = 2.215, g_{22} = 2.032, g_{33} = 1.951, $A_{11}(^{31}$P) = 322 MHz, $A_{22}(^{31}$P) = 243 MHz, $A_{33}(^{31}$P) = 136 MHz, $A_{11}(^{189}$Os) = 230 MHz, $A_{22}(^{189}$Os) and $A_{33}(^{189}$Os) not resolved. The spectrum reveals fully resolved ^{31}P hyperfine interactions (HFI) and partially resolved ^{189}Os (16% natural abundance) HFI satellites. Simulation of the spectrum assuming coaxial g and ^{31}P hyperfine A-tensors (W95EPR) yields ^{31}P hyperfine values that deviate largely from the DFT calculated ones.

However, closer inspection of the DFT calculated EPR parameters reveals that the g-tensor of complex **38** is strongly tilted with respect to the molecular symmetry axes. This is most likely caused by predominant spin-orbit coupling involving the SOMO and HOMO of **38** along these g-tensor axes.
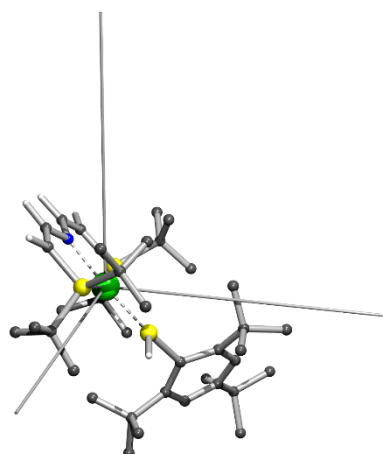
Appendix 8.3.33: Electronic g-tensor directions of **38** which are strongly tilted with respect to the molecular axis.

In contrast, the ^{31}P hyperfine A-tensor is closely aligned with the molecular symmetry axes. In combination with the abovementioned strongly tilted g-tensor directions with respect to the molecular symmetry axes, the g- and A-tensors of complex **38** are not coaxial, with large DFT computed Euler angles of $\alpha = -74.3°$, $\beta = +142.7°$, $\gamma = -7.5°$.
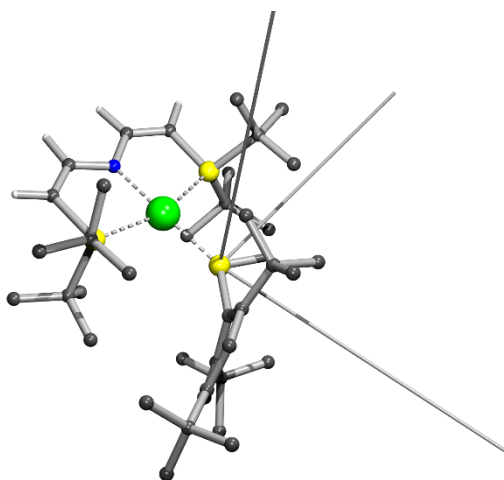
Appendix 8.3.34: HFI A-tensor of **38** which follows the molecular axis.

Similarly, the ^{189}Os hyperfine interaction (HFI) tensor (16% natural abundance; HFI tensor roughly aligned along the symmetry axes of the molecule) is rotated with respect to the electronic g-tensor, with computed Euler angles of $\alpha = +90.5°$, $\beta = +51.7°$, $\gamma = +106.5°$. It is therefore clear that the experimental spectrum needs to be simulated using non-coaxial g- and A-tensors, the thus obtained simulation provides an excellent fit with g- and A-tensor values and Euler angles that closely match the DFT calculated EPR parameters.
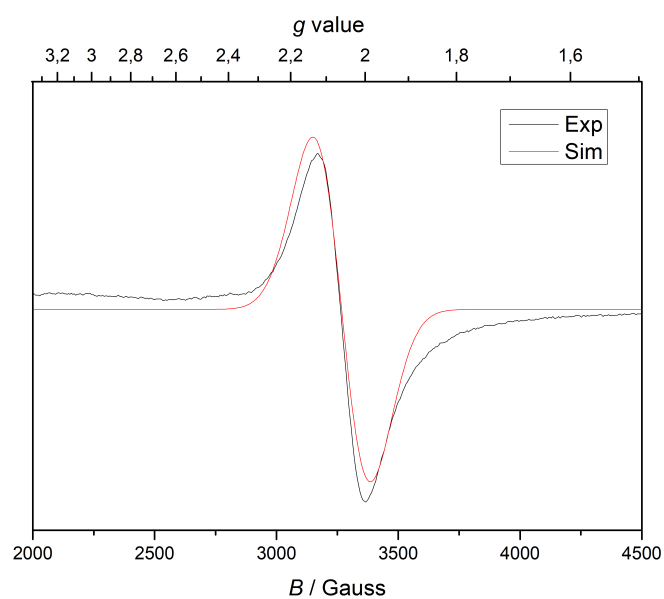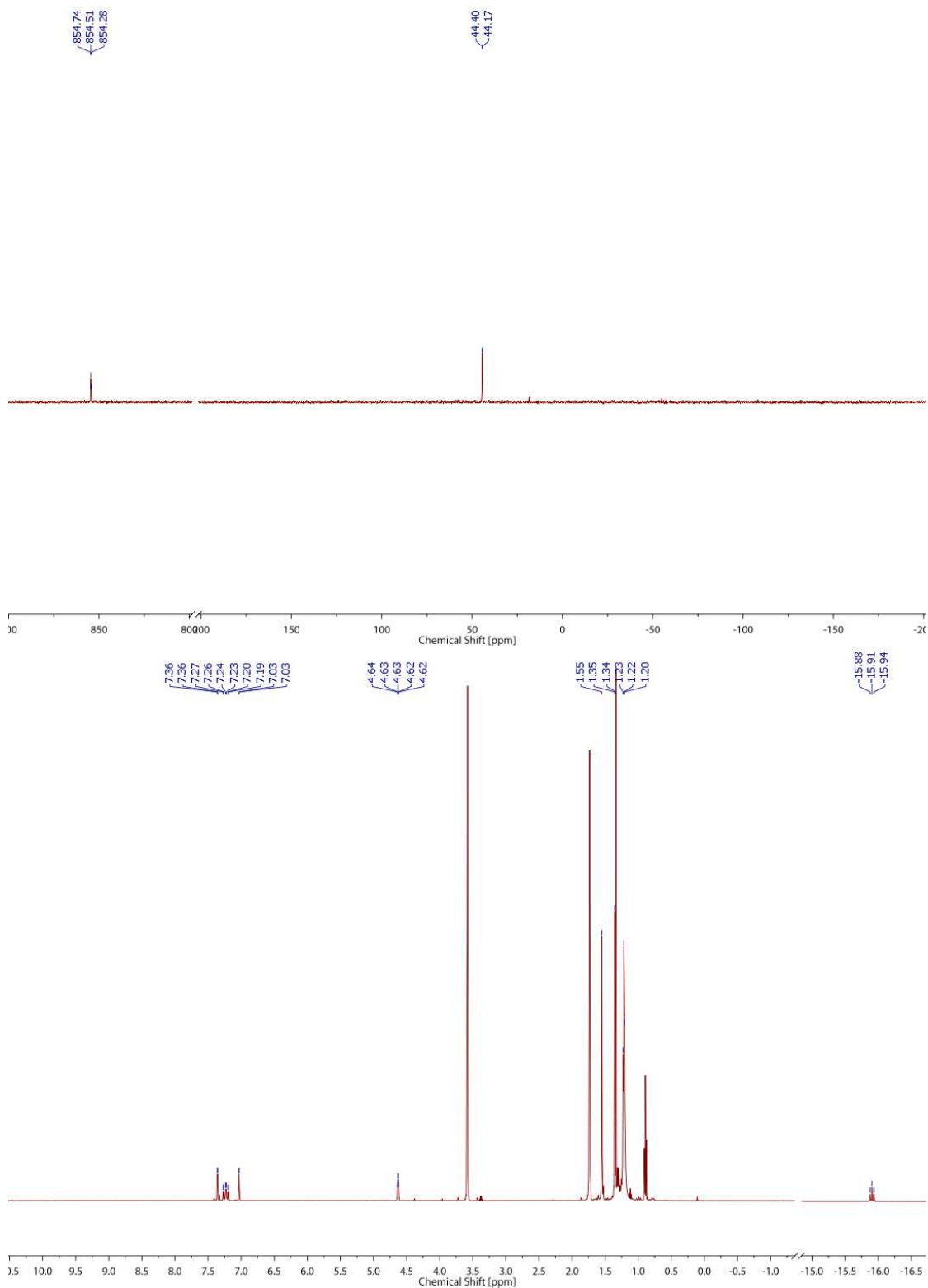
Appendix 8.3.35: EPR spectrum of **38** (black), toluene, 293 K, 9.4262 GHz, simulation (red) using parameters $g_{iso} = 2.0611$.
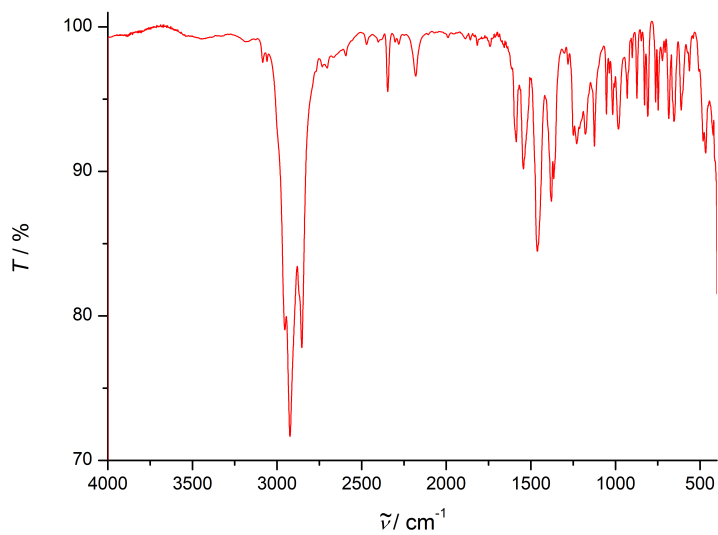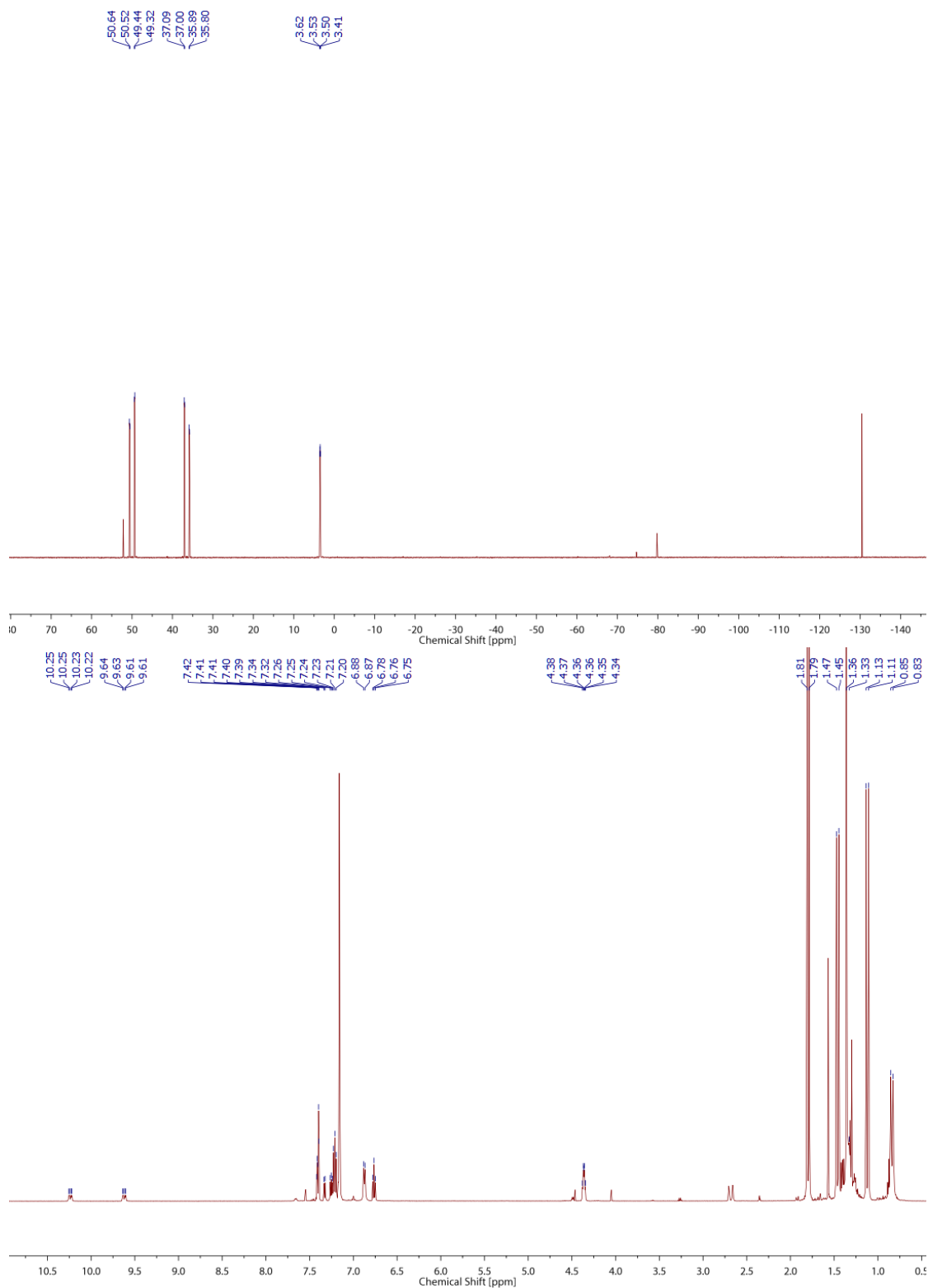

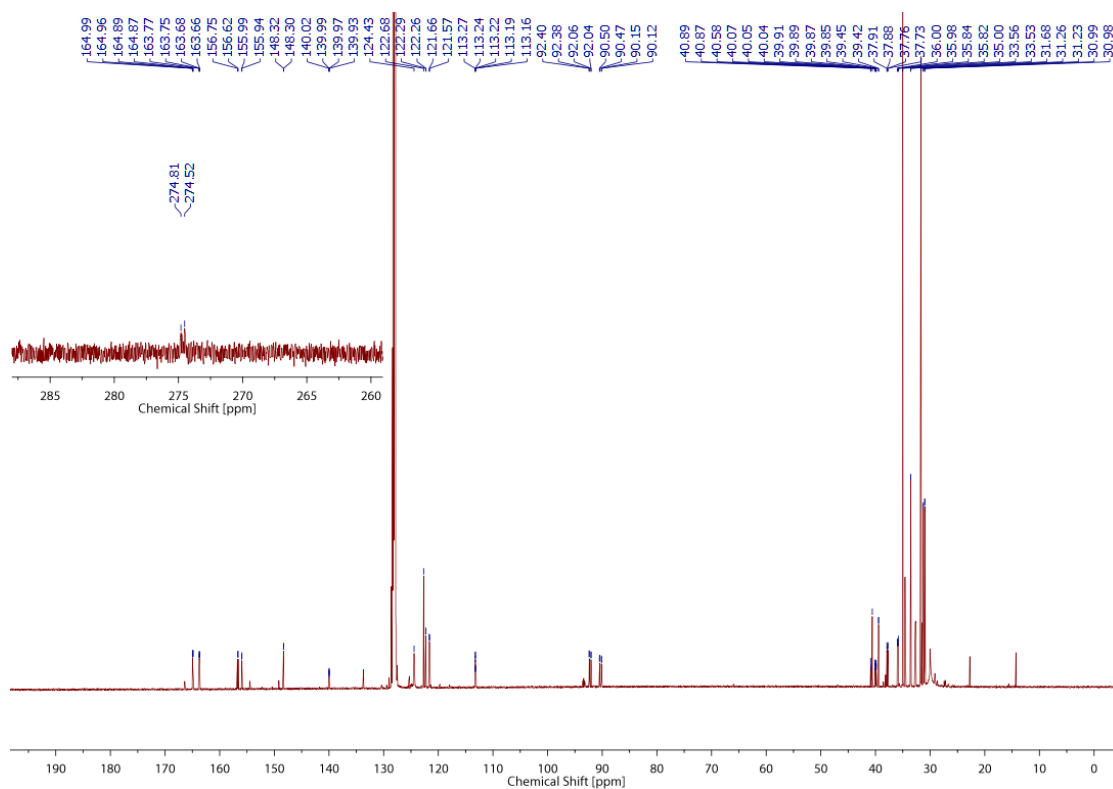**Appendix 8.3.36:** IR spectrum of **38**, Nujol, RT.
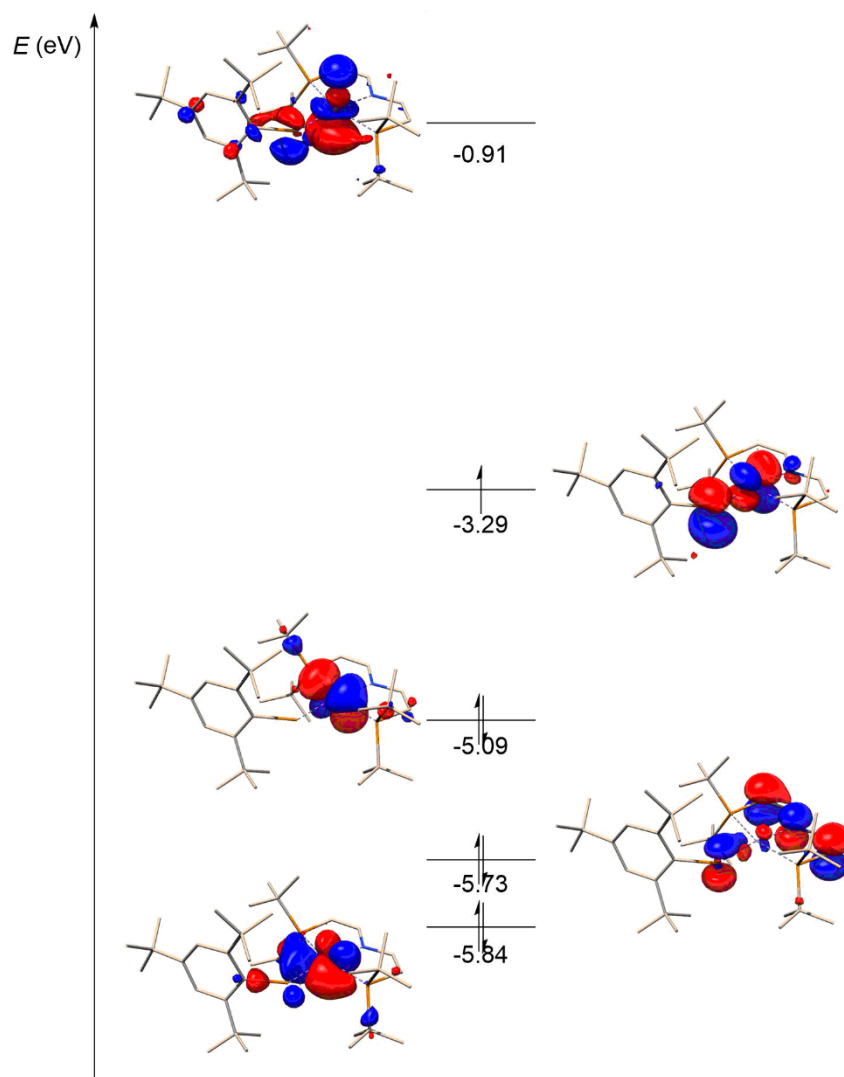
Appendix 8.3.37: Frontier molecular orbital scheme (quasi-restricted orbitals) of **38** (D3BJ-PBE0-RIJCOSX/def2-TZVP//D3BJ-PBE-RI/def2-SVP).
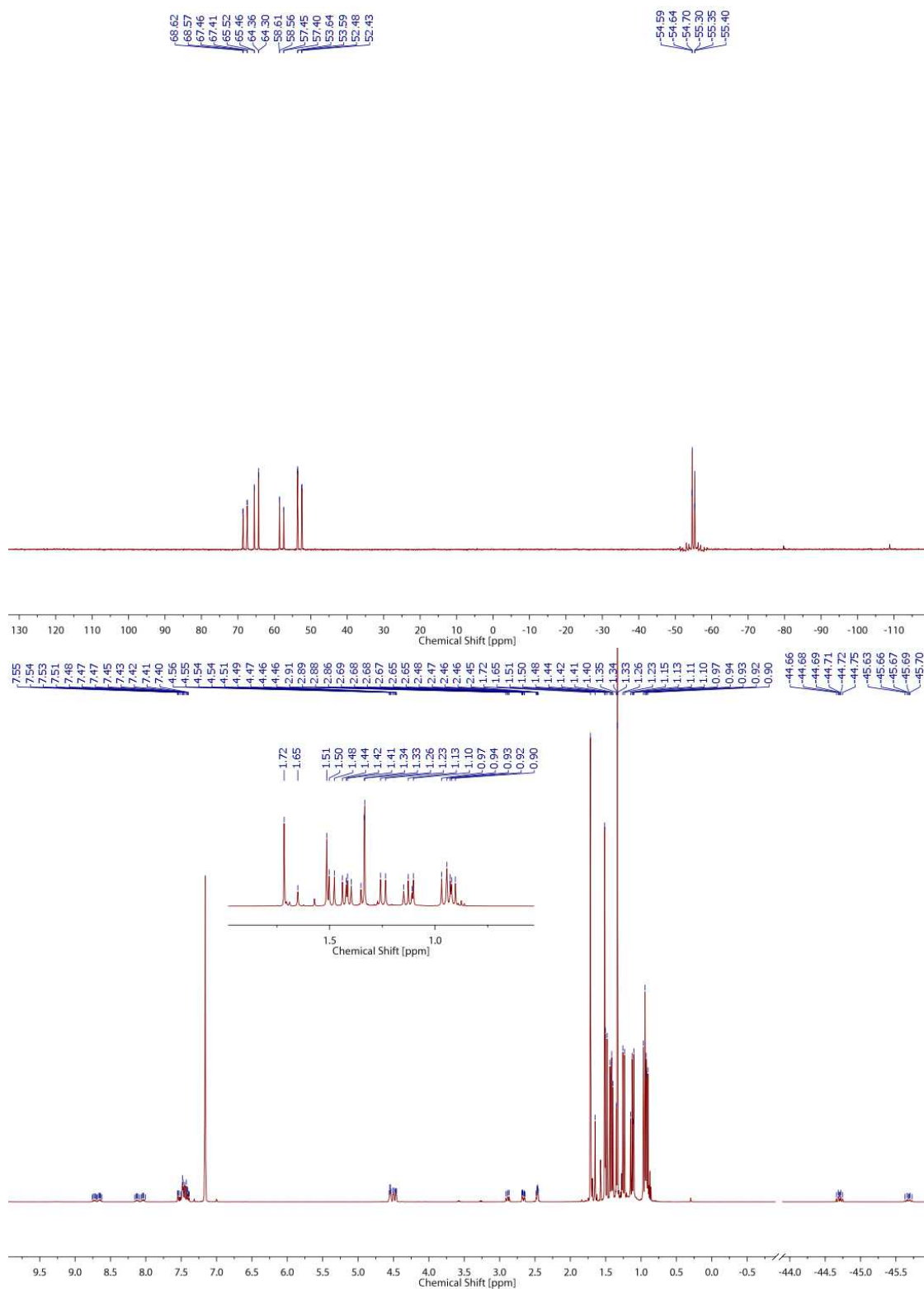
Appendix 8.3.38: Top: $^{31}P\{^1H\}$ NMR spectrum of **39**, THF-d$_8$, $-30°$C; Bottom: ^{1}H NMR spectrum of **39**, THF-d$_8$, $-30°$C.

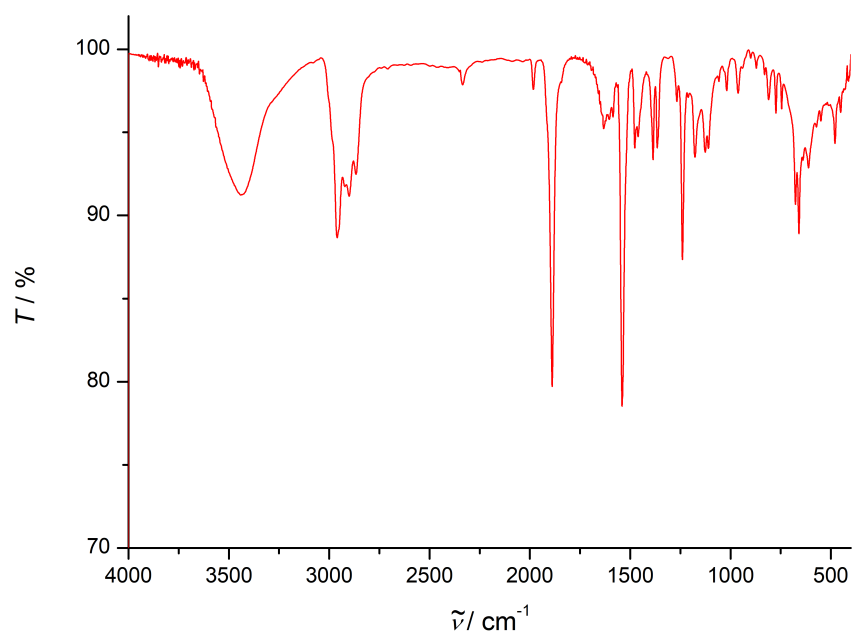*Appendix 8.3.39:* Top: $^{31}P\{^1H\}$ NMR spectrum of **42**, C_6D_6, RT; Bottom: ^1H NMR spectrum of **42**, C_6D_6, RT.
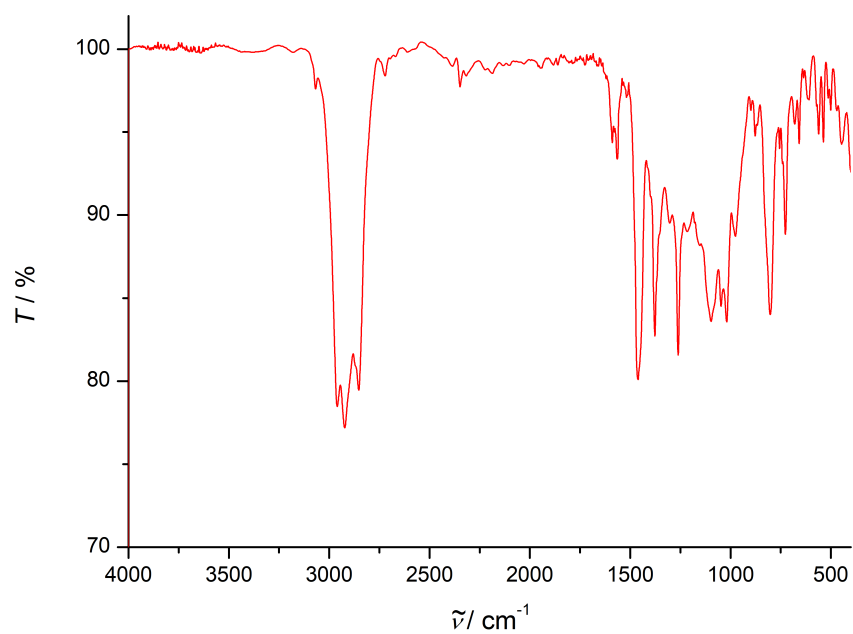
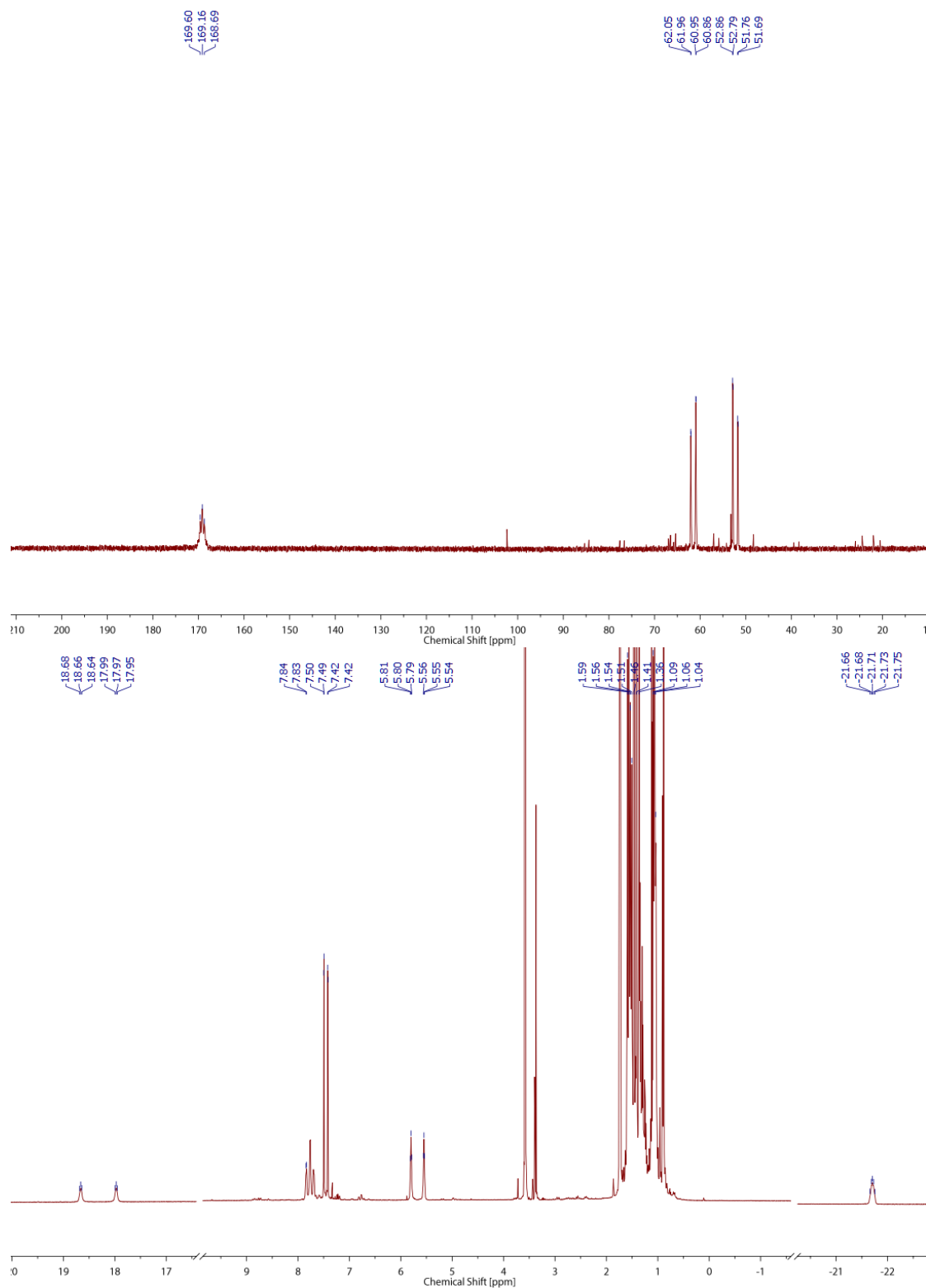***Appendix 8.3.40:*** ^{13}C{^{1}H} NMR spectrum of **42**, C$_6$D$_6$, RT.

Appendix 8.3.41: Top: $^{31}P\{^1H\}$ NMR spectrum of **40**, C_6D_6, RT; Bottom: ^1H NMR spectrum of **40**, C_6D_6, RT.
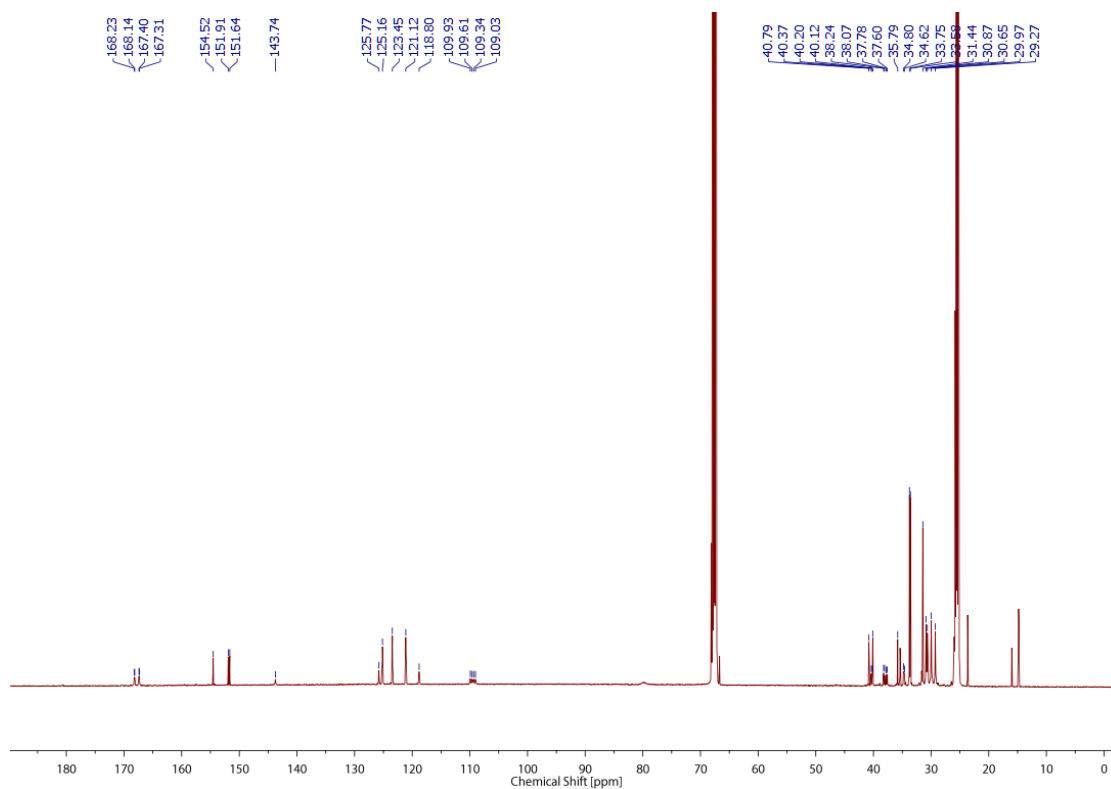
Appendix 8.3.42: IR spectrum of **38**, KBr, RT.

Appendix 8.3.43: IR spectrum of **43**, Nujol, RT.

Appendix 8.3.44: Top: ^{31}P{^{1}H} NMR spectrum of **43**, THF-d$_8$, −30°C; Bottom: ^{1}H NMR spectrum of **43**, THF-d$_8$, −30°C.
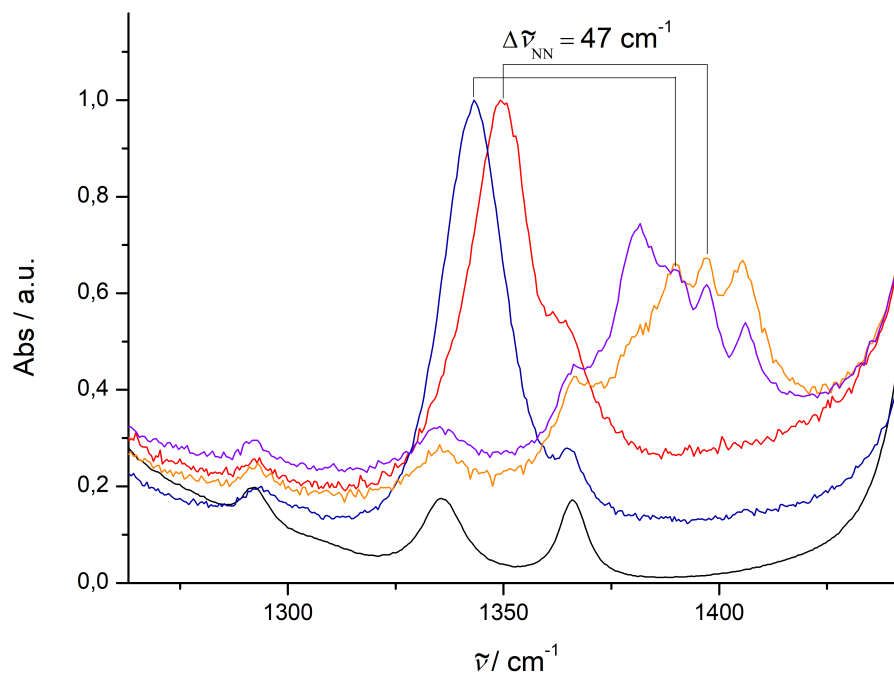
Appendix 8.3.45: ^{13}C{^{1}H} NMR spectrum of **43**, THF-d$_8$, $-30°$C.

8.4 Proton-Induced Splitting of Dinitrogen by Dimeric Mo PNP Pincer Complexes
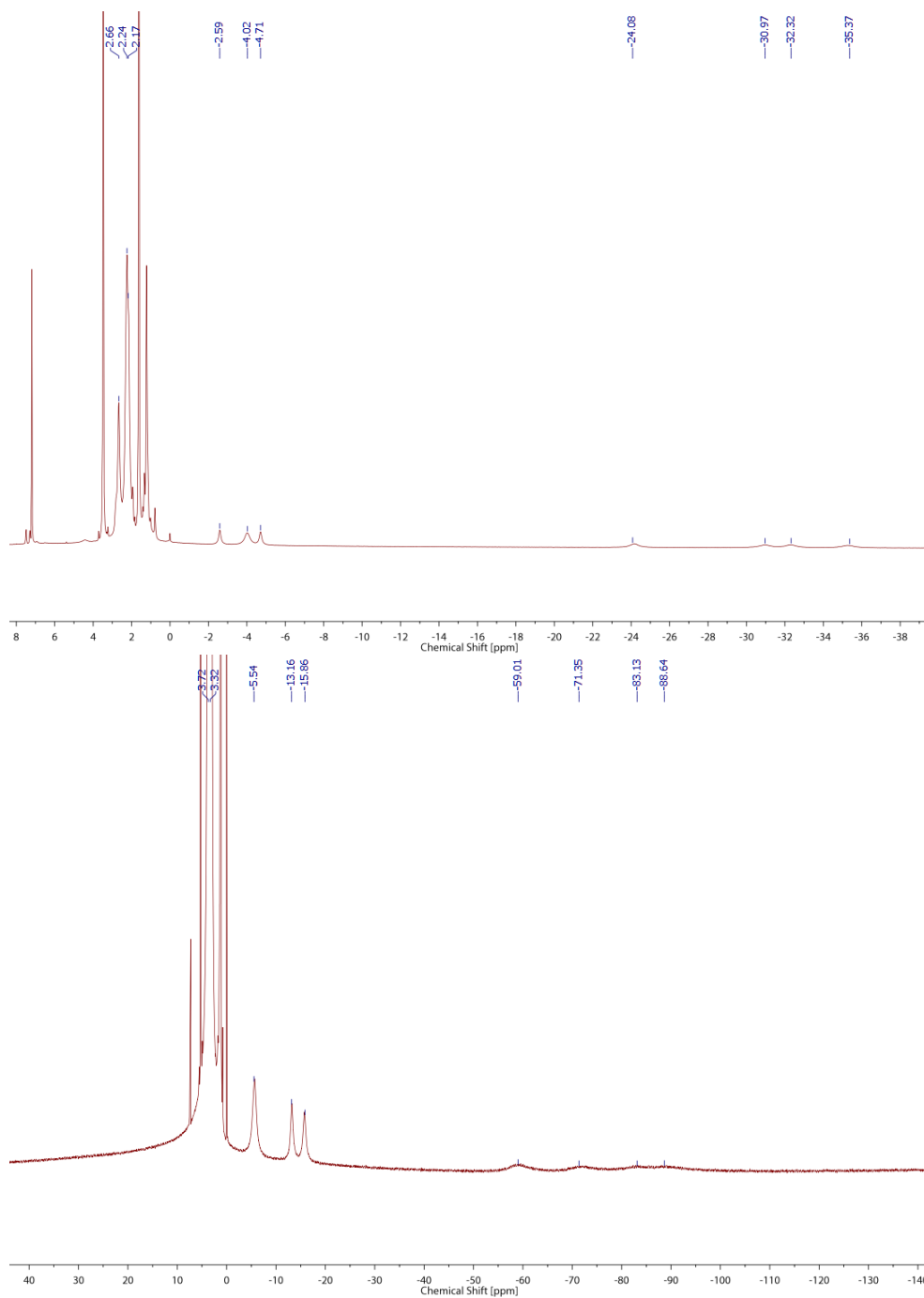
Appendix 8.4.1: Top: ^{1}H NMR spectrum of **48**, THF-d$_8$, RT; Bottom: ^{1}H NMR spectrum of **49**, CD$_2$Cl$_2$, RT.

Appendix 8.4.2: rRaman spectra of **48** (orange), **48-^{15}N$_2$** (red),**49** (purple), **49-^{15}N$_2$** (purple), THF (black), 100 K, $\lambda_{\text{ex}} = 514$ nm.
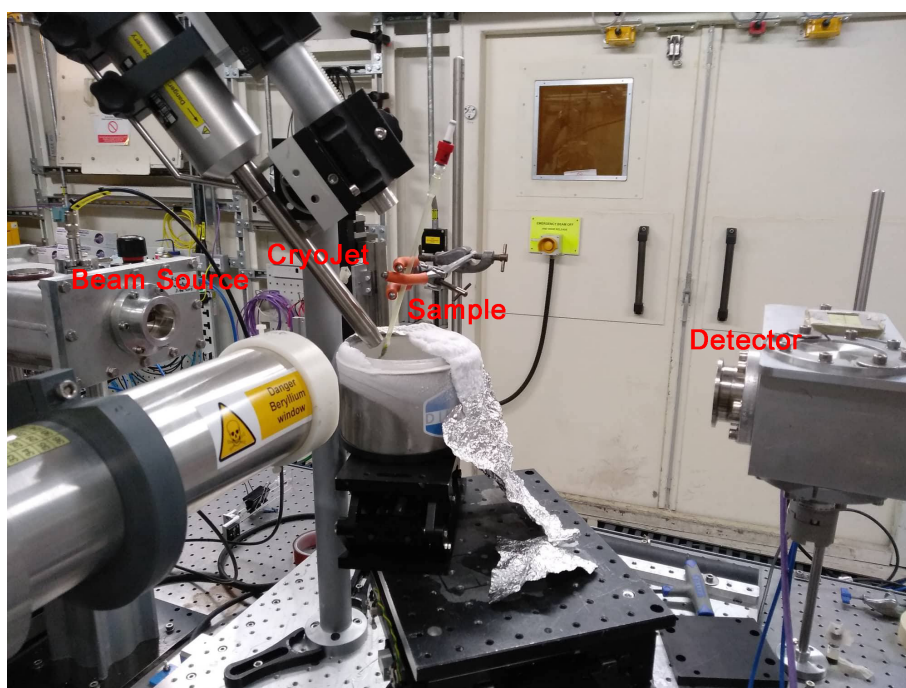
Appendix 8.4.3: Experimental setup of the XAS measurement performed at the B18 Beamline (Diamond Light Source). The sample is partly emerged in liquid nitrogen and additionally cooled by a CryoJet keeping the solution near $-100°$C. The measurements were perfomed in transmission mode.
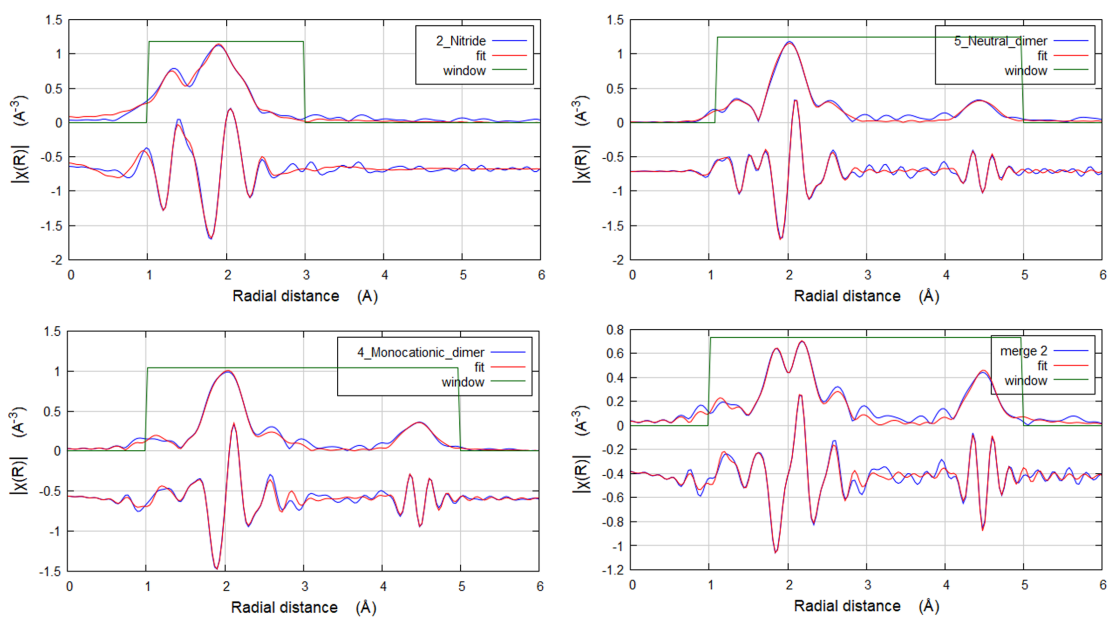
Appendix 8.4.4: Mo-K Edge EXAFS spectra **XCIX**, **XCVII**, **48** and **49**, R space.

Table 8.2: Structural parameters of **XCIX**, **XCVII**, **48**, **49** and **XCVIII** derived by EXAFS spectroscopy, [a]: For **XCIX** the nitride bond length is given.

Complex	Mo-N$_{PNP}$	Mo-N$_2$[a]	Mo-P	Mo-Cl	Mo-Mo	N-N	Mo-C
XCIX	2.11(3)	1.62(1)	2.54(3)	2.37(1)			
XCVII	1.99(2)	1.80(1)	2.50(2)	2.44(2)	4.74(2)	1.27(4)	3.11(3)
48	1.99(2)	1.82(3)	2.50(2)	2.41(2)	4.74(1)	1.22(4)	3.00(8)
49	1.92(4)	1.80(4)	2.55(1)	2.37(1)	4.74(8)	1.20(1)	2.99(1)
XCVIII	2.30(9)	1.87(2)	2.60(8)	2.48(6)	5.17(3)	n.a.	n.a.

Table 8.3: Experimental and computational structural parameters of **XCVII**, **48** and **49** in solution derived by Mo-K edge EXAFS spectroscopy and single crystal X-Ray diffraciton in Å, THF, 100°C.[280]

	Mo-N$_{PNP}$			Mo-N$_2$			Mo-Mo		
	XRD	XAS	DFT	XRD	XAS	DFT	XRD	XAS	DFT
XCVII	1.917(7)	1.99(2)	2.05	1.799(49	1.80(1)	1.84	4.846(1)	4.74(2)	4.93
48	1.974(4) 1.974(4)	1.99(2)	1.97 1.99	1.825(4) 1.804(4)	1.82(3)	1.81 1.77	4.846(1)	4.74(1)	4.81
49	1.958(8) 1.963(8)	1.99(2)	1.97 1.97	1.803(8) 1.810(8)	1.82(3)	1.79 1.79	4.847(2)	4.74(8)	4.80
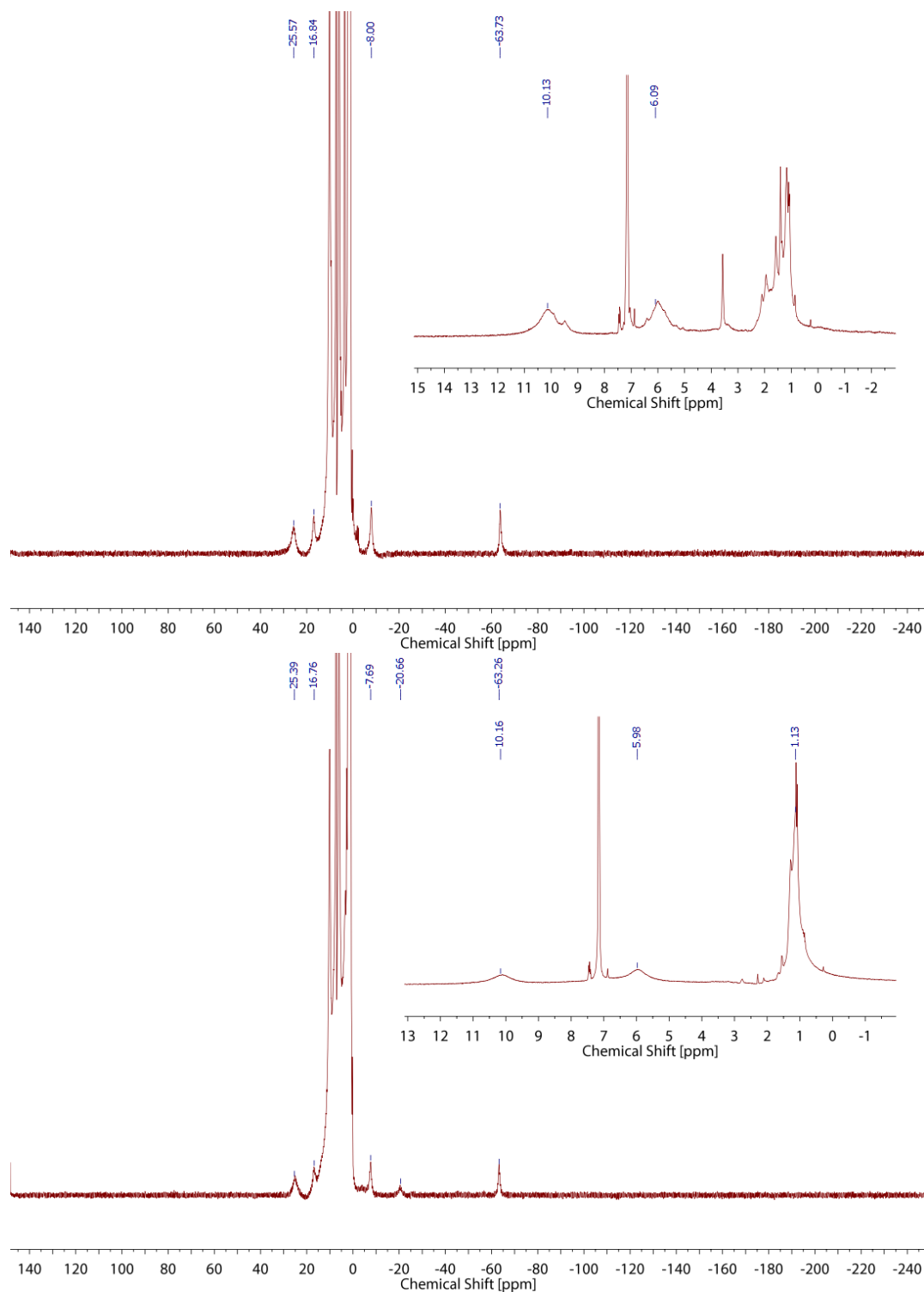
Appendix 8.4.5: Top: ^{1}H NMR spectrum of the attempted complexation of $[MoCl_3(thf)_3]$ by ^{Me}L, DCM/THF 1:2 as solvents, C_6D_6, RT; Bottom: ^{1}H NMR spectrum of the attempted complexation of $[MoCl_3(thf)_3]$ by ^{Me}L, PhCl as solvent, C_6D_6, RT.
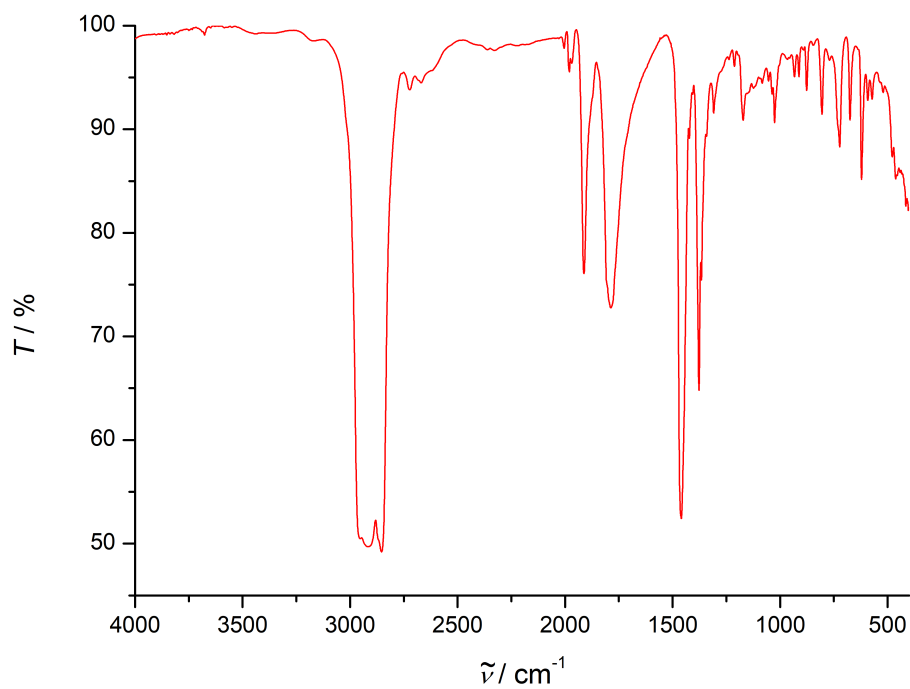
Appendix 8.4.6: IR spectrum of **51**, ATR, RT.
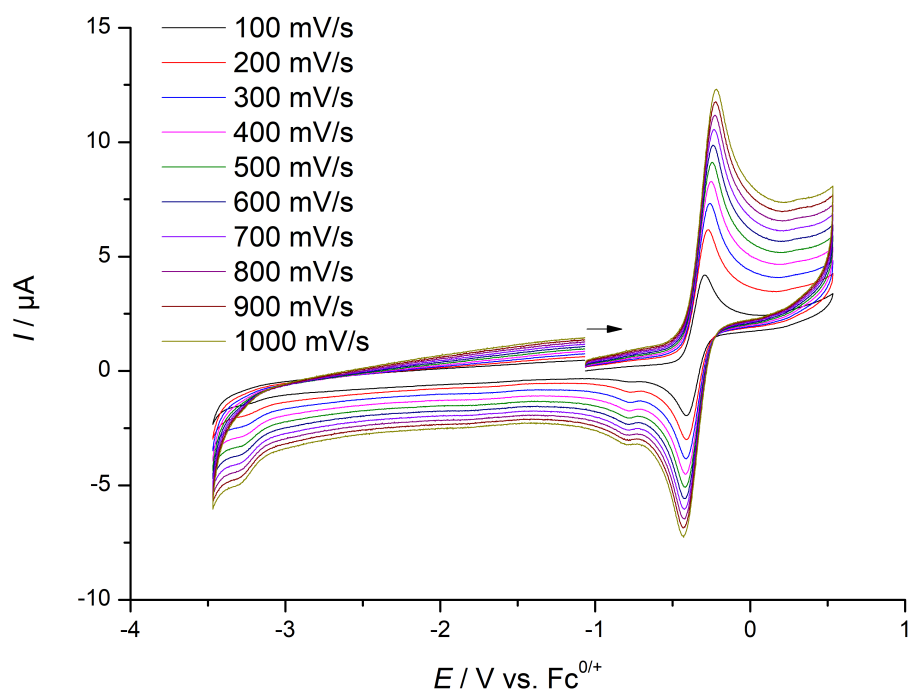
Appendix 8.4.7: Cyclic voltammetry of **51**, 1 mM, 0.1 M NBu$_4$PF$_6$, THF, RT.

Used Abbreviations

9   Used Abbreviations

a.u.	Atomic units / arbitrary units
ATP	Adenosine triphosphate
bipy	2,2'-Bipyridine
BD(F)E	Bond dissociation (free) energy
CAAC	Cyclic alkyl amino carbenes
CASSCF	Complete active space self constistent field
ClP**A**	chloro-substituted dibenzo-7λ^3-phosphanorbornadiene
COSY	Correlated spectroscopy
Cp	Cyclopentadienyl-
Cys	Cysteine
δ	Chemical shift
DCM	CH_2Cl_2
DFT	Density functional theory
Dipp	2,6-^{i}Pr$_2$C$_6$H$_3$
diox	1,4-Dioxane
DMAD	Acetylenedicarboxylate
EDA	Energy decomposition analysis
ESI	Electron spray ionisation
EPR	Electron paramagnetic resonance
$E_{1/2}$	Half-cell potential
$E_{\text{p.a.}}$	Anodic peak current
$E_{\text{p.c.}}$	Cathodic peak current
EXAFS	Extended X-ray absorption fine structure
Fc / FeCp / [FeCp]	Ferrocene, [Fe(C$_5$H$_5$)$_2$]
FT-ICR	Fourier-transform ion cyclotron resonance mass spectrometry
GB	Gray-Ballhausen
GVB	Generalized valence bond
HAT	Hydrogen atom transfer
HFI	Hyperfine interaction
His	Histidin
HMBC	Heteronuclear multiple bond correlation
HOMO	Highest occupied molecular orbital
$^{\text{H}}$PyrPz	3-(1H-pyrazol-3-yl)-pyridine
HSQC	Heteronuclear single quantum coherence
^{i}Pr	iso-propyl
ITC	Isothermal titration calorimetry
K_{a}	Acid dissociation constant
LIFDI	Liquid injection field desorption ionization
LUMO	Lowest unoccupied molecular orbital
L^1	N(CH$_2$CH$_2$P^{t}Bu$_2$)$_2$
$^{\text{H}}$L^1	HN(CH$_2$CH$_2$P^{t}Bu$_2$)$_2$
$^{\text{Me}}$L^1	(Me)N(CH$_2$CH$_2$P^{t}Bu$_2$)$_2$
L^2	N(CH$_2$CH$_2$P^{t}Bu$_2$)(CHCHP^{t}Bu$_2$)

L^3	$N(CHCHP^tBu_2)_2$
L^{Si}	$N(SiMe_2CH_2P^tBu_2)_2$
L^{SiO}	$O(SiMe_2CH_2P^tBu_2)_2$
μ_B	Bohr magneton
μ_{eff}	Effective magnetic moment
Me	Methyl
Mes	$2,4,6\text{-}Me_3C_6H_2$
Mes*	$2,4,6\text{-}^tBu_3C_6H_2$
Mes*O	$2,4,6\text{-}^tBu_3C_6H_2O$
MO	Molecular orbital
MS	Mass spectrometry
NBO	Natural bonding orbital
NEVPT	N-electron valence state perturbation theory
NHC	N-heterocyclic carbene
NMR	Nuclear magnetic resonance
NPA	Natural population analysis
OTf	Triflate
PBE(0)	Perdew–Burke-Ernzerhof
PCET	Proton coupled electron transfer
PDI	Pyridinediimine
Ph	Phenyl
^{Ph}Tpy	4'-phenyl-2,2':6',2"-terpyridine
PI	Paramagnetic impurity
pK_a	$-log10(K_a)$
ppm	Parts per million
Pyr	Pyridine
$^{H}PyrPz$	3-(1H-pyrazol-3-yl)-pyridine
QDPT	Quasi-degenerate pertubation theory
rRaman	Resonance Raman
RT / r.t.	Room temperature
SOC	Spin-orbit coupling
SOMO	Singly occupied molecular orbital
SQUID	Superconducting quantum interference device
SVP	Split valence polarization
THF	Tetrahydrofurane
TBA	*Tetra*-butyl ammonium
^tBu	*tert*-butyl
TEMPO	2,2,6,6-Tetramethylpiperidinyloxyl
TIP	Temperature independent paramagnetism
Tpy	Terpyridine
TZVP	Triple ζ valence plus polarization
vs.	versus
WBI	Wiberg bond index
XAS	X-ray absorption
ZORA	Zeroth order regular approximation

References

References

[1] G. S. Girolami, *J. Chem. Educ.* **2009**, *86*, 1200.

[2] B. M. Hoffman, D. Lukoyanov, Z. Y. Yang, D. R. Dean, L. C. Seefeldt, *Chem. Rev.* **2014**, *114*, 4041.

[3] M. Appl, *Ullmann's Encyclopedia of Industrial Chemistry*, 7. Aufl., WILEY-VCH Verlag GmbH, Weinheim, **2001**.

[4] F. Schüth, R. Palkovits, R. Schlögl, D. S. Su, *Energy Environ. Sci.* **2012**, *5*, 6278.

[5] A. Hellman, K. Honkala, I. N. Remediakis, Á. Logadóttir, A. Carlsson, S. Dahl, C. H. Christensen, J. K. Nørskov, *Surf. Sci.* **2006**, *600*, 4264.

[6] G. Ertl, *Angew. Chem. Int. Ed.* **2008**, *47*, 3524.

[7] B. M. Hoffman, D. Lukoyanov, Z.-Y. Yang, D. R. Dean, L. C. Seefeldt, *Chem. Rev.* **2014**, *114*, 4041.

[8] T. Spatzal, M. Aksoyoglu, L. Zhang, S. L. Andrade, E. Schleicher, S. Weber, D. C. Rees, O. Einsle, *Science* **2011**, *334*, 940.

[9] K. M. Lancaster, M. Roemelt, P. Ettenhuber, Y. Hu, M. W. Ribbe, F. Neese, U. Bergmann, S. DeBeer, *Science* **2011**, *334*, 974.

[10] O. Einsle, F. A. Tezcan, S. L. Andrade, B. Schmid, M. Yoshida, J. B. Howard, D. C. Rees, *Science* **2002**, *297*, 1696.

[11] B. M. Hoffman, D. R. Dean, L. C. Seefeldt, *Acc. Chem. Res.* **2009**, *42*, 609.

[12] N. N. Greenwood, A. Earnshaw, *Chemistry of the Elements*, 2. Aufl., Butterworth-Heinemann, Oxford, **1997**.

[13] E. Wiberg, N. Wiberg, *Lehrbuch der anorganische Chemie*, 102. Aufl., Walter de Gruyter & Co., Berlin, New York, **2007**.

[14] F. Wolfe-Simon, J. Switzer Blum, T. R. Kulp, G. W. Gordon, S. E. Hoeft, J. Pett-Ridge, J. F. Stolz, S. M. Webb, P. K. Weber, P. C. W. Davies, A. D. Anbar, R. S. Oremland, *Science* **2011**, *332*, 1163.

[15] J. T. Waber, D. T. Cromer, *J. Chem. Phys.* **1965**, *42*, 4116.

[16] K. P. Huber, G. Herzberg, *Molecular Spectra and Molecular Structure of Diatomic Molecules*, Nostrand, New York, **1979**.

[17] W. Kutzelnigg, *Angew. Chem. Int. Ed.* **1984**, *23*, 272.

[18] P. Jerabek, G. Frenking, *Theor. Chem. Acc.* **2014**, *133*, 1.

[19] M. von Hopffgarten, G. Frenking, *Wiley Interdiscip. Rev. Comput. Mol. Sci.* **2012**, *2*, 43.

[20] L. T. Xu, T. H. Dunning, *J. Chem. Theory Comput.* **2015**, *11*, 2496.

[21] W. A. Goddard, T. H. Dunning, W. J. Hunt, P. J. Hay, *Acc. Chem. Res.* **1973**, *6*, 368.

[22] R. A. Eikey, M. Abu-Omar, *Coord. Chem. Rev.* **2003**, *243*, 83.

[23] C. E. Laplaza, W. M. Davis, C. C. Cummins, *Angew. Chem. Int. Ed.* **1995**, *34*, 2042.

[24] M. Scheer, *Coord. Chem. Rev.* **1997**, *163*, 271.

[25] G. Becker, W. Becker, R. Knebl, H. Schmidt, U. Weber, W. M, *Nov. Acta Leopoldina* **1985**, *59*, 55.

[26] G. Becker, W. Becker, R. Knebl, H. Schmidt, U. Hildenbrand, M. Westerhausen, *Phosphorous Sulfur Relat. Elem.* **1987**, *30*, 349.

[27] M. Scheer, K. Schuster, T. A. Budzichowski, M. H. Chisholm, William E. Streib, *J. Chem. Soc., Chem. Comm.* **1995**, 1671.

[28] M. L. Ziegler, H.-P. Neumann, *Chem. Ber.* **1989**, *122*, 25.

[29] C. Caballero, D. Lehne, B. Nuber, M. L. Ziegler, *Chem. Ber.* **1991**, *124*, 1327.

[30] F. P. Arnold, D. P. Ridge, A. L. Rheingold, *J. Am. Chem. Soc.* **1995**, *117*, 4427.

[31] I. Klopsch, E. Yuzik-Klimova, „Functionalization of N2 by Mid to Late Transition Metals via N-N Bond Cleavage" in *Top. Organomet. Chem.*, **2017**.

[32] M. F. Espada, S. Bennaamane, Q. Liao, N. Saffon-Merceron, S. Massou, E. Clot, N. Nebra, M. Fustier-Boutignon, N. Mézailles, *Angew. Chem. Int. Ed.* **2018**, *57*, 12865.

[33] I. Klopsch, F. Schendzielorz, C. Volkmann, C. Würtele, S. Schneider, *Z. anorg. allg. Chem.* **2018**, *644*, 916.

[34] L. M. Duman, L. R. Sita, *J. Am. Chem. Soc.* **2017**, *139*, 17241.

[35] F. Schendzielorz, M. Finger, J. Abbenseth, C. Würtele, V. Krewald, S. Schneider, *Angew. Chem. Int. Ed.* **2018**, *2*, 840.

[36] Y. Ashida, K. Arashiba, K. Nakajima, Y. Nishibayashi, *Nature* **2019**, *568*, 536.

[37] Z.-j. Lv, Z. Huang, W.-x. Zhang, Z. Xi **2019**, *DOI: 10.10*.

[38] Y. Nishibayashi, *Transition Metal-Dinitrogen Complexes - Preparation and Reactivity*, WILEY-VCH Verlag GmbH, Weinheim, **2019**.

[39] S. M. Bhutto, P. L. Holland, *Eur. J. Inorg. Chem.* **2019**, 1861.

[40] B. M. Lindley, R. S. Van Alten, M. Finger, F. Schendzielorz, C. Würtele, A. J. Miller, I. Siewert, S. Schneider, *J. Am. Chem. Soc.* **2018**, *140*, 7922.

[41] M. J. Chalkley, T. J. Del Castillo, B. D. Matson, J. C. Peters, *J. Am. Chem. Soc.* **2018**, *140*, 6122.

[42] T. J. Del Castillo, N. B. Thompson, J. C. Peters, *J. Am. Chem. Soc.* **2016**, *138*, 5341.

[43] R. Cai, S. D. Minteer, M. Pita, D. Leech, A. L. De Lacey, R. D. Milton, S. Abdellaoui, *Angew. Chem. Int. Ed.* **2017**, *56*, 2680.

[44] E. Y. Jeong, C. Y. Yoo, C. H. Jung, J. H. Park, Y. C. Park, J. N. Kim, S. G. Oh, Y. Woo, H. C. Yoon, *ACS Sustain. Chem. Eng.* **2017**, *5*, 9662.

[45] N. Ostermann, I. Siewert, *Curr. Opin. Electrochem.* **2019**, DOI: 10.1016/j.coelec.2019.04.024.

[46] C. E. Laplaza, C. C. Cummins, R. E. T. Hill, A. L. Boettcher, *Science* **1995**, *268*, 861.

[47] J. J. Curley, T. R. Cook, S. Y. Reece, P. Müller, C. C. Cummins, *J. Am. Chem. Soc.* **2008**, *130*, 9394.

[48] C. E. Laplaza, M. J. Johnson, J. C. Peters, A. L. Odom, E. Kim, C. C. Cummins, G. N. George, I. J. Pickering, *J. Am. Chem. Soc.* **1996**, *118*, 8623.

[49] D. V. Yandulov, R. R. Schrock, *Science* **2003**, *301*, 76.

[50] G. Christian, J. Driver, R. Stranger, *Faraday Discuss.* **2003**, *124*, 331.

[51] G. Chrstian, R. Stranger, B. F. Yates, D. C. Graham, *Dalton Trans.* **2005**, 962.

[52] I. Klopsch, M. Finger, C. Würtele, B. Milde, D. B. Werz, S. Schneider, *J. Am. Chem. Soc.* **2014**, *136*, 6881.

[53] I. Klopsch, M. Kinauer, M. Finger, C. Würtele, S. Schneider, *Angew. Chem. Int. Ed.* **2016**, *55*, 4786.

[54] W. A. Nugent, R. J. Mckinney, V. Kasowski, F. A. Van-Catledge, *Inorganica Chim. Acta* **1982**, *65*, 91.

[55] M. J. Bezdek, S. Guo, P. J. Chirik, *Inorg. Chem.* **2016**, *55*, 3117.

[56] J. J. Curley, N. A. Piro, C. C. Cummins, *Inorg. Chem.* **2009**, *48*, 9599.

[57] M. Scheer, J. Miiller, M. Haser, *Angew. Chem. Int. Ed.* **1996**, *35*, 2492.

[58] J. S. Figueroa, C. C. Cummins, *J. Am. Chem. Soc.* **2003**, *125*, 4020.

[59] J. S. Figueroa, C. C. Cummins, *Angew. Chem. Int. Ed.* **2004**, *43*, 984.

[60] O. J. Scherer, *Acc. Chem. Res.* **1999**, *32*, 751.

[61] B. P. Johnson, G. Balázs, M. Scheer, *Coord. Chem. Rev.* **2006**, *250*, 1178.

[62] C. C. Cummins, *Angew. Chem. Int. Ed.* **2006**, *45*, 862.

[63] G. Balázs, L. J. Gregoriades, M. Scheer, *Organometallics* **2007**, *26*, 3058.

[64] J. A. Buss, P. H. Oyala, T. Agapie, *Angew. Chem. Int. Ed.* **2017**, *56*, 14502.

[65] M. Joost, W. J. Transue, C. C. Cummins, *Chem. Commun.* **2017**, *53*, 10731.

[66] G. Balázs, M. Sierka, M. Scheer, *Angew. Chem. Int. Ed.* **2005**, *44*, 4920.

[67] A. Velian, M. Nava, M. Temprado, Y. Zhou, R. W. Field, C. C. Cummins, *J. Am. Chem. Soc.* **2014**, *136*, 13586.

[68] J. M. Goicoechea, H. Grützmacher, *Angew. Chem. Int. Ed.* **2018**, *57*, 16968.

[69] A. Hinz, J. M. Goicoechea, *Angew. Chem. Int. Ed.* **2016**, *55*, 8536.

[70] L. N. Grant, B. Pinter, B. C. Manor, R. Suter, H. Grützmacher, D. J. Mindiola, *Chem. Eur. J.* **2017**, *23*, 6272.

[71] L. Weber, *Eur. J. Inorg. Chem.* **2018**, 2175.

[72] Z. J. Quan, X. C. Wang, *Org. Chem. Front.* **2014**, *1*, 1128.

[73] G. Hierlmeier, A. Hinz, R. Wolf, J. M. Goicoechea, *Angew. Chem. Int. Ed.* **2017**, *57*, 431.

[74] L. Liu, D. A. Ruiz, F. Dahcheh, G. Bertrand, R. Suter, A. M. Tondreau, H. Grützmacher, *Chem. Sci.* **2016**, *7*, 2335.

[75] Y. Lu, H. Wang, Y. Xie, H. Liu, H. F. Schaefer, *Inorg. Chem.* **2014**, *53*, 6252.

[76] G. L. Hou, B. Chen, W. J. Transue, Z. Yang, H. Grützmacher, M. Driess, C. C. Cummins, W. T. Borden, X. B. Wang, *J. Am. Chem. Soc.* **2017**, *139*, 8922.

[77] C. J. Ballhausen, H. B. Gray, *Inorg. Chem.* **1962**, *1*, 111.

[78] J. R. Winkler, H. B. Gray, *Electronic Structures of Oxo-Metal Ions*, Berlin, Heidelberg, **2011**, S. 17.

[79] M. G. Scheibel, J. Abbenseth, M. Kinauer, F. W. Heinemann, C. Würtele, B. De Bruin, S. Schneider, *Inorg. Chem.* **2015**, *54*, 9290.

[80] M. G. Scheibel, B. Askevold, F. W. Heinemann, E. J. Reijerse, B. de Bruin, S. Schneider, *Nature Chem.* **2012**, *4*, 552.

[81] B. Askevold, J. T. Nieto, S. Tussupbayev, M. Diefenbach, E. Herdtweck, M. C. Holthausen, S. Schneider, *Nature Chem.* **2011**, *3*, 532.

[82] M. G. Scheibel, Y. Wu, A. C. Stückl, L. Krause, E. Carl, D. Stalke, B. De Bruin, S. Schneider, *J. Am. Chem. Soc.* **2013**, *135*, 17719.

[83] F. S. Schendzielorz, M. Finger, C. Volkmann, C. Würtele, S. Schneider, *Angew. Chem. Int. Ed.* **2016**, *55*, 11417.

[84] J. Schöffel, A. Y. Rogachev, S. D. George, P. Burger, *Angew. Chem. Int. Ed.* **2009**, *48*, 4734.

[85] J. Schöffel, N. Šušnjar, S. Nückel, D. Sieh, P. Burger, *Eur. J. Inorg. Chem.* **2010**, 4911.

[86] A. Walstrom, M. Pink, X. Yang, J. Tomaszewski, M. H. Baik, K. G. Caulton, *J. Am. Chem. Soc.* **2005**, *127*, 5330.

[87] D. R. Lide, *CRC Handbook of CHemistry and Physics*, 90. Aufl., Francis, CRC Press/Taylor and Francis, Boco Raton, FL, **2010**.

[88] K. K. Pandey, G. Frenking, *Eur. J. Inorg. Chem.* **2004**, *3*, 4388.

[89] J. M. Smith, *Prog. Inorg. Chem.* **2014**, *58*, 417.

[90] M. G. Scheibel, I. Klopsch, H. Wolf, P. Stollberg, D. Stalke, S. Schneider, *Eur. J. Inorg. Chem.* **2013**, 3454.

[91] D. Sieh, J. Schöffel, P. Burger, *Dalton Trans.* **2011**, *40*, 9512.

[92] T. J. Crevier, J. M. Mayer, *J. Am. Chem. Soc.* **1998**, *120*, 5595.

[93] T. J. Crevier, B. K. Bennett, J. D. Soper, J. A. Bowman, A. Dehestani, D. A. Hrovat, S. Lovell, W. Kaminsky, J. M. Mayer, *J. Am. Chem. Soc.* **2001**, *123*, 1059.

[94] T. A. Betley, J. C. Peters, *J. Am. Chem. Soc.* **2004**, *126*, 6252.

[95] J. J. Scepaniak, M. D. Fulton, R. P. Bontchev, E. N. Duesler, M. L. Kirk, J. M. Smith, *J. Am. Chem. Soc.* **2008**, *130*, 10515.

[96] A. Walstrom, H. Fan, M. Pink, K. G. Caulton, *Inorganica Chim. Acta* **2010**, *363*, 633.

[97] N. Tsvetkov, M. Pink, H. Fan, J.-H. Lee, K. G. Caulton, *Eur. J. Inorg. Chem.* **2010**, 4790.

[98] H. Kunkely, A. Vogler, *Angew. Chem. Int. Ed.* **2010**, *49*, 1591.

[99] M. M. Konnick, S. M. Bischof, D. H. Ess, R. A. Periana, B. G. Hashiguchi, *J. Mol. Catal. A Chem.* **2014**, *382*, 1.

[100] N. A. Piro, J. S. Figueroa, J. T. McKellar, C. C. Cummins, *Science* **2006**, *313*(September), 1276–1279.

[101] M. J. A. Johnson, A. L. Odom, C. C. Cummins, *Chem. Comm* **1997**, 1523.

[102] N. A. Piro, C. C. Cummins, *J. Am. Chem. Soc.* **2009**, *131*, 8764.

[103] G. Balázs, J. C. Green, M. Scheer, *Chem. Eur. J.* **2006**, *12*, 8603.

[104] C. Che, H. Lam, W.-o. Tong, T. Lai, T. Lau, *J. Chem. Soc., Chem. Comm.* **1989**, 1883.

[105] O. Krahe, E. Bill, F. Neese, *Angew. Chem. Int. Ed.* **2014**, *53*, 8727.

[106] L. A. Kane-Maguire, P. S. Sheridan, F. Basolo, R. G. Pearson, *J. Am. Chem. Soc.* **1970**, *92*, 5865.

[107] K. D. Demadis, T. J. Meyer, P. S. White, *Inorg. Chem.* **1997**, *36*, 5678.

[108] J. D. Buhr, H. Taube, *Inorg. Chem.* **1979**, *18*, 2208.

[109] D. C. Ware, H. Taube, *Inorg. Chem.* **1991**, *30*, 4605.

[110] R. M. Clarke, T. Storr, *J. Am. Chem. Soc.* **2016**, *138*, 15299.

[111] V. Krewald, L. González, *Chem. Eur. J.* **2018**, *24*, 5112.

[112] T. Chantarojsiri, A. H. Reath, J. Y. Yang, *Angew. Chem. Int. Ed.* **2018**, *57*, 14037.

[113] J. Abbenseth, M. Finger, C. Würtele, M. Kasanmascheff, S. Schneider, *Inorg. Chem. Front.* **2016**, *3*, 469.

[114] D. Tofan, C. C. Cummins, *Angew. Chem. Int. Ed.* **2010**, *49*, 7516.

[115] Y. Wang, Y. Xie, P. Wei, R. B. King, H. F. Schaefer, P. V. R. Schleyer, G. H. Robinson, *J. Am. Chem. Soc.* **2008**, *130*, 14970.

[116] M. Y. Abraham, Y. Wang, Y. Xie, P. Wei, H. F. Schaefer, P. R. Von Schleyer, G. H. Robinson, *Chem. Eur. J.* **2010**, *16*, 432.

[117] O. Back, G. Kuchenbeiser, B. Donnadieu, G. Bertrand, *Angew. Chem. Int. Ed.* **2009**, *48*, 5530.

[118] L. Liu, D. A. Ruiz, D. Munz, G. Bertrand, *Chem* **2016**, *1*, 147.

[119] A. Hinz, J. M. Goicoechea, *Angew. Chem. Int. Ed.* **2016**, *55*, 15515.

[120] S. Yao, Y. Xiong, T. Szilvási, H. Grützmacher, M. Driess, *Angew. Chem. Int. Ed.* **2016**, *55*, 4781.

[121] Y. Xiong, S. Yao, T. Szilvási, E. Ballestero-Martínez, H. Grützmacher, M. Driess, *Angew. Chem. Int. Ed.* **2017**, *56*, 4333.

[122] T. Krachko, A. W. Ehlers, M. Nieger, M. Lutz, J. C. Slootweg, *Angew. Chem. Int. Ed.* **2018**, *57*, 1683.

[123] B. M. Cossairt, N. A. Piro, C. C. Cummins, *Chem. Rev.* **2010**, *110*, 4164.

[124] M. Caporali, L. Gonsalvi, A. Rossin, M. Peruzzini, *Chem. Rev.* **2010**, *110*, 4178.

[125] S. Marque, P. Tordo, *Top. Curr. Chem.* **2005**, *250*, 43.

[126] P. P. Power, *Chem. Rev.* **2003**, *103*, 789.

[127] A. Armstrong, T. Chivers, M. Parvez, R. T. Boeré, *Angew. Chem. Int. Ed.* **2004**, *43*, 502.

[128] C. D. Martin, M. Soleilhavoup, G. Bertrand, *Chem. Sci.* **2013**, *4*, 3020.

[129] V. Nesterov, D. Reiter, P. Bag, P. Frisch, R. Holzner, A. Porzelt, S. Inoue, *Chem. Rev.* **2018**, *118*, 9678.

[130] U. Schmidt, F. Geiger, A. Müller, K. Markau, *Angew. Chem.* **1963**, *13*, 640.

[131] S. K. Wong, J. K. Wan, *Spectrosc. Lett.* **1970**, *3*, 135.

[132] W. T. Cook, J. S. Vincent, I. Bernal, F. Ramirez, *J. Chem. Phys.* **1974**, *61*, 3479.

[133] B. W. Fullam, S. P. Mishra, M. C. Symons, *J. Chem. Soc. Dalt. Trans.* **1974**, 2145.

[134] M. Geoffroy, E. Lucken, C. Mazeline, *Mol. Phys.* **2006**, *28*, 839.

[135] T. Berclaz, M. Geoffroy, *Helv. Chim. Acta* **1978**, *61*, 684.

[136] Y. Sakaguchi, *Chem. Phys. Lett.* **1995**, *245*, 591.

[137] P. Tordo, M. Boyer, F. Vila, L. Pujol, *Phosphorous Sulfur Relat. Elem.* **2007**, *3*, 43.

[138] D. Ajo, M. B. Biagini Cingi, I. Fragala, G. Granozzi, *Spectrosc. Lett.* **1977**, *10*, 757.

[139] A. Albert, C. N. R. Composti, C. Eteroatcmi, *Tetrahedron* **1986**, *42*, 2533.

[140] R. Leardini, A. Tundo, G. Zanardi, G. F. Peduiii, *J. Chem. Soc. Perkin Trans. II* **1985**, 1117.

[141] B. Ndiaye, S. Bhat, A. Jouaiti, T. Berclaz, G. Bernardinelli, M. Geoffroy, *J. Phys. Chem. A* **2006**, *110*, 9736.

[142] Y. Sueishi, Y. Miyake, *Bull. Chem. Soc. Jpn.* **1997**, *70*, 397.

[143] Y. Sueishi, Y. Nishihara, *J. Chem. Res.* **2001**, *S*, 84.

[144] S. L. Hinchley, C. A. Morrison, D. W. Rankin, C. L. Macdonald, R. J. Wiacek, A. Voigt, A. H. Cowley, M. F. Lappert, G. Gundersen, J. A. Clyburne, P. P. Power, *J. Am. Chem. Soc.* **2001**, *123*, 9045.

[145] J. Bezombes, K. B. Borisenko, P. B. Hitchcock, M. F. Lappert, J. E. Nycz, W. H. Rankin, H. E. Robertson, *Dalton Trans.* **2004**, 1980.

[146] S. Ito, M. Kikuchi, M. Yoshifuji, A. J. Arduengo, T. A. Konovalova, L. D. Kispert, *Angew. Chem. Int. Ed.* **2006**, *45*, 4341.

[147] R. Kinjo, B. Donnadieu, G. Bertrand, *Angew. Chem. Int. Ed.* **2010**, *49*, 5930.

[148] O. Back, M. A. Celik, G. Frenking, M. Melaimi, B. Donnadieu, G. Bertrand, *J. Am. Chem. Soc.* **2010**, *132*, 10262.

[149] O. Back, B. Donnadieu, M. von Hopffgarten, S. Klein, R. Tonner, G. Frenking, G. Bertrand, *Chem. Sci.* **2011**, *2*, 858.

[150] S. Ishida, F. Hirakawa, T. Iwamoto, *J. Am. Chem. Soc.* **2011**, *133*, 12968.

[151] X. Pan, X. Weng, Y. Zhao, Y. Sui, X. Wang, *J. Am. Chem. Soc.* **2014**, *136*, 9834.

[152] K. Schwedtmann, S. Schulz, F. Hennersdorf, T. Strassner, E. Dmitrieva, J. J. Weigand, *Angew. Chem. Int. Ed.* **2015**, *54*, 11054.

[153] K. Schwedtmann, G. Zanoni, J. J. Weigand, *Chem. Asian J.* **2018**, *13*, 1388.

[154] P. Agarwal, N. A. Piro, K. Meyer, P. Müller, C. C. Cummins, *Angew. Chem. Int. Ed* **2007**, *46*, 3111.

[155] M. Scheer, C. Kuntz, M. Stubenhofer, M. Linseis, R. F. Winter, M. Sierka, *Angew. Chem. Int. Ed.* **2009**, *48*, 2600.

[156] G. Tan, J. Li, L. Zhang, C. Chen, Y. Zhao, X. Wang, Y. Song, Y. Q. Zhang, M. Driess, *Angew. Chem. Int. Ed.* **2017**, *56*, 12741.

[157] U. Fischbach, M. Trincado, H. Grützmacher, *Dalton Trans.* **2017**, *46*, 3443.

[158] Y.-E. Kim, Y. Lee, *Angew. Chem. Int. Ed* **2018**, *57*, 14159.

[159] M. M. Hansmann, R. Jazzar, G. Bertrand, *J. Am. Chem. Soc.* **2016**, *138*, 8356.

[160] K. Lammertsma, *Top. Curr. Chem.* **2003**, *229*, 95.

[161] H. Aktaş, J. Chris Slootweg, K. Lammertsma, *Angew. Chem. Int. Ed.* **2010**, *49*, 2102.

[162] R. Waterman, *Dalton Trans.* **2009**, 18.

[163] M. J. Amme, A. B. Kazi, T. R. Cundari, *Int. J. Quant. Chem.* **2010**, *110*, 1702.

[164] K. Pal, O. B. Hemming, B. M. Day, T. Pugh, D. J. Evans, R. A. Layfield, *Angew. Chem. Int. Ed.* **2016**, *55*, 1690.

[165] J. K. Pagano, B. J. Ackley, R. Waterman, *Chem. Eur. J.* **2018**, *24*, 2554.

[166] G. Dequirez, V. Pons, P. Dauban, *Angew. Chem. Int. Ed.* **2012**, *51*, 7384.

[167] J. L. Roizen, M. E. Harvey, J. D. Bois, *Acc. Chem. Res.* **2012**, *45*, 911.

[168] P. F. Kuijpers, J. I. van der Vlugt, S. Schneider, B. de Bruin, *Chem. Eur. J.* **2017**, *23*, 13819.

[169] N. V. Barkovskii, V. I. Tsirel'nikov, A. M. Emel'yanov, Y. S. Khodeev, *Teplofiz. Vys. Temp.* **1991**, *29*, 474.

[170] J. Berkowitz, L. A. Curtiss, S. T. Gibson, J. P. Greene, G. L. Hillhouse, J. A. Pople, *J. Chem. Phys.* **1986**, *84*, 375.

[171] J. D. Cox, D. D. Wagman, V. A. Medvedev, *CODATA Key Values for Thermodynamics*, Hemisphere Publishing Corp., New York, **1984**.

[172] M. W. Chase, *NIST-JANAF Thermochemical Tables, J. Phys. Chem. Ref. Data, Monograph 9*, **1998**.

[173] M. J. Bezdek, S. Guo, P. J. Chirik, *Science* **2016**, *354*, 730.

[174] S. S. Kolmar, J. M. Mayer, *J. Am. Chem. Soc.* **2017**, *139*, 10687.

[175] D. J. Mindiola, G. L. Hillhouse, *J. Am. Chem. Soc.* **2001**, *123*, 4623.

[176] M. H. V. Huynh, T. J. Meyer, *Proc. Natl. Acad. Sci. U. S. A.* **2000**, *101*, 13138.

[177] R. E. Cowley, R. P. Bontchev, J. Sorrell, O. Sarracino, Y. Feng, H. Wang, J. M. Smith, *J. Am. Chem. Soc.* **2007**, *129*, 2424.

[178] I. Nieto, F. Ding, R. P. Bontchev, H. Wang, J. M. Smith, *J. Am. Chem. Soc.* **2008**, *130*, 2716.

[179] R. E. Cowley, N. A. Eckert, S. Vaddadi, T. M. Figg, T. R. Cundari, P. L. Holland, *J. Am. Chem. Soc.* **2011**, *133*, 9796.

[180] V. M. Iluc, A. J. Miller, J. S. Anderson, M. J. Monreal, M. P. Mehn, G. L. Hillhouse, *J. Am. Chem. Soc.* **2011**, *133*, 13055.

[181] S. Wiese, J. L. McAfee, D. R. Pahls, C. L. McMullin, T. R. Cundari, T. H. Warren, *J. Am. Chem. Soc.* **2012**, *134*, 10114.

[182] C. Milsmann, S. P. Semproni, P. J. Chirik, *J. Am. Chem. Soc.* **2014**, *136*, 12099.

[183] I. Pappas, P. J. Chirik, *J. Am. Chem. Soc.* **2016**, *138*, 13379.

[184] D. M. Spasyuk, S. H. Carpenter, C. E. Kefalidis, W. E. Piers, M. L. Neidig, L. Maron, *Chem. Sci.* **2016**, *7*, 5939.

[185] P. J. Chirik, M. Bezdek, *Angew. Chem. Int. Ed.* **2018**, *24*, 1.

[186] R. Melenkivitz, D. J. Mindiola, G. L. Hillhouse, *J. Am. Chem. Soc.* **2002**, *124*, 3846.

[187] V. M. Iluc, G. L. Hillhouse, *J. Am. Chem. Soc.* **2010**, *132*, 15148.

[188] C. Gunanathan, D. Milstein, *Acc. Chem. Res.* **2011**, *44*, 588.

[189] L. C. Liang, *Coord. Chem. Rev.* **2006**, *250*, 1152.

[190] S. Schneider, J. Meiners, B. Askevold, *Eur. J. Inorg. Chem.* **2012**, 412.

[191] B. Askevold, M. M. Khusniyarov, W. Kroener, K. Gieb, P. Müller, E. Herdtweck, F. W. Heinemann, M. Diefenbach, M. C. Holthausen, V. Vieru, L. F. Chibotaru, S. Schneider, *Chem. Eur. J.* **2015**, *21*, 579.

[192] P. O. Lagaditis, B. Schluschaß, S. Demeshko, C. Würtele, S. Schneider, *Inorg. Chem.* **2016**, *55*, 4529.

[193] J. Meiners, M. G. Scheibel, M.-H. Lemée-Cailleau, S. A. Mason, M. B. Boeddinghaus, T. F. Fässler, E. Herdtweck, M. M. Khusniyarov, S. Schneider, *Angew. Chem. Int. Ed.* **2011**, *50*, 8184.

[194] B. Askevold, M. M. Khusniyarov, E. Herdtweck, K. Meyer, S. Schneider, *Angew. Chem. Int. Ed.* **2010**, *49*, 7566.

[195] M. A. Esteruelas, F. J. Modrego, E. Oñate, E. Royo, *J. Am. Chem. Soc.* **2003**, *125*, 13344.

[196] J. T. Anhaus, T. P. Kee, M. H. Schofield, R. R. Schrock, *J. Am. Chem. Soc.* **1990**, *112*, 1642.

[197] M. L. Buil, J. J. Cardo, M. A. Esteruelas, E. Oñate, *J. Am. Chem. Soc.* **2016**, *138*, 9720.

[198] B. H. Werner, A. Michenfelder, *Angew. Chem. Int. Ed.* **1991**, *30*, 596.

[199] D. Coskun, S. V. Jerome, R. A. Friesner, *J. Chem. Theory Comput.* **2016**, *12*, 1121.

[200] F. Wätjen, Dissertation, Georg-August-Universität Göttingen, **2019**.

[201] F. Schneck, M. Finger, M. Tromp, S. Schneider **2017**, *23*, 33.

[202] A. W. Addison, T. N. Rao, J. Reedijk, J. van Rijn, G. C. Verschoor, *J. Chem. Soc., Dalt. Trans.* **1984**, 1349.

[203] A. Soncini, W. Van Den Heuvel, *J. Chem. Phys.* **2013**, *138*, 021103.

[204] D. M. D'Alessandro, P. H. Dinolfo, M. S. Davies, J. T. Hupp, F. R. Keene, *Inorg. Chem.* **2006**, *45*, 3261.

[205] J. Chatt, G. J. Leigh, D. M. P. Mingos, *J. Chem. Soc. A* **1969**, 2972.

[206] M. Atanasov, D. Aravena, E. Suturina, E. Bill, D. Maganas, F. Neese, *Coord. Chem. Rev.* **2015**, *289-290*, 177.

[207] S. P. Semproni, W. S. McNeil, R. A. Baillie, B. O. Patrick, C. F. Campana, P. Legzdins, *Organometallics* **2010**, *29*, 867.

[208] J. M. Narayanam, C. R. Stephenson, *Chem. Soc. Rev.* **2011**, *40*, 102.

[209] R. Ziessel, *J. Am. Chem. Soc* **1993**, *115*, 118.

[210] K. J. Watson, R. Ziessel, *Inorganica Chim. Acta* **1992**, *197*, 125.

[211] R. Ziessel, *Angew. Chem. Int. Ed* **1991**, *30*, 844.

[212] R. Ziessel, *J. Chem. Soc. Chem. Commun.* **1988**, 16.

[213] T. Suenobu, D. M. Guldi, S. Ogo, S. Fukuzumi, *Angew. Chem. Int. Ed.* **2003**, *42*, 5492.

[214] M. B. Chambers, D. A. Kurtz, C. L. Pitman, M. K. Brennaman, A. J. Miller, *J. Am. Chem. Soc.* **2016**, *138*, 13509.

[215] F. Schneck, J. Ahrens, M. Finger, A. C. Stückl, C. Würtele, D. Schwarzer, S. Schneider, *Nat. Commun.* **2018**, *9*, 1.

[216] M. Irwin, R. K. Jenkins, M. S. Denning, T. Krämer, F. Grandjean, G. J. Long, R. Herchel, J. E. McGrady, J. M. Goicoechea, *Inorg. Chem.* **2010**, *49*, 6160.

[217] P. Milko, M. A. Iron, *J. Chem. Theory Comput.* **2014**, *10*, 220.

[218] F. Neese, *Coord. Chem. Rev.* **2009**, *253*, 526.

[219] Y. Gloaguen, C. Rebreyend, M. Lutz, P. Kumar, M. Huber, J. I. van der Vlugt, S. Schneider, B. de Bruin, *Angew. Chem. Int. Ed.* **2014**, *53*, 6814.

[220] J. J. Scepaniak, C. G. Margarit, J. N. Harvey, J. M. Smith, *Inorg. Chem.* **2011**, *50*, 9508.

[221] J. F. Berry, *Comments Inorg. Chem.* **2009**, *30*, 28.

[222] M. H. V. Huynh, E. S. El-Samanody, K. D. Demadis, P. S. White, T. J. Meyer, *Inorg. Chem.* **2000**, *39*, 3075.

[223] M. H. V. Huynh, P. S. White, T. J. Meyer, *Angew. Chem. Int. Ed.* **2000**, *39*, 4101.

[224] M. H. V. Huynh, P. S. White, C. A. Carter, T. J. Meyer, *Angew. Chem. Int. Ed* **2001**, *40*, 3037.

[225] M. H. V. Huynh, R. T. Baker, D. L. Jameson, A. Labouriau, T. J. Meyer, *J. Am. Chem. Soc.* **2002**, *124*, 4580.

[226] S. N. Brown, *J. Am. Chem. Soc.* **1999**, *121*, 9752.

[227] W. L. Man, W. W. Lam, T. C. Lau, *Acc. Chem. Res.* **2014**, *47*, 427.

[228] A. Glüer, B. Askevold, B. Schluschaß, F. W. Heinemann, S. Schneider, *Z. anorg. allg. Chem.* **2015**, *641*, 49.

[229] G. Rossi, M. Gardini, G. Pennesi, C. Ercolani, V. L. Goedken, *J. Chem. Soc. Dalton Trans.* **1989**, 193.

[230] L. Bonomo, E. Solari, R. Scopelliti, C. Floriani, *Angew. Chem. Int. Ed.* **2001**, *40*, 2529.

[231] G. Wu, D. Rovnyak, M. J. Johnson, N. C. Zanetti, D. G. Musaev, K. Morokuma, R. R. Schrock, R. G. Griffin, C. C. Cummins, *J. Am. Chem. Soc.* **1996**, *118*, 10654.

[232] R. C. Fischer, P. P. Power, *Chem. Rev.* **2010**, 3877.

[233] P. Macchi, A. Sironi, *Coord. Chem. Rev.* **2003**, *238-239*, 383.

[234] J. I. Schweizer, M. G. Scheibel, M. Diefenbach, F. Neumeyer, C. Würtele, N. Kulminskaya, R. Linser, N. Auner, S. Schneider, M. C. Holthausen, *Angew. Chem. Int. Ed* **2016**, *55*, 1782.

[235] D. Stalke, *Chem. Eur. J.* **2011**, *17*, 9264.

[236] L. J. Farrugia, C. S. Frampton, J. A. Howard, P. R. Mallinson, R. D. Peacock, G. T. Smith, B. Stewart, *Acta Crystallogr.* **2006**, *B62*, 236.

[237] S. Mebs, J. Henn, B. Dittrich, C. Paulmann, P. Luger, *J. Phys. Chem. A* **2009**, *113*, 8366.

[238] M. E. Weeks, *J. Chem. Ed.* **1932**, *9*, 11.

[239] E. J. Zegers, E. M. Fisher, *Combust. Flame* **1998**, *115*, 230.

[240] O. P. Korobeinichev, S. B. Ilyin, V. M. Shvartsberg, A. A. Chernov, *Combust. Flame* **1999**, *118*, 718.

[241] L. B. Knight, G. C. Jones, G. M. King, R. M. Babb, A. J. McKinley, *J. Chem. Phys.* **1995**, *103*, 497.

[242] C. W. Bauschlicher, M. Zhou, L. Andrews, *J. Phys. Chem. A* **2002**, *104*, 3566.

[243] B. T. Sterenberg, L. Scoles, A. J. Carty, *Coord. Chem. Rev.* **2002**, *231*, 183.

[244] M. McCluskey, L. Andrews, *J. Phys. Chem.* **1991**, *95*, 2988.

[245] J. S. Francisco, *J. Chem. Phys.* **2002**, *117*, 3190.

[246] A. Bauzá, A. Frontera, *ChemPhysChem* **2017**, *18*, 2191.

[247] Y. Pak, *J. Chem. Phys.* **1996**, *104*, 5547.

[248] C. Xu, E. de Beer, D. M. Neumark, *J. Chem. Phys.* **1996**, *104*, 2749.

[249] L. L. Lohr, *J. Phys. Chem.* **1984**, *88*, 5569.

[250] H. B. Qian, P. B. Davies, I. K. Ahmad, P. A. Hamilton, *Chem. Phys. Lett.* **1995**, *235*, 255.

[251] L. L. Lohr, *J. Phys. Chem.* **1992**, *96*, 119.

[252] L. Andrews, M. McCluskey, Z. Mielke, R. Withnall, *J. Mol. Struct.* **1990**, *222*, 95.

[253] M. A. Hitchman, G. L. Rowbottom, *Coord. Chem. Rev.* **1982**, *42*, 55.

[254] A. J. Timmons, M. D. Symes, *Chem. Soc. Rev.* **2015**, *44*, 6708.

[255] R. Eisenberg, C. D. Meyer, *Acc. Chem. Res.* **1975**, *8*, 26.

[256] P. F. Bernath, *Astrophys. J.* **1987**, *312*, 358.

[257] C. Cummins, *Chem. Commun.* **1998**, 1777.

[258] Y. Xie, P. v. R. Schleyer, Y. Wang, P. Wei, H. F. Schaefer, G. H. Robinson, *J. Am. Chem. Soc.* **2013**, *135*, 19139.

[259] O. J. Scherer, S. Weigel, G. Wolmershäuser, *Angew. Chem. Int. Ed* **1999**, *38*, 3688.

[260] A. S. Pronin, A. I. Smolentsev, S. G. Kozlova, I. N. Novozhilov, Y. V. Mironov, *Inorg. Chem.* **2019**, *DOI: 10.10*.

[261] N. Elgrishi, K. J. Rountree, B. D. McCarthy, E. S. Rountree, T. T. Eisenhart, J. L. Dempsey, *J. Chem. Educ.* **2018**, *95*, 197.

[262] D. M. Murphy, *EPR (Electron Paramagnetic Resonance) Spectroscopy of Polycrystalline Oxide Systems - Chapter 1*, WILEY-VCH Verlag GmbH, Weinheim, **2009**.

[263] M. L. Munzarova, P. Kubacek, M. Kaupp, *J. Am. Chem. Soc.* **2000**, *122*, 11900.

[264] P. A. Haase, M. Repisky, S. Komorovsky, J. Bendix, S. P. Sauer, *Chem. Eur. J.* **2018**, *24*, 5124.

[265] M. Bennati, *eMagRes* **2017**, *6*, 271.

[266] F. Neese, *eMagRes* **2017**, *6*, 1.

[267] J. A. McCleverty, T. J. Meyer, *Comprehensive Coordination Chemistry II - Volume: Transition Metal Group 7 and 8*, Elsevier, **2003**.

[268] J. J. Warren, T. A. Tronic, J. M. Mayer, *Chem. Rev.* **2010**, *110*, 6961.

[269] J. D. Masuda, K. C. Jantunen, O. V. Ozerov, K. J. Noonan, D. P. Gates, B. L. Scott, J. L. Kiplinger, *J. Am. Chem. Soc.* **2008**, *130*, 2408.

[270] M. C. Puerta, P. Valerga, *Coord. Chem. Rev.* **1999**, *193-195*, 977.

[271] N. Shida, J. A. Buss, T. Agapie, *Chem. Commun.* **2018**, *54*, 767.

[272] A. Velian, C. C. Cummins, *Science* **2015**, *348*, 1001.

[273] W. J. Transue, A. Velian, M. Nava, M. A. Martin-Drumel, C. C. Womack, J. Jiang, G. L. Hou, X. B. Wang, M. C. McCarthy, R. W. Field, C. C. Cummins, *J. Am. Chem. Soc.* **2016**, *138*, 6731.

[274] M. A. Courtemanche, W. J. Transue, C. C. Cummins, *J. Am. Chem. Soc.* **2016**, *138*, 16220.

[275] M. P. Duffy, F. Mathey, *J. Am. Chem. Soc.* **2009**, *131*, 7534.

[276] K. Vaheesar, C. M. Kuntz, B. T. Sterenberg, *J. Organomet. Chem.* **2013**, *745*, 347.

[277] J. F. Hartwig, *Organotransition Metal Chemistry, from Bonding to Catalysis*, New York, **2010**.

[278] Y. Wang, G. H. Robinson, *Dalton Trans.* **2012**, *41*, 337.

[279] Y. Wang, G. H. Robinson, *Inorg. Chem.* **2014**, *53*, 11815.

[280] G. A. Silantyev, M. Förster, B. Schluschaß, J. Abbenseth, C. Würtele, C. Volkmann, M. C. Holthausen, S. Schneider, *Angew. Chem. Int. Ed.* **2017**, *56*, 5872.

[281] M. B. Robin, P. Day, *Adv. Inorg. Chem. Radiochem.* **1968**, *10*, 247.

[282] P. P. Borbat, A. J. Costa-Filho, K. A. Earle, J. K. Moscicki, J. H. Freed, *Science* **2001**, *291*, 266.

[283] P. Dauber, A. T. Hagler, *Acc. Chem. Res.* **1980**, *46*, 105.

[284] M. A. Buntine, V. J. Hall, F. J. Kosovel, E. R. T. Tiekink, *J. Phys. Chem. A* **1998**, *102*, 2472.

[285] A. Gavezzotti, *Crystallogr. Rev.* **1998**, *7*, 5.

[286] F. De Groot, *Chem. Rev.* **2001**, *101*, 1779.

[287] G. Vlaic, L. Olivi, *Croat. Chem. Acta* **2004**, *77*, 427.

[288] D. C. Koningsberger, R. Prins, „X-Ray Absorption: Principles, Applications, Technique of EXAFS, SEXAFS and XANES" in *Chem. Anal. Vol. 92*, John Wiley & Sons, Inc., New York, **1988**.

[289] J. H. Choi, N. E. Schloerer, J. Berger, M. H. Prechtl, *Dalton Trans.* **2014**, *43*, 290.

[290] M. Tamizmani, C. Sivasankar, *J. Organomet. Chem.* **2017**, *845*, 82.

[291] M. Brookhart, B. Grant, A. F. Volpe, *Organometallics* **1992**, *11*, 3920.

[292] J. Meiners, A. Friedrich, E. Herdtweck, S. Schneider, *Organometallics* **2009**, *28*, 6331.

[293] V. W. Manner, T. F. Markle, J. H. Freudenthal, J. P. Roth, J. M. Mayer, *Chem. Commun.* **2008**, *246*, 256.

[294] A. C. Coelho, S. S. Balula, S. M. Bruno, J. C. Alonso, N. Bion, P. Ferreira, M. Pillinger, A. A. Valente, J. Rocha, I. S. Gonçalves, *Adv. Synth. Catal.* **2010**, *352*, 1759.

[295] G. S. Girolami, A. P. Sattelberger, *Inorganic Synthesis 36*, John Wiley & Sons, Inc., Hoboken, New Jersey, **2014**.

[296] D. Heift, Z. Benko, H. Grützmacher, *Dalton Trans.* **2014**, *43*, 831.

[297] I. Klopsch, Dissertation, Georg-August-Universität Göttingen, **2016**.

[298] G. P. Elliot, N. M. McAuley, W. R. Roper, P. A. Shapley, *Inorganic Synthesis, Volume 15*, John Wiley & Sons, Inc., New York, Chichester, Brisbane, Toronto, Singapore, **1989**.

[299] W. Haberditzl, *Angew. Chem. Int. Ed.* **1966**, *5*, 288.

[300] E. Bill, „julX, Program for Simulation of Molecular Magnetic Data", **2008**.

[301] I. Ivancic, D. Degobbis, *Water Resour.* **1984**, *18*, 1143.

[302] B. Ravel, M. Newville, *J. Synchrotron Rad.* **2005**, *12*, 537.

[303] „Gaussian 09, Revision D.01".

[304] J. P. Perdew, M. Ernzerhof, K. Burke, *J. Chem. Phys.* **1996**, *105*, 9982.

[305] C. Adamo, V. Barone, *J. Chem. Phys.* **2008**, *6158*, 6158.

[306] S. Grimme, S. Ehrlich, L. Goerigk, *J. Comput. Chem* **2011**, *32*, 1456.

[307] F. Weigend, R. Ahlrichs, *Phys. Chem. Chem. Phys.* **2005**, *7*, 3297.

[308] D. Andrae, U. Häußermann, M. Dolg, H. Stoll, H. Preuss, *Theor. Chim. Acta* **1990**, *77*, 123.

[309] „MolPro 2015.1", **2015**.

[310] S. Ten-no, *Chem. Phys. Lett.* **2004**, *398*, 56.

[311] T. B. Adler, G. Knizia, H.-J. Werner, *J. Chem. Phys.* **2007**, *127*, 221106.

[312] K. A. Peterson, T. B. Adler, H. J. Werner, *J. Chem. Phys.* **2008**, *128*, 084102.

[313] K. E. Yousaf, K. A. Peterson, *J. Chem. Phys.* **2008**, *129*, 184108.

[314] S. Kritikou, J. G. Hill, *J. Chem. Theory Comput.* **2015**, *11*, 5269.

[315] D. Figgen, K. A. Peterson, M. Dolg, H. Stoll, *J. Chem. Phys.* **2009**, *130*, 164108.

[316] J. G. Hill, *J. Chem. Phys.* **2011**, *135*, 044105.

[317] J. G. Hill, K. A. Peterson, G. Knizia, H. J. Werner, *J. Chem. Phys.* **2009**, *131*, 194105.

[318] F. Neese, *Wiley Interdiscip. Rev. Comput. Mol. Sci.* **2012**, *2*, 73.

[319] C. Van Wüllen, *J. Chem. Phys.* **1998**, *109*, 392.

[320] F. Neese, F. Wennmohs, A. Hansen, U. Becker, *Chem. Phys.* **2009**, *356*, 98.

[321] C. Haettig, *Phys. Chem. Chem. Phys.* **2005**, *7*, 59.

[322] C. Angeli, R. Cimiraglia, J. P. Malrieu, *Chem. Phys. Lett.* **2001**, *350*, 297.

[323] C. Angeli, R. Cimiraglia, S. Evangelisti, T. Leininger, J. P. Malrieu, *J. Chem. Phys.* **2001**, *114*, 10252.

[324] C. Angeli, R. Cimiraglia, J. P. Malrieu, *J. Chem. Phys.* **2002**, *117*, 9138.

[325] B. A. Heß, C. M. Marian, U. Wahlgren, O. Gropen, *Chem. Phys. Lett.* **1996**, *251*, 365.

[326] J. P. Perdew, K. Burke, M. Ernzerhof, *Phys. Rev. Lett.* **1996**, *77*, 3865.

[327] O. Treutler, R. Ahlrichs, *J. Chem. Phys.* **1995**, *102*, 346.

[328] Karin E, Oliver T, Holger O, Marco H, Reinhart A, *Chem. Phys. Lett.* **1995**, *240*, 283.

[329] K. Eichkorn, F. Weigend, O. Treutler, R. Ahlrichs, *Theor. Chem. Acc.* **1997**, *97*, 119.

[330] S. Grimme, J. Antony, S. Ehrlich, H. Krieg, *J. Chem. Phys.* **2010**, *132*, 154104.

[331] A. V. Marenich, C. J. Cramer, D. G. Truhlar, *J. Phys. Chem. B* **2009**, *113*, 6378.

[332] D. A. Pantazis, X.-Y. Chen, C. R. Landis, F. Neese, *J. Chem. Theory Comput.* **2008**, *4*, 908.

[333] M. D. Hanwell, D. E. Curtis, D. C. Lonie, T. Vandermeersch, E. Zurek, H. G. R., *J. Cheminform.* **2012**, *4*, 17.

[334] E. F. Pettersen, T. D. Goddard, C. C. Huang, G. S. Couch, D. M. Greenblatt, E. C. Meng, T. E. Ferrin, *J. Comput. Chem.* **2004**, *25*, 1605.

[335] M. Dolg, U. Wedig, H. Stoll, H. Preuss, *J. Chem. Phys.* **1987**, *86*, 866.

[336] A. Bergner, M. Dolg, W. Küchle, H. Stoll, H. Preuß, *Mol. Phys.* **1993**, *80*, 1431.

[337] J. D. Chai, M. Head-Gordon, *Phys. Chem. Chem. Phys.* **2008**, *10*, 6615.

[338] Y. Minenkov, Å. Singstad, G. Occhipinti, V. R. Jensen, *Dalton Trans.* **2012**, *41*, 5526.

[339] K. L. Schuchardt, B. T. Didier, T. Elsethagen, L. Sun, V. Gurumoorthi, J. Chase, J. Li, T. L. Windus, *J. Chem. Inf. Model.* **2007**, *47*, 1045.

[340] D. Feller, *J. Comput. Chem.* **1996**, *17*, 1571.

[341] T. H. Dunning, P. J. Hay, *Modern Theoretical Chemistry*, Plenum, New York, **1977**, S. 1.

[342] A. D. McLean, G. S. Chandler, *J. Chem. Phys.* **1980**, *72*, 5639.

[343] R. Krishnan, J. S. Binkley, R. Seeger, J. A. Pople, *J. Chem. Phys.* **1980**, *72*, 650.

[344] R. C. Binning, L. A. Curtiss, *J. Comput. Chem.* **1990**, *11*, 1206.

[345] L. A. Curtiss, M. P. McGrath, J. P. Blaudeau, N. E. Davis, R. C. Binning, L. Radom, *J. Chem. Phys.* **1995**, *103*, 6104.

[346] G. Schreckenbach, T. Ziegler, *J. Phys. Chem.* **1995**, *99*, 606.

[347] S.-t. Orbitals, M. Krykunov, T. O. M. Ziegler, E. V. A. N. Lenthe, *Int. J. Quantum Chem.* **2009**, *109*, 1676.

[348] G. T. E. Velde, F. M. Bickelhaupt, E. J. Baerends, C. F. Guerra, S. J. A. V. A. N. Gisbergen, *J. Comput. Chem.* **2001**, *22*, 931.

[349] S. K. Wolff, T. Ziegler, E. Van Lenthe, E. J. Baerends, *J. Chem. Phys.* **1999**, *110*, 7689.

[350] E. van Lenthe, J. G. Snijders, E. J. Baerends, *J. Chem. Phys.* **1996**, *105*, 6505.

[351] E. van Lenthe, E. J. Baerends, J. G. Snijders, *J. Chem. Phys.* **1994**, *101*, 9783.

[352] J. P. Perdew, K. Burke, M. Ernzerhof, *Phys. Rev. Lett.* **1997**, *78*, 1396.

[353] E. van Lenthe, E. J. Baerends, *J. Phys. Chem.* **2003**, *24*, 1142.

[354] S. O. Grimm, W. McFariane, E. F. Davidoff, *J. Phys. Chem.* **1966**, *70*, 581.

[355] A. Klamt, G. Schüürmann, *J. Chem. Soc., Perkin Trans. 2* **1993**, *5*, 799.

[356] C. C. Pye, T. Ziegler, *Theor. Chem. Acc.* **1999**, *101*, 396.

[357] R. Ahlrichs, „Turbomole 7.3.1", **2018**.

[358] I. Baker, *J. Comput. Chem.* **1986**, *7*, 385.

[359] P. H. M. Budzelaar, *J. Comput. Chem.* **2007**, *28*, 2226.

[360] A. D. Becke, *Phys. Rev. A* **1988**, *38*, 3098.

[361] J. P. Perdew, *Phys. Rev. B* **1986**, *7*, 385.

[362] M. Sierka, A. Hogekamp, R. Ahlrichs, *J. Chem. Phys.* **2003**, *118*, 9136.

[363] F. Weigend, H. Häser, H. Patzelt, R. Ahlrichs, *Chem. Phys. Lett.* **1998**, *294*, 143.

[364] S. Grimme, J. Antony, S. Ehrlich, H. Krieg, *J. Chem. Phys.* **2010**, *132*, 154104.

[365] E. van Lenthe, A. van der Avoird, P. E. S. Wormer, *J. Chem. Phys.* **1997**, *107*, 2488.

[366] E. van Lenthe, A. van der Avoird, P. E. S. Wormer, *J. Chem. Phys.* **1998**, *108*, 4783.

[367] E. J. Baerends, D. E. Ellis, P. Ros, *Chem. Phys.* **1973**, *2*, 41.

[368] L. Versluis, T. Ziegler, *J. Chem. Phys.* **1988**, *88*, 322.

[369] G. te Velde, E. J. Baerends, *J. Comput. Phys.* **1992**, *99*, 84.

[370] C. Fonseca Guerra, J. G. Smijders, G. te Velde, E. J. Baerends, *Theor. Chim. Acta* **1998**, *99*, 391.

[371] A. L. Spek, *Acta Crystallogr.* **2015**, *C7-1*, 9.